

Helically Twisted Graphene Nanoribbons: Bottom-up Stereospecific Synthesis and Characterization



Dissertation zur Erlangung
des naturwissenschaftlichen Doktorgrades der
Julius-Maximilians-Universität Würzburg

vorgelegt von

Asim Swain
aus Bhubaneswar /
Indien

Würzburg 2024

Eingereicht bei der Fakultät für Chemie und Pharmazie am

19.03.2024

Gutachter der schriftlichen Arbeit

1. Gutachter: PD Dr. Prince Ravat

2. Gutachter: Prof. Dr. Dr. h.c. Todd B. Marder

Prüfer des öffentlichen Promotionskolloquiums

1. Prüfer: PD Dr. Prince Ravat

2. Prüfer: Prof. Dr. Dr. h.c. Todd B. Marder

3. Prüfer: Prof. Dr. Joanna Wencel-Delord

Datum des öffentlichen Promotionskolloquiums

14.05.2024

Doktorurkunde ausgehändigt am

Die vorliegende Arbeit wurde in der Zeit von
Dezember 2019 bis Dezember 2023
am Institut für Organische Chemie der
Julius-Maximilians-Universität Würzburg angefertigt

Mein besonderer Dank gilt

Herrn PD Dr. Prince Ravat

für die Vergabe des vielseitigen und interessanten Themas, den damit
verbundenen Diskussionen die mehr als hilf- und lehrreich für mich waren,
dem Vertrauen und den Freiheiten bei der Bearbeitung

Herrn Prof. Dr. Christoph Lambert

für die Bereitstellung von Spektrometern sowie für die nützlichen Tipps
während der Gruppenseminare

Table of Contents

1. Summary	1
1. Zusammenfassung	2
2. Introduction	4
3. Motivation and Objective	21
4. Summary of Research Projects	23
4.1. Pyrene Fused [5]- and [7]Helicenes Connected via Hexagonal and Heptagonal Rings.....	24
4.2. Pyrene Bridged Double [7]Helicenes Embedded with a Heptagonal Ring	27
4.3. Helically Twisted Nanoribbons Using [7]Helicenes as Molecular Wrench	29
5. Publications List	31
6. References	32
7. Compiled Publications	41
7.1. C_2 - and C_1 -Symmetric Configurationally Stable Pyrene-Fused [5]Helicenes Connected via Hexagonal and Heptagonal Rings	42
7.2. Pyrene-Fused [7]Helicenes Connected via Hexagonal and Heptagonal Rings: Stereospecific Synthesis and Chiroptical Properties	47
7.3. Pyrene Bridged Double[7]helicene Embedded with a Heptagonal ring	55
7.4. Helically Twisted Nanoribbons via Stereospecific Annulative π -Extension Reaction Employing [7]Helicene as a Molecular Wrench	68
8. Compiled Supporting Information	79
9. Individual Contributions	219
10. Acknowledgement	221

1. Summary

The electronic properties of graphene nanoribbons (GNRs) are intricately linked to their shape, width, and most importantly, their edge structures. Cove-edged GNRs are of special interest, due to the potential chirality arising from the non-planarity induced by steric repulsion in the cove regions. However, their low configurational and conformational stability hinders their practical applications. Additionally, the synthesis of GNRs via bottom-up synthesis is often considered an insurmountable challenge. Addressing these obstacles, this thesis is focused on developing atomically precise, bottom-up stereospecific synthesis of GNRs, where [*n*]helicenes are employed as a strain inducing moiety to ensure the configurational and conformational stability of a cove-edged pyrene NR.

In the first two projects, the influence of molecular symmetry and ring fusion on the chiroptical response of pyrene fused [5]- and [7]helicenes was highlighted. The molecules with C_1 symmetry containing a central heptagonal ring in the helicenes exhibited higher configurational stability, along with enhanced chiroptical properties relative to the C_2 symmetric pyrene K-region fused helicene with a central hexagonal ring. The molecules with the [7]helicene moieties exhibited superior (chir)optical responses compared to their corresponding [5]helicene congeners.

Driven by the intriguing chiroptical responses of the C_1 symmetric molecules from the first two projects, in the third project the goal was to synthesize a monkey saddle-shaped pyrene-bridged double[7]helicene compound incorporating two heptagonal rings. Unfortunately, all the efforts lead to over-oxidized products due to uncontrollable Scholl cyclodehydrogenation. Despite the setback, a C_1 symmetric pyrene bridged double[7]helicene compound comprising one hexagonal and one heptagonal rings was synthesized, merging the C_1 and C_2 symmetric molecules from the second project. Notably, this molecule exhibited higher configurational stability along with improved chiroptical responses compared to the monomeric congeners discussed in the second project.

While the first three projects emphasize the influence of molecular symmetry on the (chir)optical properties and configurational stability of π -extended helicenes, the fourth project emphasized on the bottom-up synthesis of a helically twisted NRs, where [7]helicenes were stitched to the terminal K-regions of the conjugated pyrene NR through a stereospecific annulative π -extension (APEX) reaction. The cove-edged NRs exhibited exceptional configurational stability along with precise control over conformational

stability with a relative Boltzmann population of the helical NR amounting to 99.9% at room temperature. Notably, the structurally robust helical NR with 171° end-to-end twist, ranked as the second most twisted acene core.

This thesis highlights the potential of employing helicenes as a molecular wrench to produce atomically precise helically twisted nanoribbons. The efficient bottom-up synthetic methods introduced in the thesis facilitate rapid access to π -extended helicenes in abundant enantiopure quantities, and with distinct functionalities.

1. Zusammenfassung

Die elektronischen Eigenschaften von Graphen-Nanobändern (GNRs) sind eng mit ihrer Form, Breite und vor allem ihren Kantenstrukturen verbunden. Besonders interessant sind Strukturen mit einer *Cove*-Kante aufgrund der potenziellen Chiralität, die durch sterische Abstoßung und damit Nicht-Planarität in den *Cove*-Regionen entsteht. Ihre geringe Konfigurations- und Konformationsstabilität behindert jedoch ihre praktische Anwendbarkeit. Darüber hinaus wird die *Bottom-Up*-Synthese von GNRs oft als unüberwindbare Aufgabe angesehen. Um diese Herausforderungen anzugehen, beschäftigt sich diese Arbeit mit der Entwicklung einer atomar präzisen und von Grund auf stereospezifischen Synthese von GNRs, bei der [*n*]Helicene als spannungs-induzierende Gruppe verwendet werden, um die Konfigurations- und Konformationsstabilität eines Pyren-NR mit *Cove*-Kanten zu gewährleisten.

In den ersten beiden Projekten wurde der Einfluss der Molekülsymmetrie und der Ringfusion auf die chiralen Eigenschaften von Pyren-verknüpften [5]- und [7]Helicenen hervorgehoben. Die Moleküle mit C_1 -Symmetrie, die einen zentralen heptagonalen Ring in den Helicenen enthalten, zeigten eine höhere Konfigurationsstabilität sowie verbesserte chirale Eigenschaften im Vergleich zu den C_2 -symmetrischen Pyren-K-Region-fusionierten Helicenen mit einem zentralen hexagonalen Ring. Die Moleküle mit [7]Helicenen wiesen bessere (chir)optische Eigenschaften verglichen mit ihren entsprechenden [5]Helicenen-Verwandten auf.

Motiviert durch die faszinierenden chiroptischen Eigenschaften der C_1 -symmetrischen Moleküle aus den ersten beiden Projekten war das Ziel des dritten Projekts, eine Affensattelförmige, Pyren-verbrückte Doppel-[7]Helicenenverbindung zu synthetisieren, die zwei heptagonale Ringe enthält. Leider führten alle Bemühungen zu überoxidierten

Produkten aufgrund unkontrollierbarer Scholl-Cyclodehydrogenierung. Trotz des Rückschlags wurde eine C_1 -symmetrische, Pyren-verbrückte Doppel-[7]Helicenverbindung hergestellt, die einen hexagonalen und einen heptagonalen Ring enthält, und somit die C_1 - und C_2 -symmetrischen Moleküle aus dem zweiten Projekt vereint. Bemerkenswert ist, dass dieses Molekül im Vergleich zu den monomeren Kongenern aus dem zweiten Projekt eine höhere Konfigurationsstabilität und verbesserte chiroptische Eigenschaften aufwies.

Während die ersten drei Projekte den Einfluss der Molekülsymmetrie auf die (chir)optischen Eigenschaften und die Konfigurationsstabilität von π -erweiterten Helicenen zeigten, konzentrierte sich das vierte Projekt auf die *Bottom-up*-Synthese von helikal verdrehten Nanobändern (NRs), bei der [7]Helicene an die terminalen K-Regionen des konjugierten Pyren-NRs durch eine stereospezifische annulative π -Verlängerungsreaktion (APEX) angehängt wurden. Die NRs mit *Cove*-Kante zeigten eine außergewöhnliche Konfigurationsstabilität sowie eine präzise Kontrolle über die Konformationsstabilität mit einer relativen Boltzmann-Population des helikalen NRs von 99,9% bei Raumtemperatur. Bemerkenswert ist, dass das strukturell robuste helikale NR mit einer End-zu-End-Verdrehung von 171° als der am zweitmeisten verdrehte Acen-Kern eingestuft wurde.

Diese Dissertation zeigt das Potenzial der Verwendung von Helicenen als molekulares Werkzeug zur Herstellung atomar präziser helikal verdrehter Nanobänder. Die effiziente *Bottom-up*-Synthese, die in der Dissertation vorgestellt wird, ermöglichen einen schnellen Zugang zu π -erweiterten enantiomerenreinen Helicenen in üppigen Mengen und mit unterschiedlichen Funktionalitäten.

2. Introduction

Benzene is typically the first molecule that comes to mind when discussing aromatic hydrocarbons. It can combine multi-dimensionally to form a wide range of polycyclic aromatic hydrocarbons (PAHs).¹ PAHs can be categorized based on their fusion type– (i) linearly fused one dimensional (1D) [*n*]acene, and their zig-zag analogue [*n*]phenacene. (ii) two-dimensional (2D) peri fused graphene flakes called nanographene and (iii) orthogonally fused three-dimensional (3D) carbo[*n*]helicene. Additionally, 2D graphene sheets can stack in parallel on top of each other, resulting in graphite, a well-recognized carbon allotrope. *Geim* and *Novoselov* were awarded the 2010 Nobel Prize in physics for isolating graphene sheets from graphite², an accomplishment that sparked considerable interest among material chemists for in-depth research of nanographenes in the last decade, aiming to explore their functional properties and applications.

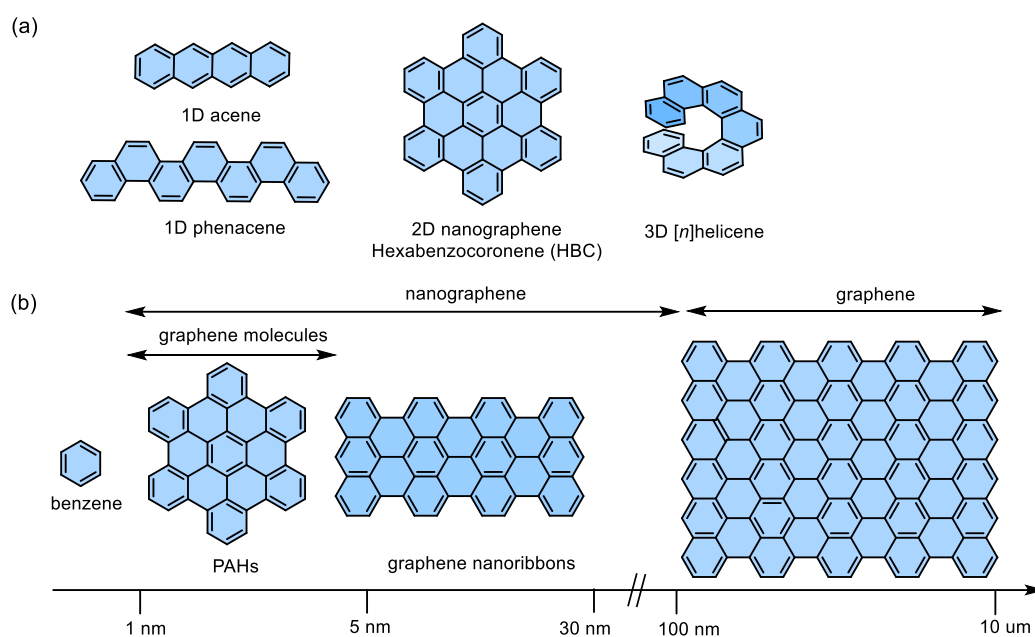


Figure. 2.1. (a) Representative structures of different groups of PAHs (1D – 3D), (b) Schematic representation of graphene terminology based on their sizes.

Nanographenes (NGs) are broadly characterized as finite graphitic units, primarily composed of fused six-membered sp^2 hybridized carbons, with sizes between 1–100 nm (Figure 2.1b). The excitonic properties of these small segments of NGs can be more easily tuned by modifying the aromaticity, molecular symmetry, hetero atom doping and ring defects, thereby making them well-suited for optoelectronic devices. The electronic properties of NG are exquisitely sensitive to their size, shape, and edge structures. NGs

bearing armchair or cove edges usually manifest semi-conducting properties, while the zigzag-edged NGs are associated with remarkable spin-polarization due to the multi-electron correlation of unpaired electrons present on the zigzag edges.

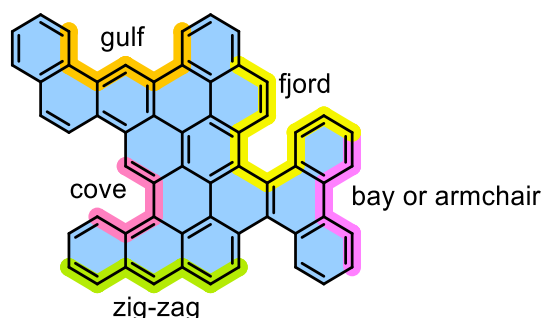


Figure. 2.2. Representative edge structures of nanographene.

GNRs, usually 3 – 30 nm in size, have attracted significant interest in recent years owing to their potential applications in transistors, photovoltaics and quantum electronic devices. In response to the escalating demands for GNRs, material scientists commonly employ top-down methodologies such as – (i) lithographic cutting of graphene³, (ii) sonochemical extraction from expanded graphite⁴ and (iii) unzipping of carbon nanotubes.⁵⁻⁷ The synthesis of GNRs through bottom-up processes, involving the fusion of smaller PAHs, has conventionally been deemed unrealistic. However, recent advancements in Scholl cyclodehydrogenation have played a pivotal role in the success of the bottom-up approach.⁸⁻⁹ External mechanical deformation or distortions can affect GNRs, leading to the adoption of twisted geometries and resulting in different electronic properties.¹⁰ The GNRs with zig-zag and arm-chair edges can undergo twisting via bulky substitution or periodic benzyl annulation along the edges.¹¹ Whereas, GNRs with cove and fjord edges can adopt a twisted conformation, either helical or wagging, due to steric congestion in the cove/fjord regions or when subjected to external strain. Their potential for chirality arises from the non-planarity caused by steric hindrance in the cove or fjord regions. Prior to the establishment of graphene chemistry, the twisting of planar structures was well established through phenyl substitution of acene.

Acenes are the linearly fused benzene rings with a general formula of $C_{4n+2}H_{2n+2}$, known for its small optical gap, energetically low triplet states, low ionization potentials and high electron affinities.¹²⁻¹³ These properties make acenes of high importance for application in semiconductors, organic field-effect transistors (OFETs) and in singlet fission research. While acenes are flat, they can be manipulated into helical or wagging conformations

through the strategic application of crowded substitutions. Pascal Jr. *et al.* pioneered the act of twisting acenes in the late 1990s.¹⁴⁻¹⁹ The current record for highest end-to-end twist in a solid state acene is 184° by Kilway *et al.*²⁰ To propagate a twist from one end to other, all the zig-zag positions in the acene need to be substituted, which is synthetically cumbersome and challenging, explaining the 15 years gap between synthesis of pentacene analogue (I) to hexacene analogue.¹⁹⁻²⁰

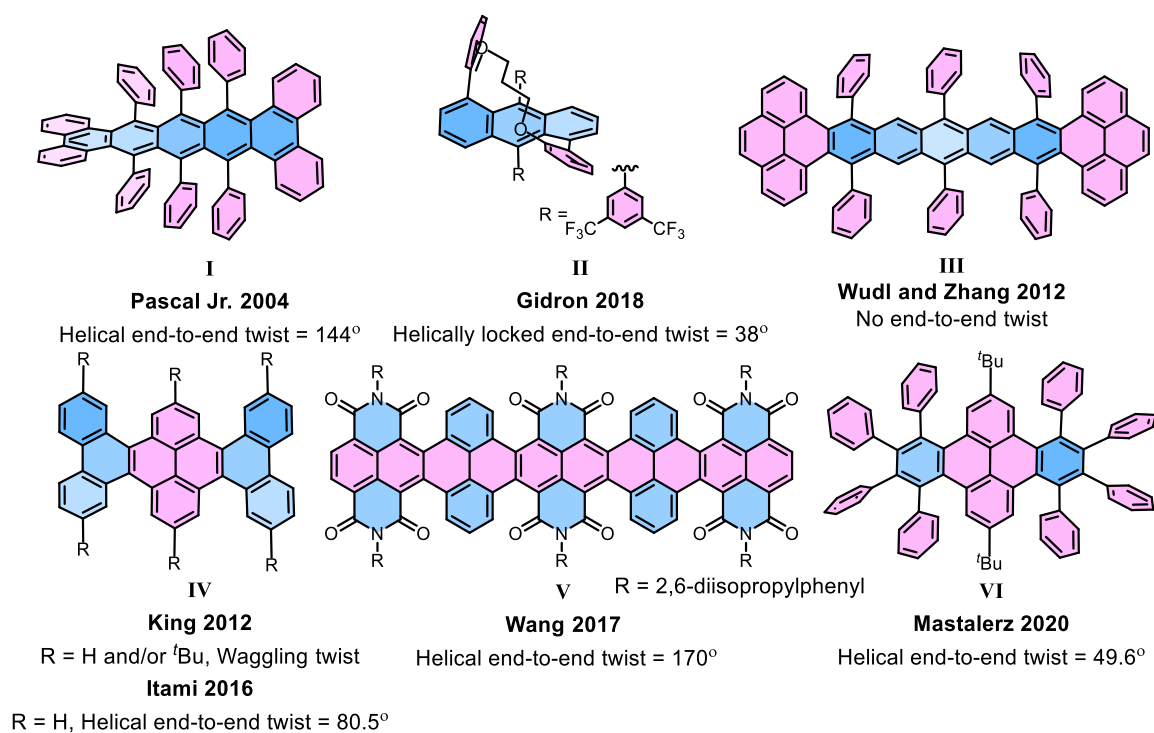


Figure 2.3. Strain induced twistacenes (I, II and III) and twisted pyrene cored molecules (IV, V and VI).

Twistacenes usually possess a low enantiomerization barrier. The twisted pentacene (I) with 144° twist racemizes within 9.5 hours at 25°C , while twistacenes with a twist lower than 100° racemize within minutes. The enantiomerization barrier can be increased by incorporating bulky substituents on the outer edges, thereby enhancing the twist, and creating a crowded transition state.²¹ More recently, Gidron *et al.* engineered helically locked tethered anthracenes (II), which can be isolated in an enantiopure form, achieving an end-to-end twist of up to 38° .²²⁻²⁴ Several attempts were made to incorporate promising π -electron-rich cores, such as pyrenes, into twisted acenes, aiming to produce longer acene-cored molecules with a high enantiomerization barrier and better functional properties.²⁵ Wudl and Zhang developed a molecule with a pentacene core terminally locked by two

pyrenes (**III**).²⁶ However, it failed to propagate a uniform twist from one end to the other as the twist reverses at the central benzene ring due to the absence of steric groups at crucial positions in the central acene core. King *et al.* prepared a K-region phenanthrene annulated pyrene exhibiting waggling conformation (**IV**).²⁷ In contrast, later Itami *et al.* achieved the helical conformation of **IV** with an unsubstituted core.²⁸ Wang *et al.* in 2017 developed helically twisted decatwistacene (**V**) with a remarkable end-to-end torsion twist of 170° arising from the steric hindrance between imide groups and benzene rings in the cove region.²⁹ Recently, eight phenyl substituted dibenzo[e, l]pyrene (**VI**) by Mastalerz *et al.* showed the helical structure with an end-to-end twist of 49.6°.³⁰

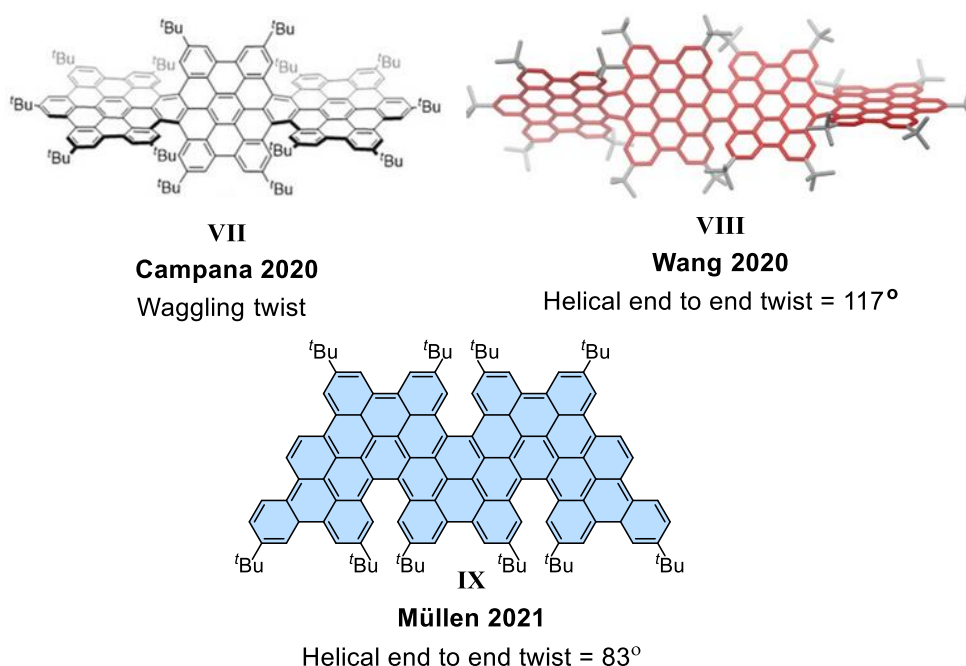


Figure 2.4. Strain induced twisted nanographenes with fjord region. The molecular structures (**VII** and **VIII**) are adapted with permission from ref. [33] and [32]. © 2020, American Chemical Society and Wiley-VCH Verlag GmbH & Co. KGaA, Weinheim.

The nanographenes with fjord region³¹, such as supertwistacene (**VIII**) by Wang *et al.*³² and triply conjugated HBC (hexa-peri-hexabenzocoronene) (**VII**) by Campana *et al.*³³—display a significantly higher barrier, allowing their chiral resolution at room temperature. The end-to-end twist (117° in supertwistacene) is significantly enhanced compared to the twistacenes, attributed to their ability to adopt the helical or single handed conformation because of the steric repulsion from the neighboring bulky *tert*-butyl group and the peripheral hydrogens in the [5]helicene sub-units in the fjord region. The increase in twist ultimately results in increasing the enantiomerization barrier to 44.7 kcal mol⁻¹. Müllen *et*

al. developed a fully fjord edged nanographene (**IX**) with an end-to-end twist of 83° by employing Suzuki coupling and Scholl cyclodehydrogenation reactions.³¹

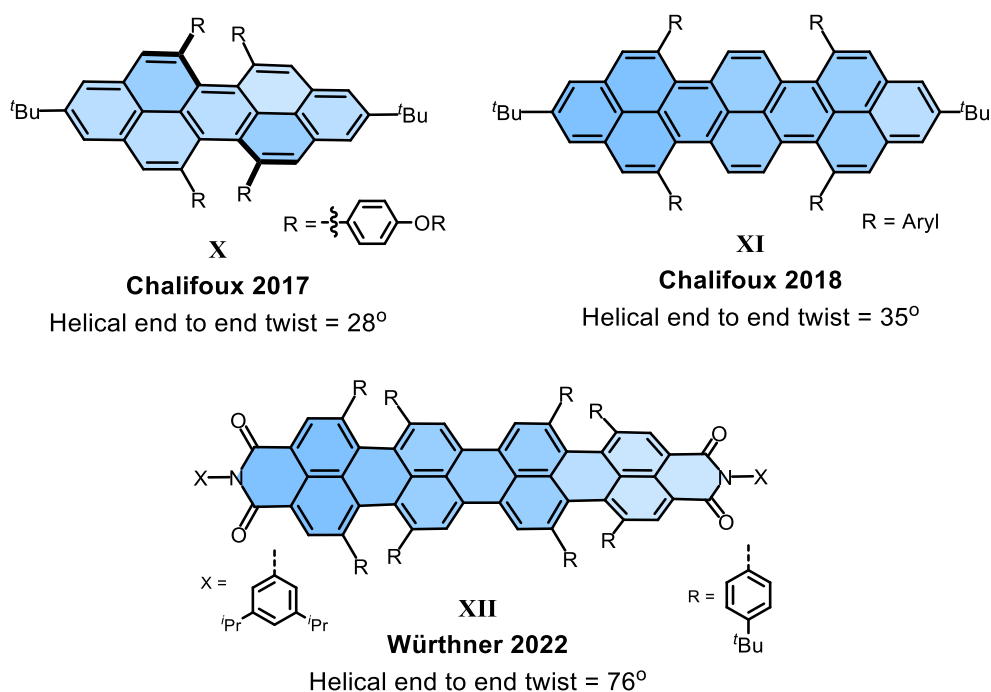


Figure 2.5. Strain induced twisted nanographenes with bay region.

The nanographenes with the bay region are relatively difficult to twist, as the majority of the rings lie flat in the orthogonal plane with limited options for substitution. Chalifoux *et al.* achieved a 28° end-to-end twist by substituting all four sites in the bay region of peropyrene(**X**).³⁴ Later they achieved 35° end-to-end twist in teropyrene by substituting only one side of the bay region (**XI**)³⁵, while Würthner *et al.* substituted all positions in the bay region, resulting in an enhanced twist of 76° in quaterrylene bisimide (**XII**) with a enantiomerization barrier of 30 kcal mol^{-1} .³⁶ From the discussed molecules, it is evident that both the size of nanographene and appropriate substitution play a crucial role in achieving a higher end-to-end twist. Müllen *et al.* synthesized a gulf-edged NR exceeding 200 nm in length by employing Diels-Alder polymerization, followed by Scholl cyclodehydrogenation.³⁷

While the previously mentioned examples of strain induced twisted nanographenes are impressive in terms of structural beauty, they lack the ability to regulate the conformation of the molecule. The solid-state structure can adopt either a helical or wagging form based on the steric congestion and cannot be effectively regulated. Moreover, the conformational population attained by the helical or wagging conformation is quite moderate at room

temperature, raising questions about their suitability for chiroptical applications. To achieve precise conformational and configurational control over the NR, the first step is to increase the twist angle, which is easier to attain in cove-edged NRs (e.g. pyrene NRs). However, to maintain the twist, annulation with a steric, yet flexible molecules, such as $[n]$ helicenes are necessary. Secondly, the annulation of bulkier groups (e.g. *tert*-butyl groups) is required for additional buttressing effect³⁸ and to make the transition state crowded, elevating the barrier resulting in an increased configurational stability.

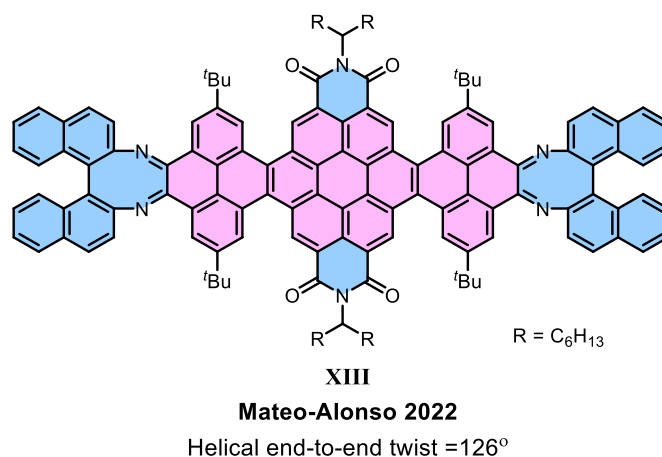


Figure 2.6. Strain induced single handed helical nanoribbon.

Recently, Mateo-Alonso *et al.* synthesized a helical NR (**XIII**), which closely resembles to NR (**V**) with pyrene-coronene core, whereas enantiopure 1,1'-binaphthyl-2,2'-diamine was fused at both terminal ends to form a [5]helicenoid with four cove region [4]helicene subunits.³⁹ The molecule exhibits an overall end-to-end twist of 281° due to the strained octagonal ring at the terminal K-region of pyrene, while the inner core has a twist of only 126°. While there is no mention of configurational stability, the helical conformer of the NR showed a 94 % relative conformational population at room temperature. The VT-CD (variable temperature circular dichroism) measurements challenges the robust chirality of the NR, as the CD signals vary significantly with respect to the temperature. The presence of nitrogen atoms in the non-aromatic octagonal ring of [5]helicinoids along with the two imide groups exclude it from being classified as an aromatic NRs.

Brief history of $[n]$ helicenes

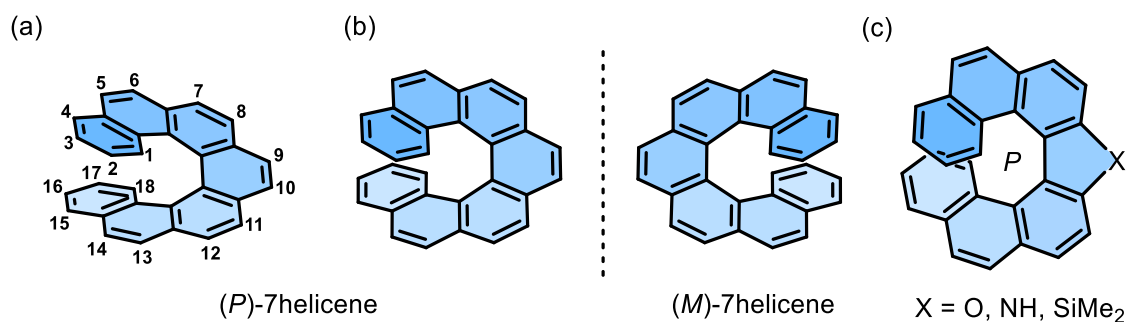


Figure. 2.7. (a) IUPAC numbering of [7]helicene, (b) enantiomers of carbo[7]helicene, (c) heteroatom doped [7]helicene.

According to IUPAC, helicenes are classified as “*ortho*-fused polycyclic aromatic or hetero aromatic compounds in which all rings (minimum five) are angularly arranged so as to give helically shaped molecules, which are thus chiral.”¹ Currently being considered as one of the dynamically evolving field of research interest, the first isolation of a helicene traces back to 1903, with Meisenheimer and Witte isolating 7-aza[5]helicene and 7,8-diaza[5]helicene. Weitzenböck synthesized the first carbo[n]helicenes ($n = 4$ and 5) in the 1910s. Later McIntosh *et al.* confirmed the helical structure of [5]helicene through X-ray crystallography.⁴⁰⁻⁴¹ In 1956, Newman's successful resolution of [6]helicene⁴²⁻⁴³ revolutionized the helicene research which was later led by Mallory⁴⁴⁻⁴⁵, Carruthers⁴⁶, Scholz⁴⁷⁻⁴⁸, and Martin⁴⁹⁻⁵³.

Structural features of $[n]$ helicene

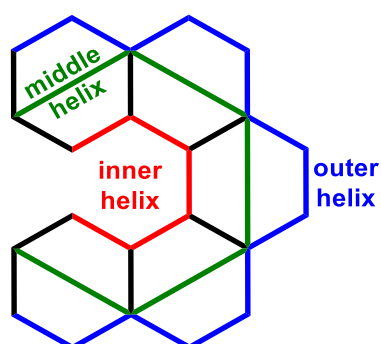


Figure 2.8. Structural characteristics of [5]helicene.

The intriguing structural arrangement of $[n]$ helicenes highlights several notable geometrical features.⁵⁴ All the carbon atoms present in a $[n]$ helicene can be categorized into

three helices according to their position (Figure 2.8). (i) inner helix and (ii) middle helix, each containing $n+1$ carbons, and (iii) outer helix with $2n$ carbons. In comparison to benzene (mean: 1.39 Å), the C–C bond length is larger in the inner helix (mean: 1.41 Å), but smaller in the outer helix (mean: 1.36 Å). Although there is no direct correlation between the dihedral angle of the inner helix with the angularly fused benzene units (n), a typical dihedral angle exists around $23^\circ \pm 0.5^\circ$ (Figure 2.9a). The pitch length increases gradually from inner to outer helix. The helical pitch calculated from the centroid of the rings increases from $n = 4 - 6$ (the distance between terminal rings is considered here), while for higher helicenes [$n \geq 7$], the pitch length decreases (Figure 2.9b).

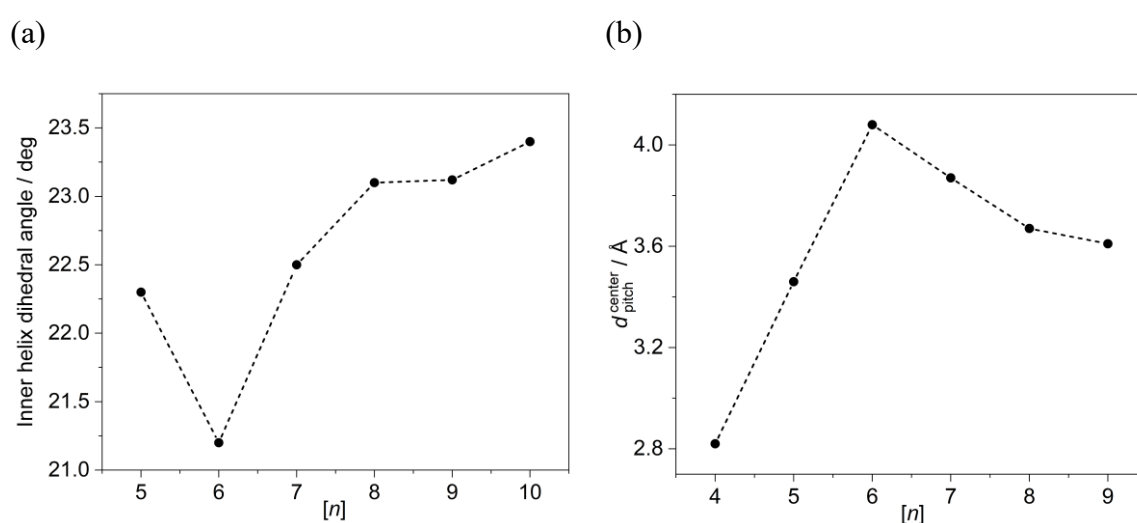


Figure 2.9. (a) inner helix dihedral angle and (b) Helical pitch calculated from DFT optimized (DFT-D2-B97-D/TZVP Level) structures of $[n]$ helicenes ($n = 4-10$).⁵⁵

Configurational stability of $[n]$ helicene

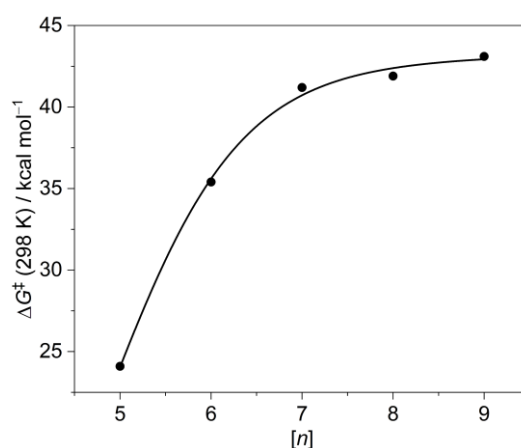


Figure 2.10. Exponential increase of ΔG^\ddagger (298 K) values for $[n]$ helicenes ($n = 5-9$).

Majority of twistacenes undergo rapid racemization under ambient conditions, with a half-life of few minutes. Conversely, $[n]$ helicenes demonstrate increased barriers to racemization (Figure 2.10). While [5]helicene racemizes within few days at room temperature, $[n]$ helicenes ($n \geq 6$) demand notably higher energy for inversion. The alternation of handedness in helicenes involves an achiral conformation at the transition state, as suggested by Martin *et al.*⁵⁶ and later supported by subsequent theoretical calculations. The racemization of $[n]$ helicene is a concerted process for $n = 4-7$, whereas higher helicenes utilize a multi-step mechanism involving $2n-14$ intermediates.⁵⁷ The configuration stability (ΔG^\ddagger) tends to be significantly influenced by factors such as – (i) substitution at the inner and/or middle helix, (ii) ring defects (iii) the helical diameter and pitch, and (iv) hetero atom doping.⁵⁸⁻⁶¹

Commonly in hetero $[n]$ helicenes, heteroatoms are doped in the outer helix and linked to ring defects.⁶² For instance, oxa-, sila- and aza $[n]$ helicene are commonly depicted with a pentagonal ring (Figure 2.7c). However, using the same nomenclature when heteroatoms are in the middle helix or in absence of any ring defects, can lead to confusion.⁶³ Alternatively, it is prudent to specify the position of the heteroatoms in the helicene as per IUPAC convention. Unsubstituted hetero $[n]$ helicenes generally exhibit a relatively low barrier for enantiomerization when compared to their carbo $[n]$ helicene congeners, i.e., aza[7]helicene⁶⁴, sila[7]helicene⁶⁵, oxa[9]helicene⁶⁶ show enantiomerization barriers of 29.5, 37.4, 39.6 kcal mol⁻¹ respectively, compared to the 41.2 kcal mol⁻¹ barrier observed for carbo[7]helicene.⁵⁸ Direct comparison of configurational stability between heteroatom doped- and carbo $[n]$ helicene is challenging, as the enantiomerization barrier depends on the presence of ring defects and position of the heteroatoms. For instance, when one carbon atom in the outer helix of [5]helicene is replaced with nitrogen, the helicene with nitrogen at the 4-position of the [5]helicene showed a slightly higher barrier of enantiomerization compared to substitutions at any of the 7 available sites.⁶³ In cases where multiple heteroatoms are present in the outer helix of helicene, the configurational barrier usually remains lower than the corresponding carbo $[n]$ helicene congener.⁶⁷⁻⁶⁸ However, this can be improved through suitable lateral π -extensions.⁶⁹ It is advisable to use a chiral π -extender over the planar molecules, for achieving better configurational stability due to presence of multiple chiral sub-units.

Photophysical properties of $[n]$ helicene

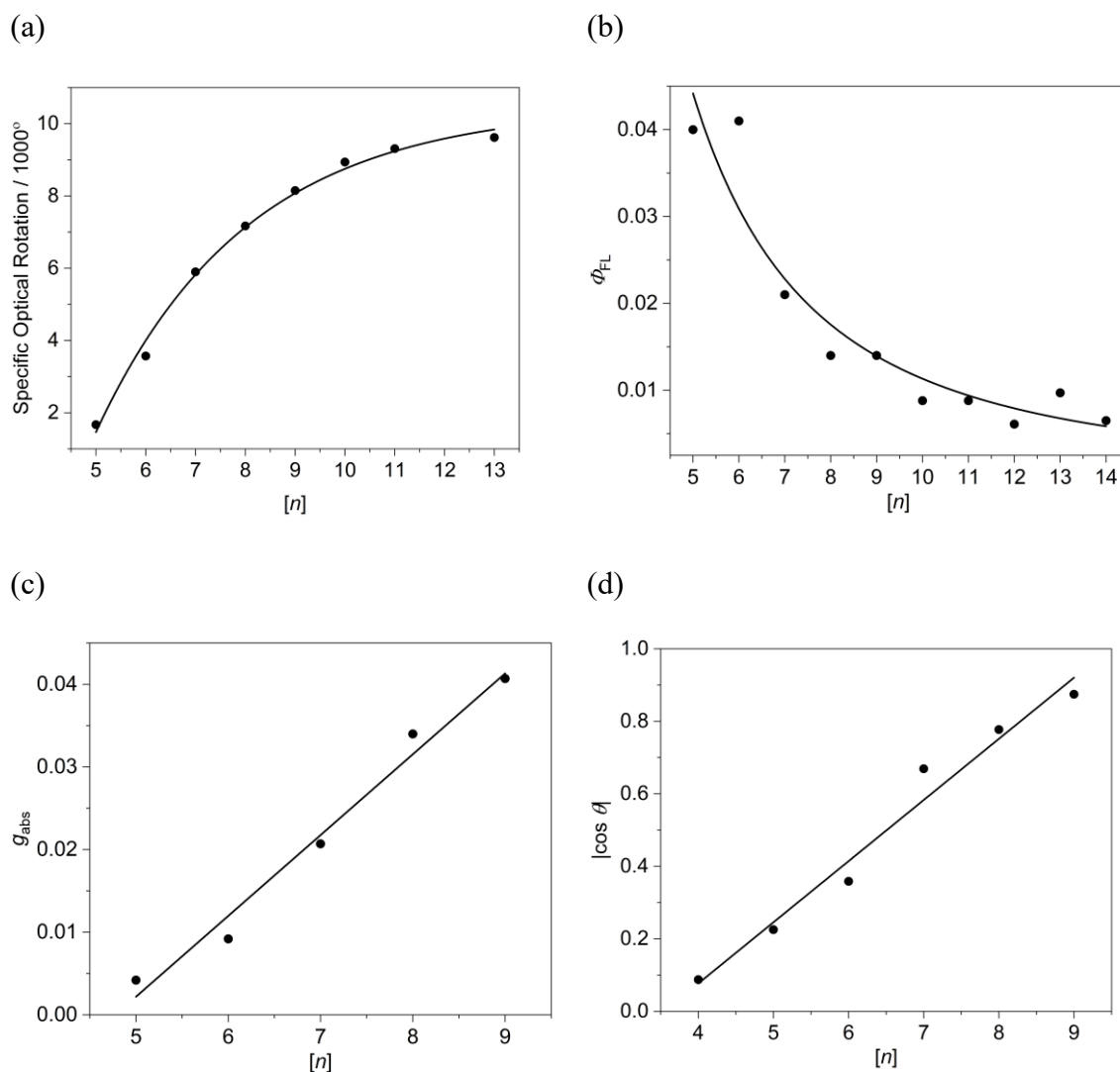


Figure 2.11. (Chir)optical properties of $[n]$ helicenes. (a) Specific optical rotation (experimental), (b) fluorescence quantum yields (experimental), (c) absorptive dissymmetry factor and (d) $\cos \theta$ values, θ is the angle between transition electric and magnetic dipole moments (calculated at RICC2/TZVPP level).⁵⁵

Helicenes are recognized for their exceptionally large specific optical rotation (OR) compared to point or axially chiral molecules. The OR value increases exponentially with the helicity, with $[13]$ helicene reaching an experimental value of 10,000° (Figure 2.11a). The P and M helicenes display clockwise or counterclockwise rotations of plane polarized light, respectively.⁷⁰ The molar extinction coefficient (ϵ) for the lowest energy transition in $[n]$ helicene decreases as the helicity increases, possibly due to a decrease in effective π -conjugation on increasing helicity. Helicenes demonstrate low fluorescence quantum yields

(FQYs), which diminish from 4% for [5]helicenes to <1% for [14]helicene (Figure 2.11b).⁷¹⁻⁷² The low FQYs can be attributed to the competitive intersystem crossing and an enhanced rate constant for $S_1 \rightarrow T_1$ transition with increased helicity.⁷³

Helicenes exhibit circular dichroism (CD) and circular polarized luminescence (CPL) due to their inherent chirality arising from their helical shape.⁷⁴⁻⁷⁶ The magnitude of CD is quantified by the absorption dissymmetry factor (g_{abs}), defined as the ratio of difference in molar extinction coefficients of left and right-handed circularly polarized light ($\Delta\varepsilon = \varepsilon_L - \varepsilon_R$) to net molar extinction coefficients ($\varepsilon = 0.5 * (\varepsilon_L + \varepsilon_R)$).⁷⁷ In quantum chemical calculations, g_{abs} is expressed as $g_{\text{abs}} = 4R/D$, where R (rotational strength) = $|\mu_e||\mu_m| \cos \theta$ and D (dipole strength) = $|\mu_e|^2 + |\mu_m|^2$, μ_e and μ_m represent the transition electric and magnetic dipole moments (TEDM and TMDM, respectively), and θ is the angle between them.⁵⁵ While there is no direct correlation between μ_e and μ_m , the $|\cos \theta|$ value increases linearly with helicity (Figure 2.11d). In general, μ_m is significantly smaller than μ_e , but the mutual compensation between μ_e and μ_m , and $\cos \theta$ results in an enhanced g_{abs} with an increase in helicity (Figure 2.11c). However, the g_{abs} value remains much smaller than the maximum theoretical value of ± 2 . Similar to CD, CPL can be quantified in terms of luminescence dissymmetry factor (g_{lum}). Although no systematic study has been reported in literature for pristine $[n]$ helicenes, it is reasonable to assume that the g_{lum} value increases with helicity, following the global regression expression of $g_{\text{lum}} = 0.6 * g_{\text{abs}}$ for $[n]$ helicene and helicinoids.⁷⁸⁻⁷⁹ To quantify the brightness of CPL, Bari *et al.* defined the term B_{CPL} as the product of molar extinction coefficient, FQY and emission dissymmetry factor (g_{lum}).⁸⁰ Through appropriate structural modification or hetero atom doping, it is possible to increase the FQY to unity, along with higher molar extinction coefficient. Therefore, the overall CPL brightness can be tuned regardless of lower g_{lum} .⁸¹⁻⁸⁶

Practical applications of any CPL-active materials require a high CPL brightness value,⁸⁰ which is not achievable for carbo $[n]$ helicenes as FQY is less than 0.05. The key to increase the CPL brightness in $[n]$ helicene is to enhance the FQY and increase the g_{lum} by bringing the ratio of magnitude of TEDM and TMDM close to unity. It is well established that the FQY and fluorescence lifetime can be regulated by the proper design of the molecular structure. However, there is limited information available in the literature regarding the tuning of TEDM and TMDM, and, until now, it has largely relied on a trial-and-error basis. Isobe *et al.* achieved FQY of 0.8 and a g_{lum} of 0.152 by tuning the TMDM to nearly 28

times that of TEDM in a carbon nanohoop with cylindrical helicity.⁸⁷ The perfect alignment (parallel or anti-parallel) of TEDM and TMDM ($\cos \theta = \pm 1$) increased the rotatory strength, and ultimately the dissymmetry factors. Mori *et. al.* reported that, with proper molecular design in terms of molecular symmetry, the arrangement of TEDM and TMDM can be tuned.⁸⁸ Tanaka *et. al.* achieved g_{lum} of 0.032 by incorporating a central pentagonal ring in a [7]helicene derivative.⁸⁹

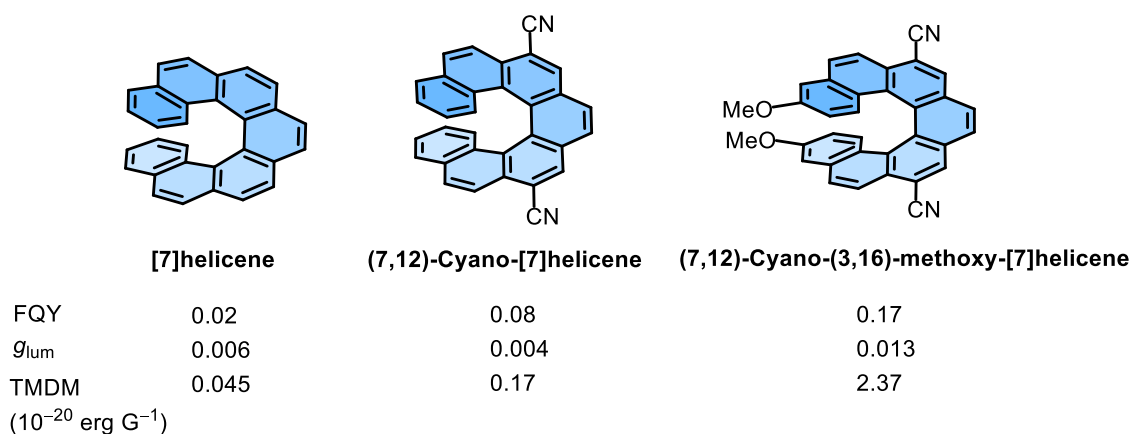


Figure 2.12. Improved chiroptical parameters of [7]helicene upon substitution.⁹⁰

Matsuda *et. al.* tuned the TEDM and TMDM in [7]helicene by substituting electron donating and/or electron withdrawing group at the selective position in outer helix where molecular orbital coefficients are high (Figure 2.12).⁹⁰ The substitution altered the symmetries of FMOs resulting in 100 times higher oscillator strength than that of pristine [7]helicene. The difference in symmetry and shapes of FMOs affect the magnitude of TEDM and TMDM. The TMDM of substituted [7]helicene is 50 times higher than that of pristine [7]helicene (Figure 2.12).

In summary, to enhance the g_{lum} (and ultimately CPL brightness) the following points should be considered. (i) The TMDM and TEDM must be parallel or antiparallel to each other and preferably propagates along the helix of the [n]helicene.⁸⁷ (ii) Achieving different symmetries of frontier orbitals involved in S_0 and S_1 state through proper functional group substitutions.⁹⁰ (iii) Lowering the ratio of TEDM and TMDM (usually $TEDM \gg TMDM$) by H-type aggregation⁹¹⁻⁹³ or by designing charge transfer type electronic state with lower orbital overlap between HOMO and LUMO⁹⁴.

Effect of twist on aromaticity of $[n]$ helicene

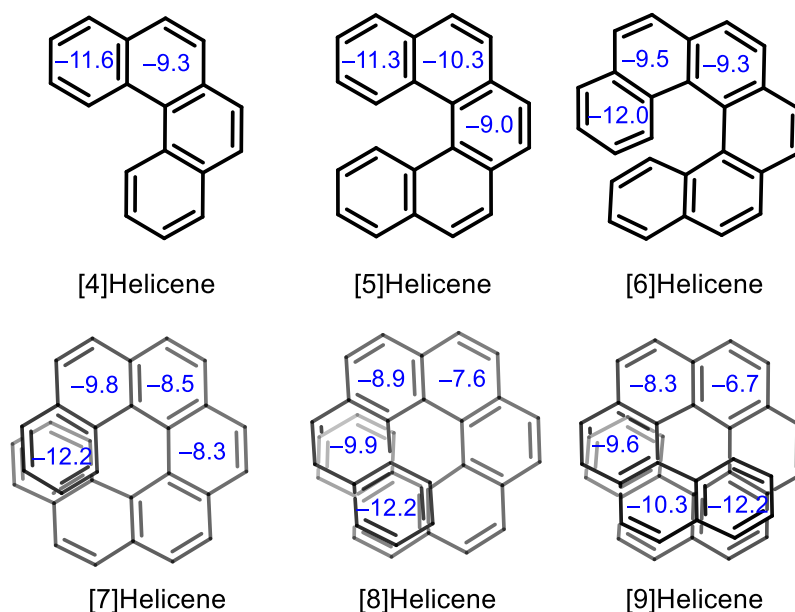


Figure 2.13. Calculated NICS(1)_{zz} values for $[n]$ helicenes ($n = 4-9$) at the B3LYP/6-311+G* level.⁹⁶

To evaluate the effect of twisting on aromaticity of $[n]$ helicenes ($n = 4-9$), the nucleus-independent chemical shift (NICS)⁹⁵ values were computed by Poater and Solà *et. al.*⁹⁶ Given the twisted structure of $[n]$ helicenes, the NICS(1)_{zz} values are considered for precise comparison. All the benzene rings within the $[n]$ helicenes exhibited negative NICS(1)_{zz} values, signifying their aromatic nature (Figure 2.13). The terminal rings exhibited relatively higher NICS values compared to benzene (-9.7 ppm), showing a gradual decrease on moving towards the central ring of $[n]$ helicene.⁹⁶⁻⁹⁷

Applications of $[n]$ helicene

Due to their elevated thermodynamic stability and distinct chiroptical characteristics compared to acenes, $[n]$ helicenes have been applied in wide range of applications. They serve as chiral auxiliaries in asymmetric synthesis⁹⁸, used as semiconductors and constitute attractive optoelectronic devices such as CPL-OFETs⁹⁹⁻¹⁰⁰, CPL-OLEDs (organic light emitting diodes)¹⁰¹⁻¹⁰³, perovskite solar cell¹⁰⁴⁻¹⁰⁸, transistors¹⁰⁹⁻¹¹¹, non-linear optics¹¹² and function as enantioselective fluorescent sensors¹¹³⁻¹¹⁵. Additionally, their flexible and compressible structures make them versatile materials for molecular springs and inductors.¹¹⁶⁻¹¹⁸

Brief history of Pyrene

Pyrene, an *ortho*- and *peri*-fused polycyclic aromatic hydrocarbon (PAH) composed of four benzene rings, forms a planar aromatic system. Gräbe proposed the correct chemical formula of pyrene in 1871, while the chemical structure was elucidated by Bamberger and Philip in 1887.¹¹⁹⁻¹²⁰ Applying Clar's sextet rule, pyrene can be represented with two sextets and two double bonds (Figure 2.14). The two double bond regions, termed as the K-region, display more double bond character rather than solely aromatic bond characteristics.

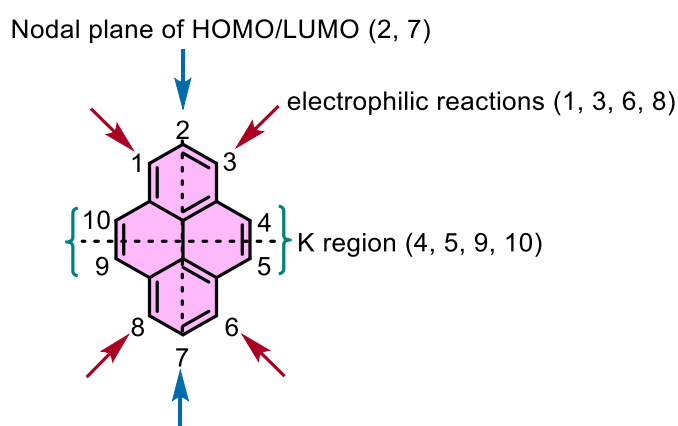


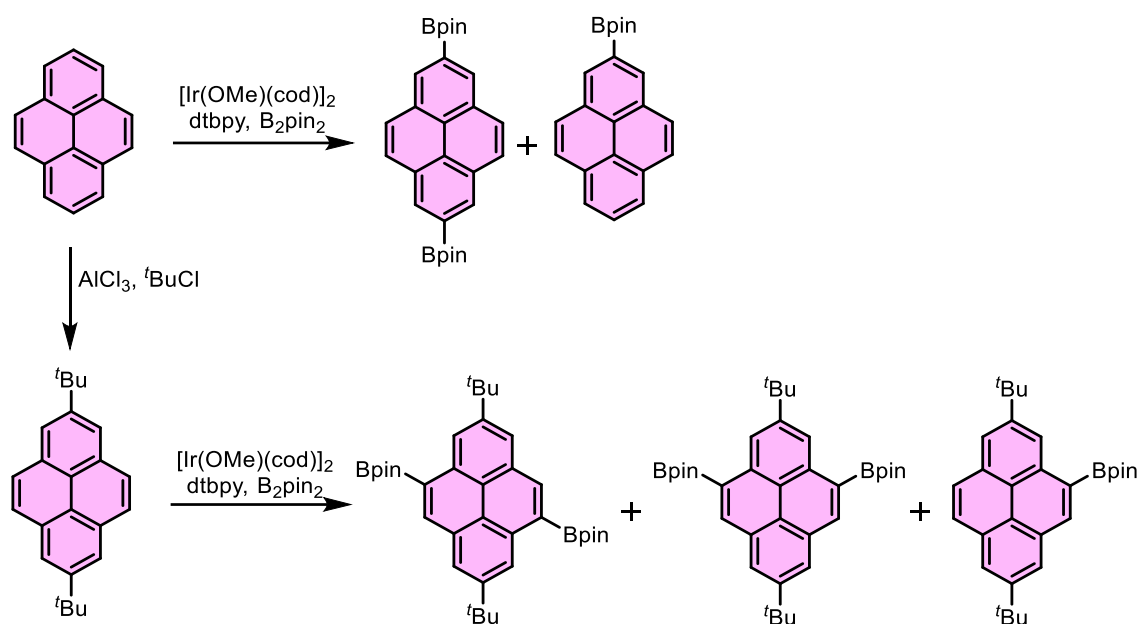
Figure 2.14. Different reaction sites of pyrene.

The positions 1, 3, 6, and 8 in pyrene are electron-rich, making them particularly susceptible to electrophilic substitutions. In contrast, the 2 and 7 positions, situated on the nodal plane of HOMO-LUMO orbitals of the pyrene, are the least reactive among all the sites. The presence of bulky groups at 2, 7 hinders the electrophilic substitution at 1, 3, 6 and 8 positions, thereby directing the substitution towards the K-regions (Scheme 2.1).

Pyrene demonstrates remarkable photophysical attributes, with emission between 370 – 400 nm, a long fluorescence lifetime, and high fluorescence quantum yield. It can form excimer which emits around 460 nm, displaying a red-shifted emission compared to its monomer. These remarkable characteristics have led numerous attempts towards integration of pyrene with larger PAHs to enhance the overall photophysical properties of the resultant hybrid molecule. The binding capabilities of pyrene, involving π -stacking and C–H– π interactions, are highly regarded. These distinctive features have found widespread applications in the non-covalent modification of various extended planar π -systems, such as carbon nanotubes and graphene sheets.¹²¹⁻¹²³

Pyrene embedded cove-edged NR

The selective functionalization of pyrene is challenging due to the presence of multiple reaction sites with similar reactivity. The use of aluminum chloride as a Lewis acid in conjunction with *tert*-butyl chloride, enables effective alkylation at 2 and 7 positions, which then acts a directing agent, facilitating access to the K-region of pyrene.¹²⁴



Scheme 2.1. One-pot iridium catalyzed borylation of pyrene using bis(pinacolato)di-boron by Marder *et al.*

The direct borylation of pyrene at positions 2 and 7 was achieved by Marder *et al.*,¹²⁵ in the presence of an Iridium catalyst and bipyridyl ligand (Scheme 2.1). Subsequently, in presence of bulky *tert*-butyl group the borylation selectively directs to the K-region (Scheme 2.1).¹²⁶ Alternatively, K-region of 2,7-di-*tert*-butylpyrene can be directly brominated, however purification of brominated pyrene substrates is cumbersome involving multiple repetitive recrystallization.¹²⁷

As previously mentioned, the cove-edged NRs, have drawn considerable attention due to the chirality arising from the cove region, offering the potential to enhance macro chirality in a single-handed helical conformation of NRs. Among the pyrene-incorporated NRs, fully cove-edged hydrocarbon NRs are a rarity. In 2016, Zhao and Ba *et al.* attempted the bottom-up synthesis of ladder-type cove-edged pyrene NRs (**XIV**) by employing successive Suzuki coupling and Scholl cyclohydrogenation reactions using the K-region borylated pyrene developed by Marder *et al.*¹²⁷ Despite the apparent promise of the synthetic route, longer

pyrene NRs could not be synthesized due to incomplete Scholl reactions or chlorination in the terminal K-region.

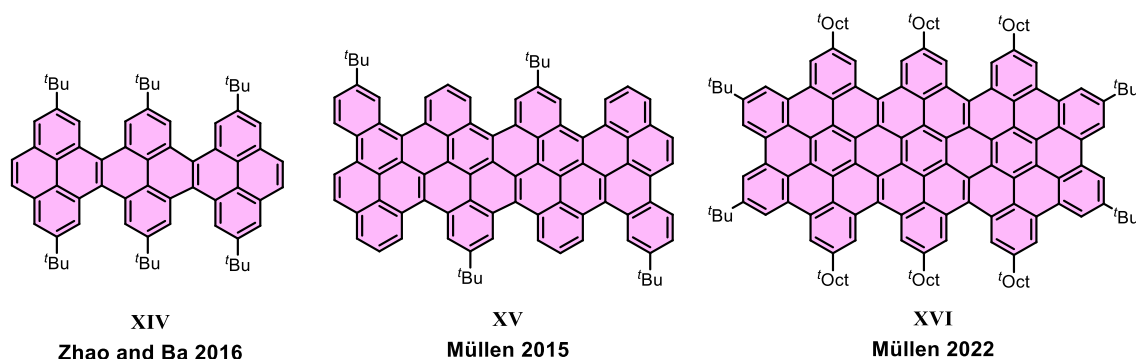


Figure. 2.15. Reported fully cove-edged pyrene nanoribbons.

Significant contributions in the development of fully cove-edged hydrocarbon NR have been made by Müllen *et al.* **XV** was synthesized from 11,11'-dibromo-5,5'-bischrysene by employing Ullmann coupling followed by Scholl cyclodehydrogenation.¹²⁸ However once again, the production of longer NRs was hindered by incomplete Scholl reactions. The bottom-up synthesis of **XVI** was achieved using transition metal-catalyzed alkyne annulation followed by Scholl cyclodehydrogenation under harsh acidic condition.¹²⁹

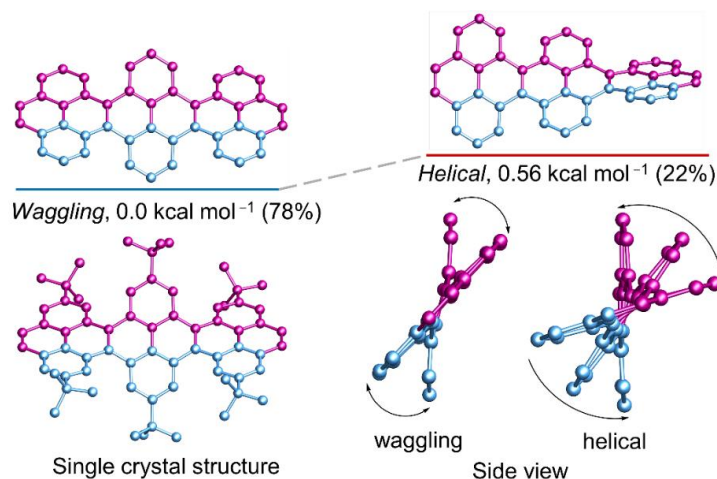


Figure 2.16 DFT (ω B97XD/6-31G(d,p)) calculated conformational isomers and single crystal structure of **XIV** with relative total energy and population at 298 K. Hydrogen atoms in all and *tert*-butyl groups in calculated structures are omitted for clarity.

Directing the cove-edged NRs to achieve a single-handed helicity presents considerable challenges, given their tendency to adopt wagging conformation, resulting in tilted upward and downward topologies. Based on the helicity all cove-edged NRs exhibit broadly three

possible conformations– (a) single handed helicity (*P* or *M*), (b) double handed opposite helicity (resembling like a butterfly structure) with no end-to-end twist (c) wagging conformation. Moreover, the minimal energy difference between conformers makes them prone to racemization in absence of significant external strain (or annulation of bulky groups).

For example, the conformational stability of **XIV** was assessed through DFT calculations (Figure 2.16). At room temperature, the wagging conformer of **XIV** prevails as the most stable, constituting 78% of the population, while the remaining portion corresponds to the helical conformer which is only 0.56 kcal mol⁻¹ higher in energy. These calculations were supported by the obtained single crystal structure of **XIV**, revealing a wagging twist. With no net end-to-end twist, the twist direction reverses in the middle. To control the twist and achieve unidirectionality, opposite strain should be induced on the terminal K-regions of **XIV**, which is the primary objective of this thesis.

3. Motivation and Objective

Among the variety of nanoribbons (NRs), cove-edged NRs stand out as an important class, as their nonplanar structure enhances solubility, offers distinctive solid-state packing, and facilitates easy access for further tuning of electronic properties.¹³⁰ However, the synthesis of fully cove-edged graphene NRs poses significant challenges due to the absence of efficient synthetic strategies and precise precursor designs. The production of longer cove-edged graphene NR has proven to be difficult, often resulting in formation of small oligomers.¹²⁸

Helicenes^{49, 131-132} and twistacenes^{12, 19-20, 133}, being helically twisted π -conjugated PAHs¹³⁴, present unique opportunities to explore various phenomena arising from their inherent axial chirality and distinctive optoelectronic properties. Both classes of molecules have been extensively studied, with various synthetic methods and structural alternations for diverse applications. The concept in this thesis was to incorporate helicene at both ends of cove-edged pyrene NRs to dictate the overall conformation of NR by utilizing the structural and chiral information encoded in the $[n]$ helicenes. Despite recent advancements in π -extended $[n]$ helicene embedded compounds, there are still several challenges yet to be addressed.

- (i) Obtaining sufficient quantity of enantiomerically pure π -extended helicenes.
- (ii) Conducting a systematic study on the effect of molecular symmetry on π -extended helicenes.
- (iii) Ensuring high configurational stability under ambient conditions.
- (iv) Controlling the conformation of helically twisted molecular ribbons.

To tackle the aforementioned challenges, this thesis is centered on bottom-up stereospecific synthesis of nanometer-sized, helically twisted chiral NRs with well-defined structural conformations.

- (i) Obtaining enantiopure $[n]$ helicenes through chiral stationary phase–high performance liquid chromatography is cumbersome and falls short in meeting the requirement of gram quantities. As an alternative, separating enantiomers can be achieved through routine column chromatography in gram quantities, employing a chiral auxiliary to the racemic mixture.¹³⁵
- (ii) Despite recent advancements, a thorough investigation focused on the effect of molecular symmetry on the functionalities of π -extended helicenes has not been adequately addressed in the literature. To conduct a comprehensive study, pyrene is

chosen as the π -extender because of its multiple reaction sites, which could be accessed differently by varying reaction conditions, resulting in pyrene-helicene hybrids with different molecular symmetry.

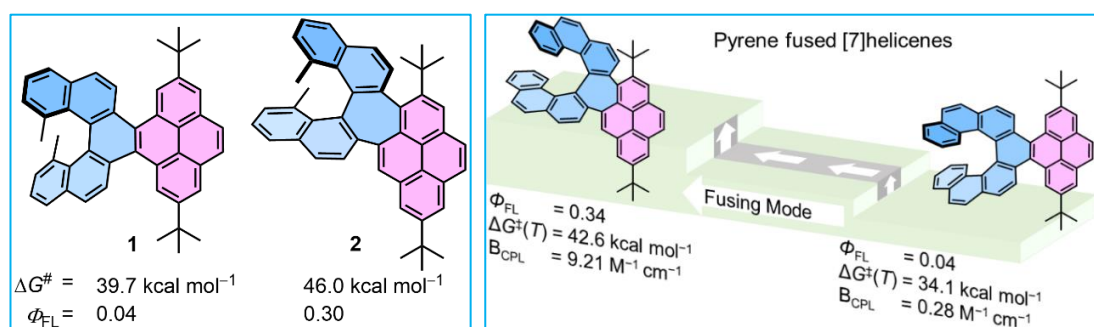
- (iii) The configurational stability of [*n*]helicene embedded PAHs can be enhanced through inner helix substitutions or by buttressing effect from appropriate substitutions.⁵⁸ While the conformational stability relies on locking of a specific conformation of the PAHs through induced strain facilitated by bulkier group substitutions.
- (iv) The incorporation of enantiopure [*n*]helicene of same helicity, with terminal K-regions of pyrene can potentially result in three twists within the central core – helical (*P* or *M*) and wagging. DFT-optimized geometries and calculations have revealed that the most stable conformation involves the opposite helicity between the helicene and the central core, whereas identical helicity results in the highest energy conformation. TD-DFT calculations indicate that as the size of the central core increases, the twist angle amplifies, thereby generating a highly twisted NR with an increased dissymmetric factor (g_{abs} and g_{lum}).

4. Summary of the research projects

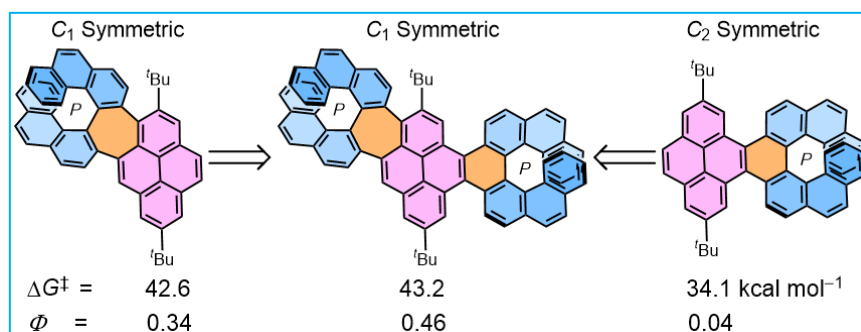
During this thesis, while working on the synthesis of the helically twisted nanoribbon, a range of π -extended $[n]$ helicene–pyrene molecules were developed by altering the fusion mode of $[n]$ helicene with pyrene, thereby resulting in PAHs of different molecular symmetries. These molecules are classified into following three categories.

(1) Pyrene Fused [5]- and [7]Helicenes Connected via Hexagonal and Heptagonal Rings¹³⁶⁻

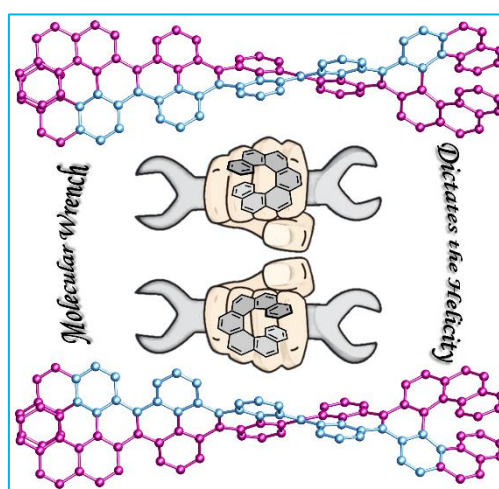
137



(2) Pyrene Bridged Double [7]Helicenes Embedded with a Heptagonal Ring¹³⁸



(3) Helically Twisted Nanoribbons Using [7]Helicenes as Molecular Wrench



4.1. Pyrene Fused [5]- and [7]Helicenes Connected via Hexagonal and Heptagonal Rings

Polycyclic aromatic hydrocarbons fused with [*n*]helicenes offer, in addition to intriguing physical properties, a feature of chirality, which results in non-superimposable mirror-image structures of these compounds that can be resolved into optically active enantiomers. This process, however, is cumbersome, which largely restricts the availability of materials in an optically active form and represents a great hurdle for their applications. The stereospecific synthesis of *C*₂- and *C*₁-symmetric pyrene-fused [5]helicene molecules **1** and **2** — connected via hexagonal and heptagonal rings — was achieved through a one-pot Suzuki coupling–C–H activation and two-step Suzuki coupling–Scholl reaction, respectively, from enantiopure 2,2'-diiodo-8,8'-dimethyl-1,1'-binaphthalene.¹³⁶ [5]helicene-pyrene hybrid molecules **1** and **2** exhibited a high barrier for the enantiomerization due to the presence of methyl groups in the inner helix, as revealed by kinetics measurements along with distinctive functional properties, which was attributed to the fusing mode of [5]helicene with the pyrene and molecular symmetry. Notably, the estimated Gibbs activation energy for enantiomerization (45.8 kcal mol⁻¹), and the absorption dissymmetry factor (2.3 × 10⁻³) for **2**, are one of the highest reported values for any π -conjugated molecules incorporating the [5]helicene-moiety.

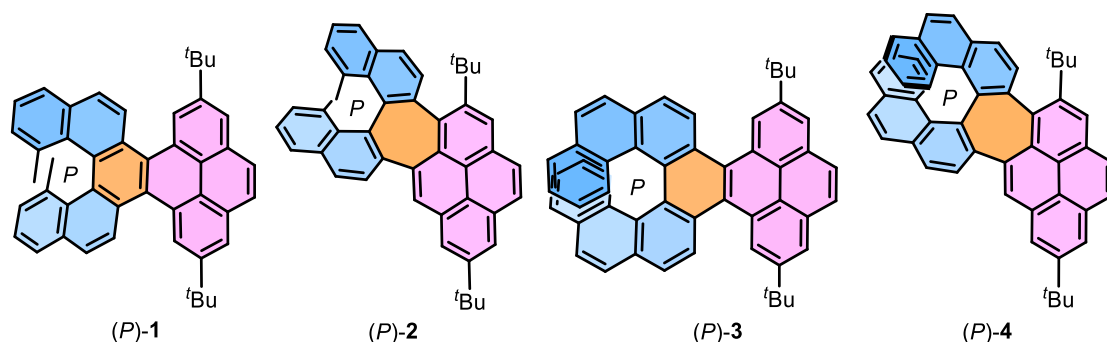
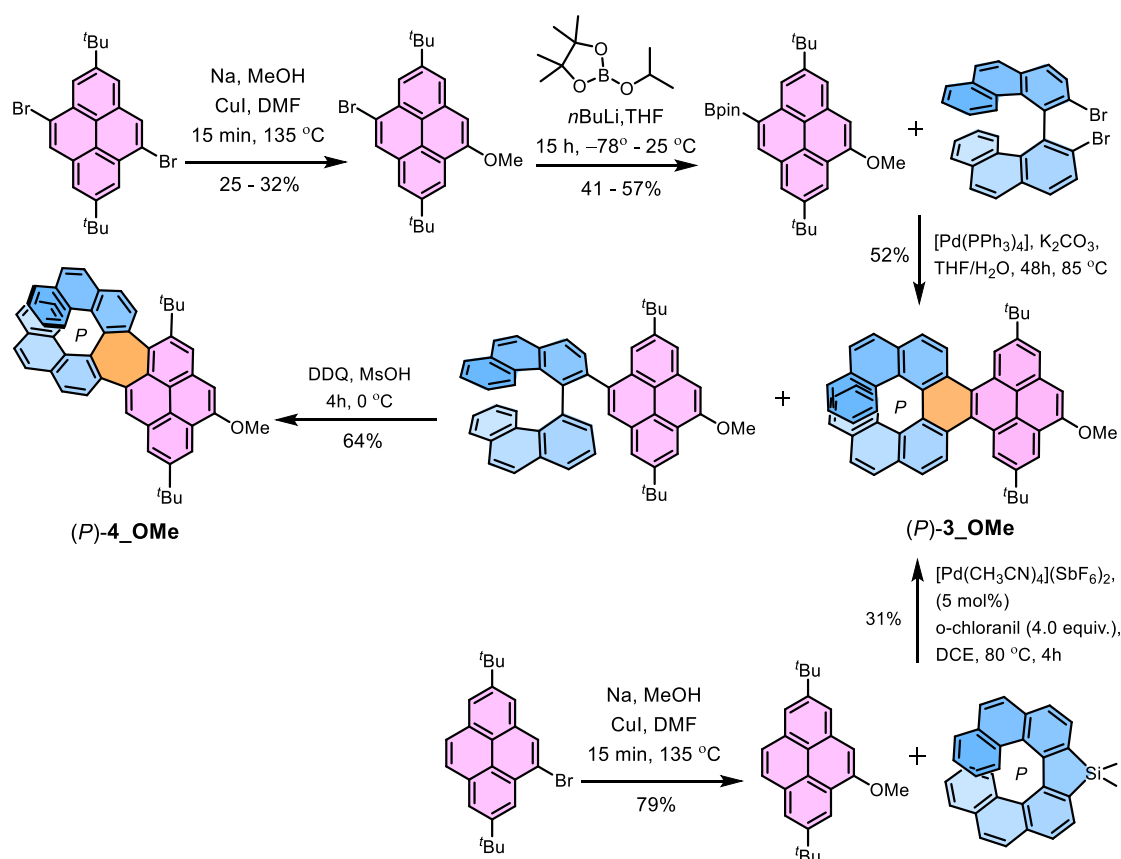


Figure 4.1. Pyrene fused [5]- and [7]helicenes. *Org. Lett.* **2021**, *23* (4), 1339; *J. Org. Chem.* **2022**, *87* (2), 993.

Subsequently, the substitution of [5]helicenes with the [7]helicene through a similar stereospecific approach resulted in formation of *C*₂- and *C*₁-symmetric pyrene-fused [7]helicene molecules **3** and **4**, derived from enantiopure 3,3'-dibromo-4,4'-biphenanthrene.¹³⁷ Similar to the observations with [5]helicene congeners, the [7]helicene-pyrene hybrid molecules **3** and **4** exhibited high configurational stability and distinct

functional properties, which was attributed to the fusion mode of [7]helicene with the pyrene and molecular symmetry. In comparison to the previously studied pyrene-fused [5]helicene congeners, the molecules featuring a [7]helicene moiety exhibited an enhanced chiroptical response with increased brightness values for circularly polarized luminescence (Figure 4.2 and 4.3).⁸⁰ The findings provide valuable insights into the influence of molecular symmetry on the (chir)optical properties and configurational stability of π -extended helicenes.

Effect of methoxy group on (chir)optical properties



Scheme 4.1. K-region methoxylated pyrene fused [7]helicenes.

The (chir)optical parameters of [*n*]helicenes can be readily tuned upon suitable substitution with electron-donating and/or -withdrawing groups along the outer helix of [*n*]helicene.⁹⁰ To prepare the targeted twisted ribbon (**9**), the synthesis of K-region functionalized molecules of **3** and **4** was aimed for. However, attachment of two different functional groups in pyrene proves to be quite challenging because of multiple reaction sites with similar reactivity (Figure 2.14). Even when functional groups are added stoichiometrically, it often leads to the formation of multiple products. However, with careful optimization and

monitoring, the reaction can be intermittently quenched to yield the desired product in moderate yields. A similar strategy was employed to transform 4,9-dibromo-2,7-di-*tert*-butylpyrene into 4-bromo-2,7-di-*tert*-butyl-9-methoxypyrene, which was subsequently boronated to generate the desired methoxylated pyrene precursor for Suzuki coupling with 3,3'-dibromo-4,4'-biphenanthrene (Scheme 4.1). (*P*)-**3**_OMe was obtained with a 52% yield, accompanied by 26% of the uncyclized product. The latter was then subjected to Scholl cyclodehydrogenation, resulting in the production of (*P*)-**4**_OMe with a 64% yield. Alternatively, (*P*)-**3**_OMe can be conveniently synthesized through a palladium catalyzed K-region annulative π -extension (APEX) reaction using readily available 2,7-di-*tert*-butyl-4-methoxypyrene and (*P*)-dimethylsila[7]helicene.

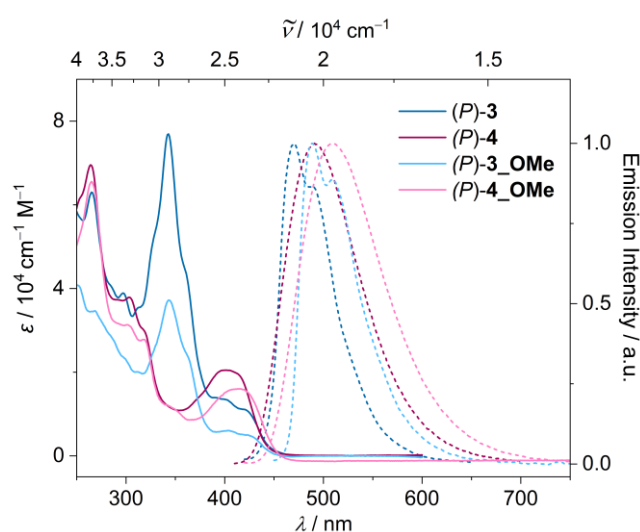


Figure 4.2. UV-Vis absorption (solid) and emission (dashed) spectra of **3** (dark blue), **4** (dark pink), **3**_OMe (light blue) and **4**_OMe (light pink) in dichloromethane ($c \sim 10^{-5}$ M).

The C_1 -symmetric compounds ((*P*)-**3**_OMe and (*P*)-**4**_OMe) exhibited red-shifted absorption and emission spectra profiles compared to (*P*)-**3** and (*P*)-**4** (Figure 4.2). The lowest energy transition in all four compounds consisted of a HOMO \rightarrow LUMO transition, with similar oscillator strengths of 0.14 for (*P*)-**3** / **3**_OMe and 0.52 for (*P*)-**4** / **4**_OMe. Although the time-resolved fluorescence decay was similar for (*P*)-**3** / **3**_OMe and (*P*)-**4** / **4**_OMe, the methoxylated compounds exhibited higher FQY (0.17 for **3**_OMe, 0.46 for **4**_OMe) compared to compounds without the methoxy group (0.04 for **3**, 0.34 for **4**). The higher FQY is possibly due to a reduced optical energy gap and a higher radiative rate constant.

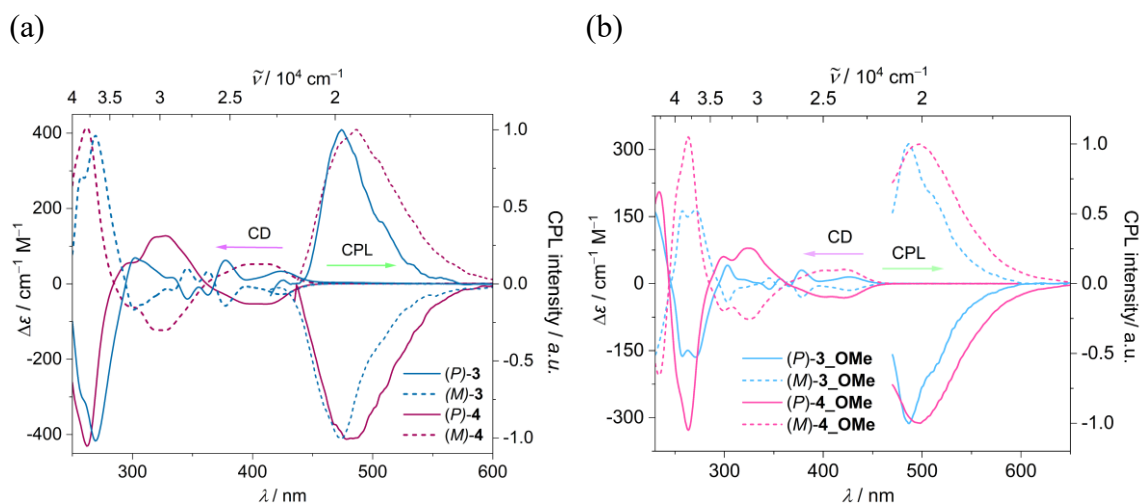


Figure 4.3. ECD (solid) and CPL (dashed) spectra of (a) **3** (dark blue), **4** (dark pink) and (b) **3_OMe** (light blue), **4_OMe** (light pink) in dichloromethane ($c \sim 10^{-5} \text{ M}$).

The molecular dipole strength increased 23 times for (*P*)-**3_OMe** and 8 times for (*P*)-**4_OMe** due to the presence of the electron-donating methoxy group in the K-region of the pyrene. The chiroptical parameters remain quite similar for (*P*)-**3_OMe** compared to (*P*)-**3**; however, the CPL signal is opposite to the lowest energy CD signal. i.e., (*P*)-**3_OMe** showed a positive CD signal in the lowest energy CD signal, while exhibiting a negative CPL upon photoexcitation (Figure 4.3). This phenomenon can only occur when the electronic transitions involved in absorption and emission are different.⁹⁰ In contrast to (*P*)-**3** and (*P*)-**3_OMe**, the chiroptical parameters of (*P*)-**4_OMe** are slightly higher compared to (*P*)-**4** due to a higher transition magnetic dipole moment.

4.2. Pyrene Bridged Double [7]Helicenes Embedded with a Heptagonal Ring

To develop efficient circularly polarized materials with [*n*]helicene-embedded polycyclic aromatic hydrocarbons, it's essential to enhance the (chir)optical responses. Previous two studies on pyrene fused mono[*n*]helicene ($n = 5$ and 7) have illustrated that the fusing mode and molecular symmetry can significantly influence the resultant (chir)optical properties.¹³⁶⁻¹³⁷ To further consolidate this outcoming,¹³⁶⁻¹³⁷ a synthesis similar to the previously reported stereospecific method was employed to prepare pyrene bridged double [7]helicenes.

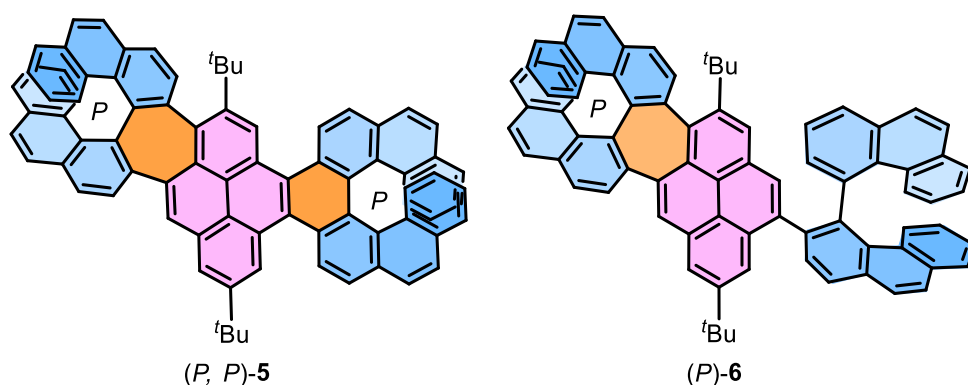


Figure 4.4. Pyrene bridged double[7]helicenes featuring a heptagonal ring and a pyrene fused heptagonal[7]helicene incorporating an axially chiral biphenanthrene unit. *Org. Chem. Front.* **2023**, *10* (15), 3714.

The one pot Suzuki coupling and partial C–H activation between 3,3'-dibromo-4,4'-biphenanthrene¹³⁷ and 2-(2,7-di-*tert*-butylpyren-4-yl)-4,4,5,5-tetramethyl-1,3,2-dioxaborolane¹²⁶ followed by Scholl reaction produced C_1 -symmetric pyrene bridged double [7]helicenes (**5**).¹³⁸ The helicene units are connected via hexagonal and heptagonal rings, merging two molecules from the previous study of pyrene fused [7]helicene (**3** and **4**).¹³⁷ This hybrid molecule exhibited a unique combination of properties inherited from both molecules, with particular emphasis on the characteristics of the heptagonal ring. In line with single helicene congener, C_1 -symmetric heptagon containing double helicene exhibited higher absorption (2.7×10^{-3}) and emission dissymmetric factors (2.5×10^{-3}) along with a significant increase in FQY (0.46) as well as enhanced configurational stability ($43.2 \text{ kcal mol}^{-1}$). Furthermore, the compound (**6**) derived from only Suzuki coupling, followed by partial Scholl reaction in presence of catalytic amount of methanesulphonic acid (MsOH), produced a heptagonally fused [7]helicene and an axially chiral biphenanthrene unit, which exhibited enhanced (chir)optical properties (FQY = 0.41, dissymmetric factor $\sim 3.2 \times 10^{-3}$) compared to the monomer congeners (**3** and **4**). These findings offer valuable insights into the influence of molecular symmetry on the (chir)optical properties of both single and double helicenes.

4.3. Helically Twisted Nanoribbons using [7]Helicenes as Molecular Wrench

As mentioned earlier in the introduction section, the conformational stability of strain-induced twistacene was improved significantly with phenyl substitution along zigzag edges, leading to the isolation of stable conformers of twisted pentacenes. This approach was later then applied to create twisted bay and fjord-edged nanoribbons (NRs) by substitution of bulkier groups. Most of these NRs exhibit limited chiroptical responses due to their moderate end-to-end twist. On the other hand, cove-edged NRs can achieve a higher degree of twist due to their increased flexibility. However, controlling the stereoselectivity of cove-edged NRs is challenging because of their dynamic nature, as they fluctuate between helical and wagging conformations because of low energy barriers. In this study, the conformation and twist of cove-edged NRs was systematically adjusted by incorporating terminal [7]helicenes as strain-inducing tensors, effectively acting as molecular wrenches to determine the overall NR conformation.¹³⁹

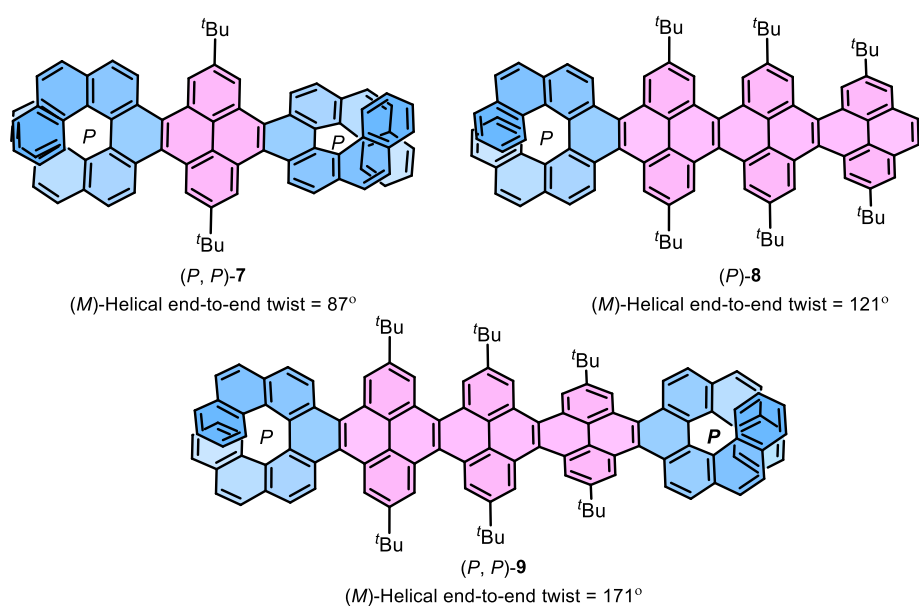


Figure 4.5. Strain induced helically twisted nanoribbons. *Chem. Sci.* **2024**, [10.1039/D4SC01814A](https://doi.org/10.1039/D4SC01814A).

A palladium catalyzed double C–Si/C–H activation through stereospecific and site-selective annulative π -extension (APEX) reaction was employed for the late stage incorporation of enantiopure [7]helicenes at the terminal K-regions of a cove-edged pyrene NR to produce single handed twisted NR with opposite helicity to the [7]helicene. The end-to-end twist in (*P, P*)-9 is nearly twice that of (*P, P*)-7 and significantly higher from (*P*)-8,

illustrating that the terminal [7]helicenes act as a molecular wrench in maintaining the stereoselective twist. The helically twisted NR (**9**) with an end-to-end twist of 171° records the second most twisted acene core after twisted hexacene (184°) by Kilway *et al.*²⁰ Extensive quantum chemical calculations provided insights into the energetically favored conformers and their relative Boltzmann populations. These chiral NRs exhibited exceptional configurational ($37.7 \text{ kcal mol}^{-1}$ for **7**) and conformational stability with a relative population of helical NR amounting to 99.9% at room temperature. The gradual increase in chiroptical responses from (*P, P*)-**7** to (*P, P*)-**9** highlights the emergence of macro chirality resulting from the overall twist of the NR. The structural robustness of (*P*)-**8** and (*P, P*)-**9** was evident from the unchanged chiroptical responses with variation of temperature. The outlined strategy, allowing the late-stage introduction of [*n*]helicene units by APEX reaction, holds promise for facilitating the synthesis of diverse cove edge NR variants with desired conformations.

5. Publications List

Parts of this thesis have been published in following peer-reviewed journals:

1. A. Swain, K. Kolanji, C. Stapper, P. Ravat, C_2 - and C_1 -Symmetric Configurationally Stable Pyrene-Fused [5]Helicenes Connected via Hexagonal and Heptagonal Rings, *Org. Lett.* **2021**, *23*, 1339.
2. A. Swain, K. Radacki, H. Braunschweig, P. Ravat, Pyrene-Fused [7]Helicenes connected via Hexagonal and Heptagonal Rings: Stereospecific Synthesis and Chiroptical Properties, *J. Org. Chem.* **2022**, *87*, 993.
3. A. Swain, P. Ravat, Pyrene Bridged Double[7]helicene Embedded with a Heptagonal Ring, *Org. Chem. Front.* **2023**, *10*, 3714.
4. A. Swain, K. Radacki, H. Braunschweig, P. Ravat, Helically Twisted Nanoribbons via Stereospecific Annulative π -Extension Reaction Employing [7]Helicene as a Molecular Wrench, *Chem. Sci.* **2024**, 10.1039/D4SC01814A.

All the published work incorporated in this thesis has been included with the necessary permissions. Publications during the PhD tenure which are not included in this thesis are listed below:

5. J. Selby, M. Holzapfel, K. Radacki, A. Swain, H. Braunschweig, C. Lambert, Polymeric Indolenine–Squaraine Foldamers with a Preferred Helix Twist Sense and Their Chiroptical Absorption and Emission Properties, *Macromolecules* **2022**, *55*, 421.
6. E. Freytag, M. Holzapfel, A. Swain, G. Bringmann, M. Stolte, F. Würthner, C. Lambert, Axially Chiral Indolenine Derived Chromophore Dimers and Their Chiroptical Absorption and Emission Properties, *Chem. Sci.* **2022**, *13*, 12229.
7. F. Zhang, F. Rauch, A. Swain, T. B. Marder, P. Ravat, Efficient Narrowband Circularly Polarized Light Emitters Based on 1,4-B,N-Embedded Rigid Donor–Acceptor Helicenes, *Angew. Chem. Int. Ed.* **2023**, *62*, e202218965.
8. Fridolin Saal, A. Swain, A. Schmiedel, M. Holzapfel, C. Lambert, P. Ravat, Push-Pull [7]Helicene Diimide: Excited-State Charge Transfer and Solvatochromic Circularly Polarised Luminescence, *Chem. Commun.*, **2023**, *59*, 14005.

6. References

1. Moss, G. P.; Smith, P. A. S.; Tavernier, D., Glossary of class names of organic compounds and reactivity intermediates based on structure (IUPAC Recommendations 1995). *Pure Appl. Chem.* **1995**, *67*, 1307–1375.
2. Gerstner, E., Nobel Prize 2010: Andre Geim & Konstantin Novoselov. *Nat. Phys.* **2010**, *6*, 836–836.
3. Yan, L.; Zheng, Y. B.; Zhao, F.; Li, S.; Gao, X.; Xu, B.; Weiss, P. S.; Zhao, Y., Chemistry and physics of a single atomic layer: strategies and challenges for functionalization of graphene and graphene-based materials. *Chem. Soc. Rev.* **2012**, *41*, 97–114.
4. Xu, H.; Suslick, K. S., Sonochemical Preparation of Functionalized Graphenes. *J. Am. Chem. Soc.* **2011**, *133*, 9148–9151.
5. Mondal, S.; Ghosh, S.; Raj, C. R., Unzipping of Single-Walled Carbon Nanotube for the Development of Electrocatalytically Active Hybrid Catalyst of Graphitic Carbon and Pd Nanoparticles. *ACS Omega* **2018**, *3*, 622–630.
6. Kosynkin, D. V.; Higginbotham, A. L.; Sinitskii, A.; Lomeda, J. R.; Dimiev, A.; Price, B. K.; Tour, J. M., Longitudinal unzipping of carbon nanotubes to form graphene nanoribbons. *Nature* **2009**, *458*, 872–876.
7. Ko, D.; Choi, J.; Yan, B.; Hwang, T.; Jin, X.; Kim, J. M.; Piao, Y., A facile and scalable approach to develop electrochemical unzipping of multi-walled carbon nanotubes to graphene nanoribbons. *J. Mat. Chem. A* **2020**, *8*, 22045–22053.
8. Zhang, Y.; Pun, S. H.; Miao, Q., The Scholl Reaction as a Powerful Tool for Synthesis of Curved Polycyclic Aromatics. *Chem. Rev.* **2022**, *122*, 14554–14593.
9. Jassas, R. S.; Mughal, E. U.; Sadiq, A.; Alsantali, R. I.; Al-Rooqi, M. M.; Naeem, N.; Moussa, Z.; Ahmed, S. A., Scholl reaction as a powerful tool for the synthesis of nanographenes: a systematic review. *RSC Adv.* **2021**, *11*, 32158–32202.
10. Xia, D.; Li, Q.; Xue, Q.; Liang, C.; Dong, M., Super flexibility and stability of graphene nanoribbons under severe twist. *Phys. Chem. Chem. Phys.* **2016**, *18*, 18406–18413.
11. Senese, A. D.; Chalifoux, W. A. Nanographene and Graphene Nanoribbon Synthesis via Alkyne Benzannulations *Molecules*, **2019**, *24*, 118.
12. Pascal, R. A., Twisted Acenes. *Chem. Rev.* **2006**, *106*, 4809–4819.
13. Tönshoff, C.; Bettinger, H. F., Pushing the Limits of Acene Chemistry: The Recent Surge of Large Acenes. *Chem. Eur. J.* **2021**, *27*, 3193–3212.
14. Pascal, R. A.; McMillan, W. D.; Van Engen, D., 9,18-Diphenyltetrabenz[a,c,h,j]anthracene: a remarkably twisted polycyclic aromatic hydrocarbon. *J. Am. Chem. Soc.* **1986**, *108*, 5652–5653.
15. Pascal, R. A., Jr.; McMillan, W. D.; Van Engen, D.; Eason, R. G., Synthesis and structure of longitudinally twisted polycyclic aromatic hydrocarbons. *J. Am. Chem. Soc.* **1987**, *109*, 4660–4665.
16. Smyth, N.; Van Engen, D.; Pascal, R. A., Jr., Synthesis of longitudinally twisted polycyclic aromatic hydrocarbons via a highly substituted aryne. *J. Org. Chem.* **1990**, *55*, 1937–1940.

17. Qiao, X.; Padula, M. A.; Ho, D. M.; Vogelaar, N. J.; Schutt, C. E.; Pascal, R. A., Octaphenylnaphthalene and Decaphenylanthracene. *J. Am. Chem. Soc.* **1996**, *118*, 741–745.
18. Schuster, I. I.; Craciun, L.; Ho, D. M.; Pascal, R. A., Synthesis of a strained, air-sensitive, polycyclic aromatic hydrocarbon by means of a new 1,4-benzadiyne equivalent. *Tetrahedron* **2002**, *58*, 8875–8882.
19. Lu, J.; Ho, D. M.; Vogelaar, N. J.; Kraml, C. M.; Pascal, R. A., A Pentacene with a 144° Twist. *J. Am. Chem. Soc.* **2004**, *126*, 11168–11169.
20. Clevenger, R. G.; Kumar, B.; Menuey, E. M.; Kilway, K. V., Synthesis and Structure of a Longitudinally Twisted Hexacene. *Chem. Eur. J.* **2018**, *24*, 3113–3116.
21. Walters, R. S.; Kraml, C. M.; Byrne, N.; Ho, D. M.; Qin, Q.; Coughlin, F. J.; Bernhard, S.; Pascal, R. A., Jr., Configurationally Stable Longitudinally Twisted Polycyclic Aromatic Compounds. *J. Am. Chem. Soc.* **2008**, *130*, 16435–16441.
22. Bedi, A.; Shimon, L. J. W.; Gidron, O., Helically Locked Tethered Twistacenes. *J. Am. Chem. Soc.* **2018**, *140*, 8086–8090.
23. Bedi, A.; Gidron, O., The Consequences of Twisting Nanocarbons: Lessons from Tethered Twisted Acenes. *Acc. Chem. Res.* **2019**, *52*, 2482–2490.
24. Bedi, A.; Gidron, O., Chiroptical Properties of Twisted Acenes: Experimental and Computational Study. *Chem. Eur. J.* **2019**, *25*, 3279–3285.
25. Figueira-Duarte, T. M.; Müllen, K., Pyrene-Based Materials for Organic Electronics. *Chem. Rev.* **2011**, *111*, 7260–7314.
26. Xiao, J.; Duong, H. M.; Liu, Y.; Shi, W.; Ji, L.; Li, G.; Li, S.; Liu, X.-W.; Ma, J.; Wudl, F.; Zhang, Q., Synthesis and Structure Characterization of a Stable Nonatwistacene. *Angew. Chem. Int. Ed.* **2012**, *51*, 6094–6098.
27. Kumar, B.; Strasser, C. E.; King, B. T., t-Butyl Biphenylation of o-Dibromoarenes: A Route to Soluble Polycyclic Aromatic Hydrocarbons. *J. Org. Chem.* **2012**, *77*, 311–316.
28. Yano, Y.; Ito, H.; Segawa, Y.; Itami, K., Helically Twisted Tetracene: Synthesis, Crystal Structure, and Photophysical Properties of Hexabenz[a,c,fg,j,l,op]tetracene. *Synlett* **2016**, *27*, 2081–2084.
29. Fan, W.; Winands, T.; Doltsinis, N. L.; Li, Y.; Wang, Z., A Decatwistacene with an Overall 170° Torsion. *Angew. Chem. Int. Ed.* **2017**, *56*, 15373–15377.
30. Elbert, S. M.; Baumgärtner, K.; Esteves, J. A.; Weber, L.; Rominger, F.; Mastalerz, M., Pyrene-Based Diarynes as Precursors for Twisted Fused Polycyclic Aromatic Hydrocarbons: A Comparison of Two Routes. *Organic Materials* **2020**, *02*, 358–361.
31. Yao, X.; Zheng, W.; Osella, S.; Qiu, Z.; Fu, S.; Schollmeyer, D.; Müller, B.; Beljonne, D.; Bonn, M.; Wang, H. I.; Müllen, K.; Narita, A., Synthesis of Nonplanar Graphene Nanoribbon with Fjord Edges. *J. Am. Chem. Soc.* **2021**, *143*, 5654–5658.
32. Ma, S.; Gu, J.; Lin, C.; Luo, Z.; Zhu, Y.; Wang, J., Supertwistacene: A Helical Graphene Nanoribbon. *J. Am. Chem. Soc.* **2020**, *142*, 16887–16893.
33. Castro-Fernández, S.; Cruz, C. M.; Mariz, I. F. A.; Márquez, I. R.; Jiménez, V. G.; Palomino-Ruiz, L.; Cuerva, J. M.; Maçôas, E.; Campaña, A. G., Two-Photon Absorption Enhancement by the Inclusion of a Tropone Ring in Distorted Nanographene Ribbons. *Angew. Chem. Int. Ed.* **2020**, *59*, 7139–7145.

34. Yang, W.; Longhi, G.; Abbate, S.; Lucotti, A.; Tommasini, M.; Villani, C.; Catalano, V. J.; Lykhin, A. O.; Varganov, S. A.; Chalifoux, W. A., Chiral Peropyrene: Synthesis, Structure, and Properties. *J. Am. Chem. Soc.* **2017**, *139*, 13102–13109.
35. Yang, W.; Kazemi, R. R.; Karunathilake, N.; Catalano, V. J.; Alpuche-Aviles, M. A.; Chalifoux, W. A., Expanding the scope of peropyrenes and teropyrenes through a facile InCl₃-catalyzed multifold alkyne benzannulation. *Org. Chem. Front.* **2018**, *5*, 2288–2295.
36. Mahlmeister, B.; Mahl, M.; Reichelt, H.; Shoyama, K.; Stolte, M.; Würthner, F., Helically Twisted Nanoribbons Based on Emissive Near-Infrared Responsive Quaterylene Bisimides. *J. Am. Chem. Soc.* **2022**, *144*, 10507–10514.
37. Narita, A.; Feng, X.; Hernandez, Y.; Jensen, S. A.; Bonn, M.; Yang, H.; Verzhbitskiy, I. A.; Casiraghi, C.; Hansen, M. R.; Koch, A. H. R.; Fytas, G.; Ivasenko, O.; Li, B.; Mali, K. S.; Balandina, T.; Mahesh, S.; De Feyter, S.; Müllen, K., Synthesis of structurally well-defined and liquid-phase-processable graphene nanoribbons. *Nature Chem.* **2014**, *6*, 126–132.
38. Theilacker, W.; Böhm, H., Optically Active 2,2'-Dimethylbiphenyl, the Simplest Atropisomeric Hydrocarbon. *Angew. Chem. Int. Ed.* **1967**, *6*, 251–251.
39. Dubey, R. K.; Melle-Franco, M.; Mateo-Alonso, A., Inducing Single-Handed Helicity in a Twisted Molecular Nanoribbon. *J. Am. Chem. Soc.* **2022**, *144*, 2765–2774.
40. McIntosh, A. O.; Robertson, J. M.; Vand, V., The crystal structure and molecular shape of 3 : 4-5 : 6-dibenzophenanthrene. *J. Chem. Soc.* **1954**, 1661–1668.
41. McIntosh, A. O.; Robertson, J. M.; Vand, V., Crystal Structure of 3.4 ; 5.6 Dibenzophenanthrene. *Nature* **1952**, *169*, 322–323.
42. Newman, M. S.; Lednicer, D., The Synthesis and Resolution of Hexahelicene1. *J. Am. Chem. Soc.* **1956**, *78*, 4765–4770.
43. Newman, M. S.; Lutz, W. B.; Lednicer, D., A New Reagent for Resolution by Complex Formation; The Resolution of Phenanthro-[3,4-c]Phenanthrene. *J. Am. Chem. Soc.* **1955**, *77*, 3420–3421.
44. Mallory, F. B.; Wood, C. S.; Gordon, J. T., Photochemistry of Stilbenes. III. Some Aspects of the Mechanism of Photocyclization to Phenanthrenes. *J. Am. Chem. Soc.* **1964**, *86*, 3094–3102.
45. Wood, C. S.; Mallory, F. B., Photochemistry of Stilbenes. IV. The Preparation of Substituted Phenanthrenes1a-c. *J. Org. Chem.* **1964**, *29*, 3373–3377.
46. Carruthers, W., Photocyclisation of some stilbene analogues. Synthesis of dibenzo[a,l]pyrene. *J. Chem. Soc. C* **1967**, 1525–1527.
47. Scholz, M.; Mühlstädt, M.; Dietz, F., Chemie angeregter zustände. I. Mitt. Die richtung der photocyclisierung naphthalinsubstituierter äthylene. *Tetrahedron Lett.* **1967**, *8*, 665–668.
48. Dietz, F.; Scholz, M., Chemie angeregter zustände—IV: Die photocyclisierung der drei isomeren distyrylbenzole. *Tetrahedron* **1968**, *24*, 6845–6849.
49. Martin, R. H., The Helicenes. *Angew. Chem. Int. Ed.* **1974**, *13*, 649–660.
50. Martin, R. H.; Baes, M., Helicenes: Photosyntheses of [11], [12] and [14]helicene. *Tetrahedron* **1975**, *31*, 2135–2137.
51. Flammang-Barbieux, M.; Nasielski, J.; Martin, R. H., Synthesis of heptahelicene (1) benzo [c] phenanthro [4, 3-g]phenanthrene. *Tetrahedron Lett.* **1967**, *8*, 743–744.

52. Martin, R. H.; Eyndels, C.; Defay, N., Double helicenes: Diphenanthro[4,3-a; 3',4'-o]picene and benzo[s]diphenanthro[4,3-a; 3',4'-o]picene. *Tetrahedron* **1974**, *30*, 3339–3342.
53. Tribout, J.; Martin, R. H.; Doyle, M.; Wynberg, H., Chemical assignment of absolute configurations in the helicene and heterohelicene series. Part XXXIV 1. Hexahelicene 2. Benzo [d] naphtho [1,2-d'] benzo [1,2-b; 4,3-b'] dithiophene. *Tetrahedron Lett.* **1972**, *13*, 2839–2842.
54. Somers, J. B. M.; Borkent, J. H.; Laarhoven, W. H., Conformational studies on helicenes VI. A comparison between experimental and calculated conformations. *Recueil des Travaux Chimiques des Pays-Bas* **1981**, *100*, 110–114.
55. Nakai, Y.; Mori, T.; Inoue, Y., Theoretical and Experimental Studies on Circular Dichroism of Carbo[n]helicenes. *J. Phys. Chem. A* **2012**, *116*, 7372–7385.
56. Martin, R. H.; Marchant, M.-J., Thermal racemisation of [6], [7], [8] and [9] helicene. *Tetrahedron Lett.* **1972**, *13*, 3707–3708.
57. Barroso, J.; Cabellos, J. L.; Pan, S.; Murillo, F.; Zarate, X.; Fernandez-Herrera, M. A.; Merino, G., Revisiting the racemization mechanism of helicenes. *Chem. Commun.* **2018**, *54*, 188–191.
58. Ravat, P., Carbo[n]helicenes Restricted to Enantiomerize: An Insight into the Design Process of Configurationally Stable Functional Chiral PAHs. *Chem. Eur. J.* **2021**, *27*, 3957–3967.
59. Ravat, P.; Hinkelmann, R.; Steinebrunner, D.; Prescimone, A.; Bodoky, I.; Juríček, M., Configurational Stability of [5]Helicenes. *Org. Lett.* **2017**, *19*, 3707–3710.
60. Yamamoto, K.; Okazumi, M.; Suemune, H.; Usui, K., Synthesis of [5]Helicenes with a Substituent Exclusively on the Interior Side of the Helix by Metal-catalyzed Cycloisomerization. *Org. Lett.* **2013**, *15*, 1806–1809.
61. Sakai, M.; Wakabayashi, S.; Hasegawa, K.; Imayoshi, A.; Imai, Y.; Sasamori, T.; Tsubaki, K., Synthesis and Optical Properties of Chiral Dinaphthofuran Possessing Two Methyl Groups in the Bay Region. *Chem. Lett.* **2024**, 10.1093/chemle/upae013.
62. Shen J.-J., Y. W.-W., Recent advances in multiple heterohelicenes. *ChemRxiv.* **2022**, 10.26434/chemrxiv-2022-14vbd.
63. Caronna, T.; Mele, A.; Famulari, A.; Mendola, D.; Fontana, F.; Juza, M.; Kamuf, M.; Zawatzky, K.; Trapp, O., A Combined Experimental and Theoretical Study on the Stereodynamics of Monoaza[5]helicenes: Solvent-Induced Increase of the Enantiomerization Barrier in 1-Aza-[5]helicene. *Chem. Eur. J.* **2015**, *21*, 13919–13924.
64. Chen, X.-Y.; Li, J.-K.; Wang, C.; Wang, X.-Y., Synthesis of Methyl-Substituted Aza[7]helicene with Enhanced Configurational Stability and Chiroptical Performance. *ChemRxiv.* **2024**, 10.26434/chemrxiv-2024-4qrlv.
65. Terada, N.; Uematsu, K.; Higuchi, R.; Tokimaru, Y.; Sato, Y.; Nakano, K.; Nozaki, K., Synthesis and Properties of Spiro-double Sila[7]helicene: The LUMO Spiro-conjugation. *Chem. Eur. J.* **2021**, *27*, 9342–9349.
66. Hossain, M. S.; Akter, M.; Shahabuddin, M.; Salim, M.; Iimura, K.-i.; Karikomi, M., Synthesis of Enantiomerically Pure Oxa[9]helicene Derivatives by a Nucleophilic Cyclodehydration Reaction of Helical 1,1'-Bibenzo[c]phenanthrenylidene-2,2'-dione. *Synlett* **2021**, *33*, 277–282.

67. Full, J.; Panchal, S. P.; Götz, J.; Krause, A.-M.; Nowak-Król, A., Modular Synthesis of Organoboron Helically Chiral Compounds: Cutouts from Extended Helices. *Angew. Chem. Int. Ed.* **2021**, *60*, 4350–4357.
68. Volland, D.; Niedens, J.; Geppert, P. T.; Wildervanck, M. J.; Full, F.; Nowak-Król, A., Synthesis of a Blue-Emissive Azaborathia[9]helicene by Silicon-Boron Exchange from Unusual Atropisomeric Teraryls. *Angew. Chem. Int. Ed.* **2023**, *62*, e202304291.
69. Full, F.; Wölflick, Q.; Radacki, K.; Braunschweig, H.; Nowak-Król, A., Enhanced Optical Properties of Azaborole Helicenes by Lateral and Helical Extension. *Chem. Eur. J.* **2022**, *28*, e202202280.
70. Katzenelson, O.; Edelstein, J.; Avnir, D., Quantitative chirality of helicenes. *Tetrahedron: Asymmetry* **2000**, *11*, 2695–2704.
71. Vander Donckt, E.; Nasielski, J.; Greenleaf, J. R.; Birks, J. B., Fluorescence of the helicenes. *Chem. Phys. Lett.* **1968**, *2*, 409–410.
72. Birks, J. B.; Birch, D. J. S.; Cordemans, E.; Vander Donckt, E., Fluorescence of the higher helicenes. *Chem. Phys. Lett.* **1976**, *43*, 33–36.
73. Dey, M.; Ghosh, D., Curious Case of Singlet Triplet Gaps in Nonlinear Polyaromatic Hydrocarbons. *J. Phys. Chem. Lett.* **2022**, *13*, 11795–11800.
74. Abbate, S.; Longhi, G.; Mori, T., Chiroptical Properties of Helicenes. In *Helicenes*, 2022; pp 373–394.
75. Mori, T., Chiroptical Properties of Symmetric Double, Triple, and Multiple Helicenes. *Chem. Rev.* **2021**, *121*, 2373–2412.
76. Martin, R. H.; Marchant, M. J., Resolution and optical properties ($[\alpha]_{\text{max}}$, ord and cd) of hepta-, octa- and nonahelicene. *Tetrahedron* **1974**, *30*, 343–345.
77. Warnke, I.; Furche, F., Circular dichroism: electronic. *WIREs Comput. Mol. Sci.* **2012**, *2*, 150–166.
78. Cei, M.; Di Bari, L.; Zinna, F., Circularly polarized luminescence of helicenes: A data-informed insight. *Chirality* **2023**, *35*, 192–210.
79. Tanaka, H.; Inoue, Y.; Mori, T., Circularly Polarized Luminescence and Circular Dichroisms in Small Organic Molecules: Correlation between Excitation and Emission Dissymmetry Factors. *ChemPhotoChem* **2018**, *2*, 386–402.
80. Arrico, L.; Di Bari, L.; Zinna, F., Quantifying the Overall Efficiency of Circularly Polarized Emitters. *Chem. Eur. J.* **2021**, *27*, 2920–2934.
81. Greenfield, J. L.; Wade, J.; Brandt, J. R.; Shi, X.; Penfold, T. J.; Fuchter, M. J., Pathways to increase the dissymmetry in the interaction of chiral light and chiral molecules. *Chem. Sci.* **2021**, *12*, 8589–8602.
82. Wade, J.; Brandt, J. R.; Reger, D.; Zinna, F.; Amsharov, K. Y.; Jux, N.; Andrews, D. L.; Fuchter, M. J., 500-Fold Amplification of Small Molecule Circularly Polarised Luminescence through Circularly Polarised FRET. *Angew. Chem. Int. Ed.* **2021**, *60*, 222–227.
83. Qiu, Z.; Ju, C. W.; Frederic, L.; Hu, Y.; Schollmeyer, D.; Pieters, G.; Mullen, K.; Narita, A., Amplification of Dissymmetry Factors in pi-Extended [7]- and [9]Helicenes. *J. Am. Chem. Soc.* **2021**, *143*, 4661–4667.
84. Kiel, G. R.; Bergman, H. M.; Samkian, A. E.; Schuster, N. J.; Handford, R. C.; Rothenberger, A. J.; Gomez-Bombarelli, R.; Nuckolls, C.; Tilley, T. D., Expanded [23]-

Helicene with Exceptional Chiroptical Properties via an Iterative Ring-Fusion Strategy. *J. Am. Chem. Soc.* **2022**, *144*, 23421–23427.

85. Saal, F.; Swain, A.; Schmiedel, A.; Holzapfel, M.; Lambert, C.; Ravat, P., Push–pull [7]helicene diimide: excited-state charge transfer and solvatochromic circularly polarised luminescence. *Chem. Commun.* **2023**, *59*, 14005–14008.

86. Zhang, F.; Rauch, F.; Swain, A.; Marder, T. B.; Ravat, P., Efficient Narrowband Circularly Polarized Light Emitters Based on 1,4-B,N-embedded Rigid Donor-Acceptor Helicenes. *Angew. Chem. Int. Ed.* **2023**, e202218965.

87. Sato, S.; Yoshii, A.; Takahashi, S.; Furumi, S.; Takeuchi, M.; Isobe, H., Chiral intertwined spirals and magnetic transition dipole moments dictated by cylinder helicity. *Proc. Natl. Acad. Sci. U.S.A.* **2017**, *114*, 13097–13101.

88. Tanaka, H.; Ikenosako, M.; Kato, Y.; Fujiki, M.; Inoue, Y.; Mori, T., Symmetry-based rational design for boosting chiroptical responses. *Commun. Chem.* **2018**, *1*, 38.

89. Sawada, Y.; Furumi, S.; Takai, A.; Takeuchi, M.; Noguchi, K.; Tanaka, K., Rhodium-Catalyzed Enantioselective Synthesis, Crystal Structures, and Photophysical Properties of Helically Chiral 1,1'-Bitriphenylenes. *J. Am. Chem. Soc.* **2012**, *134*, 4080–4083.

90. Kubo, H.; Hirose, T.; Nakashima, T.; Kawai, T.; Hasegawa, J.-y.; Matsuda, K., Tuning Transition Electric and Magnetic Dipole Moments: [7]Helicenes Showing Intense Circularly Polarized Luminescence. *J. Phys. Chem. Lett.* **2021**, *12*, 686–695.

91. Kumar, J.; Nakashima, T.; Tsumatori, H.; Kawai, T., Circularly Polarized Luminescence in Chiral Aggregates: Dependence of Morphology on Luminescence Dissymmetry. *J. Phys. Chem. Lett.* **2014**, *5*, 316–321.

92. Kumar, J.; Nakashima, T.; Kawai, T., Circularly Polarized Luminescence in Chiral Molecules and Supramolecular Assemblies. *J. Phys. Chem. Lett.* **2015**, *6*, 3445–3452.

93. Sang, Y.; Han, J.; Zhao, T.; Duan, P.; Liu, M., Circularly Polarized Luminescence in Nanoassemblies: Generation, Amplification, and Application. *Adv. Mater.* **2020**, *32*, 1900110.

94. Hu, Y.; Wang, X.-Y.; Peng, P.-X.; Wang, X.-C.; Cao, X.-Y.; Feng, X.; Müllen, K.; Narita, A., Benzo-Fused Double [7]Carbohelicene: Synthesis, Structures, and Physicochemical Properties. *Angew. Chem. Int. Ed.* **2017**, *56*, 3374–3378.

95. Schleyer, P. v. R.; Maerker, C.; Dransfeld, A.; Jiao, H.; van Eikema Hommes, N. J. R., Nucleus-Independent Chemical Shifts: A Simple and Efficient Aromaticity Probe. *J. Am. Chem. Soc.* **1996**, *118*, 6317–6318.

96. Portella, G.; Poater, J.; Bofill, J. M.; Alemany, P.; Solà, M., Local Aromaticity of [n]Acenes, [n]Phenacenes, and [n]Helicenes (n = 1–9). *J. Org. Chem.* **2005**, *70*, 2509–2521.

97. Rulíšek, L.; Exner, O.; Cwiklik, L.; Jungwirth, P.; Starý, I.; Pospíšil, L.; Havlas, Z., On the Convergence of the Physicochemical Properties of [n]Helicenes. *J. Phys. Chem. C* **2007**, *111*, 14948–14955.

98. Aillard, P.; Voituriez, A.; Marinetti, A., Helicene-like chiral auxiliaries in asymmetric catalysis. *Dalton Trans.* **2014**, *43*, 15263–15278.

99. Shang, X.; Wan, L.; Wang, L.; Gao, F.; Li, H., Emerging materials for circularly polarized light detection. *J. Mat. Chem. C* **2022**, *10*, 2400–2410.

100. Yang, Y.; Rice, B.; Shi, X.; Brandt, J. R.; Correa da Costa, R.; Hedley, G. J.; Smilgies, D.-M.; Frost, J. M.; Samuel, I. D. W.; Otero-de-la-Roza, A.; Johnson, E. R.; Jelfs, K. E.; Nelson, J.; Campbell, A. J.; Fuchter, M. J., Emergent Properties of an Organic Semiconductor Driven by its Molecular Chirality. *ACS Nano* **2017**, *11*, 8329–8338.
101. Brandt, J. R.; Wang, X.; Yang, Y.; Campbell, A. J.; Fuchter, M. J., Circularly Polarized Phosphorescent Electroluminescence with a High Dissymmetry Factor from PHOLEDs Based on a Platinahelicene. *J. Am. Chem. Soc.* **2016**, *138*, 9743–9746.
102. Jhulki, S.; Mishra, A. K.; Chow, T. J.; Moorthy, J. N., Helicenes as All-in-One Organic Materials for Application in OLEDs: Synthesis and Diverse Applications of Carbo- and Aza[5]helical Diamines. *Chem. Eur. J.* **2016**, *22*, 9375–9386.
103. Deng, Y.; Wang, M.; Zhuang, Y.; Liu, S.; Huang, W.; Zhao, Q., Circularly polarized luminescence from organic micro-/nano-structures. *Light Sci Appl* **2021**, *10*, 76.
104. Lewińska, G.; Danel, K. S.; Sanetra, J., The bulk heterojunction cells based on new helicenes – Preparation, implementation and surface examination. *Solar Energy* **2016**, *135*, 848–853.
105. He, L.; Zhang, Y.; Wei, Y.; Cai, Y.; Zhang, J.; Wang, P., A helicene-based semiconducting polymer for stable and efficient perovskite solar cells. *Matter* **2023**, *6*, 4013–4031.
106. Wei, Y.; Cai, Y.; He, L.; Zhang, Y.; Yuan, Y.; Zhang, J.; Wang, P., Molecular engineering of nitrogen-rich helicene based organic semiconductors for stable perovskite solar cells. *Chem. Sci.* **2023**, *14*, 10285–10296.
107. Wang, J.; Wang, Y.; Xie, X.; Ren, Y.; Zhang, B.; He, L.; Zhang, J.; Wang, L.-D.; Wang, P., A Helicene-Based Molecular Semiconductor Enables 85 °C Stable Perovskite Solar Cells. *ACS Energy Lett.* **2021**, *6*, 1764–1772.
108. Fatima, R.; Iqbal, J.; Bibi, S.; Yaseen, M., Exploring Acceptor Modification in Helicene-Phenylamine-Based Small Molecules for Organic and Perovskite Solar Cells. *Energy Technol.* **2023**, 2301019.
109. Kim, C.; Marks, T. J.; Facchetti, A.; Schiavo, M.; Bossi, A.; Maiorana, S.; Licandro, E.; Todescato, F.; Toffanin, S.; Muccini, M.; Graiff, C.; Tiripicchio, A., Synthesis, characterization, and transistor response of tetrathia-[7]-helicene precursors and derivatives. *Organic Electronics* **2009**, *10*, 1511–1520.
110. Bracciale, M. P.; Kwon, G.; Ho, D.; Kim, C.; Santarelli, M. L.; Marrocchi, A. Synthesis, Characterization, and Thin-Film Transistor Response of Benzo[i]pentahelicene-3,6-dione *Molecules*, **2022**, *27*, 863.
111. Yu, Y.; Wang, L.; Wang, C.; Liu, F.; Ling, H.; Liu, J., Intramolecular Alkyne Aromatization: Unexpected Synthesis of Expanded [9]Helicene and π -Extended Double [4]Helicene, and Their Molecular Geometry Effect on Transistor Memory. *Small Sci.* **2023**, *3*, 2300040.
112. Verbiest, T.; Elshocht, S. V.; Kauranen, M.; Hellemans, L.; Snauwaert, J.; Nuckolls, C.; Katz, T. J.; Persoons, A., Strong Enhancement of Nonlinear Optical Properties Through Supramolecular Chirality. *Science* **1998**, *282*, 913–915.
113. Tsuji, G.; Kawakami, K.; Sasaki, S., Enantioselective binding of chiral 1,14-dimethyl[5]helicene–spermine ligands with B- and Z-DNA. *Bioorg. Med. Chem.* **2013**, *21*, 6063–6068.

114. Teichmann, B.; Krause, A.-M.; Lin, M.-J.; Würthner, F., Enantioselective Recognition of Helicenes by a Tailored Chiral Benzo[ghi]perylene Trisimide π -Scaffold. *Angew. Chem. Int. Ed.* **2022**, *61*, e202117625.
115. Reetz, M. T.; Sostmann, S., 2,15-Dihydroxy-hexahelicene (HELIXOL): synthesis and use as an enantioselective fluorescent sensor. *Tetrahedron* **2001**, *57*, 2515–2520.
116. Nakakuki, Y.; Hirose, T.; Sotome, H.; Miyasaka, H.; Matsuda, K., Hexa-peri-hexabenz[7]helicene: Homogeneously π -Extended Helicene as a Primary Substructure of Helically Twisted Chiral Graphenes. *J. Am. Chem. Soc.* **2018**, *140*, 4317–4326.
117. Guo, Y.-D.; Yan, X.-H.; Xiao, Y.; Liu, C.-S., U-shaped relationship between current and pitch in helicene molecules. *Sci. Rep.* **2015**, *5*, 16731.
118. Karak, P.; Choudhury, J., Conformationally flexible heterohelicenes as stimuli-controlled soft molecular springs. *Chem. Sci.* **2022**, *13*, 11163–11173.
119. Bamberger, E. G.; Philip, M., Untersuchungen über hochmolekulare Kohlenwasserstoffe; Ueber das Pyren. *Justus Liebigs Annalen der Chemie* **1887**, *240*, 147–192.
120. Goldschmiedt, G., Ueber die Structur des Pyrens. *Justus Liebigs Annalen der Chemie* **1907**, *351*, 218–232.
121. Billing, B. K.; Mayank; Agnihotri, P. K.; Singh, N., Development of pyrene-stacked carbon nanotube-based hybrid: measurement of NO₃⁻ ions using fluorescence spectroscopy. *Analyst* **2018**, *143*, 3343–3352.
122. Matiyani, M.; Pathak, M.; Bohra, B. S.; Sahoo, N. G., Noncovalent Functionalization of Carbon Nanotubes. In *Handbook of Carbon Nanotubes*, Springer International Publishing: **2022**; pp 421–448.
123. Gavrel, G.; Jusselme, B.; Filoramo, A.; Campidelli, S., Supramolecular Chemistry of Carbon Nanotubes. In *Making and Exploiting Fullerenes, Graphene, and Carbon Nanotubes*, Springer Berlin Heidelberg: **2014**; pp 95–126.
124. Liu, Z.; Wang, Y.; Chen, Y.; Liu, J.; Fang, Q.; Kleeberg, C.; Marder, T. B., Ir-Catalyzed Direct Borylation at the 4-Position of Pyrene. *J. Org. Chem.* **2012**, *77*, 7124–7128.
125. Coventry, D. N.; Batsanov, A. S.; Goeta, A. E.; Howard, J. A. K.; Marder, T. B.; Perutz, R. N., Selective Ir-catalysed borylation of polycyclic aromatic hydrocarbons: structures of naphthalene-2,6-bis(boronate), pyrene-2,7-bis(boronate) and perylene-2,5,8,11-tetra(boronate) esters. *Chem. Commun.* **2005**, 2172–2174.
126. Ji, L.; Krummenacher, I.; Friedrich, A.; Lorbach, A.; Haehnel, M.; Edkins, K.; Braunschweig, H.; Marder, T. B., Synthesis, Photophysical, and Electrochemical Properties of Pyrenes Substituted with Donors or Acceptors at the 4- or 4,9-Positions. *J. Org. Chem.* **2018**, *83*, 3599–3606.
127. Liu, F.; Shen, X.; Wu, Y.; Bai, L.; Zhao, H.; Ba, X., Synthesis of ladder-type graphene ribbon oligomers from pyrene units. *Tetrahedron Lett.* **2016**, *57*, 4157–4161.
128. Liu, J.; Li, B.-W.; Tan, Y.-Z.; Giannakopoulos, A.; Sanchez-Sanchez, C.; Beljonne, D.; Ruffieux, P.; Fasel, R.; Feng, X.; Müllen, K., Toward Cove-Edged Low Band Gap Graphene Nanoribbons. *J. Am. Chem. Soc.* **2015**, *137*, 6097–6103.
129. Gu, Y.; Vega-Mayoral, V.; Garcia-Orrit, S.; Schollmeyer, D.; Narita, A.; Cabanillas-González, J.; Qiu, Z.; Müllen, K., Cove-Edged Hexa-peri-hexabenzobis-peri-octacene:

- Molecular Conformations and Amplified Spontaneous Emission. *Angew. Chem. Int. Ed.* **2022**, *61*, e202201088.
130. Wang, X.; Ma, J.; Zheng, W.; Osella, S.; Arisnabarreta, N.; Droste, J.; Serra, G.; Ivasko, O.; Lucotti, A.; Beljonne, D.; Bonn, M.; Liu, X.; Hansen, M. R.; Tommasini, M.; De Feyter, S.; Liu, J.; Wang, H. I.; Feng, X., Cove-Edged Graphene Nanoribbons with Incorporation of Periodic Zigzag-Edge Segments. *J. Am. Chem. Soc.* **2022**, *144*, 228–235.
131. Gingras, M.; Félix, G.; Peresutti, R., One hundred years of helicene chemistry. Part 2: stereoselective syntheses and chiral separations of carbohelicenes. *Chem. Soc. Rev.* **2013**, *42*, 1007–1050.
132. Shen, Y.; Chen, C. F., Helicenes: synthesis and applications. *Chem. Rev.* **2012**, *112*, 1463–535.
133. Xiao, Y.; Mague, J. T.; Schmehl, R. H.; Haque, F. M.; Pascal Jr, R. A., Dodecaphenyltetracene. *Angew. Chem. Int. Ed.* **2019**, *58*, 2831–2833.
134. Rickhaus, M.; Mayor, M.; Juríček, M., Strain-induced helical chirality in polyaromatic systems. *Chem. Soc. Rev.* **2016**, *45*, 1542–1556.
135. Nakano, K.; Hidehira, Y.; Takahashi, K.; Hiyama, T.; Nozaki, K., Stereospecific Synthesis of Hetero[7]helicenes by Pd-Catalyzed Double N-Arylation and Intramolecular O-Arylation. *Angew. Chem. Int. Ed.* **2005**, *44*, 7136–7138.
136. Swain, A. K.; Kolanji, K.; Stapper, C.; Ravat, P., C₂- and C₁-Symmetric Configurationally Stable Pyrene-Fused [5]Helicenes Connected via Hexagonal and Heptagonal Rings. *Org. Lett.* **2021**, *23*, 1339–1343.
137. Swain, A. K.; Radacki, K.; Braunschweig, H.; Ravat, P., Pyrene-Fused [7]Helicenes Connected Via Hexagonal and Heptagonal Rings: Stereospecific Synthesis and Chiroptical Properties. *J. Org. Chem.* **2022**, *87*, 993–1000.
138. Swain, A.; Ravat, P., Pyrene bridged double[7]helicene embedded with a heptagonal ring. *Org. Chem. Front.* **2023**, *10*, 3714–3725.
139. Swain, A.; Radacki, K.; Braunschweig, H.; Ravat, P., Helically twisted nanoribbons via stereospecific annulative π -extension reaction employing [7]helicene as a molecular wrench, *Chem. Sci.* **2024**, 10.1039/D4SC01814A.

7. Compiled Publications

7.1. C_2 - and C_1 -Symmetric Configurationally Stable Pyrene-Fused [5]Helicenes Connected via Hexagonal and Heptagonal Rings	43
7.2. Pyrene-Fused [7]Helicenes Connected via Hexagonal and Heptagonal Rings: Stereospecific Synthesis and Chiroptical Properties	48
7.3. Pyrene Bridged Double[7]helicene Embedded with a Heptagonal ring	56
7.4. Helically Twisted Nanoribbons via Stereospecific Annulative π -Extension Reaction Employing [7]Helicene as a Molecular Wrench	69

The published publications have been reprinted with the necessary copyright permissions, and all authors have been duly informed about their individual contributions, which are listed in section 9 of the thesis.

The copyright information are as follows—

- 7.1. A. Swain, K. Kolanji, C. Stapper, P. Ravat, C_2 - and C_1 -Symmetric Configurationally Stable Pyrene-Fused [5]Helicenes Connected via Hexagonal and Heptagonal Rings, Reprinted with permission from *Org. Lett.* **2021**, *23*, 1339. © 2021 American Chemical Society.
- 7.2. A. Swain, K. Radacki, H. Braunschweig, P. Ravat, Pyrene-Fused [7]Helicenes connected via Hexagonal and Heptagonal Rings: Stereospecific Synthesis and Chiroptical Properties, Reprinted with permission from *J. Org. Chem.* **2022**, *87*, 993. © 2022 American Chemical Society.
- 7.3. A. Swain, P. Ravat, Pyrene Bridged Double[7]helicene Embedded with a Heptagonal Ring, Reproduced from *Org. Chem. Front.* **2023**, *10*, 3714 with permission from the Chinese Chemical Society (CCS), Shanghai Institute of Organic Chemistry (SIOC), and the Royal Society of Chemistry.
- 7.4. A. Swain, K. Radacki, H. Braunschweig, P. Ravat, Helically Twisted Nanoribbons via Stereospecific Annulative π -Extension Reaction Employing [7]Helicene as a Molecular Wrench, Reproduced from *Chem. Sci.* **2024**, 10.1039/D4SC01814A with permission from the Royal Society of Chemistry.

C₂- and C₁-Symmetric Configurationally Stable Pyrene-Fused [5]Helicenes Connected via Hexagonal and Heptagonal Rings

Asim kumar Swain,[†] Kubandiran Kolanji,[†] Christoph Stapper, and Prince Ravat*



Cite This: *Org. Lett.* 2021, 23, 1339–1343



Read Online

ACCESS |



Metrics & More

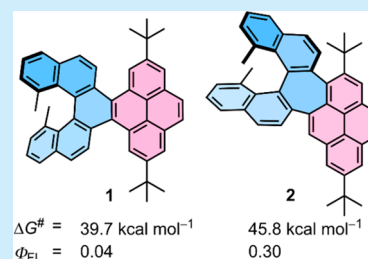


Article Recommendations



Supporting Information

ABSTRACT: In this paper, we describe the stereospecific synthesis and functional properties of C₂- and C₁-symmetric pyrene-fused [5]helicene molecules **1** and **2** connected via hexagonal and heptagonal rings, respectively. Both molecules showed high configurational stability and distinct functional properties, which were attributed to the fusing mode of [5]helicene with the pyrene and molecular symmetry. The estimated Gibbs activation energy for enantiomerization of **2** is one of the highest reported values for any π -conjugated molecules incorporating [5]helicene moiety.



In the past few years, polycyclic aromatic hydrocarbons (PAHs) fused with one or multiple [*n*]helicene¹ units have gained significant attention as they offer improved optical and electronic properties compared to naked carbo[*n*]helicenes.² On the other hand, the PAHs benefit from inherent helical chirality and excellent chiroptical properties³ of [*n*]helicenes. Most synthetic approaches toward helicene-fused PAHs yield a mixture of stereoisomers that are typically separated using HPLC employing chiral stationary phase columns. This process, however, is cumbersome and restricts the available quantity of enantiopure compounds, hence their applicability. The enantioselective synthesis of unfunctionalized hydrocarbon molecules is challenging and still in the development stage, which offers limited substrate scope.⁴ However, the en route key precursors used in the synthesis of helicene-fused PAHs can be obtained in an enantiopure form either using asymmetric catalysis or by chiral resolution using the readily available optically active auxiliaries.⁵ Employing the enantiopure starting materials and adequate synthetic method would allow the synthesis of large helicene-fused PAHs in a stereospecific manner with the desired stereochemistry. Following this strategy, recently we achieved the stereospecific synthesis of a propeller-shaped PAH (C₉₀H₄₈) in gram quantities as a single enantiomer by nickel-mediated Yamamoto-type [2 + 2 + 2] cyclotrimerization of configurationally stable (*M*)-9,10-dibromo[7]helicene.⁶ Our synthetic design took advantage of the thermodynamic stability of stereoisomers of the product and kinetic (in)stability of [*n*]helicenes.⁷

Herein, we show the stereospecific synthesis of pyrene-fused [5]helicene compounds **1** and **2** via one-pot Suzuki coupling–C–H activation and two-step Suzuki coupling–Scholl reaction, respectively, from enantiopure 2,2'-diiodo-8,8'-dimethyl-1,1'-binaphthalene (**6**). The earlier examples of pyrene-fused [*n*]helicenes suffer from low configurational stability and

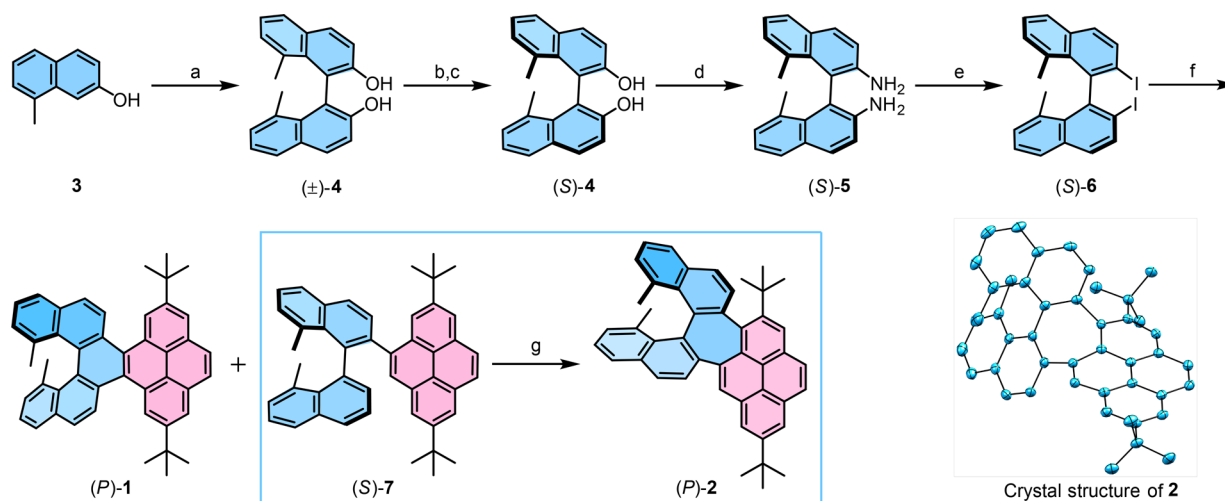
limited (chir)optical properties.⁸ The helicene–pyrene hybrid molecules **1** and **2** showed a high barrier for the enantiomerization process—owing to the two methyl groups in the *fiord* region of [5]helicene subunit—revealed by kinetics measurements. The functional properties of **1** and **2** were investigated by UV–vis absorption, emission, and electronic circular dichroism (ECD) spectroscopies as well as the cyclic voltammetry.

Synthesis of enantiopure **1** was achieved in six steps from 8-methylnaphthalen-2-ol (**3**) as depicted in Scheme 1. Oxidative homocoupling of **3** using Cu-TMEDA catalyst yielded (\pm)-**4** in 78% yield.⁹ Compound **4** could be resolved into enantiomers using (1*S*)-10-camphorsulfonyl chloride as a chiral auxiliary. Esterification of **4** with (1*S*)-10-camphorsulfonyl chloride gave a diastereomeric mixture which was separated using routine column chromatography on silica gel followed by removal of auxiliary afforded enantiopure **4** in 78% yield over two steps. The synthesis was continued separately with each enantiomers of **4**. The key intermediate (*S*)-**6** (er 96:04, er = enantiomeric ratio) was obtained in two steps via functional group transformation from hydroxyl to iodo: (i) conversion of hydroxyl groups to amines using 2-bromopropionamide in an enantioselective switchable Smiles rearrangement¹⁰ and (ii) diazotization–iodination¹¹ of amines **5**. The one-pot Suzuki coupling–C–H activation¹² reaction between (*S*)-**6** and 2-(2,7-di-*tert*-butylpyren-4-yl)-4,4,5,5-tetramethyl-1,3,2-dioxaborolane—using Pd(PPh₃)₄ and K₂CO₃ in a 3:1 THF/H₂O mixture—took place in an enantioselective manner

Received: January 2, 2021

Published: February 2, 2021



Scheme 1. Synthesis of **1** and **2**

^aStereospecific synthesis of **1** and **2**: (a) Cu-TMEDA, DCM, 25 °C, 50 min, 78% yield; (b) (1*S*)-10-camphorsulfonyl chloride, DMF/triethylamine, DMAP, 0 °C, 15 h, 91% yield of mixture of diastereomers which were separated by column chromatography; (c) (+)-diastereomer, NaOH, THF/MeOH, 90 °C, 15 h, 86% yield; (d) (i) 2-Bromopropionamide, K₂CO₃, KI, DMSO, 50 °C, 12 h, (ii) KOH, 150 °C, 4 h, 81% yield; (e) (i) Triflic acid, NaNO₂, 0 °C, 50 min, (ii) KI, H₂O, 25 °C, 20 min, 76% yield (er 96:04); (f) 2-(2,7-di-*tert*-butylpyren-4-yl)-4,4,5,5-tetramethyl-1,3,2-dioxaborolane, Pd(PPh₃)₄, K₂CO₃, 85 °C, 20 h, solvent system 1: THF/H₂O (3:1), 59% yield of **1** (er 95:05) and 28% yield of **7**, solvent system 2: toluene/EtOH/H₂O (5:3:1), 62% yield of **7**; (g) triflic acid, DDQ, DCM, 0 °C, 30 min, 86% yield (er 96:04). The *M*-enantiomers of **1** and **2** were synthesized from (*R*)-**6** in comparable yields and enantiopurity. ORTEP diagram of **2**. Thermal ellipsoids are shown at the 50% probability level. Hydrogen atoms are omitted for clarity.

to give the target compound (*P*)-**1** (er 95:05) in 59% yield as a major product together with an uncyclized compound **7** in 28% yield. The er of (*P*)-**1** is similar to that of the initial material (*S*)-**6** indicating >99% stereoselectivity of this reaction step. When the same reaction was performed using a different solvent system—toluene/EtOH/H₂O (5:3:1)—exclusively **7** was formed in 62% yield. The ratios and yield of **1** and **7** were varied depending on the reaction conditions (Table S1). The Scholl-type oxidative cyclodehydrogenation¹³ of **7**, to our surprise, selectively yielded compound (*P*)-**2** (er 96:04) with a heptagonal ring¹⁴ in 86% yield with the retention of configuration. This is another example of an unexpected Scholl reaction providing an intriguing product. The selective ring closure at position 1 of pyrene during the Scholl reaction can be attributed to the higher aromaticity of the corresponding ring.¹⁵

The structures of **1** and **2** were confirmed with the aid of COSY, NOESY, HMBC, and HSQC 2D NMR experiments by unambiguous assignment of all proton and carbon resonance signals to their respective atoms (Figure S11). Compounds **1** and **2** showed 8 and 16 resonance signals in the typical aromatic region of ¹H NMR spectrum (Figure 1b,c), corroborating with their C₂- and C₁-symmetric structures, respectively. The nucleus-independent chemical shift (NICS) calculations were performed to gain insight into the aromaticity of each ring and obtain the values of chemical shift—NICS(1)_{ZZ} values of respective rings shown in Figure 1a. The experimental NMR spectrum of **1** was well reproduced by calculations. The larger downfield shift of protons e and f is because of the through-space interaction in the cove region which was also supported by NOESY experiments. For both compounds, six-membered rings showed the negative NICS(1)_{ZZ} values in the range −2.43 to −30.88 ppm corresponding to aromaticity.¹⁶ Only the heptagonal ring in **2** exhibited a positive NICS(1)_{ZZ} value indicating antiaroma-

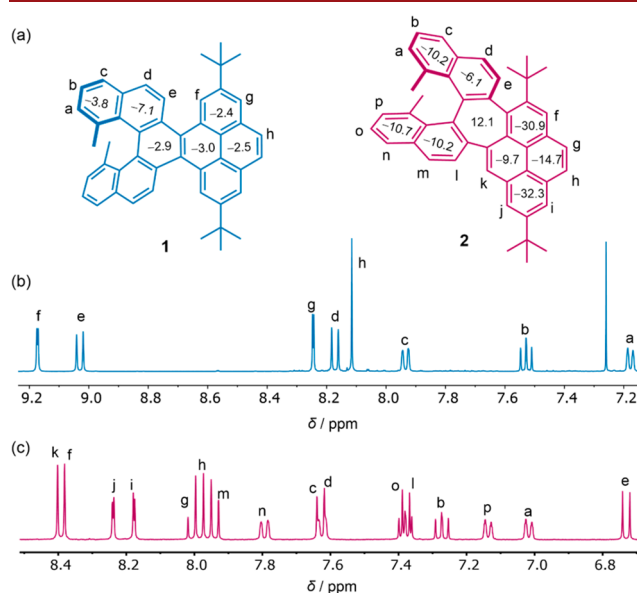


Figure 1. (a) Calculated NICS(1)_{ZZ} values and assignment of ¹H NMR signals. ¹H NMR spectrum of (b) **1** and (c) **2** in CDCl₃ and CD₂Cl₂, respectively, recorded at 298 K.

ticity, which could also account for the upfield shift of proton e. Additionally, the structure of **2** was confirmed by single-crystal X-ray analysis (Scheme 1). All attempts to grow single crystals of **1** failed; therefore, the structural features of **1** and **2** were compared using the DFT-optimized geometries. Interestingly, the [5]helicene subunit of **1** (1.45 Å, 28.0°) and **2** (1.45 Å, 29.1°) showed average C–C bond length and torsional twist at the inner helix comparable to that of the 1,14-dimethyl[5]helicene¹⁷ congener (1.45 Å, 28.1°). The main geometrical difference between the [5]helicene units of **1** and **2** is the distance between the carbon atom (attached to methyl groups)

Table 1. Summary of Optical, Electrochemical and Kinetics Parameters

compd	E_g^a (eV)	λ_{\max}^b (FL) (nm)	Φ_{FL}	τ_{FL} (ns)	k_{FL}^c (10^6 s^{-1})	k_{NR}^d (10^7 s^{-1})	$E_{\text{ox}}^{1/2e}$ (V)	E_{HOMO}^f (eV)	ΔG^\ddagger (T) (kcal mol $^{-1}$)
1	2.79	471	0.04	2.60 (8.13)	15.4 (4.92)	36.9 (11.8)	0.65	-5.81	39.7 (493 K)
2	2.80	502	0.30	2.83	106	24.7	0.54	-5.70	45.8 (503 K)
[5]helicene ^g	3.54	360	0.04	25.5	1.57	3.76			25.0 (503 K)
2,7-di- <i>tert</i> -butylpyrene ^h	3.55	378	0.12						

^aEstimated from crossing of absorption and fluorescence spectra. ^bFluorescence band. ^cRate constant for the radiative decay. ^dRate constant for the nonradiative decay. ^eVolt vs Fc/Fc⁺ in DCM. ^f $E_{\text{HOMO}} = -(E_{\text{ox}}^{1/2}[\text{vs Fc/Fc}^+] + 5.16)$. ^gReferences 3c, 17, and 20 ^hReference 8d.

in the inner helix. Owing to the saddle shape curvature of the heptagonal ring, the distance between these two carbon atoms was much larger in **2** (3.68 Å) in comparison to **1** (3.36 Å).

Typically, PAHs with a [5]helicene subunit exhibit poor configurational stability (ΔG^\ddagger (503 K) = ~ 25 kcal mol $^{-1}$). Our previous study on configurational stability of carbo[*n*]helicenes suggested that the enantiomerization barrier of [5]helicenes can be significantly improved by introducing substituents in the inner helix.^{17,18} To ensure the stereostability, **1** and **2** were subjected to kinetic measurements, following the change in ee with time at a temperature of 493 and 503 K, respectively (Figure S5). The influence of the methyl substituent on configurational stability was well reflected in the estimated $\Delta G^\ddagger(T)$ for **1** (39.7 kcal mol $^{-1}$) and **2** (45.8 kcal mol $^{-1}$). The latter is the highest reported value for any [5]helicene compound and also substantially larger than that of [9]-helicene (ΔG^\ddagger (503 K) = 44.1 kcal mol $^{-1}$).¹⁹ The exceptionally high $\Delta G^\ddagger(T)$ for **2** was attributed to the additional steric effect by the neighboring *tert*-butyl group of the pyrene unit as well as the larger distance between the carbon atoms in the inner helix, which may stabilize the ground-state structure to a greater extent than the transition state structure involved in the enantiomerization process. It should be noted that compound **1** possesses, in addition to a configurationally stable [5]-helicene subunit, two configurationally labile [4]helicene units which are in dynamic equilibrium at room temperature (Figure S6)—the NMR spectrum of **1** ruled out any possibility of the diastereomeric mixture at room temperature.

The optical properties of **1** and **2** were investigated by UV-vis absorption and emission spectroscopy in dichloromethane (DCM). The UV-vis absorption and fluorescence spectra of **1** and **2** showed a considerable bathochromic shift compared to [5]helicene and 2,7-di-*tert*-butylpyrene (Figure 2, Table 1). While both compounds showed distinct absorption spectra, the optical energy gap is similar (2.79–2.80 eV) and much smaller than that of [5]helicene (3.54 eV)^{3c} and 2,7-di-*tert*-butylpyrene (3.55 eV).^{8d} TD-DFT calculations provided further insights into electronic transitions (Figure S8, Table S4). The absorption spectra of *C*₂-symmetric **1** exhibited the same characteristic low energy transition as for [5]helicene. The two lowest energy transitions were accordingly, mainly composed of HOMO → LUMO+1/HOMO-1 → LUMO and HOMO → LUMO transition with oscillator strengths (*f*) of 0.01 and 0.14, respectively. Interestingly, for *C*₁-symmetric molecule **2**, the order of these two transitions—HOMO → LUMO and HOMO → LUMO+1/HOMO-1 → LUMO with *f* = 0.40 and 0.03, respectively—was reversed. This clearly shows the effect of molecular symmetry on the shape and intensity of electronic transitions, which was further reflected in their emission properties. The fluorescence spectrum of compound **2** (5071 cm $^{-1}$) showed a much larger Stokes shift compared to **1** (3706 cm $^{-1}$). While the fluorescence quantum

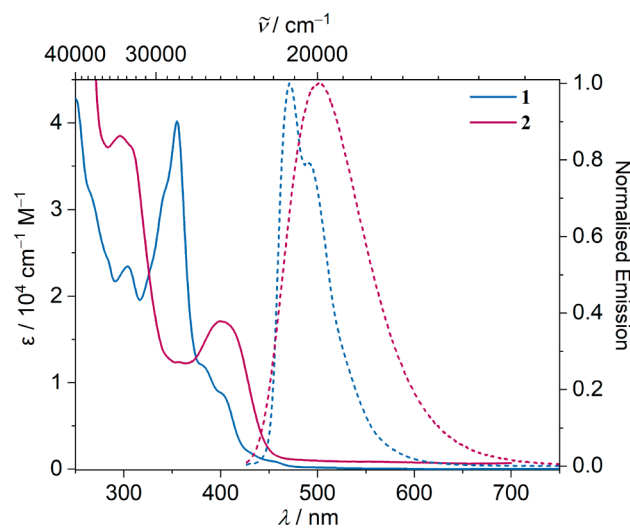


Figure 2. UV-vis absorption (solid line, $c = \sim 10^{-5}$ M) and emission (dashed line, excitation at 28249 cm $^{-1}$ for **1** and 24691 cm $^{-1}$ for **2**, $c = \sim 10^{-6}$ M) spectra of **1** and **2** in DCM.

yield (FQY) of **1** (0.04) is similar to that of [5]helicene,²⁰ **2** (0.30) showed a roughly 8-fold increase. The low FQY of **1** can be attributed to the forbidden S1 state as revealed by TD-DFT calculations and the higher rate of nonradiative decay. The FQY of **2** is three times higher than that for the recently reported large negatively curved nanographenes with [5]-helicene subunit and heptagonal as well as octagonal rings, which can be attributed to its structural rigidity.²¹ Time-resolved fluorescence decay of **1** and **2** could be fitted with bi- and monoexponential function giving the fluorescence lifetime of $\tau_1 = 2.60$ ns, $\tau_2 = 8.13$ ns, and $\tau_1 = 2.83$ ns, respectively, both of which are much shorter than that for [5]helicene (Table 1). The biexponential fluorescence decay of **1** is likely due to its dynamic structure.²²

The CV of **1** and **2** in DCM revealed one and two reversible oxidation processes, respectively. No reduction redox process was observed in the solvent window. The first oxidation couple for **1** and **2** occurred at half-wave potentials of 0.65 and 0.54 V, respectively, versus Fc/Fc⁺ as an internal standard (Figure S1). Accordingly, the calculated HOMO energy level for **1** (-5.81 eV) is slightly lower than that for **2** (-5.70 eV).

ECD measurements were performed to assign the absolute configuration and probe the chiroptical properties of **1** and **2**. The absolute configurations were assigned by comparing the experimental CD spectra with TD-DFT-calculated spectra for a *P*-enantiomer (Figure S9). The *P/M* enantiomers of both compounds showed perfect mirror-image CD spectra with opposite Cotton effects (Figure 3). While the lowest energy transition for **1** showed a weak and positive Cotton effect, that for **2** was much stronger and negative. Accordingly, the

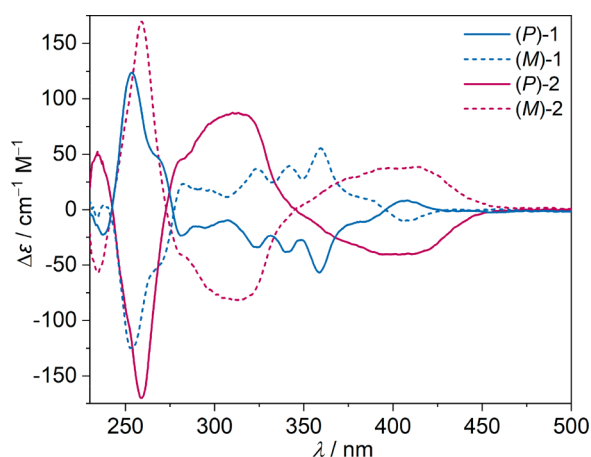


Figure 3. Electronic CD spectra of *P*- and *M*-enantiomers of **1** and **2** in DCM ($c = \sim 10^{-5}$ M).

absorption dissymmetry factor (g_{abs}) for **2** (2.3×10^{-3} at 415 nm) was slightly higher compared to **1** (1.5×10^{-3} at 415 nm) (Figure S4).

In conclusion, we have demonstrated a straightforward stereoselective synthesis of configurational stable pyrene-fused helicene compounds **1** and **2** utilizing a one-pot Suzuki coupling–C–H activation and two-step Suzuki coupling–Scholl reaction, respectively, from enantiopure starting material **6**. The synthesis can be easily scaled up, and enantiopure compounds can be obtained in gram quantities. In comparison to **1** and naked [5]helicene, **2** showed substantially higher fluorescence quantum yields as well as exceptionally high configurational stability. Our study revealed that the π -extended helicene with seven-membered ring exhibit beneficial functional properties. In our future work, we aim to synthesize negatively curved functional chiral nanographenes incorporating seven-membered rings, which are stable toward enantio-merization.

■ ASSOCIATED CONTENT

Supporting Information

The Supporting Information is available free of charge at <https://pubs.acs.org/doi/10.1021/acs.orglett.1c00005>.

Experimental and calculation details, cyclic voltammograms, crystallographic details, copy of NMR spectra, and HPLC plots (PDF)

Accession Codes

CCDC 2052372 contains the supplementary crystallographic data for this paper. These data can be obtained free of charge via www.ccdc.cam.ac.uk/data_request/cif, or by emailing data_request@ccdc.cam.ac.uk, or by contacting The Cambridge Crystallographic Data Centre, 12 Union Road, Cambridge CB2 1EZ, UK; fax: +44 1223 336033.

■ AUTHOR INFORMATION

Corresponding Author

Prince Ravat – Institut für Organische Chemie, Universität Würzburg, D-97074 Würzburg, Germany; orcid.org/0000-0002-7553-9188; Email: princekumar.ravat@uni-wuerzburg.de

Authors

Asim kumar Swain – Institut für Organische Chemie, Universität Würzburg, D-97074 Würzburg, Germany
 Kubandiran Kolanji – Institut für Organische Chemie, Universität Würzburg, D-97074 Würzburg, Germany
 Christoph Stapper – Institut für Organische Chemie, Universität Würzburg, D-97074 Würzburg, Germany

Complete contact information is available at: <https://pubs.acs.org/doi/10.1021/acs.orglett.1c00005>

Author Contributions

†A.k.S. and K.K. contributed equally.

Notes

The authors declare no competing financial interest.

■ ACKNOWLEDGMENTS

This project has received funding from the Julius-Maximilians-Universität Würzburg within the “Excellent Ideas” program and Deutsche Forschungsgemeinschaft (RA 3163/4-1). We thank Fangyuan Zhang and Fridolin Saal for their help with CD and fluorescence measurements and Ana-Maria Krause for single-crystal X-ray structure analysis (University of Würzburg). We sincerely thank Prof. C. Lambert (University of Würzburg) for generously supporting our research.

■ REFERENCES

- (1) (a) Shen, Y.; Chen, C.-F. Helicenes: Synthesis and Applications. *Chem. Rev.* **2012**, *112*, 1463–1535. (b) Martin, R. H. The Helicenes. *Angew. Chem., Int. Ed. Engl.* **1974**, *13*, 649–660.
- (2) Selected recent examples. Earlier examples can be found in cited reviews. (a) Ma, S.; Gu, J.; Lin, C.; Luo, Z.; Zhu, Y.; Wang, J. Supertwistacene: A Helical Graphene Nanoribbon. *J. Am. Chem. Soc.* **2020**, *142*, 16887–16893. (b) Ma, J.; Fu, Y.; Dmitrieva, E.; Liu, F.; Komber, H.; Hennersdorf, F.; Popov, A. A.; Weigand, J. J.; Liu, J.; Feng, X. Helical Nanographenes Containing an Azulene Unit: Synthesis, Crystal Structures, and Properties. *Angew. Chem., Int. Ed.* **2020**, *59*, 5637–5642. (c) Zhu, Y.; Guo, X.; Li, Y.; Wang, J. Fusing of Seven HBCs toward a Green Nanographene Propeller. *J. Am. Chem. Soc.* **2019**, *141*, 5511–5517. (d) Kato, K.; Segawa, Y.; Itami, K. Symmetric Multiple Carbohelicenes. *Synlett* **2019**, *30*, 370–377. (e) Hu, Y.; Paternò, G. M.; Wang, X.-Y.; Wang, X.-C.; Guizzardi, M.; Chen, Q.; Schollmeyer, D.; Cao, X.-Y.; Cerullo, G.; Scotognella, F.; Müllen, K.; Narita, A. π -Extended Pyrene-Fused Double [7]-Carbohelicene as a Chiral Polycyclic Aromatic Hydrocarbon. *J. Am. Chem. Soc.* **2019**, *141*, 12797–12803. (f) Cruz, C. M.; Márquez, I. R.; Castro-Fernández, S.; Cuerva, J. M.; Maçôas, E.; Campaña, A. G. A Triskelion-Shaped Saddle–Helix Hybrid Nanographene. *Angew. Chem., Int. Ed.* **2019**, *58*, 8068–8072. (g) Nakakuki, Y.; Hirose, T.; Sotome, H.; Miyasaka, H.; Matsuda, K. Hexa-peri-hexabenz[7]-helicene: Homogeneously π -Extended Helicene as a Primary Substructure of Helically Twisted Chiral Graphenes. *J. Am. Chem. Soc.* **2018**, *140*, 4317–4326. (h) Lin, W.-B.; Li, M.; Fang, L.; Chen, C.-F. Recent progress on multidimensional construction of helicenes. *Chin. Chem. Lett.* **2018**, *29*, 40–46. (i) Li, C.; Yang, Y.; Miao, Q. Recent Progress in Chemistry of Multiple Helicenes. *Chem. - Asian J.* **2018**, *13*, 884–894. (j) Fernández-García, J. M.; Evans, P. J.; Medina Rivero, S.; Fernández, I.; García-Fresnadillo, D.; Perles, J.; Casado, J.; Martín, N. π -Extended Corannulene-Based Nanographenes: Selective Formation of Negative Curvature. *J. Am. Chem. Soc.* **2018**, *140*, 17188–17196. (k) Yang, W.; Longhi, G.; Abbate, S.; Lucotti, A.; Tommasini, M.; Villani, C.; Catalano, V. J.; Lykhin, A. O.; Varganov, S. A.; Chalifoux, W. A. Chiral Peropyrene: Synthesis, Structure, and Properties. *J. Am. Chem. Soc.* **2017**, *139*, 13102–13109.
- (3) (a) Zhao, W.-L.; Li, M.; Lu, H.-Y.; Chen, C.-F. Advances in helicene derivatives with circularly polarized luminescence. *Chem.*

Commun. **2019**, *55*, 13793–13803. (b) Tanaka, H.; Inoue, Y.; Mori, T. Circularly Polarized Luminescence and Circular Dichroisms in Small Organic Molecules: Correlation between Excitation and Emission Dissymmetry Factors. *ChemPhotoChem.* **2018**, *2*, 386–402. (c) Nakai, Y.; Mori, T.; Inoue, Y. Theoretical and Experimental Studies on Circular Dichroism of Carbo[n]helicenes. *J. Phys. Chem. A* **2012**, *116*, 7372–7385.

(4) (a) Yubuta, A.; Hosokawa, T.; Gon, M.; Tanaka, K.; Chujo, Y.; Tsurusaki, A.; Kamikawa, K. Enantioselective Synthesis of Triple Helicenes by Cross-Cyclotrimerization of a Helicenyl Aryne and Alkynes via Dynamic Kinetic Resolution. *J. Am. Chem. Soc.* **2020**, *142*, 10025–10033. (b) Takano, H.; Shiozawa, N.; Imai, Y.; Kanyiva, K. S.; Shibata, T. Catalytic Enantioselective Synthesis of Axially Chiral Polycyclic Aromatic Hydrocarbons (PAHs) via Regioselective C–C Bond Activation of Biphenylenes. *J. Am. Chem. Soc.* **2020**, *142*, 4714–4722.

(5) (a) Stará, I. G.; Starý, I. Helically Chiral Aromatics: The Synthesis of Helicenes by [2 + 2 + 2] Cycloisomerization of π -Electron Systems. *Acc. Chem. Res.* **2020**, *53*, 144–158. (b) Link, A.; Sparr, C. Stereoselective arene formation. *Chem. Soc. Rev.* **2018**, *47*, 3804–3815. (c) Gingras, M.; Felix, G.; Peresutti, R. One hundred years of helicene chemistry. Part 2: stereoselective syntheses and chiral separations of carbohelicenes. *Chem. Soc. Rev.* **2013**, *42*, 1007–1050. (d) Nakano, K.; Hidehira, Y.; Takahashi, K.; Hiyama, T.; Nozaki, K. Stereospecific Synthesis of Hetero[7]helicenes by Pd-Catalyzed Double N-Arylation and Intramolecular O-Arylation. *Angew. Chem., Int. Ed.* **2005**, *44*, 7136–7138.

(6) Zhang, F.; Michail, E.; Saal, F.; Krause, A.-M.; Ravat, P. Stereospecific Synthesis and Photophysical Properties of Propeller-Shaped C₉₀H₄₈ PAH. *Chem. - Eur. J.* **2019**, *25*, 16241–16245.

(7) Ravat, P. Carbo[n]helicenes Restricted to Enantiomerize: An Insight into the Design Process of Configurationally Stable Functional Chiral PAHs. *Chem. - Eur. J.* **2020**, DOI: 10.1002/chem.202004488.

(8) (a) Wang, L.; Han, Y.; Zhang, J.; Li, X.; Liu, X.; Xiao, J. Stable Double and Quadruple [5]Helicene Derivatives: Synthesis, Structural Analysis, and Physical Properties. *Org. Lett.* **2020**, *22*, 261–264. (b) Bam, R.; Yang, W.; Longhi, G.; Abbate, S.; Lucotti, A.; Tommasini, M.; Franzini, R.; Villani, C.; Catalano, V. J.; Olmstead, M. M.; Chalifoux, W. A. Four-Fold Alkyne Benzannulation: Synthesis, Properties, and Structure of Pyrene[a]pyrene-Based Helicene Hybrids. *Org. Lett.* **2019**, *21*, 8652–8656. (c) Yano, Y.; Ito, H.; Segawa, Y.; Itami, K. Helically Twisted Tetracene: Synthesis, Crystal Structure, and Photophysical Properties of Hexabenz[a,c,f,g,j,l,op]-tetracene. *Synlett* **2016**, *27*, 2081–2084. (d) Hu, J.-Y.; Paudel, A.; Seto, N.; Feng, X.; Era, M.; Matsumoto, T.; Tanaka, J.; Elsegood, M. R. J.; Redshaw, C.; Yamato, T. Pyrene-cored blue-light emitting [4]helicenes: synthesis, crystal structures, and photophysical properties. *Org. Biomol. Chem.* **2013**, *11*, 2186–2197. (e) Bédard, A.-C.; Vlassova, A.; Hernandez-Perez, A. C.; Bessette, A.; Hanan, G. S.; Heuft, M. A.; Collins, S. K. Synthesis, Crystal Structure and Photophysical Properties of Pyrene–Helicene Hybrids. *Chem. - Eur. J.* **2013**, *19*, 16295–16302.

(9) (a) Pedersen, S. K.; Eriksen, K.; Pittelkow, M. Symmetric, Unsymmetrical, and Asymmetric [7]-, [10]-, and [13]Helicenes. *Angew. Chem., Int. Ed.* **2019**, *58*, 18419–18423. (b) Terrasson, V.; Roy, M.; Moutard, S.; Lafontaine, M.-P.; Pepe, G.; Felix, G.; Gingras, M. Benzylic-type couplings provide an important asymmetric entry to functionalized, non-racemic helicenes. *RSC Adv.* **2014**, *4*, 32412–32414.

(10) Chang, X.; Zhang, Q.; Guo, C. Switchable Smiles Rearrangement for Enantioselective O-Aryl Amination. *Org. Lett.* **2019**, *21*, 4915–4918.

(11) Kracsenciová, K.; Walla, P.; Kasák, P.; Uray, G.; Kappe, C. O.; Putala, M. Stereocconservative Negishi arylation and alkynylation as an efficient approach to enantiopure 2,2'-diarylated 1,1'-binaphthyls. *Chem. Commun.* **2004**, 2606–2607.

(12) (a) Tu, J.; Li, G.; Zhao, X.; Xu, F. Synthesis of triphenylene derivatives by Pd-catalyzed Suzuki coupling/intramolecular CH activation between arylboronic acids and dibromobiphenyls. *Tetra-*

dron Lett. **2019**, *60*, 44–47. (b) Shimizu, M.; Nagao, I.; Tomioka, Y.; Hiyama, T. Palladium-Catalyzed Annulation of vic-Bis-(pinacolatoboryl)alkenes and -phenanthrenes with 2,2'-Dibromobiphenyls: Facile Synthesis of Functionalized Phenanthrenes and Dibenzo-[g,p]chrysenes. *Angew. Chem., Int. Ed.* **2008**, *47*, 8096–8099.

(13) Grzybowski, M.; Sadowski, B.; Butenschön, H.; Gryko, D. T. Synthetic Applications of Oxidative Aromatic Coupling—From Biphenols to Nanographenes. *Angew. Chem., Int. Ed.* **2020**, *59*, 2998–3027.

(14) Miao, Q. Heptagons in Aromatics: From Monocyclic to Polycyclic. *Chem. Rec.* **2015**, *15*, 1156–1159.

(15) (a) Liu, J.; Narita, A.; Osella, S.; Zhang, W.; Schollmeyer, D.; Beljonne, D.; Feng, X.; Müllen, K. Unexpected Scholl Reaction of 6,7,13,14-Tetraarylbenzo[k]tetraphene: Selective Formation of Five-Membered Rings in Polycyclic Aromatic Hydrocarbons. *J. Am. Chem. Soc.* **2016**, *138*, 2602–2608. (b) Lorbach, D.; Wagner, M.; Baumgarten, M.; Müllen, K. The right way to self-fuse bi- and terpyrenyls to afford graphenic cutouts. *Chem. Commun.* **2013**, *49*, 10578–10580.

(16) Randić, M. Aromaticity of Polycyclic Conjugated Hydrocarbons. *Chem. Rev.* **2003**, *103*, 3449–3606.

(17) Ravat, P.; Hinkelmann, R.; Steinebrunner, D.; Prescimone, A.; Bodoky, I.; Juríček, M. Configurational Stability of [5]Helicenes. *Org. Lett.* **2017**, *19*, 3707–3710.

(18) Saal, F.; Zhang, F.; Holzapfel, M.; Stolte, M.; Michail, E.; Moos, M.; Schmiedel, A.; Krause, A.-M.; Lambert, C.; Würthner, F.; Ravat, P. [n]Helicene Diimides (n = 5, 6, and 7): Through-Bond versus Through-Space Conjugation. *J. Am. Chem. Soc.* **2020**, *142*, 21298–21303.

(19) Martin, R. H.; Marchant, M. J. Thermal racemisation of hepta-, octa-, and nonahelicene: Kinetic results, reaction path and experimental proofs that the racemisation of hexa- and heptahelicene does not involve an intramolecular double diels-alder reaction. *Tetrahedron* **1974**, *30*, 347–349.

(20) Birks, J. B.; Birch, D. J. S.; Cordemans, E.; Vander Donckt, E. Fluorescence of the higher helicenes. *Chem. Phys. Lett.* **1976**, *43*, 33–36.

(21) (a) Qiu, Z.; Asako, S.; Hu, Y.; Ju, C.-W.; Liu, T.; Rondin, L.; Schollmeyer, D.; Lauret, J.-S.; Müllen, K.; Narita, A. Negatively Curved Nanographene with Heptagonal and [5]Helicene Units. *J. Am. Chem. Soc.* **2020**, *142*, 14814–14819. (b) Medel, M. A.; Tapia, R.; Blanco, V.; Miguel, D.; Morcillo, S. P.; Campaña, A. G. Octagon-embedded carbohelicene as chiral motif for CPL emission of saddle-helix nanographenes. *Angew. Chem., Int. Ed.* **2020**. (c) Márquez, I. R.; Fuentes, N.; Cruz, C. M.; Puente-Muñoz, V.; Sotorrios, L.; Marcos, M. L.; Choquesillo-Lazarte, D.; Biel, B.; Crovetto, L.; Gómez-Bengoa, E.; González, M. T.; Martín, R.; Cuerva, J. M.; Campaña, A. G. Versatile synthesis and enlargement of functionalized distorted heptagon-containing nanographenes. *Chem. Sci.* **2017**, *8*, 1068–1074.

(22) Kel, O.; Sherin, P.; Mehanna, N.; Laleu, B.; Lacour, J.; Vauthey, E. Excited-state properties of chiral [4]helicene cations. *Photochem. Photobiol. Sci.* **2012**, *11*, 623–631.

Pyrene-Fused [7]Helicenes Connected Via Hexagonal and Heptagonal Rings: Stereospecific Synthesis and Chiroptical Properties

Asim Kumar Swain, Krzysztof Radacki, Holger Braunschweig, and Prince Ravat*



Cite This: *J. Org. Chem.* 2022, 87, 993–1000



Read Online

ACCESS |



Metrics & More

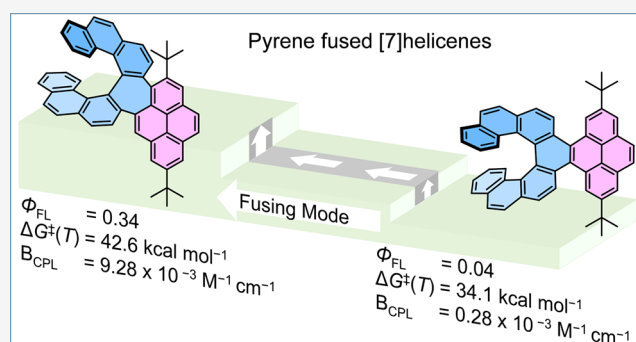


Article Recommendations



Supporting Information

ABSTRACT: In this manuscript, we portrayed a stereospecific synthesis of C_2 - and C_1 -symmetric pyrene-fused [7]helicene compounds **1** and **2**, respectively. Compounds **1** and **2** were synthesized via a one-pot Suzuki coupling–C–H activation and two-step Suzuki coupling–Scholl reaction, respectively, with complete retention of configuration. The synthesized molecules differ in the fusing mode of [7]helicene units with pyrene via six- and seven-membered rings for **1** and **2**, respectively. There was a significant difference in the functional properties and enantiomerization barrier of both compounds because of their distinct molecular symmetry as well as fusing mode to pyrene moiety. The heptagon-containing molecule **2** showed remarkable photophysical and chiroptical properties with commendable configurational stability compared to **1** and pristine [7]helicene as well as its [5]helicene congener.



INTRODUCTION

Over the past decade, a number of trials have been made to ameliorate the functional properties of [n]helicenes¹ by stitching them with polycyclic aromatic hydrocarbons (PAHs). Significant attempts were made to improve the overall functional properties of [n]helicene-attached PAHs by combining the chiroptical properties of [n]helicene with photophysical properties of PAHs.² However, in the majority of cases the synthetic route suffered from the cumbersome separation of a stereoisomeric mixture, providing enantiopure compounds in limited quantities. On several occasions the configurational stabilities of these hybrid structures decreased drastically compared to their parent [n]helicenes, which ultimately limits further exploration.³ Recent studies from our group demonstrated that a large-scale stereospecific synthesis of helicene-fused PAHs⁴ and phthalocyanine⁵ with appropriate stereochemistry is feasible utilizing enantiopure starting materials with stereospecific synthetic strategies. In our previous report, we developed pyrene-fused methyl-capped [5]helicene compounds⁶ and studied their configurational stability as well as electronic and (chir)optical properties, which were remarkably superior to those of pristine [5]-helicene,⁷ [5]helicene-embedded nanographenes,^{2f,8} and other pyrene-based helicenes.⁹ But for practical applicability, further improvements on functional properties are desired. Recent investigations on [n]helicene–PAH hybrids show that higher homologues of [n]helicenes boost the chiroptical and electronic properties significantly.^{2d,e,10}

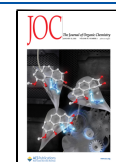
Herein, we report stereospecific syntheses of pyrene-fused [7]helicene compounds **1** and **2**, connected via hexagonal and heptagonal rings, respectively. The functional properties of **1** and **2** were thoroughly investigated by means of UV–vis absorption, emission, electronic circular dichroism (ECD), circularly polarized luminescence (CPL), and cyclic voltammetry (CV). Experimental data were supported by the quantum-chemical calculations—with a comparison to their [5]helicene congeners.⁶

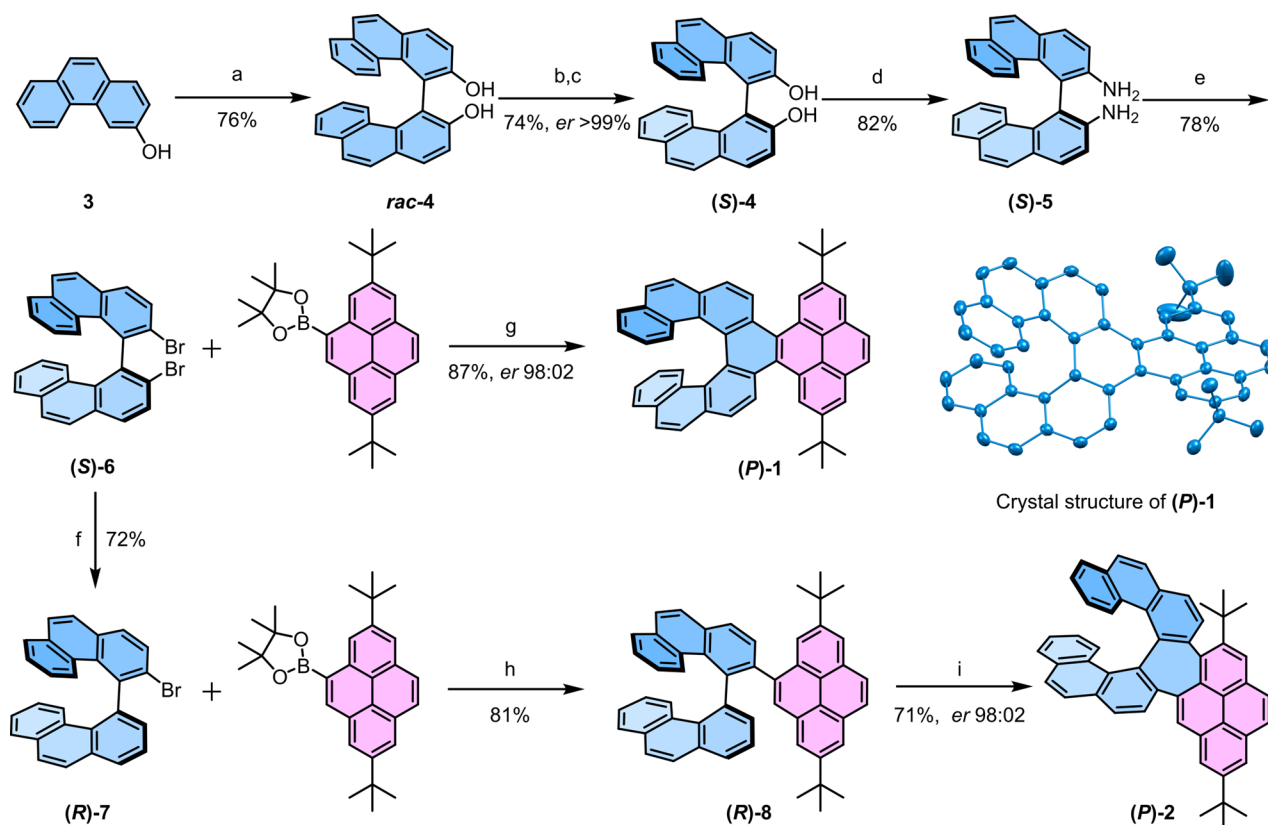
RESULTS AND DISCUSSION

The syntheses of enantiopure **1** and **2** from separate enantiomers (*R*- and *S*-) of 4,4'-biphenanthrene-3,3'-diol (**4**) (*er* > 99%) was accomplished as shown in Scheme 1. A chiral separation of *rac*-**4** was achieved with the aid of (1*S*)-10-camphorsulfonyl chloride acting as a chiral auxiliary following the known protocols.¹¹ The key precursor (*S*)-**6** was synthesized from (*S*)-**4** over two steps: (i) a functional group transformation from hydroxyl to amine using 2-bromopropionamide in an enantioselective switchable Smiles

Received: September 17, 2021

Published: January 6, 2022



Scheme 1. Stereospecific Synthesis^a of (*P*)-1 and (*P*)-2

^aStereospecific synthesis of (*P*)-1 and (*P*)-2: (a) Cu-tetramethylethylenediamine (TMEDA), DCM, 25 °C, 1 h, 76% yield. (b) (1*S*)-10-Camphorsulfonyl chloride, DCM/triethylamine, DMAP, 0 °C, 30 min, 86% yield of mixture of diastereomers, which were separated by column chromatography. (c) (+)-diastereomer (*er* 98:02), THF/MeOH, 90 °C, 15 h, 86% yield. (d) (i) 2-Bromopropionamide, K₂CO₃, KI, dimethylsulfoxide (DMSO), 50 °C, 8 h, (ii) KOH, 150 °C, 4 h, 82% yield; (e) NaNO₂, BrCCl₃, acetic acid (AcOH), DCM/H₂O (1:1), 25 °C, 1 h, 78% yield; (f) *n*-BuLi, THF, 4 h, 72% yield; (g) Pd(PPh₃)₄, K₂CO₃, THF/H₂O (3:1), 85 °C, 15 h, 87% yield (*er* 98:02); (h) Pd(PPh₃)₄, K₂CO₃, THF/H₂O (3:1), 85 °C, 2 h, 81% yield; (i) DDQ, Triflic acid, DCM, 0 °C, 4 h, 71% yield (*er* 98:02). The *M* enantiomers of **1** and **2** were duly synthesized from (*R*)-**6** with comparable yields and enantiopurity. ORTEP diagram of (*P*)-**1**. Thermal ellipsoids are shown at the 50% probability level. Hydrogen atoms are omitted for clarity.

rearrangement¹² with a yield of 82% and (ii) a Sandmeyer-type conversion of amine to bromine with BrCCl₃ (78%).¹³ Unlike our previous studies on [1,1'-binaphthalene]-2,2'-diamine, the iodination of diazonium intermediates of [4,4'-biphenanthrene]-3,3'-diamine ((*S*)-**5**) produced a mixture of over-iodinated product at the 9 and/or 10 position. A one-pot Suzuki coupling–C–H activation¹⁴ between (*S*)-**6** and 2-(2,7-di-*tert*-butylpyren-4-yl)-4,4,5,5-tetramethyl-1,3,2-dioxaborolane using [Pd(PPh₃)₄] and K₂CO₃ in a tetrahydrofuran (THF)/H₂O (3:1) mixture was executed in an enantioselective manner giving (*P*)-**1** (*er* 98:02) as the major product in excellent 87% yield along with ~9% of uncyclized (*R*)-**8**. A significant increase in the yield of cyclized (*P*)-**1** was observed compared to its [5]helicene congener where coupling was performed with an iodo counterpart.⁵ (*R*)-**8** was also synthesized from (*S*)-**6**—via a selective mono-debromination by lithiation with *n*-BuLi and an addition of MeOH/H₂O to give (*R*)-**7**—followed by a Suzuki coupling with 2-(2,7-di-*tert*-butylpyren-4-yl)-4,4,5,5-tetramethyl-1,3,2-dioxaborolane in 58% yield over two steps. A Scholl-type oxidative cyclodehydrogenation¹⁵ of (*R*)-**8** produced the intriguing (*P*)-**2** embodied with a heptagonal ring¹⁶ in 71% yield, while retaining the original configuration (*er* 98:02). Influenced by the higher aromaticity of the corresponding ring of pyrene, the unusual ring closure at

the 1 position of the pyrene moiety occurred selectively.¹⁷ The enantiopurity of **1** and **2** (*er* 98:02) is similar to that of (*S*)-**4** (*er* > 99%) indicating the exceptional stereospecificity of the overall reaction scheme. The (*M*)-enantiomers of both the compounds were synthesized from the corresponding (*R*)-**6** with comparable yields and enantiopurity.

The structures of **1** and **2** were validated by an unambiguous assignment of proton and carbon resonance signals to their respective atoms (Figure S11) with the help of COSY, NOESY, HMBC, and HSQC two-dimensional (2D) NMR experiments. The C₂ and C₁ symmetry of **1** and **2** clearly manifested from the 11 and 22 resonance signals, respectively, present in the aromatic region of ¹H NMR spectrum (Figures S12 and S18). Additionally, the structure of compound **1** was confirmed by single-crystal X-ray diffraction (Scheme 1). However, all the attempts to grow single crystals for **2** were unsuccessful. Therefore, to compare the geometrical features, the structure of both the compounds was optimized using density functional theory (DFT) at ωB97XD/6-31G(d,p). The main geometrical difference between these two compounds lies at the torsional twist in the inner helix and the distance between two terminal benzene rings. Because of the saddle-shaped geometry of the heptagonal ring, compound **2** showed a slightly higher torsional twist and, consequently, a longer

distance between two terminal rings (26.5° , 4.47 \AA) compared to that of **1** (23.9° , 3.77 \AA). The experimental NMR spectra were in harmony with the calculations (Table S6). In both compounds, six-membered rings showed negative NICS(1_{zz}) values in the range between -0.8 and -30.4 ppm correlating to their aromaticity (Table S4). The heptagonal ring in **2** showed a positive NICS(1_{zz}) value of 15.5 ppm justifying its antiaromatic character.¹⁸

To gain insights into the effect of ring fusion and π -extension on the inversion process and configurational stability, the kinetics measurements were performed at elevated temperatures. The configurational stability for **1** and **2** was evaluated using the Gibbs activation energy $\Delta G^\ddagger(T)$ for enantiomerization. The values of $\Delta G^\ddagger(T)$ of **1** and **2** were calculated by following the decay of the enantiomeric excess (*ee*) of the enantio-enriched samples at 438 K for **1** and 498 K for **2** over time (*t*) by high-performance liquid chromatography (HPLC) on a chiral stationary phase column (Supporting Information section S5). To our surprise, compound **1** showed a much smaller ΔG^\ddagger (438 K) of $34.1 \text{ kcal mol}^{-1}$, whereas **2** showed a slightly enhanced inversion barrier (ΔG^\ddagger (498 K) = $42.6 \text{ kcal mol}^{-1}$) compared to that of [7]helicene (ΔG^\ddagger (300 K) = $41.2 \text{ kcal mol}^{-1}$).¹⁹ The high configurational stability of **2** can be attributed to the additional steric effect from the neighboring *tert*-butyl group of the pyrene unit and the inclusion of a seven-membered ring instead of the typical six-membered ring. As per our previous studies on [5]helicenes,²⁰ the configurational stability for both **1** and **2** can be further improved by the introduction of suitable substituents in the inner helix. In addition to configurationally stable [7]helicene subunit, (*P*)-**1** also possesses two configurationally labile [4]helicenes that lead to three possible diastereomers (Figure S6). In the solution, all three diastereomers likely coexist in a dynamic equilibrium at room temperature, as any possibility of a diastereomeric mixture has been excluded by the ^1H NMR spectra as well as a chiral stationary-phase HPLC (Figure S4b). Concomitant with single-crystal X-ray structure, the DFT calculation showed that, among the three possible diastereomers, the one with the opposite helicity for [7]- and [4]helicene subunits is thermodynamically the most stable isomer. The bulky *tert*-butyl group in the bay region of compound **2** may also lead to another possible diastereomer (Figure S7). However, for steric reasons, it is unlikely that this diastereomer is formed during the reaction, which is 25.8 kcal/mol higher in energy.

The photophysical properties of **1** and **2** were investigated by UV–vis absorption and emission spectroscopy in dichloromethane (DCM) (Figure 1a). Both UV–vis absorption and fluorescence spectra for **1** and **2** showed considerable bathochromic shifts compared to [7]helicene and 2,7-di-*tert*-butylpyrene. Spectroscopic profiles are identical to those of a [5]helicene congener⁶ with an enhanced magnitude of molar extinction coefficients, which can be attributed to the extended π -conjugation. On the one hand, irrespective of their distinct absorption spectral features, both **1** and **2** showed similar optical energy gaps (2.83 – 2.85 eV), which are slightly higher than those of their [5]helicene congeners (2.79 – 2.80 eV).⁶ On the other hand, the energy gap is much lower compared to [7]helicene (3.06 eV)^{7,21} and 2,7-di-*tert*-butylpyrene (3.55 eV).²² Time-dependent (TD) DFT calculations provided further insights into electronic transitions. Irrespective of their different symmetry, both **1** and **2** showed similar characteristic low-energy transitions, mainly composed of

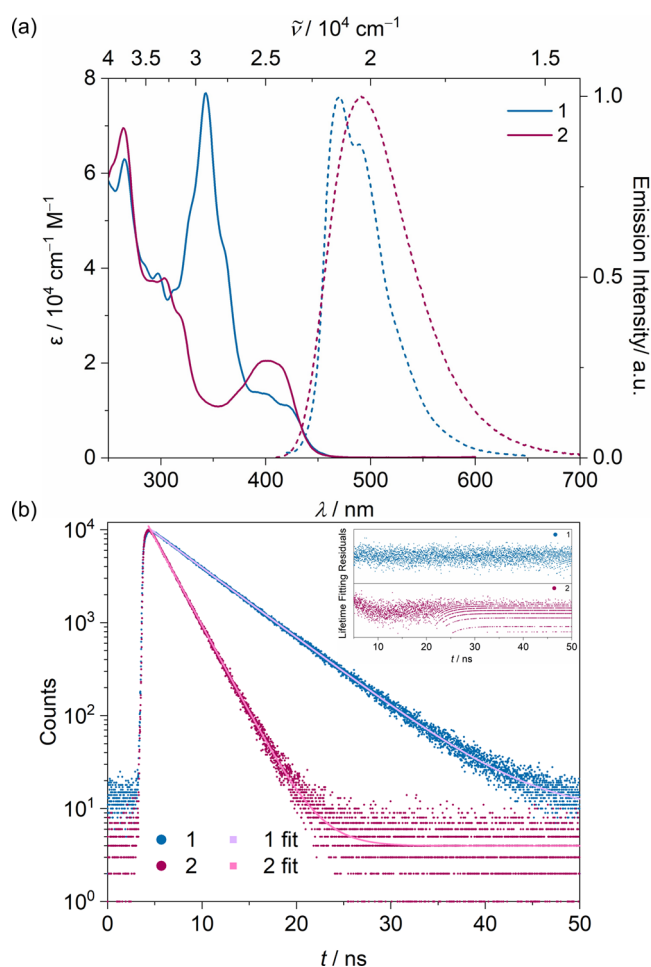


Figure 1. (a) UV–vis absorption (solid line) and emission (dashed line) spectra (excited at $29\,152 \text{ cm}^{-1}$ for **1** and at $24\,876 \text{ cm}^{-1}$ for **2**) of **1** and **2** in DCM ($c \approx 10^{-5} \text{ M}$). (b) Time-resolved fluorescence decay (excited at $24\,154 \text{ cm}^{-1}$) of **1** and **2** in DCM. (inset) Monoexponential fitting residuals of **1** and **2**.

highest occupied molecular orbital (HOMO) \rightarrow lowest unoccupied molecular orbital (LUMO) and HOMO \rightarrow LUMO+1/HOMO–1 \rightarrow LUMO transitions with oscillator strengths (*f*) of 0.14 and 0.27 for **1** and 0.57 and 0.02 for **2**, respectively (Figure S8, Table S3a). In addition to this, HOMO \rightarrow LUMO+2/HOMO–2 \rightarrow LUMO transitions also have a major contribution with oscillator strengths (*f*) of 0.83 in the case of **1**. The lowest energy transition in both **1** and **2** differ from that of [7]helicene, where it is mainly composed of HOMO \rightarrow LUMO+1/HOMO–1 \rightarrow LUMO and HOMO–2 \rightarrow LUMO transitions.⁷ Both the compounds appeared to be emissive in solution as well as solid state (Figures 1a and S2). In DCM, **1** and **2** exhibited distinct emission profiles with large Stokes shifts. The fluorescence spectrum of **2** (4509 cm^{-1}) showed an almost double Stokes shift than that of **1** (2476 cm^{-1}) indicating a much higher structural relaxation in the excited state of **2** due to the nonplanar heptagonal ring.

To understand the excited-state dynamics, the time-resolved fluorescence decay of **1** and **2** was measured in DCM using a pulsed laser light (excited at $24\,154 \text{ cm}^{-1}$) (Figure 1b). Decay curves of **1** and **2** were well-fitted with the monoexponential function giving lifetimes of 5.76 and 2.31 ns , respectively, both of which are much shorter than that of [7]helicene (13.8 ns). While the fluorescence quantum yield (FQY) for **1** (4%) is

Table 1. Summary of Optical and Electrochemical and Kinetics Parameters of **1**, **2**, and [7]Helicene

compound	E_{gr}^a eV	Φ_{FL}	τ_{FL} , ns	k_{FL}^b 10^6 s $^{-1}$	k_{NR}^c 10^7 s $^{-1}$	g_{abs}^d 10^{-3}	g_{lum}^e 10^{-3}	$E_{ox}^{1/2,f}$ V	E_{HOMO}^g eV	ΔG^\ddagger (T), kcal mol $^{-1}$
1	2.83	0.04	5.76	6.94	16.67	2.64–7.47	1.27	0.56	–5.72	34.1 (438 K)
2	2.85	0.34	2.31	147.18	28.57	2.95–7.96	2.64	0.41	–5.57	42.6 (498 K)
[7]helicene ^h	3.06	0.02	13.8	1.45	7.10				–5.36 ⁱ	41.2 (298 K) ^j
2,7-di- <i>tert</i> -butylpyrene ^k	3.55	0.12								

^aEstimated from a crossing of absorption and fluorescence spectra. ^bRate constant for the radiative decay. ^cRate constant for the nonradiative decay. ^dWavelength range from 250 to 450 nm. ^eWavelength range from 450 to 600 nm. ^fVolts vs Fc/Fc⁺ in DCM. ^g $E_{HOMO} = -(E_{ox}^{1/2}[\text{vs Fc/Fc}^+] + 5.16)$. ^hRefs 7 and 21. ⁱRef 25. ^jRef 19. ^kRef 9c.

twice that of [7]helicene (2%), **2** showed a 17-fold increase (34%).²¹ The very high FQY of **2** compared to that of **1** can be explained because of a larger oscillator strength for $S_0 \rightarrow S_1$ transition and a much higher radiative rate constant (Table 1). The fluorescence quantum yield for **2** is among one of the highest reported for [7]helicene-embedded nanographenes.^{2e,23} Fluorescence measurements in the solid state are largely dependent on the texture of the compound, which reasonably affects the quantum yield. As compared to solution, crystalline **1** retained the fluorescence quantum yield (3%), but powdery **2** suffered a nearly fourfold aggregation caused by fluorescence quenching (9%).²⁴

The redox properties of compounds **1** and **2** were evaluated by means of cyclic voltammetry (CV) and differential pulse voltammetry (DPV) in dichloromethane (Figure S1). The CV plot showed one and two (quasi)reversible oxidation processes for **1** and **2**, respectively. The first oxidation couples for **1** and **2** were observed at 0.56 and 0.41 V, respectively, with Fc/Fc⁺ as an internal reference. Correspondingly, the estimated HOMO energy for **1** (–5.72 eV) is lower than that of **2** (–5.57 eV). The trend is duly followed from their [5]helicene congeners with marginally reduced HOMO energy.

Furthermore, chiroptical properties were investigated by ECD and CPL measurements. An absolute configuration for enantiomers of **1** and **2** was assigned with the aid of TD-DFT calculated CD spectra for the *P* enantiomer (Figure S9). The *P* and *M* enantiomers for both **1** and **2** showed complementary mirror image CD spectra with opposite Cotton effects in the UV–vis region (Figure 2a). The Cotton effect of the lowest energy transition differs in both compounds; while **1** showed a weak and positive Cotton effect, **2** showed relatively larger and negative Cotton effect. A similar trend was also observed in our previous studies with [5]helicene congeners; however, as anticipated the CD signals are significantly enhanced by replacing the [5]helicene with the [7]helicene substructure. The absorption dissymmetry factor (g_{abs}) increased considerably from the [5] to [7]helicene congener for **1** (2.5×10^{-3} at 421 nm) and **2** (2.7×10^{-3} at 402 nm) (Figure 2b). Both **1** and **2** showed good CPL responses, as *P* and *M* enantiomers showed complementary mirror images, which are in accord with corresponding CD signals (Figure 2a). The luminescence dissymmetry factor (g_{lum}) for **2** (2.6×10^{-3} at 490 nm) is slightly higher than that of **1** (1.3×10^{-3} at 471 nm) (Figure 2b), while both of their [5]helicene counterparts exhibit a similar g_{lum} (2.1×10^{-3}) (Figure S3b). The g_{lum}/g_{abs} value as a measure of the excited-state relaxation for **1** (0.53) closely resembles the linearly fitted regression value of 0.61 for helicenes and heliceneoids,²⁶ while for **2** it is significantly higher and close to unity (0.94), corroborating its structural rigidity²⁷ and making it a strong contender for further exploration. In order to quantify the efficiency of a CPL emitter, recently Bari et al. coined the term “Brightness of CPL” following the

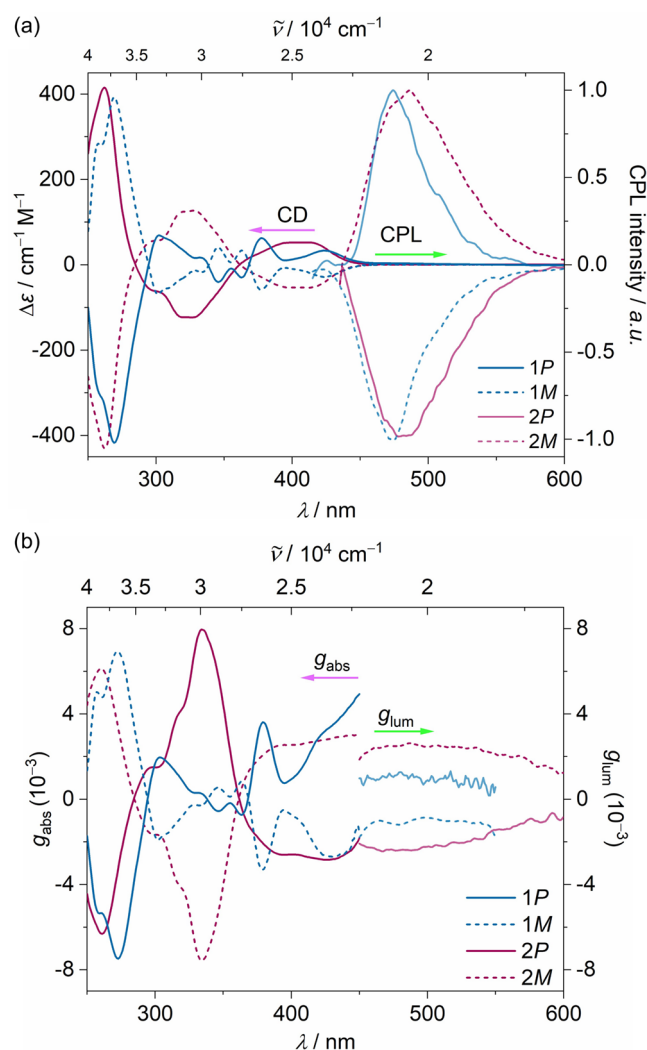


Figure 2. (a) Electronic CD spectra (250–450 nm) and CPL spectra (450–600 nm) of *P* and *M* enantiomers of **1** and **2** in DCM at 25 °C ($c \approx 10^{-5}$ M). (b) Absorption dissymmetry factor (g_{abs}) (250–450 nm) and luminescence dissymmetry factor (g_{lum}) (450–600 nm) of **1** and **2**.

principle of fluorescence brightness, which is defined as product of molar extinction coefficient (ϵ) and quantum efficiency (ϕ) with emission dissymmetry factor (g_{lum})²⁸

$$B_{cpl} = \epsilon\phi \frac{g_{lum}}{2}$$

The calculated CPL brightness for compound **1** is 0.28 M $^{-1}$ cm $^{-1}$, whereas **2** showed a much higher brightness (9.21 M $^{-1}$ cm $^{-1}$) that was nearly twice that of its [5]helicene congener.

The latter is one of the highest reported CPL brightnesses compared to homologues [7]helicene compounds.²⁸

CONCLUSION

In conclusion, a straightforward stereospecific pathway has been shown for pyrene-fused [7]helicene compounds **1** and **2** with a fully retained enantiomeric excess. On the basis of symmetry and fusion mode to pyrene, both compounds showed distinct functional properties, while the heptagon-fused compound **2** stands out with enhanced (chir)optical properties and configurational stability. Moreover the CPL brightness for **2** is significantly enhanced compared to that of the [5]helicene congener. In the future, we aim to achieve the stereospecific synthesis of pyrene-bridged manifold helicenes incorporating multiple heptagonal rings with further improved photophysical and chiroptical properties.

EXPERIMENTAL PROCEDURES

General Information. All chemicals and solvents were purchased from commercial sources and were used without further purification unless stated otherwise. Compounds **4–6** were prepared with a slight modification of the literature procedure,^{11,29} while 2-(2,7-di-*tert*-butylpyren-4-yl)-4,4,5,5-tetramethyl-1,3,2-dioxaborolane was synthesized according to known literature protocols.³⁰ The reactions and experiments sensitive to dioxygen were performed using Schlenk techniques and with nitrogen-saturated solvents. All the glassware and NMR tubes prior to use for experiments were dried in an oven at 80 °C for 12 h.

NMR Spectroscopy. The NMR experiments were performed at 298 K on NMR spectrometers operating at 400 MHz proton and 101 MHz ¹³C frequencies. Standard pulse sequences were used, and the data were processed using twofold zero-filling in the indirect dimension for all 2D experiments. Chemical shifts (δ) are reported in parts per million relative to the solvent residual peak (¹H and ¹³C NMR, respectively): CDCl₃ (δ = 7.26 and 77.2 ppm), and *J* values are given in hertz. Structural assignments for compounds **1** and **2** were made with additional information from gCOSY, gNOESY, gHSQC, and gHMBC experiments.

High-Resolution Mass Spectrometry. The electrospray ionization high-resolution mass spectrometry (ESI-HRMS) and atmospheric pressure chemical ionization (APCI-HRMS) were measured on a Bruker micrOTOF, while the matrix-assisted laser desorption/ionization time-of-flight (MALDI-TOF) HRMS spectra were measured on Bruker ultrafleXtreme. *trans*-2-[3-(4-*tert*-Butylphenyl)-2-methyl-2-propenyldiene]malononitrile (DCTB) dissolved in chloroform was used as supporting matrix in the MALDI-TOF-HRMS measurement.

UV-Vis and Fluorescence Spectroscopy. UV-Vis spectra were measured on a JASCO V-670 spectrometer, while emission spectra were measured on an Edinburgh FLS 980 photoluminescence spectrometer. The fluorescence lifetimes were measured in DCM using a 418.6 nm pulsed laser diode with a pulse frequency of 1/50 ns. The fluorescence quantum yields were measured in DCM using the same spectrometer with a 450 W xenon arc lamp as the light source and a calibrated integrating sphere. The solid-state fluorescence quantum yield was measured with a Hamamatsu Absolute PL Quantum Yield Measurement System CC9920–02 upon excitation at 350 and 400 nm. The system is composed of a 150 W continuous wave (CW) xenon lamp as the excitation source, a monochromator (250–700 nm, full width at half-maximum (fwhm) 10 nm), an integrating sphere, and a multichannel spectrometer capable of simultaneously measuring multiple wavelengths between 300 and 950 nm.

CPL and CD Spectroscopy. CPL and CD spectra were recorded with a customized JASCO CPL-300/J-1500 hybrid spectrometer.

Cyclic Voltammetry. Cyclic voltammetry experiments were performed in DCM with 0.1 M [Bu₄N][PF₆] as the supporting

electrolyte using a Gamry Instruments Reference 600 potentiostat. A standard three-electrode cell configuration was employed using a platinum disk working electrode, a platinum wire counter electrode, and Ag/AgCl serving as the reference electrode. The redox potentials were referenced to the ferrocene (Fc)/ferrocenium (Fc⁺) redox couple.

Single-Crystal X-ray Crystallography. The crystal data of **1** were collected on a Rigaku XtaLAB Synergy-S diffractometer with an Hybrid Pixel Array Detectors (HPAD) and multilayer mirror monochromatic Cu K α radiation. The structure was solved using an intrinsic phasing method,³¹ refined with the ShelXL program,³² and expanded using Fourier techniques. All non-hydrogen atoms were refined anisotropically. Hydrogen atoms were included in structure factors calculations. All hydrogen atoms were assigned to idealized geometric positions. The geometry of solvent molecules (hexane) was constrained using restraints on 1–2 and 1–3 distances. The displacement parameters of atoms in disordered residues were restrained to the same value with similarity restraint. Solvent molecules were refined isotropically.

Crystal data for **1**: C₅₈H₅₄, *M_r* = 751.01, orange needle, 0.338 × 0.040 × 0.029 mm³, space group C2/c, *a* = 21.9510(2) Å, *b* = 21.30729(17) Å, *c* = 18.62947(18) Å, α = 90°, β = 108.5271(10)°, γ = 90°, *V* = 8261.74(14) Å³, *Z* = 8, ρ_{calc} = 1.208 g·cm⁻³, μ = 0.508 mm⁻¹, *F*(000) = 3216, *T* = 100.01(10) K, *R*₁ = 0.0670, *wR*₂ = 0.1550, 8923 independent reflections [$2\theta \leq 160.498^\circ$] and 554 parameters.

Quantum-Chemical Calculations. DFT calculations were performed using the Gaussian 16 suite.³³ Geometries were optimized using the ω B97XD functional and the 6-31G(d,p) basis set in the gas phase. A frequency analysis was performed to verify the stationary-state geometry. In all cases no imaginary frequency was found. TD-DFT calculations were performed on ω B97XD/6-31G(d,p) optimized geometries at the B3LYP/6-31g(d,p) level. The effect of the solvent was accounted for using the polarizable continuum model (PCM) (with dichloromethane as the solvent).

Synthesis. 16,21-Di-*tert*-butylbenzo[*a*]naphtho[8,1,2-*jk*]-phenanthro[3,4-*s*]picene ((*P*)-**1**). In a Schlenk tube (S)-**6** (88.0 mg, 0.20 mmol, 1.0 equiv) and 2-(2,7-di-*tert*-butylpyren-4-yl)-4,4,5,5-tetramethyl-1,3,2-dioxaborolane (89.5 mg, 0.20 mmol, 1.0 equiv) were dissolved in THF (3 mL); K₂CO₃ (112.3 mg, 0.81 mmol, 4.0 equiv) was dissolved in water (1 mL), and both solutions were degassed for 10 min separately and mixed together. To this mixture Pd(PPh₃)₄ (15.5 mg, 0.015 mmol, 7.5 mol %) was added under a nitrogen flow and degassed again for 10 min. The reaction flask was then sealed and heated at 85 °C for 15 h in an oil bath. The reaction was quenched by adding water and extracted with ethyl acetate, dried over anhydrous sodium sulfate. The solvent was evaporated under reduced pressure using a rotary evaporator, and the crude product was purified by column chromatography on silica gel using 1% ethyl acetate in petroleum ether to yield 99.4 mg (87%) as a green fluorescent crystalline solid (*P*)-**1**. Melting point 391–394 °C. *er* 98:02. Together with (*P*)-**1**, ~9% of (*R*)-**8** was also isolated in the above reaction as a side product. ¹H NMR (400 MHz, CDCl₃, 25 °C): δ [ppm] = 9.30 (d, *J* = 1.7 Hz, 2H), 9.09 (d, *J* = 8.6 Hz, 2H), 8.28 (d, *J* = 1.7 Hz, 2H), 8.16–8.14 (m, 4H), 7.77 (d, *J* = 8.5 Hz, 2H), 7.52 (d, *J* = 8.4 Hz, 2H), 7.36 (d, *J* = 8.4 Hz, 4H), 6.99 (t, *J* = 7.9 Hz, 2H), 6.57 (t, *J* = 8.4 Hz, 2H), 1.73 (s, 18H). ¹³C{¹H}NMR (101 MHz, CDCl₃, 25 °C): δ [ppm] = 148.3, 132.1, 131.1, 131.1, 129.6, 129.5, 128.8, 128.7, 128.1, 127.7, 127.7, 126.9, 125.8, 125.6, 125.2, 125.1, 125.0, 124.9, 123.7, 123.5, 122.1, 35.7, 32.1. HRMS (MALDI-TOF): *m/z*: [M] Calcd for [C₅₂H₄₀] 664.3130; Found 664.3116.

9,14-Di-*tert*-butyldiphenanthro[3',4':4,5;4'',3':6,7]cyclohepta[1,2,3-*cd*]pyrene ((*P*)-**2**). In a Schlenk tube (*R*)-**8** (50.0 mg, 0.075 mmol, 1.0 equiv) was dissolved in dry DCM and stirred at 0 °C for 10 min. The solution was added dropwise to a flask containing 2,3-dichloro-5,6-dicyano-1,4-benzoquinone (DDQ) (17.1 mg, 0.075 mmol, 1.0 equiv) and stirred at 0 °C for 20 min followed by an addition of triflic acid (7.95 μ L, 8.90 μ mol, 12 mol %). The reaction mixture continued to stir at 0 °C for 4 h under a nitrogen atmosphere. The reaction was quenched by a saturated NaHCO₃ solution; the organic layer was extracted with DCM and dried over anhydrous

sodium sulfate. The solvent was evaporated under reduced pressure using a rotary evaporator, and the crude product was purified by column chromatography on silica gel using 1% ethyl acetate in petroleum ether to yield 35.4 mg (71%) as the green fluorescent solid of (*P*)-2. Melting point 258–260 °C. *er* 98:02. ¹H NMR (400 MHz, CDCl₃, 25 °C): δ [ppm] = 8.58 (s, 1H), 8.39 (s, 1H), 8.25 (d, *J* = 1.7 Hz, 1H), 8.16 (d, *J* = 1.8 Hz, 1H), 8.03–8.01 (m, 2H), 7.98–7.96 (m, 1H), 7.74–7.66 (m, 3H), 7.53 (d, *J* = 8.7 Hz, 1H), 7.48 (d, *J* = 8.6 Hz, 1H), 7.44 (dd, *J* = 8.2, 1.4 Hz, 1H), 7.41–7.34 (m, 2H), 7.11–7.06 (m, 2H), 7.01 (t, *J* = 6.8 Hz, 1H), 6.96 (d, *J* = 8.3 Hz, 1H), 6.66–6.59 (m, 2H), 6.43 (d, *J* = 8.4 Hz, 1H), 1.67 (s, 9H), 1.57 (s, 9H). ¹³C{¹H} NMR (101 MHz, CDCl₃, 25 °C): δ [ppm] = 149.2, 148.5, 144.0, 143.7, 140.0, 137.1, 136.5, 134.3, 134.1, 133.9, 133.6, 132.9, 132.5, 132.3, 131.9, 131.2, 130.9, 130.7, 130.6, 130.3, 130.0, 129.1, 129.1, 128.2, 127.9, 127.7, 127.5, 127.3, 127.2, 127.1, 126.8, 126.6, 126.1, 125.7, 125.4, 124.3, 124.2, 123.1, 122.9, 121.9, 121.6, 38.0, 35.3, 35.2, 32.0. HRMS (MALDI-TOF): *m/z*: [M] Calcd for [C₅₂H₄₀] 664.3130; Found 664.3128.

rac-[4,4'-Biphenanthrene]-3,3'-diol ((±)-4). 3 (500 mg, 2.6 mmol) was dissolved in dry DCM (8 mL), and then Cu-TMEDA (59 mg, 5.0 mol %) was added in portions over 10 min to the flask. The reaction mixture was then stirred for 50 min at 25 °C and quenched by 1 M HCl followed by an extraction with 25 mL of DCM. The organic layer was dried over anhydrous sodium sulfate, and the solvent was removed under reduced pressure using a rotary evaporator. The crude product was purified by column chromatography on silica gel using 15% ethyl acetate in petrol ether to yield 378 mg (76%) of (±)-4 as a white solid. Melting point 124–126 °C. ¹H NMR (400 MHz, CDCl₃, 25 °C): δ [ppm] = 8.09 (d, *J* = 8.7 Hz, 2H), 8.03 (d, *J* = 8.7 Hz, 2H), 7.84 (t, *J* = 8.2 Hz, 4H), 7.74 (d, *J* = 8.7 Hz, 2H), 7.45 (d, *J* = 8.6 Hz, 2H), 7.40 (m, 2H), 6.95 (m, 2H), 5.03 (s, 2H). ¹³C{¹H} NMR (101 MHz, CDCl₃, 25 °C): δ [ppm] = 153.0, 133.9, 132.5, 130.1, 129.8, 129.1, 128.9, 127.7, 127.0, 126.5, 126.3, 125.1, 117.7, 116.6. HRMS (ESI): *m/z*: [M–H][–] Calcd for [C₂₈H₁₇O₂] 385.1234; Found 385.1246.

rac-[4,4'-Biphenanthrene]-3,3'-dicamphorsulfonicester. *rac*-4 (12.0 g, 31.1 mmol, 1.0 equiv) was dissolved in dry DCM (200 mL) and triethylamine (20 mL, 140 mmol, 4.5 equiv) followed by an addition of 4-dimethylaminopyridine (DMAP) (2.28 g, 18.7 mmol, 0.6 equiv). The reaction mixture was then stirred at 0 °C for 30 min. (1*S*)-(+)-10-Camphorsulfonyl chloride (27.3 g, 108 mmol, 3.5 equiv) was dissolved in 45 mL of dry DCM at 0 °C and added to the reaction mixture dropwise. The reaction mixture was stirred at 0 °C for 20 min and then warmed to 25 °C and stirred for 15 h. The reaction was quenched with water, and the product was extracted with DCM and dried over anhydrous sodium sulfate. The solvent was removed under reduced pressure using a rotary evaporator. The crude product was purified by column chromatography on silica gel using 0.5% ethyl acetate in DCM to isolate both diastereomers separately. Yield: 21.7 g (86%) (9.5 g of *P* and 12.2 g of *M*) as a white crystalline solid. *er* 98:02. Melting point 129–131 °C. ¹H NMR (400 MHz, CDCl₃, 25 °C): δ [ppm] = 8.11 (d, *J* = 8.6 Hz, 1H), 8.06 (d, *J* = 8.7 Hz, 1H), 7.92–7.86 (m, 3H), 7.72 (d, *J* = 8.7 Hz, 1H), 7.46 (t, *J* = 7.9 Hz, 1H), 7.02 (t, *J* = 7.9 Hz, 1H), 2.42 (d, *J* = 14.8 Hz, 1H), 2.27–2.20 (m, 1H), 2.02–1.93 (m, 2H), 1.89 (d, *J* = 14.8 Hz, 1H), 1.78 (d, *J* = 18.4 Hz, 1H), 1.32–1.17 (m, 3H), 0.82 (s, 3H), 0.63 (s, 3H). ¹³C{¹H} NMR (101 MHz, CDCl₃, 25 °C): δ [ppm] = 213.5, 145.7, 133.5, 131.8, 131.2, 130.8, 130.6, 129.0, 128.7, 127.4, 127.3, 126.8, 126.7, 125.8, 121.5, 57.6, 48.2, 47.8, 42.8, 42.4, 26.9, 24.6, 19.5, 19.4. HRMS (ESI): *m/z*: [M + Na⁺] Calcd for [C₄₈H₄₆O₈S₂Na] 837.2501; Found 837.2526.

(*S*)-[4,4'-Biphenanthrene]-3,3'-diol ((*S*)-4). (*S*)-[4,4'-Biphenanthrene]-3,3'-dicamphorsulfonicester (2.0 g, 2.7 mmol) was dissolved in THF (40 mL), MeOH (20 mL), and 5 M NaOH (20 mL) and refluxed at 90 °C in an oil bath for 15 h. Then 1 M hydrochloric acid was added to the reaction mixture until it was acidic (pH 3–4). The reaction mixture was then concentrated by evaporating methanol under reduced pressure using a rotary evaporator, and the product was extracted with DCM, dried over anhydrous sodium sulfate. The solvent was then removed under reduced pressure, and the crude

product was purified by column chromatography on silica gel using 5% ethyl acetate in petroleum ether to yield 1.08 g (86%) of (*S*)-4 as white crystalline solid. *er* 99:01. Melting point 124–126 °C. ¹H NMR (400 MHz, CDCl₃, 25 °C): δ [ppm] = 8.09 (d, *J* = 8.7 Hz, 2H), 8.03 (d, *J* = 8.7 Hz, 2H), 7.84 (t, *J* = 8.2 Hz, 4H), 7.74 (d, *J* = 8.7 Hz, 2H), 7.45 (d, *J* = 8.6 Hz, 2H), 7.40 (m, 2H), 6.95 (m, 2H), 5.03 (s, 2H). ¹³C{¹H} NMR (101 MHz, CDCl₃, 25 °C): δ [ppm] = 153.0, 133.9, 132.5, 130.1, 129.8, 129.1, 128.9, 127.7, 127.0, 126.5, 126.3, 125.1, 117.7, 116.6. HRMS (ESI): *m/z*: [M–H][–] Calcd for [C₂₈H₁₇O₂] 385.1234; Found 385.1246.

(*S*)-[4,4'-Biphenanthrene]-3,3'-diamine ((*S*)-5). K₂CO₃ (1.07 g, 7.7 mmol, 3.0 equiv) and 2-bromopropionamide (1.18 g, 7.7 mmol, 3.0 equiv) were dissolved in DMSO (5 mL) and stirred for 20 min at 25 °C. KI (42.9 mg, 0.25 mmol, 0.1 equiv) was added to the solution and stirred for 10 min. (*S*)-4 (1.0 g, 2.59 mmol, 1.0 equiv) was added to the reaction mixture, which was stirred for 8 h at 55 °C in an oil bath. Once all the starting material was consumed, as confirmed by thin-layer chromatography (TLC), KOH (1.74 g, 31.05 mmol, 12 equiv) was added to the reaction mixture and heated at 150 °C for 4 h in an oil bath. The reaction was then quenched with water and extracted with ethyl acetate. The solvent was removed under reduced pressure using a rotary evaporator, and the crude product was purified by column chromatography on silica gel using 40% ethyl acetate in petroleum ether to yield 816 mg (82%) as an off-white solid (*S*)-5. Melting point 111–113 °C. ¹H NMR (400 MHz, CDCl₃, 25 °C): δ [ppm] = 8.24 (d, *J* = 8.7 Hz, 2H), 7.89 (d, *J* = 8.5 Hz, 2H), 7.78 (d, *J* = 8.8 Hz, 4H), 7.60 (d, *J* = 8.7 Hz, 2H), 7.35 (t, *J* = 7.3 Hz, 2H), 7.16 (d, *J* = 8.4 Hz, 2H), 6.92 (t, *J* = 7.8 Hz, 2H), 3.56 (s, 4H). The broad amine peak can be seen around 3.56 ppm. ¹³C{¹H} NMR (101 MHz, CDCl₃, 25 °C): δ [ppm] = 143.2, 133.9, 130.8, 130.7, 130.1, 128.5, 128.1, 127.9, 126.5, 125.9, 125.4, 124.6, 119.3, 118.1. HRMS (ESI): *m/z*: [M + Na⁺] Calcd for [C₂₈H₂₀N₂Na] 407.1519; Found 407.1541.

3,3'-Dibromo-4,4'-biphenanthrene ((*S*)-6). (*S*)-5 (1.0 g, 2.6 mmol, 1.0 equiv) and NaNO₂ (1.8 g, 26.0 mmol, 10.0 equiv) were dissolved in dry DCM (8 mL) followed by the dropwise addition of BrCCl₃ (1.2 mL, 10.4 mmol, 4.0 equiv). Eight milliliters of H₂O was added to the reaction mixture and stirred at 25 °C for 5 min. Then glacial AcOH (2.9 mL, 52.1 mmol, 20.0 equiv) was added and stirred at 25 °C for 1 h. The reaction was quenched by adding a sodium thiosulfate solution, and the organic layer was extracted with DCM. The solvent was removed under reduced pressure using a rotary evaporator, and the crude product was purified by column chromatography on silica gel using 1% ethyl acetate in petroleum ether to yield 1.04 g (78%) of (*S*)-6 as a white powder. Melting point 191–193 °C. ¹H NMR (400 MHz, CDCl₃, 25 °C): δ [ppm] = 7.98–7.93 (m, 4H), 7.89–7.82 (m, 6H), 7.79 (d, *J* = 8.7 Hz, 2H), 7.39 (t, *J* = 8.7 Hz, 2H), 6.93 (t, *J* = 8.7 Hz, 2H). ¹³C{¹H} NMR (101 MHz, CDCl₃, 25 °C): δ [ppm] = 141.3, 133.5, 133.2, 132.0, 131.4, 130.7, 130.3, 129.0, 128.8, 127.5, 126.9, 126.7, 125.8, 124.9. HRMS (APCI): *m/z*: [M + H⁺] Calcd for [C₂₈H₁₇Br₂] 510.9697; Found 510.9670.

3-Dibromo-4,4'-biphenanthrene ((*R*)-7). (*S*)-6 (280 mg, 0.55 mmol, 1.0 equiv) was dissolved in dry THF (20 mL), degassed, and stirred at –78 °C for 1 h. *n*-BuLi (0.22 mL, 2.5 M in hexane, 1.0 equiv) was added dropwise, and the reaction mixture was stirred for 4 h at –78 °C. Once the lithiated product formation was confirmed by TLC, the reaction was quenched with a methanol (MeOH) and water mixture and warmed to 25 °C. The organic layer was extracted with ethyl acetate, and the solvent was removed under reduced pressure using a rotary evaporator. The crude product was purified by column chromatography on silica gel using 1% ethyl acetate in petroleum ether to yield 170 mg (72%) of (*R*)-7 as a white powder. Melting point 113–115 °C. ¹H NMR (400 MHz, CDCl₃, 25 °C): δ [ppm] = 8.09–8.03 (m, 2H), 7.95–7.80 (m, 8H), 7.76 (d, *J* = 8.8 Hz, 1H), 7.63 (t, *J* = 8.0 Hz, 1H), 7.43 (t, *J* = 8.0 Hz, 1H), 7.35 (t, *J* = 8.0 Hz, 1H), 7.16 (d, *J* = 8.7 Hz, 1H), 7.06–7.01 (m, 1H), 6.90–6.84 (m, 1H). ¹³C{¹H} NMR (101 MHz, CDCl₃, 25 °C): δ [ppm] = 142.5, 141.7, 133.9, 133.8, 133.4, 133.1, 131.4, 130.9, 130.8, 130.4, 129.8, 129.8, 129.5, 128.8, 128.7, 128.7, 128.1, 128.0, 127.8, 127.3, 126.6, 126.5, 126.1, 125.4, 125.2. HRMS (APCI): *m/z*: [M + H⁺] Calcd for [C₂₈H₁₈Br] 433.0599; Found 433.0592.

4-([4,4'-Biphenanthren]-3-yl)-2,7-di-tert-butylpyrene ((R)-8). In a Schlenk tube (R)-7 (120.0 mg, 0.28 mmol, 1.0 equiv) and 2-(2,7-di-tert-butylpyren-4-yl)-4,4,5,5-tetramethyl-1,3,2-dioxaborolane (122.0 mg, 0.028 mmol, 1.0 equiv) were dissolved in dry THF (3 mL); K_2CO_3 (153.1 mg, 1.11 mmol, 4 equiv) was dissolved in water (1 mL), and both solutions were degassed for 10 min separately and mixed together. To this mixture $Pd(PPh_3)_4$ (24.0 mg, 0.02 mmol, 7.5 mol %) was added under a nitrogen flow and degassed again for 10 min. The reaction flask was then sealed and heated at 85 °C for 2 h in an oil bath. The reaction was quenched by adding water, and the organic layer was extracted with ethyl acetate, dried over anhydrous sodium sulfate. The solvent was evaporated under reduced pressure using a rotary evaporator, and the crude product was purified by column chromatography on silica gel using 1% ethyl acetate in petroleum ether to yield 149.8 mg (81%) as a clear white oil of (R)-8. Melting point 164–166 °C. 1H NMR (400 MHz, $CDCl_3$, 25 °C): δ [ppm] = 8.47 (d, J = 8.5 Hz, 1H), 8.27 (d, J = 8.3 Hz, 1H), 8.17 (d, J = 8.1 Hz, 1H), 8.06 (d, J = 8.9 Hz, 1H), 7.98–7.91 (m, 4H), 7.84–7.78 (m, 3H), 7.68 (d, J = 8.0 Hz, 1H), 7.58 (t, J = 7.9 Hz, 1H), 7.41 (t, J = 8.0 Hz, 1H), 7.36 (d, J = 1.8 Hz, 1H), 7.23 (t, J = 8.5 Hz, 1H), 7.17–7.11 (m, 2H), 7.06–7.04 (m, 2H), 6.98 (d, J = 8.9 Hz, 1H), 6.93 (t, J = 8.6 Hz, 1H), 6.79 (t, J = 7.6 Hz, 1H), 6.67 (s, 1H), 1.47 (s, 9H), 1.34 (s, 9H). $^{13}C\{^1H\}$ NMR (101 MHz, $CDCl_3$, 25 °C): δ [ppm] = 147.9, 147.2, 142.1, 140.2, 139.3, 137.4, 134.1, 134.0, 133.3, 132.7, 131.8, 131.3, 130.4, 130.3, 130.3, 130.1, 130.0, 129.9, 129.2, 129.2, 128.8, 128.5, 128.4, 128.2, 128.1, 128.0, 127.8, 127.7, 127.3, 127.3, 127.1, 126.9, 126.6, 126.3, 126.2, 126.0, 125.9, 125.5, 123.7, 122.1, 122.0, 121.8, 121.4, 121.2, 121.1, 32.0, 31.9. HRMS (MALDI-TOF): m/z : [M] Calcd for $[C_{52}H_{42}]$ 666.3287; Found 666.3352.

■ ASSOCIATED CONTENT

SI Supporting Information

The Supporting Information is available free of charge at <https://pubs.acs.org/doi/10.1021/acs.joc.1c02281>.

Cyclic voltammograms, solid-state fluorescence spectra, CPL data for [5]helicene congeners, chiral stationary-phase HPLC plots, crystallographic details and ORTEP diagram, kinetics data, 1H and $^{13}C\{^1H\}$ NMR spectra, HRMS plots, and details of (TD)DFT calculations including Cartesian coordinates of optimized geometries (PDF)

Accession Codes

CCDC 2103307 contains the supplementary crystallographic data for this paper. These data can be obtained free of charge via www.ccdc.cam.ac.uk/data_request/cif, or by emailing data_request@ccdc.cam.ac.uk, or by contacting The Cambridge Crystallographic Data Centre, 12 Union Road, Cambridge CB2 1EZ, UK; fax: + 44 1223 336033.

■ AUTHOR INFORMATION

Corresponding Author

Prince Ravat – Institut für Organische Chemie, Universität Würzburg, D-97074 Würzburg, Germany; orcid.org/0000-0002-7553-9188; Email: princekmar.ravat@uniwuerzburg.de

Authors

Asim Kumar Swain – Institut für Organische Chemie, Universität Würzburg, D-97074 Würzburg, Germany

Krzysztof Radacki – Institut für Anorganische Chemie, Universität Würzburg, D-97074 Würzburg, Germany;

orcid.org/0000-0003-3088-6327

Holger Braunschweig – Institut für Anorganische Chemie, Universität Würzburg, D-97074 Würzburg, Germany;

orcid.org/0000-0001-9264-1726

Complete contact information is available at:

<https://pubs.acs.org/10.1021/acs.joc.1c02281>

Author Contributions

The manuscript was written through contributions of all authors.

Funding

This project received funding from Deutsche Forschungsgemeinschaft (DFG) (Project No. 448604676). The CPL/CD hybrid spectrometer was funded by the DFG (Project No. 444286426).

Notes

The authors declare no competing financial interest.

■ ACKNOWLEDGMENTS

P.R. thanks Julius-Maximilians-Universität Würzburg for “Excellent Ideas” program. P.R. and A.K.S. sincerely thank Prof. C. Lambert (University of Würzburg) for generously supporting our research. We thank T. Schembri and M. Stolte (University of Würzburg) for solid-state fluorescence measurements.

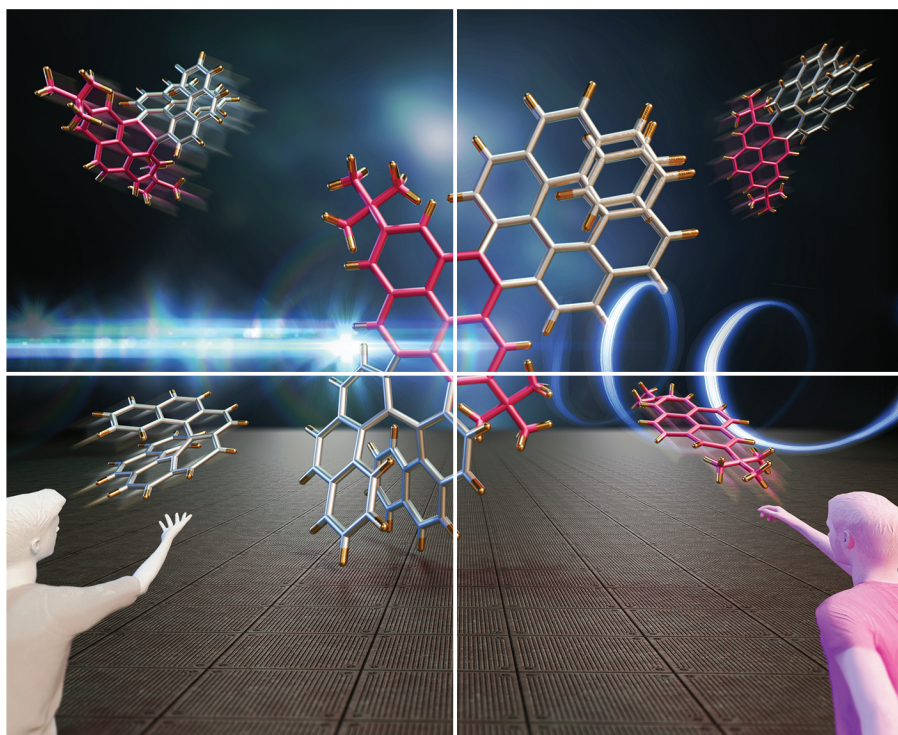
■ REFERENCES

- (1) (a) Shen, Y.; Chen, C.-F. Helicenes: Synthesis and Applications. *Chem. Rev.* **2012**, *112*, 1463–1535. (b) Martin, R. H. The Helicenes. *Angew. Chem., Int. Ed.* **1974**, *13*, 649–660.
- (2) (a) Tsurusaki, A.; Kamikawa, K. Multiple Helicenes Featuring on the Synthetic Approaches and Molecular Structures. *Chem. Lett.* **2021**, *50*, 1913–1932. (b) Mori, T. Chiroptical Properties of Symmetric Double, Triple, and Multiple Helicenes. *Chem. Rev.* **2021**, *121*, 2373–2412. (c) Reger, D.; Haines, P.; Amsharov, K. Y.; Schmidt, J. A.; Ullrich, T.; Bönsch, S.; Hampel, F.; Göring, A.; Nelson, J.; Jelfs, K. E.; Guldi, D. M.; Jux, N. A Family of Superhelicenes: Easily Tunable, Chiral Nanographenes by Merging Helicity with Planar π Systems. *Angew. Chem., Int. Ed.* **2021**, *60*, 18073–18081. (d) Qiu, Z.; Ju, C.-W.; Frédéric, L.; Hu, Y.; Schollmeyer, D.; Pieters, G.; Müllen, K.; Narita, A. Amplification of Dissymmetry Factors in π -Extended [7]- and [9]Helicenes. *J. Am. Chem. Soc.* **2021**, *143*, 4661–4667. (e) Xiao, X.; Pedersen, S. K.; Aranda, D.; Yang, J.; Wiscons, R. A.; Pittelkow, M.; Steigerwald, M. L.; Santoro, F.; Schuster, N. J.; Nuckolls, C. Chirality Amplified: Long, Discrete Helicene Nanoribbons. *J. Am. Chem. Soc.* **2021**, *143*, 983–991. (f) Medel, M. A.; Tapia, R.; Blanco, V.; Miguel, D.; Morcillo, S. P.; Campaña, A. G. Octagon-Embedded Carbohelicene as a Chiral Motif for Circularly Polarized Luminescence Emission of Saddle-Helix Nanographenes. *Angew. Chem., Int. Ed.* **2021**, *60*, 6094–6100. (g) Fernández-García, J. M.; Evans, P. J.; Filippone, S.; Herranz, M. A.; Martín, N. Chiral Molecular Carbon Nanostructures. *Acc. Chem. Res.* **2019**, *52*, 1565–1574. (h) Yang, W.; Longhi, G.; Abbate, S.; Lucotti, A.; Tommasini, M.; Villani, C.; Catalano, V. J.; Lykhin, A. O.; Varganov, S. A.; Chalifoux, W. A. Chiral Peropyrene: Synthesis, Structure, and Properties. *J. Am. Chem. Soc.* **2017**, *139*, 13102–13109.
- (3) Ikai, T.; Yamakawa, S.; Suzuki, N.; Yashima, E. One-Step Simultaneous Synthesis of Circularly Polarized Luminescent Multiple Helicenes Using a Chrysene Framework. *Chem.-Asian J.* **2021**, *16*, 769–774.
- (4) Zhang, F.; Michail, E.; Saal, F.; Krause, A.-M.; Ravat, P. Stereospecific Synthesis and Photophysical Properties of Propeller-Shaped C90H48 PAH. *Chem. Eur. J.* **2019**, *25*, 16241–16245.
- (5) Zhang, F.; Radacki, K.; Braunschweig, H.; Lambert, C.; Ravat, P. Zinc-[7]helicencyanine and Its Discrete π -Stacked Homochiral Dimer. *Angew. Chem., Int. Ed.* **2021**, *60*, 23656–23660.
- (6) Swain, A. K.; Kolanji, K.; Stapper, C.; Ravat, P. C2- and C1-Symmetric Configurationally Stable Pyrene-Fused [5]Helicenes Connected via Hexagonal and Heptagonal Rings. *Org. Lett.* **2021**, *23*, 1339–1343.

- (7) Nakai, Y.; Mori, T.; Inoue, Y. Theoretical and Experimental Studies on Circular Dichroism of Carbo[n]helicenes. *J. Phys. Chem. A* **2012**, *116*, 7372–7385.
- (8) Qiu, Z.; Asako, S.; Hu, Y.; Ju, C.-W.; Liu, T.; Rondin, L.; Schollmeyer, D.; Lauret, J.-S.; Müllen, K.; Narita, A. Negatively Curved Nanographene with Heptagonal and [5]Helicene Units. *J. Am. Chem. Soc.* **2020**, *142*, 14814–14819.
- (9) (a) Bam, R.; Yang, W.; Longhi, G.; Abbate, S.; Lucotti, A.; Tommasini, M.; Franzini, R.; Villani, C.; Catalano, V. J.; Olmstead, M. M.; Chalifoux, W. A. Four-Fold Alkyne Benzannulation: Synthesis, Properties, and Structure of Pyreno[a]pyrene-Based Helicene Hybrids. *Org. Lett.* **2019**, *21*, 8652–8656. (b) Yano, Y.; Ito, H.; Segawa, Y.; Itami, K. Helically Twisted Tetracene: Synthesis, Crystal Structure, and Photophysical Properties of Hexabenz[a,c,fg,j,op]-tetracene. *Synlett* **2016**, *27*, 2081–2084. (c) Hu, J.-Y.; Paudel, A.; Seto, N.; Feng, X.; Era, M.; Matsumoto, T.; Tanaka, J.; Elsegood, M. R. J.; Redshaw, C.; Yamato, T. Pyrene-cored blue-light emitting [4]helicenes: synthesis, crystal structures, and photophysical properties. *Org. Biomol. Chem.* **2013**, *11*, 2186–2197. (d) Bédard, A.-C.; Vlassova, A.; Hernandez-Perez, A. C.; Bessette, A.; Hanan, G. S.; Heuft, M. A.; Collins, S. K. Synthesis, Crystal Structure and Photophysical Properties of Pyrene–Helicene Hybrids. *Chem. Eur. J.* **2013**, *19*, 16295–16302.
- (10) (a) Saal, F.; Ravat, P. Imide-Functionalized Helical PAHs: A Step towards New Chiral Functional Materials. *Synlett* **2021**, *32*, 1879–1890. (b) Zhu, Y.; Xia, Z.; Cai, Z.; Yuan, Z.; Jiang, N.; Li, T.; Wang, Y.; Guo, X.; Li, Z.; Ma, S.; Zhong, D.; Li, Y.; Wang, J. Synthesis and Characterization of Hexapole [7]Helicene, A Circularly Twisted Chiral Nanographene. *J. Am. Chem. Soc.* **2018**, *140*, 4222–4226.
- (11) Nakano, K.; Hidehira, Y.; Takahashi, K.; Hiyama, T.; Nozaki, K. Stereospecific Synthesis of Hetero[7]helicenes by Pd-Catalyzed Double N-Arylation and Intramolecular O-Arylation. *Angew. Chem., Int. Ed.* **2005**, *44*, 7136–7138.
- (12) Chang, X.; Zhang, Q.; Guo, C. Switchable Smiles Rearrangement for Enantioselective O-Aryl Amination. *Org. Lett.* **2019**, *21*, 4915–4918.
- (13) Leas, D. A.; Dong, Y.; Vennerstrom, J. L.; Stack, D. E. One-Pot, Metal-Free Conversion of Anilines to Aryl Bromides and Iodides. *Org. Lett.* **2017**, *19*, 2518–2521.
- (14) Shimizu, M.; Nagao, I.; Tomioka, Y.; Hiyama, T. Palladium-Catalyzed Annulation of vic-Bis(pinacolatoboryl)alkenes and -phenanthrenes with 2,2'-Dibromobiaryls: Facile Synthesis of Functionalized Phenanthrenes and Dibenzo[g,p]chrysenes. *Angew. Chem., Int. Ed.* **2008**, *47*, 8096–8099.
- (15) Grzybowski, M.; Sadowski, B.; Butenschön, H.; Gryko, D. T. Synthetic Applications of Oxidative Aromatic Coupling—From Biphenols to Nanographenes. *Angew. Chem., Int. Ed.* **2020**, *59*, 2998–3027.
- (16) Miao, Q. Heptagons in Aromatics: From Monocyclic to Polycyclic. *Chem. Rec.* **2015**, *15*, 1156–1159.
- (17) Lorbach, D.; Wagner, M.; Baumgarten, M.; Müllen, K. The right way to self-fuse bi- and terpyrenyls to afford graphenic cutouts. *Chem. Commun.* **2013**, *49*, 10578–10580.
- (18) (a) Fallah-Bagher-Shaidaei, H.; Wannere, C. S.; Corminboeuf, C.; Puchta, R.; Schleyer, P. v. R. Which NICS Aromaticity Index for Planar π Rings Is Best? *Org. Lett.* **2006**, *8*, 863–866. (b) Schleyer, P. v. R.; Maerker, C.; Dransfeld, A.; Jiao, H.; van Eikema Hommes, N. J. R. Nucleus-Independent Chemical Shifts: A Simple and Efficient Aromaticity Probe. *J. Am. Chem. Soc.* **1996**, *118*, 6317–6318.
- (19) Ravat, P. Carbo[n]helicenes Restricted to Enantiomerize: An Insight into the Design Process of Configurationally Stable Functional Chiral PAHs. *Chem. Eur. J.* **2021**, *27*, 3957–3967.
- (20) (a) Saal, F.; Zhang, F.; Holzapfel, M.; Stolte, M.; Michail, E.; Moos, M.; Schmiedel, A.; Krause, A.-M.; Lambert, C.; Würthner, F.; Ravat, P. [n]Helicene Diimides (n = 5, 6, and 7): Through-Bond versus Through-Space Conjugation. *J. Am. Chem. Soc.* **2020**, *142*, 21298–21303. (b) Ravat, P.; Hinkelmann, R.; Steinebrunner, D.; Prescimone, A.; Bodoky, I.; Juriček, M. Configurational Stability of [5]Helicenes. *Org. Lett.* **2017**, *19*, 3707–3710. (c) Ravat, P.; Solomek, T.; Häussinger, D.; Blacque, O.; Juriček, M. Dimethylcethrene: A Chiroptical Diradicaloid Photoswitch. *J. Am. Chem. Soc.* **2018**, *140*, 10839–10847.
- (21) Birks, J. B.; Birch, D. J. S.; Cordemans, E.; Vander Donckt, E. Fluorescence of the higher helicenes. *Chem. Phys. Lett.* **1976**, *43*, 33–36.
- (22) Hu, J.-Y.; Paudel, A.; Seto, N.; Feng, X.; Era, M.; Matsumoto, T.; Tanaka, J.; Elsegood, M. R. J.; Redshaw, C.; Yamato, T. Pyrene-cored blue-light emitting [4]helicenes: synthesis, crystal structures, and photophysical properties. *Org. Biomol. Chem.* **2013**, *11*, 2186–2197.
- (23) (a) Yamano, R.; Shibata, Y.; Tanaka, K. Synthesis of Single and Double Dibenzohelicenes by Rhodium-Catalyzed Intramolecular [2 + 2+2] and [2 + 1+2 + 1] Cycloaddition. *Chem. Eur. J.* **2018**, *24*, 6364–6370. (b) Oyama, H.; Akiyama, M.; Nakano, K.; Naito, M.; Nobusawa, K.; Nozaki, K. Synthesis and Properties of [7]Helicene-like Compounds Fused with a Fluorene Unit. *Org. Lett.* **2016**, *18*, 3654–3657.
- (24) Ma, X.; Sun, R.; Cheng, J.; Liu, J.; Gou, F.; Xiang, H.; Zhou, X. Fluorescence Aggregation-Caused Quenching versus Aggregation-Induced Emission: A Visual Teaching Technology for Undergraduate Chemistry Students. *J. Chem. Educ.* **2016**, *93*, 345–350.
- (25) Sakai, H.; Shinto, S.; Kumar, J.; Araki, Y.; Sakanoue, T.; Takenobu, T.; Wada, T.; Kawai, T.; Hasobe, T. Highly Fluorescent [7]Carbohelicene Fused by Asymmetric 1,2-Dialkyl-Substituted Quinoxaline for Circularly Polarized Luminescence and Electrochromism. *J. Phys. Chem. C* **2015**, *119*, 13937–13947.
- (26) Tanaka, H.; Inoue, Y.; Mori, T. Circularly Polarized Luminescence and Circular Dichroisms in Small Organic Molecules: Correlation between Excitation and Emission Dissymmetry Factors. *ChemPhotoChem.* **2018**, *2*, 386–402.
- (27) Tanaka, H.; Ikenosako, M.; Kato, Y.; Fujiki, M.; Inoue, Y.; Mori, T. Symmetry-based rational design for boosting chiroptical responses. *Commun. Chem.* **2018**, *1*, 38.
- (28) Arrico, L.; Di Bari, L.; Zinna, F. Quantifying the Overall Efficiency of Circularly Polarized Emitters. *Chem. Eur. J.* **2021**, *27*, 2920–2934.
- (29) (a) Terada, N.; Uematsu, K.; Higuchi, R.; Tokimaru, Y.; Sato, Y.; Nakano, K.; Nozaki, K. Synthesis and Properties of Spiro-double Sila[7]helicene: The LUMO Spiro-conjugation. *Chem. Eur. J.* **2021**, *27*, 9342–9349. (b) Terrasson, V.; Roy, M.; Moutard, S.; Lafontaine, M.-P.; Pepe, G.; Felix, G.; Gingras, M. Benzylic-type couplings provide an important asymmetric entry to functionalized, non-racemic helicenes. *RSC Adv.* **2014**, *4*, 32412–32414.
- (30) Liu, Z.; Wang, Y.; Chen, Y.; Liu, J.; Fang, Q.; Kleeberg, C.; Marder, T. B. Ir-Catalyzed Direct Borylation at the 4-Position of Pyrene. *J. Org. Chem.* **2012**, *77*, 7124–7128.
- (31) Sheldrick, G. SHELXT - Integrated space-group and crystal-structure determination. *Acta Crystallogr., Sect. A* **2015**, *71*, 3–8.
- (32) Sheldrick, G. A short history of SHELX. *Acta Crystallogr., Sect. A* **2008**, *64*, 112–122.
- (33) Frisch, M. J.; Trucks, G. W.; Schlegel, H. B.; Scuseria, G. E.; Robb, M. A.; Cheeseman, J. R.; Scalmani, G.; Barone, V.; Petersson, G. A.; Nakatsuji, H.; Li, X.; Caricato, M.; Marenich, A. V.; Bloino, J.; Janesko, B. G.; Gomperts, R.; Mennucci, B.; Hratchian, H. P.; Ortiz, J. V.; Izmaylov, A. F.; Sonnenberg, J. L.; Williams, J.; Ding, F.; Lipparini, F.; Egidi, F.; Goings, J.; Peng, B.; Petrone, A.; Henderson, T.; Ranasinghe, D.; Zakrzewski, V. G.; Gao, J.; Rega, N.; Zheng, G.; Liang, W.; Hada, M.; Ehara, M.; Toyota, K.; Fukuda, R.; Hasegawa, J.; Ishida, M.; Nakajima, T.; Honda, Y.; Kitao, O.; Nakai, H.; Vreven, T.; Throssell, K.; Montgomery, Jr., J. A.; Peralta, J. E.; Ogliaro, F.; Bearpark, M. J.; Heyd, J. J.; Brothers, E. N.; Kudin, K. N.; Staroverov, V. N.; Keith, T. A.; Kobayashi, R.; Normand, J.; Raghavachari, K.; Rendell, A. P.; Burant, J. C.; Iyengar, S. S.; Tomasi, J.; Cossi, M.; Millam, J. M.; Klene, M.; Adamo, C.; Cammi, R.; Ochterski, J. W.; Martin, R. L.; Morokuma, K.; Farkas, O.; Foresman, J. B.; Fox, D. J. *Gaussian 16*, rev. C.01; Gaussian, Inc.: Wallingford, CT, 2016.

Volume 10 | Number 15 | 7 August 2023

10
YEARS
ANNIVERSARY



ORGANIC CHEMISTRY

FRONTIERS



CHINESE
CHEMICAL
SOCIETY



ROYAL SOCIETY
OF CHEMISTRY

rsc.li/frontiers-organic

RESEARCH ARTICLE

View Article Online
View Journal | View IssueCite this: *Org. Chem. Front.*, 2023,
10, 3714Received 15th March 2023,
Accepted 12th May 2023

DOI: 10.1039/d3qo00386h

rsc.li/frontiers-organic

Pyrene bridged double[7]helicene embedded with a heptagonal ring†

Asim Swain and Prince Ravat *

To utilize [*n*]helicene-embedded polycyclic aromatic hydrocarbons in the development of circularly polarized materials high luminescence quantum yield and dissymmetric factors are essential to boost (chir)optical properties. Previously we have shown that the (chir)optical properties of pyrene fused mono helicenes can be significantly influenced by the fusing mode and molecular symmetry. We report in this manuscript the stereospecific synthesis and (chir)optical properties of C_1 symmetric pyrene fused double [7]helicene, where the helicene units are connected *via* hexagonal and heptagonal rings. In line with single helicene congeners, lower symmetric heptagon containing double helicene exhibited higher absorption and emission dissymmetric factors along with a significant increase in fluorescence quantum yield. Our findings in this manuscript provide further insights into the effect of molecular symmetry on the (chir)optical properties of single and double helicenes.

Introduction

A rapid growth in the development of [*n*]helicene chemistry^{1–3} was witnessed during the last decade because of their wide range of demanding applications in organic electronics,^{4,5} asymmetric catalysis,^{6–8} molecular machines,⁹ and bio imaging¹⁰ owing to their inherent chirality. Overcoming the shortcomings of pristine [*n*]helicenes, helicene fused polycyclic aromatic hydrocarbons (PAHs) have shown a significant increase in the overall functional properties.^{11–24} Moreover during the last few years multiple [*n*]helicene-embedded nanographenes with numerous aromatic cores have been developed.^{23,25–30} Preserving their core properties, multi[*n*]helicene showed unique characteristics due to an increased π -conjugation and molecular packing.^{23,31–36} Although these molecules provided an opportunity for synthetic chemists to explore the limits of aromaticity and π -bonding by designing extremely twisted PAHs,^{37–42} often the key challenge remained with the configurational stability and isolation of enantiopure [*n*]helicene derivatives as well as their stereoselective synthesis. Several stable conformers are possible for multiple [*n*]helicene-embedded PAHs, hence the isolation and availability of enantiopure multi[*n*]helicenes are cumbersome.^{22,23} To overcome these challenges, we follow a stereospecific synthetic pathway,

which allows us to synthesize configurationally stable enantiopure helicene-containing functional molecules.^{19,20,30,34}

Recently, we reported stereospecific synthesis of C_2 and C_1 symmetric pyrene fused [5]helicenes¹⁹ and [7]helicenes,²⁰ with excellent stereoselectivity. While investigating photophysical properties, we found a significant enhancement in (chir)optical properties from [5]helicene to [7]helicene-embedded compounds (Fig. 1, molecules 1 and 2). Especially heptagon-

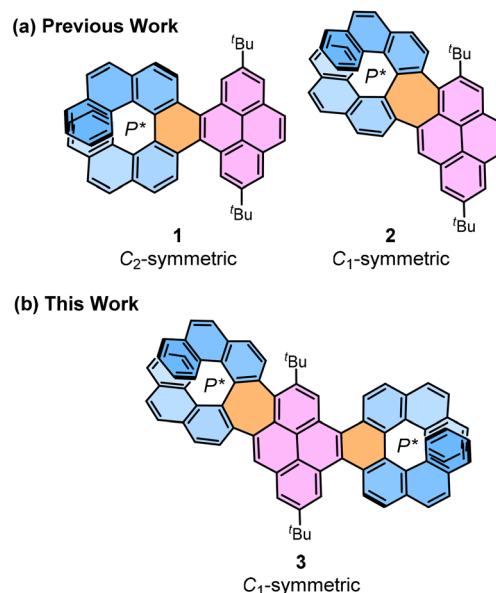


Fig. 1 Pyrene embedded mono and double [7]helicenes.

Julius-Maximilians-Universität Würzburg, Institut für Organische Chemie, Am
Hubland, D-97074 Würzburg, Germany.

E-mail: princekumar.ravat@uni-wuerzburg.de

† Electronic supplementary information (ESI) available. See DOI: <https://doi.org/10.1039/d3qo00386h>

ally fused^{43–45} C_1 symmetric **2** showed remarkable improvement in fluorescence quantum yield and configurational stability compared to hexagonally fused C_2 symmetric congener **1** as well as other pyrene fused helicenes.^{46–49} Inspired by the overall functional properties of **1** and **2**, we envisage to investigate whether heptagonal-fused-[7]helicene will be dominant over the hexagonally-fused-[7]helicene if stitched together with pyrene (molecule **3**). Also, to further improve (chir)optical properties, we aimed to prepare a monkey-saddled⁵⁰ molecule **9** with two heptagonal rings.

We herein report the stereospecific synthesis of pyrene-bridged double[7]helicene **3** connected *via* hexagonal and heptagonal rings. Additionally, to compare the photophysical properties, we synthesized (*P,M*)*-diastereomers of **3**. We investigated their (chir)optical properties through UV-vis absorption, emission, electronic circular dichroism (ECD), and circularly polarized luminescence (CPL) spectroscopies as well as kinetic measurements to estimate the inversion barrier. Experimental data were well fitted to quantum-chemical calculations (ESI Section S4†) with a thorough comparison to their distinctive monomeric [7]helicene congeners.²⁰

Results and discussion

The stereospecific synthesis of enantiopure (*P,P*)- and (*M,M*)-**3** was achieved in two steps from corresponding (*R*)- and (*S*)-3,3'-dibromo-4,4'-biphenanthrene (**4**), respectively (Scheme 1).^{20,51,52} The one-pot Suzuki coupling followed by C–H activation^{53,54} between **4** and 2-(2,7-di-*tert*-butylpyren-4-yl)-4,4,5,5-tetramethyl-1,3,2-dioxaborolane (**5**),^{55,56} in presence of [Pd(PPh₃)₄] and K₂CO₃ in a tetrahydrofuran (THF)/water (3 : 1) mixture produced **6** and **7**. Due to the low R_f (0.07–0.04) difference between the two products in the thin layer chromatography and tailing of products in the column chromatography, **6** and **7** could not be isolated in complete pure fraction. But two different fractions were collected with a major component of **6** and **7**, respectively, from silica column chromatography. The two fractions showed distinct mass spectra peaks in MALDI-HRMS (ESI Fig. S21 and S22†). The fractions of **6** and **7** were used in a Scholl-type oxidative cyclodehydrogenation reaction^{57,58} without any further purification. The reaction of **6** with methanesulfonic acid (MsOH) and 2,3-dichloro-5,6-dicyano-1,4-benzoquinone (DDQ) gave **3** in 57% yield as a yellowish-green fluorescent solid compound. The unusual ring closure⁵⁹ is mainly driven by the higher ring aromaticity of the corresponding pyrene⁶⁰ ring compared to others, as observed in our earlier studies with [5] and [7]helicenes. To obtain double-saddled compound **9** from **7**, two successive ring closures are necessary. Under the above-mentioned mild acidic condition, only one ring closure was observed leading to compound **8**. The oxidative Scholl reaction was then repeated with **7** and also with **8** in various combinations of acids (such as Triflic acid,^{45,61} MsOH, and Boron trifluoride etherate⁶²) and oxidants (such as DDQ, chloranil, and ferric chloride⁶³) at various reaction temperatures (–30 to 50 °C), however all

attempts produced a mixture of multiple over-oxidized products, which could not be isolated. It is previously observed that the [*n*]helicene-containing PAHs readily convert to quasi [*n*]circulene during oxidative Scholl reaction.^{61,64} To understand the failure of second ring closure in molecule **8** under mild reaction conditions, we calculated the spin density for the radical cation of **8**. The calculations revealed that the spin densities are primarily distributed over pyrene and the heptagonally attached [7]helicene (Fig. 2). There are no spin densities detected over the axially attached biphenanthrene unit. Considering the radical cation mechanism for the oxidative cyclodehydrogenation step, the lack of positive spin density over the phenanthrene units hinders the ring closure with pyrene.^{65,66} The enantiopurity of **3** (er 98 : 02) is retained to that of **4** (er 99 : 01). Both (*P,P*) and (*M,M*) enantiomers of **3** were synthesized from *S*- and *R*-enantiomers of **4**, respectively, in comparable yields and enantiopurity following identical reaction conditions. To synthesize (*P,M*)*-diastereomer of **3**, the Suzuki coupling – C–H activation was performed with a *rac*-**4** and **5**. The resolution of a diastereomeric mixture of **3** with HPLC equipped with chiral stationary phase columns (CSP-HPLC) showed the formation of diastereomers (*P,P*)*-**3** and (*P,M*)*-**3** in a ratio of 4.3 : 1. Attempts for enantiomeric resolution of (*P,M*)*-**3** were not successful. The structures of (*P,P*)-**3** and (*P,M*)*-**3** were confirmed by the unambiguous assignment of ¹H peaks to the respective atoms (ESI Fig. S6†) by gCOSY, gNOESY, and gTOCSY 2D NMR measurements.

(*P,P*)*-**3** and (*P,M*)*-**3** are assigned to C_1 symmetry. The two *tert*-butyl groups attached to pyrene showed two singlets at 1.72 and 1.81 (1.83 for (*P,M*)*-**3**) ppm each corresponds to 9 protons in the ¹H NMR spectrum due to unresolved J_{HH} couplings as well as the shorter effective correlation time because of the rapid rotation of methyl groups along with the *tert*-butyl group. The four larger downfield shifted protons in ¹H NMR spectrum of both (*P,P*)*-**3** and (*P,M*)*-**3** correspond to the two [4]helicene cove regions present in the structure, confirmed by NOESY experiments. Steric hindrance between the adjacent protons in the cove region caused higher deshielding of those proton signals. To get insights into the ring aromaticity of the molecules, nucleus-independent chemical shift (NICS) calculations were performed on ωB97XD/6-31G(d,p) optimized geometry at GIAO-B3LYP/6-311+G(2d,p) level (ESI Table S4†). The NICS(1)_{zz} values are negative for all the six-membered rings present in the structures of (*P,P*)-**3** signifying their aromaticity character, while the positive NICS(1)_{zz} value of 14.45 ppm for the heptagonal ring in (*P,P*)-**3** indicates its anti-aromatic character. Nevertheless in both [7]helicene units the aromaticity decreased on moving from external to central rings, which is quite similar to pristine [7]helicene.^{67,68} The major geometrical features in two different types of [7]helicenes because of their central hexagonal and heptagonal rings are (i) the distance between the terminal benzene rings and (ii) the torsional twist of the inner helix of [7]helicene. The distance between the centroid of terminal benzene rings of [7]helicene is 3.78 Å and 4.48 Å, respectively, for hexagonally and heptagonally attached [7]helicenes. However, the torsional twist in the inner

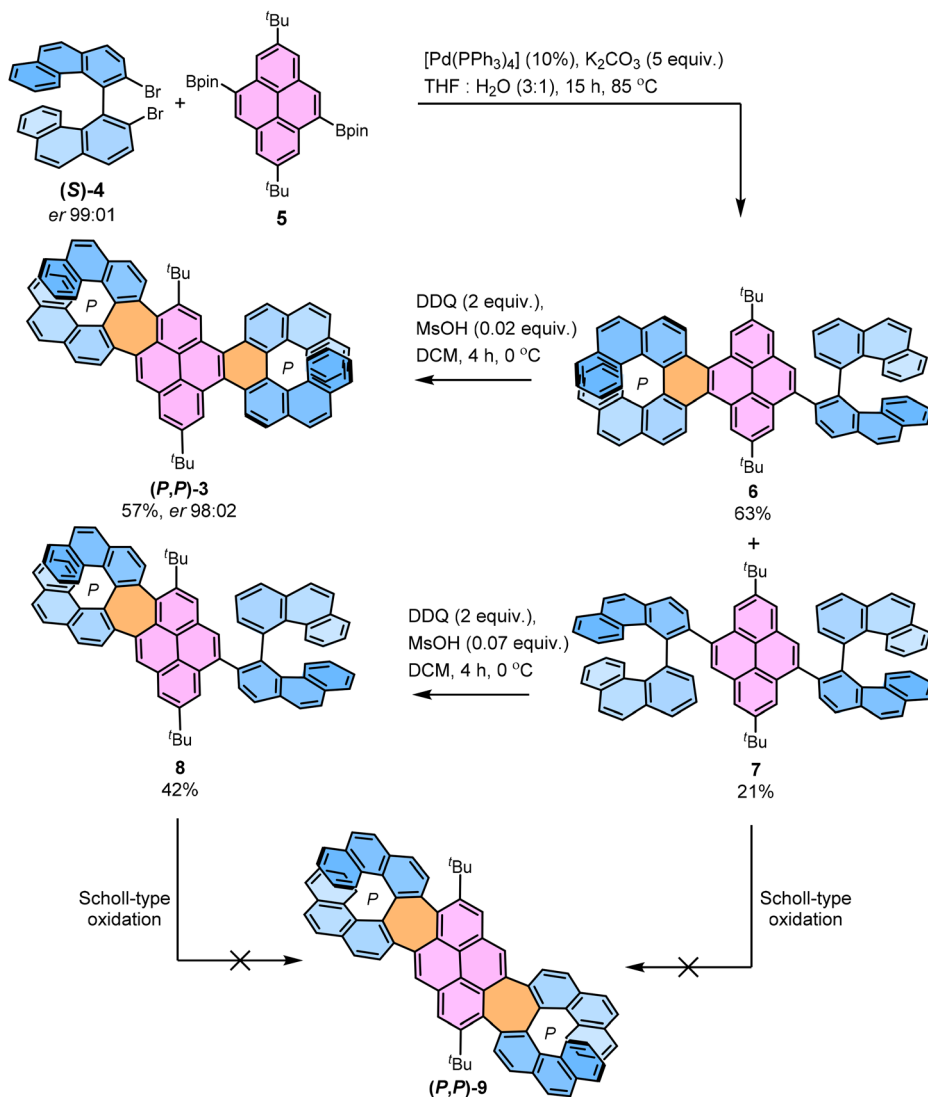
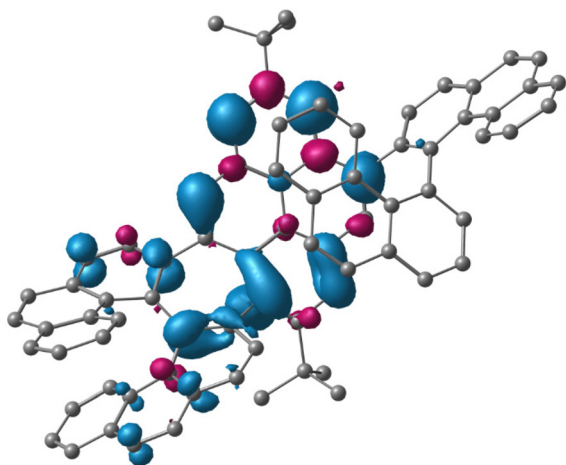
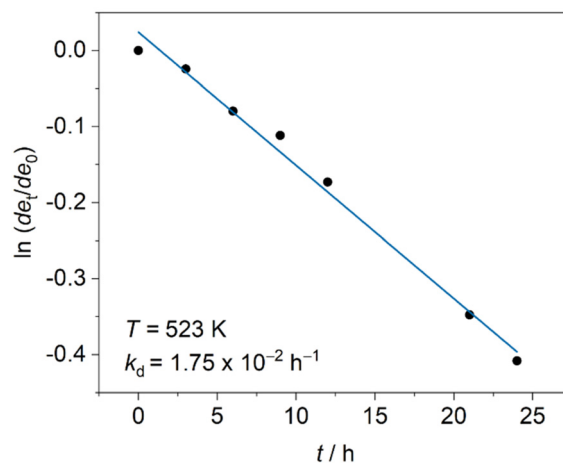
Scheme 1 Stereospecific synthesis of (P,P) -3 and (P) -8.

Fig. 2 Calculated spin density distribution for the radical cation of 8. Hydrogen atoms are omitted for clarity.

Fig. 3 Plot of $\ln(de_t/de_0)$ against t for $(P,M)^*-3$ fitted linearly to obtain the k_d and $\Delta G^\ddagger(T)$ values.

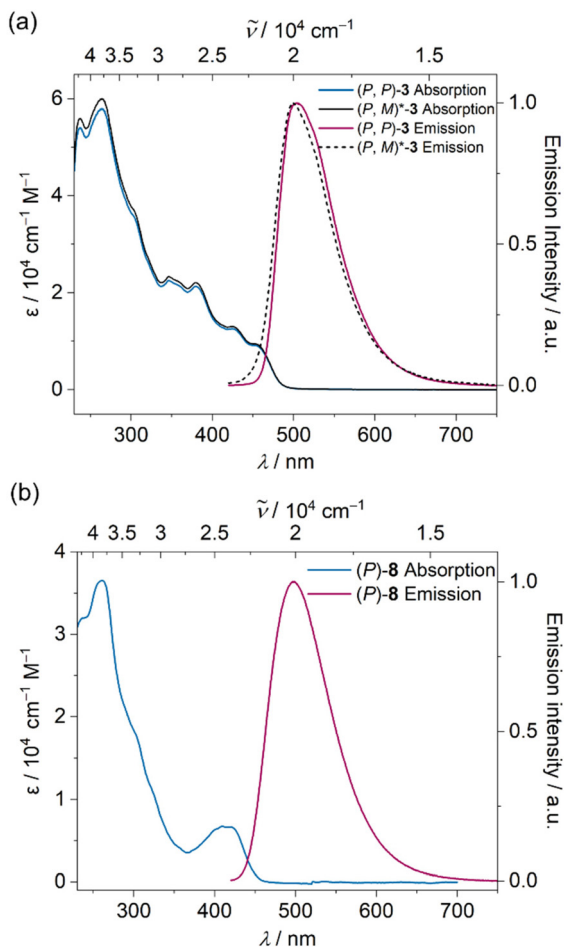


Fig. 4 UV-vis absorption (blue, $c \sim 10^{-5}$ M) and emission (red, $c \sim 10^{-6}$ M), spectra of (a) (P,P) -3, $(P,M)^*$ -3 (black) and (b) (P) -8 in dichloromethane.

helix of both [7]helicenes is quite similar (23°). Similar geometrical parameters were also observed in case of (P,M) -3.

Although our synthetic pathway allows firm control over the chirality of the [7]helicenes, there are six possible diastereomers for **3** based on the helicity of the [4]helicene sub-units present on top and bottom of the hexagonally fused ring (ESI Fig. S4†) along with the positioning of the *tert*-butyl group to the heptagonally fused [7]helicene. The TD-DFT optimized

geometry and energies showed the diastereomer with opposite chirality of [4]helicenes to [7]helicene is more stable compared to other diastereomers. The diastereomer with *tert*-butyl group positioned away from the heptagonal [7]helicene is more stable by $28.4 \text{ kcal mol}^{-1}$. The two configurationally labile [4]helicene sub-units exist in dynamic equilibrium at room temperature as no diastereomeric mixture signals were observed in ^1H NMR spectra of (P,P) -3 and $(P,M)^*$ -3 recorded at room temperature.

To confirm the configurational stability, the diastereomeric mixture of $(P,M)^*$ -3 was heated at 523 K to observe the formation of the $(P,P)^*$ -3 diastereomers with time. The Gibbs activation energy ΔG^\ddagger (523 K) for diastereomerization of **3** was obtained by following the decay of the diastereomeric excess (de) over time (t) by CSP-HPLC. The rate of diastereomerization (k_d) was calculated from the linear fitting of $\ln(\text{de}_t/\text{de}_0)$ against time (Fig. 3). The $\Delta G^\ddagger(T)$ value was calculated using the equation $\Delta G^\ddagger(T) = -RT \ln(k_d h / \kappa k_B T)$, where R is the gas constant ($R = 8.31446 \text{ J K}^{-1}$), h is the Planck constant ($h = 6.62607 \times 10^{-34} \text{ J s}$), k_B is the Boltzmann constant ($k_B = 1.38064852 \times 10^{-23} \text{ J K}^{-1}$), and κ is the transmission coefficient ($\kappa = 0.5$ or 1). The transmission coefficient $\kappa = 0.5$ was used because the diastereomerization of **3** is a reversible first-order process. The obtained ΔG^\ddagger (523 K) for diastereomerization of **3** is $43.2 \text{ kcal mol}^{-1}$, which is slightly higher than the inversion barrier for pristine [7]helicene ($41.2 \text{ kcal mol}^{-1}$) and **2** ($42.6 \text{ kcal mol}^{-1}$).^{3,69,70} The higher value of the diastereomerization barrier of **3** is because of the inclusion of the heptagon ring along with the steric repulsion from the neighboring *tert*-butyl group of pyrene along with relatively larger distance between terminal rings of the [7]helicene which may stabilize the ground state structure to a greater extent.

The photophysical properties of (P,P) -3 and $(P,M)^*$ -3 and (P) -8 were studied by absorption and emission spectroscopy (Fig. 4). The optoelectronic features of **3** are unaffected by the conformational change in the [7]helicenes as (P,P) -3 and $(P,M)^*$ -3 showed nearly identical absorption and emission spectra suggesting the electronic structure in both ground and excited state are similar for (P,P) -3 and $(P,M)^*$ -3. Observation of such similarity despite different configurations of [7]helicenes is rare in the literature^{38,71–75} but not unknown.^{21,76} Moreover, the calculated frontier molecular orbitals of **3** remained identical regardless of the configuration of [7]helicenes (ESI

Table 1 Summary of (chir)optical and kinetic parameters

Compd	$\lambda_{\text{max abs}} (\text{nm})/\epsilon$ ($\text{cm}^{-1} \text{M}^{-1}$)	$\lambda_{\text{max em}}$ (nm)	E_g^a/eV	Φ_{FL}	$\tau_{\text{FL}}/\text{ns}$	$k_{\text{FL}}/10^8 \text{ s}^{-1}$	$k_{\text{NR}}/10^8 \text{ s}^{-1}$	$g_{\text{abs}}^d/10^{-3}$	$g_{\text{lum}}/10^{-3}$	μ/D^e	$\Delta G^\ddagger(T)/$ kcal mol^{-1}
1	430 (8509)	470	2.83	0.04	5.76	0.07	1.67	2.64–7.47	1.27	0.06	34.1 (438 K)
2	414 (19464)	491	2.85	0.34	2.31	1.47	2.86	2.95–7.96	2.64	0.27	42.6 (498 K)
(P,P) -3	445 (9366)	504	2.67	0.46	3.19 ^b	1.44 ^c	1.69 ^c	2.43–2.68	2.47	0.21	43.2 (523 K)
$(P,M)^*$ -3	448 (9534)	500	2.67	0.43	3.67 ^b	1.17 ^c	1.55 ^c	—	—	0.31	—
(P) -8	410 (6718)	498	2.81	0.41	2.21	1.85	2.67	2.63–3.15	3.17	—	—
[7]helicene	423 (200) ^f	443 ^f	3.06	0.02	13.8	0.01	0.71	30.0 ^f	6.0 ^f	—	41.2 (298 K) ^g

^a Estimated from crossing of absorption and fluorescence spectra. ^b $\tau_{\text{avg}} = (\alpha_1\tau_1^2 + \alpha_2\tau_2^2)/(\alpha_1\tau_1 + \alpha_2\tau_2)$. ^c Calculated for τ_{avg} . ^d Wavelength range 230–450 nm. ^e Calculated dipole moment. ^f Ref. 80. ^g Ref. 3 and 70.

Table S2†). An increase in π -conjugation results in bathochromic shifted absorption and emission spectra for **3** compared to monomer congeners **1** and **2**. The optical energy gap calculated from intersection of absorption and emission spectra for **8** (2.81 eV) is, similar to that of **1** and **2** (2.83 and 2.85 eV, respectively) while that for **3** (2.67 eV), is slightly smaller (Table 1). Nevertheless, both compounds showed much lower

optical energy gap compared to the [7]helicene (3.06 eV)^{77,78} and 2,7-di-*tert*-butylpyrene (3.55 eV).⁷⁹

TD-DFT simulated spectra provided further insights into the electronic transitions of **3** (ESI Fig. S5a†). Similar to **1** and **2**, the lowest energy transition of (*P,P*)-**3** is mainly stemming from HOMO \rightarrow LUMO at 445 with an oscillator strength (f) of 0.35 (ESI Table S3a†). This differs from pristine [7]helicene, where the lowest energy transition is assigned to HOMO \rightarrow LUMO+1, HOMO-1 \rightarrow LUMO, and HOMO-2 \rightarrow LUMO.^{80,81} Apart from this, another major transition mainly stemming from the hexagonally attached [7]helicene was observed at 390 nm with an oscillator strength of 0.43 corresponding to HOMO \rightarrow LUMO+1 and HOMO-1 \rightarrow LUMO transitions. With both low-energy key transitions of **1** and **2** present in compound **3**, the absorption profile of **3** resembles a combination of **1** and **2** (ESI Fig. S1a†). Similar features were also observed in the calculated spectra of (*P,M*)-**3** (ESI Table S3b†).

Both **3** and **8** are emissive in solution and solid state. The emission maxima in dichloromethane for **3** and **8** are recorded at 504 nm (19 841 cm^{-1}) and 498 nm (20 080 cm^{-1}), respectively. The fluorescence quantum yield (FQY) for (*P,P*)-**3**, (*P,M*)

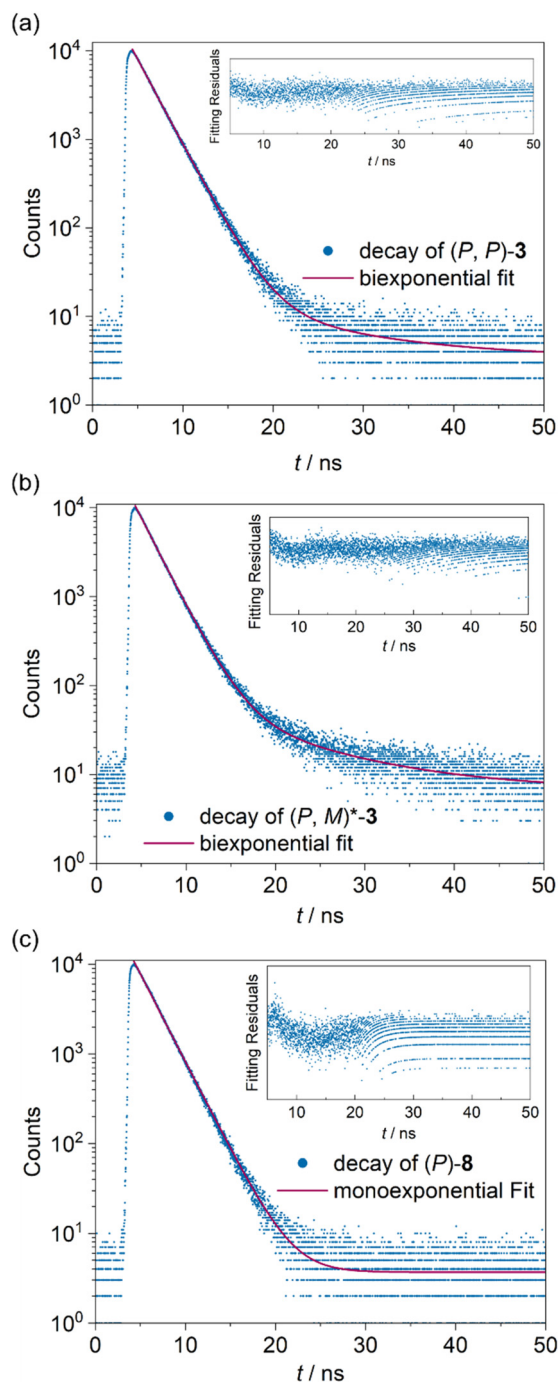


Fig. 5 Time resolved fluorescence decay (excited at 24 154 cm^{-1}) of (a) (*P,P*)-**3**, (b) (*P,M*)-**3**, (c) (*P*)-**8** in dichloromethane ($c \sim 10^{-5}$ M). Inset – exponential tail-fitting residuals.

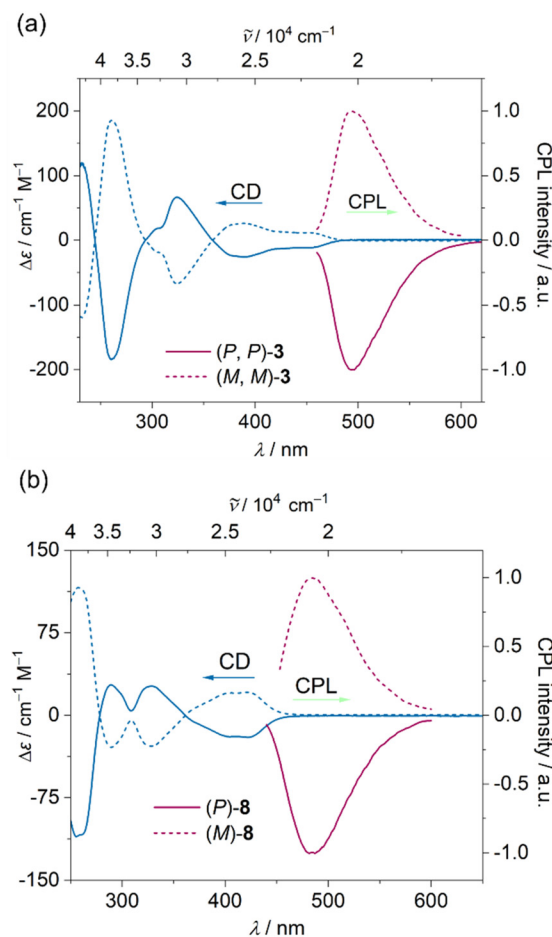


Fig. 6 ECD spectra (blue) and CPL spectra (red) of (*P,P*) (solid line) and (*M,M*) (dashed line) enantiomers of (a) **3** and (b) **8** in dichloromethane ($c \sim 10^{-5}$ M).

-3, and (P)-8 is 46%, 43%, and 41%, respectively. Both (P,P)-3 and (P,M)-3 showed a huge increase in the FQY compared to that of **1** (4% in dichloromethane). While the radiative rate constant of (P,P)-3 remained similar to **2**, the lower non-radiative rate constant of (P,P)-3 ($1.69 \times 10^8 \text{ s}^{-1}$) compared to **2** ($2.86 \times 10^8 \text{ s}^{-1}$) corroborated its high FQY (Table 1). The molecular dipole moment of **3** is directed from hexagonally attached [7]helicene towards heptagonally attached [7]helicene through the short axis of pyrene (ESI Fig. S4†). The anti-aromatic character along with the saddle curvature of the heptagonal ring,

lowers the delocalization of the π -electrons making it a less delocalized region for the π -electrons of the molecule, resulting in the direction of the dipolar moment from hexagonally-fused-[7]helicene to heptagonally-fused-[7]helicene.

To gain a further understanding of the excited-state dynamics, the time-resolved fluorescence decay of (P,P)-3, (P,M)*-3, and (P)-8 were measured *via* time-correlated single photon counting technique using a pulsed laser light excited at $24\,154 \text{ cm}^{-1}$ (Fig. 5). Unlike mono-exponential fitting of **1** and **2**, the decay curves of **3** were fitted with bi-exponential function giving two lifetimes with different fractional contributions. The fitted lifetimes for (P,P)-3 are 2.26 ns (0.98) and 11.87 ns (0.02), while for (P,M)*-3 are 2.17 ns (0.96) and 10.99 ns (0.04). The area-weighted average lifetime⁸² of (P,P)-3 and (P,M)*-3 is calculated to be 3.19 ns and 3.67 ns, respectively, which are significantly shorter than that of [7]helicene (13.8 ns).⁸³ The decay curve of (P)-8 was fitted with a mono-exponential function to give a lifetime of 2.21 ns similar to that of **2**.

The chiroptical properties of **3** and **8** were investigated through ECD and CPL measurements in dichloromethane (Fig. 6). The absolute configuration of the (P,P) enantiomer of **3** was verified by TD-DFT calculated ECD spectra (ESI Fig. S5b†). The enantiomeric pair of **3** and **8** showed complementary mirror image ECD spectra with multiple opposite Cotton effects in the UV-vis region. Both (P,P)-3 and (P)-8 exhibit a negative and relatively small Cotton effect for the lowest energy transition. However, the pristine [7]helicene shows the opposite phenomenon: a strong and positive cotton effect for the lowest energy transition. Unlike the absorption spectra where major transitions of **1** and **2** manifest in **3**, the ECD spectra of **3** resemble that of **2** with a diminished intensity for the $S_0 \rightarrow S_1$ transition.

The experimentally determined absorption dissymmetry factor ($g_{\text{abs}} = \Delta\epsilon/\epsilon$) of **3** is in the range of 2.43×10^{-3} – 2.68×10^{-3} and for **8**, it is in the range of 2.63×10^{-3} – 3.15×10^{-3} (Fig. 7), which is similar to that of **1** and **2**. The experimental g_{abs} for **3** was in harmony with the TD-DFT calculated dissymmetry value (Table 2). Although **3** showed nearly three-fold lower magnetic transition dipole moment (μ'_m) for $S_0 \rightarrow S_1$ transition compared to **1** and **2**, the similar g_{abs} values are because of much higher $|\cos \theta|$ for **3**.

Both (P,P) and (M,M) enantiomers of **3** and **8** showed complementary mirror image CPL signals (Fig. 6), which are in harmony with their respective lower energy CD signals, signifying that both low energy absorption in $S_0 \rightarrow S_1$ and emission ($S_1 \rightarrow S_0$) involved same electronic transitions. The shifted CPL

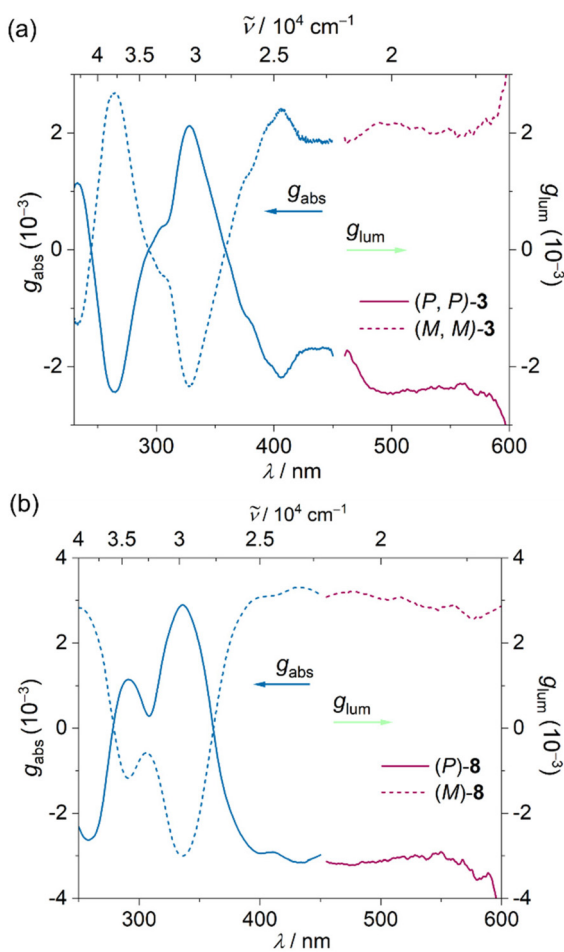


Fig. 7 Absorption dissymmetry factor (g_{abs}) (blue) and luminescence dissymmetry factor (g_{lum}) (red) of (P,P) (solid line) and (M,M) (dashed line) enantiomers of (a) **3** and (b) **8** in dichloromethane ($c \sim 10^{-5} \text{ M}$).

Table 2 Calculated electric and magnetic transition dipole moments, and dissymmetry factor for $S_0 \rightarrow S_1$ and $S_1 \rightarrow S_0$ transitions for **1**, **2** and (P,P)-**3**

Compd	$S_0 \rightarrow S_1$				$S_1 \rightarrow S_0$			
	$ \mu'_e /10^{-20} \text{ esu cm}$	$ \mu'_m /10^{-20} \text{ erg G}^{-1}$	$ \cos \theta $	$ g_{\text{abs}} /10^{-3}$	$ \mu_e /10^{-20} \text{ esu cm}$	$ \mu_m /10^{-20} \text{ erg G}^{-1}$	$ \cos \theta $	$ g_{\text{lum}} /10^{-3}$
1	363.86	1.32	0.11	1.6	478.20	1.34	0.11	1.2
2	711.16	1.29	0.29	2.1	987.54	1.72	0.21	1.5
(P,P)- 3	587.14	0.42	0.76	2.2	913.89	0.55	0.65	1.6

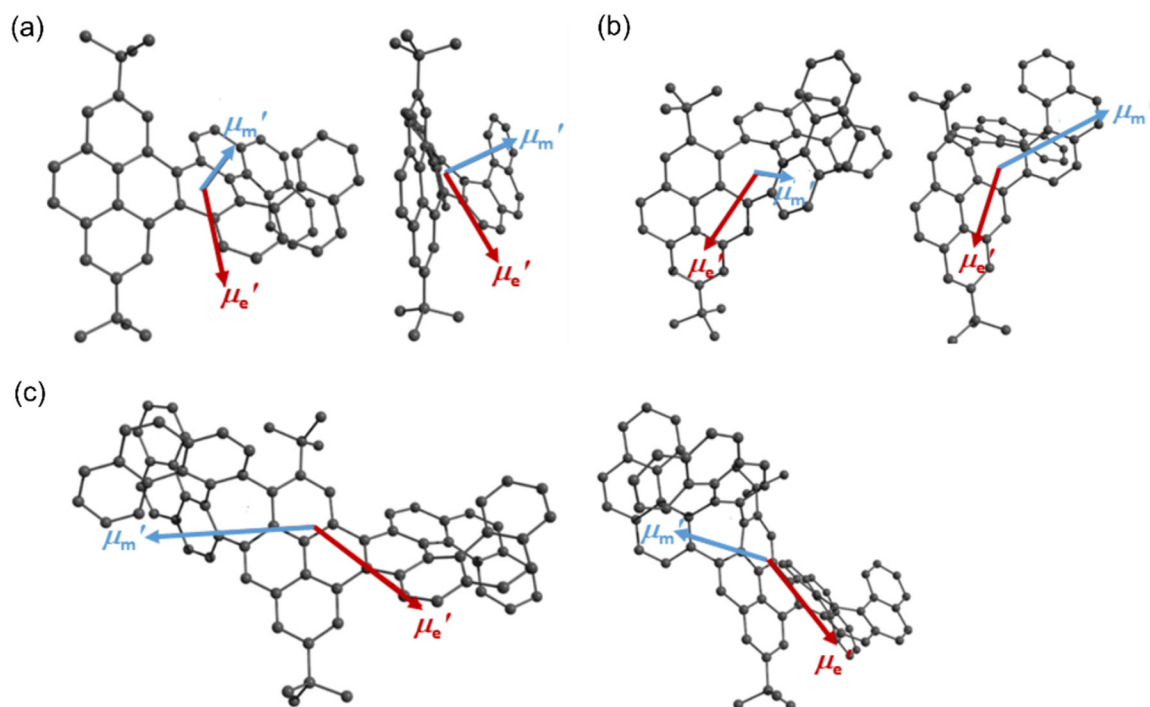


Fig. 8 The spatial arrangement of electric (μ_e') and magnetic (μ_m') dipole moment vectors for the $S_0 \rightarrow S_1$ transition of (a) *(P)*-1 (μ_e' decreased by 200) (b) *(P)*-2 (μ_e' decreased by 400 and μ_m' increased by 2) (c) *(P,P)*-3 (μ_e' decreased by 400 and μ_m' increased by 5). Hydrogen atoms are omitted for clarity.

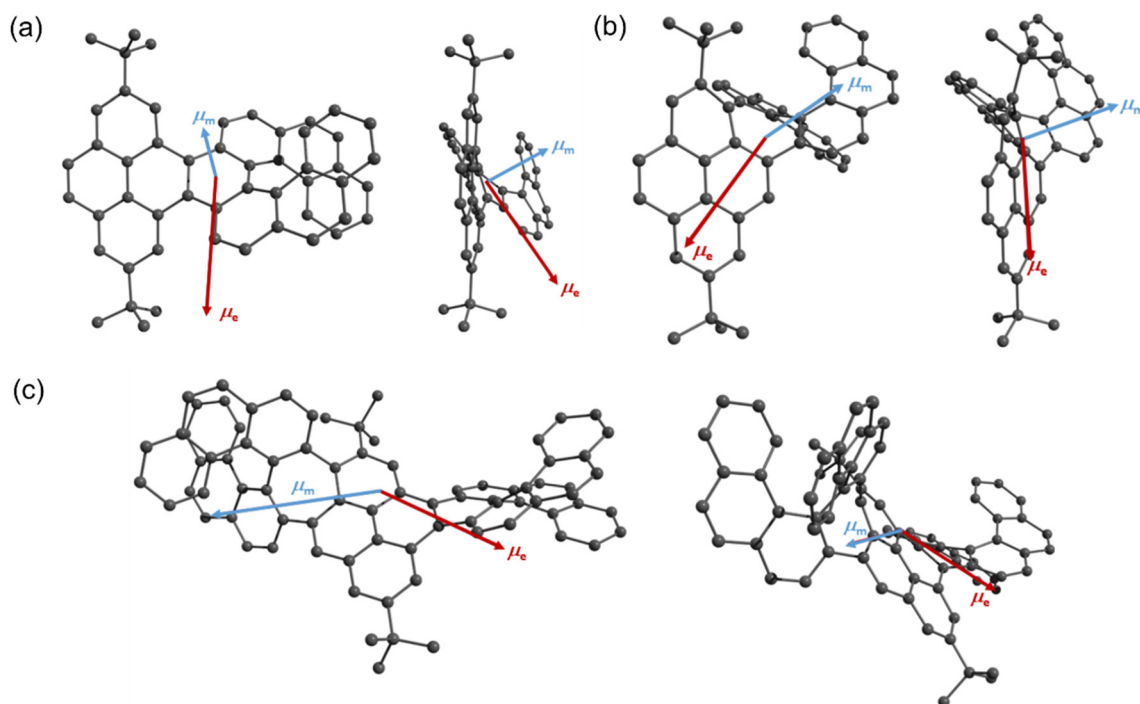


Fig. 9 The spatial arrangement of electric (μ_e) and magnetic (μ_m) dipole moment vectors for the $S_1 \rightarrow S_0$ transition of (a) *(P)*-1 (μ_e decreased by 300 and μ_m increased by 5) (b) *(P)*-2 (μ_e decreased by 800 and μ_m increased by 5) (c) *(P,P)*-3 (μ_e decreased by 400). Hydrogen atoms are omitted for clarity.

maxima to that of fluorescence can be explained because of different measurement angles set up for light path in the respective instruments and different calibrations in both spectrometers.^{84,85} The CPL and fluorescence spectrometers follow a 180° and 90° path set up, respectively, for measurements. The experimentally obtained luminescence dissymmetry factor (g_{lum}) of **3** and **8** is 2.47×10^{-3} (at 494 nm) and 3.17×10^{-3} (at 484 nm), respectively. **3** showed nearly double the g_{lum} of **1** and similar to that of **2** (Fig. 7). From the TD-DFT calculations for the $S_1 \rightarrow S_0$ transition, g_{lum} was calculated to be 1.6×10^{-3} for **3** (Table 2). The solid-state CPL spectra for enantiomers of **3** and **8** were measured in a drop-casted thin film (ESI Fig. S2b†). The enantiomers exhibited consistent CPL signals in both solution and solid-state measurements. The solid-state luminescence dissymmetry factor ($g_{lum, solid}$) of **3** and **8** is 1.41×10^{-3} (at 507 nm) and 1.33×10^{-3} (at 489 nm), respectively, which is slightly less than that in dichloromethane.

The spatial arrangement of μ_e and μ_m in the case of **1** and **2** is quite different from **3**. For **1** and **2**, the dipole moments move out of the molecular plane mainly originating at the central ring of the [7]helicene, unit whereas for **3**, μ_e and μ_m mainly move along the pyrene plane. The similar spatial arrangement of electric and magnetic dipole moments in both $S_0 \rightarrow S_1$ (Fig. 8) and $S_1 \rightarrow S_0$ transitions (Fig. 9) of **3** implies the comparable electronic structure involved in these transitions corroborating the structural rigidity of **3**. Also, the g_{lum}/g_{abs} value for **3** and **8** is nearly unity symbolizing its higher structural rigidity. The g_{lum}/g_{abs} value is much higher than the linearly fitted regression value of 0.6 for conventional [*n*]helicene and heliceneoids.⁸⁶ Comparison of dissymmetry factors between **3** and **8** indicates that the key (chir)optical responses are dominated by the heptagonal [7]helicene compared to the hexagonally attached [7]helicene.

Conclusion

In summary, we achieved a stereospecific synthesis of C_1 symmetric pyrene bridged double [7]helicene, (*P,P*)*-**3** and (*P,M*)*-**3**, employing Suzuki coupling – C–H activation and Scholl-type oxidative cyclodehydrogenation. Irrespective of [7]helicene conformation, (*P,P*)*-**3** and (*P,M*)*-**3** showed identical absorption and emission spectra, suggesting that the conformation of [7]helicenes in **3** does not affect electronic structural properties. No significant changes were observed in the dissymmetry factors despite the addition of a [7]helicene to **1** and **2**. Major photophysical properties of **3** were dominated by the heptagonally fused [7]helicene compared to the hexagonally fused [7]helicene. However, considerable enhancement in FQY is observed for double helicene **3**, compared to **1** and **2**. The Gibbs activation energy barrier for diastereomerization of **3** is determined to be $43.2 \text{ kcal mol}^{-1}$, which is among the highest experimental values reported for [7]helicene fused PAHs. The compound **8** consists of a heptagonal embedded [7]helicene and axially chiral biphenanthrene unit was also fully characterized. Also **8** exhibited enhanced FQY to **1**, **2** and comparable to **3**.

Experimental section

General information

All chemicals and solvents were purchased from commercial sources and were used without further purification unless stated otherwise. 3,3'-Dibromo-4,4'-biphenanthrene,²⁰ and 2-(2,7-di-*tert*-butylpyrene-4-yl)-4,4,5,5-tetramethyl-1,3,2-dioxaborolane⁵⁵ were synthesized according to literature known protocols and purity was confirmed by ¹H NMR.^{20,55} The reactions and experiments sensitive to dioxygen were performed using Schlenk techniques and with nitrogen-saturated solvents. Before using all the glassware and NMR tubes were dried in the oven at 80 °C for 12 h.

Synthesis of **6** and **7**

In a Schlenk tube (*S*)-3,3'-dibromo-4,4'-biphenanthrene (70.0 mg, 0.13 mmol, 2.0 equiv.) and 2,2'-(2,7-di-*tert*-butylpyrene-4,9-diyl)bis(4,4,5,5-tetramethyl-1,3,2-dioxaborolane) (36.5 mg, 0.065 mmol, 1.0 equiv.) were dissolved in 3 mL THF, and potassium carbonate (44.5 mg, 0.32 mmol, 5.0 equiv.) was dissolved in water (1 mL), and both solutions were degassed for 10 min separately and mixed. To this mixture tetrakis(triphenylphosphine)palladium(0) [Pd(PPh₃)₄] (7.5 mg, 0.0065 mmol, 10.0 mol%) was added under nitrogen flow and degassed again for 10 min. The reaction flask was then sealed with Teflon tape and heated at 85 °C for 15 h in an oil bath. The reaction was quenched by adding water and extracted with ethyl acetate. The collected organic phase was dried over anhydrous sodium sulfate. The solvent was removed under reduced pressure using a rotary evaporator, and the crude product was passed through a silica column using 1–2% ethyl acetate in petroleum ether to isolate two different fractions corresponding to **6** and **7** in 63% (41.3 mg) and 21% (13.8 mg) yield respectively. For **6** and **7**, containing fractions the ¹H NMR spectrum showed densely populated aromatic signals, out of which major parts could not be integrated, possibly because of the detection of diastereomeric protons. The HRMS of two fractions were listed below.

For 6 HRMS (MALDI-TOF) *m/z*: [M] calcd for [C₈₀H₅₆] 1016.4382; found 1016.4397.

For 7 HRMS (MALDI-TOF) *m/z*: [M] calcd for [C₈₀H₅₈] 1018.4539; found 1018.4569.

Synthesis of (*P,P*)-**3**

In an oven dried Schlenk tube, the isolated **6** (40.0 mg, 0.04 mmol, 1.0 equiv.) was dissolved in dry dichloromethane (DCM) and stirred at 0 °C for 10 min. The solution was added dropwise to a flask containing DDQ (17.9 mg, 0.08 mmol, 2.0 equiv.) and stirred at 0 °C for 20 min followed by addition of methanesulfonic acid (MsOH) (0.1 mL, 1.54 μmol, 0.02 equiv.). The reaction mixture was continued to stir at 0 °C for 4 h under the nitrogen atmosphere. Once the TLC confirmed full consumption of **6**, the reaction was quenched by saturated NaHCO₃ solution and extracted with DCM. The collected organic phase was dried over anhydrous sodium sulfate. The solvent was evaporated under reduced pressure using a rotary

evaporator, and the crude product was purified by column chromatography on silica gel using 5% ethyl acetate in petroleum ether to yield 22.6 mg (57%) as a green fluorescent solid of (*P,P*)-3. The (*M,M*)-3 was prepared following the above-mentioned reaction conditions with similar yields from (*R*)-4.

Characterization of (*P,P*)-3

Melting point: 240–244 °C.

HRMS (MALDI-TOF) *m/z*: [M] calcd for [C₈₀H₅₄] 1014.4226; found 1014.4235.

¹H NMR (400 MHz, CD₂Cl₂, 25 °C): δ [ppm] = 9.47 (s, 1H), 9.31–9.25 (m, 2H), 9.13 (d, *J* = 8.5 Hz, 1H), 8.76 (s, 1H), 8.43 (d, *J* = 1.6 Hz, 1H), 8.31 (d, *J* = 8.6 Hz, 1H), 8.23 (d, *J* = 8.7 Hz, 1H), 8.13 (d, *J* = 8.4 Hz, 1H), 7.94 (d, *J* = 8.4 Hz, 1H), 7.87 (d, *J* = 8.6 Hz, 1H), 7.83 (d, *J* = 8.6 Hz, 1H), 7.80 (d, *J* = 8.2 Hz, 1H), 7.75 (d, *J* = 8.7 Hz, 1H), 7.66 (d, *J* = 8.7 Hz, 1H), 7.59–7.34 (m, 11H), 7.16–7.06 (m, 3H), 7.04–6.98 (m, 2H), 6.75–6.68 (m, 2H), 6.61–6.52 (m, 3H), 1.81 (s, 9H), 1.72 (s, 9H).

¹³C NMR (101 MHz, CD₂Cl₂, 25 °C): δ [ppm] = 149.18, 147.35, 144.44, 144.31, 140.13, 137.59, 136.19, 134.53, 134.32, 134.25, 133.25, 133.21, 133.11, 133.10, 132.49, 132.37, 131.63, 131.41, 130.91, 130.88, 130.54, 130.23, 130.05, 129.76, 129.73, 129.57, 129.11, 129.09, 129.03, 129.01, 128.99, 128.77, 128.75, 128.61, 128.58, 128.45, 128.12, 128.08, 127.97, 127.95, 127.91, 127.85, 127.78, 127.74, 127.73, 127.15, 127.11, 127.05, 127.03, 126.59, 126.57, 126.12, 126.01, 125.97, 125.79, 125.53, 125.42, 124.71, 124.68, 124.63, 124.05, 123.16, 123.09, 122.33, 38.60, 35.82, 34.91, 31.99.

Synthesis of (*P,M*)*-3

To obtain (*P,M*)*-3, the Suzuki coupling-C–H activation was performed under identical reaction conditions for (*P,P*)*-3 using a 1 : 1 mixture of (*S*)- and (*R*)-3,3'-dibromo-4,4'-biphenanthrene followed by Scholl-type cyclodehydrogenation reaction with the diastereomeric mixture of 6. The isolated diastereomeric mixture of 3 from column chromatography was injected into CSP-HPLC to separate (*P,P*)*-3 and (*P,M*)*-3 in a 4.3 : 1 ratio.

Characterization of (*P,M*)*-3

Melting point: 239–244 °C.

HRMS (MALDI-TOF) *m/z*: [M] calcd for [C₈₀H₅₄] 1014.4226; found 1014.4251

¹H NMR (400 MHz, CD₂Cl₂, 25 °C): δ [ppm] = 9.53 (s, 1H), 9.32 (s, 1H), 9.09 (d, *J* = 2.2 Hz, 1H), 9.07 (d, *J* = 1.7 Hz, 1H), 8.70 (s, 1H), 8.39 (d, *J* = 1.3 Hz, 1H), 8.23–8.13 (m, 3H), 7.86–7.74 (m, 4H), 7.71–7.74 (m, 2H), 7.60–7.53 (m, 5H), 7.48–7.43 (m, 2H), 7.42–7.34 (m, 3H), 7.21–7.13 (m, 2H), 7.11–7.09 (m, 1H), 7.05–6.96 (m, 3H), 6.73–6.67 (m, 2H), 6.61–6.55 (m, 2H), 6.49 (d, *J* = 8.5 Hz, 1H), 1.83 (s, 9H), 1.72 (s, 9H).

¹³C NMR (151 MHz, CD₂Cl₂, 25 °C): δ [ppm] = 149.57, 149.47, 143.91, 143.39, 140.40, 137.08, 136.59, 134.62, 134.35, 133.96, 133.28, 133.24, 133.07, 132.76, 132.67, 132.51, 132.49, 131.95, 131.52, 131.39, 131.31, 130.80, 130.55, 130.50, 130.49, 130.27, 129.77, 129.75, 129.73, 129.65, 129.11, 129.06, 128.98,

128.95, 128.91, 128.80, 128.73, 128.60, 128.58, 128.49, 128.16, 128.14, 127.94, 127.91, 127.74, 127.69, 127.15, 127.12, 126.96, 126.57, 126.49, 126.11, 126.08, 125.88, 125.79, 125.71, 125.69, 125.55, 125.40, 125.39, 125.34, 125.30, 124.75, 124.64, 124.01, 123.21, 122.44, 122.14, 38.52, 35.17, 32.01, 30.08.

Synthesis of (*P*)-8

In an oven dried Schlenk tube, 7 (20.0 mg, 0.02 mmol, 1.0 equiv.) was dissolved in dry DCM and stirred at 0 °C for 10 min. The solution was added dropwise to a flask containing DDQ (8.9 mg, 0.04 mmol, 2.0 equiv.) and stirred at 0 °C for 20 min followed by addition of MsOH (0.1 mL, 1.54 μmol, 0.07 equiv.). The reaction mixture was stirred at 0 °C for 4 h under the nitrogen atmosphere. Once the TLC confirmed full consumption of 7, the reaction was quenched by saturated NaHCO₃ solution and extracted with DCM. The collected organic phase was dried over anhydrous sodium sulfate. The solvent was evaporated under reduced pressure using a rotary evaporator, and the crude product was purified by column chromatography on silica gel using 5% ethyl acetate in petroleum ether to yield 8.4 mg (42%) of (*P*)-8 as green fluorescent solid.

Melting point: 133–137 °C.

HRMS (MALDI-TOF) *m/z*: [M] calcd for [C₈₀H₅₆] 1016.4382; found 1016.4389.

¹H NMR (400 MHz, CD₂Cl₂, 25 °C): δ [ppm] = 8.51 (d, *J* = 8.7 Hz, 1H), 8.41 (s, 1H), 8.29 (d, *J* = 8.1 Hz, 1H), 8.24 (d, *J* = 8.1 Hz, 1H), 8.10 (d, *J* = 8.9 Hz, 1H), 8.03–8.00 (m, 2H), 8.00–7.96 (m, 2H), 7.93 (d, *J* = 8.3 Hz, 1H), 7.75 (d, *J* = 8.0 Hz, 1H), 7.71–7.64 (m, 3H), 7.60 (d, *J* = 8.2 Hz, 1H), 7.49 (t, *J* = 7.7 Hz, 2H), 7.46–7.41 (m, 2H), 7.40–7.34 (m, 2H), 7.31–7.25 (m, 2H), 7.13–7.09 (m, 2H), 7.08–7.04 (m, 2H), 7.03–7.00 (m, 2H), 6.97–6.91 (m, 2H), 6.81–6.77 (m, 1H), 6.69–6.61 (m, 3H), 6.40 (d, *J* = 8.2 Hz, 1H), 1.53 (s, 9H), 1.34 (s, 9H).

¹³C NMR (101 MHz, CD₂Cl₂, 25 °C): δ [ppm] = 148.22, 148.19, 144.24, 144.16, 142.37, 140.40, 139.42, 139.30, 137.42, 137.16, 135.82, 134.49, 134.39, 134.35, 134.14, 133.62, 133.53, 133.20, 133.19, 132.95, 132.86, 132.13, 131.97, 131.84, 131.40, 130.79, 130.74, 130.61, 130.55, 130.53, 130.20, 130.01, 129.99, 129.39, 129.34, 129.11, 129.00, 128.86, 128.41, 128.24, 128.19, 128.17, 128.04, 127.96, 127.93, 127.82, 127.73, 127.70, 127.67, 127.61, 127.29, 127.23, 127.05, 127.01, 126.93, 126.67, 126.57, 126.54, 126.48, 126.21, 125.94, 125.85, 125.69, 124.62, 124.55, 122.82, 122.49, 121.01, 120.53, 37.92, 35.28, 35.04, 31.76.

Conflicts of interest

There are no conflicts to declare.

Acknowledgements

P. R. thanks Julius-Maximilians-Universität Würzburg for “Excellent Ideas” program. We sincerely thank Prof. C. Lambert (University of Würzburg) for generously sup-

porting our research. Funding: This project received funding from Deutsche Forschungsgemeinschaft (DFG) (Project No. 448604676). The CPL/CD hybrid spectrometer was funded by the DFG (Project No. 444286426).

References

- 1 Y. Shen and C. F. Chen, Helicenes: synthesis and applications, *Chem. Rev.*, 2012, **112**, 1463–1535.
- 2 R. H. Martin, The Helicenes, *Angew. Chem., Int. Ed. Engl.*, 1974, **13**, 649–660.
- 3 P. Ravat, Carbo[n]helicenes Restricted to Enantiomerize: An Insight into the Design Process of Configurationally Stable Functional Chiral PAHs, *Chem. – Eur. J.*, 2021, **27**, 3957–3967.
- 4 S. T. J. Ryan and M. J. Fuchter, in *Helicenes*, 2022, pp. 473–503, DOI: [10.1002/9783527829415.ch15](https://doi.org/10.1002/9783527829415.ch15).
- 5 P. Ravat, T. Šolomek and M. Juriček, Helicenes as Chiroptical Photoswitches, *ChemPhotoChem*, 2019, **3**, 180–186.
- 6 M. J. Narcis and N. Takenaka, Helical-Chiral Small Molecules in Asymmetric Catalysis, *Eur. J. Org. Chem.*, 2014, 21–34.
- 7 P. Aillard, A. Voituriez and A. Marinetti, Helicene-like chiral auxiliaries in asymmetric catalysis, *Dalton Trans.*, 2014, **43**, 15263–15278.
- 8 D. Sakamoto, I. Gay Sánchez, J. Rybáček, J. Vacek, L. Bednářová, M. Pazderková, R. Pohl, I. Čísařová, I. G. Stará and I. Starý, Cycloiridated Helicenes as Chiral Catalysts in the Asymmetric Transfer Hydrogenation of Imines, *ACS Catal.*, 2022, **12**, 10793–10800.
- 9 T. R. Kelly, Progress toward a Rationally Designed Molecular Motor, *Acc. Chem. Res.*, 2001, **34**, 514–522.
- 10 P. A. Summers, A. P. Thomas, T. Kench, J. B. Vannier, M. K. Kuimova and R. Vilar, Cationic helicenes as selective G4 DNA binders and optical probes for cellular imaging, *Chem. Sci.*, 2021, **12**, 14624–14634.
- 11 Q. Xu, C. Wang, J. He, X. Li, Y. Wang, X. Chen, D. Sun and H. Jiang, Corannulene-based nanographene containing helical motifs, *Org. Chem. Front.*, 2021, **8**, 2970–2976.
- 12 T. Otani, A. Tsuyuki, T. Iwachi, S. Someya, K. Tateno, H. Kawai, T. Saito, K. S. Kanyiva and T. Shibata, Facile Two-Step Synthesis of 1,10-Phenanthroline-Derived Polyaza[7]helicenes with High Fluorescence and CPL Efficiency, *Angew. Chem., Int. Ed.*, 2017, **56**, 3906–3910.
- 13 S. K. Pedersen, K. Eriksen and M. Pittelkow, Symmetric, Unsymmetrical, and Asymmetric [7]-, [10]-, and [13] Helicenes, *Angew. Chem., Int. Ed.*, 2019, **58**, 18419–18423.
- 14 Y. Yamamoto, H. Sakai, J. Yuasa, Y. Araki, T. Wada, T. Sakanoue, T. Takenobu, T. Kawai and T. Hasobe, Synthetic Control of the Excited-State Dynamics and Circularly Polarized Luminescence of Fluorescent “Push-Pull” Tetrathia [9]helicenes, *Chem. – Eur. J.*, 2016, **22**, 4263–4273.
- 15 Y. Nakakuki, T. Hirose, H. Sotome, H. Miyasaka and K. Matsuda, Hexa-peri-hexabenz[7]helicene: Homogeneously pi-Extended Helicene as a Primary Substructure of Helically Twisted Chiral Graphenes, *J. Am. Chem. Soc.*, 2018, **140**, 4317–4326.
- 16 H. Oyama, M. Akiyama, K. Nakano, M. Naito, K. Nobusawa and K. Nozaki, Synthesis and Properties of [7]Helicene-like Compounds Fused with a Fluorene Unit, *Org. Lett.*, 2016, **18**, 3654–3657.
- 17 Z. Qiu, C. W. Ju, L. Frederic, Y. Hu, D. Schollmeyer, G. Pieters, K. Mullen and A. Narita, Amplification of Dissymmetry Factors in pi-Extended [7]- and [9]Helicenes, *J. Am. Chem. Soc.*, 2021, **143**, 4661–4667.
- 18 Y. Zhu and J. Wang, Helical Synthetic Nanographenes with Atomic Precision, *Acc. Chem. Res.*, 2023, **56**, 363–373.
- 19 A. K. Swain, K. Kolanji, C. Stapper and P. Ravat, C₂- and C₁-Symmetric Configurationally Stable Pyrene-Fused [5] Helicenes Connected via Hexagonal and Heptagonal Rings, *Org. Lett.*, 2021, **23**, 1339–1343.
- 20 A. K. Swain, K. Radacki, H. Braunschweig and P. Ravat, Pyrene-Fused [7]Helicenes Connected Via Hexagonal and Heptagonal Rings: Stereospecific Synthesis and Chiroptical Properties, *J. Org. Chem.*, 2022, **87**, 993–1000.
- 21 F. Zhang, F. Rauch, A. K. Swain, T. B. Marder and P. Ravat, Efficient Narrowband Circularly Polarized Light Emitters Based on 1,4-B,N-embedded Rigid Donor–Acceptor Helicenes, *Angew. Chem., Int. Ed.*, 2023, e202218965.
- 22 T. Ikai, K. Oki, S. Yamakawa and E. Yashima, Stereospecific Synthesis of Enantiopure [6]Helicene Containing a Seven-Membered Ring and [7]Helicene via Acid-Promoted Stepwise Alkyne Annulations of Doubly Axial-Chiral Precursors, *Angew. Chem., Int. Ed.*, 2023, e202301836.
- 23 A. Tsurusaki and K. Kamikawa, Multiple Helicenes Featuring Synthetic Approaches and Molecular Structures, *Chem. Lett.*, 2021, **50**, 1913–1932.
- 24 F. Saal, F. Zhang, M. Holzapfel, M. Stolte, E. Michail, M. Moos, A. Schmiedel, A.-M. Krause, C. Lambert, F. Würthner and P. Ravat, [n]Helicene Diimides (n = 5, 6, and 7): Through-Bond versus Through-Space Conjugation, *J. Am. Chem. Soc.*, 2020, **142**, 21298–21303.
- 25 R. Yamano, Y. Shibata and K. Tanaka, Synthesis of Single and Double Dibenzohelicenes by Rhodium-Catalyzed Intramolecular [2 + 2 + 2] and [2 + 1 + 2 + 1] Cycloaddition, *Chem. – Eur. J.*, 2018, **24**, 6364–6370.
- 26 L. Wang, Y. Han, J. Zhang, X. Li, X. Liu and J. Xiao, Stable Double and Quadruple [5]Helicene Derivatives: Synthesis, Structural Analysis, and Physical Properties, *Org. Lett.*, 2020, **22**, 261–264.
- 27 Y. Hu, G. M. Paterno, X. Y. Wang, X. C. Wang, M. Guizzardi, Q. Chen, D. Schollmeyer, X. Y. Cao, G. Cerullo, F. Scotognella, K. Mullen and A. Narita, pi-Extended Pyrene-Fused Double [7] Carbohelicene as a Chiral Polycyclic Aromatic Hydrocarbon, *J. Am. Chem. Soc.*, 2019, **141**, 12797–12803.
- 28 A. Ushiyama, S. Hiroto, J. Yuasa, T. Kawai and H. Shinokubo, Synthesis of a figure-eight azahelicene dimer with high emission and CPL properties, *Org. Chem. Front.*, 2017, **4**, 664–667.
- 29 F. Saal and P. Ravat, Imide-Functionalized Helical PAHs: A Step towards New Chiral Functional Materials, *Synlett*, 2021, 1879–1890.

- 30 F. Zhang, E. Michail, F. Saal, A. M. Krause and P. Ravat, Stereospecific Synthesis and Photophysical Properties of Propeller-Shaped C₉₀ H₄₈ PAH, *Chem. – Eur. J.*, 2019, **25**, 16241–16245.
- 31 G. R. Kiel, H. M. Bergman, A. E. Samkian, N. J. Schuster, R. C. Handford, A. J. Rothenberger, R. Gomez-Bombarelli, C. Nuckolls and T. D. Tilley, Expanded [23]-Helicene with Exceptional Chiroptical Properties via an Iterative Ring-Fusion Strategy, *J. Am. Chem. Soc.*, 2022, **144**, 23421–23427.
- 32 T. Mori, Chiroptical Properties of Symmetric Double, Triple, and Multiple Helicenes, *Chem. Rev.*, 2021, **121**, 2373–2412.
- 33 W.-W. Yang and J.-J. Shen, Multiple Heterohelicenes: Synthesis, Properties and Applications, *Chem. – Eur. J.*, 2022, **28**, e202202069.
- 34 F. Zhang, K. Radacki, H. Braunschweig, C. Lambert and P. Ravat, Zinc-[7]helicenocyanine and Its Discrete π -Stacked Homochiral Dimer, *Angew. Chem., Int. Ed.*, 2021, **60**, 23656–23660.
- 35 K. Kato, Y. Segawa and K. Itami, Symmetric Multiple Carbohelicenes, *Synlett*, 2019, 370–377.
- 36 Y.-F. Wu, L. Zhang, Q. Zhang, S.-Y. Xie and L.-S. Zheng, Multiple [n]helicenes with various aromatic cores, *Org. Chem. Front.*, 2022, **9**, 4726–4743.
- 37 S. Miguez-Lago, I. F. A. Mariz, M. A. Medel, J. M. Cuerva, E. Macoas, C. M. Cruz and A. G. Campana, Highly contorted superhelicene hits near-infrared circularly polarized luminescence, *Chem. Sci.*, 2022, **13**, 10267–10272.
- 38 T. Fujikawa, Y. Segawa and K. Itami, Synthesis and Structural Features of Quadruple Helicenes: Highly Distorted π Systems Enabled by Accumulation of Helical Repulsions, *J. Am. Chem. Soc.*, 2016, **138**, 3587–3595.
- 39 T. Fujikawa, N. Mitoma, A. Wakamiya, A. Saeki, Y. Segawa and K. Itami, Synthesis, properties, and crystal structures of π -extended double [6]helicenes: contorted multi-dimensional stacking lattice, *Org. Biomol. Chem.*, 2017, **15**, 4697–4703.
- 40 M. Roy, V. Bereznaia, M. Villa, N. Vanthuyne, M. Giorgi, J.-V. Naubron, S. Poyer, V. Monnier, L. Charles, Y. Carissan, D. Hagebaum-Reignier, J. Rodriguez, M. Gingras and Y. Coquerel, Stereoselective Syntheses, Structures, and Properties of Extremely Distorted Chiral Nanographenes Embedding Hextuple Helicenes, *Angew. Chem., Int. Ed.*, 2020, **59**, 3264–3271.
- 41 V. Bereznaia, M. Roy, N. Vanthuyne, M. Villa, J.-V. Naubron, J. Rodriguez, Y. Coquerel and M. Gingras, Chiral Nanographene Propeller Embedding Six Enantiomerically Stable [5]Helicene Units, *J. Am. Chem. Soc.*, 2017, **139**, 18508–18511.
- 42 T. Hosokawa, Y. Takahashi, T. Matsushima, S. Watanabe, S. Kikkawa, I. Azumaya, A. Tsurusaki and K. Kamikawa, Synthesis, Structures, and Properties of Hexapole Helicenes: Assembling Six [5]Helicene Substructures into Highly Twisted Aromatic Systems, *J. Am. Chem. Soc.*, 2017, **139**, 18512–18521.
- 43 Y. Fei and J. Liu, Synthesis of Defective Nanographenes Containing Joined Pentagons and Heptagons, *Adv. Sci.*, 2022, **9**, 2201000.
- 44 J. M. Farrell, V. Grande, D. Schmidt and F. Würthner, A Highly Warped Heptagon-Containing sp² Carbon Scaffold via Vinylaphthyl π -Extension, *Angew. Chem., Int. Ed.*, 2019, **58**, 16504–16507.
- 45 Q. Miao, Heptagons in Aromatics: From Monocyclic to Polycyclic, *Chem. Rec.*, 2015, **15**, 1156–1159.
- 46 A.-C. Bédard, A. Vlassova, A. C. Hernandez-Perez, A. Bessette, G. S. Hanan, M. A. Heuft and S. K. Collins, Synthesis, Crystal Structure and Photophysical Properties of Pyrene–Helicene Hybrids, *Chem. – Eur. J.*, 2013, **19**, 16295–16302.
- 47 R. Bam, W. Yang, G. Longhi, S. Abbate, A. Lucotti, M. Tommasini, R. Franzini, C. Villani, V. J. Catalano, M. M. Olmstead and W. A. Chalifoux, Four-Fold Alkyne Benzannulation: Synthesis, Properties, and Structure of Pyreno[a]pyrene-Based Helicene Hybrids, *Org. Lett.*, 2019, **21**, 8652–8656.
- 48 Y. Yano, H. Ito, Y. Segawa and K. Itami, Helically Twisted Tetracene: Synthesis, Crystal Structure, and Photophysical Properties of Hexabenz[a,c,fg,j,l,op]tetracene, *Synlett*, 2016, 2081–2084.
- 49 M. Buchta, J. Rybáček, A. Jančařík, A. A. Kudale, M. Buděšínský, J. V. Chocholoušová, J. Vacek, L. Bednárová, I. Císařová, G. J. Bodwell, I. Starý and I. G. Stará, Chimerical Pyrene-Based [7]Helicenes as Twisted Polycondensed Aromatics, *Chem. – Eur. J.*, 2015, **21**, 8910–8917.
- 50 T. Kirschbaum, F. Rominger and M. Mastalerz, A Chiral Polycyclic Aromatic Hydrocarbon Monkey Saddle, *Angew. Chem., Int. Ed.*, 2020, **59**, 270–274.
- 51 N. Terada, K. Uematsu, R. Higuchi, Y. Tokimaru, Y. Sato, K. Nakano and K. Nozaki, Synthesis and Properties of Spiro-double Sila[7]helicene: The LUMO Spiro-conjugation, *Chem. – Eur. J.*, 2021, **27**, 9342–9349.
- 52 K. Nakano, Y. Hidehira, K. Takahashi, T. Hiyama and K. Nozaki, Stereospecific Synthesis of Hetero[7]helicenes by Pd-Catalyzed Double N-Arylation and Intramolecular O-Arylation, *Angew. Chem., Int. Ed.*, 2005, **44**, 7136–7138.
- 53 M. Shimizu, I. Nagao, Y. Tomioka and T. Hiyama, Palladium-catalyzed annulation of vic-bis(pinacolatoboryl) alkenes and -phenanthrenes with 2,2'-dibromobiaryls: facile synthesis of functionalized phenanthrenes and dibenzo[g,p]chrysenes, *Angew. Chem., Int. Ed.*, 2008, **47**, 8096–8099.
- 54 J. Tu, G. Li, X. Zhao and F. Xu, Synthesis of triphenylene derivatives by Pd-catalyzed Suzuki coupling/intramolecular CH activation between arylboronic acids and dibromobiaryls, *Tetrahedron Lett.*, 2019, **60**, 44–47.
- 55 L. Ji, I. Krummenacher, A. Friedrich, A. Lorbach, M. Haehnel, K. Edkins, H. Braunschweig and T. B. Marder, Synthesis, Photophysical, and Electrochemical Properties of Pyrenes Substituted with Donors or Acceptors at the 4- or 4,9-Positions, *J. Org. Chem.*, 2018, **83**, 3599–3606.
- 56 M. N. Eliseeva and L. T. Scott, Pushing the Ir-Catalyzed C–H Polyborylation of Aromatic Compounds to Maximum Capacity by Exploiting Reversibility, *J. Am. Chem. Soc.*, 2012, **134**, 15169–15172.





- 57 Y. Zhang, S. H. Pun and Q. Miao, The Scholl Reaction as a Powerful Tool for Synthesis of Curved Polycyclic Aromatics, *Chem. Rev.*, 2022, **122**, 14554–14593.
- 58 N. Ponugoti and V. Parthasarathy, Rearrangements in Scholl Reaction, *Chem. – Eur. J.*, 2022, **28**, e202103530.
- 59 J. Liu, A. Narita, S. Osella, W. Zhang, D. Schollmeyer, D. Beljonne, X. Feng and K. Mullen, Unexpected Scholl Reaction of 6,7,13,14-Tetraarylbenzo[k]tetraphene: Selective Formation of Five-Membered Rings in Polycyclic Aromatic Hydrocarbons, *J. Am. Chem. Soc.*, 2016, **138**, 2602–2608.
- 60 D. Lorbach, M. Wagner, M. Baumgarten and K. Müllen, The right way to self-fuse bi- and terpyrenyls to afford graphenic cutouts, *Chem. Commun.*, 2013, **49**, 10578–10580.
- 61 C. Shen, G. Zhang, Y. Ding, N. Yang, F. Gan, J. Crassous and H. Qiu, Oxidative cyclo-rearrangement of helicenes into chiral nanographenes, *Nat. Commun.*, 2021, **12**, 2786.
- 62 M. Baudillon, T. Cauchy, N. Vanthuyne, N. Avarvari and F. Pop, Configurationally stable dithia[7]helicene and dithia-quasi[8]circulene fused dithiolones, *Org. Chem. Front.*, 2022, **9**, 4260–4270.
- 63 F. Ammon, S. T. Sauer, R. Lippert, D. Lungerich, D. Reger, F. Hampel and N. Jux, Unexpected formation of [5]helicenes from hexaarylbenzenes containing pyrrole moieties, *Org. Chem. Front.*, 2017, **4**, 861–870.
- 64 D. Čavlović, D. Häussinger, O. Blacque, P. Ravat and M. Juriček, Nonacethrene Unchained: A Cascade to Chiral Contorted Conjugated Hydrocarbon with Two sp³-Defects, *JACS Au*, 2022, **2**, 1616–1626.
- 65 S. H. Pun, E. C. H. Wen, Z. Xia, H. Chen, F. R. Fischer and Q. Miao, Reactivity, Regioselectivity, and Synthetic Application of 2-Pyrenyl Units in Scholl Reactions, *ChemRxiv*, 2023, DOI: [10.26434/chemrxiv-2023-dp14j](https://doi.org/10.26434/chemrxiv-2023-dp14j).
- 66 A. Matsumoto, M. Suzuki, D. Kuzuhara, H. Hayashi, N. Aratani and H. Yamada, Tetrabenzoperipentacene: Stable Five-Electron Donating Ability and a Discrete Triple-Layered β -Graphite Form in the Solid State, *Angew. Chem., Int. Ed.*, 2015, **54**, 8175–8178.
- 67 G. Portella, J. Poater, J. M. Bofill, P. Alemany and M. Solà, Local Aromaticity of [n]Acenes, [n]Phenacenes, and [n]Helicenes (n = 1–9), *J. Org. Chem.*, 2005, **70**, 2509–2521.
- 68 L. Rulišek, O. Exner, L. Cwiklik, P. Jungwirth, I. Starý, L. Pospíšil and Z. Havlas, On the Convergence of the Physicochemical Properties of [n]Helicenes, *J. Phys. Chem. C*, 2007, **111**, 14948–14955.
- 69 J. Barroso, J. L. Cabellos, S. Pan, F. Murillo, X. Zarate, M. A. Fernandez-Herrera and G. Merino, Revisiting the racemization mechanism of helicenes, *Chem. Commun.*, 2018, **54**, 188–191.
- 70 R. H. Martin and M.-J. Marchant, Thermal racemisation of [6], [7], [8] and [9] helicene, *Tetrahedron Lett.*, 1972, **13**, 3707–3708.
- 71 T. Fujikawa, Y. Segawa and K. Itami, Synthesis, Structures, and Properties of π -Extended Double Helicene: A Combination of Planar and Nonplanar π -Systems, *J. Am. Chem. Soc.*, 2015, **137**, 7763–7768.
- 72 M. M. Hossain, K. Thakur, M. R. Talipov, S. V. Lindeman, S. Mirzaei and R. Rathore, Regioselectivity in the Scholl Reaction: Mono and Double [7]Helicenes, *Org. Lett.*, 2021, **23**, 5170–5174.
- 73 B. Liu, M. Böckmann, W. Jiang, N. L. Doltsinis and Z. Wang, Perylene Diimide-Embedded Double [8]Helicenes, *J. Am. Chem. Soc.*, 2020, **142**, 7092–7099.
- 74 H. Tanaka, M. Ikenosako, Y. Kato, M. Fujiki, Y. Inoue and T. Mori, Symmetry-based rational design for boosting chiroptical responses, *Nat. Commun.*, 2018, **1**, 38.
- 75 Y. Hu, X.-Y. Wang, P.-X. Peng, X.-C. Wang, X.-Y. Cao, X. Feng, K. Müllen and A. Narita, Benzo-Fused Double [7]Carbohelicene: Synthesis, Structures, and Physicochemical Properties, *Angew. Chem., Int. Ed.*, 2017, **56**, 3374–3378.
- 76 J.-K. Li, X.-Y. Chen, W.-L. Zhao, Y.-L. Guo, Y. Zhang, X.-C. Wang, A. C. H. Sue, X.-Y. Cao, M. Li, C.-F. Chen and X.-Y. Wang, Synthesis of Highly Luminescent Chiral Nanographene, *Angew. Chem., Int. Ed.*, 2023, **62**, e202215367.
- 77 Y. Nakai, T. Mori and Y. Inoue, Theoretical and experimental studies on circular dichroism of carbo[n]helicenes, *J. Phys. Chem. A*, 2012, **116**, 7372–7385.
- 78 E. Vander Donckt, J. Nasielski, J. R. Greenleaf and J. B. Birks, Fluorescence of the helicenes, *Chem. Phys. Lett.*, 1968, **2**, 409–410.
- 79 J.-Y. Hu, A. Paudel, N. Seto, X. Feng, M. Era, T. Matsumoto, J. Tanaka, M. R. J. Elsegood, C. Redshaw and T. Yamato, Pyrene-cored blue-light emitting [4]helicenes: synthesis, crystal structures, and photophysical properties, *Org. Biomol. Chem.*, 2013, **11**, 2186–2197.
- 80 H. Kubo, T. Hirose, T. Nakashima, T. Kawai, J.-Y. Hasegawa and K. Matsuda, Tuning Transition Electric and Magnetic Dipole Moments: [7]Helicenes Showing Intense Circularly Polarized Luminescence, *J. Phys. Chem. Lett.*, 2021, **12**, 686–695.
- 81 Y. Nakai, T. Mori and Y. Inoue, Theoretical and Experimental Studies on Circular Dichroism of Carbo[n]helicenes, *J. Phys. Chem. A*, 2012, **116**, 7372–7385.
- 82 A. Sillen and Y. Engelborghs, The Correct Use of “Average” Fluorescence Parameters, *Photochem. Photobiol.*, 1998, **67**, 475–486.
- 83 J. B. Birks, D. J. S. Birch, E. Cordemans and E. Vander Donckt, Fluorescence of the higher helicenes, *Chem. Phys. Lett.*, 1976, **43**, 33–36.
- 84 T. Harada, H. Hayakawa, M. Watanabe and M. Takamoto, A solid-state dedicated circularly polarized luminescence spectrophotometer: Development and application, *Rev. Sci. Instrum.*, 2016, **87**, 075102.
- 85 U. Resch-Genger and P. C. DeRose, Fluorescence standards: Classification, terminology, and recommendations on their selection, use, and production (IUPAC Technical Report), *Pure Appl. Chem.*, 2010, **82**, 2315–2335.
- 86 H. Tanaka, Y. Inoue and T. Mori, Circularly Polarized Luminescence and Circular Dichroisms in Small Organic Molecules: Correlation between Excitation and Emission Dissymmetry Factors, *ChemPhotoChem*, 2018, **2**, 386–402.



Cite this: DOI: 10.1039/d4sc01814a

All publication charges for this article have been paid for by the Royal Society of Chemistry

Helically twisted nanoribbons *via* stereospecific annulative π -extension reaction employing [7]helicene as a molecular wrench†

Asim Swain, ^a Krzysztof Radacki, ^b Holger Braunschweig ^b and Prince Ravat ^{*a}

Over the past decade, significant progress has been made in synthesizing atomically precise carbon nanostructures, particularly graphene nanoribbons (NRs), employing advanced synthetic methodologies. Despite these advancements, achieving control over the stereochemistry of twisted NRs has proven to be a formidable challenge. This manuscript presents a strategic approach to achieve absolute control over the single-handed helical conformation in a cove-edged NR. This strategy leverages enantiopure helicenes as a molecular wrench, intricately influencing the overall conformation of the NR. [7]helicenes stitched to the terminal K-regions of a conjugated pyrene NR through a stereospecific annulative π -extension reaction to produce a helically twisted NR with an end-to-end twist of 171°. Furthermore, a detailed investigation of the impact of twisting on the conformational population was studied by quantum chemical calculations.

Received 18th March 2024

Accepted 15th May 2024

DOI: 10.1039/d4sc01814a

rsc.li/chemical-science

Introduction

The electronic properties of graphene nanoribbons (NRs)^{1–8} composed of linearly fused polycyclic aromatic hydrocarbons (PAHs) depend on their size, shape, and most importantly, edge structures. Based on the edges NRs can be classified as cove-edge, armchair-edge, and zigzag-edge NRs.^{9–13} The cove-edge NRs¹⁴ are of special interest as they have the potential to be chiral as a result of the non-planarity arising from the steric hindrance in the cove regions. Cove-edged NRs can adopt a twisted configuration, whether helical or wagging (randomly twisted), contingent upon specific steric congestion along their edges.^{15–18} However, they suffer from low configurational stability and the minimal relative energy difference between helical and wagging conformers due to the rapid flipping of the inner cove's chirality.^{14,19,20} The NRs with *fford* regions—such as supertwistacene²¹ by Wang *et al.* and triply conjugated HBC (*hexa-peri-hexabenzocoronene*)²² by Campana *et al.*—exhibit a slightly higher barrier, allowing room temperature chiral resolution. The nanographenes with bay regions are relatively difficult to twist, as the majority of the rings lie flat in the orthogonal plane with limited options for substitution.

Chalifoux *et al.* achieved a 35° end-to-end twist by substituting only one side of the bay region,²³ while Würthner *et al.* substituted all positions in the bay region, resulting in an enhanced twist of 76° in quaterylene bisimide with an enantiomerization barrier of 30 kcal mol^{−1}.²⁴

The strategy of strain-induced twist has been widely applied to achieve longitudinally twisted acenes ('twistacenes'), the narrowest NRs, which can be manipulated into helical or wagging conformations through the strategic application of crowded substitutions or benzyl annulations (Fig. 1).^{4,25–27} In the late 1990s, Pascal Jr *et al.* pioneered the twisting of acenes by employing bulky phenyl substitutions reaching an astonishing end-to-end twist of 144° (**I**).^{28–30} This record was surpassed by Kilway *et al.* in 2018 with the hexacene derivative, achieving an end-to-end twist of 184°.³¹ In twistacenes, the strain-induced helical twist propagates along the aromatic ring planes. However, often twistacenes owing to the low configurational stability cannot be resolved into enantiomers. Gidron *et al.* engineered helically locked tethered anthracenes (**II**), which can be isolated in an enantiopure form, achieving an end-to-end twist of up to 38°.^{32,33} Several attempts were made to incorporate promising π -electron-rich cores, such as pyrenes³⁴ into twisted acenes. In most cases, the attachment takes place at the K-region of the pyrene, as it offers greater accessibilities compared to other reaction sites of pyrene. Wudl and Zhang developed a molecule (**III**) containing a pentacene core terminally locked by two pyrenes.³⁵ However, it failed to propagate a uniform twist from one end to the other as the twist reverses at the central benzene ring due to the absence of steric groups at crucial positions in the central acene. King *et al.* prepared a K-

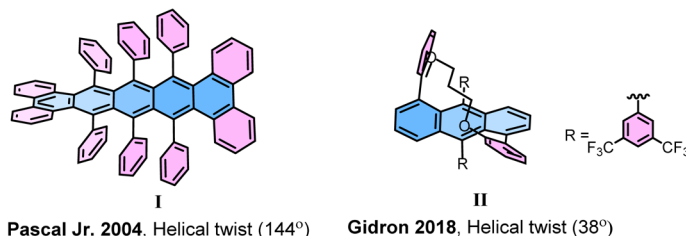
^aJulius-Maximilians-Universität Würzburg, Institut für Organische Chemie, Am Hubland, 97074 Würzburg, Germany. E-mail: princekumar.ravat@uni-wuerzburg.de

^bJulius-Maximilians-Universität Würzburg, Institut für Anorganische Chemie, Am Hubland, 97074 Würzburg, Germany

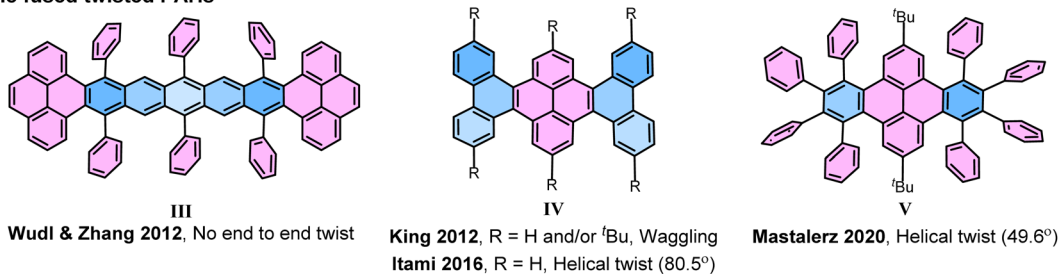
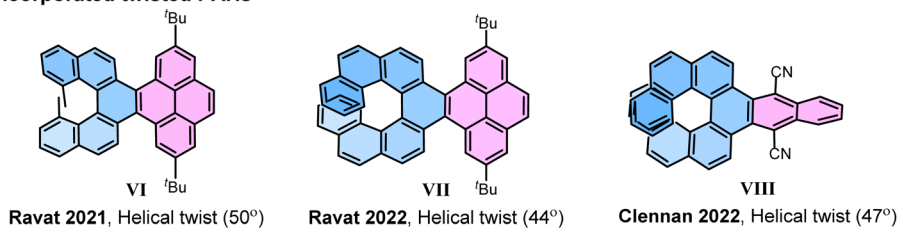
† Electronic supplementary information (ESI) available. CCDC 2315652 and 2315653. For ESI and crystallographic data in CIF or other electronic format see DOI: <https://doi.org/10.1039/d4sc01814a>



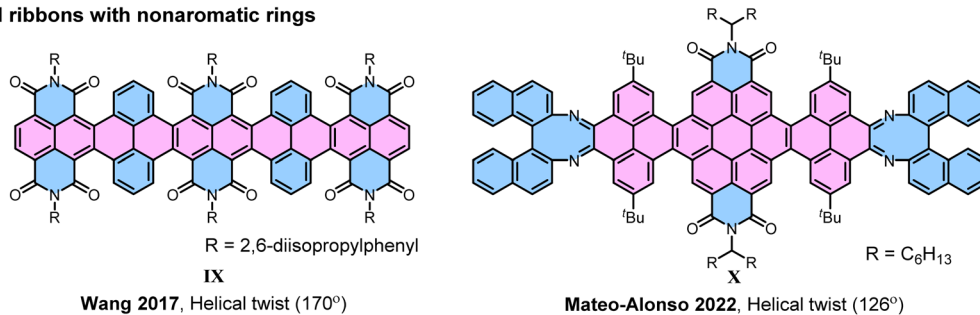
(a) Strain induced twistacene



(b) Pyrene fused twisted PAHs

(c) [*n*]Helicene incorporated twisted PAHs

(d) Twisted ribbons with nonaromatic rings



(e) This work: Stereoselective strain induced helical twist

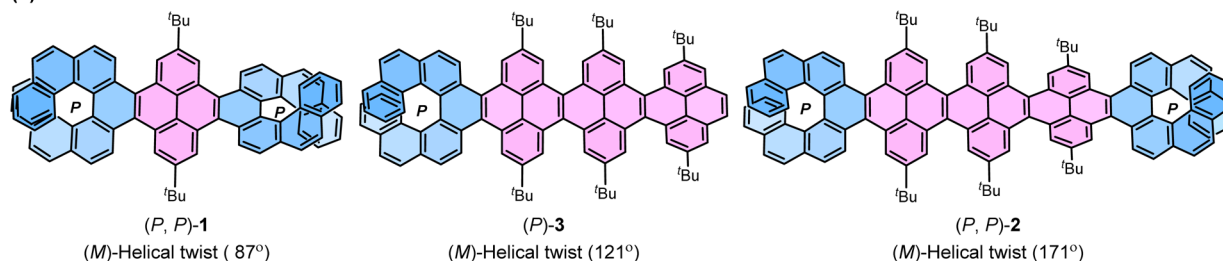


Fig. 1 Selected previous examples of twisted molecules (a)–(d) and newly synthesized helically twisted NRs (e). The helical end-to-end twist is reported in parenthesis.

region phenanthrene annulated pyrene exhibiting wagging conformation (**IV**).³⁶ In contrast, later Itami *et al.* achieved the helical conformation of **IV** with an unsubstituted core.³⁷ Lately, eight phenyl substituted dibenzo[*e, l*]pyrene (**V**) by Mastalerz *et al.* showed the helical structure with an end-to-end twist of 49.6° .³⁸ Recently, we introduced [*n*]helicene as a strain-inducing tensor for generating twisted acene core within a pyrene-fused [*n*]helicene moiety, achieving end-to-end twist of 50° by

incorporating methyl substituted [5]helicene at the K-region of pyrene (**VI**) and a 44° end-to-end twist upon using [7]helicene (**VII**).^{39–41} The helicity of twisted core was dictated by the helicity of the attached [*n*]helicene, which was opposite to each other. This approach was then followed by Clennan to produce a 47° end-to-end twist in a [7]helicene-incorporated anthracene (**VIII**).⁴² Mateo-Alonso *et al.* consequently employed this concept in making a pyrene-coronene cored helical nanoribbon (**X**),



where enantiopure 1,1'-binaphthyl-2,2'-diamine was fused to form [5]helicenoid at both terminal ends containing distorted octagonal rings with four cove region [4]helicene subunits achieving an end-to-end twist of 126° for the central core.⁴³ It is worth mentioning that, similar to **X**, Wang *et al.* in 2017 reported a helically twisted decatwistacene (**IX**) with a much higher end-to-end torsion twist of 170° which was achieved solely through steric hindrance between imide groups and benzene rings in the cove region, without the use of any external steric tensor such as [n]helicinoids, as shown in **X**.⁴⁴ The axially chiral binaphthyl moiety within the ribbon **X** is not fully conjugated and possesses multiple nonaromatic rings with two nitrogen atoms, as well as two imide moieties. Furthermore, in this ribbon, the cove-region gained additional configurational stability from the buttressing effect⁴⁵ of imide moieties. The conformation of **X** was susceptible to temperature fluctuations because of the dynamic nature of the cove regions. Hence, the challenge of developing a sturdy cove-edged hydrocarbon nanoribbon with a precisely stable conformation remains unaddressed.

Earlier investigations into strain-induced twisting suffered from limitations in controlling stereochemistry and low configurational stability, making it a challenging endeavor to synthesize helically twisted chiral hydrocarbon NRs in a stereospecific manner. To address this challenge, we aimed to exert precise control over the twist of cove-edged NRs by integrating configurationally stable enantiopure [n]helicenes^{46–49} at the terminals preceding our earlier work where we attain 99.5% conformational stability for **VII**. The incorporation of enantiopure [n]helicene on both ends of NRs gives rise to three potential stereoisomers: left-handed, right-handed, or wagging. In this study, we demonstrate that the overall conformation and twist of cove-edged NRs can be systematically adjusted by employing terminal helicene moieties, effectively acting as a molecular wrench. This article presents a strategic methodology focused on achieving helically twisted chiral nanoribbons, featuring a central pyrene core NR, securely anchored at terminal K-regions through one or two [7]helicenes *via* stereospecific APEX reactions (Fig. 1e). The influence of [7]helicene on stabilizing the conformers was explored using DFT-optimized structures and single-crystal structure analysis. The (chir)optical properties were comprehensively examined through UV-Vis absorption, emission, electronic circular dichroism (ECD), and circularly polarized luminescence (CPL) spectroscopies. Furthermore, the inversion barrier of compound **1** was estimated through kinetic measurements. The experimental findings were effectively correlated with quantum chemical calculations, providing a comprehensive understanding of the synthesized helically twisted chiral nanoribbons and their intriguing properties.

Results and discussion

Synthesis and characterization

The most straightforward instance of cove-edged nanoribbons (NRs) involves a linearly fused pyrene connected at the K-region. In this study, a central NR comprising three linearly fused pyrene units (**3Py**) was selected. The *peri*-fused benzene rings in

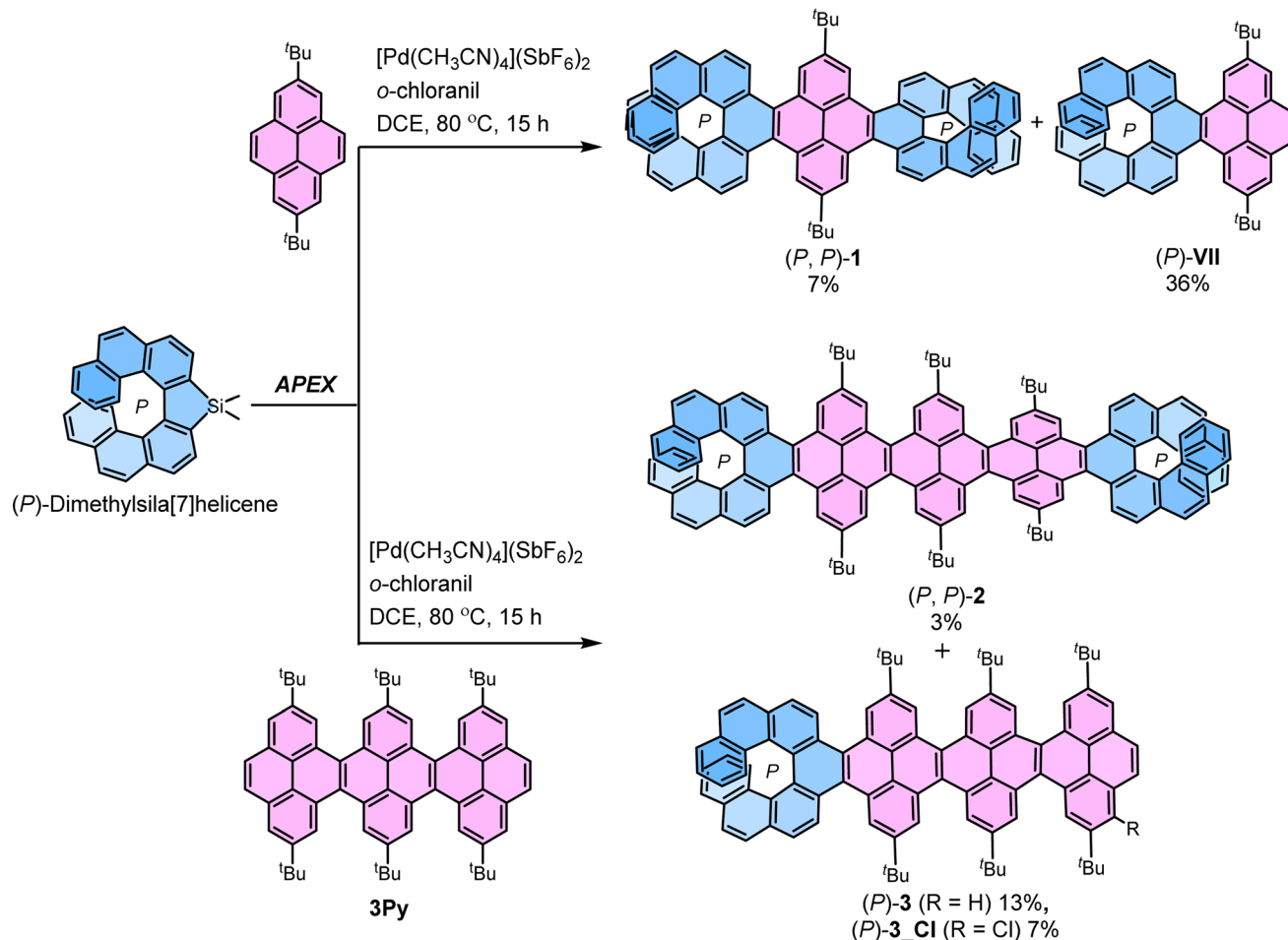
pyrene served to anchor essential points necessary for transmitting twists from one end to the other. Recently, we developed a stereospecific method for incorporating [n]helicene at the K-region of pyrene through a one-pot Suzuki coupling – C–H activation process.^{39–41} Initially, we applied the same strategy to synthesize (*P, P*)-**1** by conducting a one-pot Suzuki coupling – C–H activation reaction between (*S*)-3,3-dibromo-4,4'-biphenanthrene⁴⁰ (*ee* > 99%) and 2-(2,7-di-*tert*-butylpyren-4-yl)-4,4,5,5-tetramethyl-1,3,2-dioxaborolane.⁵⁰ (*P, P*)-**1** was successfully obtained with a moderate 35% yield, considering two Suzuki coupling and two C–H activation reaction steps (ESI Section S2†). However, this approach proved unsuitable for synthesizing **2** and **3** due to inaccessibility of required pyrene-NR (**3Py**) with boronic ester group. To surmount these obstacles, we adopted the K-region specific annulative π -extension (APEX) reaction developed by Ito and Itami (Scheme 1).⁵¹

(*P, P*)-**1** and (*P, P*)-**2** were synthesized from 2,7-di-*tert*-butylpyrene and **3Py**,⁵² and (*P*)-dimethylsila[7]helicene (*ee* > 99%),⁵³ through a palladium-catalyzed double C–H/C–Si coupling (K-region APEX reaction).⁵¹ A mixture of the respective pyrene precursor and (*P*)-dimethylsila[7]helicene was heated at 80 °C for 15 hours in the presence of [Pd(CH₃CN)₄](SbF₆)₂ and *o*-chloranil, producing the double annulative (*P, P*)-**1** and (*P, P*)-**2** with stereospecificity. The second competitive addition of [7]helicene occurs selectively at the K-region of the pyrene possibly due to its high olefinic character,⁵⁴ compared to the two K-regions of the first annulated [7]helicene where aromatic character is dominant.⁵¹ This selectivity can be rationalized by the presence of neighboring conjugated Clar's sextet. In the K-region of pyrene, four *peri*-fused benzene rings shared two Clar's sextets, whereas in the K-region of [7]helicene, it conjugates with two neighboring Clar's sextets. The APEX reactions also produced single annulated (*P*)-**3** and (*P*)-**VII** (ref. 40) with moderate yield. Similarly, (*M, M*)-**1** and (*M, M*)-**2** were synthesized from (*M*)-dimethylsila[7]helicene in comparable yields and enantiopurity. The identical enantiopurity of **1** (*ee* > 99%) in APEX reaction and Suzuki coupling–C–H activation confirms the stereospecificity of the APEX reaction (ESI Fig. S1†). To the best of our knowledge, these are the first examples of site-selective and stereospecific APEX reactions, as the enantiomeric excess (*ee*) was retained throughout the reaction scheme.⁵⁵ The structures of **1**, **2** and **3** were confirmed by unambiguous assignment of ¹H and ¹³C peaks to the respective atoms by COSY, NOESY, HSQC, and HMBC NMR measurements (ESI Fig. S10†). Additionally, the structure of **1** and **3Py** was determined by single-crystal X-ray diffraction (ESI Fig. S9†).

Pyrene bridged double [7]helicene

Before exploring longer fused pyrene NRs, an extensive study was conducted on conformational stability of pyrene bridged double [7]helicene (**1**). DFT optimized geometry and energy level analyses of (*P, P*)-**1** revealed that the diastereomer with an opposite chirality in the cove region to [7]helicene (left-handed helical conformation) is notably most stable, constituting a relative Boltzmann population of 99.9% (Fig. 2a). The remaining 0.1% encompasses the higher energy wagging conformation of (*P, P*)-





Scheme 1 Synthesis of *(P, P)*-1, *(P, P)*-2 and *(P)*-3 via stereospecific APEX reaction.

1. The theoretical calculations were substantiated by the obtained single crystal structure of *(P, P)*-1 (Fig. 2c), where all four [4]helicene subunits adopt the *M* conformation. The resemblance between the experimental (87°) and calculated (96°) end-to-end twists confirm the precision of the DFT optimized structures. In the case of *(P, M)*-1, pyrene bridged by two [7]helicenes with opposite chirality, the scenario reverses, just the opposite of *(P, P)*-1. The wagging conformation with opposite helicity to [7]helicene in the cove is the most stable, representing 99% of the relative population (Fig. 2b). The remaining 1% comprises the helical conformation. Notably, in both *(P, P)*-1 and *(P, M)*-1, the conformer with similar helicity in the cove and adjacent [7]helicene represents the highest energy conformation, with an almost negligible relative population.

The 99.9% conformational stability of *(P, P)*-1 allow us to assess the configurational stability, unlike the dynamic nanoribbon (**VII**) reported by Mateo-Alonso *et al.* where mixture of conformations exists at variable temperature for fixed helicity of the [5]helicenoid.⁴³ *(P, P)*-1 was heated at elevated temperature to observe formation of other isomers. Upon heating two new peaks appeared in HPLC, which were assigned to *(M, M)*-1 and *(P, M)*-1 (ESI Fig. S2a†). Using Eyring equation the ΔH and ΔS values were calculated to be 44.1 kcal mol⁻¹ and 21.4 cal K⁻¹ mol⁻¹, respectively (ESI Fig. S3b†). Accordingly, the Gibbs activation energy ΔG^\ddagger

(298 K) for diastereomerization of **1** was calculated to be 37.7 kcal mol⁻¹, lower than the enantiomerization barrier of pristine [7]helicene (41.2 kcal mol⁻¹).^{49,56,57} It should be noted that, both ΔH and ΔS for the diastereomerization of **1** are significantly higher than those for the enantiomerization of the [7]helicene ($\Delta H = 40.4$ kcal mol⁻¹, $\Delta S = -2.8$ cal K⁻¹ mol⁻¹).⁴⁹ Hence the decreased ΔG^\ddagger for **1** can be rationalized for the much higher and positive ΔS value—an entropically favored process. ΔG^\ddagger (438 K) of **1** (35.3 kcal mol⁻¹) is slightly higher than that of **VII** (34.1 kcal mol⁻¹)⁴⁰ indicating a more ordered conformation upon locking the structure with the second [7]helicene.⁵⁸ Upon prolonged heating *(P, P)*-1 reaches to a diastereomeric equilibrium of *(P*, P*)*-1 to meso *(P, M)*-1 at a ratio of 3.6 : 1 (ESI Fig. S1 and S2†), similar to the ratio (3.8 : 1) obtained from racemic reaction (ESI Fig. S1†). This is well in accordance with the calculated relative population of two diastereomers (3.8 : 1) by DFT.

Conformation isomers of conjugated cove-edged NR (3Py)

The cove-edged nanoribbons showcase a nonplanar geometry primarily attributed to steric repulsion between two hydrogen atoms positioned at the inner core of recurring [4]helicene units, resulting in tilted upward and downward topologies. The conformational stability of **3Py** was evaluated through DFT



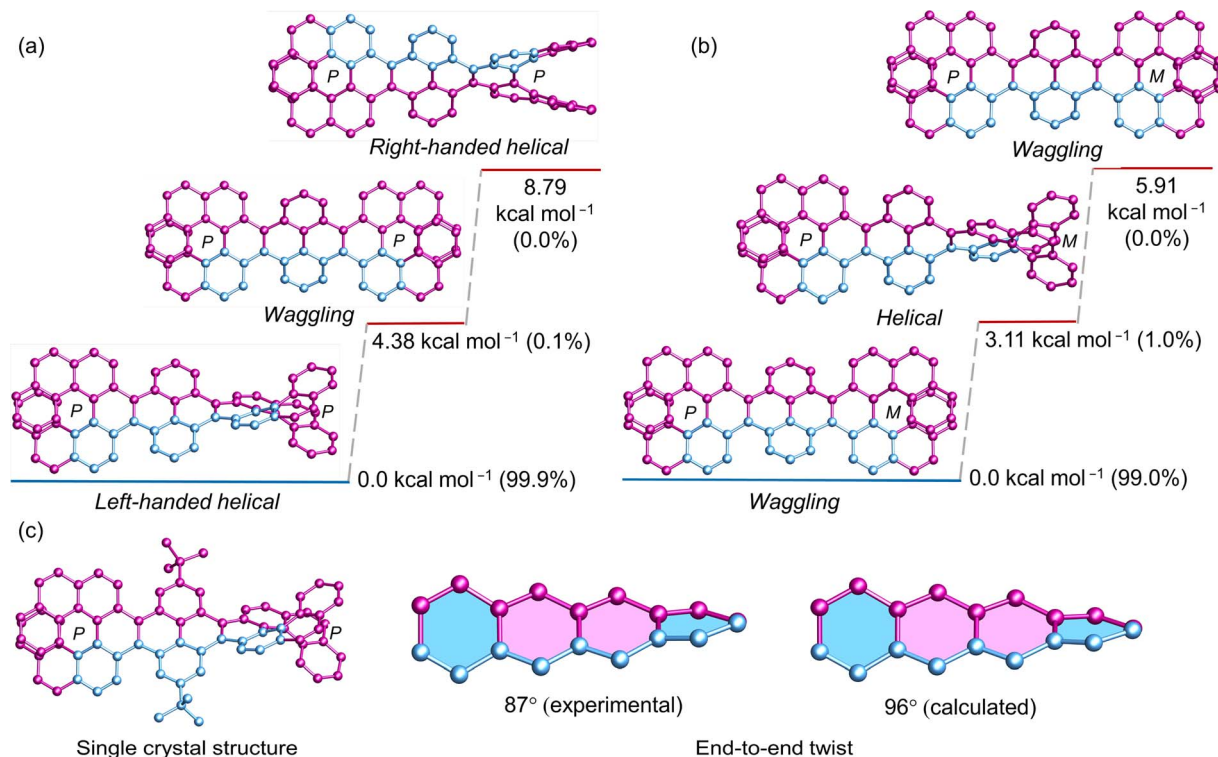


Fig. 2 DFT (ω B97XD/6-31G(d,p)) calculated conformational isomers of (a) (*P, P*)-1, (b) (*P, M*)-1 with relative total energy and population at 298 K. (c) Single crystal structure of (*P, P*)-1. Hydrogen atoms in all and *tert*-butyl groups in calculated structures are omitted for clarity.

calculations (Fig. 3). At room temperature, the wagging conformer of **3Py** prevails as the most stable, constituting 78% of the population, while the remaining portion corresponds to the helical conformer. The calculations were substantiated by the obtained single crystal of **3Py**, revealing a wagging twist. Notably, there is no net end-to-end twist observed, as the twist from one terminal to the other end does not continue consistently but instead reverses the twist direction in the middle pyrene. The rapid flipping of adjacent pyrene in wagging twist is evident from the ^1H NMR experiment, where all *tert*-butyl groups exhibit only one distinct sharp singlet at 1.63 ppm (ESI Fig. S15 †).

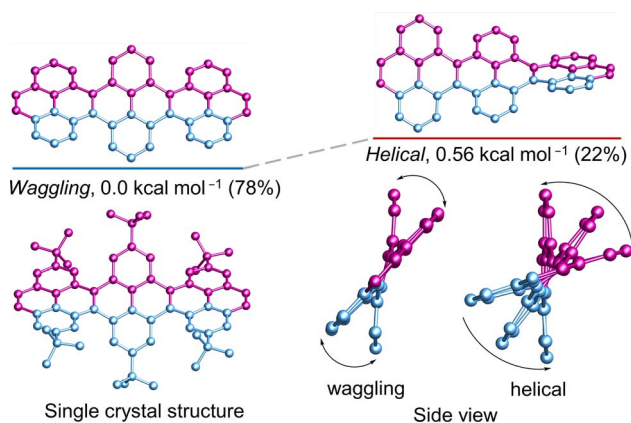


Fig. 3 DFT (ω B97XD/6-31G(d,p)) calculated conformational isomers and single crystal structure of **3Py** with relative total energy and population at 298 K. Hydrogen atoms in all and *tert*-butyl groups in calculated structures are omitted for clarity.

Effect of one terminal [7]helicene on conformational stability of cove-edged NR

Next, we investigated the influence of one (*P*)-[7]helicene unit on the conformation of **3Py**. Although (*P*)-**3** appears as flexible as **3Py**, the left-handed helical conformation emerges as the most stable, constituting a relative population of 87.9% (Fig. 4). Conversely, the lowest wagging conformer, slightly higher in energy (1.91 kcal mol $^{-1}$), accounts for a relative population of 6.3%, while combined population of all four wagging conformers amounts to 12.09%. The highest energy right-handed helical conformer (5.17 kcal mol $^{-1}$) comprises only 0.01% of the population. Despite numerous attempts in various solvent combinations and at low temperatures, obtaining a single crystal of (*P*)-**3** remained elusive. However, the twisted structure of the C_2 symmetric (*P*)-**3** is discernible in the ^1H NMR, where all three sets of *tert*-butyl groups exhibit three distinct singlet signals, each corresponding to 18 protons (ESI Fig. S32 †). Consequently, rapid flipping of adjacent pyrenes in the wagging conformation just as **3Py** is not applicable to (*P*)-**3**. The end-to-end twist of (*P*)-**3** measures 121 $^\circ$, which is 34 $^\circ$ higher than that of (*P, P*)-**1**.

Effect of two terminal [7]helicenes on conformational stability of cove-edged NR

The (*P*)-[7]helicene-locked nanoribbon (*P, P*)-**2** follows a similar trend as (*P*)-**3** and (*P, P*)-**1** established by DFT calculated energies. The left-handed helical nanoribbon represents the most stable conformer with a relative population of 99.9%, while the



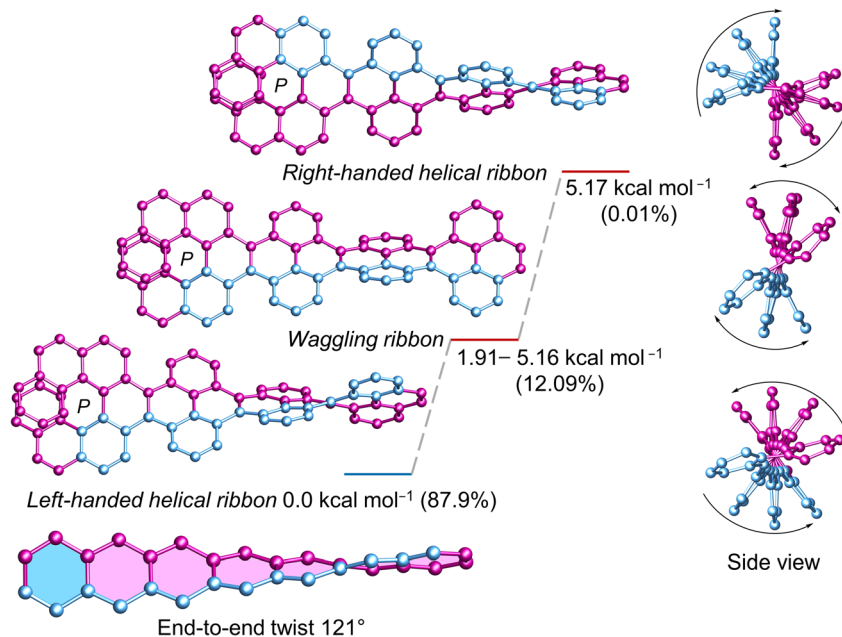


Fig. 4 DFT (ω B97XD/6-31G(d,p)) calculated conformational isomers of (*P*)-**3** with relative total energy and population at 298 K. The lowest energy wagging conformation of (*P*)-**3** is depicted here. Refer to ESI Section S6† for additional wagging conformations. Hydrogen atoms and *tert*-butyl groups are omitted for clarity.

wagging conformers account for the remainder (Fig. 5a). The right-handed helical ribbon represents the highest energy conformer ($9.22 \text{ kcal mol}^{-1}$) with a negligible population. Notably, upon locking both terminal K-regions by (*P*)-[7]helicene in 2,7-di-*tert*-butyl pyrene and **3Py**, the left-handed helical ribbon becomes stabilized by $4.37\text{--}4.38 \text{ kcal mol}^{-1}$ from the lowest wagging conformer and by $8.79\text{--}9.22 \text{ kcal mol}^{-1}$ from the right-handed helical ribbon. In the case of (*P*, *M*)-**2**, where helicenes of opposite chirality attached to the terminal of NR, the wagging conformer is stable by $2.57 \text{ kcal mol}^{-1}$ from the helical conformer, constituting a relative population of 65% (Fig. 5b). Although (*P*, *P*)-**2** possesses twice the number of labile [4]helicene subunits in comparison to the pyrene-coronene nanoribbon (**X**) described by Mateo-Alonso *et al.*,⁴³ its left-handed helical conformer shows significantly greater stability than the wagging conformers, comprising a relative population of 99.9% *versus* 93.8%. The end-to-end twist of (*P*, *P*)-**2** measures 171° making it as the second-most twisted central acene core following the twisted hexacene reported by Kilway *et al.*³¹ The end-to-end twist in (*P*, *P*)-**2** is nearly double that of (*P*, *P*)-**1** and increased significantly from (*P*)-**3** demonstrating that the terminal [7]helicenes act as a molecular wrench in maintaining the twist. The average torsion angle per benzene ring⁴ measures 21.75° and 21.38° in (*P*, *P*)-**1** and (*P*, *P*)-**2**, respectively, in contrast to 17.3° in (*P*)-**3** and 14.8° in (*P*)-**VII**, which highlights the increased strain resulting from the conformational lock imposed by the second [7]helicene. The distance between the terminal benzene centroids of [7]helicene substructure decreased significantly from 4.13 \AA in (*P*, *P*)-**1** to 3.77 \AA in (*P*, *P*)-**2**, while the torsional twist slightly increased from 22.4° (**1**) to 22.9° in **2**. This highlights the additional strain imposed by the [7]helicene in (*P*, *P*)-**2** to maintain such a high level of twist in

the central core. Regardless of its size ($\sim 3.1 \text{ nm}$), and the extensive aromatic core comprising 100 carbon atoms, (*P*, *P*)-**2** demonstrates excellent solubility in a wide range of organic solvents, owing to the highly twisted structure.

Nucleus-independent chemical shift calculations

To evaluate the effect of twisting on the aromaticity, the nucleus-independent chemical shift (NICS) values were computed for all discussed molecules (Fig. 6). All benzene rings exhibited negative NICS(1)_{zz} values, indicative of their aromaticity, except for H4 ring in (*P*)-**3** and (*P*, *P*)-**2**. The marginally positive value NICS(1)_{zz} for ring H4 in (*P*)-**3** and (*P*, *P*)-**2** corroborates to its highly distorted structure compared to other rings. In the [7]helicene subunit of NRs, the aromaticity increased on moving away from the central rings (H4 to H1) similar to pristine [7]helicene.^{59,60} Aromaticity within the acene core (P1 to P6) decreases on moving away from terminal rings into the central core in **3Py**. However, this trend reverses in (*P*, *P*)-**1** and (*P*, *P*)-**2** as terminal rings (P1 or P6) show smaller NICS(1)_{zz} values with a gradual increase to the inner core. Away from the centrally tethered twisting, the P7–P9 rings in the pyrene exhibit relatively higher negative NICS(1)_{zz} values, as do the H1 and H2 rings of the [7]helicene. In general, the NICS(1)_{zz} values of the wagging conformer of **1** and **2** are significantly higher than those of the left-handed helical conformer of (*P*, *P*)-**1** and (*P*, *P*)-**2**, likely due to absence of an end-to-end twist (ESI Table S6†).

Chiroptical properties

The absorption and emission spectra of (*P*, *P*)-**2** and (*P*)-**3** closely resemble each other, with a slight red shift compared to (*P*, *P*)-**1**, due to an increase in π -conjugation (Fig. 7a). The optical energy



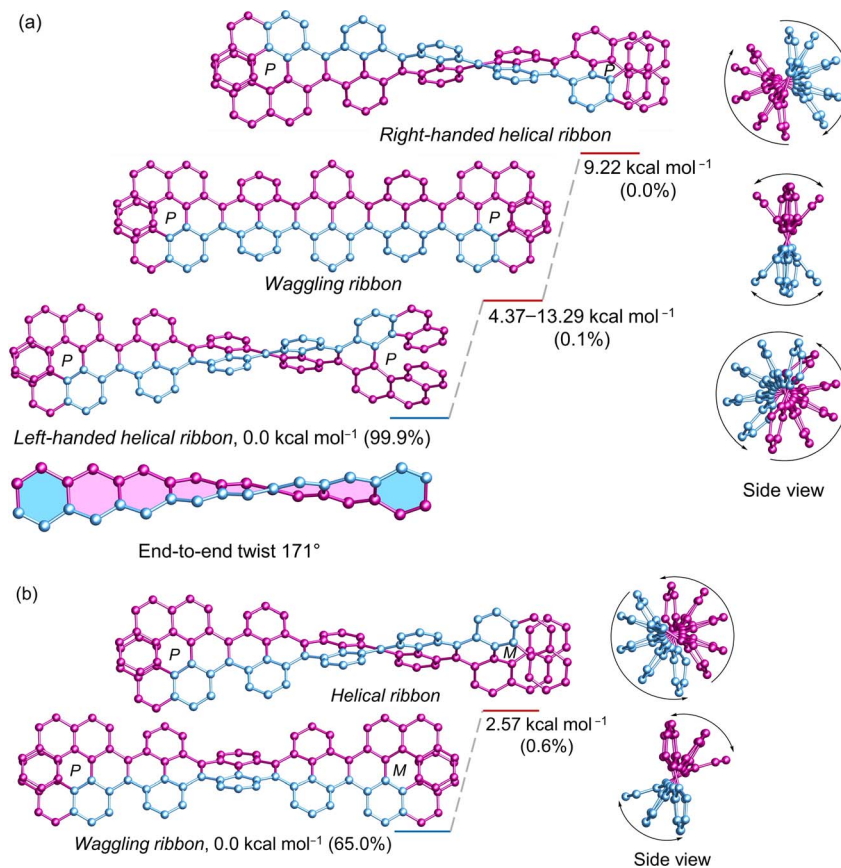


Fig. 5 DFT (ω B97XD/6-31G(d,p)) calculated conformational isomers of (a) (P, P)-2 and (b) (P, M)-2 with relative total energy and population at 298 K. The lowest energy wagging conformation of 2 is depicted here. Refer to ESI Section S6† for additional wagging conformations. Hydrogen atoms and *tert*-butyl groups are omitted for clarity.

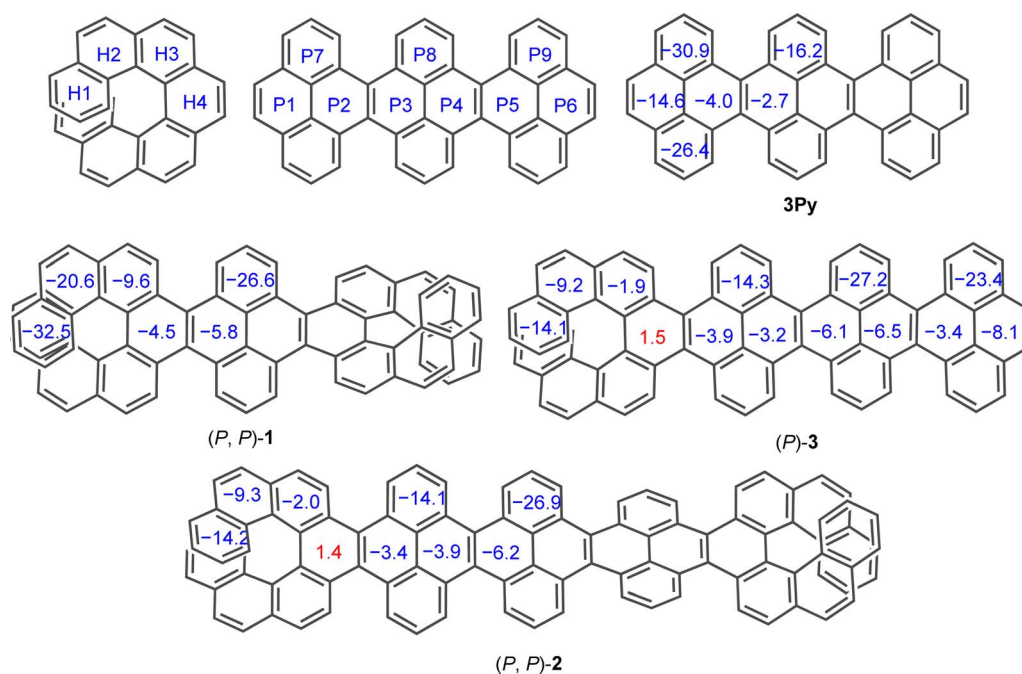


Fig. 6 Calculated (GIAO-B3LYP/6-311+G(2d,p)) NICS(1)_{zz} values for 3Py, (P, P)-1, (P, P)-2 and (P)-3. *tert*-Butyl groups are omitted for clarity.



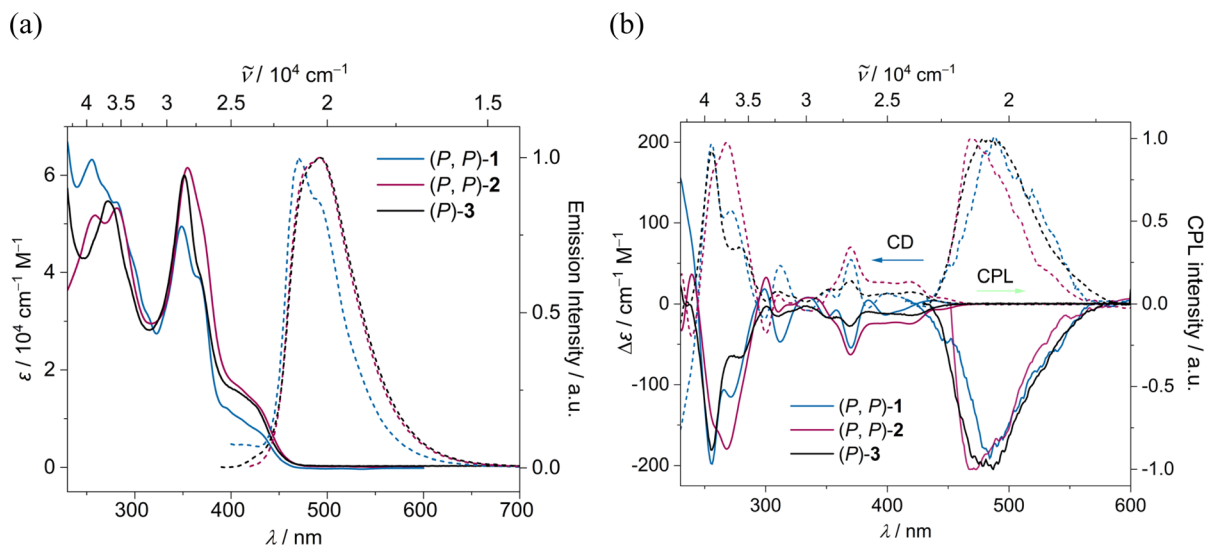


Fig. 7 (a) UV-Vis absorption (solid line) and emission (dashed line) spectra and (b) ECD and CPL spectra of (P, P) (solid line) and (M, M) (dashed line) of 1 (blue), 2 (red) and 3 (black) in DCM ($c \sim 10^{-5} \text{ M}$).

gap for (P, P) -1, (P, P) -2, and (P) -3 falls within the range of 2.79–2.83 eV, notably lower than that of [7]helicene (3.06 eV)⁶¹ and 3Py (2.92 eV) (ESI Table S2†). TD-DFT (B3LYP/6-31g(d,p)) calculations revealed that for all three compounds the lowest energy absorption band mainly stemming from HOMO \rightarrow LUMO transition with similar oscillator strength of 0.13–0.14 (ESI Table S5†). The emission maximum for (P, P) -1, (P, P) -2 and (P) -3 were recorded at 473, 492 and 493 nm respectively with fluorescence quantum yields (FQYs) of 0.05, 0.15 and 0.19 in dichloromethane. The decrease in FQY of (P, P) -2 compared to (P) -3 can be attributed to twist-enhanced inter system crossing as observed in twisted acenes.^{62,63} The fluorescence decay lifetimes of (P, P) -1, (P, P) -2, and (P) -3 range between 5.07–5.55 ns, significantly shorter than that of [7]helicene (13.8 ns).⁶⁴

The absolute configuration of the enantiomers of 1, 2, and 3 was assigned comparing experimental and TD-DFT calculated CD spectra (ESI Fig. S8†). The lowest energy CD signals are stronger for 2, followed by 1 and 3 respectively (Fig. 7b). The experimentally obtained luminescence dissymmetry factor (g_{lum}) of 2 is 1.54×10^{-3} , nearly three times that of 3 (0.63×10^{-3}) and 1 (0.54×10^{-3}) (ESI Fig. S7†). The increase in chiroptical response of 2 can be attributed to the increased twist in the NR core, resulting in macro chirality. This was further supported by TD-DFT calculations, which showed enhanced excited state magnetic transition dipole moment and higher $\cos \theta$ values for 2 compared to those for 1 and 3 (ESI Table S3†). In contrast to dynamic pyrene-coronene NR (X) reported by Mateo-Alonso *et al.*,⁴³ the variable temperature (278–333 K) ECD and CPL measurements showed minimal change (ESI Fig. S6f†), indicating the robust chirality of the (P, P) -2, corroborating its higher $g_{\text{lum}}/g_{\text{abs}}$ ratio of 0.81.⁶⁵

Conclusion

In summary, we have succeeded in achieving unparalleled control over the conformation of cove-edged graphene NRs.

Leveraging enantiopure [7]helicenes as molecular wrenches, we have integrated these helical motifs into the terminal K-regions of a conjugated pyrene NR through a stereospecific APEX reaction. Among these acene-cored NRs, (P, P) -2 displayed an impressive end-to-end twist of 171° . These robust chiral NRs exhibited exceptional configurational and conformational stability with a relative population of helical NR amounting to 99.9% at room temperature. The progressive increase in chiroptical responses from (P) -3 to (P, P) -2 highlights the emergence of macro chirality resulting from the overall twist of the nanoribbon. Our study not only addresses the longstanding challenge of controlling the stereochemistry of twisted hydrocarbon NRs but also sheds light on the impact of twisting on the conformational population. Through extensive quantum chemical calculations, we have provided a detailed understanding of the energetically favored conformers and their relative populations. The outlined strategy, allowing the late-stage introduction of helicene units by APEX reaction, holds promise for facilitating the synthesis of diverse cove edge NR variants with desired conformations.

Data availability

The experimental procedures, characterizations, spectral analysis and DFT computational details are available in the ESI.†

Author contributions

A. S. performed the experimental work, analyzed the data, and wrote the manuscript. K. R. and H. B. analyzed the crystallographic data. P. R. conceived the project, supervised the research, and prepared the final draft of the manuscript.

Conflicts of interest

There are no conflicts to declare.



Acknowledgements

We dedicate this paper to Professor Frank Würthner (University of Würzburg) on the occasion of his 60th birthday. P. R. thanks Julius-Maximilians-Universität Würzburg for “Excellent Ideas” program. A. S. and P. R. sincerely thank Prof. Christoph Lambert (University of Würzburg) for generously supporting our research. Funding: this project received funding from Deutsche Forschungsgemeinschaft (DFG) (Project No. 448604676). The CPL/CD hybrid spectrometer was funded by the DFG (Project No. 444286426). We thank the reviewers for their valuable suggestions to improve the manuscript.

References

- X.-Y. Wang, A. Narita and K. Müllen, Precision synthesis versus bulk-scale fabrication of graphenes, *Nat. Rev. Chem.*, 2017, **2**, 0100.
- J. M. Fernández-García, P. J. Evans, S. Filippone, M. Á. Herranz and N. Martín, Chiral Molecular Carbon Nanostructures, *Acc. Chem. Res.*, 2019, **52**, 1565–1574.
- Y. Segawa, H. Ito and K. Itami, Structurally uniform and atomically precise carbon nanostructures, *Nat. Rev. Mater.*, 2016, **1**, 15002.
- M. Rickhaus, M. Mayor and M. Juríček, Strain-induced helical chirality in polyaromatic systems, *Chem. Soc. Rev.*, 2016, **45**, 1542–1556.
- J. R. Sanchez-Valencia, T. Dienel, O. Gröning, I. Shorubalko, A. Mueller, M. Jansen, K. Amsharov, P. Ruffieux and R. Fasel, Controlled synthesis of single-chirality carbon nanotubes, *Nature*, 2014, **512**, 61.
- S. Eigler and A. Hirsch, Chemistry with Graphene and Graphene Oxide—Challenges for Synthetic Chemists, *Angew. Chem., Int. Ed.*, 2014, **53**, 7720–7738.
- E. Clar, *Polycyclic Hydrocarbons*, Springer, 1964.
- W. Niu, Y. Fu, Z.-L. Qiu, C. J. Schürmann, S. Obermann, F. Liu, A. A. Popov, H. Komber, J. Ma and X. Feng, π -Extended Helical Multilayer Nanographenes with Layer-Dependent Chiroptical Properties, *J. Am. Chem. Soc.*, 2023, **145**, 26824–26832.
- A. Narita, X. Feng and K. Müllen, Bottom-Up Synthesis of Chemically Precise Graphene Nanoribbons, *Chem. Rev.*, 2015, **15**, 295–309.
- A. Narita, X.-Y. Wang, X. Feng and K. Müllen, New advances in nanographene chemistry, *Chem. Soc. Rev.*, 2015, **44**, 6616–6643.
- S. Dutta and S. K. Pati, Novel properties of graphene nanoribbons: a review, *J. Mat. Chem.*, 2010, **20**, 8207–8223.
- J. Liu, R. Berger, K. Müllen and X. Feng, in *From Polyphenylenes to Nanographenes and Graphene Nanoribbons*, Springer, 2017, vol. 278, pp. 1–32.
- J. Li, S. Sanz, N. Merino-Díez, M. Vilas-Varela, A. Garcia-Lekue, M. Corso, D. G. de Oteyza, T. Frederiksen, D. Peña and J. I. Pascual, Topological phase transition in chiral graphene nanoribbons: from edge bands to end states, *Nat. Commun.*, 2021, **12**, 5538.
- J. Liu, B.-W. Li, Y.-Z. Tan, A. Giannakopoulos, C. Sanchez-Sanchez, D. Beljonne, P. Ruffieux, R. Fasel, X. Feng and K. Müllen, Toward Cove-Edged Low Band Gap Graphene Nanoribbons, *J. Am. Chem. Soc.*, 2015, **137**, 6097–6103.
- Y. Gu, R. Muñoz-Mármol, S. Wu, Y. Han, Y. Ni, M. A. Díaz-García, J. Casado and J. Wu, Cove-Edged Nanographenes with Localized Double Bonds, *Angew. Chem., Int. Ed.*, 2020, **59**, 8113–8117.
- Y. Gu, V. Vega-Mayoral, S. Garcia-Orrit, D. Schollmeyer, A. Narita, J. Cabanillas-González, Z. Qiu and K. Müllen, Cove-Edged Hexa-*peri*-hexabenzobis-*peri*-octacene: Molecular Conformations and Amplified Spontaneous Emission, *Angew. Chem., Int. Ed.*, 2022, **61**, e202201088.
- X. Wang, J. Ma, W. Zheng, S. Osella, N. Arisnabarreta, J. Droste, G. Serra, O. Ivasenko, A. Lucotti, D. Beljonne, M. Bonn, X. Liu, M. R. Hansen, M. Tommasini, S. De Feyter, J. Liu, H. I. Wang and X. Feng, Cove-Edged Graphene Nanoribbons with Incorporation of Periodic Zigzag-Edge Segments, *J. Am. Chem. Soc.*, 2022, **144**, 228–235.
- W. A. Chalifoux, The Synthesis of Non-planar, Helically Coiled Graphene Nanoribbons, *Angew. Chem., Int. Ed.*, 2017, **56**, 8048–8050.
- M. Daigle, D. Miao, A. Lucotti, M. Tommasini and J.-F. Morin, Helically Coiled Graphene Nanoribbons, *Angew. Chem., Int. Ed.*, 2017, **56**, 6213–6217.
- W. Niu, J. Ma, P. Soltani, W. Zheng, F. Liu, A. A. Popov, J. J. Weigand, H. Komber, E. Poliani, C. Casiraghi, J. Droste, M. R. Hansen, S. Osella, D. Beljonne, M. Bonn, H. I. Wang, X. Feng, J. Liu and Y. Mai, A Curved Graphene Nanoribbon with Multi-Edge Structure and High Intrinsic Charge Carrier Mobility, *J. Am. Chem. Soc.*, 2020, **142**, 18293–18298.
- S. Ma, J. Gu, C. Lin, Z. Luo, Y. Zhu and J. Wang, Supertwistacene: A Helical Graphene Nanoribbon, *J. Am. Chem. Soc.*, 2020, **142**, 16887–16893.
- S. Castro-Fernández, C. M. Cruz, I. F. A. Mariz, I. R. Márquez, V. G. Jiménez, L. Palomino-Ruiz, J. M. Cuerva, E. Maçõas and A. G. Campaña, Two-Photon Absorption Enhancement by the Inclusion of a Tropone Ring in Distorted Nanographene Ribbons, *Angew. Chem., Int. Ed.*, 2020, **59**, 7139–7145.
- W. Yang, R. R. Kazemi, N. Karunathilake, V. J. Catalano, M. A. Alpuche-Aviles and W. A. Chalifoux, Expanding the scope of peropyrenes and teropyrenes through a facile InCl₃-catalyzed multifold alkyne benzannulation, *Org. Chem. Front.*, 2018, **5**, 2288–2295.
- B. Mahlmeister, M. Mahl, H. Reichelt, K. Shoyama, M. Stolte and F. Würthner, Helically Twisted Nanoribbons Based on Emissive Near-Infrared Responsive Quaterylene Bisimides, *J. Am. Chem. Soc.*, 2022, **144**, 10507–10514.
- R. A. Pascal, Twisted Acenes, *Chem. Rev.*, 2006, **106**, 4809–4819.
- R. S. Walters, C. M. Kraml, N. Byrne, D. M. Ho, Q. Qin, F. J. Coughlin, S. Bernhard and R. A. Pascal Jr, Configurationally Stable Longitudinally Twisted Polycyclic Aromatic Compounds, *J. Am. Chem. Soc.*, 2008, **130**, 16435–16441.



- 27 I. I. Schuster, L. Craciun, D. M. Ho and R. A. Pascal, Synthesis of a strained, air-sensitive, polycyclic aromatic hydrocarbon by means of a new 1,4-benzadiyne equivalent, *Tetrahedron*, 2002, **58**, 8875–8882.
- 28 J. Lu, D. M. Ho, N. J. Vogelaar, C. M. Kraml and R. A. Pascal, A Pentacene with a 144° Twist, *J. Am. Chem. Soc.*, 2004, **126**, 11168–11169.
- 29 X. Qiao, M. A. Padula, D. M. Ho, N. J. Vogelaar, C. E. Schutt and R. A. Pascal, Octaphenylanthracene and Decaphenylanthracene, *J. Am. Chem. Soc.*, 1996, **118**, 741–745.
- 30 Y. Xiao, J. T. Mague, R. H. Schmehl, F. M. Haque and R. A. Pascal Jr, Dodecaphenyltetracene, *Angew. Chem., Int. Ed.*, 2019, **58**, 2831–2833.
- 31 R. G. Clevenger, B. Kumar, E. M. Menuey and K. V. Kilway, Synthesis and Structure of a Longitudinally Twisted Hexacene, *Chem.–Eur. J.*, 2018, **24**, 3113–3116.
- 32 A. Bedi, L. J. W. Shimon and O. Gidron, Helically Locked Tethered Twistacenes, *J. Am. Chem. Soc.*, 2018, **140**, 8086–8090.
- 33 A. Bedi and O. Gidron, The Consequences of Twisting Nanocarbons: Lessons from Tethered Twisted Acenes, *Acc. Chem. Res.*, 2019, **52**, 2482–2490.
- 34 T. M. Figueira-Duarte and K. Müllen, Pyrene-Based Materials for Organic Electronics, *Chem. Rev.*, 2011, **111**, 7260–7314.
- 35 J. Xiao, H. M. Duong, Y. Liu, W. Shi, L. Ji, G. Li, S. Li, X.-W. Liu, J. Ma, F. Wudl and Q. Zhang, Synthesis and Structure Characterization of a Stable Nonatwistacene, *Angew. Chem., Int. Ed.*, 2012, **51**, 6094–6098.
- 36 B. Kumar, C. E. Strasser and B. T. King, *t*-Butyl Biphenylation of *o*-Dibromoarenes: A Route to Soluble Polycyclic Aromatic Hydrocarbons, *J. Org. Chem.*, 2012, **77**, 311–316.
- 37 Y. Yano, H. Ito, Y. Segawa and K. Itami, Helically Twisted Tetracene: Synthesis, Crystal Structure, and Photophysical Properties of Hexabenz[a,c,f,g,j,l,op]tetracene, *Synlett*, 2016, **27**, 2081–2084.
- 38 S. M. Elbert, K. Baumgärtner, J. A. Esteves, L. Weber, F. Rominger and M. Mastalerz, Pyrene-Based Diarynes as Precursors for Twisted Fused Polycyclic Aromatic Hydrocarbons: A Comparison of Two Routes, *Org. Mater.*, 2020, **02**, 358–361.
- 39 A. K. Swain, K. Kolanji, C. Stapper and P. Ravat, C₂- and C₁-Symmetric Configurationally Stable Pyrene-Fused [5] Helicenes Connected *via* Hexagonal and Heptagonal Rings, *Org. Lett.*, 2021, **23**, 1339–1343.
- 40 A. K. Swain, K. Radacki, H. Braunschweig and P. Ravat, Pyrene-Fused [7]Helicenes Connected *Via* Hexagonal and Heptagonal Rings: Stereospecific Synthesis and Chiroptical Properties, *J. Org. Chem.*, 2022, **87**, 993–1000.
- 41 A. Swain and P. Ravat, Pyrene bridged double[7]helicene embedded with a heptagonal ring, *Org. Chem. Front.*, 2023, **10**, 3714–3725.
- 42 J. A. Weber, E. L. Clennan and N. Arulsamy, A Computational Physical Organic Study of a Torque, Lock, and Propagate Approach and Validation with the Synthesis of Configurationally Stable First-Generation Helically Twisted Acenes, *Eur. J. Org. Chem.*, 2022, e202101533.
- 43 R. K. Dubey, M. Melle-Franco and A. Mateo-Alonso, Inducing Single-Handed Helicity in a Twisted Molecular Nanoribbon, *J. Am. Chem. Soc.*, 2022, **144**, 2765–2774.
- 44 W. Fan, T. Winands, N. L. Doltsinis, Y. Li and Z. Wang, A Decatwistacene with an Overall 170° Torsion, *Angew. Chem., Int. Ed.*, 2017, **56**, 15373–15377.
- 45 W. Theilacker and H. Böhm, Optically Active 2,2'-Dimethylbiphenyl, the Simplest Atropisomeric Hydrocarbon, *Angew. Chem., Int. Ed.*, 1967, **6**, 251.
- 46 R. H. Martin, The Helicenes, *Angew. Chem., Int. Ed.*, 1974, **13**, 649–660.
- 47 Y. Shen and C. F. Chen, Helicenes: synthesis and applications, *Chem. Rev.*, 2012, **112**, 1463–1535.
- 48 M. Gingras, G. Félix and R. Peresutti, One hundred years of helicene chemistry. Part 2: stereoselective syntheses and chiral separations of carbohelicenes, *Chem. Soc. Rev.*, 2013, **42**, 1007–1050.
- 49 P. Ravat, Carbo[n]helicenes Restricted to Enantiomerize: An Insight into the Design Process of Configurationally Stable Functional Chiral PAHs, *Chem.–Eur. J.*, 2021, **27**, 3957–3967.
- 50 L. Ji, I. Krummenacher, A. Friedrich, A. Lorbach, M. Haehnel, K. Edkins, H. Braunschweig and T. B. Marder, Synthesis, Photophysical, and Electrochemical Properties of Pyrenes Substituted with Donors or Acceptors at the 4- or 4,9-Positions, *J. Org. Chem.*, 2018, **83**, 3599–3606.
- 51 K. Ozaki, K. Kawasumi, M. Shibata, H. Ito and K. Itami, One-shot K-region-selective annulative π -extension for nanographene synthesis and functionalization, *Nat. Commun.*, 2015, **6**, 6251.
- 52 F. Liu, X. Shen, Y. Wu, L. Bai, H. Zhao and X. Ba, Synthesis of ladder-type graphene ribbon oligomers from pyrene units, *Tetrahedron Lett.*, 2016, **57**, 4157–4161.
- 53 H. Oyama, K. Nakano, T. Harada, R. Kuroda, M. Naito, K. Nobusawa and K. Nozaki, Facile Synthetic Route to Highly Luminescent Sila[7]helicene, *Org. Lett.*, 2013, **15**, 2104–2107.
- 54 T. Hasegawa, M. Sekine, W. P. Schaefer and H. Taube, Preparation and characterization of a bis(pentaammineosmium(II)) pyrene complex, *Inorg. Chem.*, 1991, **30**, 449–452.
- 55 H. Ito, K. Ozaki and K. Itami, Annulative π -Extension (APEX): Rapid Access to Fused Arenes, Heteroarenes, and Nanographenes, *Angew. Chem., Int. Ed.*, 2017, **56**, 11144–11164.
- 56 R. H. Martin and M.-J. Marchant, Thermal racemisation of [6], [7], [8] and [9] helicene, *Tetrahedron Lett.*, 1972, **13**, 3707–3708.
- 57 J. Barroso, J. L. Cabellos, S. Pan, F. Murillo, X. Zarate, M. A. Fernandez-Herrera and G. Merino, Revisiting the racemization mechanism of helicenes, *Chem. Commun.*, 2018, **54**, 188–191.
- 58 J. M. Fernández-García, P. Izquierdo-García, M. Buendía, S. Filippone and N. Martín, Synthetic chiral molecular nanographenes: the key figure of the racemization barrier, *Chem. Commun.*, 2022, **58**, 2634–2645.



- 59 G. Portella, J. Poater, J. M. Bofill, P. Alemany and M. Solà, Local Aromaticity of $[n]$ Acenes, $[n]$ Phenacenes, and $[n]$ Helicenes ($n = 1-9$), *J. Org. Chem.*, 2005, **70**, 2509–2521.
- 60 L. Rulišek, O. Exner, L. Cwiklik, P. Jungwirth, I. Starý, L. Pospíšil and Z. Havlas, On the Convergence of the Physicochemical Properties of $[n]$ Helicenes, *J. Phys. Chem. C*, 2007, **111**, 14948–14955.
- 61 Y. Nakai, T. Mori and Y. Inoue, Theoretical and experimental studies on circular dichroism of carbo $[n]$ helicenes, *J. Phys. Chem. A*, 2012, **116**, 7372–7385.
- 62 P. Malakar, V. Borin, A. Bedi, I. Schapiro, O. Gidron and S. Ruhman, The impact of twisting on the intersystem crossing in acenes: an experimental and computational study, *Phys. Chem. Chem. Phys.*, 2022, **24**, 2357–2362.
- 63 K. Nagarajan, A. R. Mallia, K. Muraleedharan and M. Hariharan, Enhanced intersystem crossing in core-twisted aromatics, *Chem. Sci.*, 2017, **8**, 1776–1782.
- 64 J. B. Birks, D. J. S. Birch, E. Cordemans and E. Vander Donckt, Fluorescence of the higher helicenes, *Chem. Phys. Lett.*, 1976, **43**, 33–36.
- 65 H. Tanaka, Y. Inoue and T. Mori, Circularly Polarized Luminescence and Circular Dichroisms in Small Organic Molecules: Correlation between Excitation and Emission Dissymmetry Factors, *ChemPhotoChem*, 2018, **2**, 386–402.



8. Compiled Supporting Information

8.1. C_2 - and C_1 -Symmetric Configurationally Stable Pyrene-Fused [5]Helicenes Connected via Hexagonal and Heptagonal Rings	80
8.2. Pyrene-Fused [7]Helicenes Connected via Hexagonal and Heptagonal Rings: Stereospecific Synthesis and Chiroptical Properties	119
8.3. Pyrene Bridged Double[7]helicene Embedded with a Heptagonal ring	150
8.4. Helically Twisted Nanoribbons via Stereospecific Annulative π -Extension Reaction Employing [7]Helicene as a Molecular Wrench	171

The supporting information section has undergone changes that bear no consequences on the results. Specifically, modifications have been made to the page numbers in the table of contents, cartesian coordinates have been removed. Additionally, certain figures were converted to greyscale without altering their meaning. Unaltered versions can be freely accessed on the respective publication webpage.

8.1. Supporting Information for

***C*₂- and *C*₁-Symmetric Configurationally Stable Pyrene-Fused [5]Helicenes Connected via Hexagonal and Heptagonal Rings**

Asim kumar Swain[‡], Kubandiran Kolanji[‡], Christoph Stapper and Prince Ravat^{*}

Institut für Organische Chemie and Center for Nanosystems Chemistry, Universität Würzburg, Am Hubland, D-97074 Würzburg, Germany

Table of Contents

S1. Materials and characterization	S81
S2. Synthetic details and analytical data.....	S83
S3. Cyclic voltammetry	S90
S4. Fluorescence lifetime.....	S91
S5. Chiral stationary phase HPLC and CD.....	S92
S6. Determination and analysis of activation parameters of enantiomerization	S94
S7. Quantum chemical calculations	S96
S8. Single crystal data.....	S102
S9. NMR spectroscopy	S104
S10. High resolution mass spectrometry (HRMS)	S116
S11. References.....	S118

S1. Materials and characterization

All chemicals and solvents were purchased from commercial sources and were used without further purification unless stated otherwise. The 8-methylnaphthalen-2-ol (**3**) and 2-(2,7-di-*tert*-butylpyren-4-yl)-4,4,5,5-tetramethyl-1,3,2-dioxaborolane were synthesized according to literature known protocols^{1,2}. The reactions and experiments sensitive to dioxygen were performed using Schlenk techniques and nitrogen-saturated solvents. All the glassware and NMR tubes prior to use for experiments were kept in oven at 80 °C for 12 h.

Chromatography:

Open-column chromatography and thin-layer chromatography (TLC) were performed on silica gel (Merck silica gel 100-200 mesh). Chiral stationary phase HPLC separations were performed by SHIMADZU 223.

NMR spectroscopy:

The NMR experiments were performed at 298 K on NMR spectrometers operating at 400 MHz proton and 101 MHz ¹³C frequencies. Standard pulse sequences were used and the data was processed using 2-fold zero-filling in the indirect dimension for all 2D experiments. Chemical shifts (δ) are reported in parts per million (ppm) relative to the solvent residual peak (¹H and ¹³C NMR, respectively): CDCl₃ (δ = 7.26 and 77.16 ppm), CD₂Cl₂ (δ = 5.32 and 53.84 ppm) and *J* values are given in Hz. Structural assignments for compound **1** and **2** were made with additional information from gCOSY, gNOESY, gHSQC and gHMBC experiments.

HRMS:

The ESI-HRMS were measured on Bruker micrOTOF while the MALDI-TOF-HRMS were measured on Bruker ultrafleXtreme. *trans*-2-[3-(4-*tert*-Butylphenyl)-2-methyl-2-propenylidene]malononitrile (DCTB) dissolved in chloroform was used as supporting matrix in the MALDI-TOF-HRMS measurement.

Melting point:

Melting points were measured using an OptiMelt Automated Melting Point System.

UV–vis and Fluorescence spectroscopy:

UV–vis spectra were measured on JASCO V-670 spectrometer, while emission spectra were measured Edinburgh FLS 980 photoluminescence spectrometer. The fluorescence lifetimes were measured in DCM using a 418.6 nm pulsed laser diode with a pulse frequency of 1/100 ns. The fluorescence quantum yields were measured in DCM using same spectrometer with a 450 W xenon arc lamp as a light source and a calibrated integrating sphere.

Circular dichroism spectroscopy:

CD spectra were measured on JASCO J-810 spectrometer.

Optical rotation:

Optical rotations were measured on JASCO P-1020 polarimeter with WCG3-100 cell.

Cyclic voltammetry:

Cyclic voltammetry experiments were performed in DCM with 0.1 M $[\text{Bu}_4\text{N}][\text{PF}_6]$ as supporting electrolyte using a Gamry Instruments Reference 600 potentiostat. A standard three-electrode cell configuration was employed using a platinum disk working electrode, a platinum wire counter electrode, and an Ag/AgCl serving as reference electrode. The redox potentials were referenced to the ferrocene (Fc) / ferrocenium (Fc^+) redox couple.

S2. Synthetic details and analytical data

rac-8,8'-dimethyl-[1,1'-binaphthalene]-2,2'-diol ((±)-4)



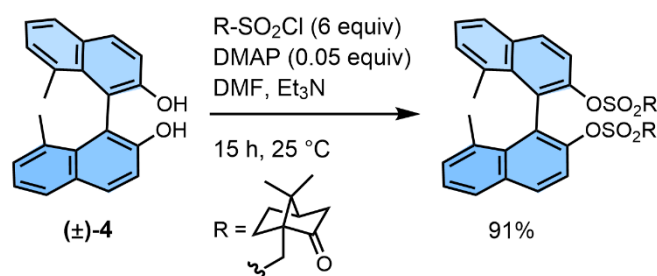
3 (500 mg, 3.16 mmol) was dissolved in dry DCM (8 mL) then Cu-TMEDA (44 mg, 3.0 mol%) was added in portions over 15 min to the flask. The reaction mixture was then stirred for 50 min at 25 °C. The reaction was quenched by 1 M HCl followed by extraction with 25 mL of DCM. The organic layer was dried over anhydrous sodium sulfate. The solvent was removed under reduced pressure using a rotary evaporator. Crude product was purified by column chromatography on silica gel using 20% ethylacetate in petrolether to yield 392 mg (78%) of **(±)-4** as white crystalline solid. Melting Point 255.8 °C.

¹H NMR (400 MHz, CDCl₃, 25 °C): δ [ppm] = 7.94 (d, J = 8.9 Hz, 1H), 7.74 (d, J = 9.3 Hz, 1H), 7.30 (d, J = 8.9 Hz, 1H), 7.19 (d, J = 6.5 Hz, 1H), 5.04 (s, 1H), 1.85 (s, 3H). (1H integrated under the CDCl₃ residual peak at δ 7.26 ppm)

¹³C NMR (101 MHz, CDCl₃, 25 °C): δ [ppm] = 153.4, 134.1, 133.1, 133.0, 131.1, 130.6, 128.2, 124.0, 116.9, 113.8, 22.7.

HRMS (ESI): m/z : [M-H]⁻ Calcd for [C₂₂H₁₇O₂] 313.1234; Found 313.1231

8,8'-dimethyl-[1,1'-binaphthalene]-2,2'-dicamphorsulfonicester



Rac-**4** (10.0 g, 31.8 mmol, 1.00 equiv) was dissolved in dry DMF (30 mL) and triethylamine (20 mL, 143 mmol, 4.50 equiv) followed by addition of DMAP (200 mg, 1.63 mmol, 0.05 equiv). The reaction mixture was then stirred at 0 °C for 30 min. (1*S*)-(+)-10-Camphorsulfonyl chloride (50.0 g, 199 mmol, 6.27 equiv) was dissolved in 45 mL dry

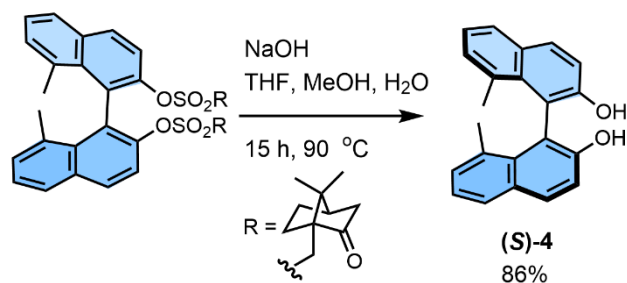
DMF at 0 °C and added to the reaction mixture dropwise via syringe. The reaction mixture was stirred at 0 °C for 20 min, then warmed up to 25 °C and stirred for 15 h. The reaction was quenched with water and the product was extracted with DCM, dried over anhydrous sodium sulfate. The solvent was removed under reduced pressure using a rotary evaporator. Crude product was purified by column chromatography on silica gel using 5% ethylacetate in toluene to isolate both the diastereomers separately. Combined Yield: 21.56 g (91%) as white crystalline solid. Melting Point 166.5 °C.

¹H NMR (400 MHz, CDCl₃, 25 °C): δ [ppm] = 7.95 (d, J = 9.0 Hz, 1H), 7.78 (d, J = 7.9 Hz, 1H), 7.62 (d, J = 8.9 Hz, 1H), 7.43 – 7.37 (m, 1H), 7.30 (d, J = 7.0 Hz, 1H), 2.59 (d, J = 14.8 Hz, 1H), 2.28 – 2.17 (m, 2H), 1.96 (m, 4H), 1.91 – 1.83 (m, 1H), 1.79 (d, J = 18.5 Hz, 1H), 1.47 – 1.16 (m, 3H), 0.82 (s, 3H), 0.61 (s, 3H).

¹³C NMR (101 MHz, CDCl₃, 25 °C): δ [ppm] = 213.4, 146.2, 136.1, 133.1, 132.6, 131.4, 131.3, 127.7, 126.2, 126.0, 120.1, 77.5, 77.2, 76.8, 57.6, 48.7, 47.9, 42.8, 42.4, 26.9, 24.7, 23.5, 19.5, 19.4.

HRMS (ESI): m/z : [2M + Na⁺] Calcd for [C₄₂H₄₆O₈S₂Na] 765.2526; Found 765.2540

(S)-8,8'-dimethyl-[1,1'-binaphthalene]-2,2'-diol ((S)-4)



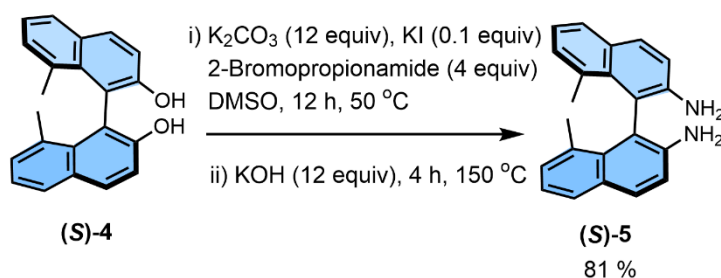
(S)- 8,8'-dimethyl-[1,1'-binaphthalene]-2,2'-dicamphorsulfonicester (2.0 g, 2.7 mmol) was dissolved in THF (40 mL), MeOH (20 mL) and 5 M NaOH (20 mL) and refluxed at 90 °C in an oil bath for 15 h. Then 1M Hydrochloric acid was added to the reaction mixture until it was acidic. The reaction mixture was then concentrated by evaporating methanol under reduced pressure using a rotary evaporator and the product was extracted with DCM, dried over anhydrous sodium sulfate. The solvent was then removed under reduced pressure and the crude product was purified by column chromatography on silica gel using 5% ethylacetate in petroleum ether to yield 1.08 g (86%) of (S)-4 as white crystalline solid. *er* 96:04. Melting point 255.7 °C.

¹H NMR (400 MHz, CDCl₃, 25 °C): δ [ppm] = 7.94 (d, *J* = 8.9 Hz, 1H), 7.74 (d, *J* = 9.3 Hz, 1H), 7.30 (d, *J* = 8.9 Hz, 1H), 7.19 (d, *J* = 6.5 Hz, 1H), 5.04 (s, 1H), 1.85 (s, 3H). (1H integrated under the CDCl₃ residual peak at δ 7.26 ppm)

¹³C NMR (101 MHz, CDCl₃, 25 °C): δ [ppm] = 153.4, 134.1, 133.1, 133.0, 131.1, 130.6, 128.2, 124.0, 116.9, 113.8, 22.7.

HRMS (ESI): *m/z*: [M-H]⁻ Calcd for [C₂₂H₁₇O₂] 313.1234; Found 313.1231

(*S*)-8,8'-dimethyl-[1,1'-binaphthalene]-2,2'-diamine ((*S*)-5)



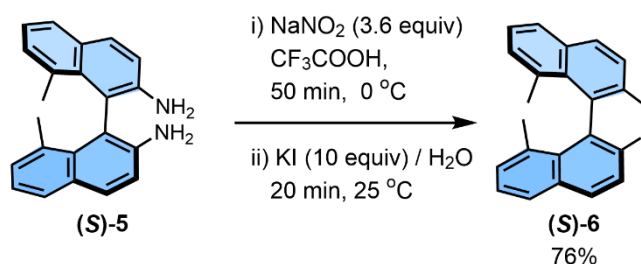
K₂CO₃ (1.58 g, 11.4 mmol, 3.0 equiv) and 2-Bromopropionamide (1.70 g, 11.4 mmol, 3.0 equiv) were dissolved in DMSO (3 mL) and stirred for 20 min at 25 °C. KI (63.1 mg, 0.03 mmol, 0.1 equiv) was added to the solution and stirred for 10 more minutes. (*S*)-4 (1.2 g, 3.8 mmol, 1.0 equiv) was added to the reaction mixture and stirred for 12 h at 50 °C in an oil bath. Once all the starting material was consumed, confirmed by TLC, KOH (1.7 g, 30.4 mmol, 8.0 equiv) was added to the reaction mixture and heated at 150 °C for 4 h in an oil bath. The reaction was then quenched with water and extracted with ethyl acetate. The solvent was removed under reduced pressure using a rotary evaporator and the crude product was purified by column chromatography on silica gel using 40% ethylacetate in petroleum ether to yield 965 mg (81%) as off-white solid (*S*)-5. Melting Point 249.8 °C.

¹H NMR (400 MHz, CDCl₃, 25 °C): δ [ppm] = 7.75 (d, *J* = 8.7 Hz, 1H), 7.63 (d, *J* = 7.3 Hz, 1H), 7.15 – 7.07 (m, 2H), 7.05 (d, *J* = 8.7 Hz, 1H), 1.90 (s, 3H). The broad amine peak can be seen around 3.30 ppm.

¹³C NMR (101 MHz, CDCl₃, 25 °C): δ [ppm] = 140.5, 134.2, 133.2, 131.4, 130.9, 130.6, 128.1, 123.3, 118.4, 118.2, 23.1.

HRMS (ESI): *m/z*: [M + H] Calcd for [C₂₂H₂₁N₂] 313.1705; Found 313.1699

Synthesis of (*S*)- 2,2'-diiodo-8,8'-dimethyl-1,1'-binaphthalene ((*S*)-6)



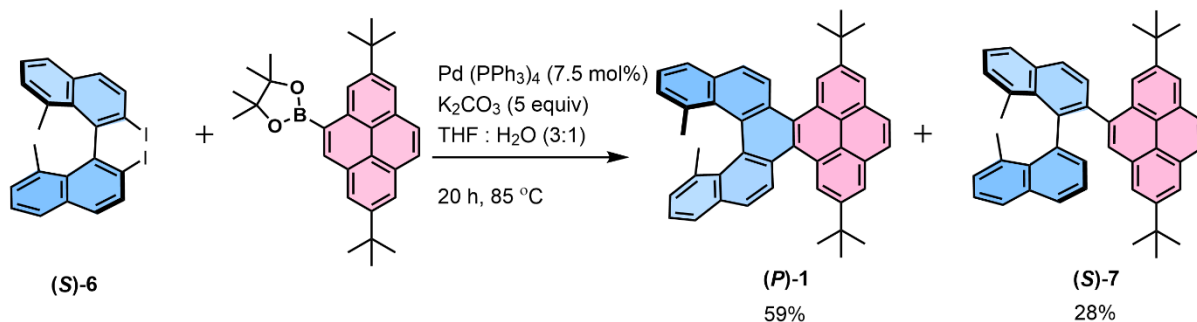
(*S*)-5 (200 mg, 0.64 mmol, 1 equiv) was dissolved in triflic acid (8 mL) and stirred at 0 °C for 10 minutes followed by addition of NaNO₂ (155 mg, 2.24 mmol, 3.5 equiv). Then the reaction mixture was continued to stir at 0 °C for 50 min followed by dropwise addition using syringe into a solution of 1.06 g KI (6.40 mmol, 10 equiv) in 4 mL H₂O. After 20 min stirring at 25 °C, the reaction was quenched with 10% solution of NaHCO₃ and washed with saturated solution of Na₂S₂O₃. The product was extracted with DCM, dried over anhydrous sodium sulfate. The solvent was removed under reduced pressure using a rotary evaporator and the crude product was purified by column chromatography on silica gel using 1% ethylacetate in petroleum ether to yield 260 mg (76%) of (*S*)-6 as white solid. Melting Point 189.3 °C. *er* 96:04.

¹H NMR (400 MHz, CDCl₃, 25 °C): δ [ppm] = 7.99 (d, *J* = 8.6 Hz, 1H), 7.78 (d, *J* = 8.6 Hz, 1H), 7.61 (d, *J* = 8.7 Hz, 1H), 7.44 – 7.36 (m, 1H), 7.24 (s, 1H), 1.79 (s, 3H).

¹³C NMR (101 MHz, CDCl₃, 25 °C): δ [ppm] = 148.3, 135.5, 135.0, 134.4, 133.5, 130.9, 130.8, 128.2, 126.4, 104.8, 24.8.

HRMS (MALDI-TOF): *m/z*: [*M*] Calcd for [C₂₂H₁₆I₂] 533.9341; Found 533.9362

12, 17-di-*tert*-butyl-4,5-dimethyldinaphtho[2,1,8-def:1',2'-s]picene ((*P*)-1) and (*S*)-2,7-di-*tert*-butyl-4-(8,8'-dimethyl-[1,1'-binaphthalen]-2-yl)pyrene ((*S*)-7)



In a Schlenk tube (*S*)-6 (30.0 mg, 0.056 mmol, 1 equiv) and 2-(2,7-di-*tert*-butylpyren-4-yl)-4,4,5,5-tetramethyl-1,3,2-dioxaborolane (30.0 mg, 0.067 mmol, 1.2 equiv) were

dissolved in dry THF (3 mL) and K₂CO₃ (38.7 mg, 0.28 mmol, 5 equiv) was dissolved in water (1 mL) and both solutions were degassed for 10 min separately and then mixed together. To this mixture Pd(PPh₃)₄ (6.50 mg, 0.0056 mmol, 0.1 equiv) was added under high nitrogen pressure and bubbled with nitrogen for 10 additional min. The reaction flask was then sealed and heated at 85 °C for 20 h in an oil bath. The reaction was quenched by adding water and extracted with DCM, dried over anhydrous sodium sulfate. The solvent was evaporated under reduced pressure using a rotary evaporator. The crude product was purified by column chromatography on silica gel using 1% ethylacetate in petroleum ether to yield 19.5 mg (59%) as a green fluorescent oil of (*P*)-**1**. Melting Point 150.7 °C. *er* 95:05.

Optical rotation: $[\alpha]_D^{25} = + 940$

¹H NMR (400 MHz, CDCl₃, 25 °C): δ [ppm] = 9.17 (d, *J* = 1.7 Hz, 1H), 9.03 (d, *J* = 8.8 Hz, 1H), 8.25 (d, *J* = 1.7 Hz, 1H), 8.17 (d, *J* = 8.9 Hz, 1H), 8.12 (s, 1H), 7.93 (d, *J* = 7.6 Hz, 1H), 7.56 – 7.49 (m, 1H), 7.18 (d, *J* = 6.8 Hz, 1H), 1.68 (s, 9H), 1.19 (s, 3H).

¹³C NMR (101 MHz, CD₂Cl₂, 25 °C): δ [ppm] = 148.2, 135.4, 133.0, 132.9, 131.1, 129.4, 129.1, 128.5, 128.2, 127.6, 127.5, 126.1, 125.8, 125.5, 124.9, 123.9, 123.4, 122.0, 35.6, 32.1, 23.1.

HRMS (MALDI-TOF): *m/z*: [M] Calcd for [C₄₆H₄₀] 592.3130; Found 592.3119

The above reaction also produced 9.4 mg (28%) as pale yellow crystalline solid **9**. Melting Point 259.6 °C.

¹H NMR (400 MHz, CDCl₃, 25 °C): δ [ppm] = 8.07 (d, *J* = 1.8 Hz, 1H), 8.04 (d, *J* = 8.5 Hz, 1H), 7.97- 7.94 (m, 2H), 7.93 – 7.86 (m, 2H), 7.81 (d, *J* = 1.8 Hz, 1H), 7.53 (d, *J* = 8.3 Hz, 1H), 7.50 – 7.46 (m, 1H), 7.42 (d, *J* = 1.8 Hz, 1H), 7.39 (s, 1H), 7.38 – 7.29 (m, 3H), 7.25 – 7.18 (m, 2H), 7.05 (dd, *J* = 7.1, 1.4 Hz, 1H), 6.62 – 6.52 (m, 1H), 2.21 (s, 3H), 1.92 (s, 3H), 1.43 (s, 9H), 1.42 (s, 9H).

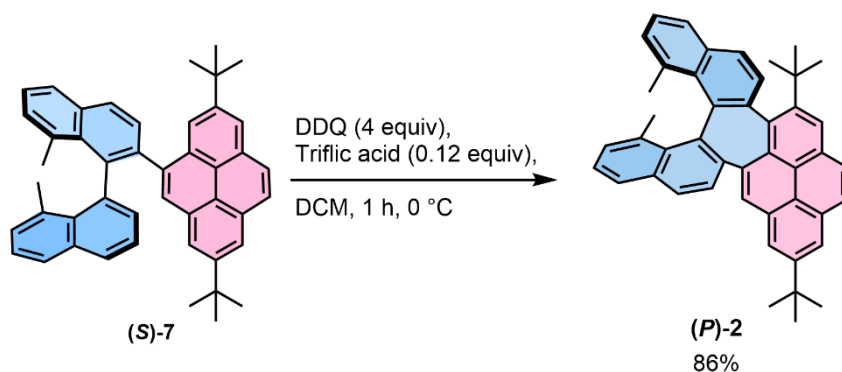
¹³C NMR (101 MHz, CD₂Cl₂, 25 °C): δ [ppm] = 148.2, 147.9, 141.3, 139.9, 138.9, 138.2, 136.7, 135.6, 134.5, 134.4, 134.0, 132.9, 131.1, 130.6, 130.3, 129.7, 129.6, 128.9, 128.6, 128.5, 128.3, 128.0, 127.7, 127.5, 127.1, 127.1, 125.8, 124.9, 123.3, 122.6, 122.1, 121.8, 121.4, 121.3, 35.3, 35.1, 32.0, 31.9, 25.2, 24.2.

HRMS (MALDI-TOF): *m/z*: [M] Calcd for [C₄₆H₄₂] 594.3287; Found 594.3228

Table S1. Optimization of Suzuki coupling with different reaction conditions.

Catalyst	Base (3 equiv)	Temp / °C	Solvent system	Yield ^a / % 1:7
Pd(PPh ₃) ₄ (10%)	K ₂ CO ₃	100	Toluene: EtOH:H ₂ O (5:3:1)	0:62
Pd(PPh ₃) ₄ (7.5%)	K ₂ CO ₃ (5 equiv)	85	THF:H ₂ O (3:1)	59:28
Pd(PPh ₃) ₄ (10%)	NHCO ₃	85	THF:H ₂ O (3:1)	32:20
Pd(PPh ₃) ₂ Cl ₂ (10%)	K ₂ CO ₃	85	THF:H ₂ O (3:1)	31:16
Pd(PPh ₃) ₂ Cl ₂ (10%)	NHCO ₃	85	THF:H ₂ O (3:1)	36:15
PdCl ₂ (PCy) ₃ (10%)	Cs ₂ CO ₃	110	Dioxane	40:13

^aIsolated yield after column chromatography.

Synthesis of 11,16-di-*tert*-butyl-4,5-dimethyldinaphtho[2',1':4,5;1'',2'':6,7]cyclohepta[1,2,3-*cd*]pyrene ((*P*)-2):

In a Schlenk tube (*S*)-7 (8.00 mg, 0.013 mmol, 1 equiv) was dissolved in dry DCM and stirred at 0 °C for 10 min. Then the solution was added dropwise to a flask containing DDQ (15.0 mg, 0.067 mmol, 5 equiv) and stirred at 0 °C for 20 min. Then triflic acid (0.14 mL, 1.50 μmol, 0.12 equiv) was added to the reaction mixture and continued to stir at 0 °C for 30 min under nitrogen atmosphere. The reaction was quenched by saturated NaHCO₃ solution in water, extracted with DCM and dried over anhydrous sodium sulfate. The solvent was then evaporated under reduced pressure using a rotary evaporator. The crude product was purified by column chromatography on silica gel using 1% ethylacetate in

petroleum ether to yield 6.8 mg (86%) as green fluorescent solid of (*P*)-**2**. Melting Point 332.1 °C. *er* 96:04.

Optical rotation: $[\alpha]_D^{25} = + 308$

¹H NMR (400 MHz, CDCl₃, 25 °C): δ [ppm] = 8.40 (s, 1H) , 8.38 (s, 1H), 8.24 (d, *J* = 1.7 Hz, 1H), 8.18 (d, *J* = 1.8 Hz, 1H), 8.00 – 7.97 (3 doublets merged, 3H) , 7.79 (d, *J* = 6.7 Hz, 1H), 7.64 – 7.62 (2 doublets merged, 2H), 7.41 – 7.35 (m, 2H), 7.30 – 7.25 (m, 1H), 7.14 (d, *J* = 8.4 Hz, 1H), 7.02 (d, *J* = 7.9 Hz, 1H), 6.73 (d, *J* = 8.5 Hz, 1H), 1.62 (s, 9H), 1.56 (s, 9H), 1.38 (s, 3H), 1.26 (s, 3H).

¹³C NMR (101 MHz, CD₂Cl₂, 25 °C): δ [ppm] = 149.6, 148.6, 143.5, 143.2, 141.0, 136.9, 136.8, 135.5, 135.3, 135.1, 134.7, 134.5, 134.5, 133.6, 132.3, 131.4, 131.2, 131.0, 130.9, 130.4, 129.9, 129.7, 129.3, 128.2, 127.6, 127.5, 127.4, 127.2, 126.9, 126.8, 126.0, 125.7, 123.4, 123.1, 121.9, 121.6, 38.1, 35.5, 34.9, 32.0, 23.5, 22.4.

HRMS (MALDI): *m/z*: [M] Calcd for [C₄₆H₄₀] 592.3130; Found 592.3162

S3. Cyclic voltammetry

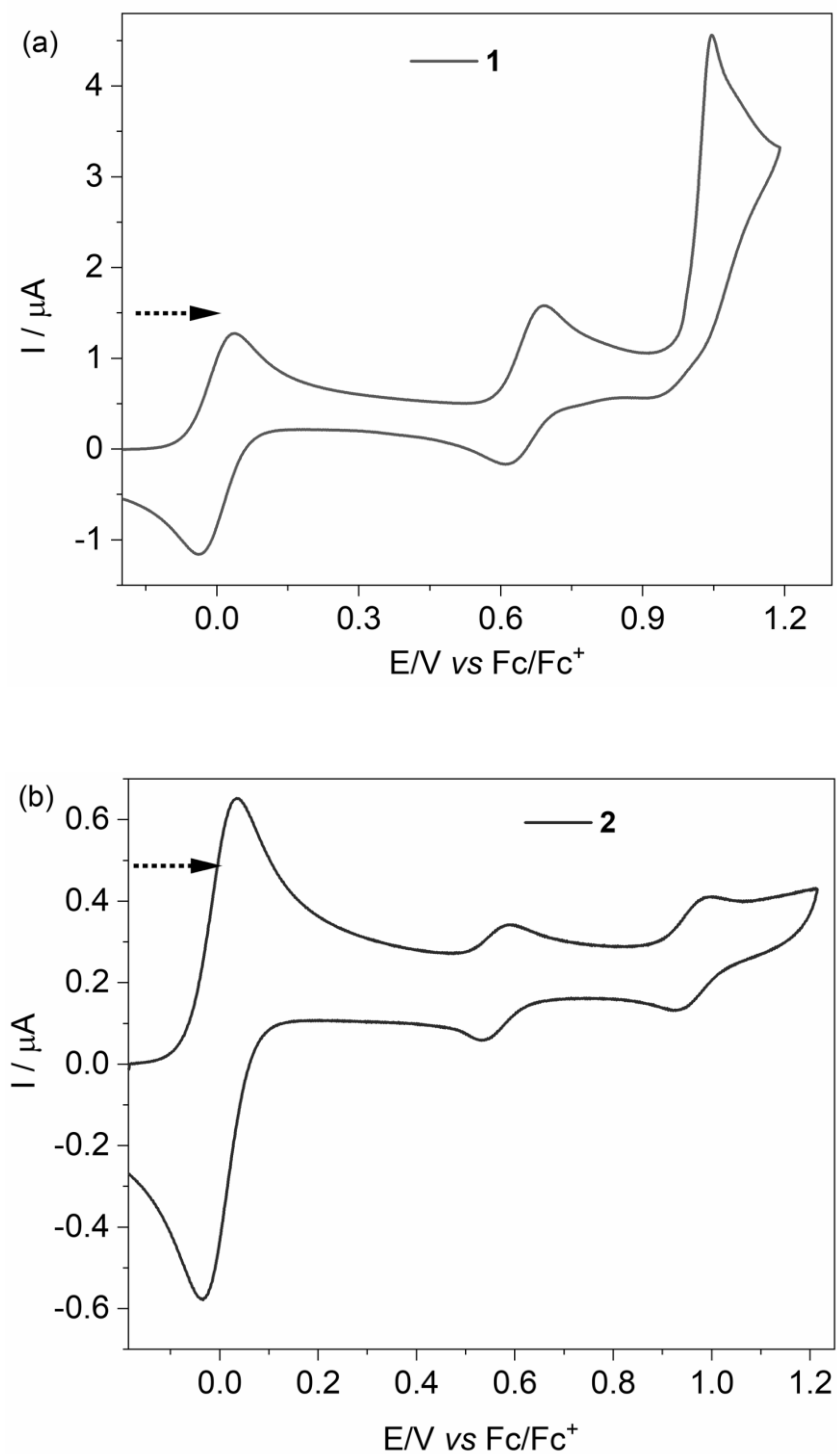


Figure S1. Cyclic voltammograms of (a) **1** and (b) **2** in DCM at 0.2 V/s scan rate, with 0.1M $(n\text{-C}_4\text{H}_9)_4\text{NBF}_4$ as supporting electrolyte, versus ferrocene/ferrocenium (Fc/Fc^+) at room temperature.

S4. Fluorescence lifetime

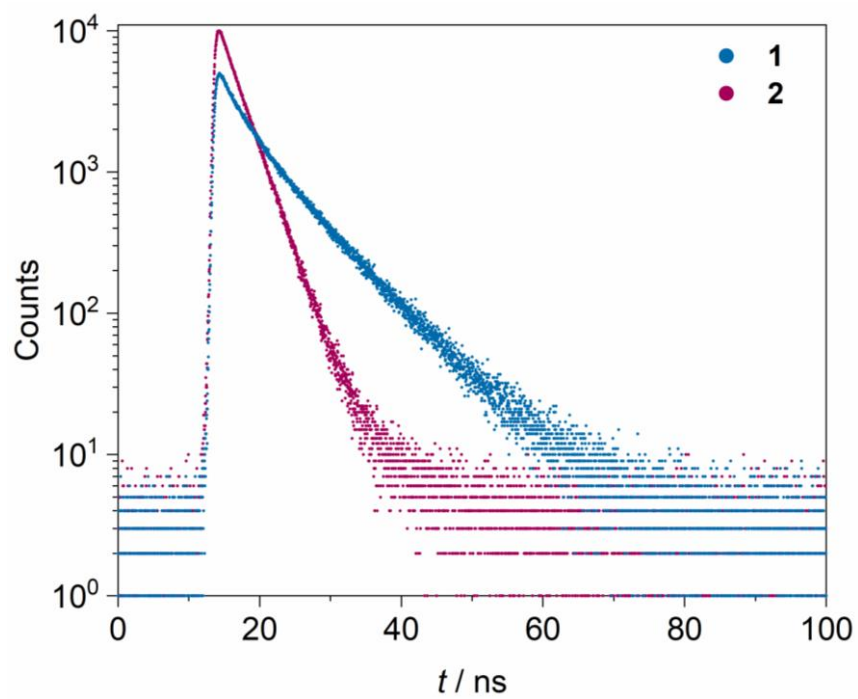


Figure S2. Fluorescence decay profile of **1** and **2** in DCM.

S5. Chiral stationary phase HPLC and CD

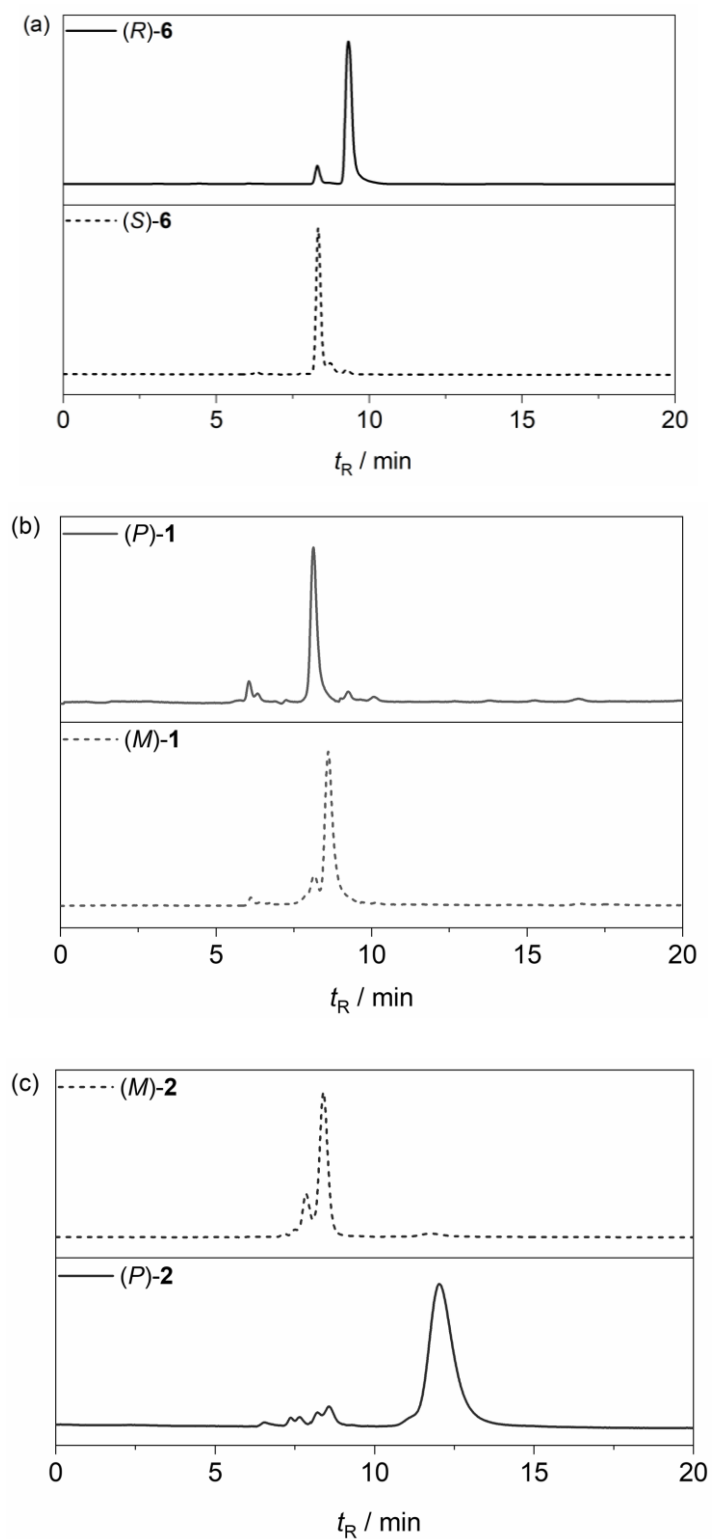


Figure S3. HPLC chromatogram of (a) **6**, (b) **1** and (c) **2** using chiral stationary phase column.

Table S2. Overview of parameters for HPLC separation of enantiomers of 1, 2 and 6.

Compound	Eluent <i>n</i> -hexane/ <i>i</i> PrOH	First fraction	Second fraction	α^b	R_s^c	<i>er</i>
6	97:3	(<i>S</i>)	(<i>R</i>)	1.12	1.22	95.84 : 4.16
1	97:3	(<i>P</i>)	(<i>M</i>)	1.05	0.61	95.31 : 4.69
2	97:3	(<i>M</i>)	(<i>P</i>)	1.43	2.33	95.91 : 4.09

^aPhenomenex Lux i-Amylose-3 5 μ m (250 x 4.6 mm). Sample injection: 5 μ L of a 1 mg/mL solution in hexane. Separation conditions: Eluent, flow rate: 0.5 mL/min, 25 $^{\circ}$ C.
^bSelectivity parameter: $\alpha = t_{R2}/t_{R1}$, where t_{R1} , and t_{R2} are elution times for first and second fraction, respectively. ^cResolution parameter: $R_s = 2(t_{R2} - t_{R1})/(w_1 + w_2)$, where w_1 and w_2 are peak widths for first and second fraction, respectively.

Absorption dissymmetry factor

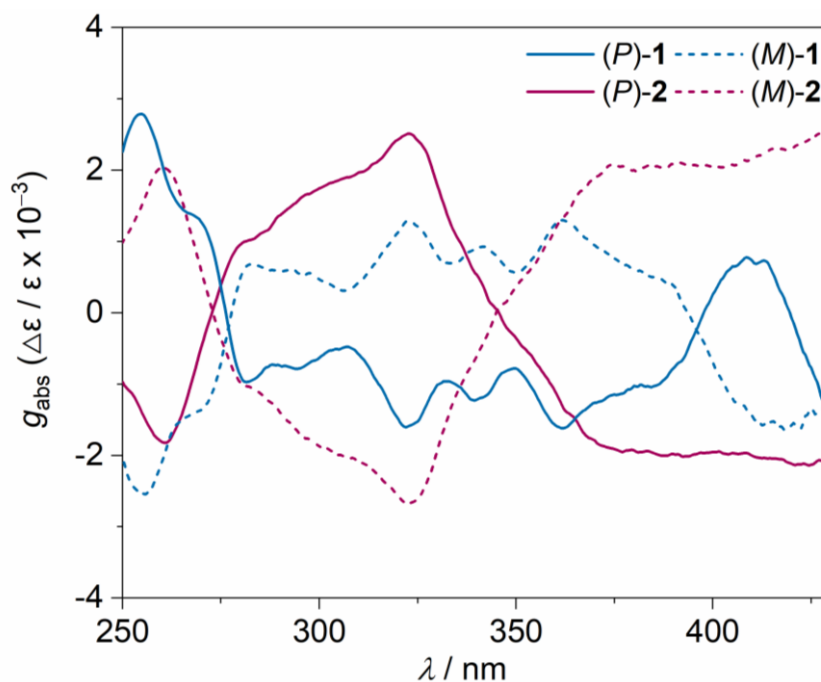


Figure S4. Absorption dissymmetry factor of **1** and **2**.

S6. Determination and analysis of activation parameters of enantiomerization

The values of the Gibbs activation energies ($\Delta G^\ddagger(T)$) for enantiomerization of **1** and **2** calculated by following the decay of the enantiomeric excess (ee) of the enantioenriched samples dissolved in diethylene glycol dibutyl ether (1-(2-(2-butoxyethoxy)ethoxy)butane) at 493 K for **1** and 503 K for **2** over time (t) by HPLC on a chiral stationary phase. To estimate the $\Delta G^\ddagger(T)$ value, the $\ln(ee_t/ee_0)$ values were plotted against the t and the data set was linearly fitted (Figures S5 (a) and (b)). Following the equations $\ln(ee_t/ee_0) = -k_{\text{rac}}t$, where k_{rac} is the rate constant of racemization, and $k_{\text{rac}} = 2k_e$, where k_e is the rate constant of enantiomerization, the k_e values were obtained and used to calculate the corresponding $\Delta G^\ddagger(T)$ values by using the Eyring equation $\Delta G^\ddagger(T) = -RT \ln(k_e h / \kappa k_B T)$, where R is the gas constant ($R = 8.31446 \text{ J K}^{-1}$), h is the Planck constant ($h = 6.62607 \times 10^{-34} \text{ J s}$), k_B is the Boltzmann constant ($k_B = 1.38064852 \times 10^{-23} \text{ J K}^{-1}$), and κ is the transmission coefficient ($\kappa = 0.5$ or 1). The transmission coefficient $\kappa = 0.5$ was used because the enantiomerization process is defined as a reversible first order reaction.

The $\Delta G^\ddagger(T)$ value for **1** was determined at 493 K, where racemization could be followed within a ~10–12 h period of time. Because the $\Delta G^\ddagger(T)$ values of **1** and **2** differ significantly, it was not possible to follow the racemization process for both compounds at the same temperature i.e., at 493 K without the process for **2** being too slow. Hence the $\Delta G^\ddagger(T)$ value for **2** was determined at 503 K, where the racemization was followed up to 3 days.

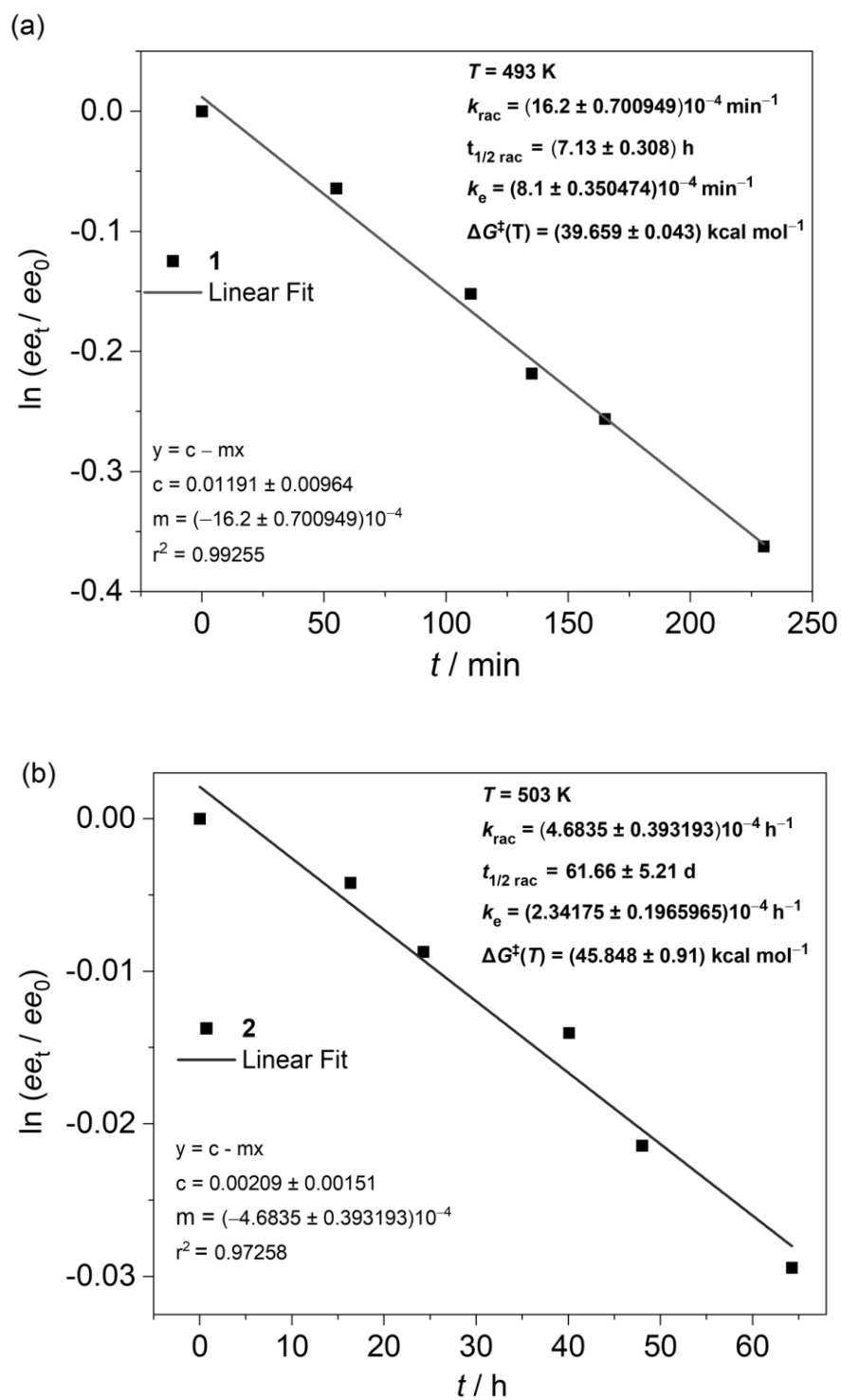


Figure S5. Plot of $\ln(ee_t/ee_0)$ against t for (a) **1** and (b) **2** and fitted linearly to obtain the k_{rac} , $t_{1/2\text{-rac}}$, k_e and ΔG^\ddagger values.

S7. Quantum chemical calculations

DFT calculations were performed using Gaussian 16 suite.³ Geometries were optimized using B3LYP functional and 6-31G(d,p) basis set in the gas phase unless stated otherwise. Frequency analysis was performed to verify the stationary state geometry. In all cases no imaginary frequency was found. TD-DFT calculations were performed on B3LYP/6-31G(d,p) optimized geometries at the B3LYP/6-31g(d,p) level. The effect of the solvent was accounted for using PCM (with dichloromethane as the solvent). SpecDis and Avogadro software were used to analyze the TD-DFT calculated spectra and to generate graphical images of frontier molecular orbitals (FMOs), respectively.

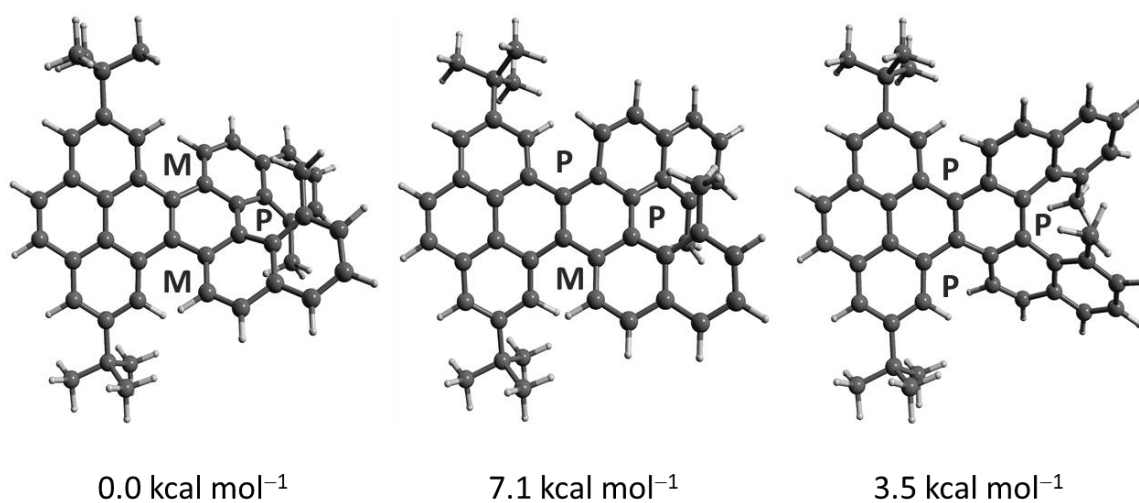


Figure S6. Relative Gibbs's free energies of diastereomers of **1**.

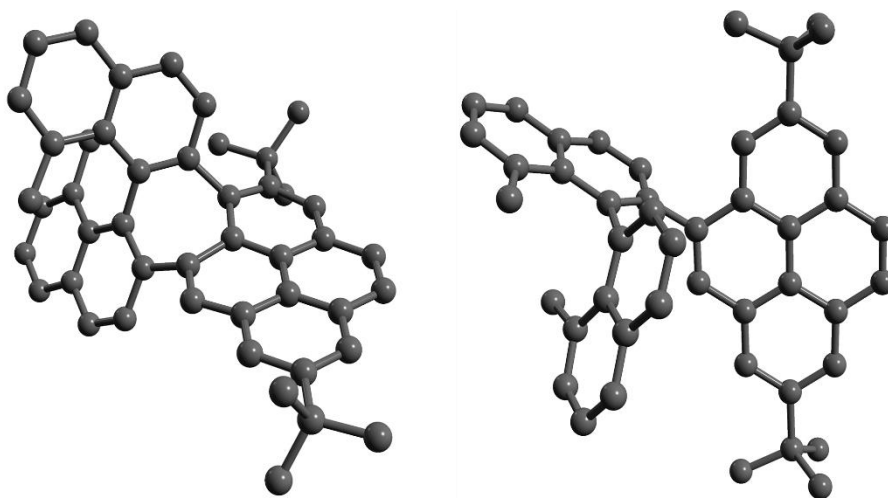
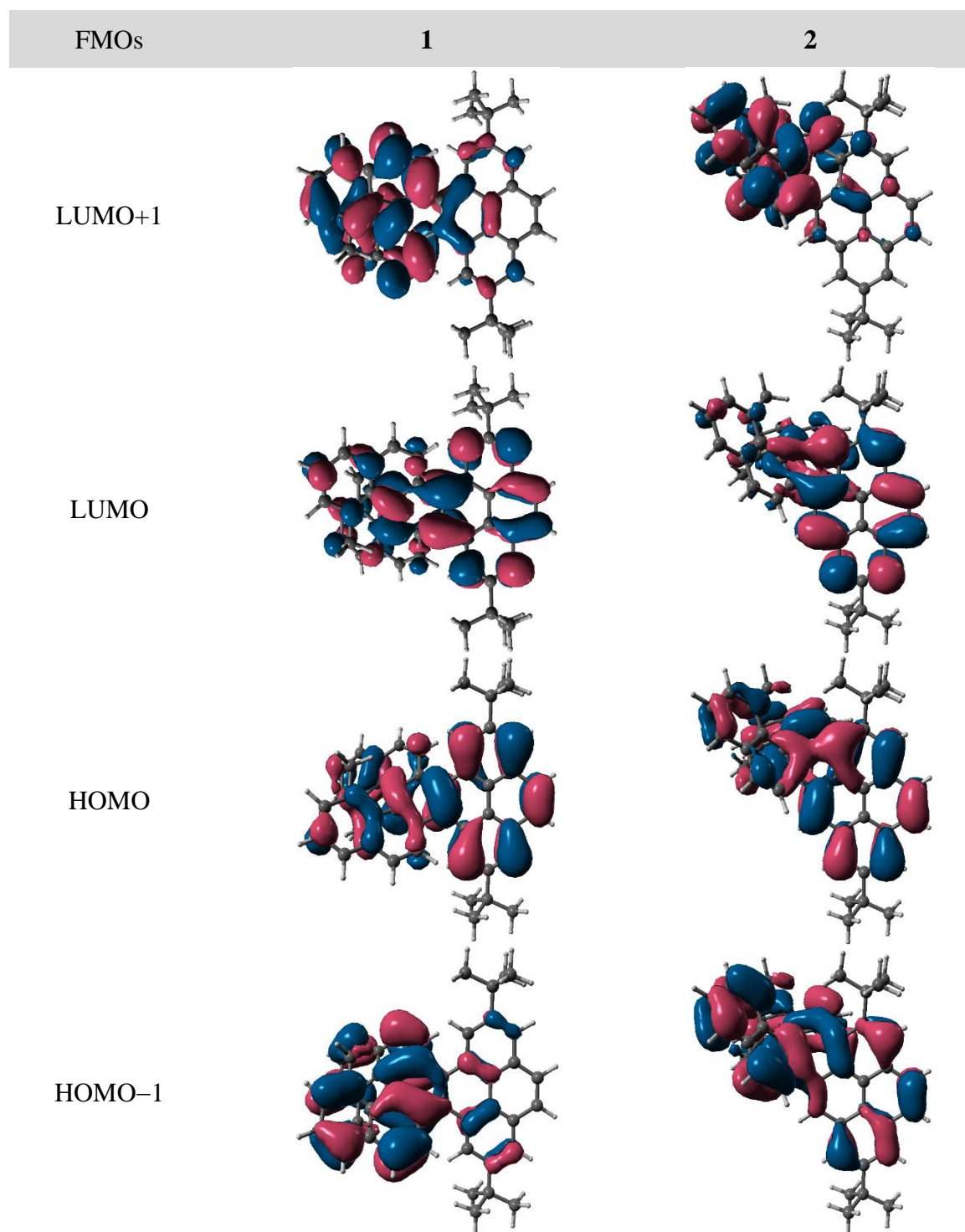


Figure S7. Optimized geometries of **2** and **7**. Hydrogen atoms are omitted for clarity

Table S3. Frontier molecular orbitals of **1** and **2**.



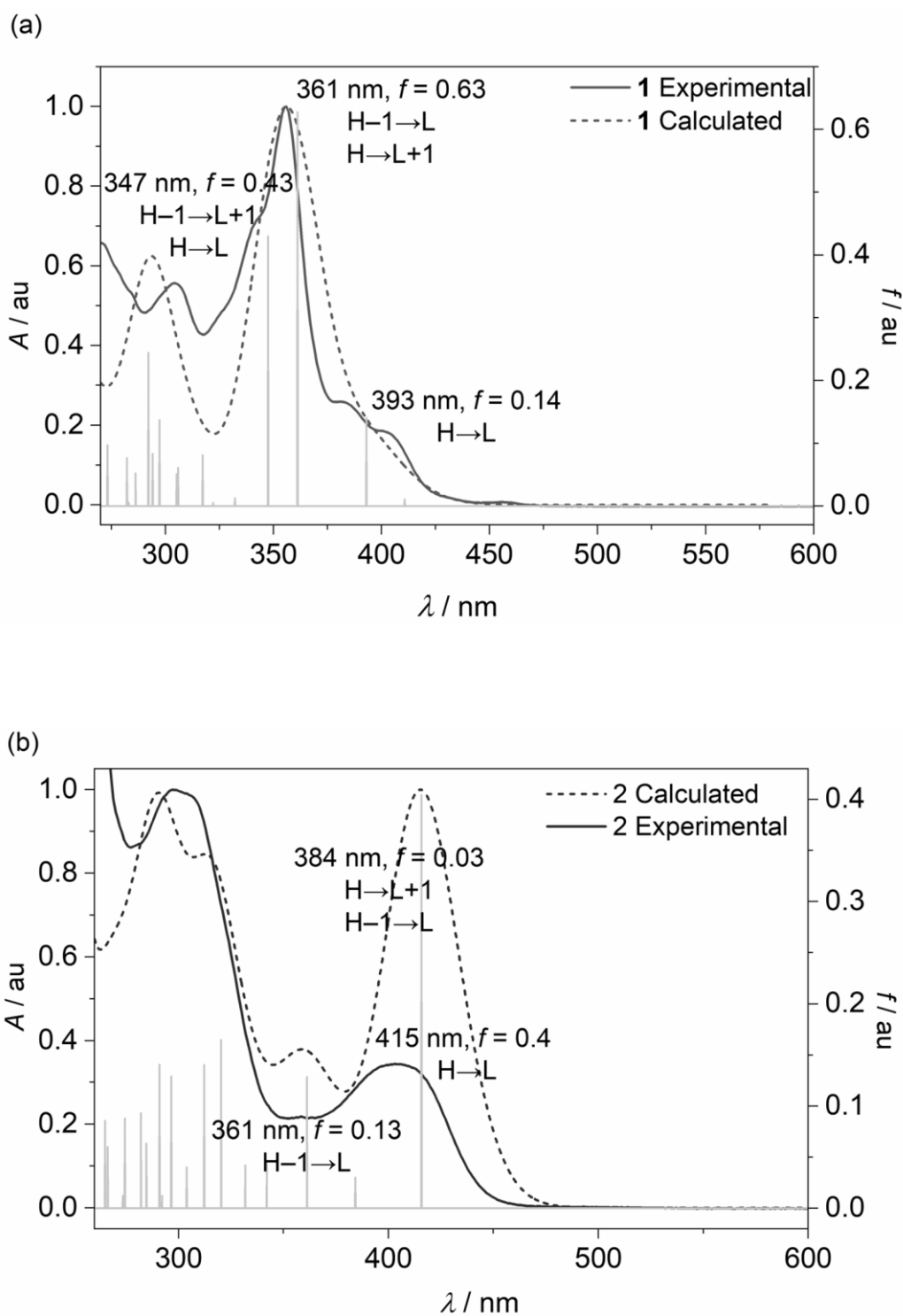


Figure S8. Comparison of experimental (solid) and TD-DFT calculated (dashed, shifted by 0.08 eV) UV-vis spectra of (a) **1** and (b) **2** along with assignments of key transitions. H = HOMO, L = LUMO, f = oscillator strength.

Table S4. Summary of TD-DFT calculated key low energy transitions.

Excited singlet state	Wavelength / nm	Energy / eV	Major transitions	Contribution	oscillator strength (<i>f</i>)
1					
1	410.73	3.02	HOMO→LUMO+1	0.41	0.01
			HOMO-1→LUMO	0.56	
2	393.03	3.15	HOMO→LUMO	0.65	0.14
3	361.09	3.43	HOMO-1→LUMO	0.41	0.63
			HOMO→LUMO+1	0.57	
4	347.51	3.57	HOMO-1→LUMO+1	0.65	0.43
			HOMO→LUMO	0.23	
2					
1	415.67	2.98	HOMO→LUMO	0.68	0.40
2	384.18	3.23	HOMO→LUMO+1	0.68	0.03
			HOMO-1→LUMO	0.16	
3	361.25	3.43	HOMO-1→LUMO	0.61	0.13

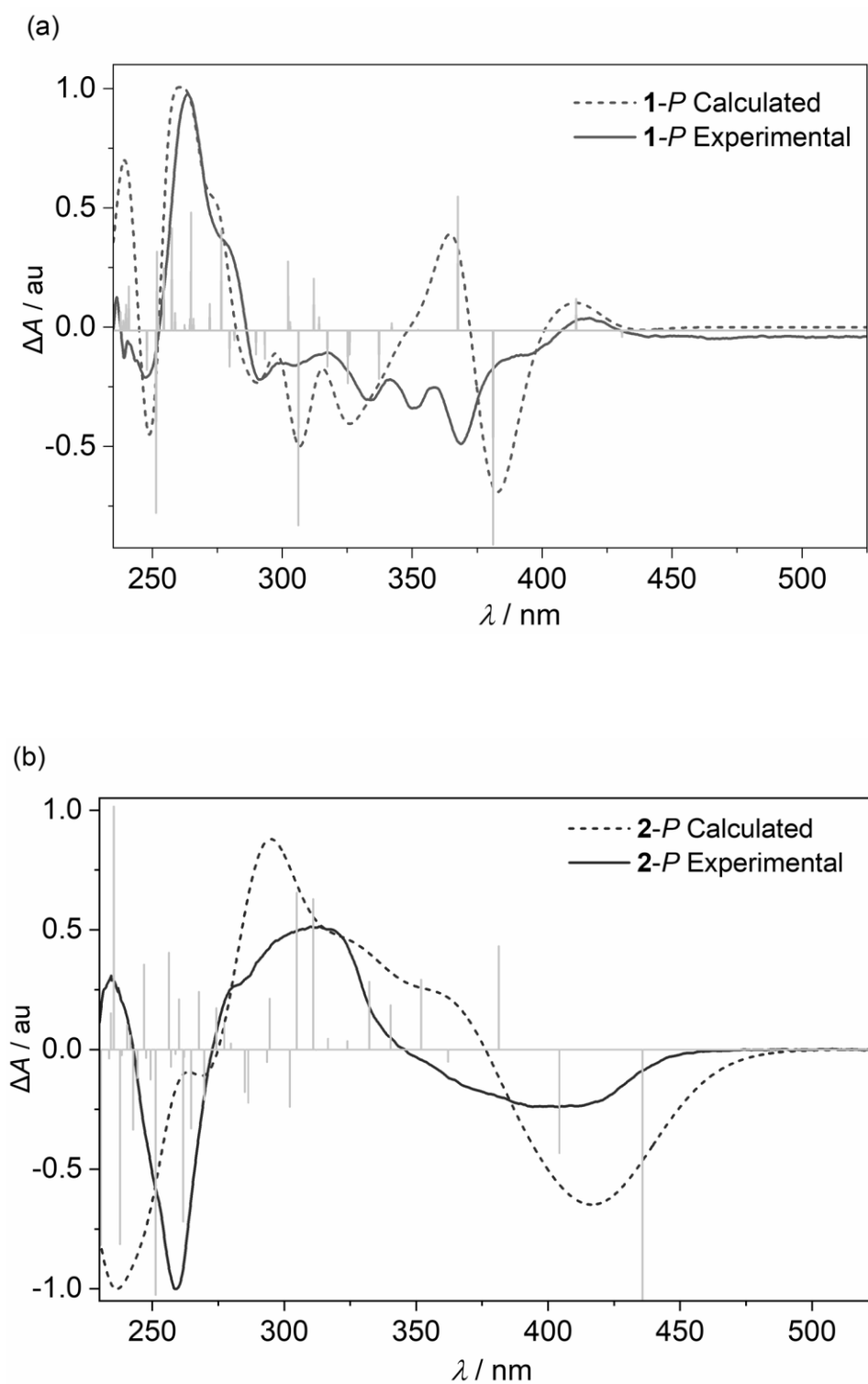


Figure S9. Comparison of experimental (solid) and TD-DFT calculated (dashed, shifted by 0.08 eV) CD spectra for *P*-enantiomer of (a) **1** and (b) **2**.

NICS calculations: The Nucleus Independent Chemical Shift (NICS) calculations were performed on B3LYP/6-31G(d,p) optimized geometry at GIAO-B3LYP/6-311+G(2d,p) level. Considering the non-planarity of molecule the NICS (1)_{zz} values were obtained by placing dummy atom at 1 Å above and below the each ring.

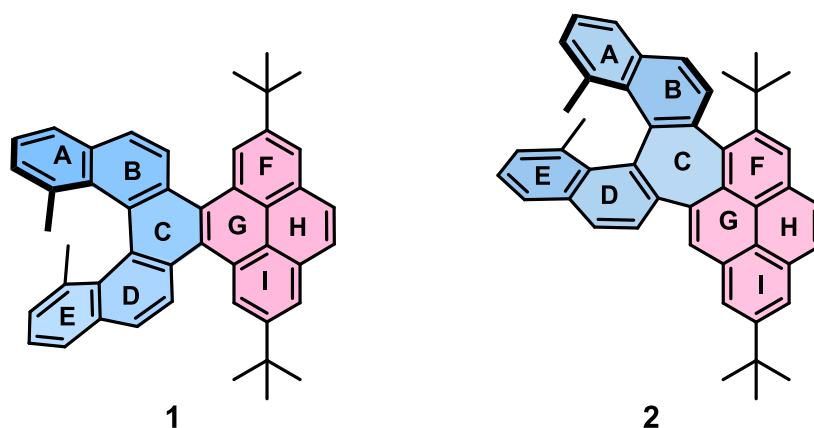


Table S5. The calculated NICS(0) and NICS(1)_{zz} values for **1** and **2**.

Ring	1			2		
	NICS(1) _{zz} (Up)	NICS(1) _{zz} (Down)	NICS(0)	NICS(1) _{zz} (Up)	NICS(1) _{zz} (Down)	NICS(0)
A	-3.83	-8.91	-8.28	-10.15	-8.40	-7.64
B	-7.09	-1.27	-5.64	-6.14	-5.39	-6.94
C	-2.93	-3.38	-3.41	12.12	14.94	7.61
D	-	-	-	-10.17	-9.09	-7.04
E	-	-	-	-10.72	-13.19	-7.59
F	-2.43	-0.84	-9.60	-30.88	-27.69	-9.57
G	-3.05	-3.17	1.42	-9.65	-14.90	-2.45
H	-2.50	-2.47	-3.37	-14.66	-14.81	-3.13
I	-	-	-	-32.28	-30.18	-10.06

S8. X-Ray crystallography

The single crystals of **2** were grown by slow diffusion of hexane to solution of **2** in chloroform in an NMR tube. Single Crystal X-ray diffraction data were collected at 100 K on a Bruker D8 Quest Kappa diffractometer with a Photon II CPAD area detector and multi-layered mirror monochromated CuK α radiation. The structures were solved using direct methods, expanded with Fourier techniques and refined with the Shelx software package.⁴ All non-hydrogen atoms were refined anisotropically. Hydrogen atoms were included in the structure factor calculation on geometrically idealized positions. Crystallographic data have been deposited with the Cambridge Crystallographic Data Centre as supplementary publication no. CCDC 2052372 for **2**. These data can be obtained free of charge from The Cambridge Crystallographic Data Centre via www.ccdc.ac.uk/data.request/cif.

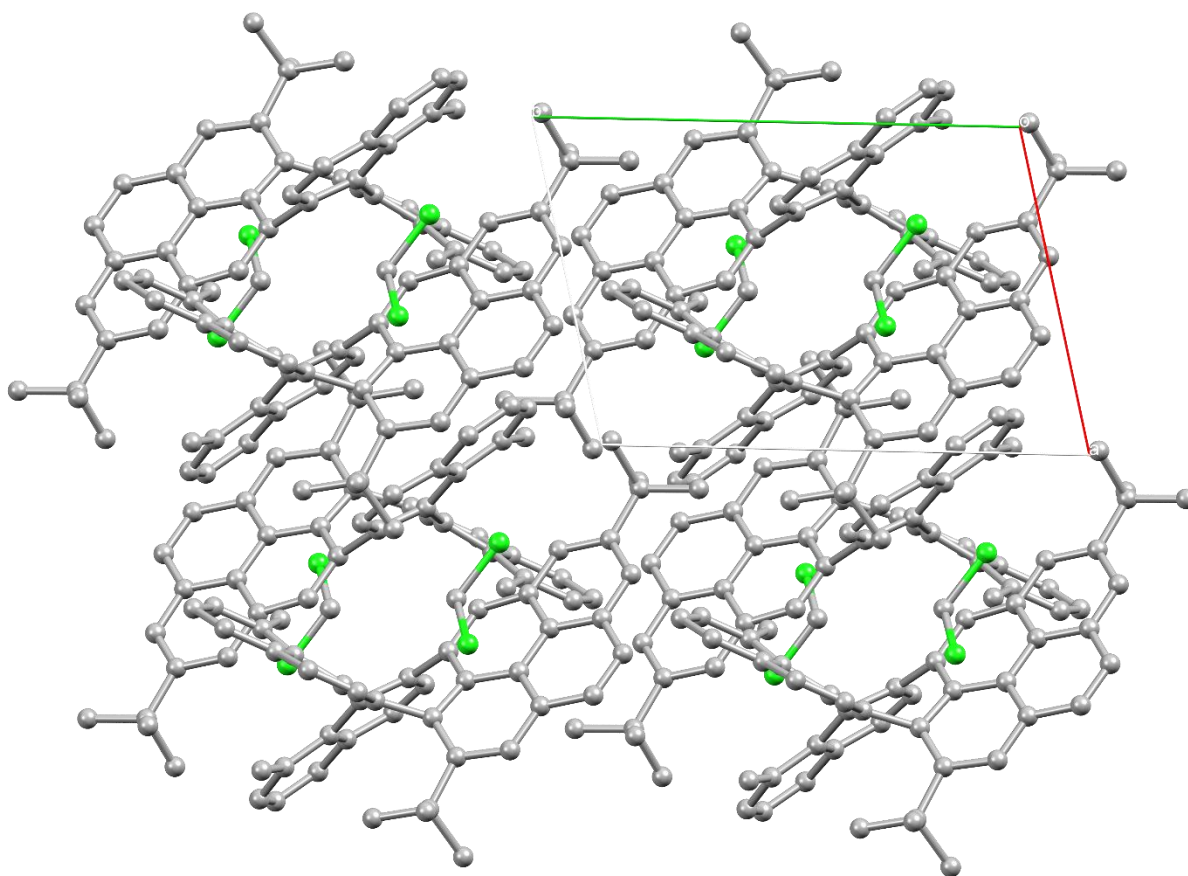


Figure S10. Crystal packing of **2**. Hydrogen atoms are omitted for clarity.

Table S6. Crystallographic table for 2.

CCDC number	2052372
Chemical formula	$C_{46}H_{40} \cdot CH_2Cl_2$
M_r	677.70
Crystal system, space group	Triclinic, $P-1$
Temperature (K)	100
a, b, c (Å)	8.4265 (6), 12.964 (1), 17.6847 (13)
α, β, γ (°)	110.250 (4), 97.265 (4), 99.701 (4)
V (Å ³)	1750.5 (2)
Z	2
Radiation type	Cu $K\alpha$
μ (mm ⁻¹)	1.91
Crystal size (mm)	0.23 × 0.03 × 0.02
T_{min}, T_{max}	0.639, 0.754
No. of measured, independent and observed [$I \geq 2\sigma(I)$] reflections	29713, 6872, 6142
R_{int}	0.031
$(\sin \theta/\lambda)_{max}$ (Å ⁻¹)	0.618
$R[F^2 > 2\sigma(F^2)], wR(F^2), S$	0.035, 0.095, 1.04
No. of reflections/parameters	6872/ 450

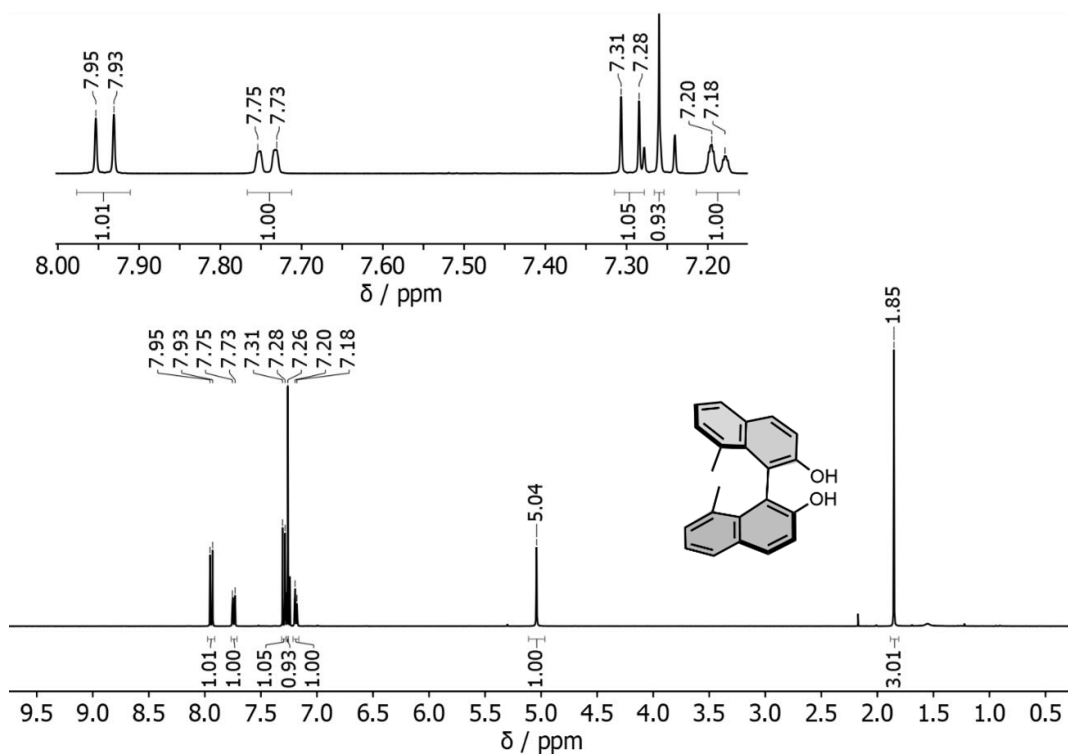


Figure S12. ^1H NMR spectrum of **4** (400 MHz, CDCl_3).

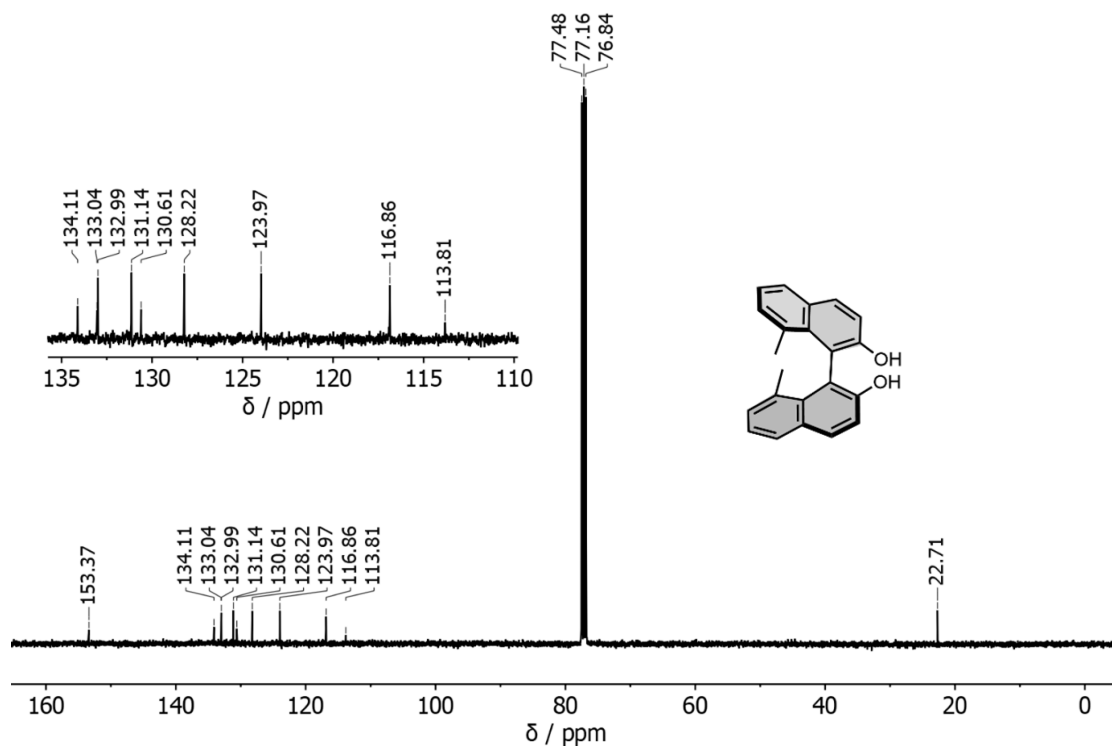


Figure S13. ^{13}C NMR spectrum of **4** (101 MHz, CDCl_3).

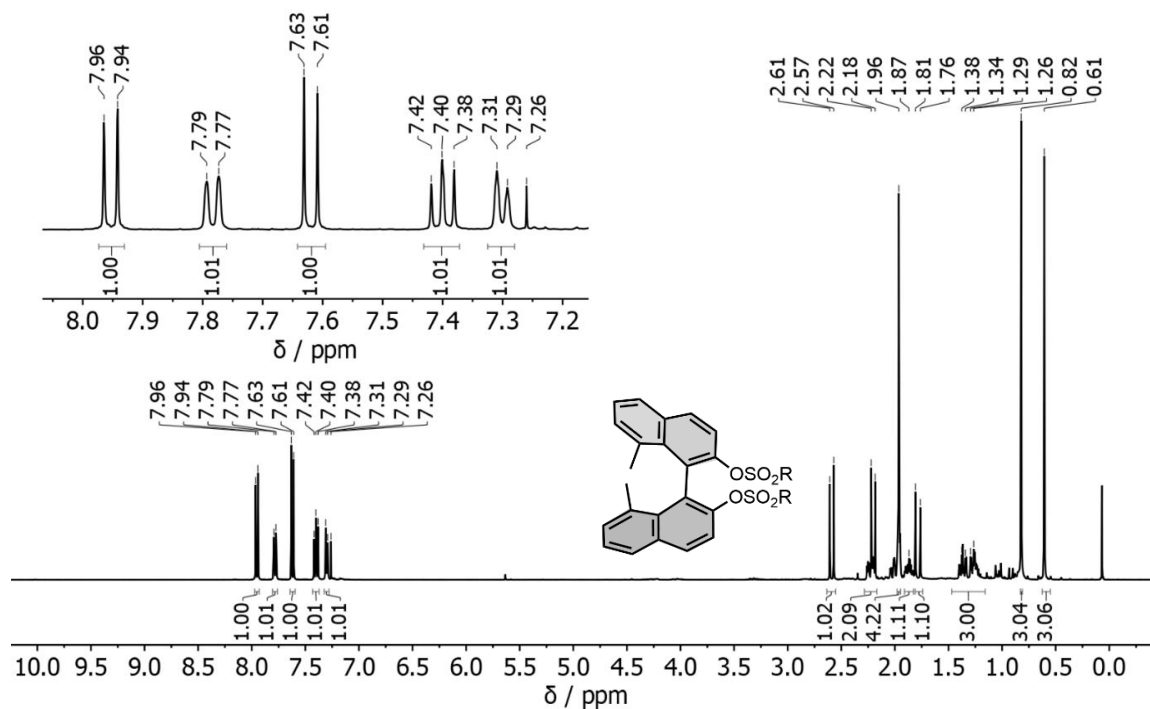


Figure S14. ^1H NMR spectrum of 8,8'-dimethyl-[1,1'-binaphthalene]-2,2'-dicamphorsulfonic ester (400 MHz, CDCl_3) (R = Camphor).

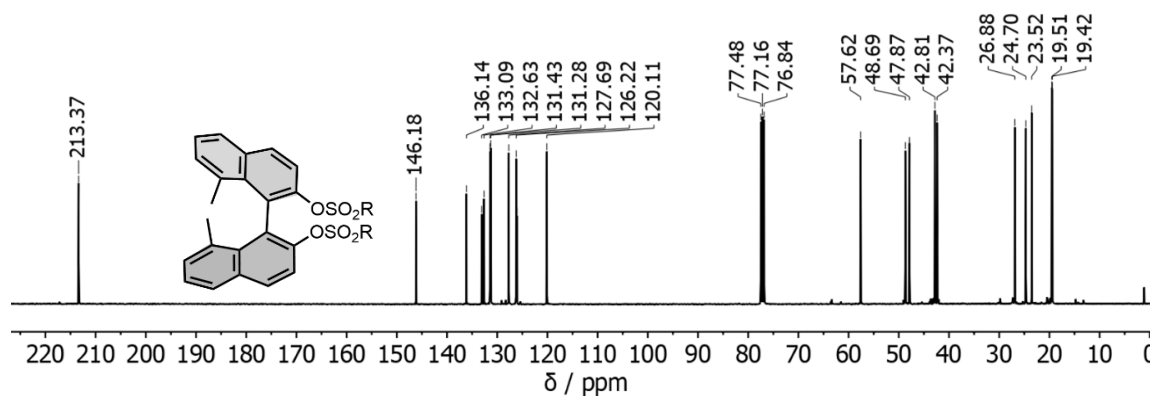


Figure S15. ^{13}C NMR spectrum of 8,8'-dimethyl-[1,1'-binaphthalene]-2,2'-dicamphorsulfonic ester (101 MHz, CDCl_3) (R = Camphor).

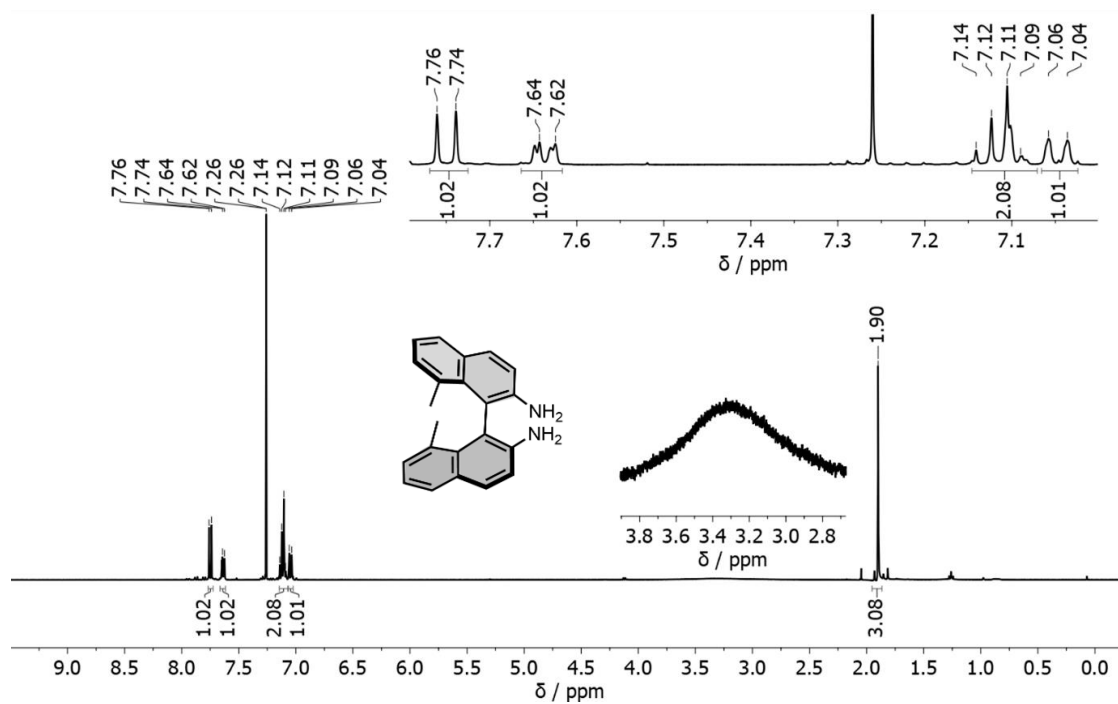


Figure S16. ^1H NMR spectrum of **5** (400 MHz, CDCl_3).

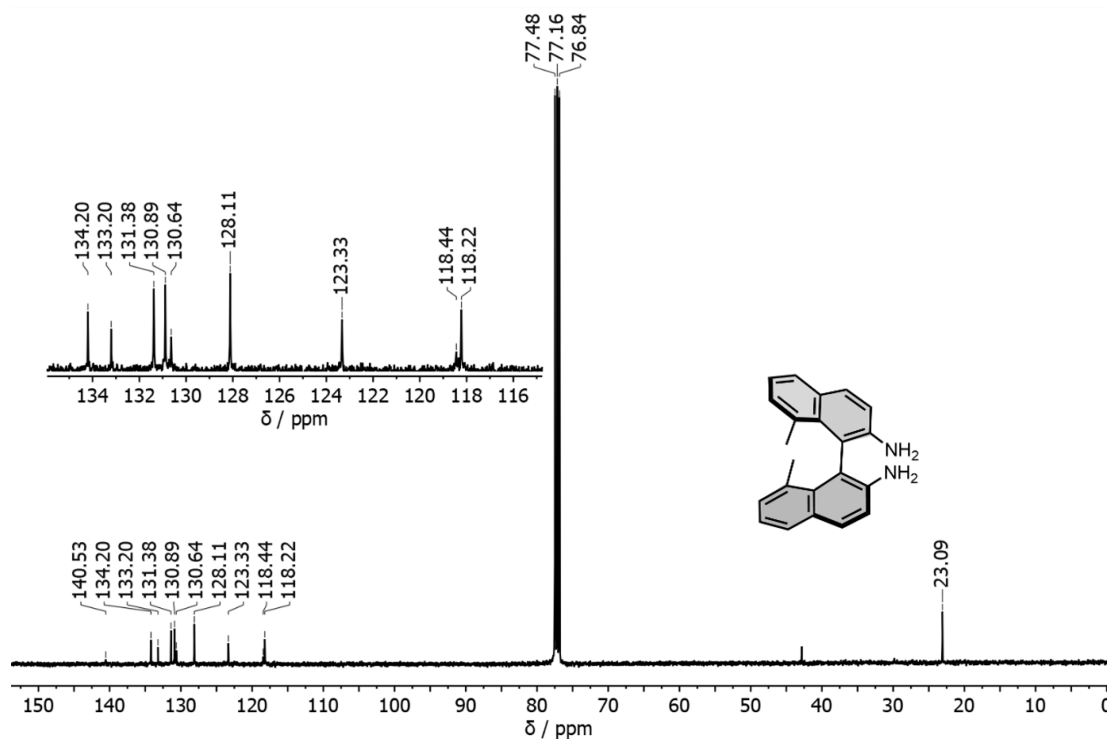


Figure S17. ^{13}C NMR spectrum of **5** (101 MHz, CDCl_3).

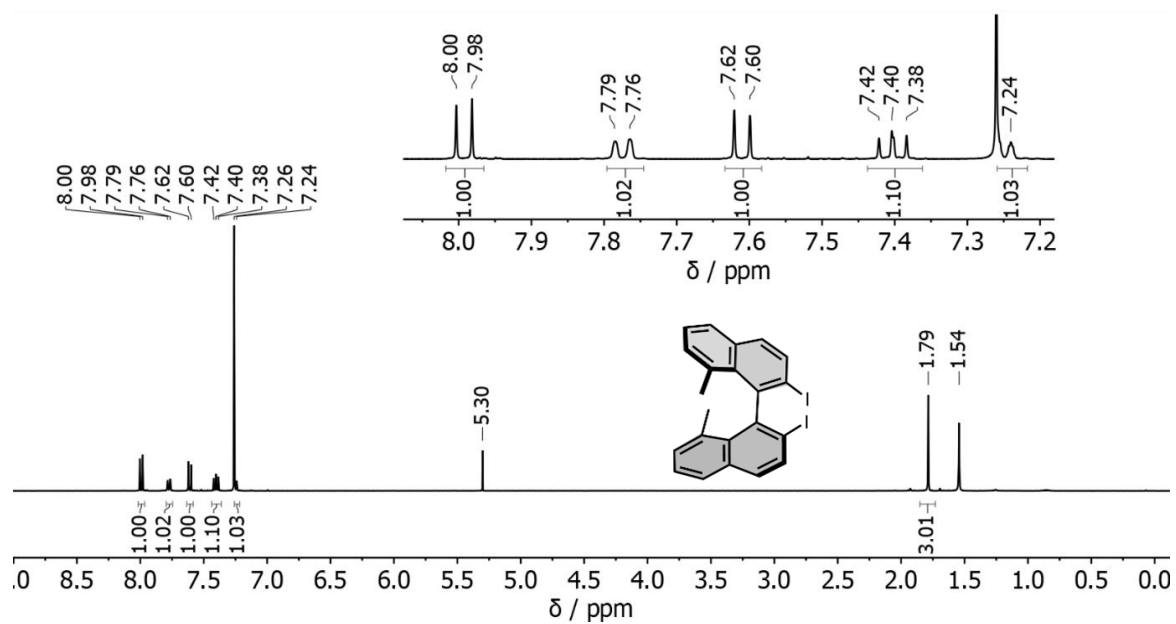


Figure S18. ^1H NMR spectrum of **6** (400 MHz, CDCl_3).

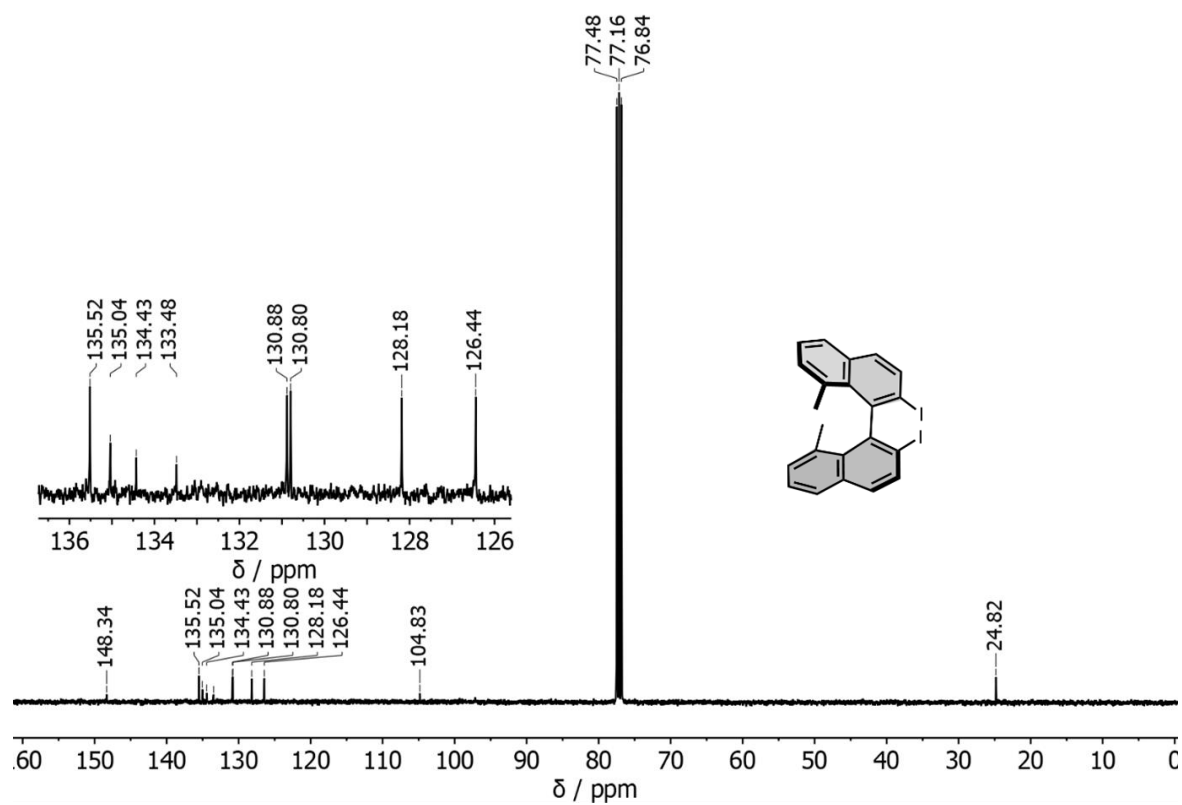


Figure S19. ^{13}C NMR spectrum of **6** (101 MHz, CDCl_3).

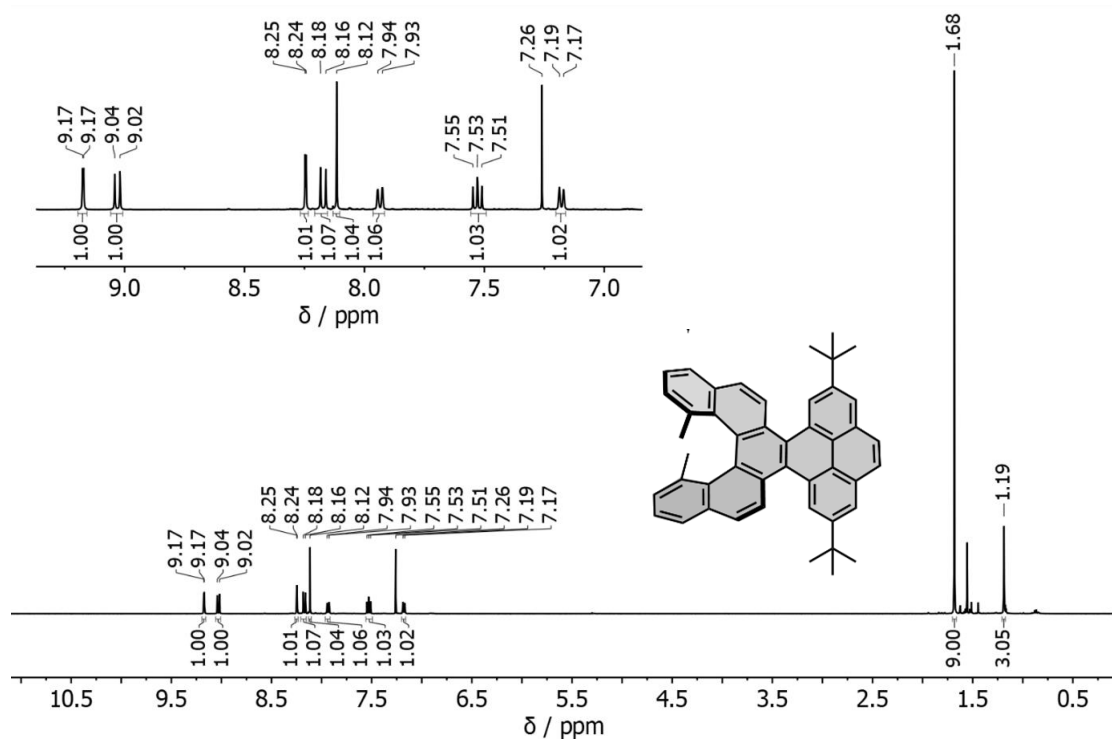


Figure S20. ^1H NMR spectrum of **1** (400 MHz, CDCl_3).

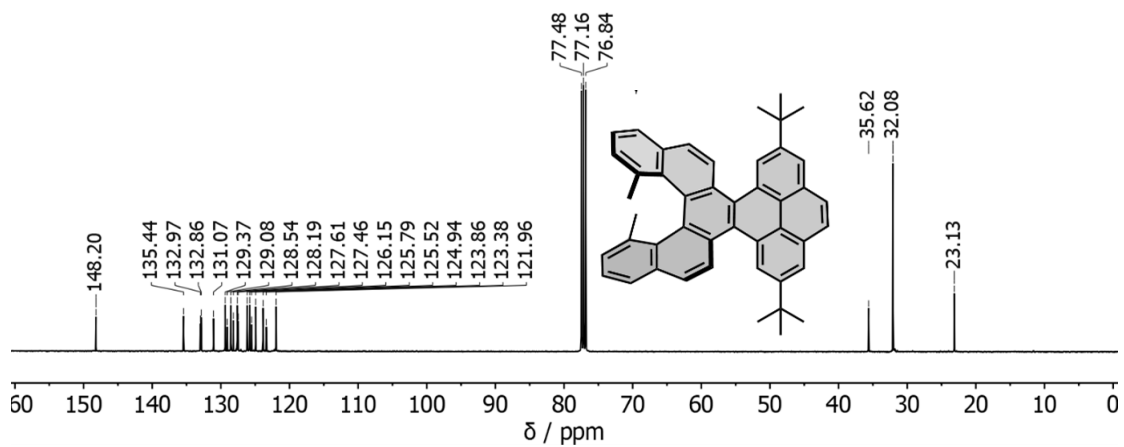


Figure S21. ^{13}C NMR spectrum of **1** (101 MHz, CDCl_3).

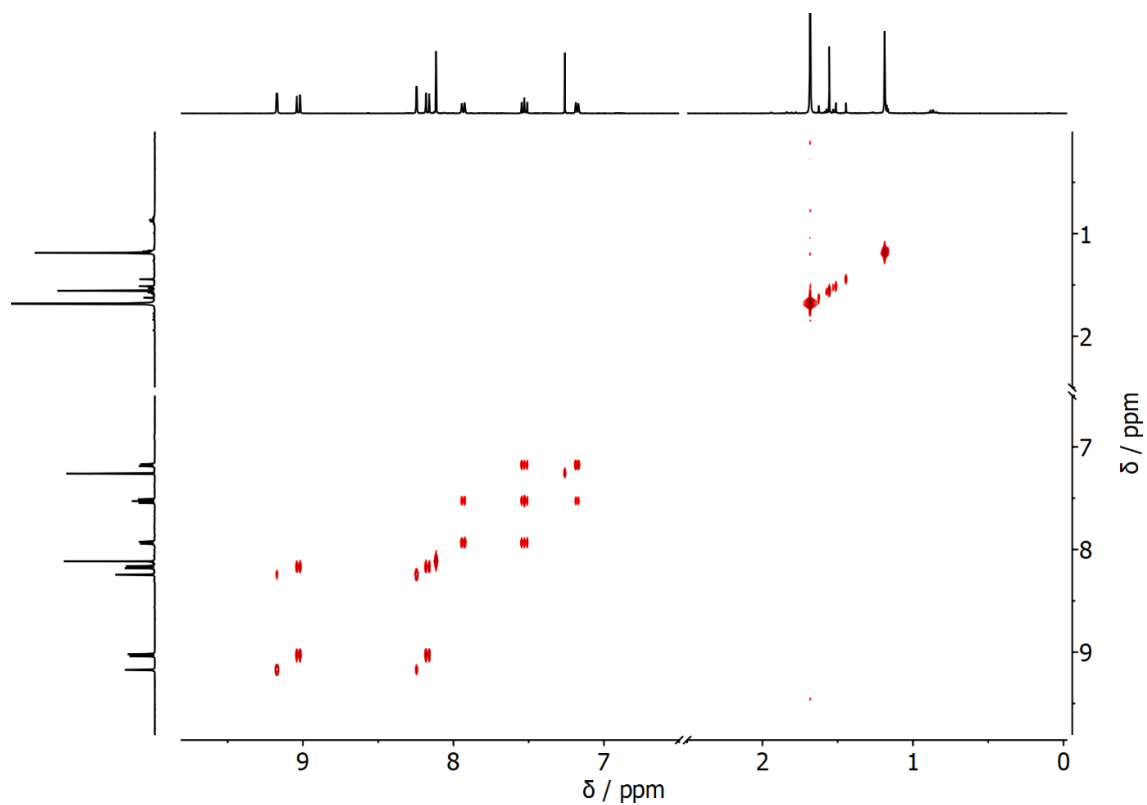


Figure S22. $^1\text{H} - ^1\text{H}$ COSY NMR spectrum of **1** (CDCl_3).

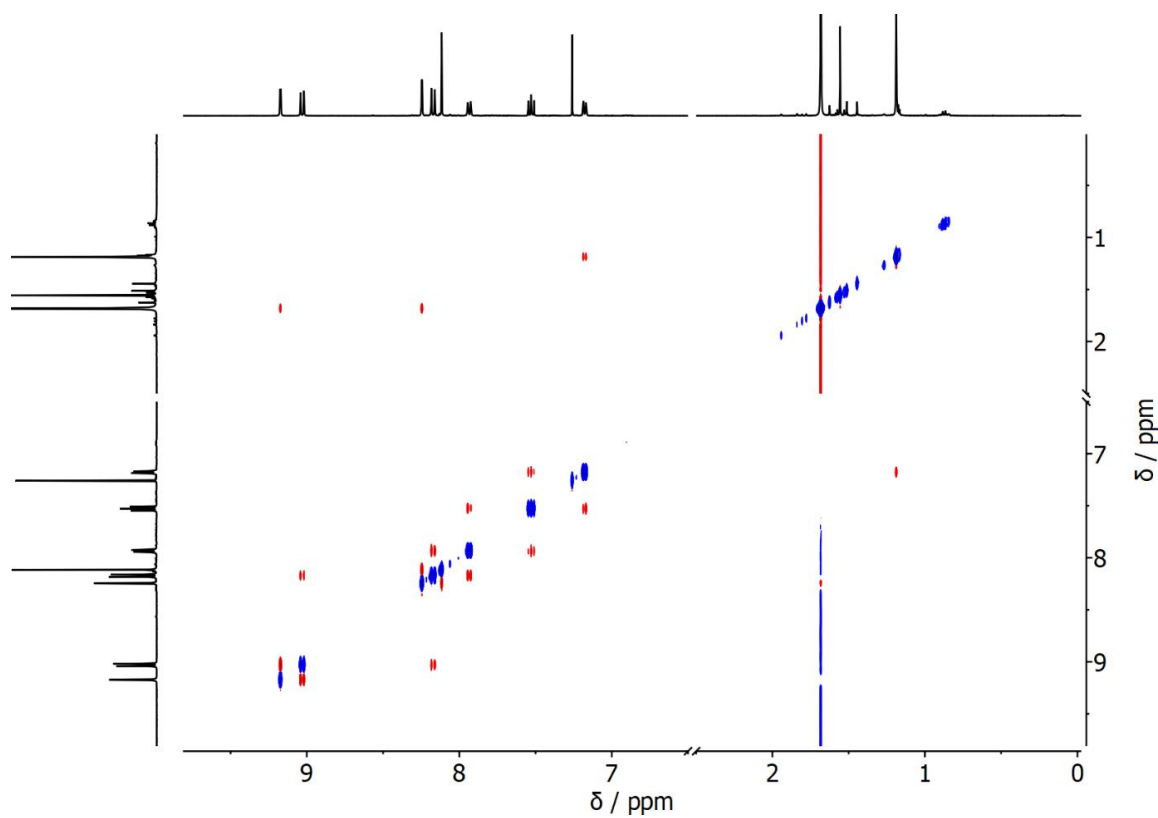


Figure S23. $^1\text{H} - ^1\text{H}$ NOESY NMR spectrum of **1** (CDCl_3).

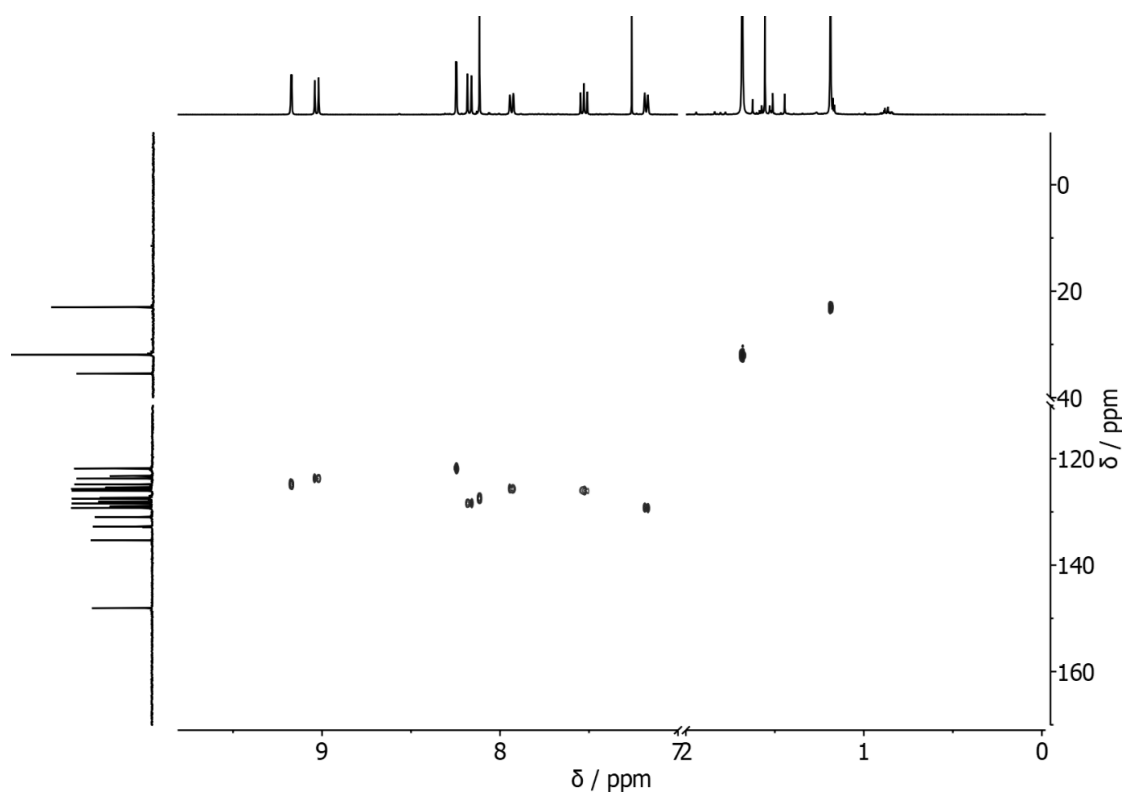


Figure S24. $^1\text{H} - ^{13}\text{C}$ HSQC NMR spectrum **1** (CDCl_3).

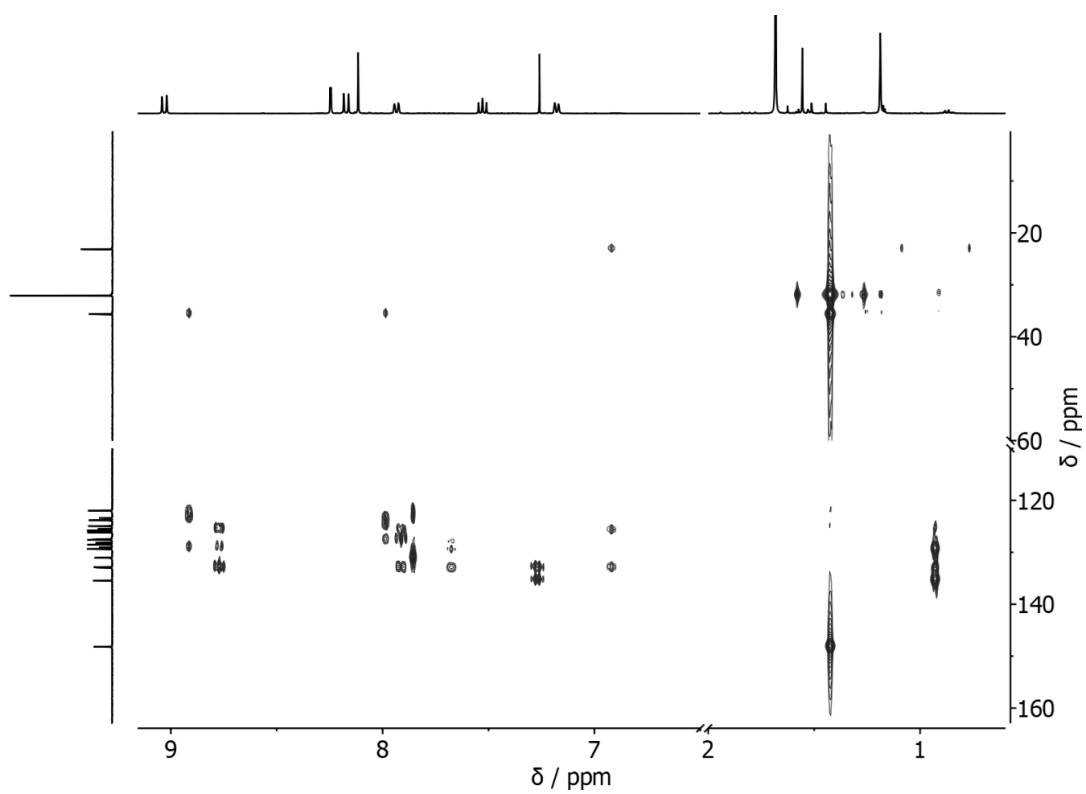


Figure S25. $^1\text{H} - ^{13}\text{C}$ HMBC NMR spectrum of **1** (CDCl_3).

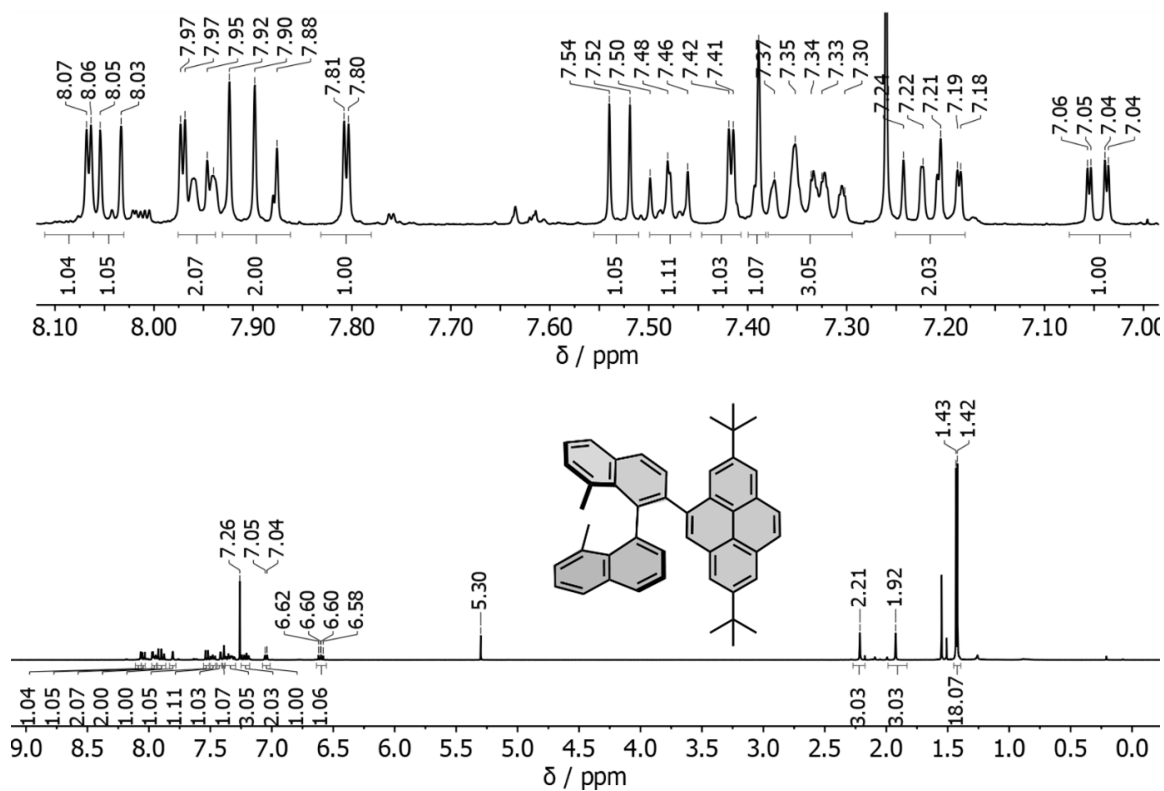


Figure S26. ^1H NMR spectrum of **7** (400 MHz, CDCl_3).

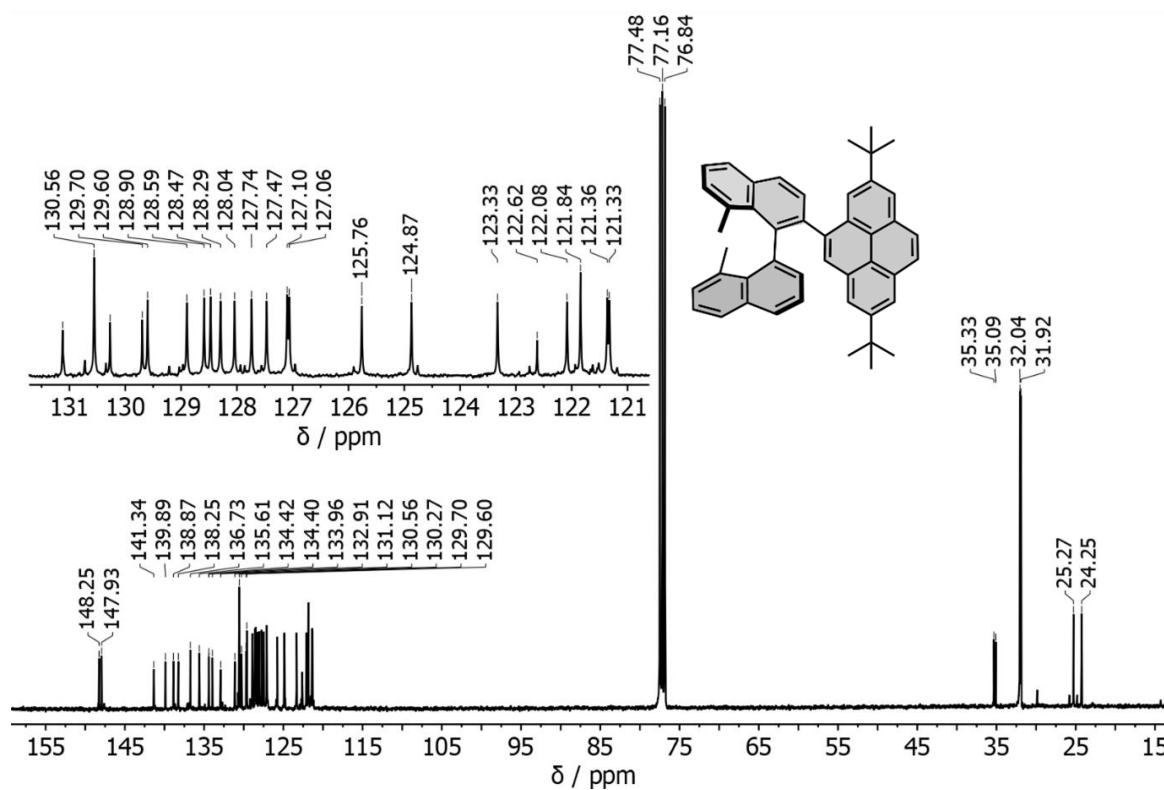


Figure S27. ^{13}C NMR spectrum of **7** (101 MHz, CDCl_3).

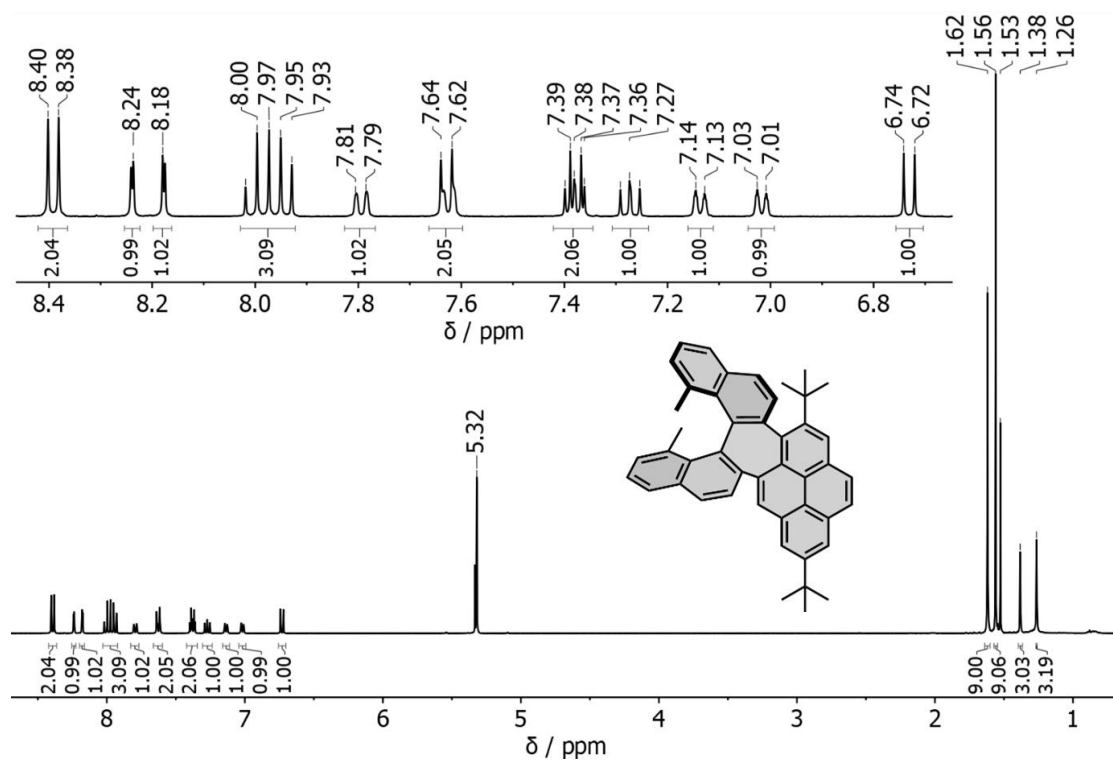


Figure S28. ¹H NMR spectrum of **2** (400 MHz, CD₂Cl₂).

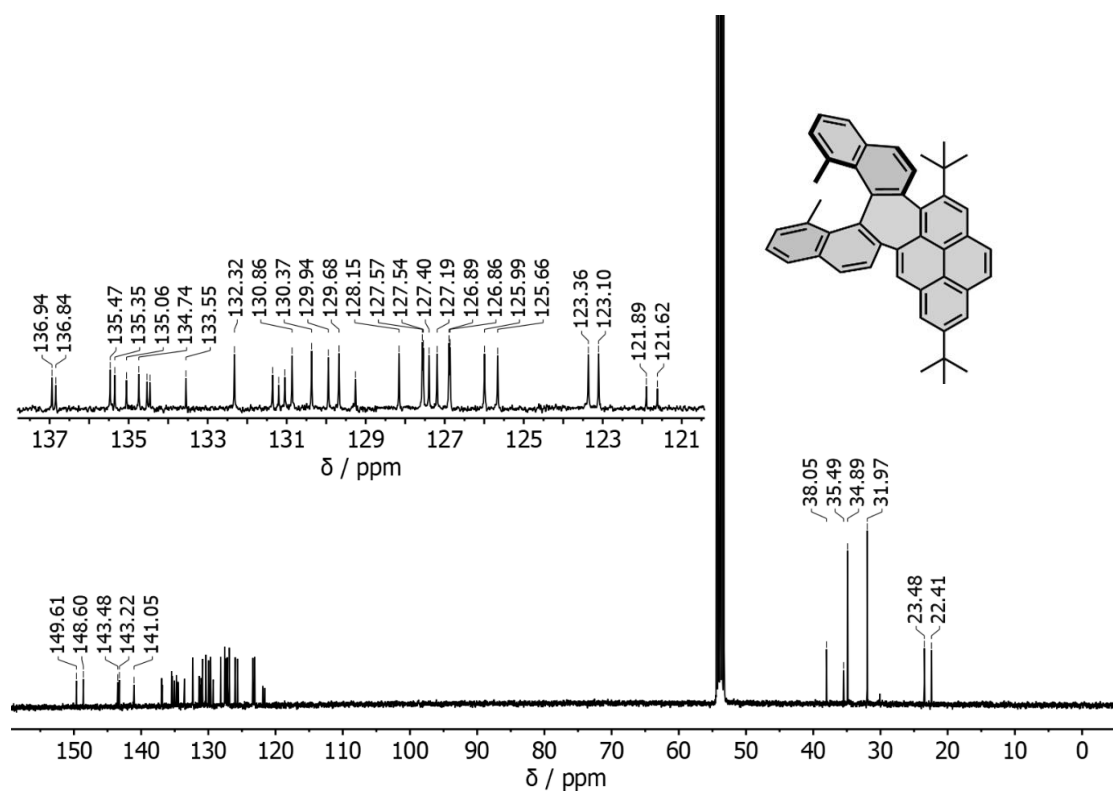


Figure S29. ¹³C NMR spectrum of **2** (101 MHz, CD₂Cl₂).

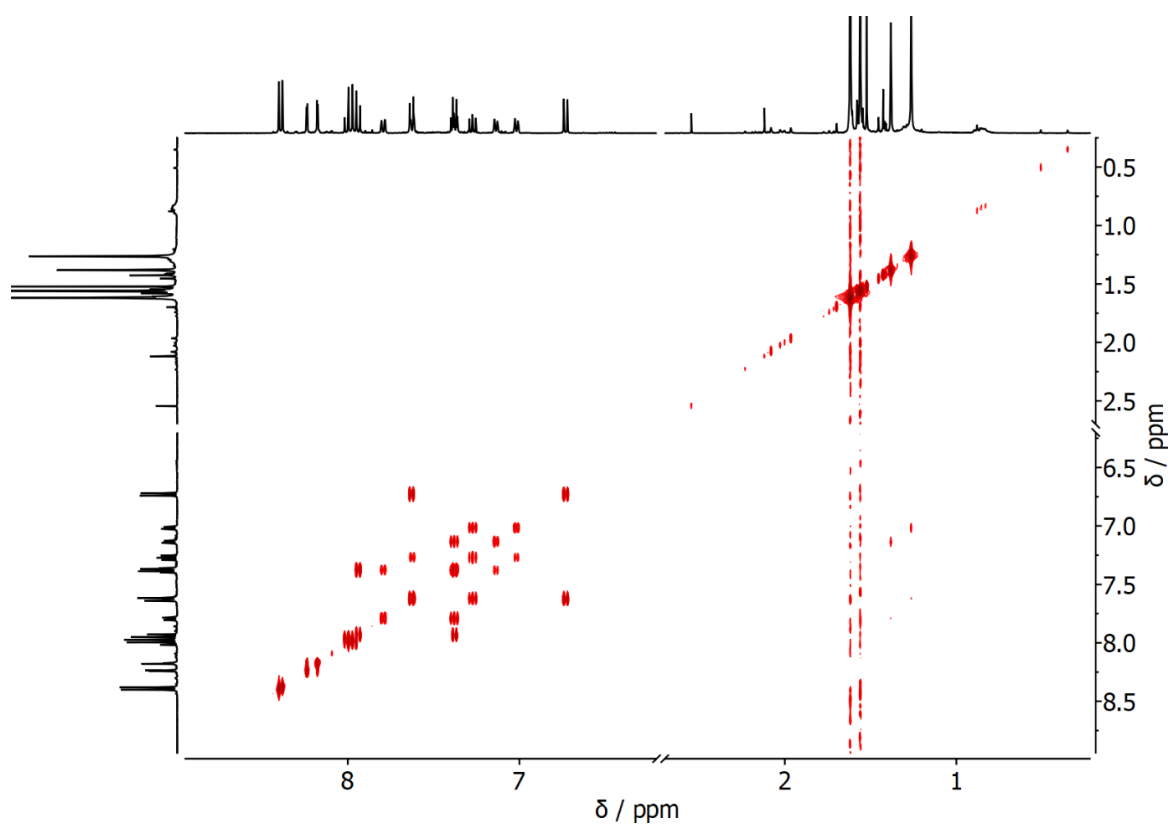


Figure S30. $^1\text{H} - ^1\text{H}$ COSY NMR spectrum of **2** (CD_2Cl_2).

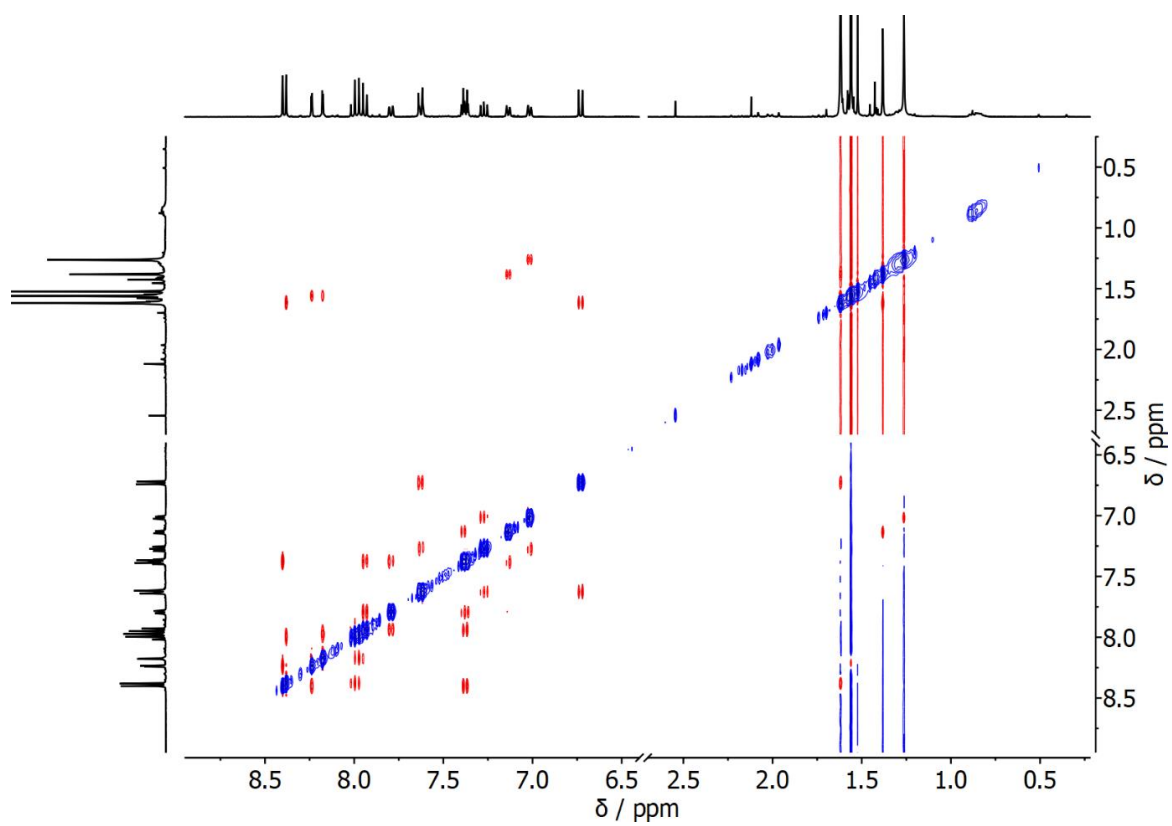


Figure S31. $^1\text{H} - ^1\text{H}$ NOESY NMR spectrum of **2** (CD_2Cl_2).

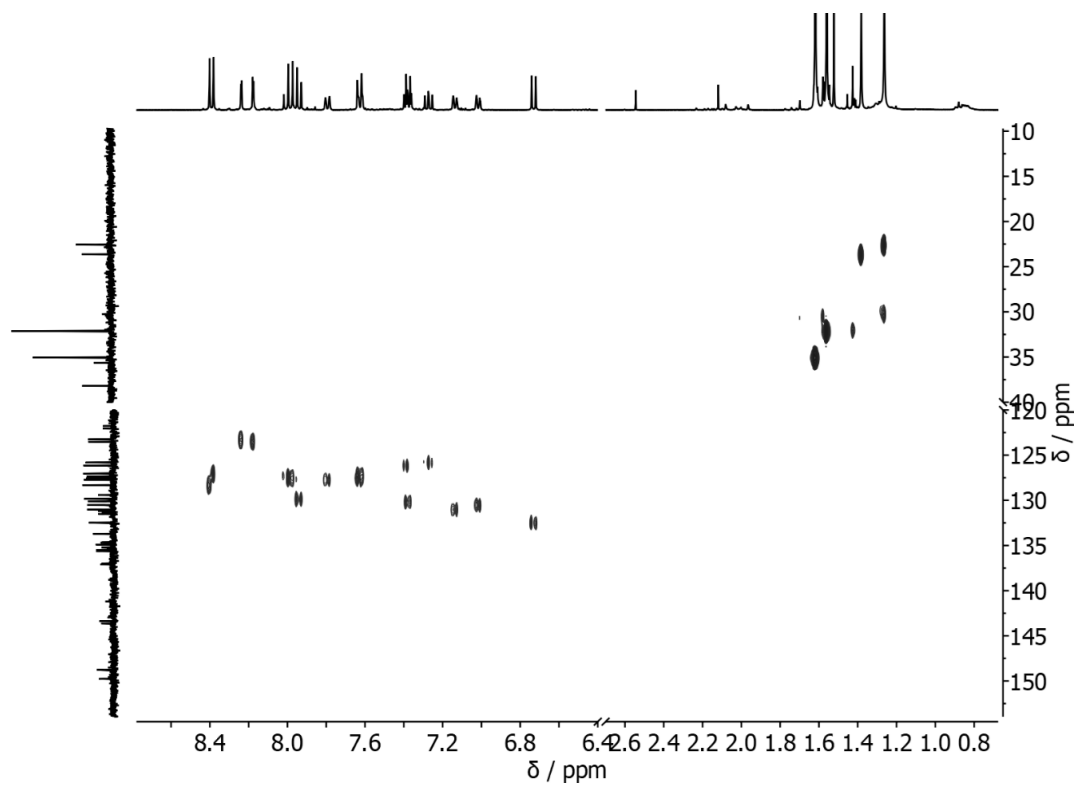


Figure S32. $^1\text{H} - ^{13}\text{C}$ HSQC NMR spectrum of **2** (CD_2Cl_2).

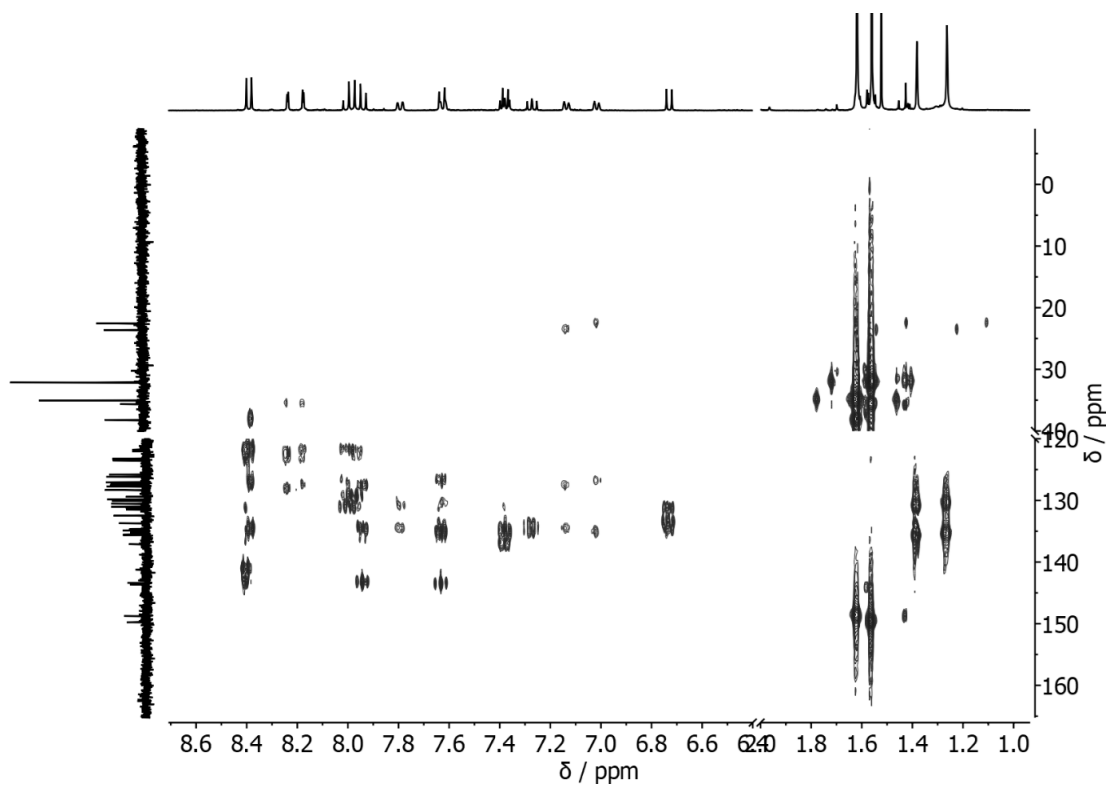


Figure S33. $^1\text{H} - ^{13}\text{C}$ HMBC NMR spectrum of **2** (CD_2Cl_2).

S10. High resolution mass spectrometry (HRMS)

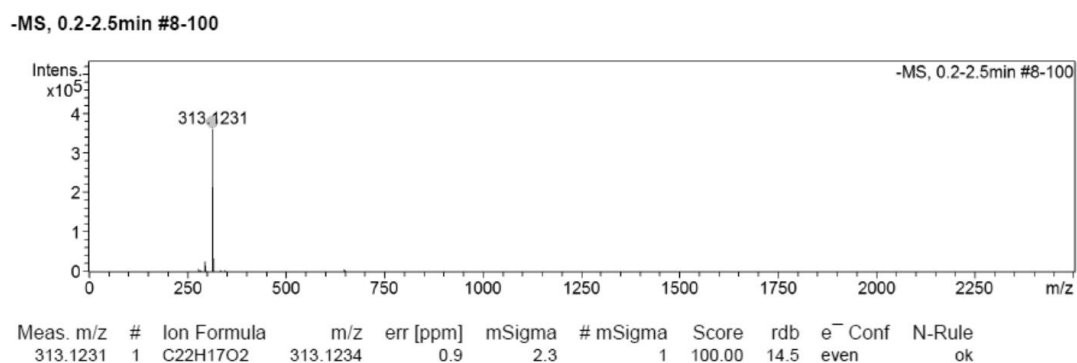


Figure S34. ESI-HRMS of **4**.

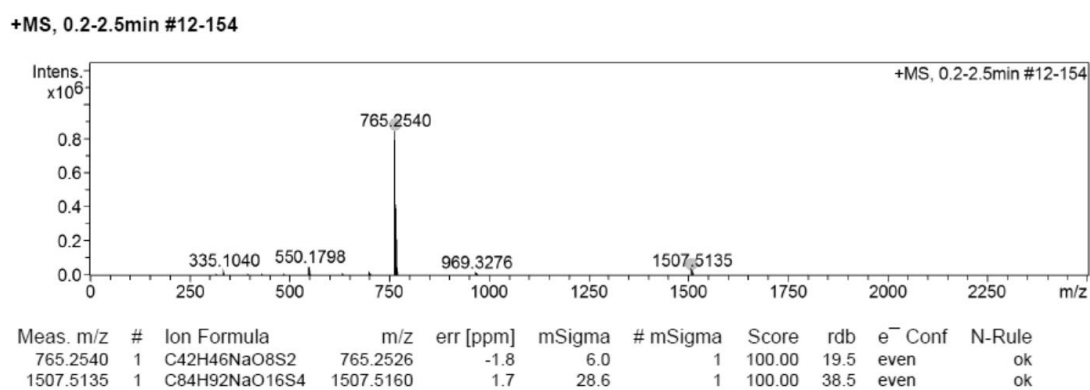


Figure S35. ESI-HRMS of **8,8'**-dimethyl-[1,1'-binaphthalene]-2,2'-dicamphorsulfonicester.

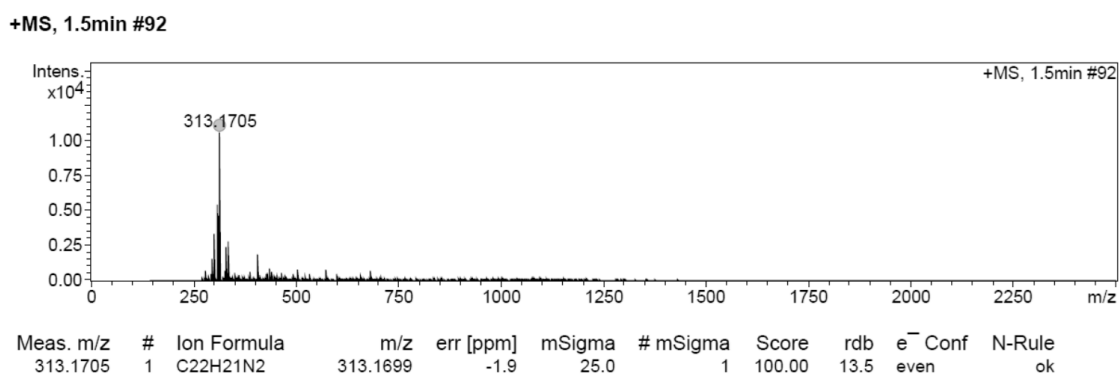


Figure S36. ESI-HRMS of **5**.

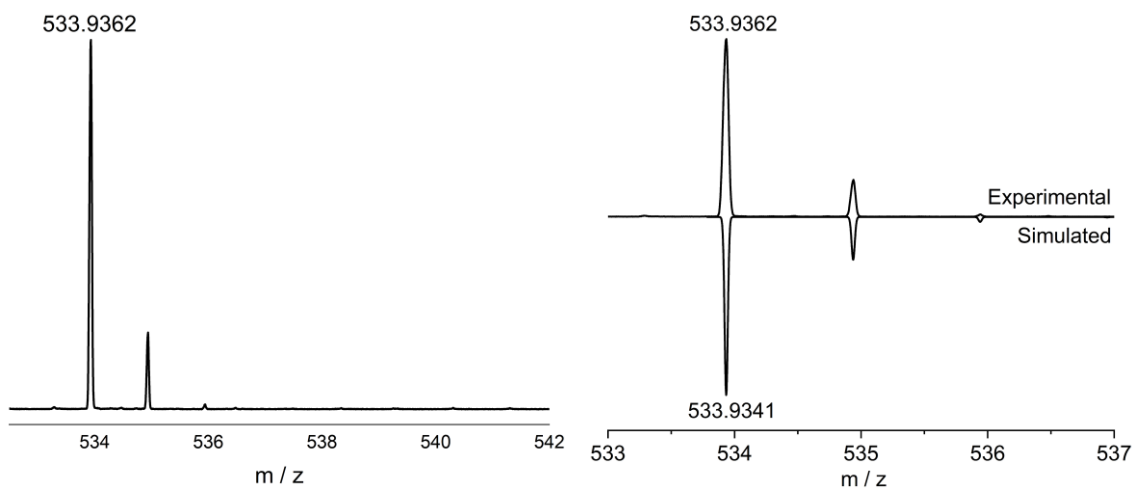


Figure S37. MALDI-TOF HRMS of **6**.

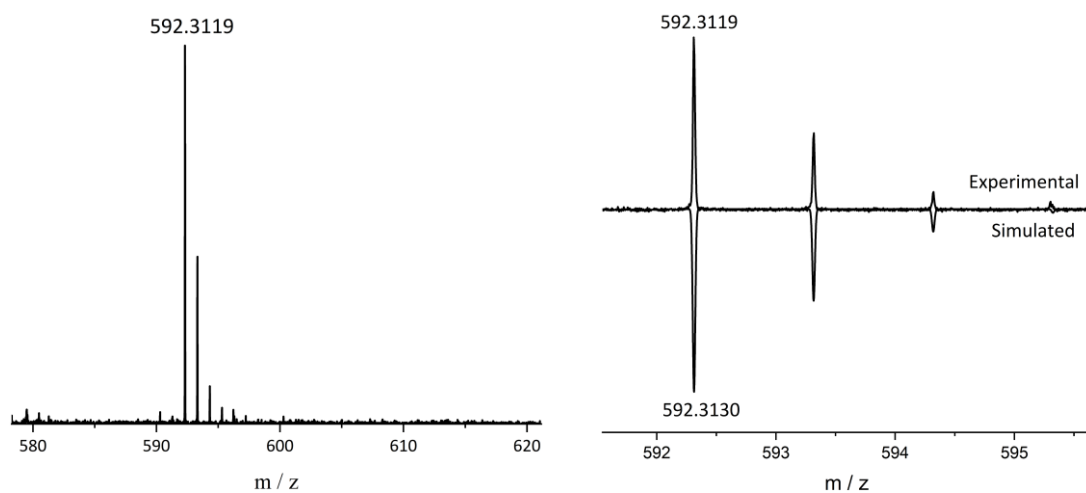


Figure S38. MALDI-TOF HRMS of **1**.

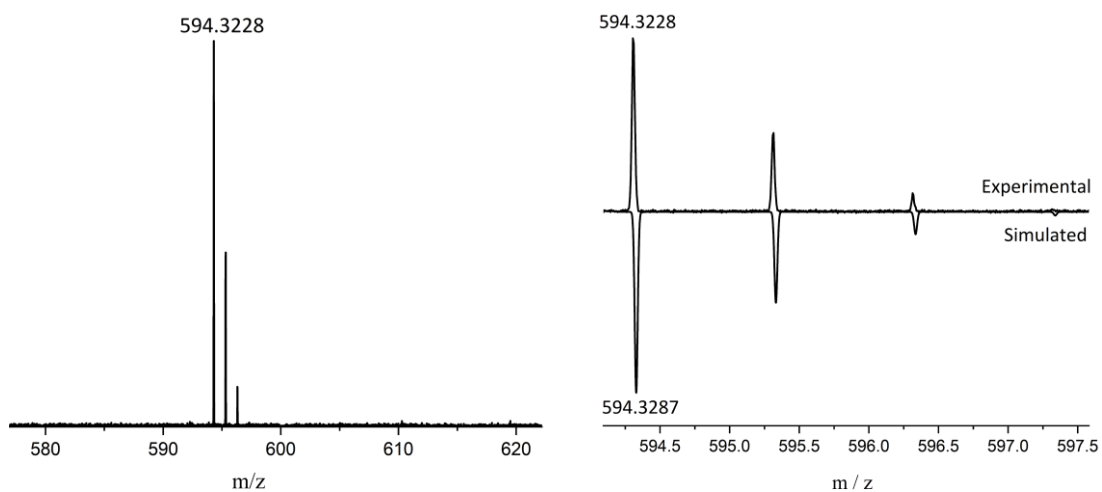


Figure S39. MALDI-TOF HRMS of **7**.

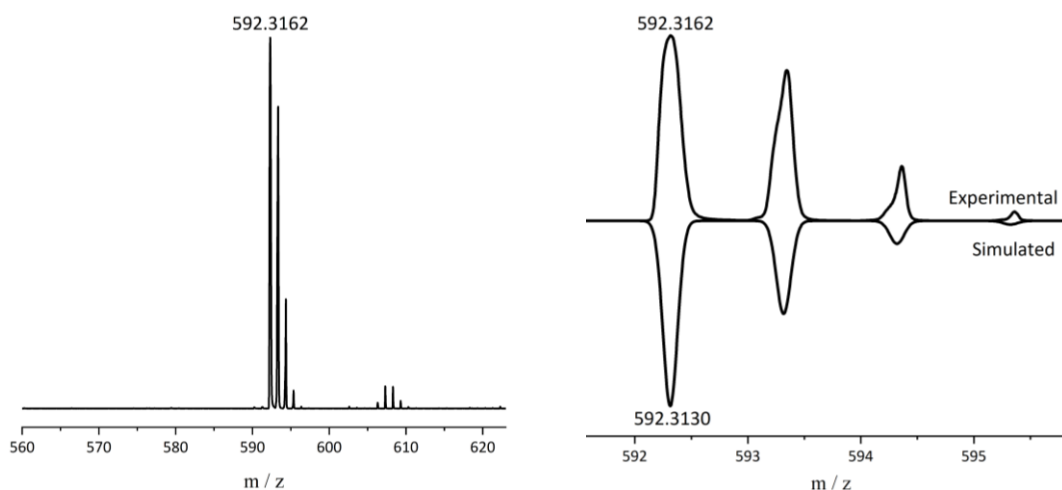


Figure S40. MALDI-TOF HRMS of **2**.

S12. References

- Misawa, N.; Nodate, M.; Otomatsu, T.; Shimizu, K.; Kaido, C.; Kikuta, M.; Ideno, A.; Ikenaga, H.; Ogawa, J.; Shimizu, S.; Shindo, K., Bioconversion of substituted naphthalenes and β -eudesmol with the cytochrome P450 BM3 variant F87V. *Applied Microbiology and Biotechnology* **2011**, *90*, 147–157.
- (a) Lorbach, D.; Wagner, M.; Baumgarten, M.; Mullen, K., The right way to self-fuse bi- and terpyrenyls to afford graphenic cutouts. *Chem Commun.* **2013**, *49*, 10578–10580; (b) Wu, Z. H.; Huang, Z. T.; Guo, R. X.; Sun, C. L.; Chen, L. C.; Sun, B.; Shi, Z. F.; Shao, X.; Li, H.; Zhang, H. L., 4,5,9,10-Pyrene Diimides: A Family of Aromatic Diimides Exhibiting High Electron Mobility and Two-Photon Excited Emission. *Angew Chem Int Ed.* **2017**, *56*, 13031–13035.
- Frisch, M. J.; Trucks, G. W.; Schlegel, H. B.; Scuseria, G. E.; Robb, M. A.; Cheeseman, J. R.; Scalmani, G.; Barone, V.; Petersson, G. A.; Nakatsuji, H.; Li, X.; Caricato, M.; Marenich, A. V.; Bloino, J.; Janesko, B. G.; Gomperts, R.; Mennucci, B.; Hratchian, H. P.; Ortiz, J. V.; Izmaylov, A. F.; Sonnenberg, J. L.; Williams; Ding, F.; Lipparini, F.; Egidi, F.; Goings, J.; Peng, B.; Petrone, A.; Henderson, T.; Ranasinghe, D.; Zakrzewski, V. G.; Gao, J.; Rega, N.; Zheng, G.; Liang, W.; Hada, M.; Ehara, M.; Toyota, K.; Fukuda, R.; Hasegawa, J.; Ishida, M.; Nakajima, T.; Honda, Y.; Kitao, O.; Nakai, H.; Vreven, T.; Throssell, K.; Montgomery Jr., J. A.; Peralta, J. E.; Ogliaro, F.; Bearpark, M. J.; Heyd, J. J.; Brothers, E. N.; Kudin, K. N.; Staroverov, V. N.; Keith, T. A.; Kobayashi, R.; Normand, J.; Raghavachari, K.; Rendell, A. P.; Burant, J. C.; Iyengar, S. S.; Tomasi, J.; Cossi, M.; Millam, J. M.; Klene, M.; Adamo, C.; Cammi, R.; Ochterski, J. W.; Martin, R. L.; Morokuma, K.; Farkas, O.; Foresman, J. B.; Fox, D. J. *Gaussian 16 Rev. C.01*, Wallingford, CT, 2016.
- (a) Sheldrick, G., Crystal structure refinement with SHELXL. *Acta Crystallogr., Sect. C: Struct. Chem.* **2015**, *71*, 3–8; (b) Sheldrick, G., SHELXT - Integrated space-group and crystal-structure determination. *Acta Crystallogr., Sect. A: Found. Adv.* **2015**, *71*, 3–8.

8.2. Supporting Information for

Pyrene-Fused [7]Helicenes Connected via Hexagonal and Heptagonal Rings: Stereospecific Synthesis and Chiroptical Properties

Asim Kumar Swain,¹ Krzysztof Radacki,² Holger Braunschweig,² and Prince Ravat^{1,*}

¹Institut für Organische Chemie, Universität Würzburg, D-97074 Würzburg, Germany.

²Institut für Anorganische Chemie, Universität Würzburg, D-97074 Würzburg, Germany.

*Email: princekumar.ravat@uni-wuerzburg.de

Table of Contents

S1. Cyclic voltammetry	S120
S2. Solid-state fluorescence	S121
S3. CPL properties of [5]helicene congeners	S121
S4. Chiral stationary phase HPLC	S122
S5. Determination and analysis of activation parameters for enantiomerization	S123
S6. Quantum chemical calculations	S125
S7. Single crystal data.....	S131
S8. NMR spectroscopy	S134
S9. High resolution mass spectrometry (HRMS)	S147

S1. Cyclic voltammetry

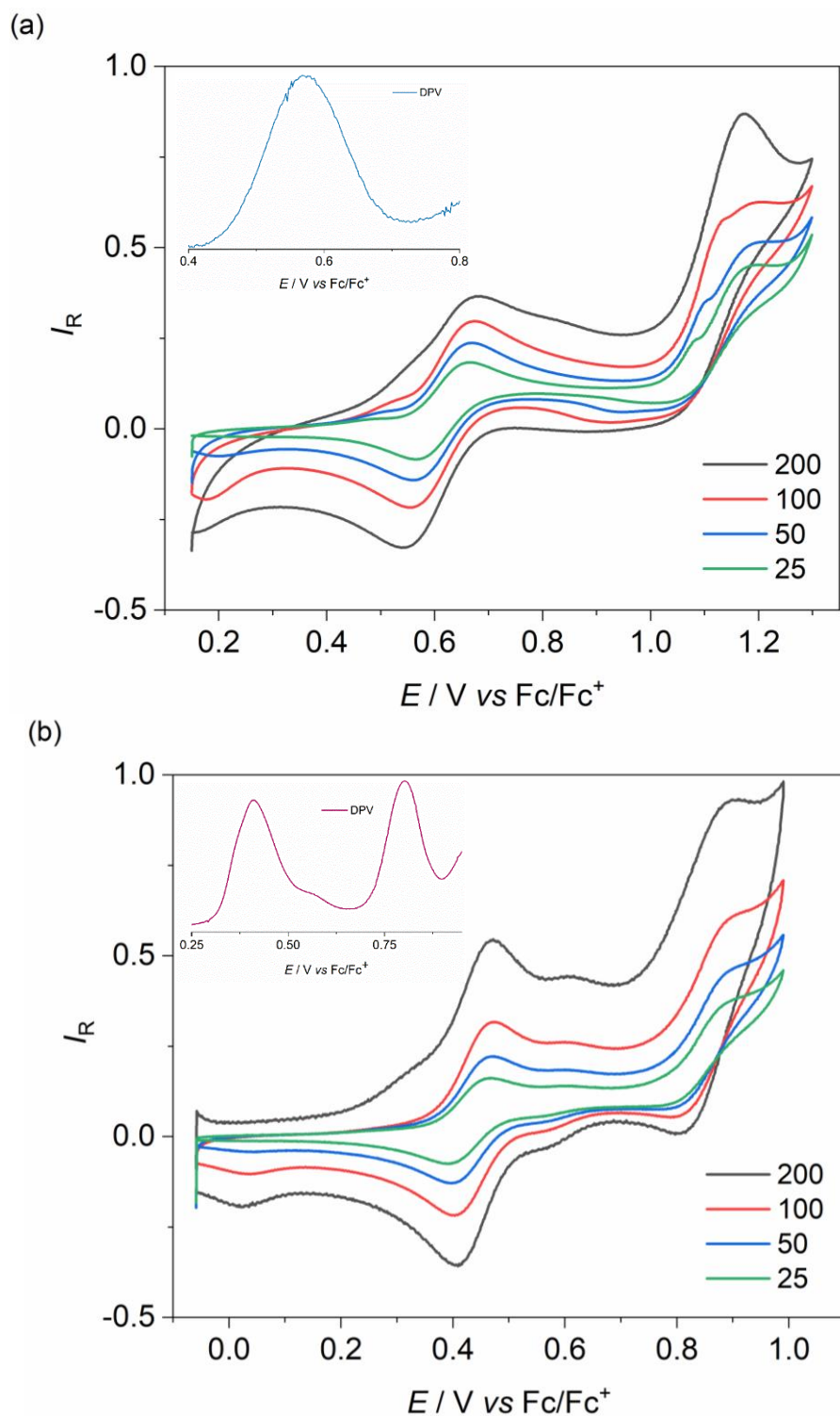


Figure S1. Cyclic voltammograms of (a) **1** and (b) **2** in DCM with 0.1 M $(n-C_4H_9)_4NPF_6$ as supporting electrolyte, versus ferrocene/ferrocenium (Fc/Fc^+) at room temperature with different scan rate. (Inset: DPV curve)

S2. Solid-state fluorescence

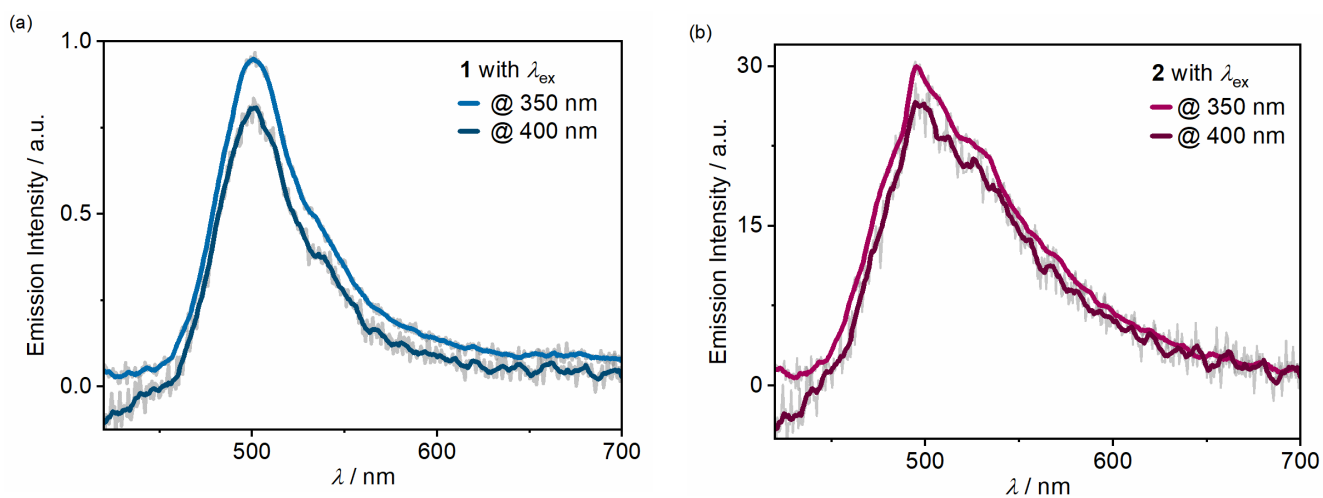


Figure S2. Solid-state emission of (a) **1** and (b) **2**.

S3. CPL properties of [5]helicene congeners

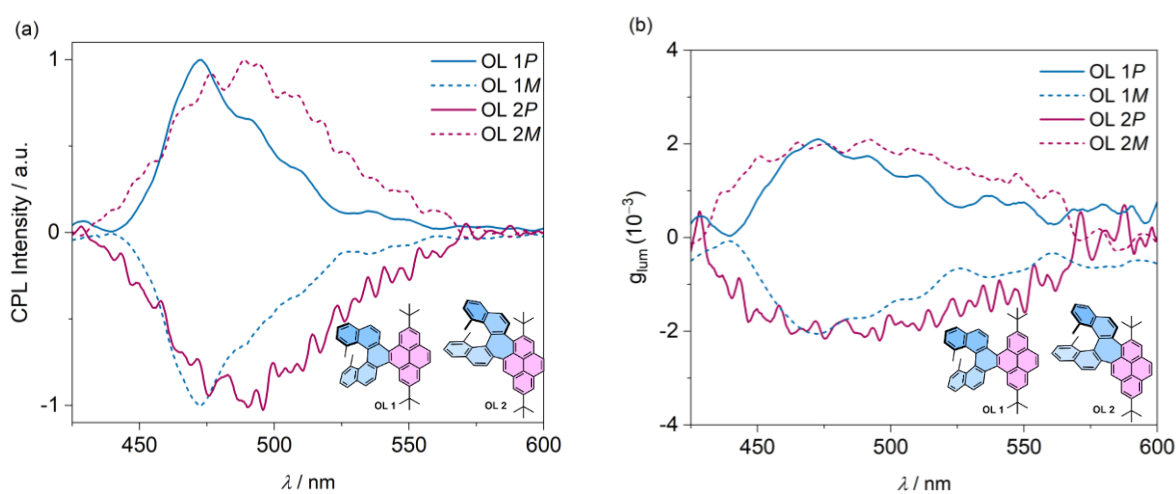


Figure S3. (a) CPL spectra and (b) Emission dissymmetry factor (g_{lum}) of [5]helicene congeners—OL **1** ($B_{CPL} = 0.37 \text{ M}^{-1} \text{ cm}^{-1}$) and OL **2** ($B_{CPL} = 5.98 \text{ M}^{-1} \text{ cm}^{-1}$).

S4. Chiral stationary phase HPLC

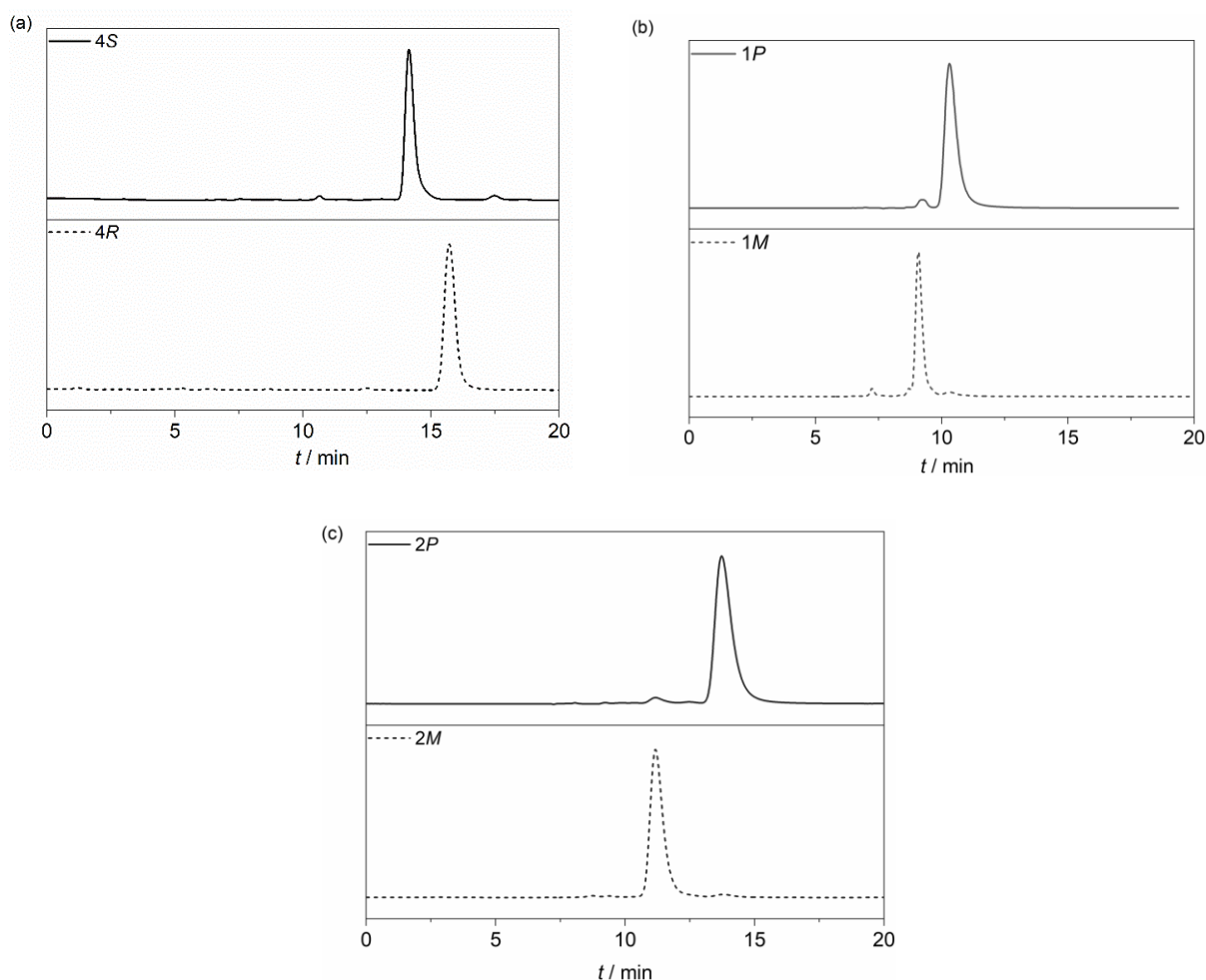


Figure S4. HPLC chromatogram of (a) **4**, (b) **1**, and (c) **2** using chiral stationary phase column.

Table S1. Overview of parameters for HPLC separation of enantiomers of **1**, **2** and **4**.

Compound	Eluent <i>n</i> -hexane/ <i>i</i> PrOH	First fraction	Second fraction	α^b	R_S^c	<i>er</i>
4	80:20	<i>S</i>	<i>R</i>	1.11	1.03	≥ 99.0
1	97:3	<i>M</i>	<i>P</i>	1.13	0.83	98.1 : 1.9
2	97:3	<i>M</i>	<i>P</i>	1.23	1.42	98.3 : 1.7

^aPhenomenex Lux i-Amylose-3 5 μm (250 x 4.6 mm). Sample injection: 5 μL of a ~ 1 mg/mL solution in hexane/*i*PrOH. Separation conditions: Eluent, flow rate: 0.5 mL/min, 25 $^\circ\text{C}$. ^bSelectivity parameter: $\alpha = t_{R2} / t_{R1}$, where t_{R1} , and t_{R2} are elution times for first and second fraction, respectively. ^cResolution parameter: $R_S = 2(t_{R2} - t_{R1}) / (w_1 + w_2)$, where w_1 and w_2 are peak widths for first and second fraction, respectively.

S5. Determination and analysis of activation parameters for enantiomerization

The values of the Gibbs activation energies ($\Delta G^\ddagger(T)$) for enantiomerization of **1** and **2** calculated by following the decay of the enantiomeric excess (ee) of the enantioenriched samples dissolved in diethylene glycol dibutyl ether (1-(2-(2-butoxyethoxy)ethoxy)butane) at 438 K for **1** and 498 K for **2** over time (t) by HPLC on a chiral stationary phase. To estimate the $\Delta G^\ddagger(T)$ value, the $\ln(ee_t/ee_0)$ values were plotted against t and the data set was linearly fitted (Figures S5 (a) and (b)). Following the equations $\ln(ee_t/ee_0) = -k_{\text{rac}}t$, where k_{rac} is the rate constant of racemization, and $k_{\text{rac}} = 2k_e$, where k_e is the rate constant of enantiomerization, the k_e values were obtained and used to calculate the corresponding $\Delta G^\ddagger(T)$ values by using the Eyring equation $\Delta G^\ddagger(T) = -RT \ln(k_e h / \kappa k_B T)$, where R is the gas constant ($R = 8.31446 \text{ J K}^{-1}$), h is the Planck constant ($h = 6.62607 \times 10^{-34} \text{ J s}$), k_B is the Boltzmann constant ($k_B = 1.38064852 \times 10^{-23} \text{ J K}^{-1}$), and κ is the transmission coefficient ($\kappa = 0.5$ or 1). The transmission coefficient $\kappa = 0.5$ was used because the enantiomerization process is defined as a reversible first order reaction.

The $\Delta G^\ddagger(T)$ value for **1** was determined at 438 K, where complete racemization could be followed within a ~ 5 h period of time. Because the $\Delta G^\ddagger(T)$ values of **1** and **2** differ significantly, it was not possible to follow the racemization process for both compounds at the same temperature i.e., at 438 K without the process for **2** being too slow. Hence the $\Delta G^\ddagger(T)$ value for **2** was determined at 498 K, where the racemization was followed up to 10 hours.

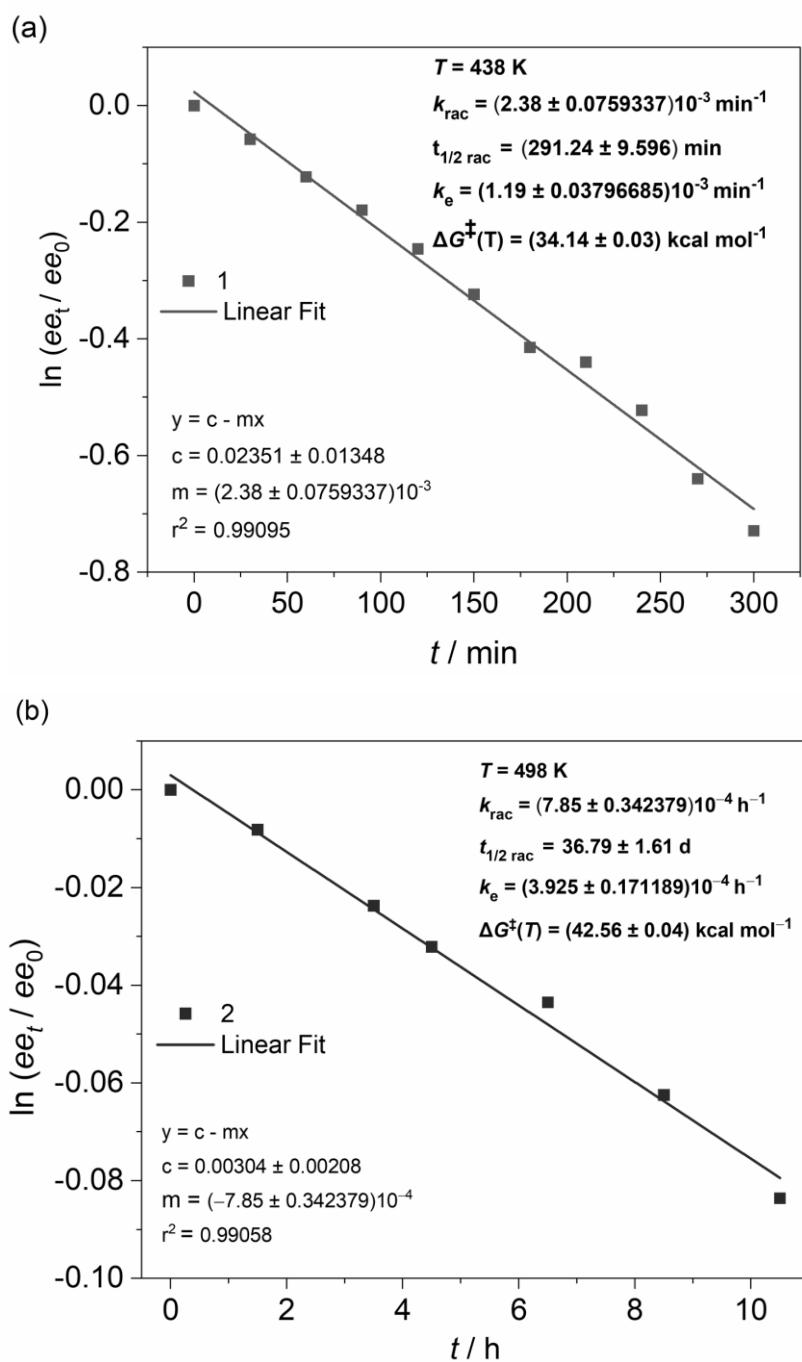


Figure S5. Plot of $\ln(ee_t/ee_0)$ against t for (a) **1** and (b) **2** and fitted linearly to obtain the k_{rac} , $t_{1/2\text{-rac}}$, k_e and ΔG^\ddagger values.

S6. Quantum chemical calculations

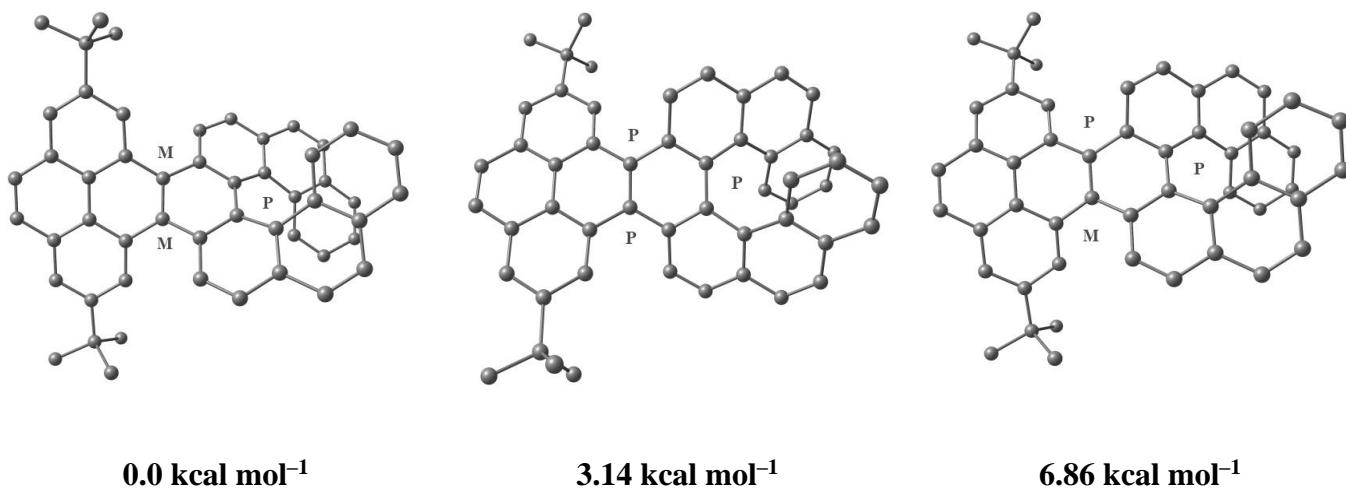


Figure S6. Relative Gibbs's free energies of diastereomers of **1**. Hydrogen atoms are omitted for clarity.

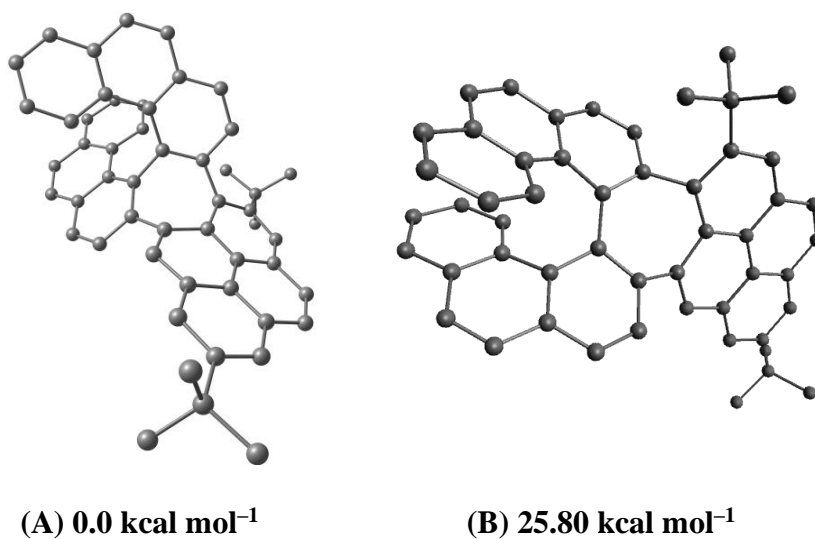
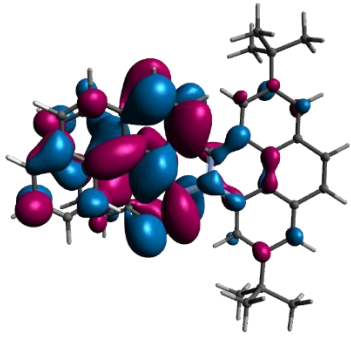
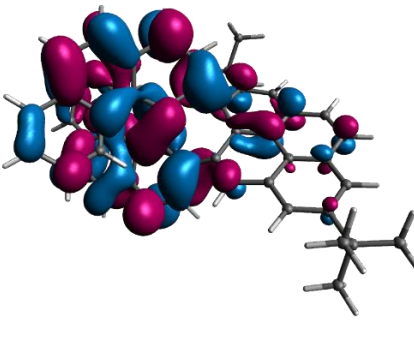
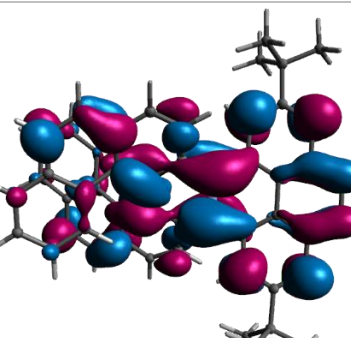
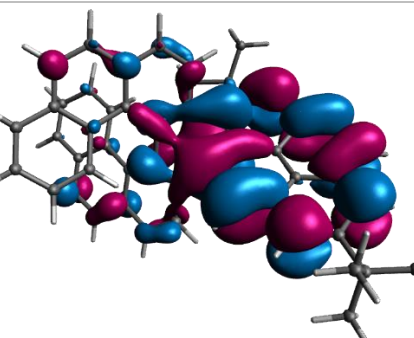
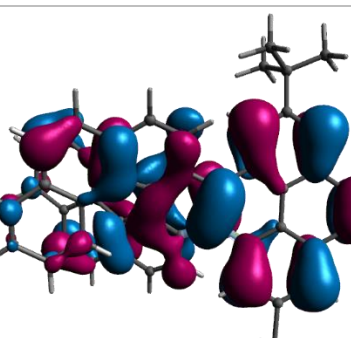
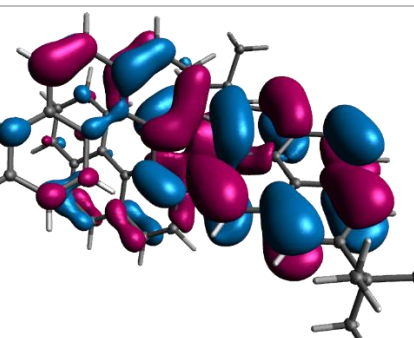
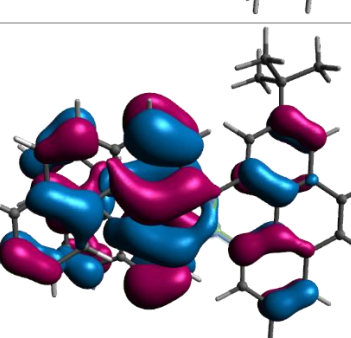
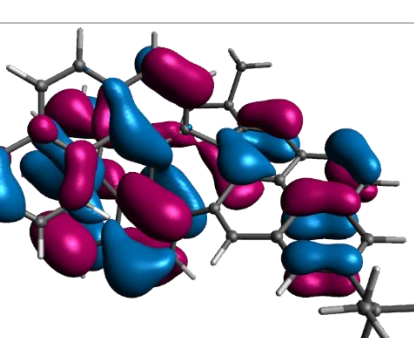


Figure S7. Relative Gibbs's free energies of diastereomers of **2**. Hydrogen atoms are omitted for clarity.

Table S2. Frontier molecular orbitals of **1** and **2** (isosurface value 0.02).

FMOs	6mem	7mem
LUMO+1		
LUMO		
HOMO		
HOMO-1		

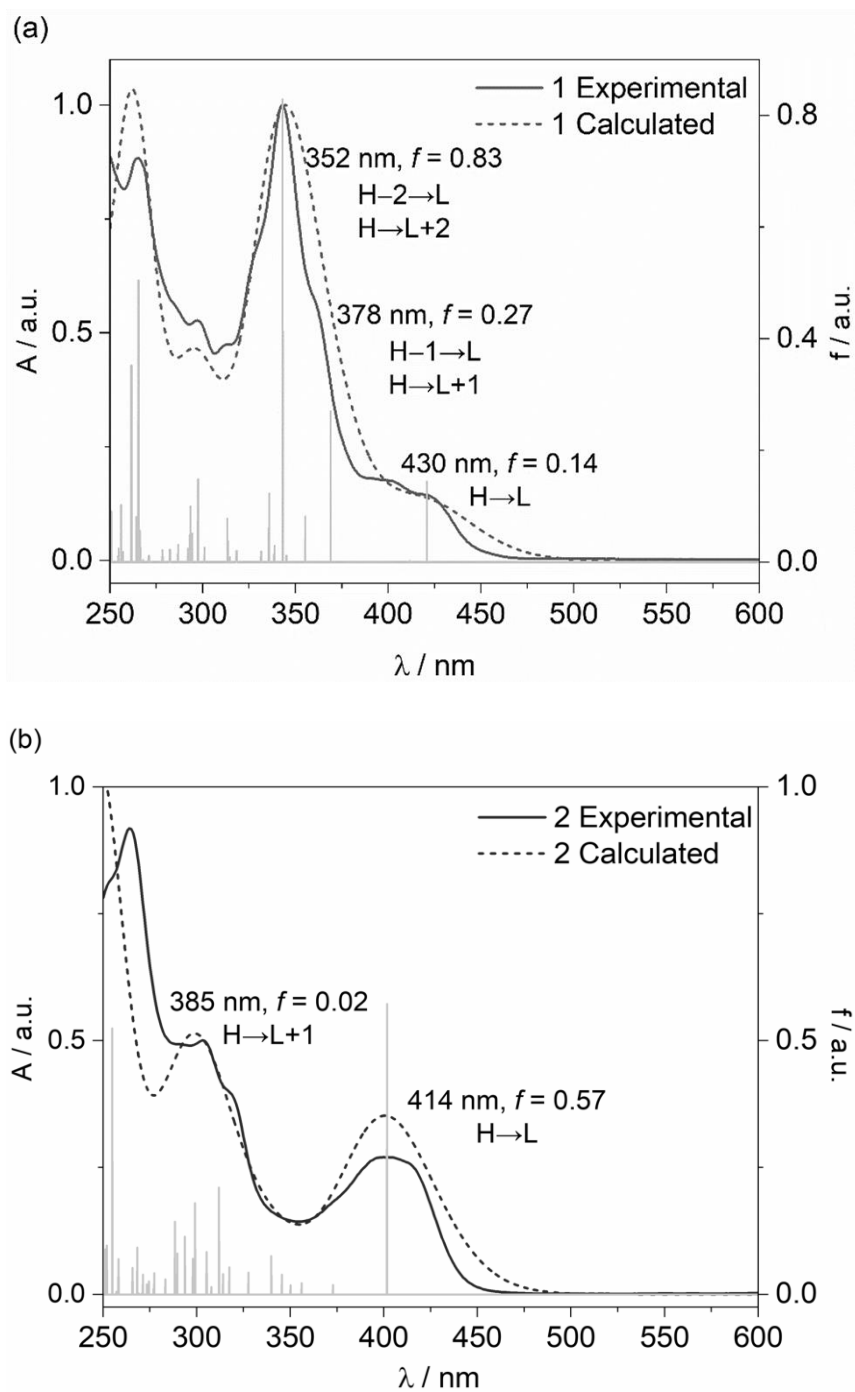


Figure S8. Comparison of experimental (solid) and TD-DFT calculated (dashed) UV-vis spectra of (a) **1** (shifted by 0.08 eV, 10 nm) and (b) **2** (shifted by 0.10 eV, 13 nm) along with assignments of key transitions. H = HOMO, L = LUMO, f = oscillator strength.

Table S3a. Summary of TD-DFT calculated key low energy transitions.

Excited singlet state	Wavelength / nm	Energy / eV	Major transitions	Contribution	oscillator strength (<i>f</i>)
1					
1	430.79	2.88	HOMO→LUMO	0.68	0.14
2	378.89	3.27	HOMO-1→LUMO	0.50	0.27
			HOMO→LUMO+1	0.42	
3	352.99	3.51	HOMO→LUMO+2	0.58	0.83
			HOMO-2→LUMO	0.35	
2					
1	414.68	2.99	HOMO→LUMO	0.69	0.57
2	385.79	3.21	HOMO→LUMO+1	0.67	0.02

Table S3b. Calculated electric and magnetic transition moments, and absorption dissymmetry factor for $S_0 \rightarrow S_1$ transition.

Molecule	Electric transition dipole moment ($ \mu $) / 10^{-20} esu cm	Magnetic transition dipole moment ($ m $) / 10^{-20} erg G ⁻¹	$\cos\theta$	Rotatory strength (R) 10^{-40} erg esu cm G ⁻¹	$g_{\text{abs.}}$ 10^{-3}
1	363.86	1.32	0.11	51.67	1.6
2	711.16	1.29	-0.29	-267.76	-2.1

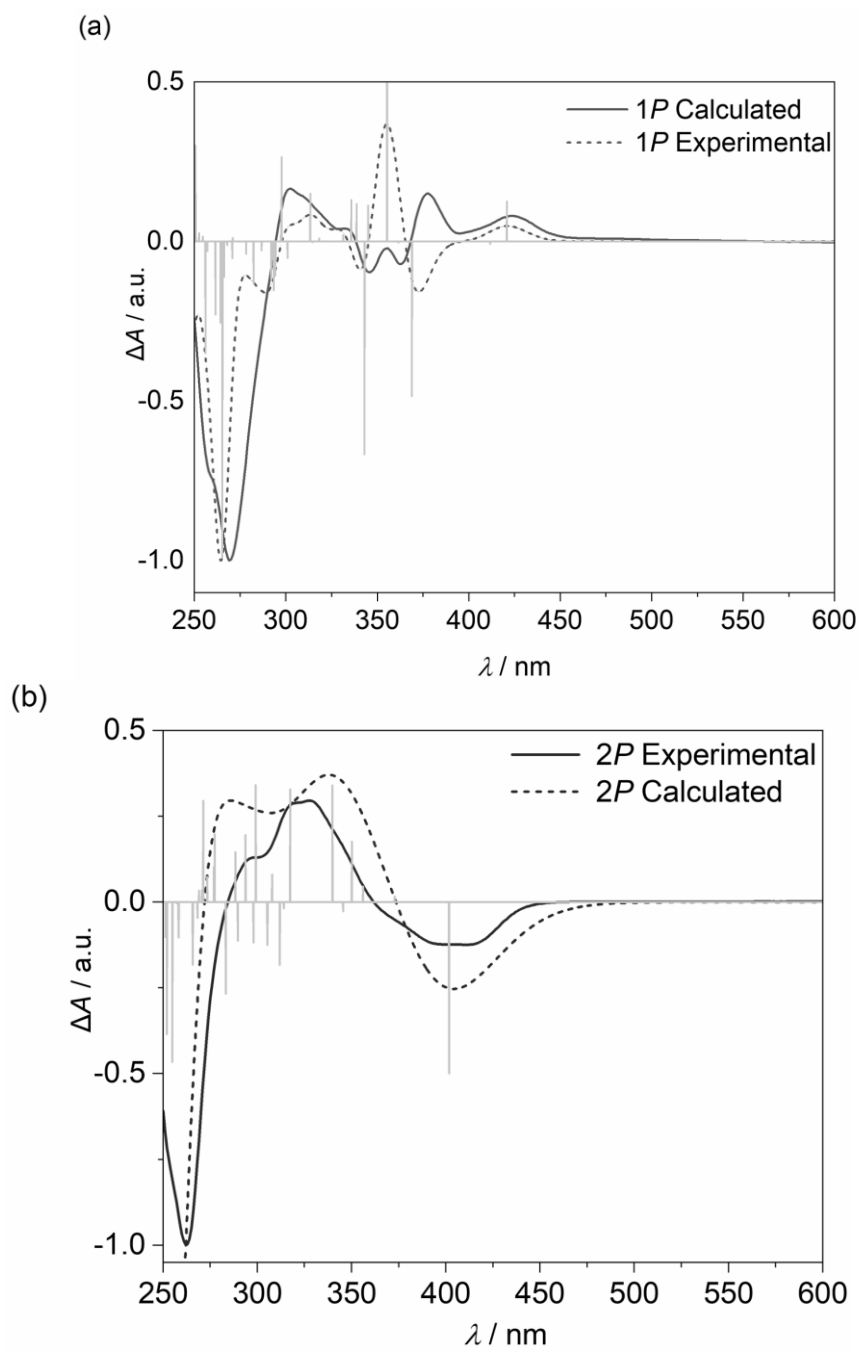


Figure S9. Comparison of experimental (solid) and TD-DFT calculated (dashed) CD spectra for *P*-enantiomer of (a) **1** (shifted by 0.08 eV) and (b) **2** (shifted by 0.10 eV).

NICS calculations: The Nucleus Independent Chemical Shift (NICS) calculations were performed on ω B97XD/6-31G(d,p) optimized geometry at GIAO-B3LYP/6-311+G(2d,p) level. Considering the non-planarity of molecule the NICS(1)_{zz} values were obtained by placing dummy atom at 1 Å above and below the each ring.

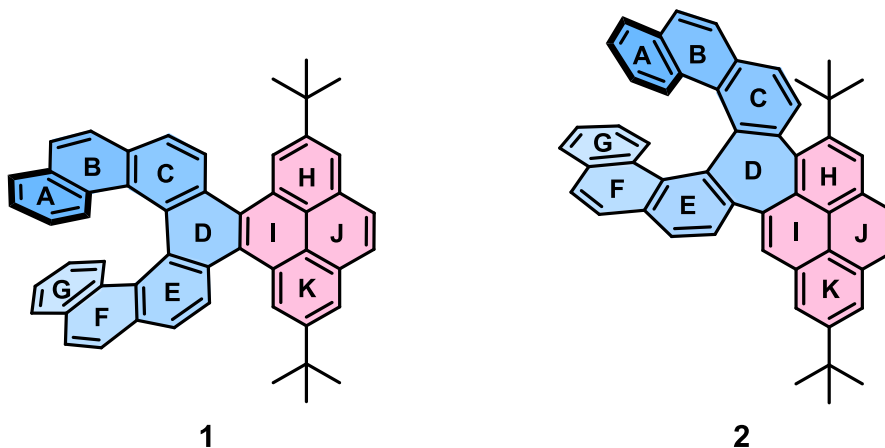


Table S4. The calculated NICS(0) and NICS(1)_{zz} values for **1** and **2**.

	1			2		
Ring	NICS(1) _{zz} (Up)	NICS(1) _{zz} (Down)	NICS(0)	NICS(1) _{zz} (Up)	NICS(1) _{zz} (Down)	NICS(0)
A	-1.49	-3.34	-5.55	-16.20	-17.72	-11.54
B	-1.44	-3.08	-5.12	-12.83	-10.65	-7.60
C	-5.13	-1.43	-6.63	-5.37	-6.20	-5.67
D	-2.76	-2.77	-5.21	13.61	15.52	24.67
E	–	–	–	-9.81	-8.22	-6.66
F	–	–	–	-11.78	-13.73	-6.67
G	–	–	–	-18.93	-16.74	-11.02
H	-2.22	-0.76	-7.11	-31.26	-27.56	-13.76
I	-2.99	-2.96	-7.43	-8.01	-13.81	8.97
J	-2.39	-2.47	-7.30	-14.53	-13.87	6.16
K	–	–	–	-31.74	-30.41	-14.47

S7. X-Ray crystallography

The single crystals of **1** were grown by slow diffusion of hexane to solution of **1** in DCM in an NMR tube. Crystallographic data have been deposited with the Cambridge Crystallographic Data Centre as supplementary publication no. CCDC 2103307 for **1**. These data can be obtained free of charge from The Cambridge Crystallographic Data Centre via www.ccdc.ac.uk/data/request/cif.

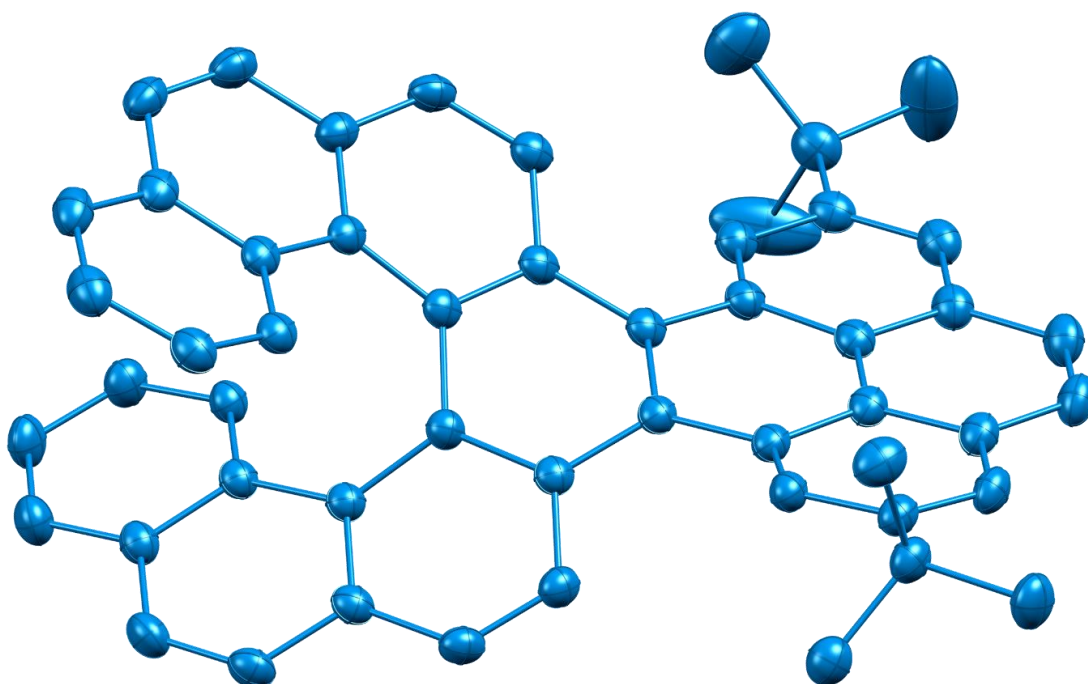


Figure S10a. ORTEP diagram of (*P*)-**1**. Thermal ellipsoids are shown at the 50% probability level. Hydrogen atoms are omitted for clarity.

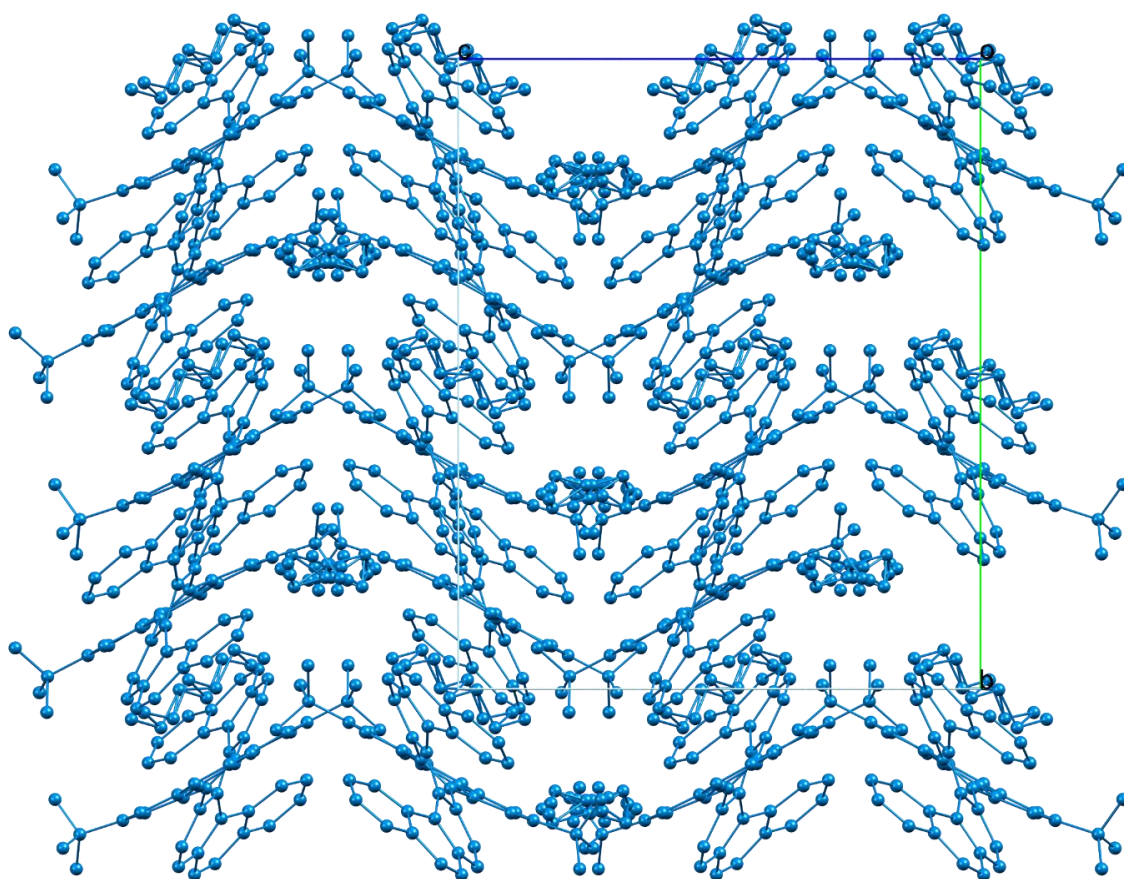
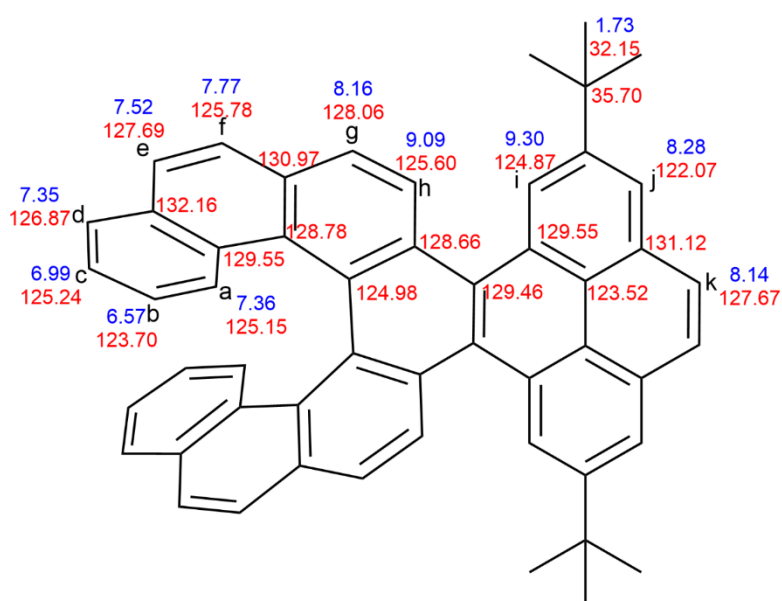


Figure S10b. Crystal packing of **1**. Hydrogen atoms are omitted for clarity.

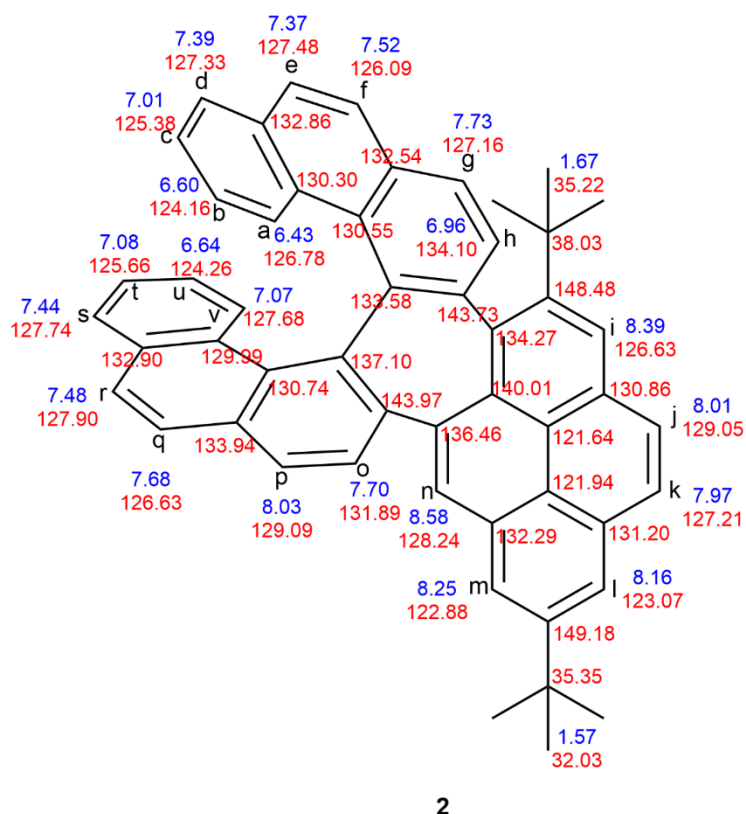
Table S5. Crystallographic table for 1.

Data	1
CCDC	2103307
Empirical formula	C ₅₈ H ₅₄
Formula weight (g·mol ⁻¹)	751.01
Temperature (K)	100.01(10)
Radiation, λ (Å)	Cu _{Kα} 1.54184
Crystal system	
Space group	C2/c
<i>Unit cell dimensions</i>	
<i>a</i> (Å)	21.9510(2)
<i>b</i> (Å)	21.30729(17)
<i>c</i> (Å)	18.62947(18)
α (°)	90
β (°)	108.5271(10)
γ (°)	90
Volume (Å ³)	8261.74(14)
<i>Z</i>	8
Calculated density (Mg·m ⁻³)	1.208
Absorption coefficient (mm ⁻¹)	0.508
<i>F</i> (000)	3216
Theta range for collection	2.968 to 80.249°
Reflections collected	63377
Independent reflections	8923
Minimum/maximum transmission	0.494/1.000
Refinement method	Full-matrix least-squares on <i>F</i> ²
Data / parameters / restraints	8923 / 554 / 58
Goodness-of-fit on <i>F</i> ²	1.051
Final R indices [<i>I</i> >2σ(<i>I</i>)]	R ₁ = 0.0586, wR ² = 0.1485
R indices (all data)	R ₁ = 0.0670, wR ² = 0.1550
Maximum/minimum residual electron density (e·Å ⁻³)	0.722 / -0.434

S8. NMR spectroscopy



Aromatic Proton Position	Exp. Shift (ppm)	Cal. Shift (ppm)
a	7.36	7.63
b	6.57	6.7
c	6.99	7.13
d	7.35	7.45
e	7.52	7.68
f	7.77	7.97
g	8.16	8.38
h	9.09	9.39
i	9.30	9.77
j	8.28	8.48
k	8.14	8.38



Aromatic Proton Position	Exp. Shift (ppm)	Cal. Shift (ppm)
a	6.43	6.81
b	6.60	6.74
c	7.01	7.17
d	7.39	7.41
e	7.37	7.41
f	7.52	7.66
g	7.73	7.81
h	6.96	7.17
i	8.39	8.74
j	8.01	8.32
k	7.97	8.24
l	8.16	8.39
m	8.25	8.62
n	8.58	8.8
o	7.70	7.81
p	8.03	8.24
q	7.68	7.81
r	7.48	7.66
s	7.44	7.56
t	7.08	7.17
u	6.64	6.74
v	7.07	7.41

Figure S11. ¹H (blue) and ¹³C NMR (red) peaks assigned to respective atoms in (a) **1** and (b) **2** and **Table S6**. Comparison between experimental and calculated aromatic ¹H NMR shift values for **1** (top) and **2** (bottom).

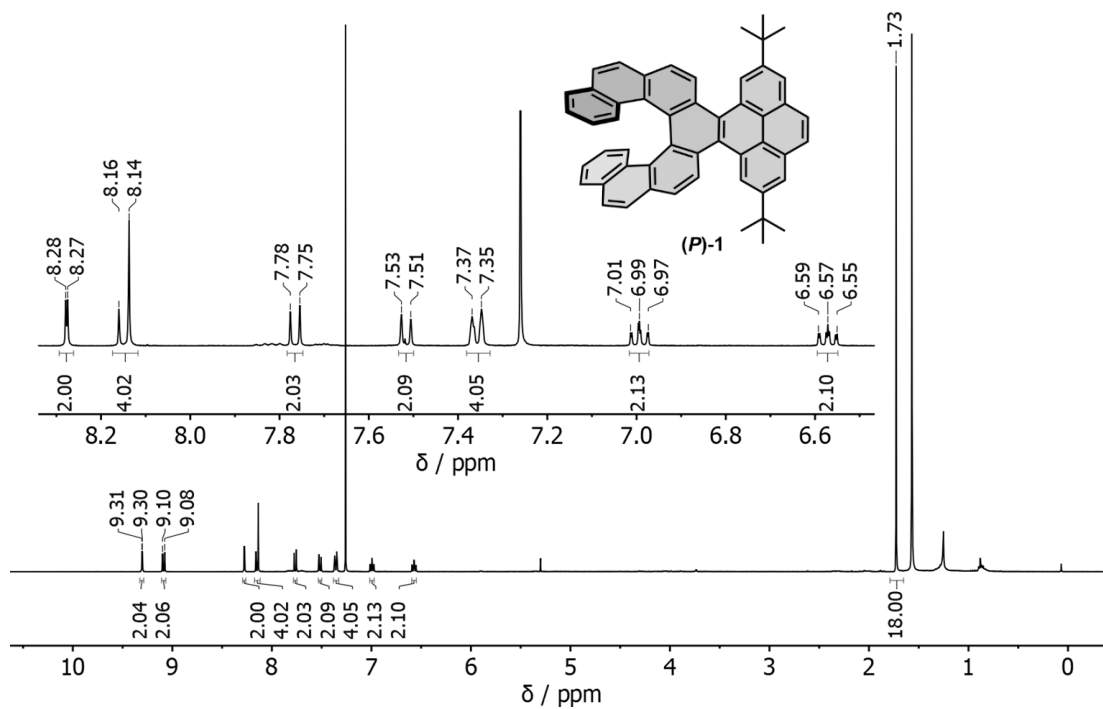


Figure S12. ^1H NMR spectrum of **1** (400 MHz, CDCl_3).

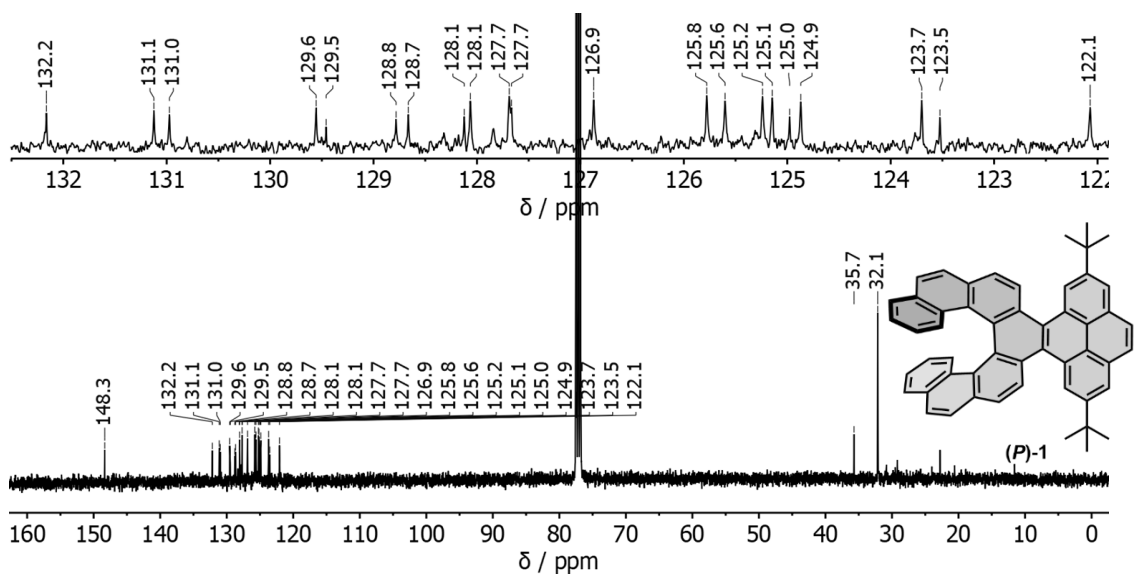


Figure S13. $^{13}\text{C}\{^1\text{H}\}$ NMR spectrum of **1** (101 MHz, CDCl_3).

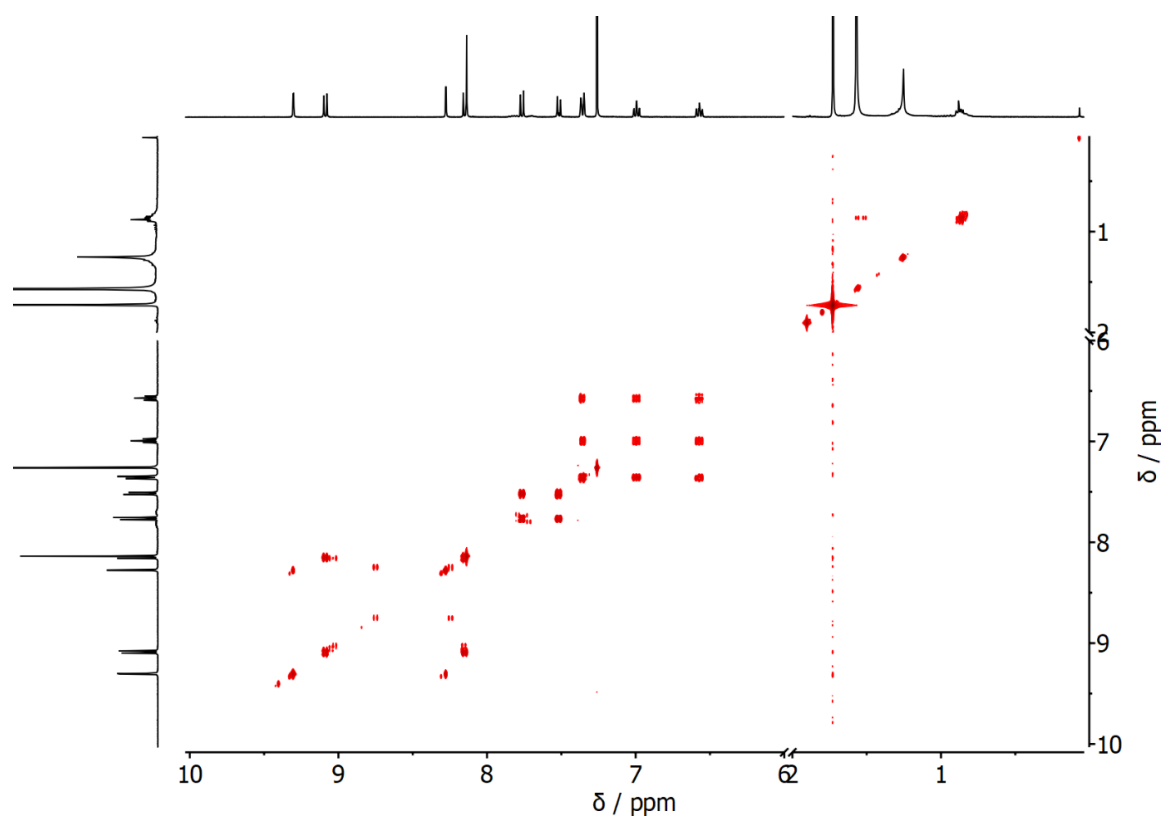


Figure S14. $^1\text{H} - ^1\text{H}$ COSY NMR spectrum of **1** (CDCl_3).

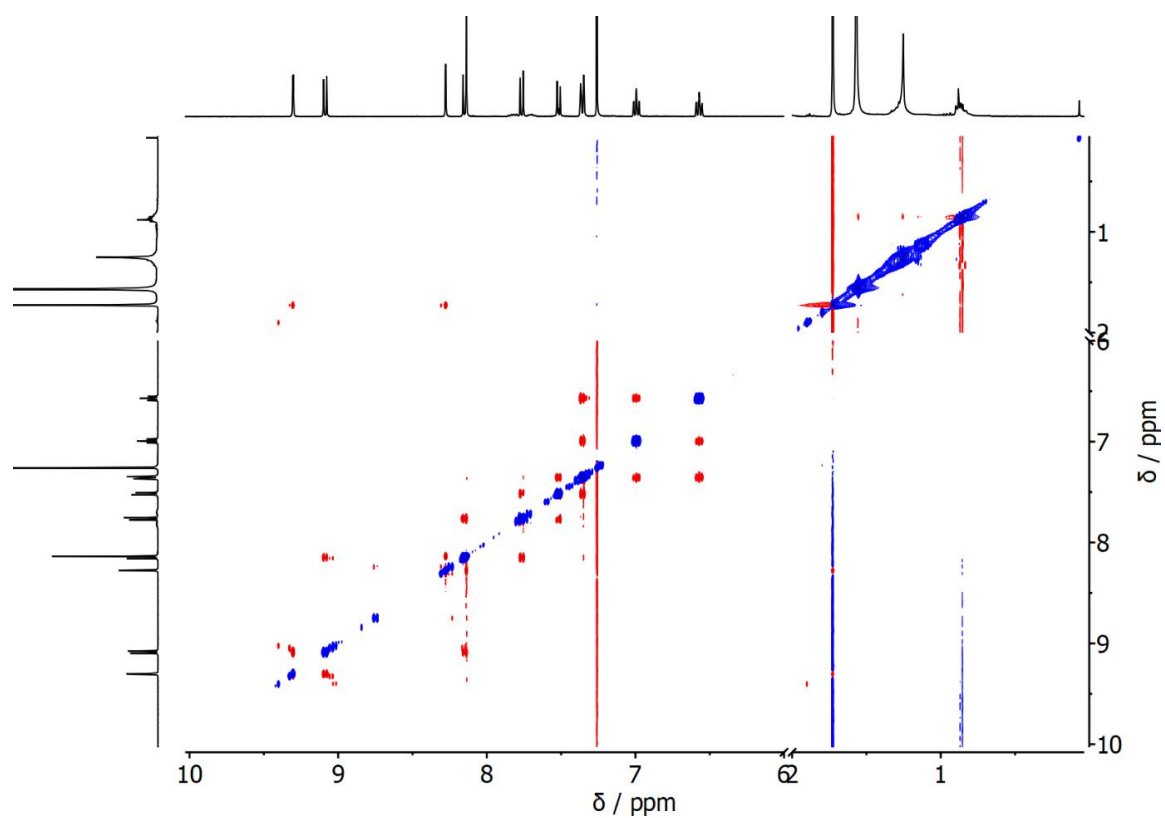


Figure S15. $^1\text{H} - ^1\text{H}$ NOESY NMR spectrum of **1** (CDCl_3).

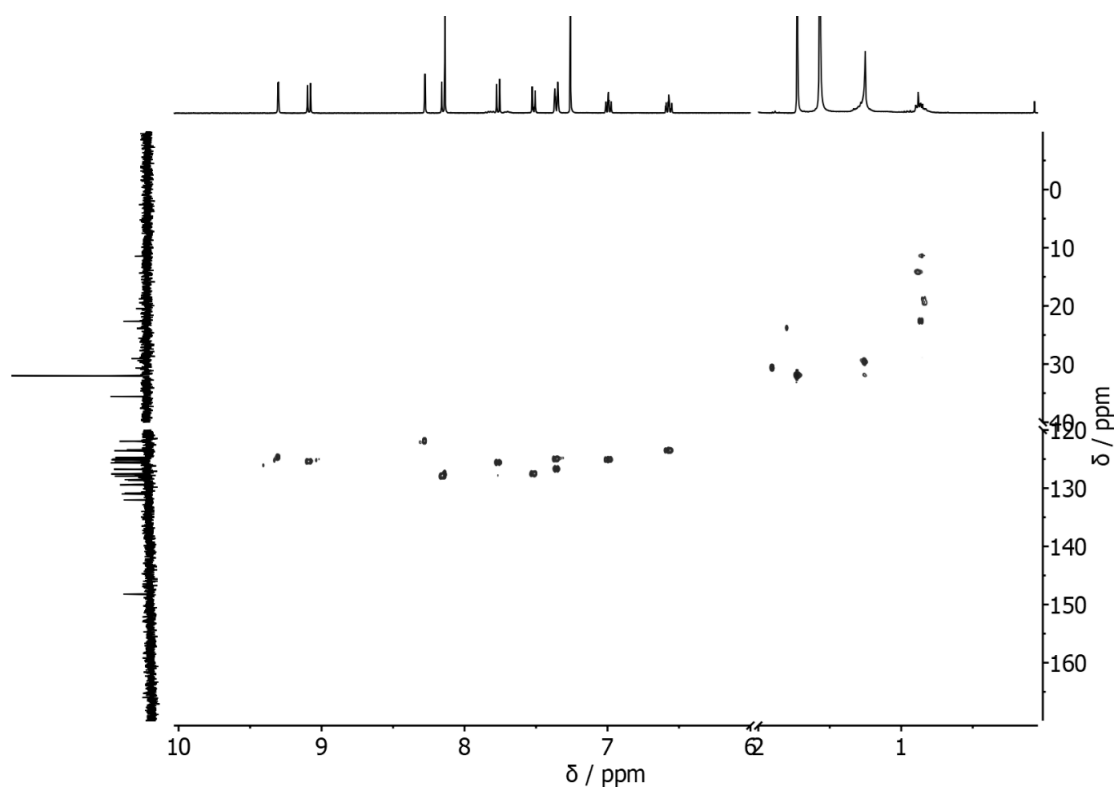


Figure S16. $^1\text{H} - ^{13}\text{C}$ HSQC NMR spectrum **1** (CDCl_3).

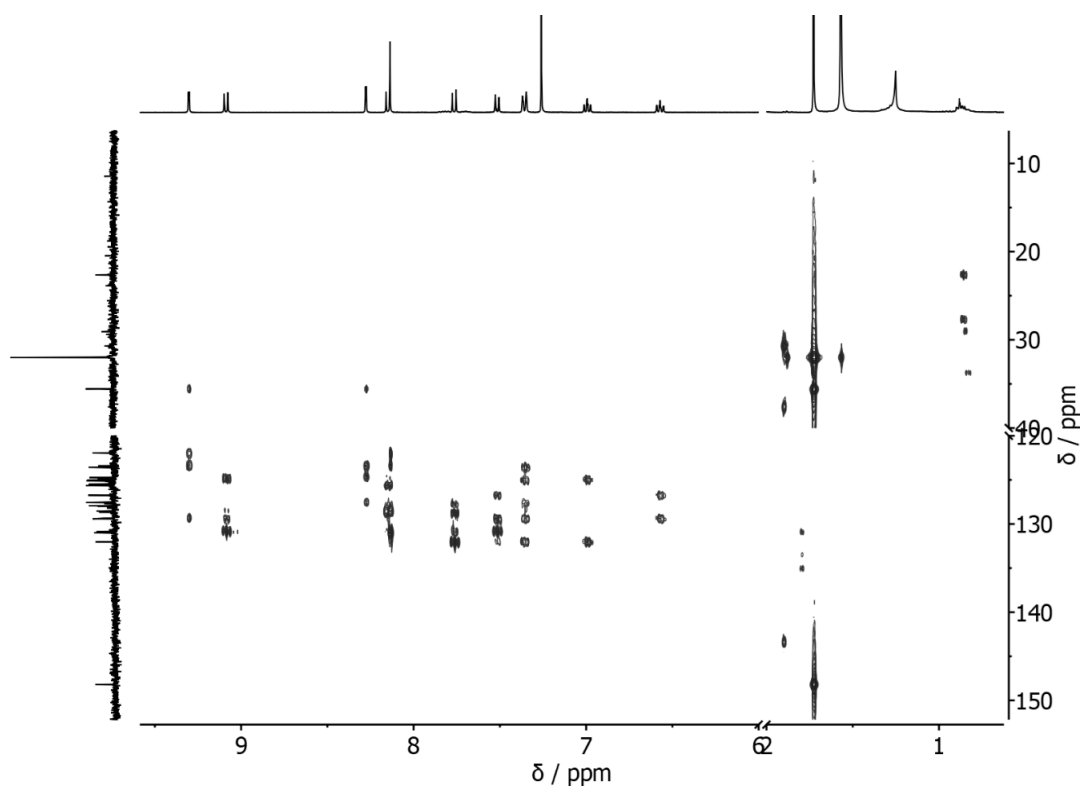


Figure S17. $^1\text{H} - ^{13}\text{C}$ HMBC NMR spectrum of **1** (CDCl_3).

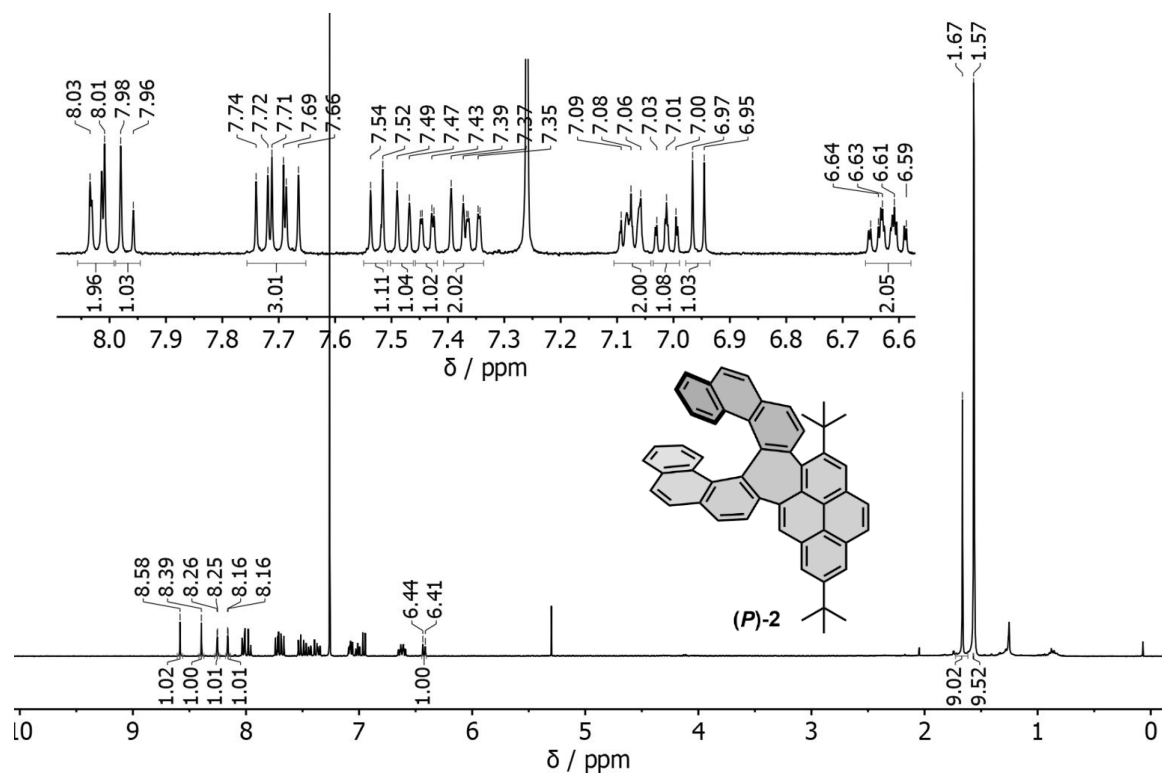


Figure S18. ^1H NMR spectrum of **2** (400 MHz, CDCl_3).

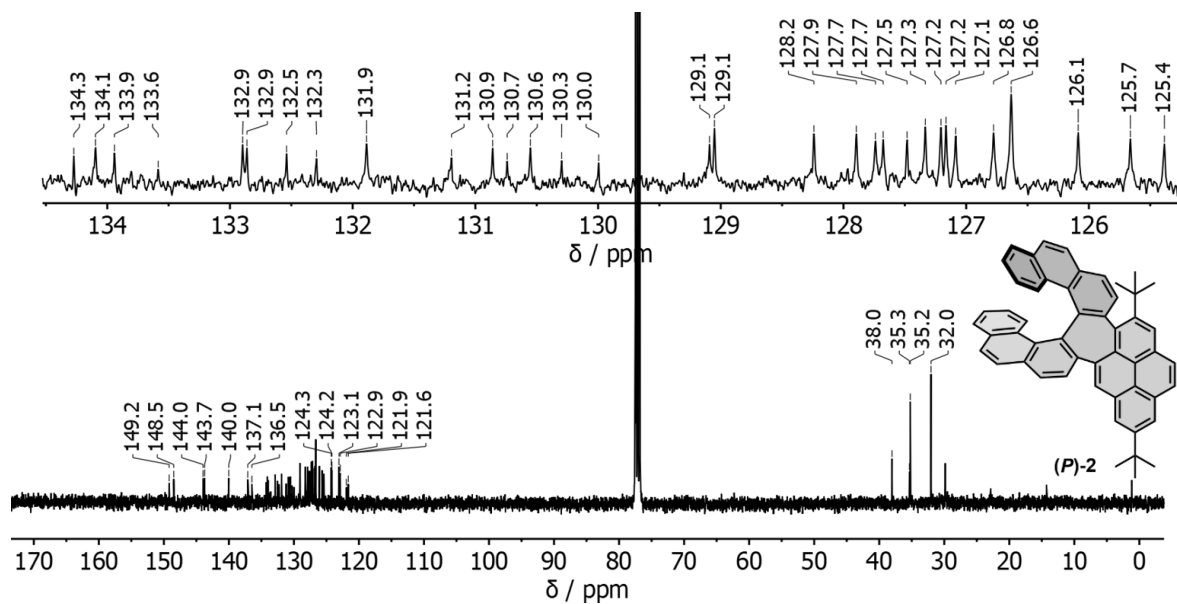


Figure S19. $^{13}\text{C}\{^1\text{H}\}$ NMR spectrum of **2** (101 MHz, CDCl_3).

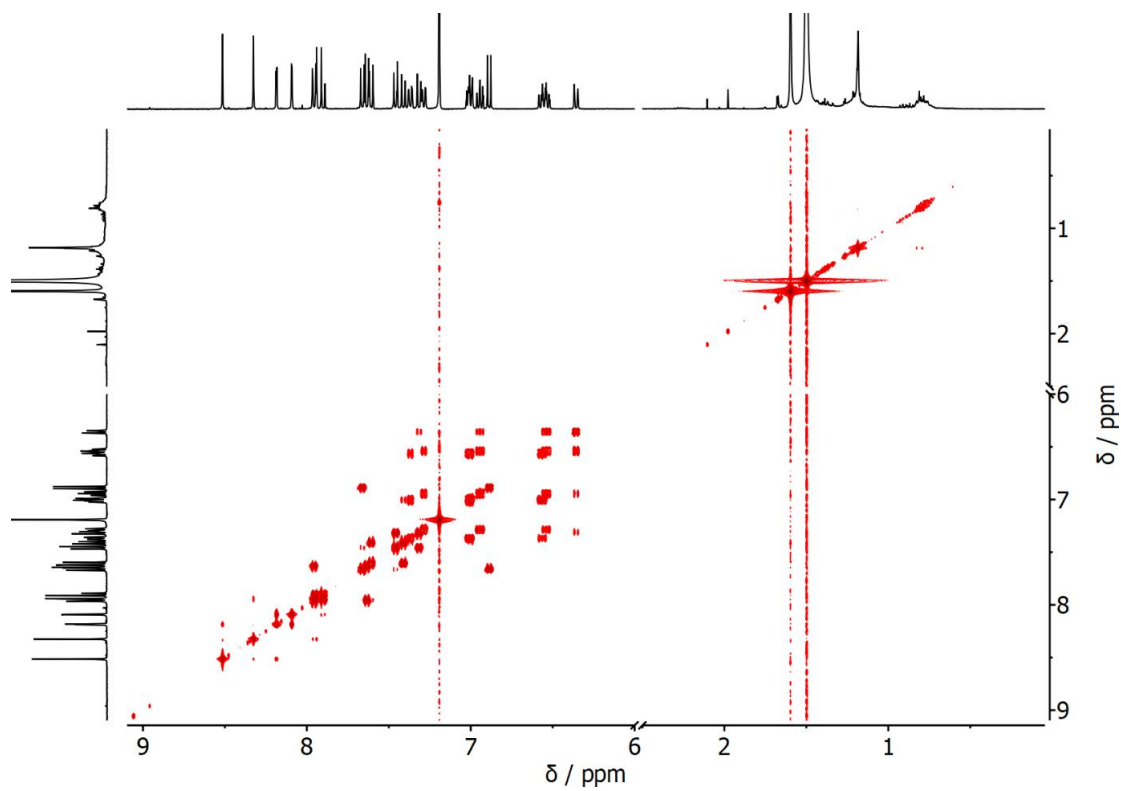


Figure S20. $^1\text{H} - ^1\text{H}$ COSY NMR spectrum of **2** (CDCl_3).

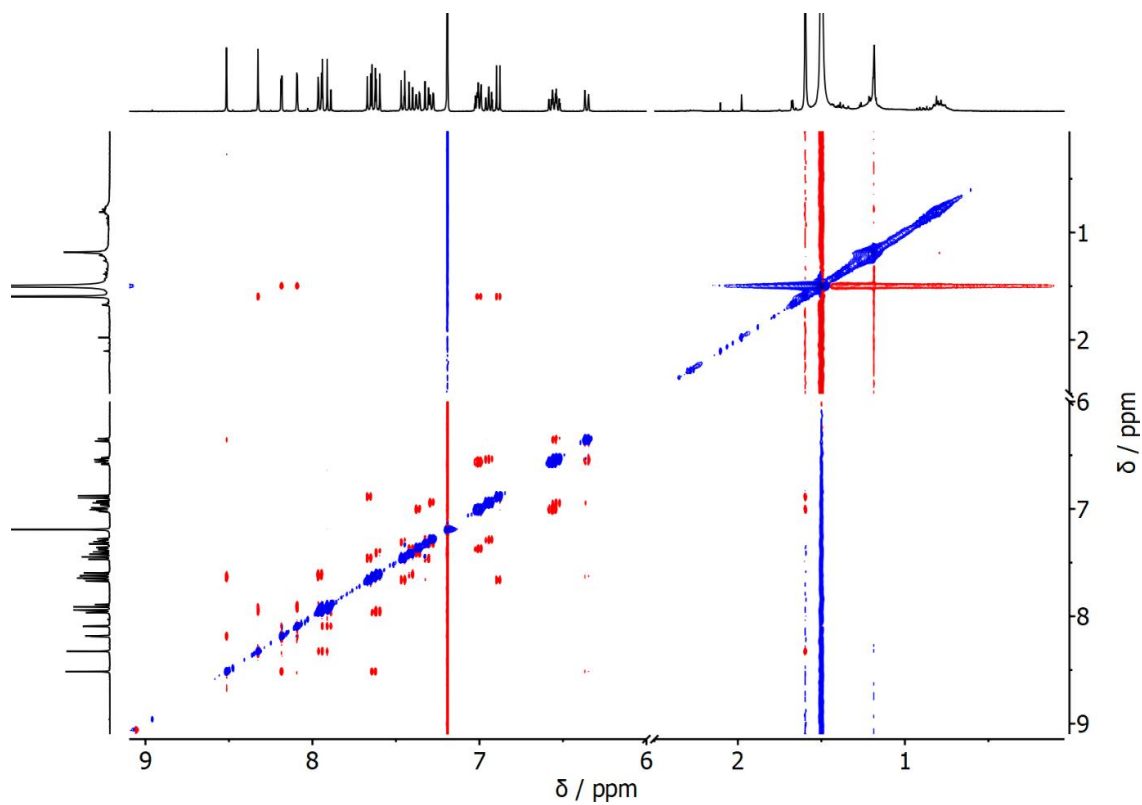


Figure S21. $^1\text{H} - ^1\text{H}$ NOESY NMR spectrum of **2** (CDCl_3).

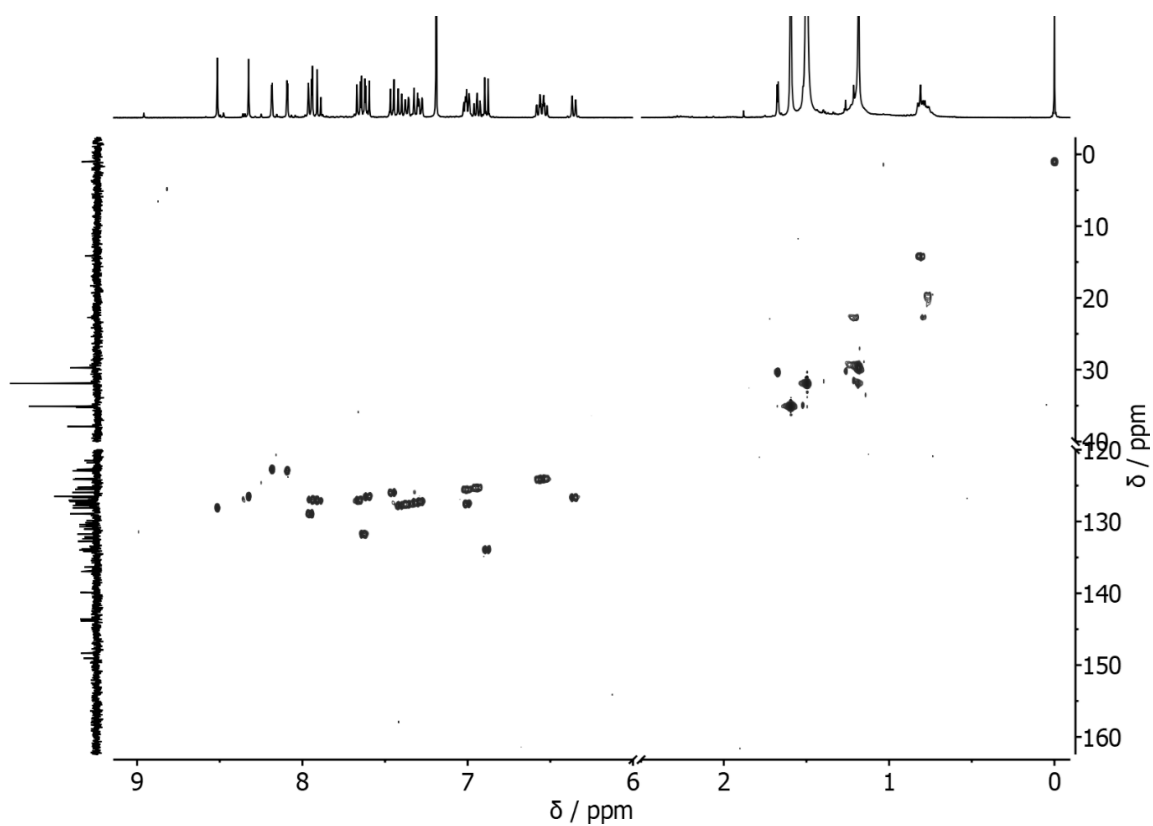


Figure S22. $^1\text{H} - ^{13}\text{C}$ HSQC NMR spectrum of **2** (CDCl_3).

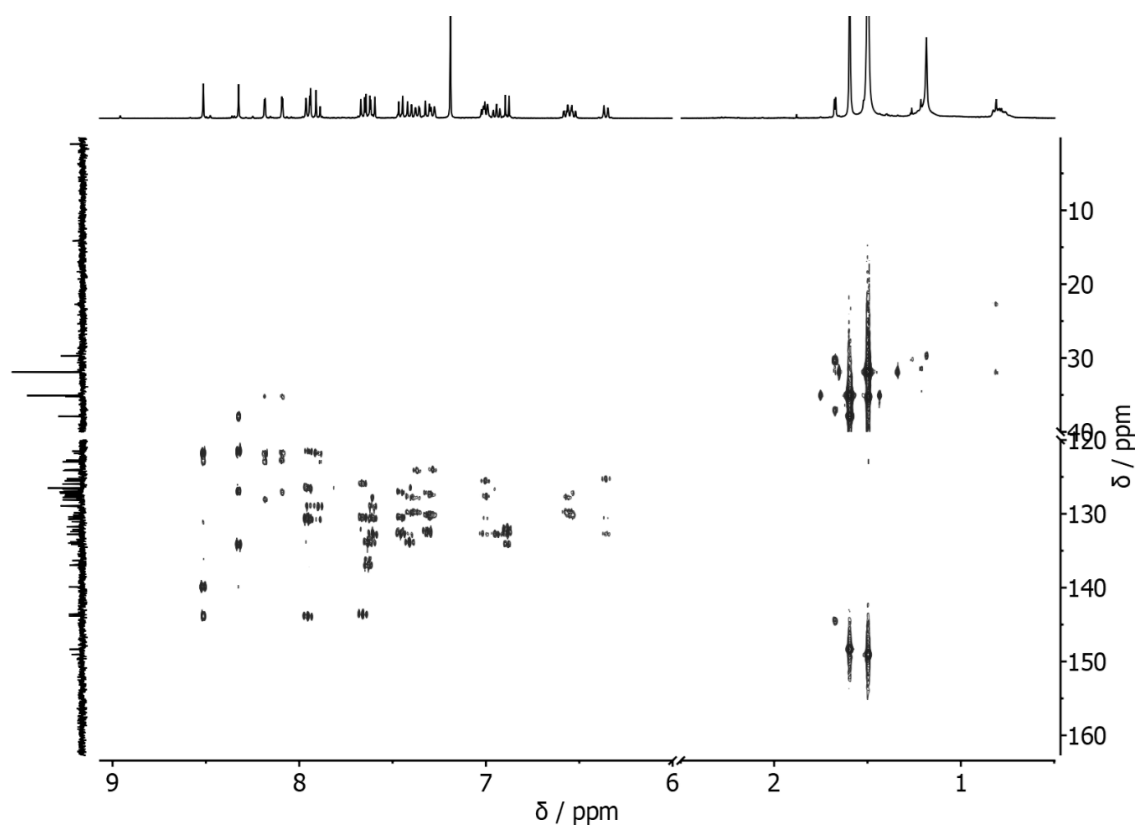


Figure S23. $^1\text{H} - ^{13}\text{C}$ HMBC NMR spectrum of **2** (CDCl_3).

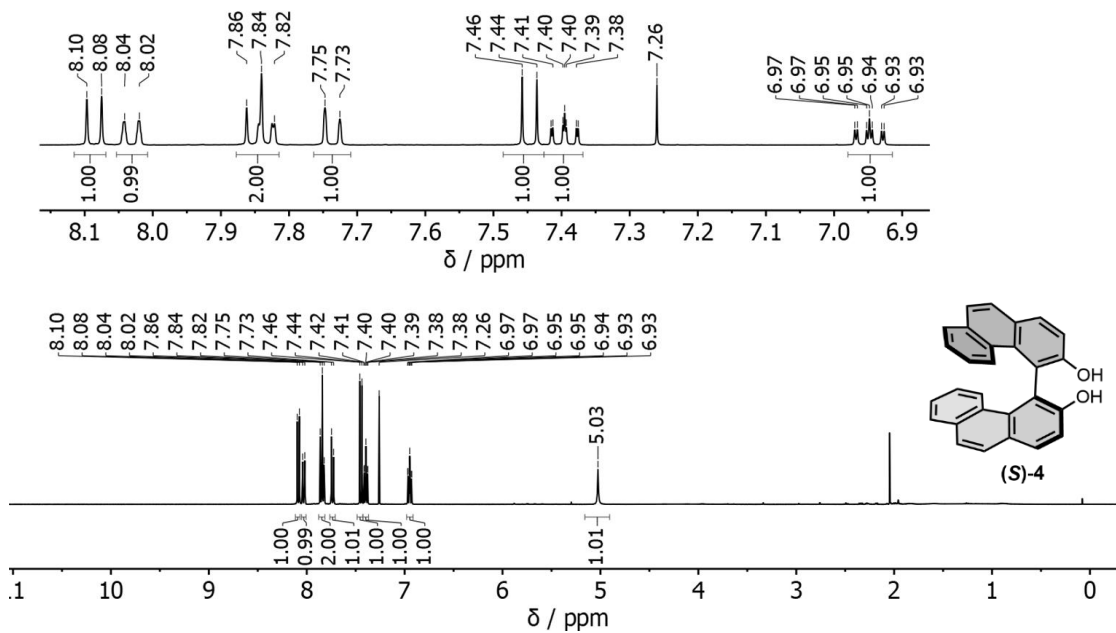


Figure S24. ^1H NMR spectrum of **4** (400 MHz, CDCl_3).

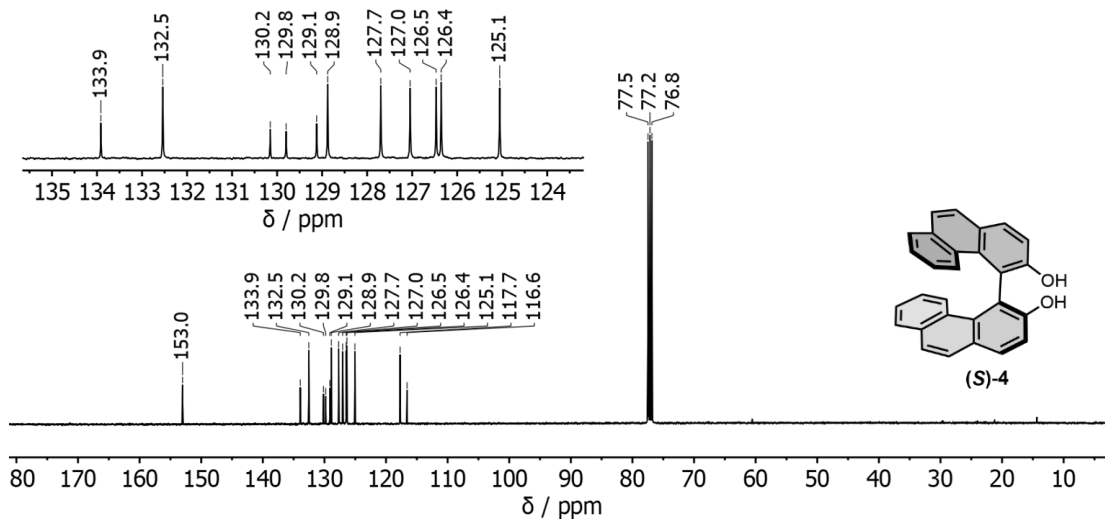
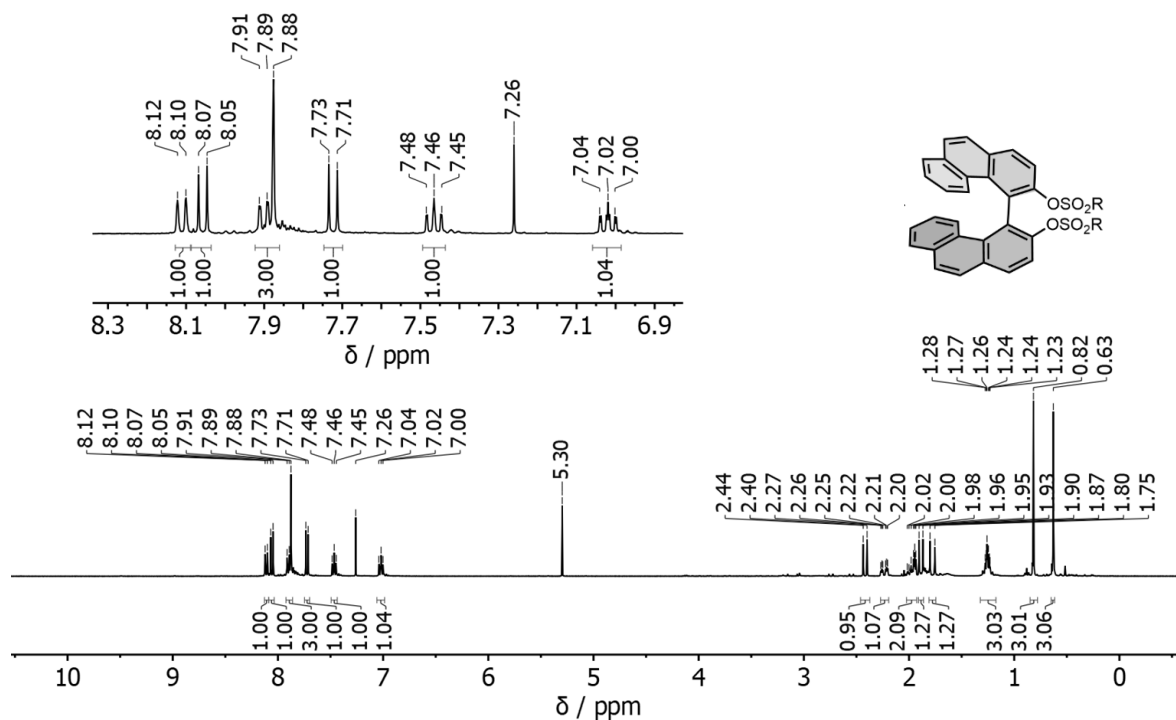
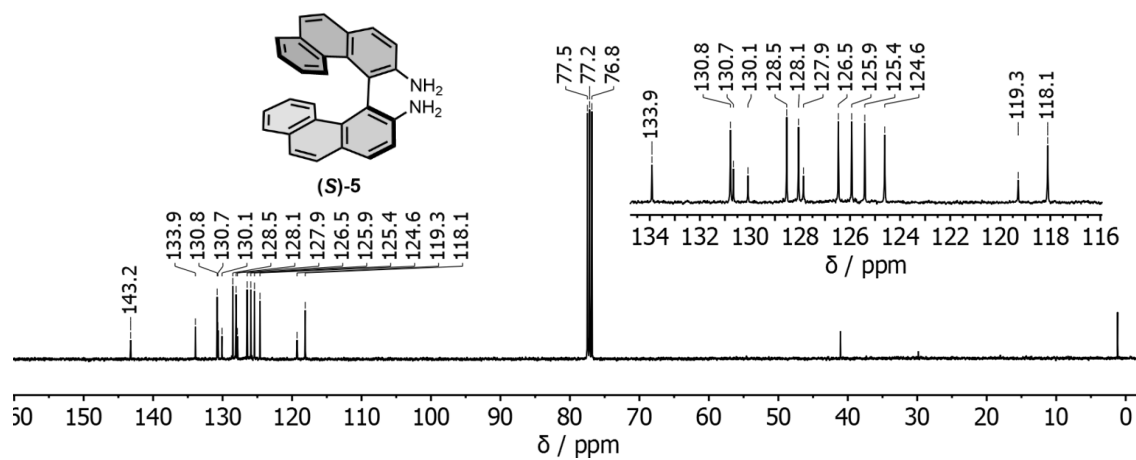
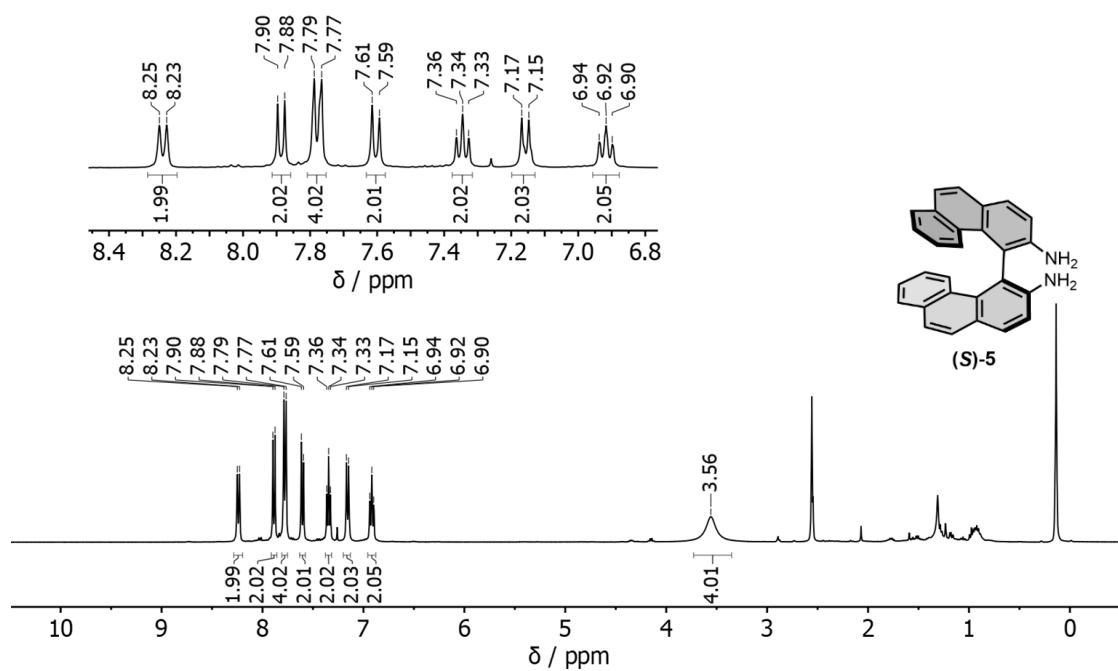


Figure S25. $^{13}\text{C}\{^1\text{H}\}$ NMR spectrum of **4** (101 MHz, CDCl_3).





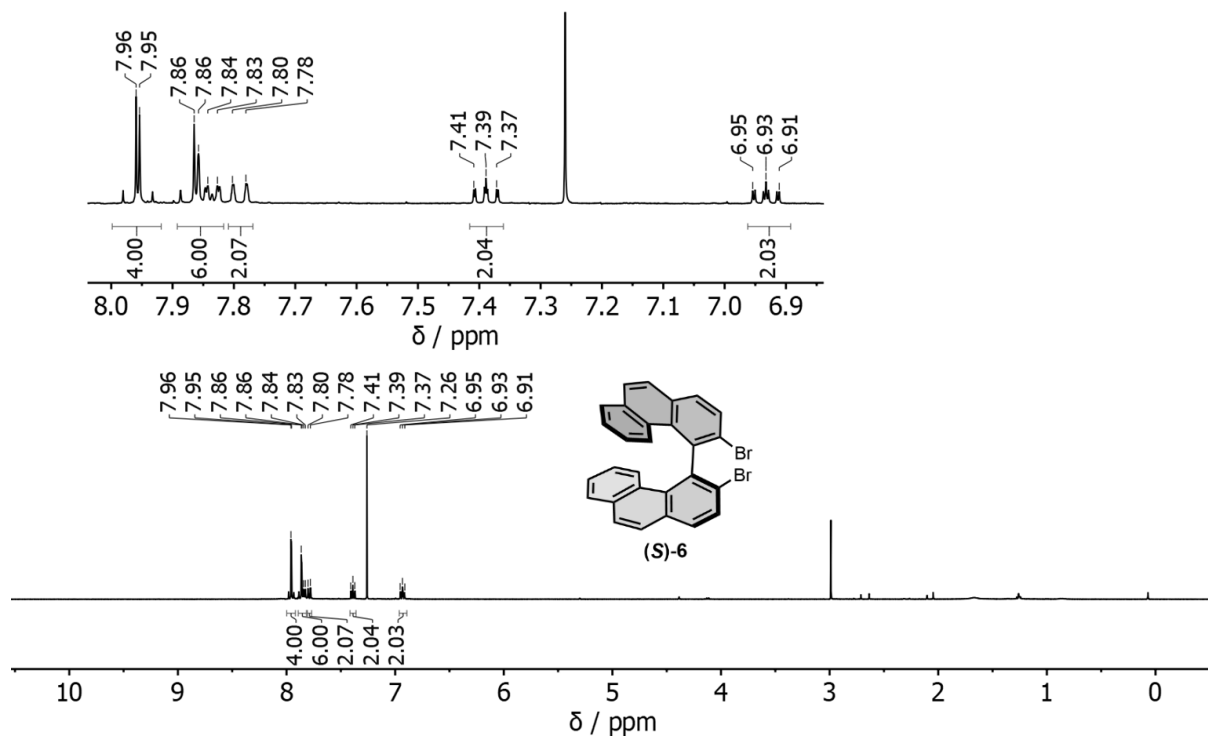


Figure S30. ^1H NMR spectrum of **6** (400 MHz, CDCl_3).

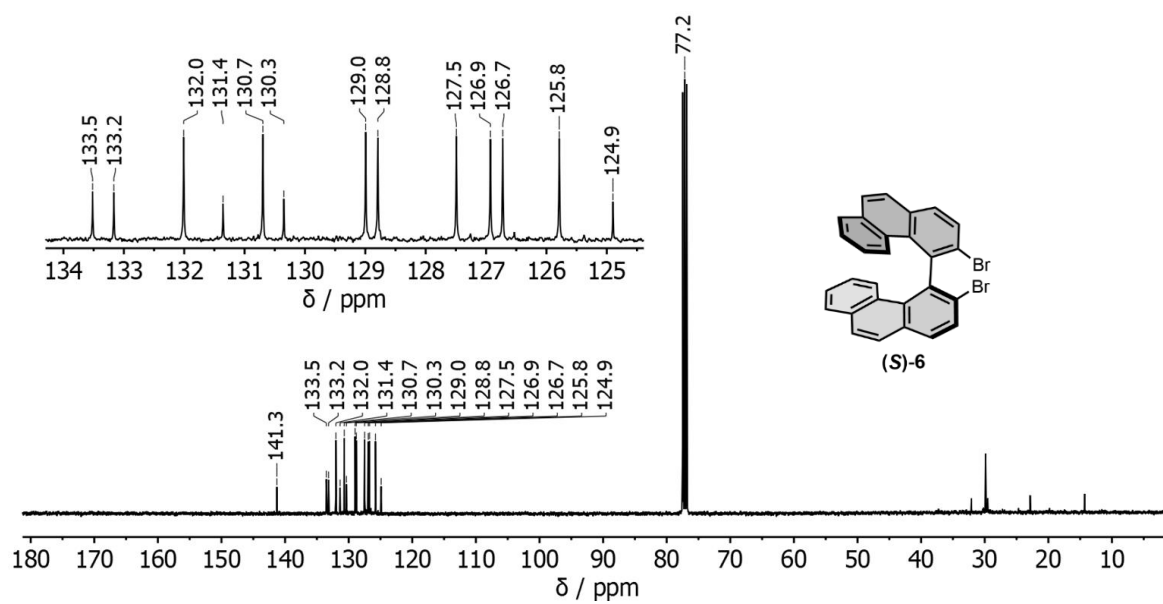


Figure S31. $^{13}\text{C}\{^1\text{H}\}$ NMR spectrum of **6** (101 MHz, CDCl_3).

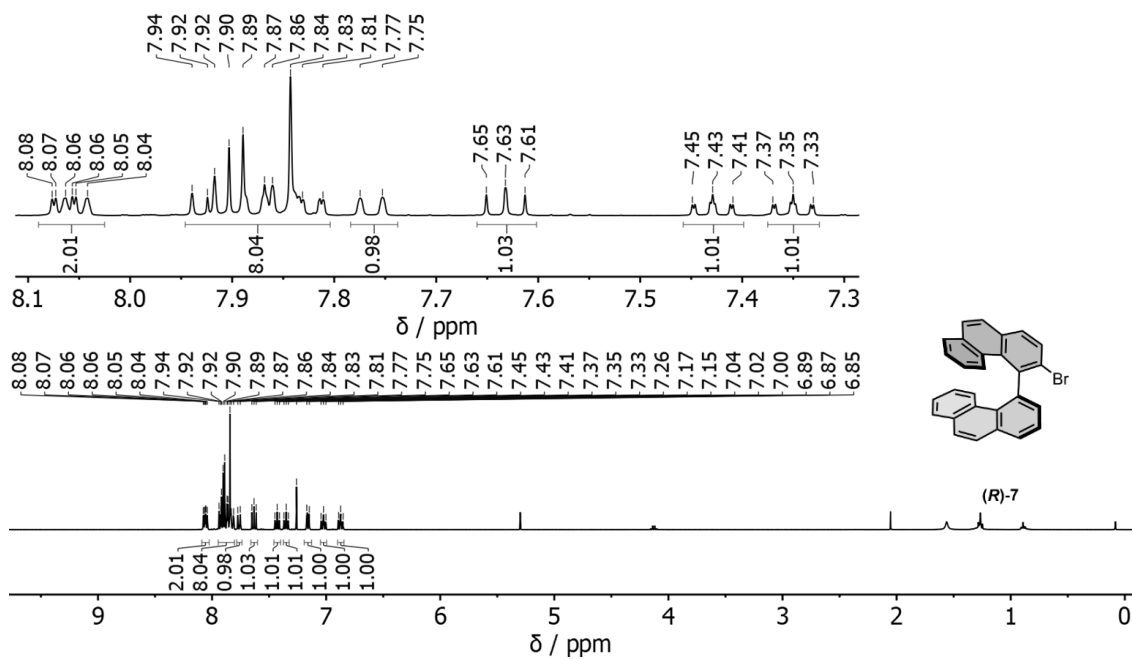


Figure S32. ^1H NMR spectrum of **7** (400 MHz, CDCl_3).

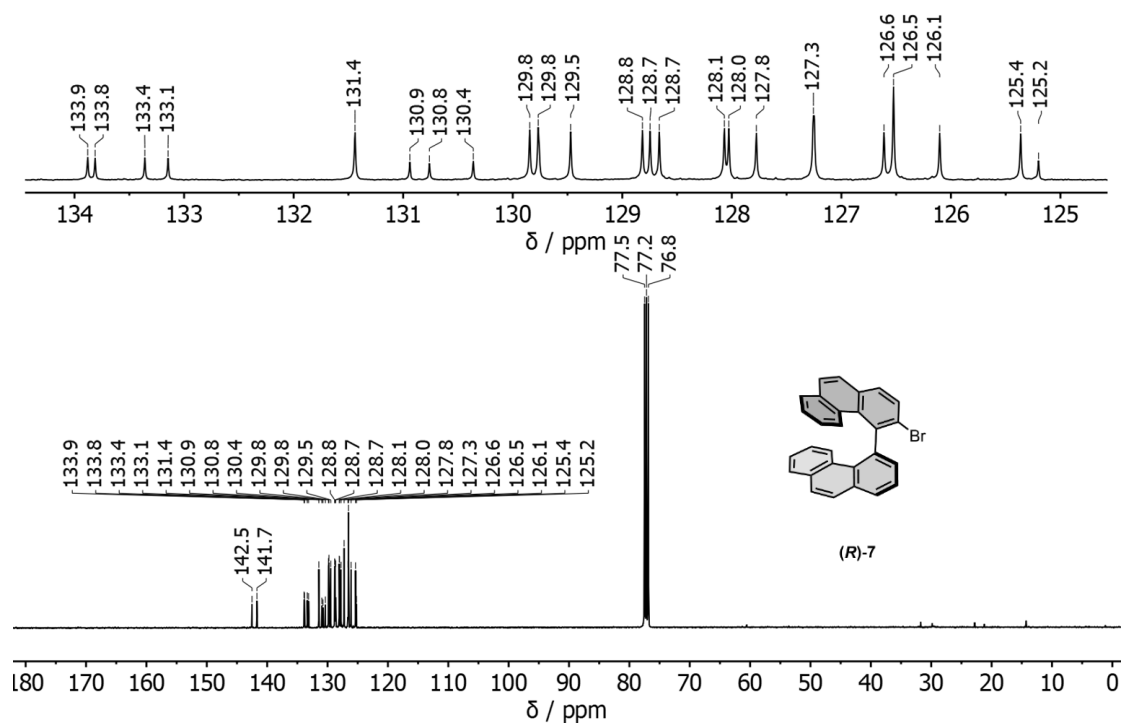


Figure S33. $^{13}\text{C}\{^1\text{H}\}$ NMR spectrum of **7** (101 MHz, CDCl_3).

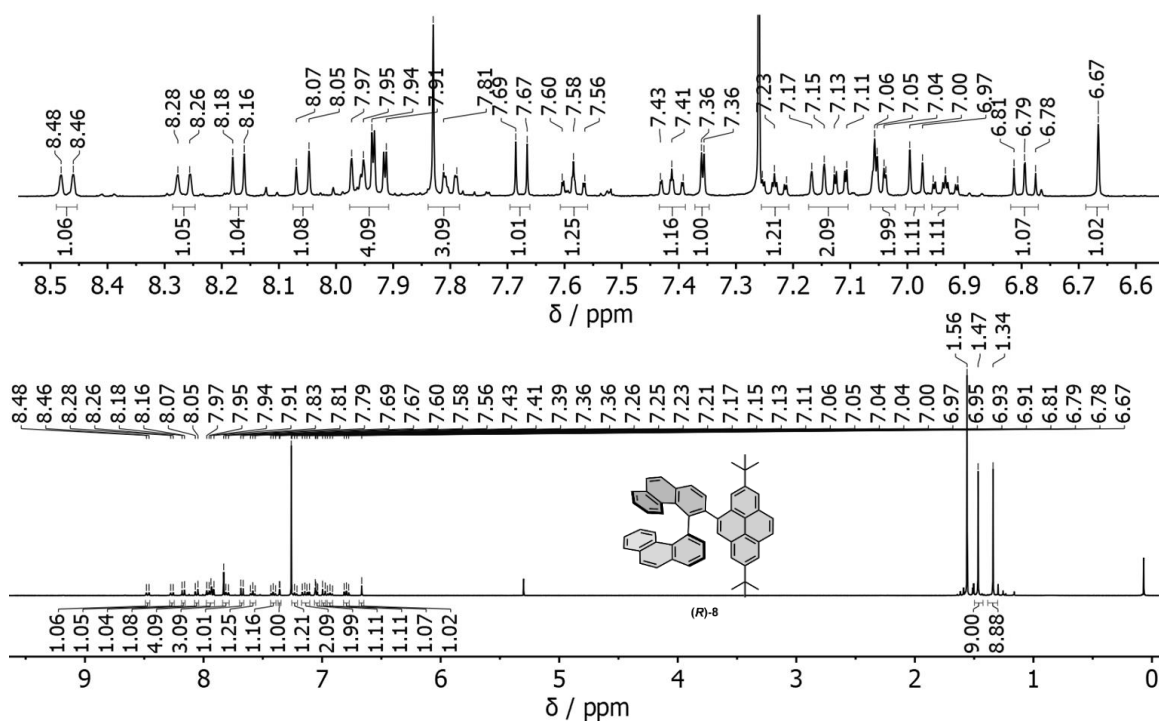


Figure S34. ^1H NMR spectrum of **8** (400 MHz, CDCl_3).

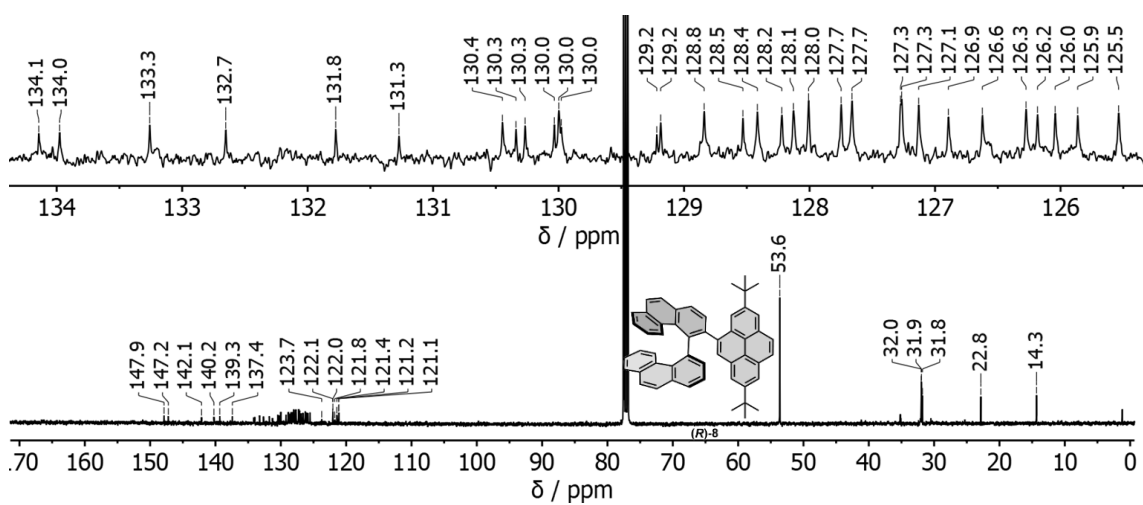


Figure S35. $^{13}\text{C}\{^1\text{H}\}$ NMR spectrum of **8** (101 MHz, CDCl_3). (DCM @ 53.6 ppm, Hexane @ 14.3, 22.8 and 31.8 ppm)

S9. High resolution mass spectrometry (HRMS)

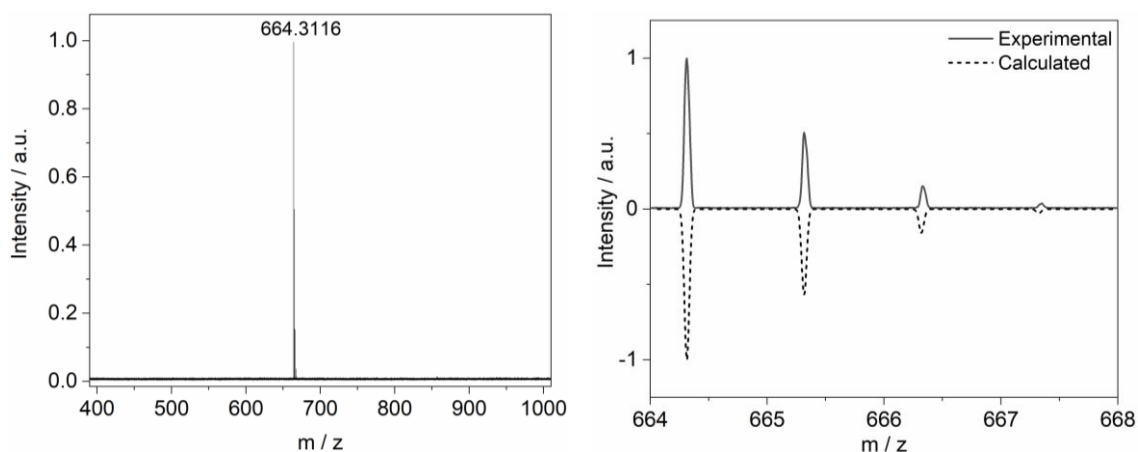


Figure S36. MALDI-TOF HRMS of 1.

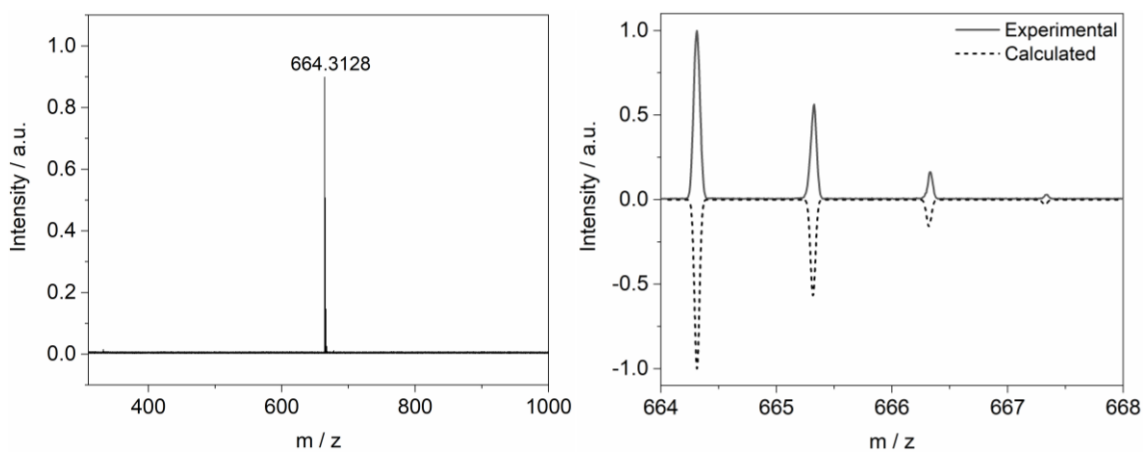


Figure S37. MALDI-TOF HRMS of 2.

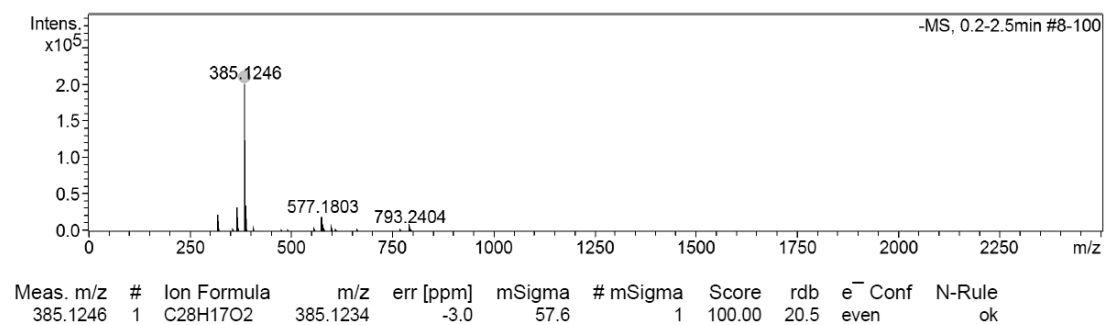
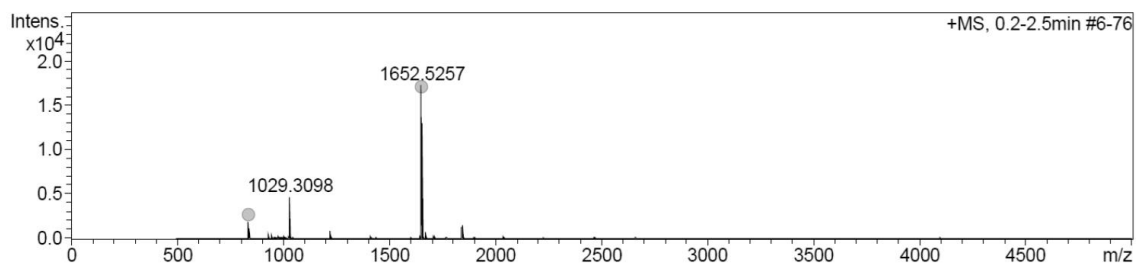
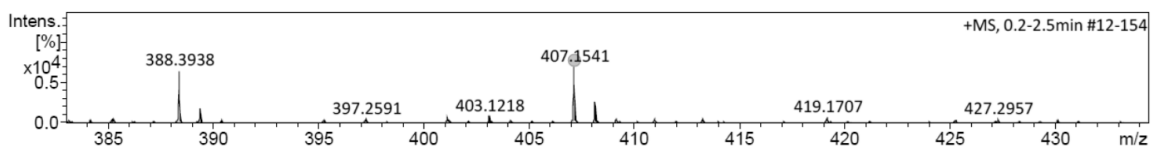


Figure S38. ESI-HRMS of 5.



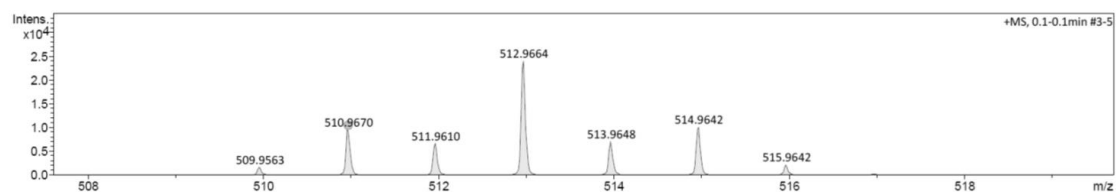
Meas. m/z	#	Ion Formula	m/z	err [ppm]	mSigma	# mSigma	Score	rdb	e ⁻ Conf	N-Rule
837.2501	1	C48H46NaO8S2	837.2526	3.0	32.8	1	100.00	25.5	even	ok
1651.5175	1	C96H92NaO16S4	1651.5160	-0.9	24.3	1	100.00	50.5	even	ok

Figure S39. ESI-HRMS of 8,8'-dimethyl-[1,1'-binaphthalene]-2,2'-dicamphorsulfonicester.



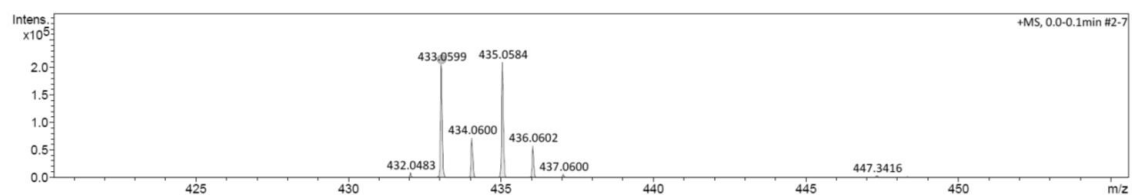
Meas. m/z	#	Ion Formula	m/z	err [ppm]	mSigma	# mSigma	Score	rdb	e ⁻ Conf	N-Rule
407.1541	1	C28H20N2Na	407.1519	-5.6	40.2	1	100.00	19.5	even	ok

Figure S40. ESI-HRMS of 6.



Meas. m/z	#	Ion Formula	m/z	err [ppm]	mSigma	# mSigma	Score	rdb	e ⁻ Conf	N-Rule
510.9670	1	C28H17Br2	510.9697	5.2	77.4	1	100.00	19.5	even	ok

Figure S41. APCI-HRMS of 7.



Meas. m/z	#	Ion Formula	m/z	err [ppm]	mSigma	# mSigma	Score	rdb	e ⁻ Conf	N-Rule
433.0599	1	C28H18Br	433.0592	-1.6	23.3	1	100.00	19.5	even	ok

Figure S42. APCI-HRMS of 8.

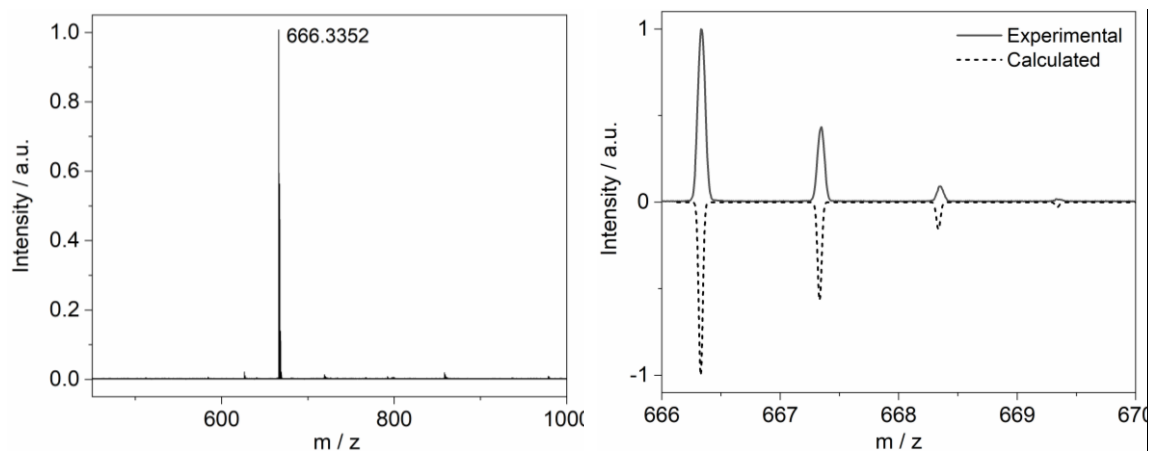


Figure S43. MALDI-TOF HRMS of **9**.

8.3. Supporting Information for

Pyrene Bridged Double [7]helicene Embedded With a Heptagonal Ring

Asim Swain,¹ Prince Ravat^{1,*}

¹Julius-Maximilians-Universität Würzburg, Institut für Organische Chemie,
Am Hubland, D-97074 Würzburg, Germany.

*Email: princekumar.ravat@uni-wuerzburg.de

Table of Contents

S1. Experimental Details	S151
S2. Photophysical Properties	S152
S3. Chiral stationary phase HPLC data	S153
S4. Quantum chemical calculations.....	S154
S5. NMR spectra.....	S160
S6. High resolution mass spectrometry (HRMS) spectra	S167
S8. References	S170

S1. Experimental Details

Chromatography. Open-column chromatography and thin-layer chromatography (TLC) were performed on silica gel (Merck silica gel 100-200 mesh). Chiral stationary phase HPLC separations were performed on SHIMADZU 223.

NMR Spectroscopy. The NMR measurements were performed at 298 K on NMR spectrometers operating at 400 MHz ^1H and 101 MHz ^{13}C frequencies (151 MHz for (*P*, *M*-**3**)). Standard pulse sequences were used, and the data was processed using 2-fold zero-filling in the indirect dimension for all 2D experiments. Chemical shifts (δ) are reported in parts per million (ppm) relative to the solvent residual peak (^1H and ^{13}C NMR, respectively): CD_2Cl_2 ($\delta = 5.32$ and 53.84 ppm) and *J* values are given in Hz.

High-resolution mass spectrometry (HRMS). The matrix-assisted laser desorption ionization-time of flight (MALDI-TOF) - HRMS were measured on Bruker ultrafleXtreme. *Trans*-2-[3-(4-*tert*-butylphenyl)-2-methyl-2-propenylidene]malononitrile (DCTB) dissolved in chloroform (30 mg/mL) was used as a supporting matrix, while Cesium iodide dissolved in acetonitrile (40 mg/mL) used as a reference in the MALDI-TOF–HRMS measurement. The calculated mass was exported from mMass software.¹

Melting point. Melting points were measured using an OptiMelt Automated Melting Point System.

UV–vis and Fluorescence spectroscopy. UV–vis spectra were measured on the JASCO V-670 spectrometer, while emission spectra were measured Edinburgh FLS 980 photoluminescence spectrometer in DCM (OD = 0.05). The fluorescence lifetimes were measured in DCM (OD = 0.05) using a 418.6 nm pulsed laser diode with a pulse frequency of 1/50 ns. The fluorescence quantum yields were measured in DCM in three different concentrations (OD = 0.2 – 0.5) using the same spectrometer with a 450 W xenon arc lamp as a light source and a calibrated integrating sphere.

CPL and CD spectroscopy. CPL and CD spectra were recorded with a customized JASCO CPL-300/J-1500 hybrid spectrometer.

S2. Photophysical Properties

A. Comparison of UV-vis absorption, emission, and CD plots in DCM.

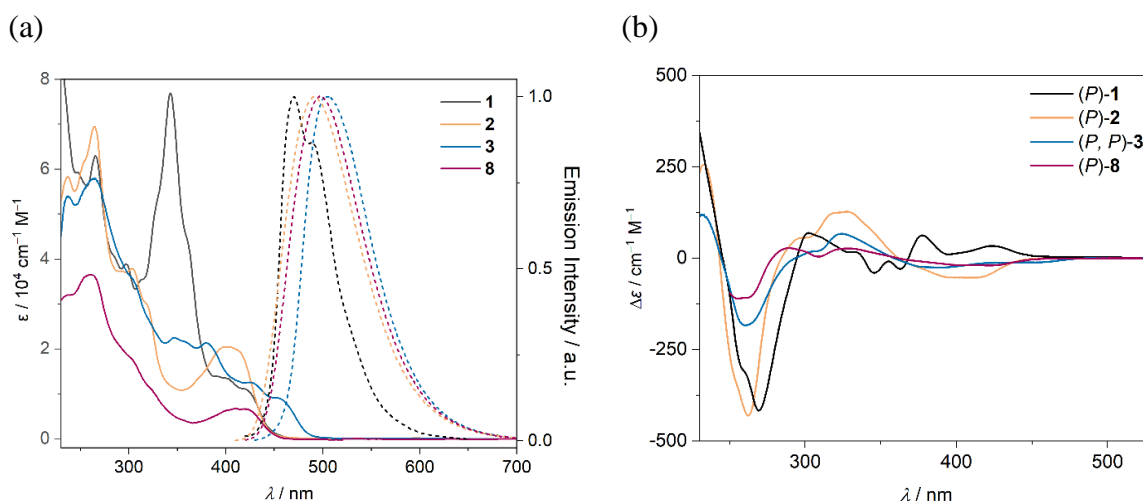


Figure S1. (a) UV-vis absorption and emission spectra of **1**, **2**, **3**, and **8** in dichloromethane. (b) Electronic CD spectra of **1**, **2**, **3**, and **8** in dichloromethane.

B. Solid state emission and CPL spectra.

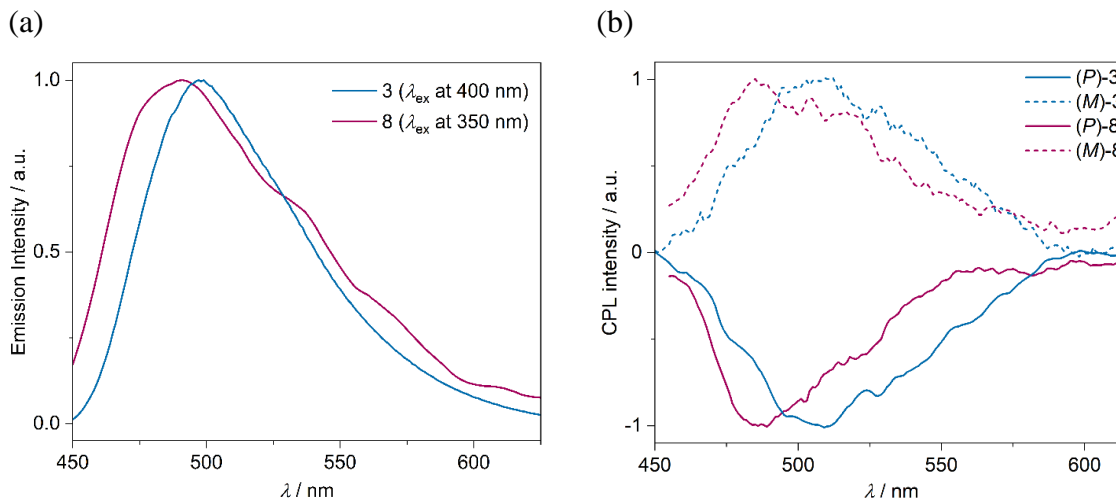


Figure S2. Solid state (a) emission spectra and (b) CPL spectra of **3** and **8** (excited at 380 nm).

S3. Chiral stationary phase HPLC data

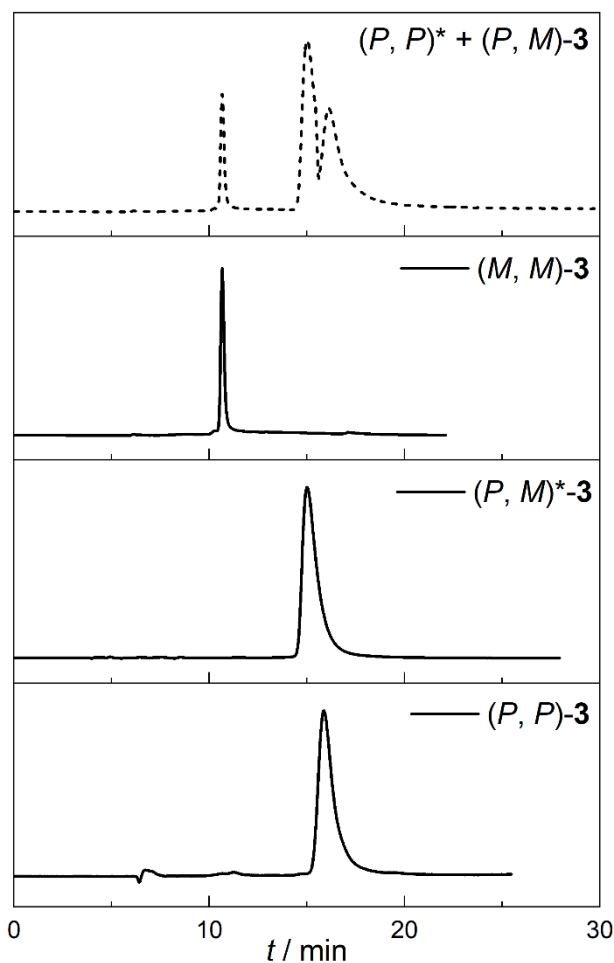


Figure S3. HPLC chromatogram of diastereomeric mixture of **3** using chiral stationary phase column. (The chromatogram detector was set at 375 nm with a bandwidth of 4 nm.)

Table S1. Overview of parameters for HPLC separation of stereoisomers of **3**.

Compound	Eluent <i>n</i> -hexane/ <i>i</i> PrOH	First fraction	Second fraction	Third fraction	α^b	R_s^c	<i>er</i>
3	94:6	<i>MM</i>	<i>PM*</i>	<i>PP</i>	1.36	2.48	98:2

^aPhenomenex Lux i-Amylose-3, 5 μ m (250 x 4.6 mm). Sample injection: 30 μ L of a ~1 mg/mL solution in hexane/*i*PrOH. Separation conditions: Eluent, flow rate: 0.5 mL/min, 25 $^{\circ}$ C. ^bSelectivity parameter: $\alpha = t_{R2} / t_{R1}$, where t_{R1} , and t_{R2} are elution times for first and second fraction, respectively. ^cResolution parameter: $R_s = 2(t_{R2} - t_{R1}) / (w_1 + w_2)$, where w_1 and w_2 are peak widths for first and second fraction, respectively. Note α and R_s for **3** was calculated only for *PP* and *MM*.

S4. Quantum chemical calculations

DFT calculations were performed using Gaussian 16 suite.² Geometries were optimized using ω B97XD functional and 6-31G(d,p) basis set in the gas phase. Frequency analysis was performed to verify the stationary state geometry. In all cases no imaginary frequency was found. TD-DFT calculations were performed on ω B97XD/6-31G(d,p) optimized geometries at the B3LYP/6-31g(d,p) level. The effect of the solvent was accounted for using PCM (with dichloromethane as the solvent). SpecDis³ and Avogadro⁴ software were used to analyze the TD-DFT calculated spectra and to generate graphical images of frontier molecular orbitals (FMOs), respectively.

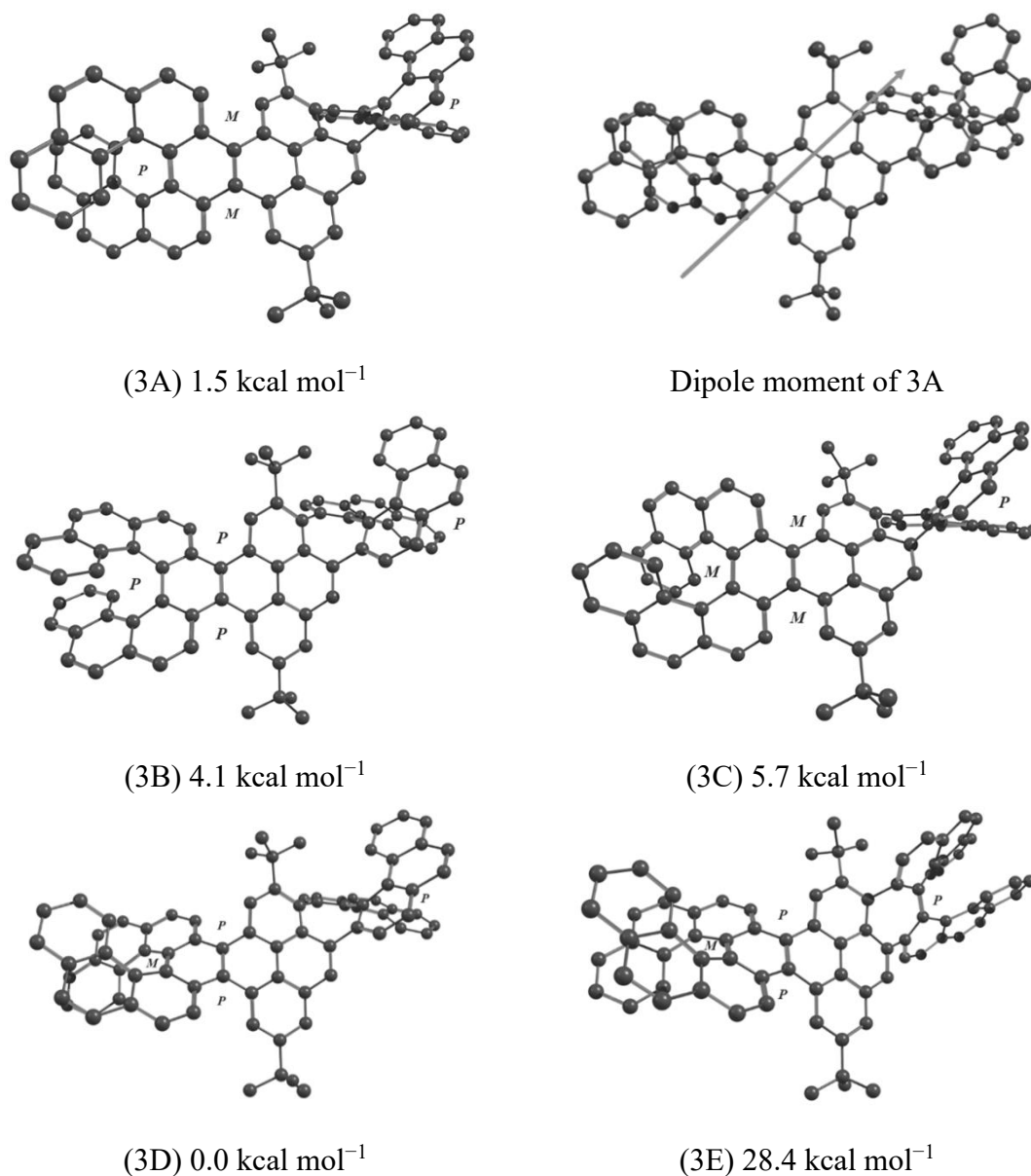


Figure S4. Relative Gibbs's free energies and optimized geometries of diastereomers of **3**. Hydrogen atoms are omitted for clarity.

Table S2. Frontier molecular orbitals of (*P, P*)-**3** and (*P, M*)-**3** (isosurface value 0.02).
Hydrogen atoms are omitted for clarity.

FMOs	(<i>P, P</i>)- 3A	(<i>P, M</i>)- 3C
LUMO+1		
LUMO		
HOMO		
HOMO-1		

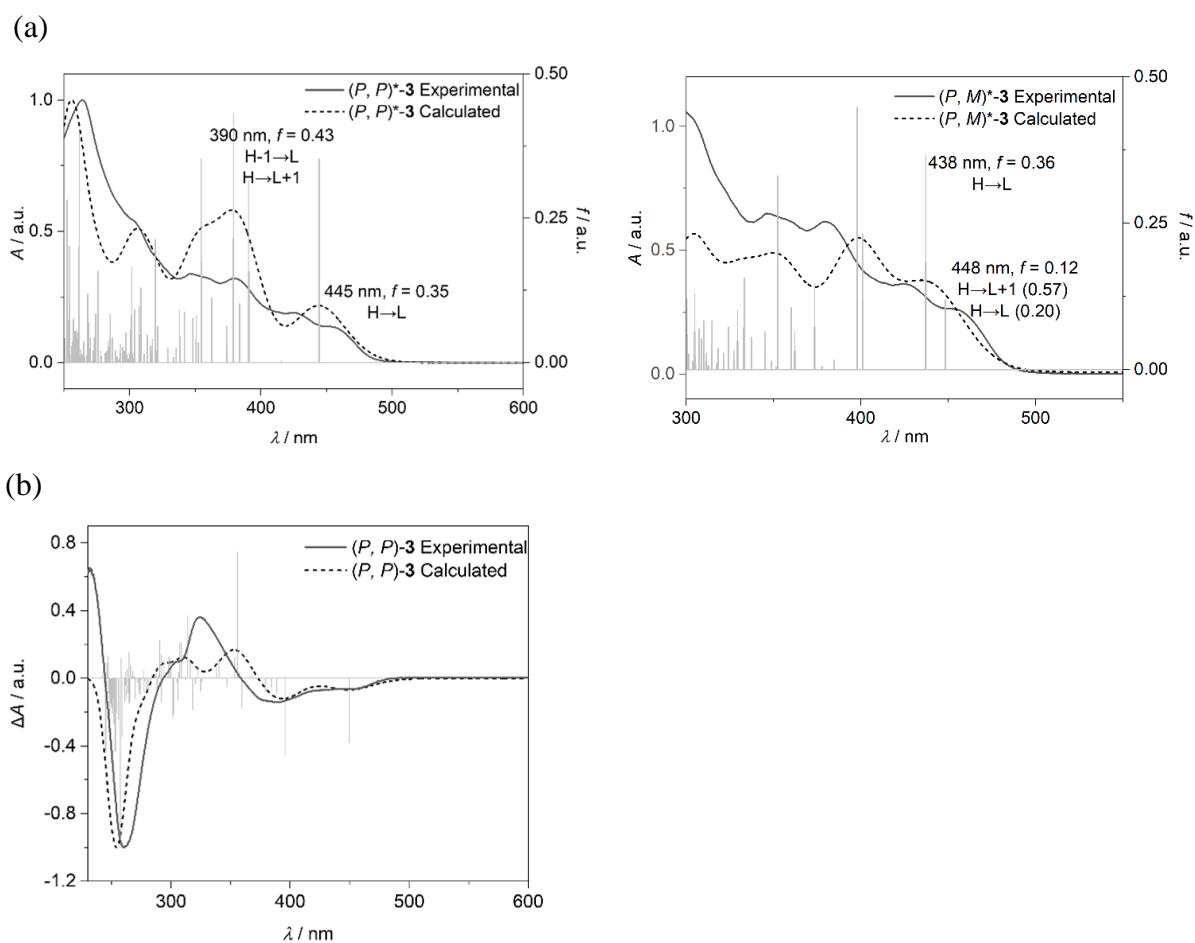


Figure S5. Comparison of experimental (solid) and TD-DFT calculated (dashed) (a) UV-vis absorption (b) ECD spectra of (P, P) -**3** (shifted by 0.07 eV, 10 nm) and (P, M) *-**3** (shifted by 0.04 eV, 15 nm) along with assignments of key transitions. H = HOMO, L = LUMO, f = oscillator strength.

Table S3a. Summary of TD-DFT calculated key transitions of (*P, P*)-**3**.

Excited singlet state	Wavelength / nm	Energy / eV	Major transitions	Contribution	oscillator strength (<i>f</i>)
1	445	2.78	HOMO→LUMO	0.69	0.35
3	390	3.18	HOMO→LUMO+2	0.53	0.43
			HOMO-1→LUMO	0.33	
8	359	3.45	HOMO→LUMO+4	0.56	0.35
			HOMO-3→LUMO	0.34	

Table S3b. Summary of TD-DFT calculated key transitions of (*P, M*)-**3**.

Excited singlet state	Wavelength / nm	Energy / eV	Major transitions	Contribution	oscillator strength (<i>f</i>)
1	448	2.76	HOMO→LUMO+1	0.57	0.12
			HOMO→LUMO	0.20	
2	438	2.83	HOMO→LUMO	0.65	0.36
4	398	3.11	HOMO-1→LUMO+1	0.49	0.45

NICS calculations: The Nucleus Independent Chemical Shift (NICS) calculations were performed on ω B97XD/6-31G(d,p) optimized geometry at GIAO-B3LYP/6-311+G(2d,p) level. Considering the non-planarity of molecule the NICS(1)_{zz} values were obtained by placing dummy atom at 1 Å above and below the each ring.

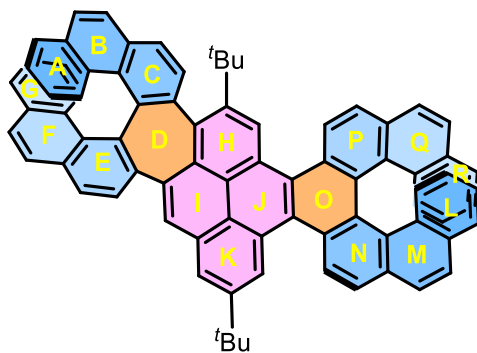


Table S4. The calculated NICS(0) and NICS(1)_{zz} values for (*P, P*)-**3**.

Ring	NICS(1) _{zz} (Up)	NICS(1) _{zz} (Down)	NICS(0) _{zz}	NICS(0) _{iso}	Ring	NICS(1) _{zz} (Up)	NICS(1) _{zz} (Down)	NICS(0) _{zz}	NICS(0) _{iso}
A	-12.28	-13.42	-9.75	-9.18	J	-4.16	-3.75	18.57	1.15
B	-10.49	-7.59	-7.69	-4.89	K	-26.23	-28.82	-10.78	-8.73
C	-3.00	-3.64	-4.81	-6.50	L	-30.30	-33.08	-17.14	-9.30
D	11.05	14.45	21.30	8.48	M	-21.17	-20.94	-6.54	-5.17
E	-7.50	-6.09	-5.99	-6.67	N	-15.95	-9.66	-4.73	-5.03
F	-9.04	-11.82	-6.81	-4.82	O	-6.31	-6.50	6.15	-1.10
G	-15.08	-12.88	-9.32	-9.23	P	-10.26	-16.67	-4.79	-5.03
H	-28.71	-22.15	-9.52	-7.88	Q	-21.39	-21.66	-6.40	-5.23
I	-6.97	-13.54	8.78	-1.63	R	-33.42	-30.53	-16.91	-9.32

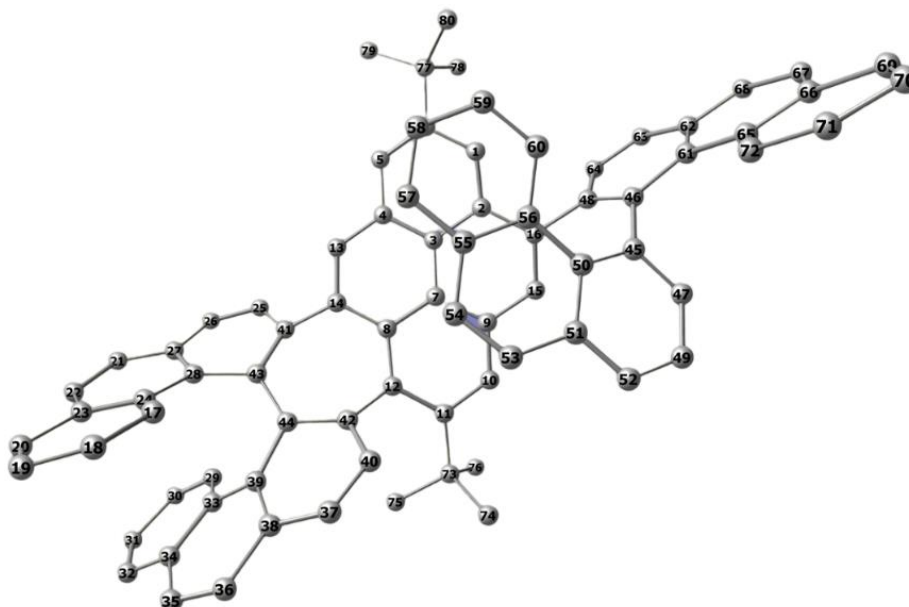


Table S5. Mulliken charges and spin densities for radical cation of **8**.

Atom no.	Mulliken charges	Spin densities	Atom no.	Mulliken charges	Spin densities	Atom no.	Mulliken charges	Spin densities
1	-0.163482	0.264863	26	-0.146228	0.067297	51	0.067740	-0.000944
2	0.108330	-0.104373	27	0.086285	-0.015958	52	-0.167475	0.001073
3	-0.006361	0.044216	28	-0.032250	0.017031	53	-0.150528	0.001419
4	0.106025	-0.057983	29	-0.132121	-0.015118	54	-0.142390	0.000910
5	-0.189932	0.195718	30	-0.125709	0.014679	55	0.075095	0.001266
6	0.138253	-0.115557	31	-0.123569	-0.012248	56	0.026335	-0.001290
7	0.007890	-0.041204	32	-0.156031	0.012179	57	-0.167624	0.002457
8	0.072874	0.007984	33	0.037175	0.027447	58	-0.120807	-0.000823
9	0.107371	0.073733	34	0.079624	-0.015933	59	-0.134576	0.001511
10	-0.167386	0.067456	35	-0.129754	0.041661	60	-0.133960	0.001937
11	0.078877	-0.038924	36	-0.153901	-0.020690	61	0.020046	-0.005642
12	-0.050876	0.190418	37	-0.143256	0.009807	62	0.076593	0.008120
13	-0.202123	0.144692	38	0.084343	0.040544	63	-0.162581	-0.006486
14	0.035401	0.000081	39	-0.042643	-0.050226	64	-0.164339	0.008810
15	-0.167778	-0.042328	40	-0.120786	0.008774	65	0.031451	0.002949
16	0.000808	0.156844	41	0.010749	0.076786	66	0.068010	-0.002468
17	-0.132083	0.003815	42	-0.014392	0.001654	67	-0.141615	0.006084
18	-0.126061	-0.002488	43	0.005813	-0.012079	68	-0.157420	-0.004168
19	-0.124110	0.005056	44	0.025105	0.115327	69	-0.162862	0.001673
20	-0.156758	-0.004181	45	-0.082325	0.000686	70	-0.121489	-0.001602
21	-0.152639	0.008820	46	-0.042610	0.013987	71	-0.140683	0.001625
22	-0.132695	-0.002825	47	-0.113216	0.000334	72	-0.122927	-0.001429
23	0.078908	0.006681	48	0.013668	-0.015999	73	-0.056146	0.002043
24	0.033430	-0.001935	49	-0.133005	0.000600	74	-0.337779	0.000622
25	-0.159308	-0.038487	50	0.029218	0.003147	75	-0.346806	0.000192
76	-0.344055	-0.000681	78	-0.345135	-0.001746	80	-0.339585	-0.001888
77	-0.074939	0.006345	79	-0.360332	-0.000012			

S5. NMR spectroscopy

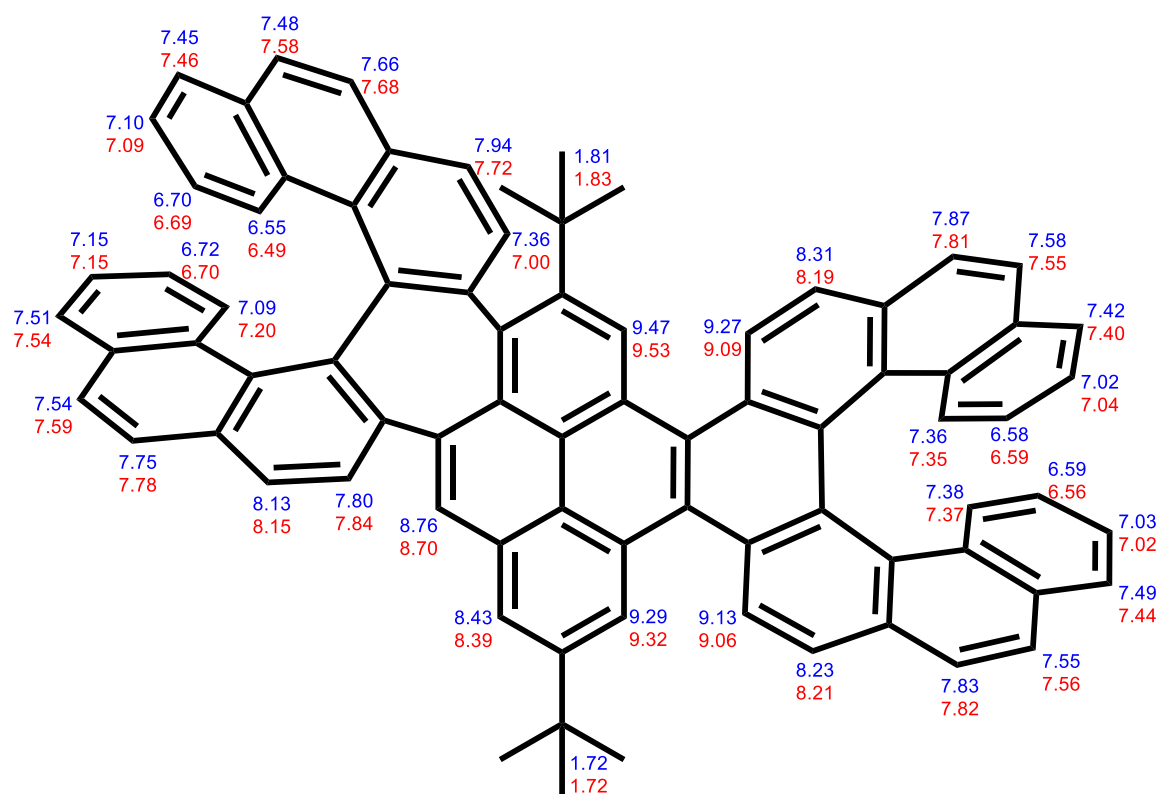


Figure S6. ^1H NMR peaks assigned to respective atoms in (*P, P*)-**3** (blue), (*P, M*)-**3** (red).

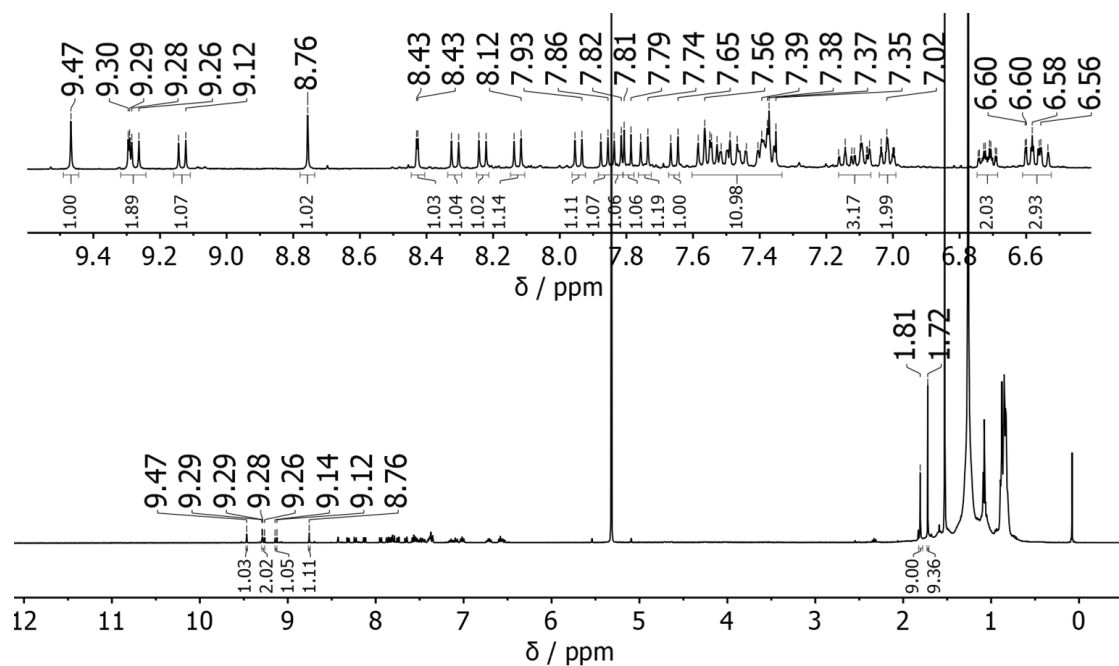


Figure S7. ^1H NMR spectrum of (P, P) -3 (400 MHz, CD_2Cl_2).

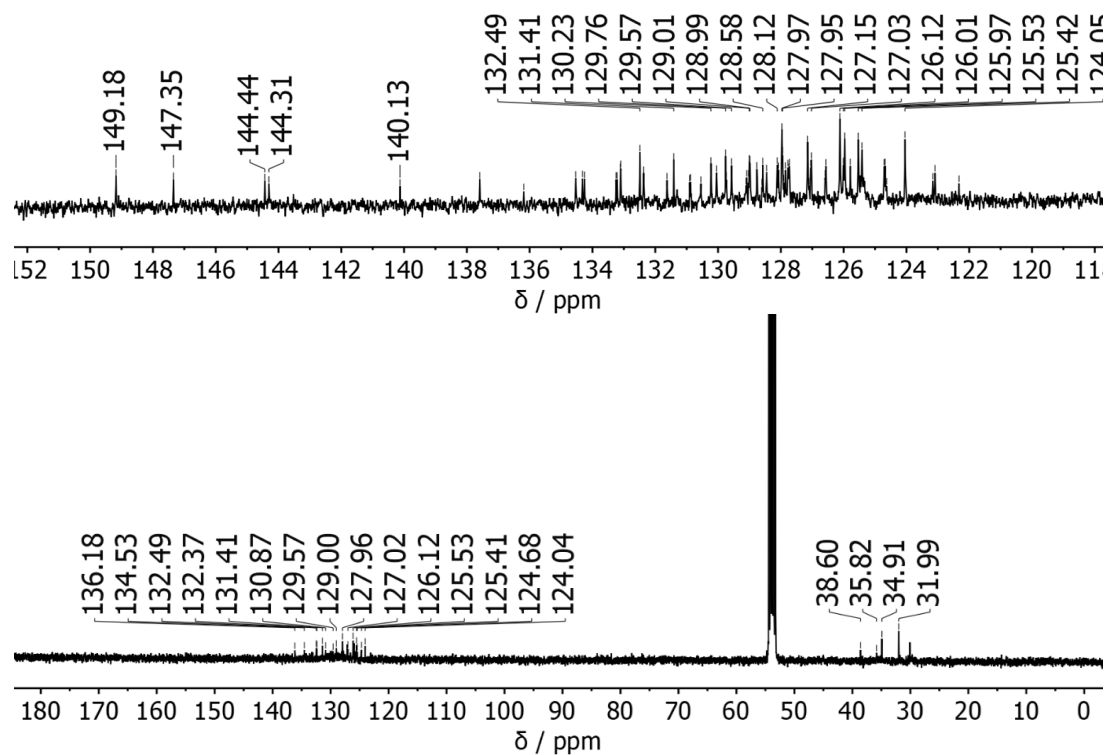


Figure S8. $^{13}\text{C}\{^1\text{H}\}$ NMR spectrum of (P, P) -3 (101 MHz, CD_2Cl_2).

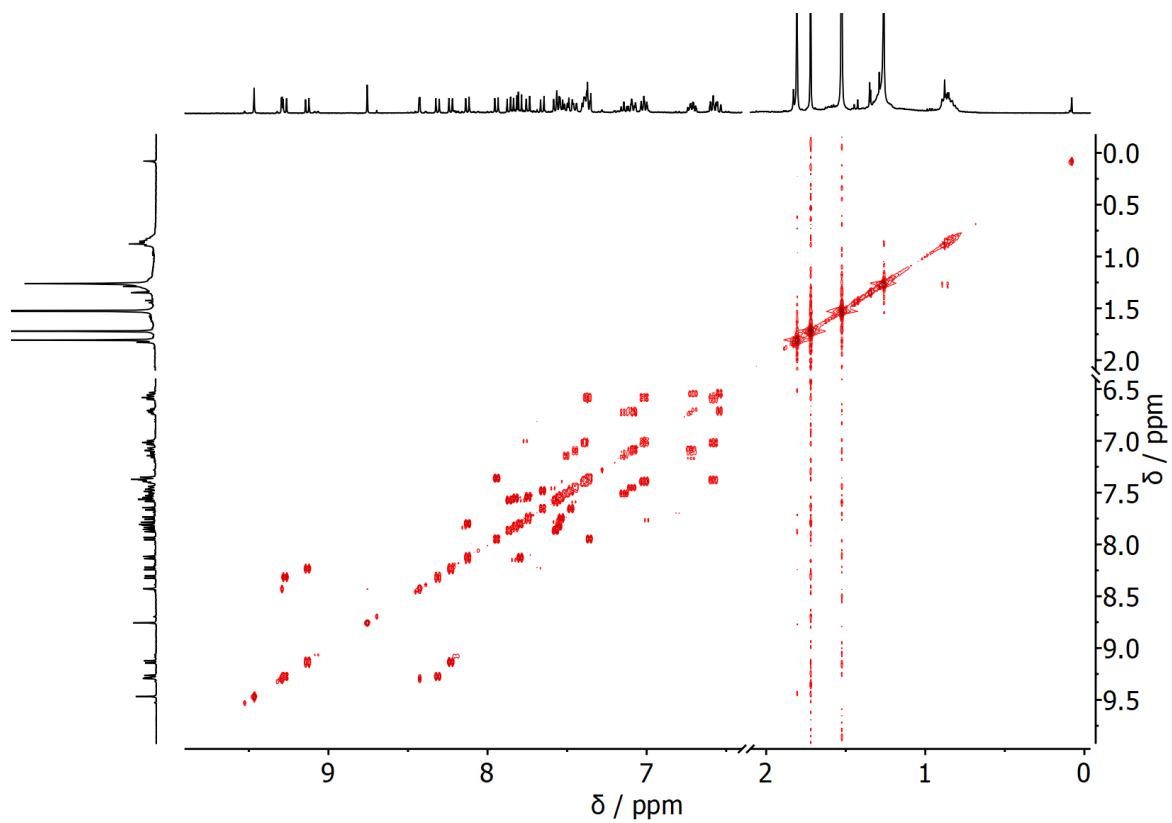


Figure S9. $^1\text{H} - ^1\text{H}$ COSY NMR spectrum of (*P, P*)-**3** (400 MHz, CD_2Cl_2).

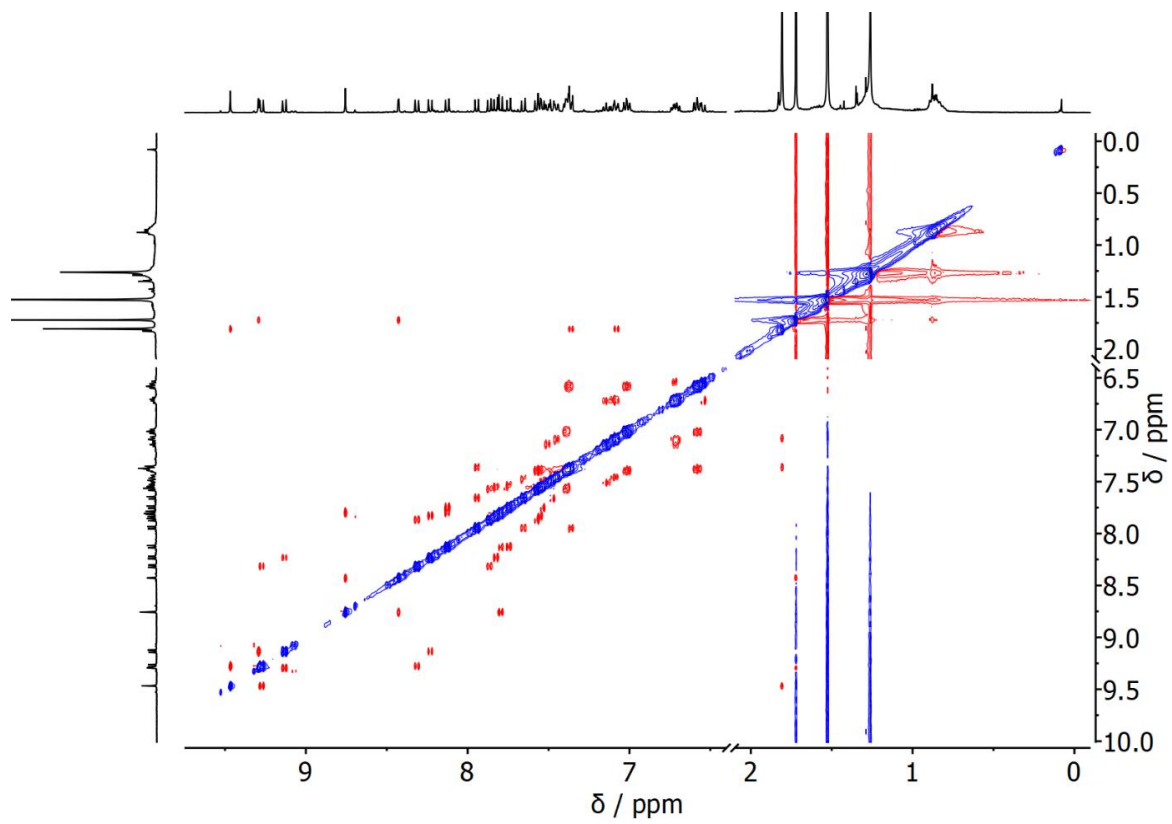


Figure S10. $^1\text{H} - ^1\text{H}$ NOESY NMR spectrum of (*P, P*)-**3** (400 MHz, CD_2Cl_2).

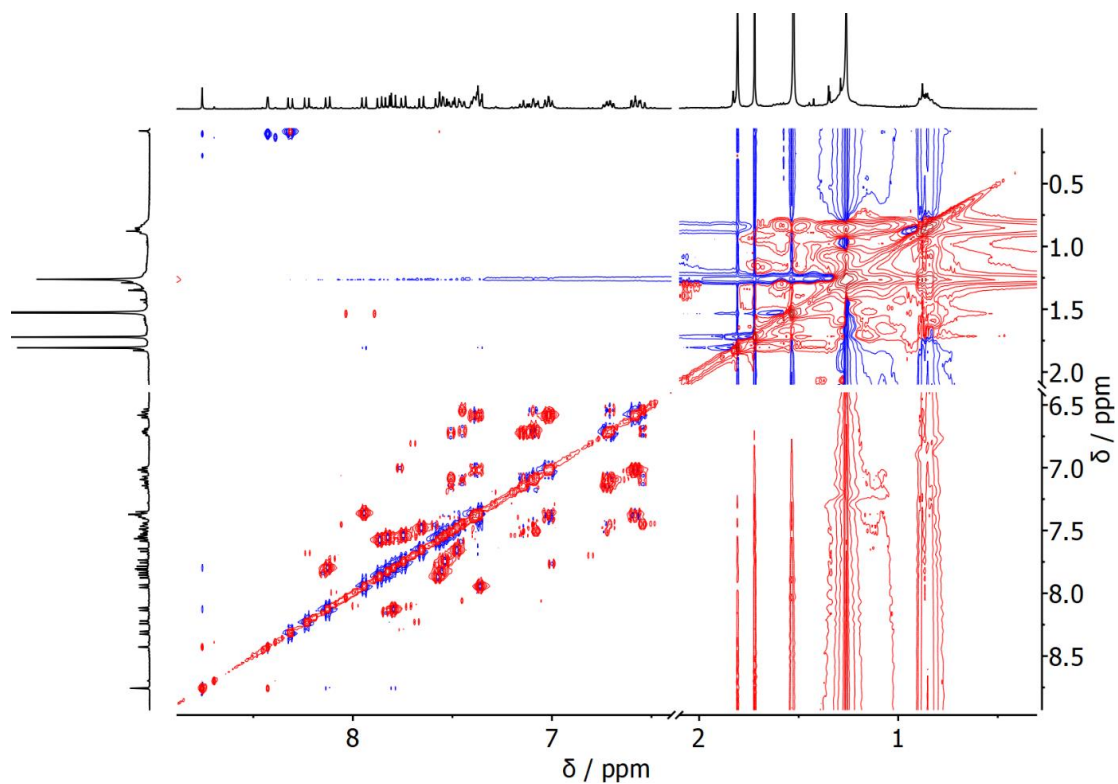


Figure S11. $^1\text{H} - ^1\text{H}$ TOCSY NMR spectrum of (*P, P*)-**3** (400 MHz, CD_2Cl_2).

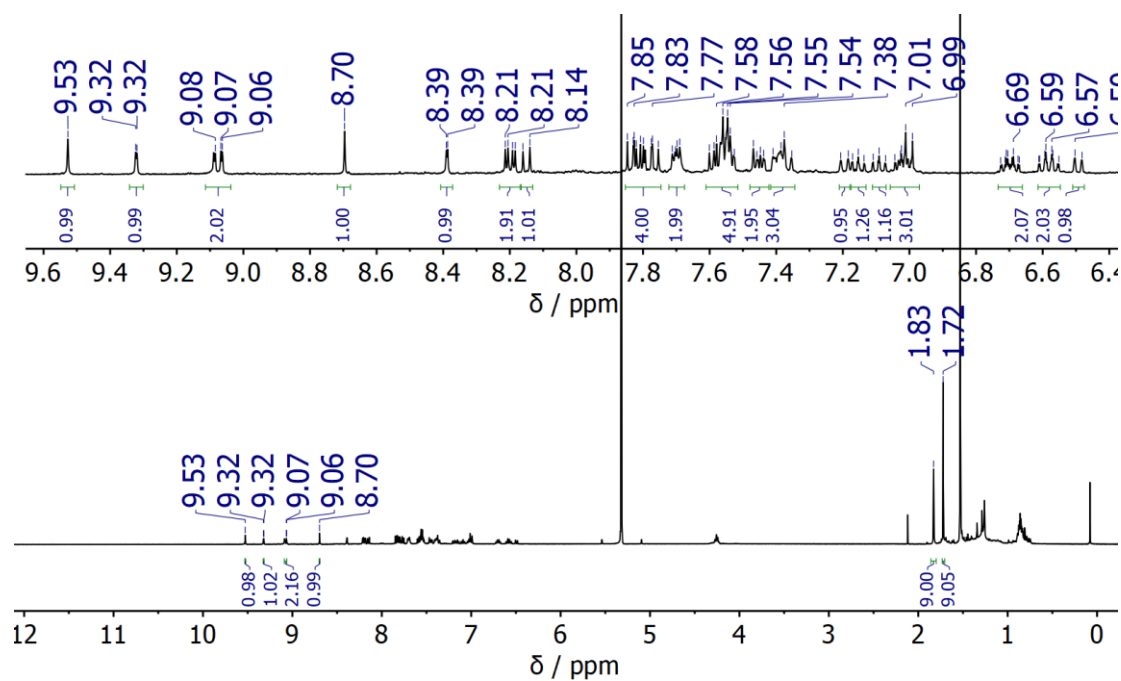


Figure S12. ^1H NMR spectrum of (*P, M*)-**3** (400 MHz, CD_2Cl_2).

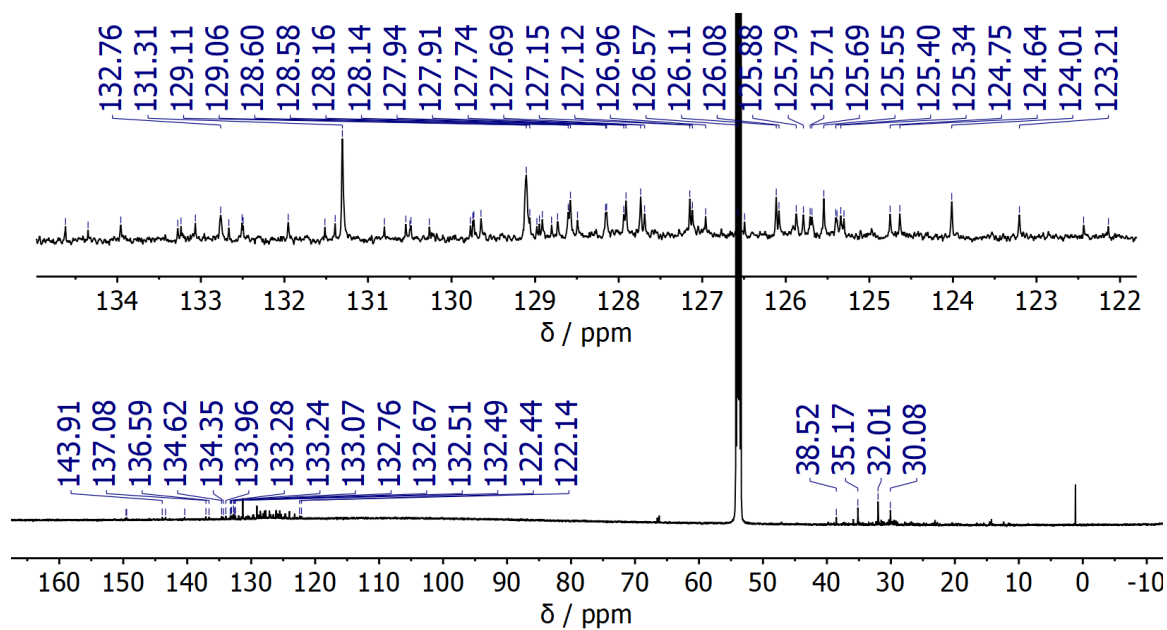


Figure S13. $^{13}\text{C}\{^1\text{H}\}$ NMR spectrum of (*P, M*)-**3** (151 MHz, CD_2Cl_2).

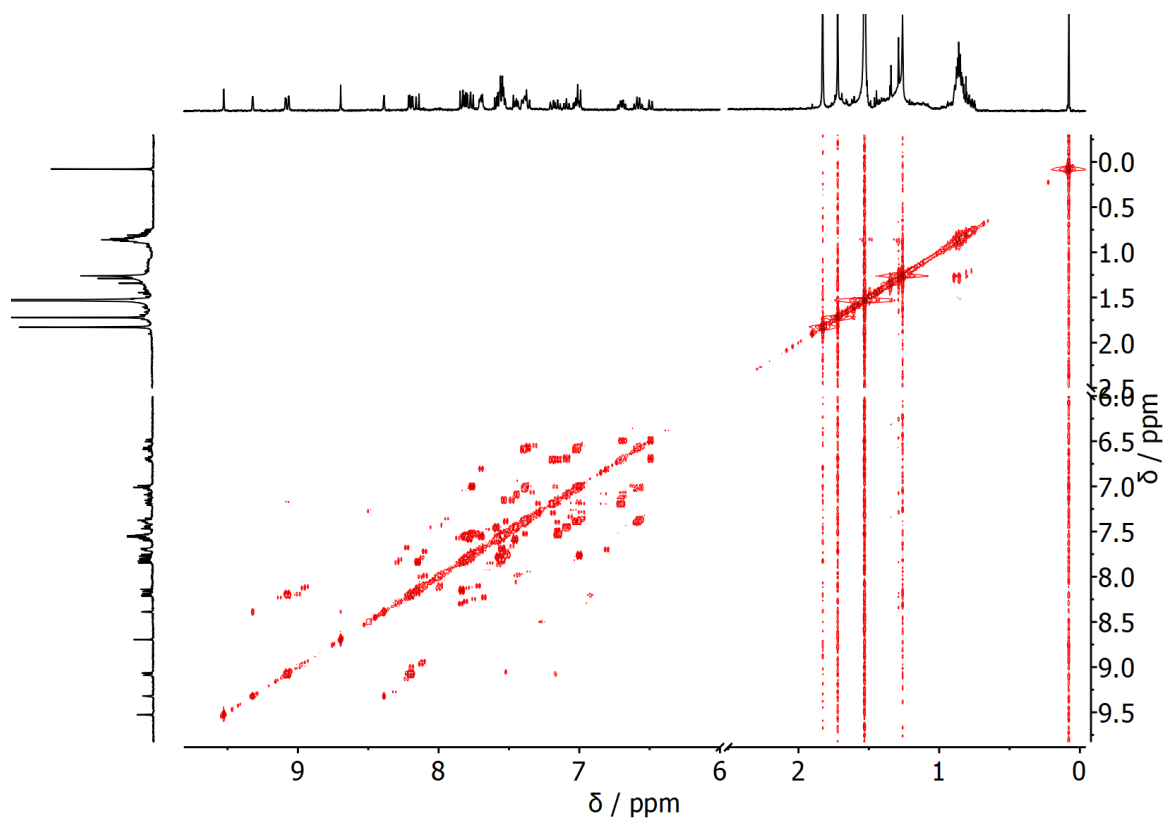


Figure S14. $^1\text{H} - ^1\text{H}$ COSY NMR spectrum of (*P, M*)-**3** (400 MHz, CD_2Cl_2).

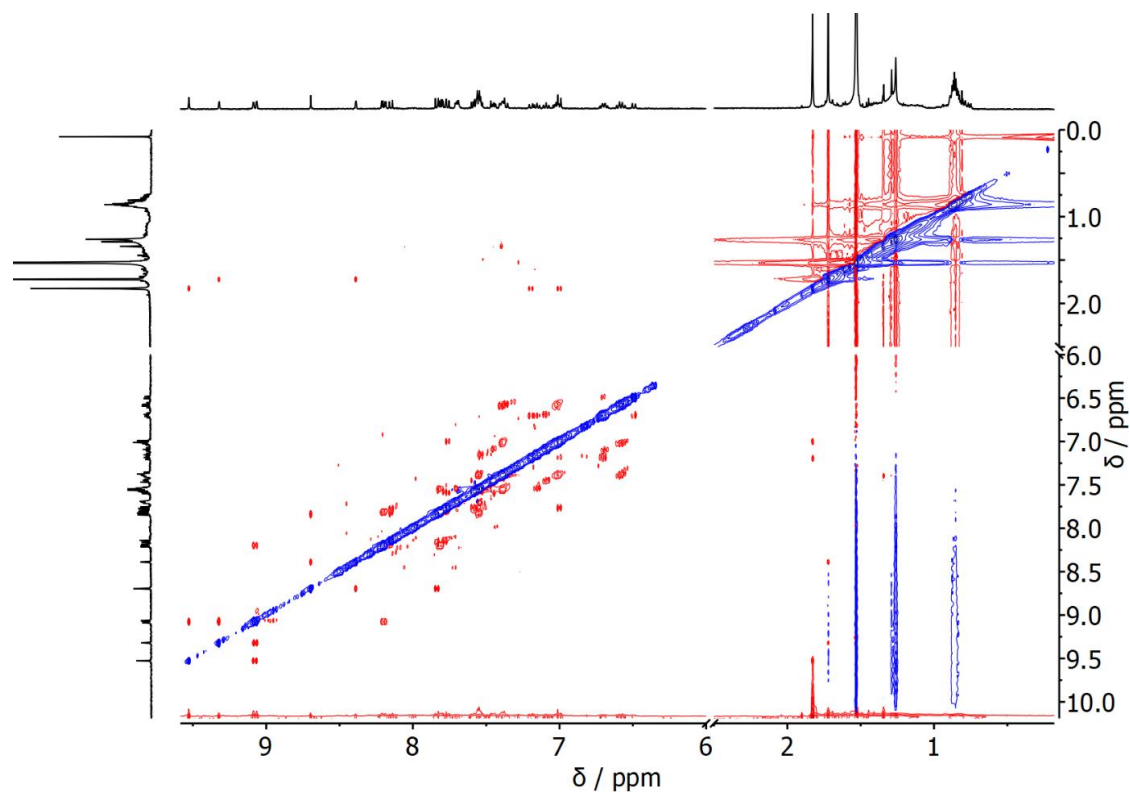


Figure S15. $^1\text{H} - ^1\text{H}$ NOESY NMR spectrum of (*P, M*)-**3** (400 MHz, CD_2Cl_2).

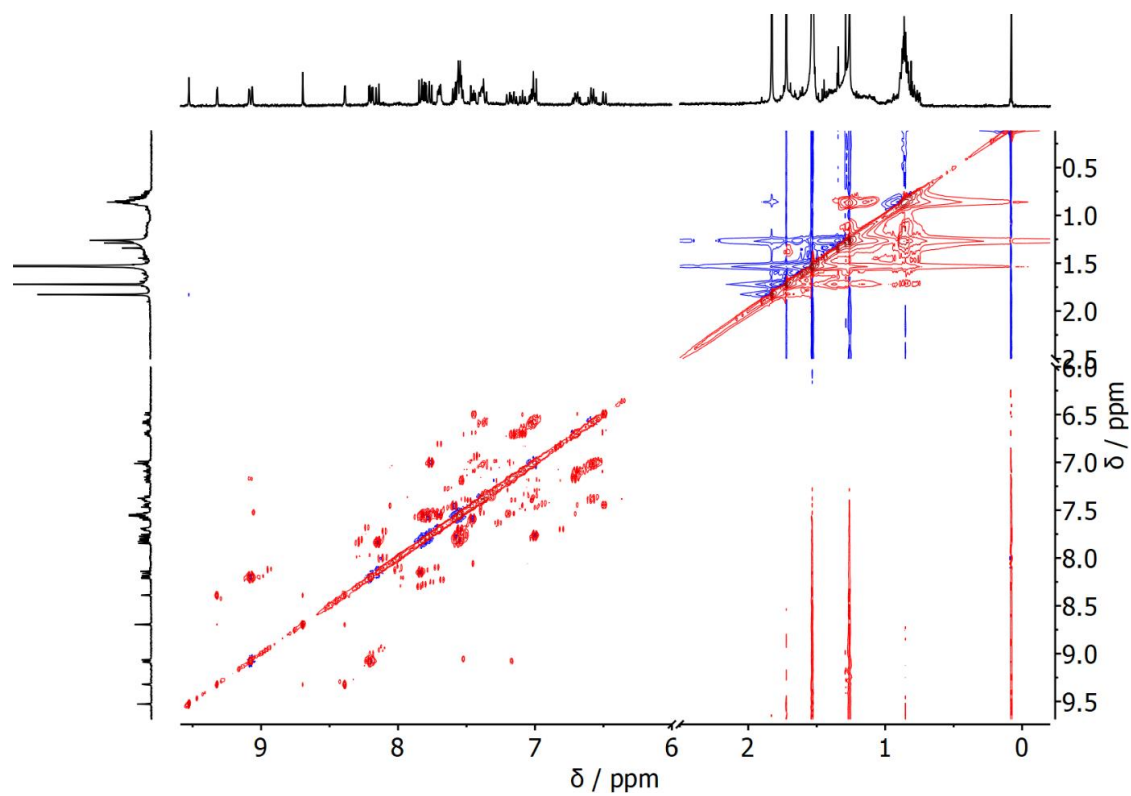


Figure S16. $^1\text{H} - ^1\text{H}$ TOCSY NMR spectrum of (*P, M*)-**3** (400 MHz, CD_2Cl_2).

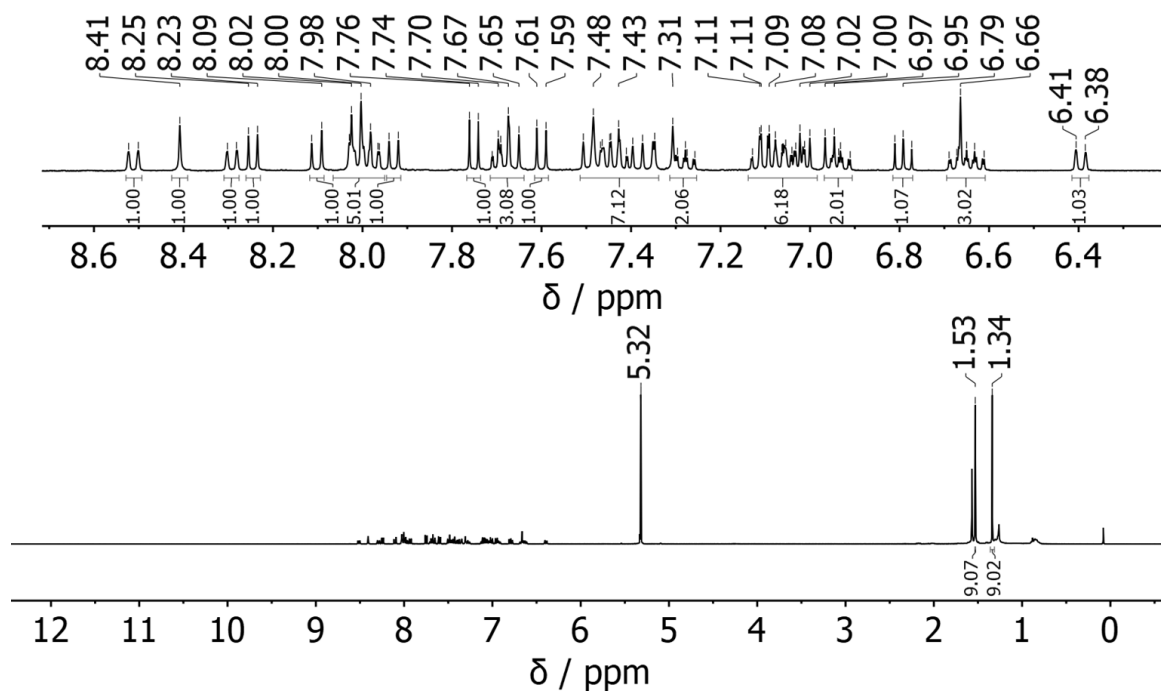


Figure S17. ^1H NMR spectrum of **8** (400 MHz, CD_2Cl_2).

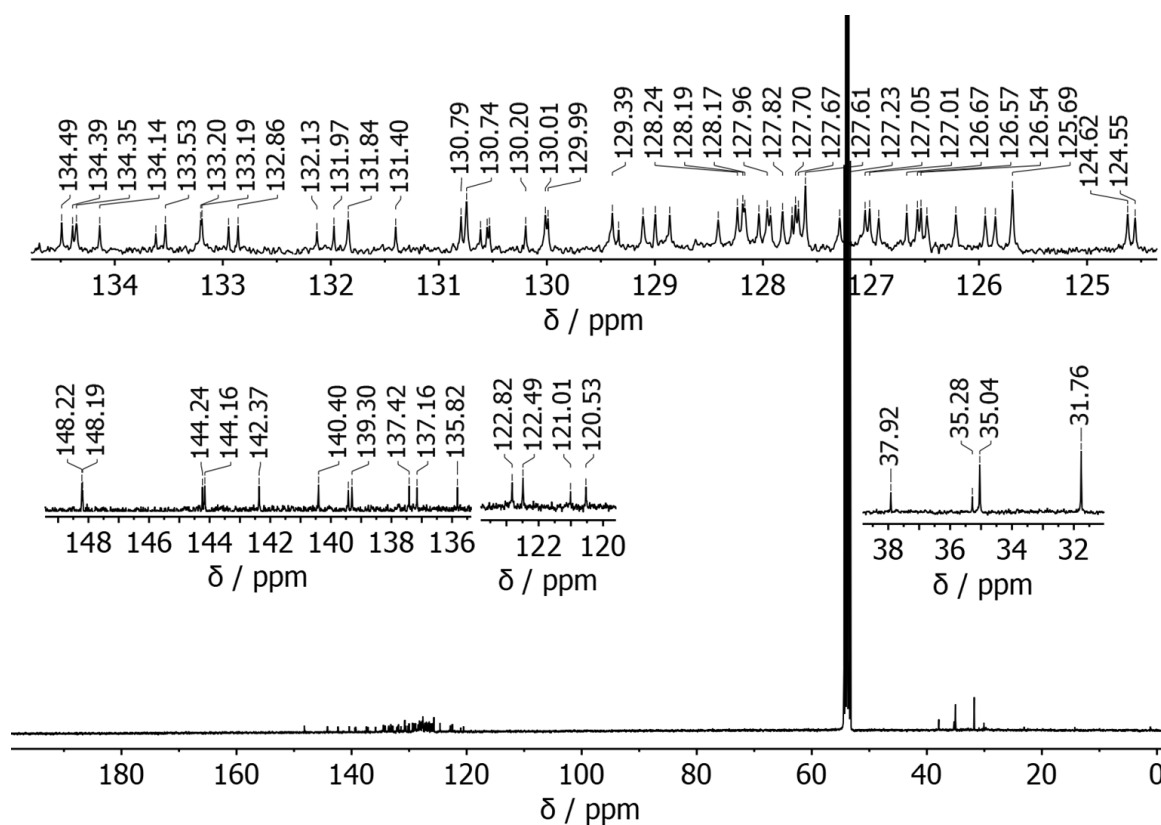


Figure S18. $^{13}\text{C}\{^1\text{H}\}$ NMR spectrum of **8** (101 MHz, CD_2Cl_2).

S6. High-resolution mass spectrometry (HRMS)

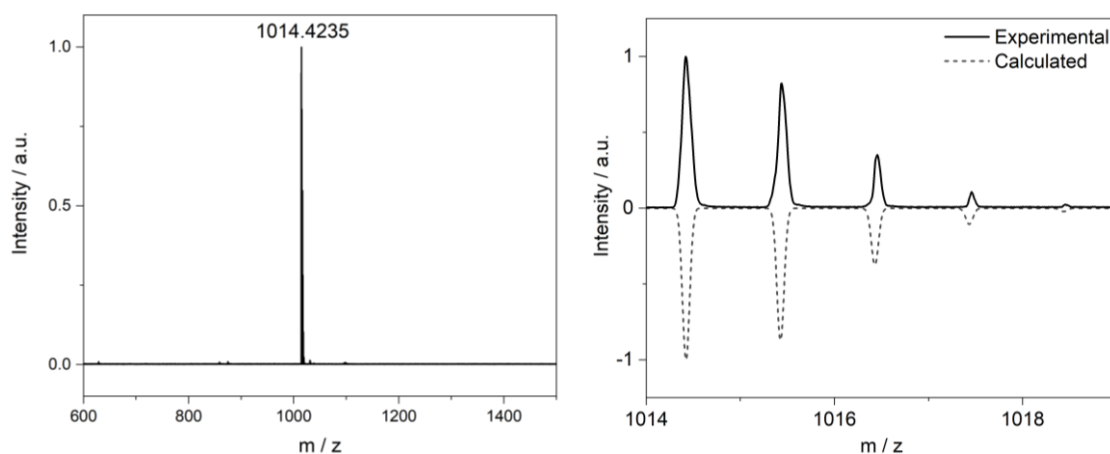


Figure S19. MALDI-TOF HRMS of *(P, P)*-3.

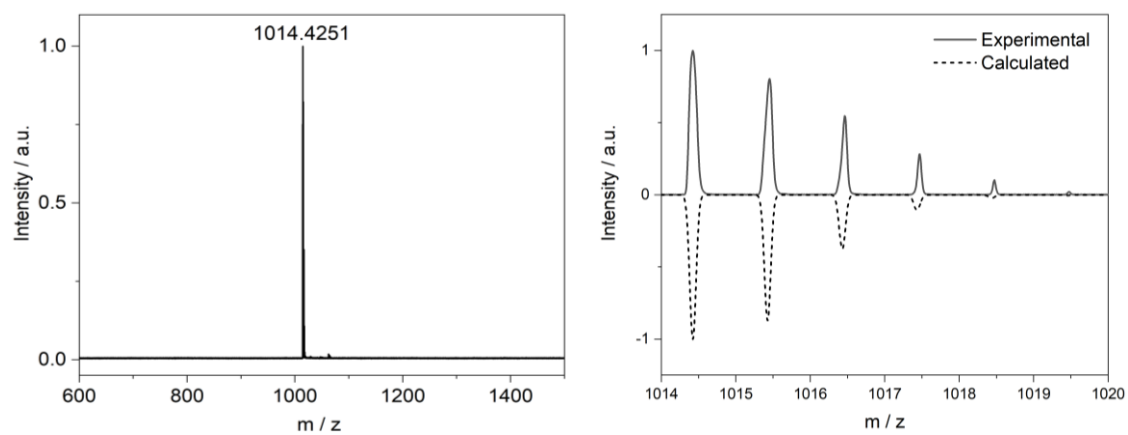


Figure S20. MALDI-TOF HRMS of *(P, M)*-3.

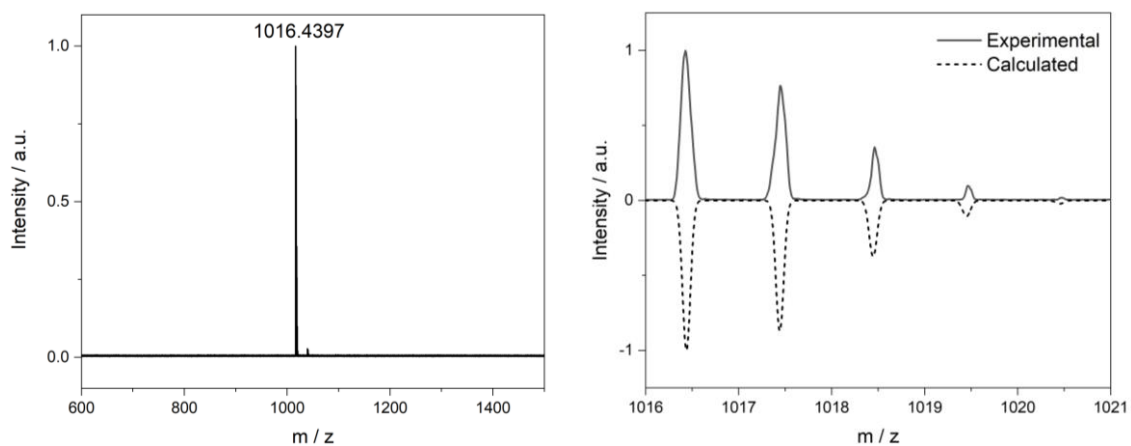


Figure S21. MALDI-TOF HRMS of 6.

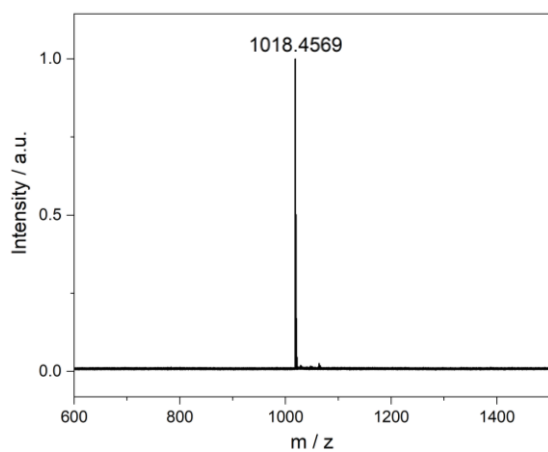


Figure S22. MALDI-TOF HRMS of **7**.

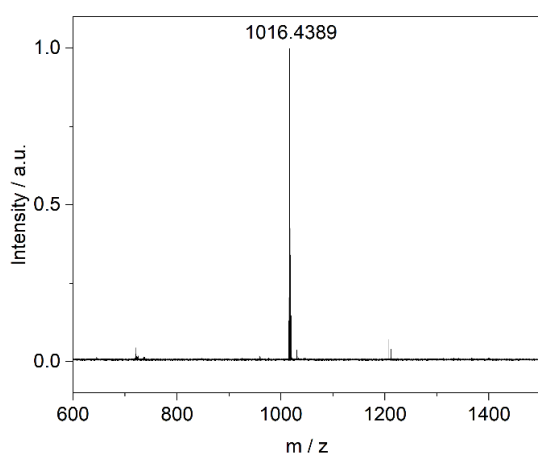
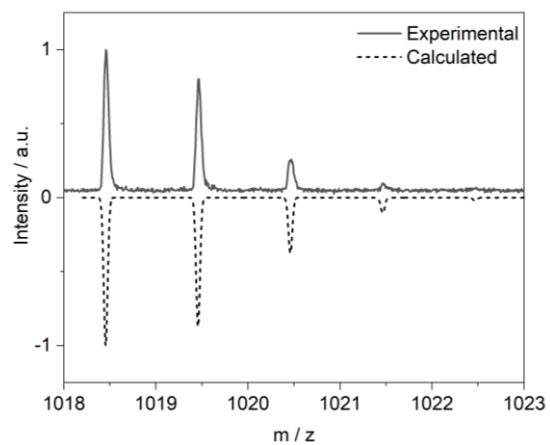
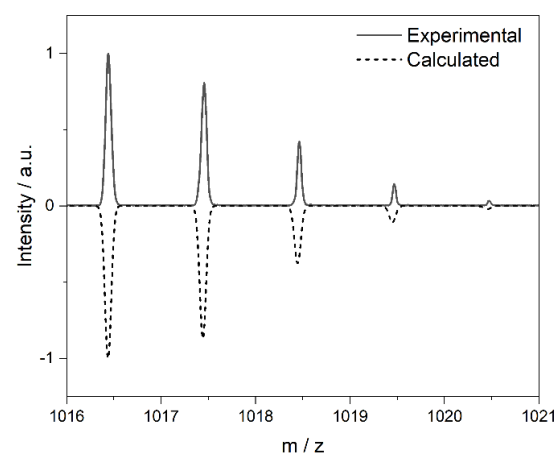


Figure S23. MALDI-TOF HRMS of **8**.



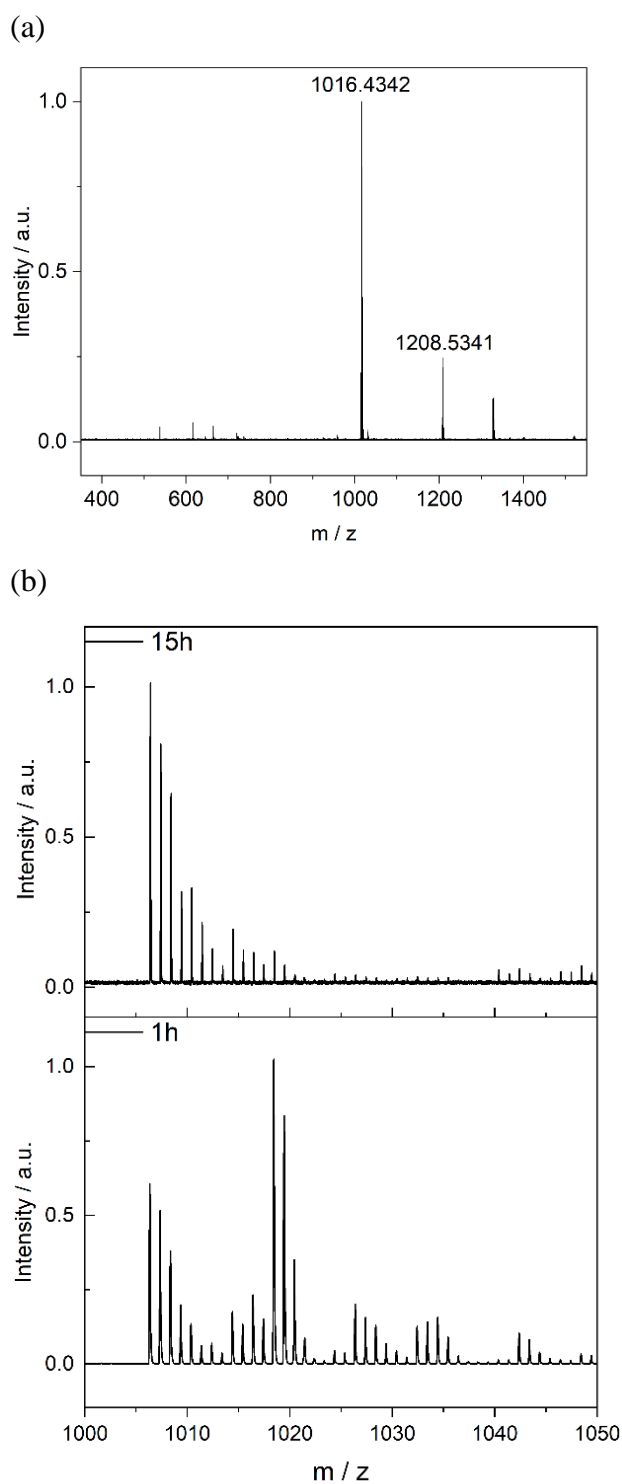


Figure S24. MALDI-TOF HRMS of reaction mixture of (a) Suzuki coupling-C-H activation after heating overnight for 15h (b) Scholl reaction with **7** in presence of triflic acid.

S8. References

1. M. Strohalm, D. Kavan, P. Novák, M. Volný and V. Havlíček, mMass 3: A Cross-Platform Software Environment for Precise Analysis of Mass Spectrometric Data, *Anal. Chem.*, 2010, **82**, 4648-4651.
2. M. J. Frisch, G. W. Trucks, H. B. Schlegel, G. E. Scuseria, M. A. Robb, J. R. Cheeseman, G. Scalmani, V. Barone, G. A. Petersson, H. Nakatsuji, X. Li, M. Caricato, A. V. Marenich, J. Bloino, B. G. Janesko, R. Gomperts, B. Mennucci, H. P. Hratchian, J. V. Ortiz, A. F. Izmaylov, J. L. Sonnenberg, Williams, F. Ding, F. Lipparini, F. Egidi, J. Goings, B. Peng, A. Petrone, T. Henderson, D. Ranasinghe, V. G. Zakrzewski, J. Gao, N. Rega, G. Zheng, W. Liang, M. Hada, M. Ehara, K. Toyota, R. Fukuda, J. Hasegawa, M. Ishida, T. Nakajima, Y. Honda, O. Kitao, H. Nakai, T. Vreven, K. Throssell, J. A. Montgomery Jr., J. E. Peralta, F. Ogliaro, M. J. Bearpark, J. J. Heyd, E. N. Brothers, K. N. Kudin, V. N. Staroverov, T. A. Keith, R. Kobayashi, J. Normand, K. Raghavachari, A. P. Rendell, J. C. Burant, S. S. Iyengar, J. Tomasi, M. Cossi, J. M. Millam, M. Klene, C. Adamo, R. Cammi, J. W. Ochterski, R. L. Martin, K. Morokuma, O. Farkas, J. B. Foresman and D. J. Fox, Gaussian 16 Rev. C.01. *Journal*, 2016.
3. T. Bruhn, A. Schaumlöffel, Y. Hemberger and G. Bringmann, SpecDis: quantifying the comparison of calculated and experimental electronic circular dichroism spectra, *Chirality*, 2013, **25**, 243-249.
4. M. D. Hanwell, D. E. Curtis, D. C. Lonie, T. Vandermeersch, E. Zurek and G. R. Hutchison, Avogadro: an advanced semantic chemical editor, visualization, and analysis platform, *J. Cheminformatics*, 2012, **4**, 17.

8.4. Supporting Information for

Helically Twisted Nanoribbons via Stereospecific Annulative π -Extension Reaction Employing [7]Helicene as a Molecular Wrench

Asim Swain¹, Krzysztof Radacki,² Holger Braunschweig,² and Prince Ravat^{1,*}

¹Julius-Maximilians-Universität Würzburg, Institut für Organische Chemie, Am Hubland, 97074 Würzburg, Germany

²Julius-Maximilians-Universität Würzburg, Institut für Anorganische Chemie, Am Hubland, 97074 Würzburg, Germany

*Email: princekumar.ravat@uni-wuerzburg.de

Table of Contents

S1. Experimental Details	S172
S2. Reaction Procedures and Characterizations	S174
S3. Chiral stationary phase HPLC	S179
S4. Determination and analysis of activation parameters for diastereomerization of 1	S180
S5. Photophysical studies.	S182
S6. Quantum chemical calculations	S186
S7. X-Ray crystallography	S197
S8. NMR spectroscopy	S199
S9. High resolution mass spectrometry (HRMS)	S215
S10. References	S218

S1. Experimental Details

General Information. All chemicals and solvents were purchased from commercial sources and were used without further purification unless stated otherwise. 3,3'-Dibromo-4,4'-biphenanthrene^[1], 2,7-di-*tert*-butylpyrene^[2], 2,2'-(2,7-di-*tert*-butylpyrene-4,9-diyl)bis(4,4,5,5-tetramethyl-1,3,2-dioxaborolane) and 2-(2,7-di-*tert*-butylpyren-4-yl)-4,4,5,5-tetramethyl-1,3,2-dioxaborolane^[3], 2,2',6,6'-tetrabromo-4,4'-di-*tert*-butyl-1,1'-biphenyl^[4] and [Pd(CH₃CN)₄](SbF₆)₂^[5] were synthesized according to literature known protocols and purity was confirmed by ¹H NMR. The reactions and experiments sensitive to dioxygen were performed using Schlenk techniques and with nitrogen-saturated solvents. Prior to use all the glassware and NMR tubes were dried in oven at 80 °C for 12 hours.

Chromatography. Open-column chromatography and thin-layer chromatography (TLC) were performed on silica gel (Merck silica gel 100-200 mesh). Chiral stationary phase HPLC separations were performed by SHIMADZU 223.

NMR Spectroscopy. The NMR measurements were performed at 298 K on NMR spectrometers operating at 400 MHz proton and 101 MHz ¹³C frequencies. Standard pulse sequences were used, and the data was processed using 2-fold zero-filling in the indirect dimension for all 2D experiments. Chemical shifts (δ) are reported in parts per million (ppm) relative to the solvent residual peak (¹H and ¹³C NMR, respectively): CDCl₃ (δ = 7.26 and 77.2 ppm), CD₂Cl₂ (δ = 5.32 and 53.84 ppm) and *J* values are given in Hz. Structural assignments for all synthesized compounds were made using additional information obtained from gCOSY, gNOESY, gHSQC, and gHMBC experiments.

High resolution mass spectrometry (HRMS). The matrix assisted laser desorption ionization-time of flight (MALDI-TOF) - HRMS were measured on Bruker ultrafleXtreme. *Trans*-2-[3-(4-*tert*-butylphenyl)-2-methyl-2-propenylidene]malononitrile (DCTB) dissolved in chloroform (30 mg/mL) was used as supporting matrix, while Caesium iodide dissolved in acetonitrile (40 mg/mL) used as reference in the MALDI-TOF–HRMS measurement. The calculated mass was exported from mMass software.^[6]

Melting point. Melting points were measured using an OptiMelt Automated Melting Point System.

UV–Vis and Fluorescence spectroscopy. UV–Vis spectra were measured on JASCO V-670 spectrometer, while emission spectra were measured Edinburgh FLS 980 photoluminescence spectrometer in DCM (OD = 0.05). The fluorescence lifetimes were measured in DCM (OD = 0.05) using a 418.6 nm pulsed laser diode with a pulse frequency of 1/50 ns. The fluorescence quantum yields were measured in DCM in three different concentration (OD = 0.2 – 0.5) using same spectrometer with a 450 W xenon arc lamp as a light source and a calibrated integrating sphere.

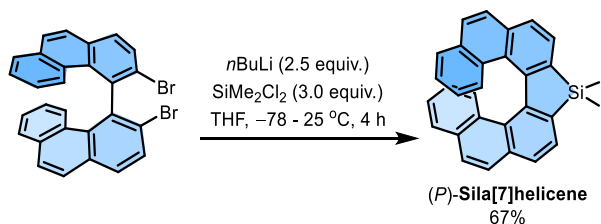
CPL and CD spectroscopy. CPL and CD spectra were recorded with a customized JASCO CPL-300/J-1500 hybrid spectrometer.

Single-Crystal X-ray Crystallography. The crystal data were collected on a RIGAKU XTALAB SYNERGY – R diffractometer with a HPA area detector and multi-layer mirror monochromated $\text{CuK}\alpha$ radiation. The structure was solved using intrinsic phasing method^[7], refined with the SHEL XL program^[8] and expanded using Fourier techniques. All non-hydrogen atoms were refined anisotropically. Hydrogen atoms were included in structure factors calculations. All hydrogen atoms were assigned to idealized geometric positions.

Quantum chemical calculations. DFT calculations were performed using Gaussian 16 suite.^[9] Geometries were optimized using ω B97XD functional and 6-31G(d,p) basis set in the gas phase. Frequency analysis was performed to verify the stationary state geometry. In all cases no imaginary frequency was found. TD-DFT calculations were performed on ω B97XD/6-31G(d,p) optimized geometries at the B3LYP/6-31g(d,p) level. The effect of the solvent was accounted for using PCM (with dichloromethane as the solvent). SpecDis^[10] and Avogadro^[11] software were used to analyze the TD-DFT calculated spectra, and to generate graphical images of frontier molecular orbitals (FMOs), respectively.

S2. Reaction Procedures and Characterizations

Synthesis of (*P*)-Dimethylsila[7]helicene.



(*P*)-Dimethylsila[7]helicene was synthesized with a modified literature procedure.^[12] In a Schlenk tube 3,3'-Dibromo-4,4'-biphenanthrene (450 mg, 0.88 mmol) was dissolved in 25 mL of dry THF (tetrahydrofuran). The reaction mixture was degassed for 20 minutes at -78°C . 1.2 mL (2.20 mmol) of *n*BuLi was added dropwise and stirred for 30 minutes. The TLC confirmed the completion of lithiation process, Me_2SiCl_2 (0.32 mL, 2.64 mmol) was added to the reaction mixture dropwise. The reaction mixture was slowly warmed to room temperature and stirred for 4 h. The reaction was quenched with water, and the organic layer was extracted with ethyl acetate and dried over sodium sulphate. The combined organic layer was evaporated under reduced pressure. The crude product was then purified with silica gel column chromatography using petrolether to yield 241 mg (67%) of sila[7]helicene as yellow crystalline solid.

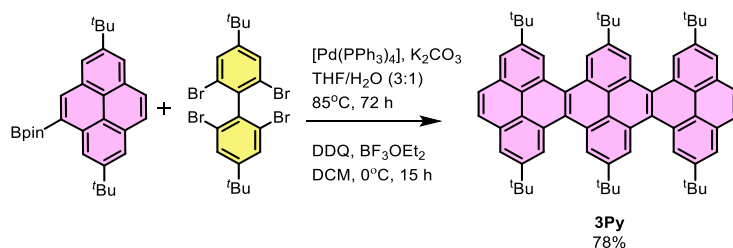
Characterization of (*P*)-Dimethylsila[7]helicene.

HRMS (MALDI-TOF) m/z : [M] Calcd for $[\text{C}_{30}\text{H}_{22}\text{Si}]$ 410.1491; Found 410.1508

^1H NMR (400 MHz, CDCl_3 , 25°C): δ [ppm] = 7.84 (d, $J = 7.3$ Hz, 2H), 7.78 (d, $J = 7.4$ Hz, 2H), 7.66 (d, $J = 8.7$ Hz, 2H), 7.51 (d, $J = 8.7$ Hz, 2H), 7.36 (d, $J = 9.4$ Hz, 2H), 7.32 (d, $J = 9.2$ Hz, 2H), 6.97 – 6.91 (m, 2H), 6.37 – 6.33 (m, 2H), 0.60 (s, 6H).

^{13}C NMR (101 MHz, CDCl_3 , 25°C): δ [ppm] = 147.73, 139.58, 134.25, 132.14, 130.33, 128.96, 128.88, 127.72, 127.25, 126.72, 126.53, 126.05, 125.05, 122.99, -2.60 .

Synthesis of 3Py.



3Py was synthesized with a modified literature procedure.^[13] In a Schlenk tube 2-(2,7-di-tert-butylpyren-4-yl)-4,4,5,5-tetramethyl-1,3,2-dioxaborolane (30 mg, 0.068 mmol) and

2,2',6,6'-tetrabromo-4,4'-di-tert-butyl-1,1'-biphenyl (20 mg, 0.034 mmol) were dissolved in 3 mL dry THF and potassium carbonate (14.1 mg, 0.102 mmol) was dissolved in water (1 mL) and both solutions were degassed for 10 min separately and mixed together. To this mixture tetrakis(triphenylphosphine)palladium(0) [Pd(PPh₃)₄] (4.0 mg, 10.0 mol %) was added under nitrogen flow and degassed again for 10 min. The reaction flask was then sealed with Teflon tape and heated at 85 °C for 72 h in an oil bath. The organic layer was extracted with ethyl acetate and dried over anhydrous sodium sulfate. The solvent was evaporated under reduced pressure using a rotary evaporator and crude product was passed through small plug of silica column using 1–2% ethyl acetate in petroleum ether to remove inorganic impurities. The crude product was then dissolved in dry DCM (3 mL) and subjected to Scholl-type cyclodehydrogenation in the presence of DDQ (10 mg, 0.044 mmol) and BF₃OEt₂ (0.15 mL, 1.21 μmol) at 0 °C and warmed up to room temperature overnight (15 h). The reaction was quenched with sodium bicarbonate and the organic layer was extracted with DCM. The collected organic phase was dried over anhydrous sodium sulphate. The solvent was evaporated under reduced pressure using a rotary evaporator and crude product was passed through silica gel column using 10% ethyl acetate in petroleum ether to isolate **3Py** in 78% yield (23.8 mg) as yellow solid over two steps.

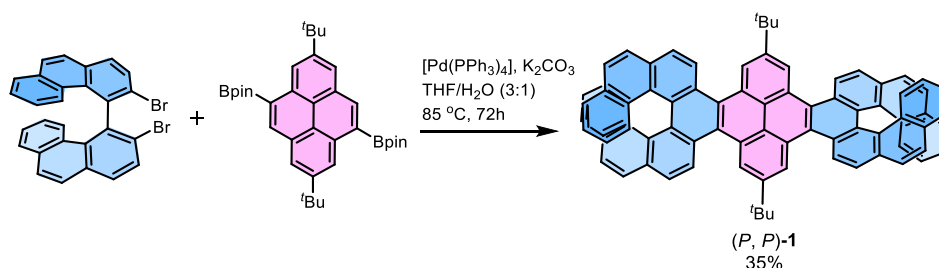
Characterization of **3Py**.

HRMS (MALDI-TOF) *m/z*: [M] Calcd for [C₆₈H₇₀] 886.5477; Found 886.5469

¹H NMR (400 MHz, CDCl₃, 25 °C): δ [ppm] = 9.26 – 9.28 (m, 8H), 8.30 (d, *J* = 1.5 Hz, 4H), 8.15 (s, 4H), 1.63 (s, 54H).

¹³C NMR (101 MHz, CDCl₃, 25 °C): δ [ppm] = 148.48, 148.28, 131.19, 129.51, 129.12, 128.96, 127.68, 123.38, 123.24, 123.00, 122.95, 122.37, 36.02, 35.67, 32.41, 32.28.

Synthesis of (*P, P*)-**1** by one pot Suzuki coupling – C-H activation.



In a Schlenk tube (*S*)-3,3'-dibromo-4,4'-biphenanthrene (70.0 mg, 0.13 mmol) and 2,2'-(2,7-di-tert-butylpyrene-4,9-diyl)bis(4,4,5,5-tetramethyl-1,3,2-dioxaborolane) (36.5 mg, 0.065 mmol) were dissolved in 3 mL dry THF and potassium carbonate (44.5 mg, 0.32

mmol) was dissolved in 1 mL water and both solutions were degassed for 10 min separately and mixed together. To this mixture $[\text{Pd}(\text{PPh}_3)_4]$ (7.5 mg, 10.0 mol %) was added under nitrogen flow and degassed again for 10 min. The reaction flask was then sealed with Teflon tape and heated at 85 °C for 72 h in an oil bath. The reaction was quenched by adding water and extracted with ethyl acetate. The collected organic phase was dried over anhydrous sodium sulfate. The solvent was evaporated under reduced pressure using a rotary evaporator and crude product was passed through silica column using 1–2% ethyl acetate in petroleum ether to isolate (*P, P*)-**1** in 35% (24.3 mg) yield.

Characterization of (*P, P*)-**1**.

Melting point: 196–198 °C

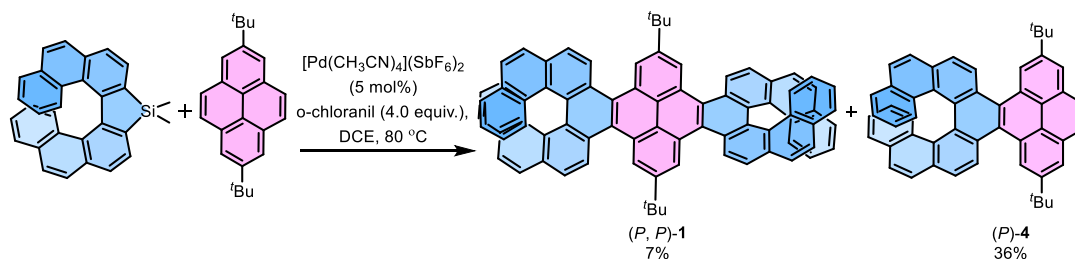
HRMS (MALDI-TOF) *m/z*: $[\text{M}]$ Calcd for $[\text{C}_{80}\text{H}_{54}]$ 1014.4226; Found 1014.4251

^1H NMR (400 MHz, CDCl_3 , 25 °C): δ [ppm] = 9.39 (s, 4H), 9.12 (d, $J = 8.6$ Hz, 4H), 8.20 (d, $J = 8.7$ Hz, 4H), 7.80 (d, $J = 8.5$ Hz, 4H), 7.55 (d, $J = 8.2$ Hz, 4H), 7.43 (d, $J = 8.9$ Hz, 4H), 7.39 (d, $J = 8.0$ Hz, 4H), 7.04 – 7.00 (m, 4H), 6.64 – 6.59 (m, 4H), 1.89 (s, 18H).

^{13}C NMR (101 MHz, CDCl_3 , 25 °C): δ [ppm] = 148.47, 132.26, 131.09, 129.64, 129.53, 128.90, 128.56, 128.23, 128.19, 127.78, 126.96, 125.90, 125.59, 125.36 (overlapped with two signals), 125.22, 124.05, 123.87, 123.78, 36.30, 32.38.

Synthesis of (*P, M*)-1**.** The Suzuki coupling–C–H activation was performed with 2,2'-(2,7-di-*tert*-butylpyrene-4,9-diyl)bis(4,4,5,5-tetramethyl-1,3,2-dioxaborolane) and *rac*-3,3'-dibromo-4,4'-biphenanthrene. The HPLC chromatogram of isolated diastereomeric mixture of **1** showed formations of chiral (*P**, *P**)-**1** to meso (*P, M*)-**1** in a 3.8:1 ratio. The (*P, M*)-**1** ^1H NMR is similar to that of (*P, P*)-**1** with a mere shift of 0.02 – 0.05 ppm in chloroform at room temperature.

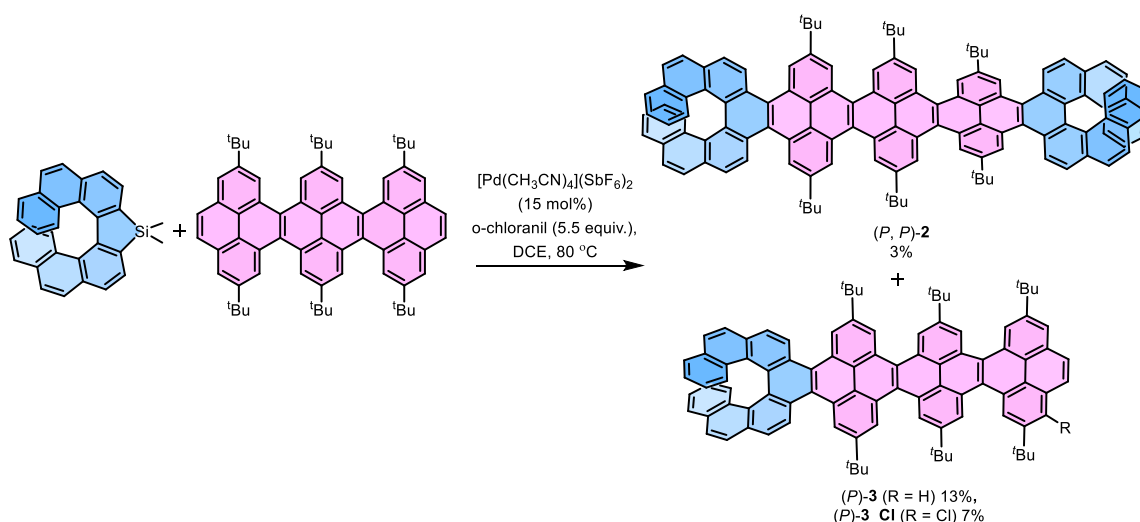
Synthesis of (*P, P*)-**1** by APEX reaction.



(*P*)-Dimethylsila[7]helicene (69 mg, 0.167 mmol, 3.5 equiv.), 2,7-di-*tert*-butylpyrene (15 mg, 0.048 mmol), $[\text{Pd}(\text{CH}_3\text{CN})_4](\text{SbF}_6)_2$ (1.8 mg, 5.0 mol%) and *o*-chloranil (47 mg, 0.191 mmol) were dissolved in dry dichloroethane (DCE) (2 mL) and degassed for 20 minutes.

The reaction mixture was heated at 80 °C for 15 h in an oil bath. The reaction mixture was cooled down to room temperature and DCE was evaporated under reduced pressure using rotary evaporator. The crude mixture was passed through silica column with petroleum ether – 2% ethyl acetate in petroleum ether to recover 7 mg (0.022 mmol) of 2,7-di-tert-butylpyrene along with (*P, P*)-**1** in 7% (1.9 mg, 0.002 mmol) and (*P*)-**4** in 36% (6.2 mg, 0.358 mmol) conversion. (The conversion efficiency is calculated considering the amount of 2,7-di-tert-butylpyrene reacted.) The isolated (*P, P*)-**1** was passed through chiral stationary phase HPLC to show single peak confirming the stereoselectivity of the reaction.

Synthesis of (*P, P*)-**2**, (*P*)-**3** and (*P*)-**3**_Cl by APEX reaction.



(*P*)-Dimethylsila[7]helicene (56mg, 0.135 mmol), **3Py** (20 mg, 0.022 mmol), $[\text{Pd}(\text{CH}_3\text{CN})_4](\text{SbF}_6)_2$ (2.5 mg, 15.0 mol%) and *o*-chloranil (30.5 mg, 0.124 mmol) were dissolved in 2 mL dry DCE and degassed for 20 minutes. The reaction mixture was heated at 80 °C for 15 h in an oil bath. The reaction mixture was cooled down to room temperature and DCE was evaporated under reduced pressure using rotary evaporator. The reaction was repeated four times and the combined crude mixture was passed through silica column with petroleum ether – 2% ethyl acetate in petroleum ether to recover 38 mg (0.043 mmol) of **3Py** along with (*P*)-**3** in 13% (7.6 mg, 0.006 mmol) and (*P*)-**3**_Cl in 7% (4.3 mg, 0.003 mmol) conversion. Further ethyl acetate concentration in the eluent mixture was increased gradually by 1 ml in each addition of 1000 ml of solvent to isolate (*P, P*)-**2** in 3% (2.1 mg, 0.001 mmol) conversion. (The conversion efficiencies are calculated considering the amount of 2,7-di-tert-butylpyrene reacted.)

Characterization of (*P*, *P*)-2.

HRMS (MALDI-TOF) m/z : [M] Calcd for [C₁₂₄H₉₈] 1587.7702; Found 1587.7721

¹H NMR (400 MHz, CD₂Cl₂, 25 °C): δ [ppm] = δ 9.44 (d, J = 1.5 Hz, 4H), 9.40 – 9.35 (m, 8H), 9.20 (d, J = 8.5 Hz, 4H), 8.27 (d, J = 8.6 Hz, 4H), 7.86 (d, J = 8.6 Hz, 4H), 7.59 (d, J = 9.0 Hz, 4H), 7.45 (d, J = 9.4 Hz, 4H), 7.42 (d, J = 9.5 Hz, 4H), 7.07 – 7.03 (m, 4H), 6.64 – 6.60 (m, 4H), 1.80 (s, 36H), 1.71 (s, 18H).

¹³C NMR (101 MHz, CD₂Cl₂, 25 °C): δ [ppm] = 149.05, 148.95, 132.53, 131.40, 130.22, 129.80, 129.76, 129.69, 129.22, 129.04, 128.87, 128.57, 128.37, 127.94, 127.18, 126.19, 125.76, 125.57, 125.46, 125.44, 124.72, 124.05, 123.69, 123.27, 122.93, 36.33, 36.29, 32.44, 32.31.

Characterization of (*P*)-3.

HRMS (MALDI-TOF) m/z : [M] Calcd for [C₉₆H₈₄] 1237.6563; Found 1237.6581

¹H NMR (400 MHz, CDCl₃, 25 °C): δ [ppm] = 9.40 (d, J = 1.3 Hz, 2H), 9.35 – 9.28 (m, 8H), 9.16 (d, J = 8.5 Hz, 2H), 8.31 (d, J = 1.7 Hz, 2H), 8.21 (d, J = 8.7 Hz, 2H), 8.16 (s, 2H), 7.81 (d, J = 8.6 Hz, 2H), 7.56 (d, J = 8.4 Hz, 2H), 7.45 (d, J = 8.5 Hz, 2H), 7.39 (d, J = 7.4 Hz, 2H), 7.05 – 7.01 (m, 2H), 6.64 – 6.60 (m, 2H), 1.78 (s, 18H), 1.66 (s, 18H), 1.64 (s, 18H).

¹³C NMR (101 MHz, CDCl₃, 25 °C): δ [ppm] = 148.52, 148.38, 148.35, 132.26, 131.22, 131.08, 129.66, 129.59, 129.53, 129.21, 129.07, 129.03, 129.00, 128.92, 128.66, 128.24, 128.19, 127.76, 127.71, 126.97, 125.91, 125.64, 125.34, 125.29, 125.24, 124.40, 123.78, 123.59, 123.42, 123.27, 123.11, 123.04, 122.98, 122.80, 122.41, 122.21, 36.16, 36.06, 35.70, 32.43, 32.38, 32.30.

Characterization of (*P*)-3_Cl.

HRMS (MALDI-TOF) m/z : [M] Calcd for [C₉₆H₈₃Cl] 1271.6183; Found 1271.6189

¹H NMR (400 MHz, CDCl₃, 25 °C): δ [ppm] = 9.41 (d, J = 1.7 Hz, 2H), 9.35 – 9.28 (m, 7H), 9.19 (d, J = 1.6 Hz, 1H), 9.16 (d, J = 8.5 Hz, 2H), 8.78 (d, J = 9.4 Hz, 1H), 8.35 (d, J = 1.7 Hz, 1H), 8.27 (d, J = 9.5 Hz, 1H), 8.21 (d, J = 8.6 Hz, 2H), 7.81 (d, J = 8.6 Hz, 2H), 7.56 (d, J = 8.5 Hz, 2H), 7.47 – 7.42 (m, 2H), 7.39 (d, J = 8.0, 2H), 7.05 – 7.01 (m, 2H), 6.64 – 6.60 (m, 2H), 1.82 – 1.76 (m, 27H), 1.68 – 1.64 (m, 27H).

¹³C NMR (101 MHz, CDCl₃, 25 °C): δ [ppm] = 149.37, 148.56, 148.52, 148.37, 148.34, 143.60, 132.26, 131.08, 130.92, 129.87, 129.65, 129.57, 129.52, 129.50, 129.42, 129.37, 129.33, 129.20, 129.11, 129.09, 129.03, 128.92, 128.87, 128.63, 128.26, 128.20, 127.78, 127.50, 126.97, 125.91, 125.61, 125.35, 125.30, 125.23, 125.09, 124.70, 124.47, 123.97,

123.86, 123.78, 123.61, 123.41, 123.39, 123.20, 123.09, 123.00, 122.76, 122.72, 122.68, 122.58, 122.57, 122.51, 37.63, 36.16, 36.08, 35.74, 32.43, 32.41, 32.38, 32.30, 32.25, 30.87, 29.90.

S3. Chiral stationary phase HPLC

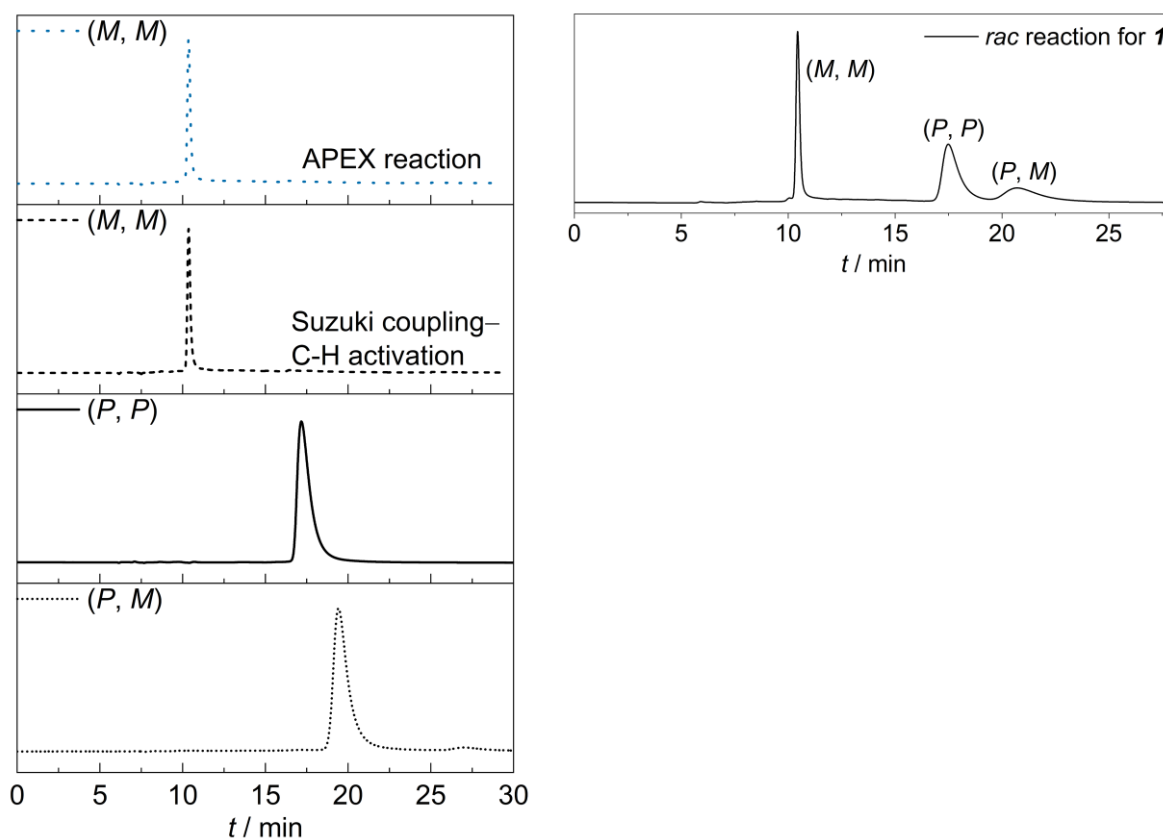


Figure S1. HPLC chromatogram of **1** using chiral stationary phase column. (The chromatogram detector was set at 354 nm with a bandwidth of 4 nm.)

Table S1. Overview of parameters for HPLC separation of enantiomers of **1**.

Compound	Eluent <i>n</i> -hexane/ <i>i</i> PrOH	First fraction	Second fraction	Third fraction	α^b	R_s^c	<i>er</i>
1	97:3	<i>MM</i>	<i>PP</i>	<i>PM</i>	1.63	1.79	99:1

^aPhenomenex Lux i-Amylose-3 5 μ m (250 x 4.6 mm). Sample injection: 30 μ L of a ~1 mg/mL solution in hexane/*i*PrOH. Separation conditions: Eluent, flow rate: 0.5 mL/min, 25 $^{\circ}$ C. ^bSelectivity parameter: $\alpha = t_{R2} / t_{R1}$, where t_{R1} , and t_{R2} are elution times for first and second fraction, respectively. ^cResolution parameter: $R_S = 2(t_{R2} - t_{R1}) / (w_1 + w_2)$, where w_1 and w_2 are peak widths for first and second fraction, respectively. Note α and R_s was calculated only for *PP* and *MM*.

S4. Determination and analysis of activation parameters for diastereomerization of **1**.

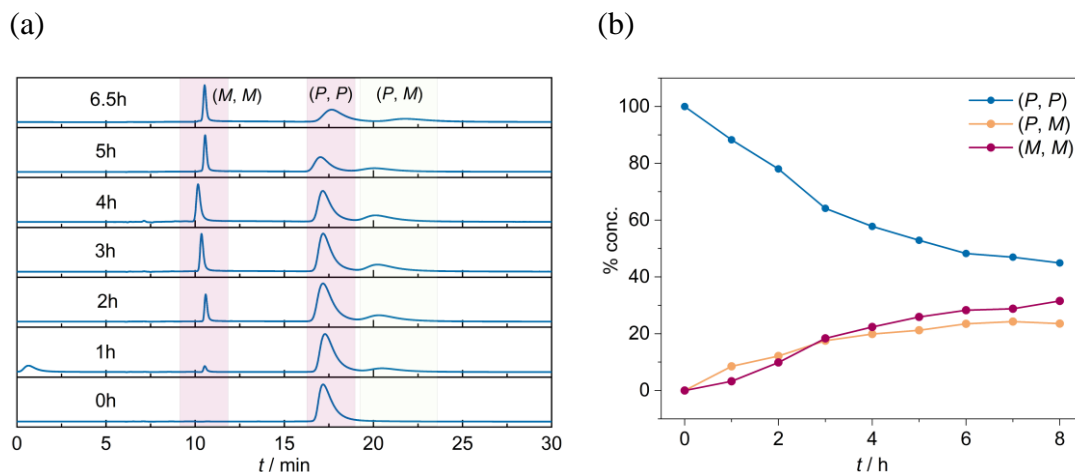


Figure S2. HPLC chromatogram of (*P, P*)-**1** upon heating at 173 °C over time using chiral stationary phase column. (The HPLC chromatogram detector was set at 354 nm with a bandwidth of 4 nm.)

The Gibbs activation energies (ΔG^\ddagger (T)) for diastereomerization of **1** calculated by following the decay of the diastereomeric excess (*de*) of (*P, P*)-**1** dissolved in diethylene glycol dibutyl ether (1-(2-(2-butoxyethoxy)ethoxy)butane) at 423, 433, 443, 453 K over time (*t*) by HPLC on a chiral stationary phase. To estimate the ΔG^\ddagger (T) value, the $\ln(de_t/de_0)$ values were plotted against *t* and the data set was linearly fitted (Figure S3). Following the equation

$$\ln\left(\frac{de_t}{de_0}\right) = -k_d t$$

the k_d (diastereomerization rate constant) values were obtained.

The enthalpy (ΔH) and entropy (ΔS) values were obtained using the following equation

$$\ln\left(\frac{k_d}{T}\right) = \left(\ln\left(\frac{\kappa k_B T}{h}\right) + \frac{\Delta S}{R}\right) - \left(\frac{\Delta H}{R}\right)\left(\frac{1}{T}\right)$$

where, R is the gas constant ($R = 8.31446 \text{ J K}^{-1}$), h is the Planck constant ($h = 6.62607 \times 10^{-34} \text{ J s}$), k_B is the Boltzmann constant ($k_B = 1.38064852 \times 10^{-23} \text{ J K}^{-1}$), and κ is the transmission coefficient ($\kappa = 0.5$ or 1). The transmission coefficient $\kappa = 0.5$ was used because the diastereomerization process is defined as a reversible first order reaction.

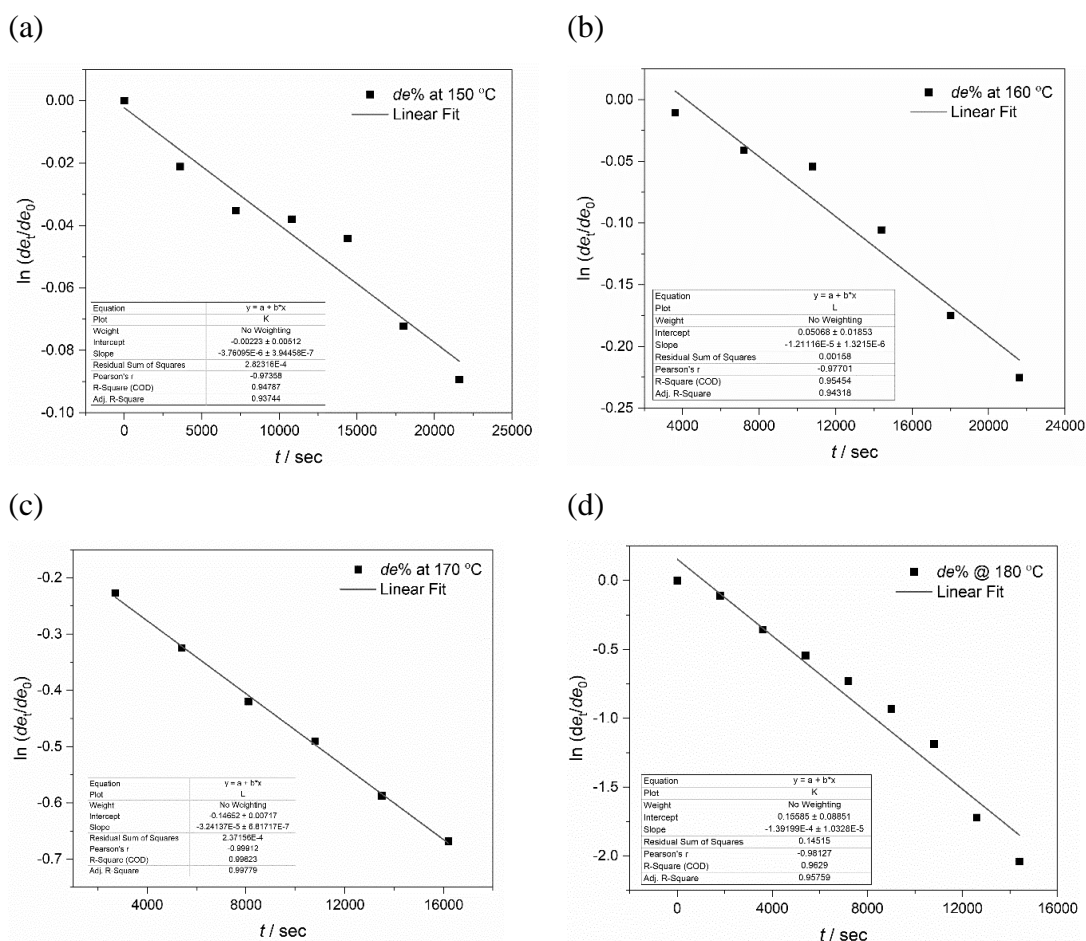


Figure S3a. Plot of $\ln(de_t/de_0)$ against t for **1** fitted linearly to obtain the k_d value.

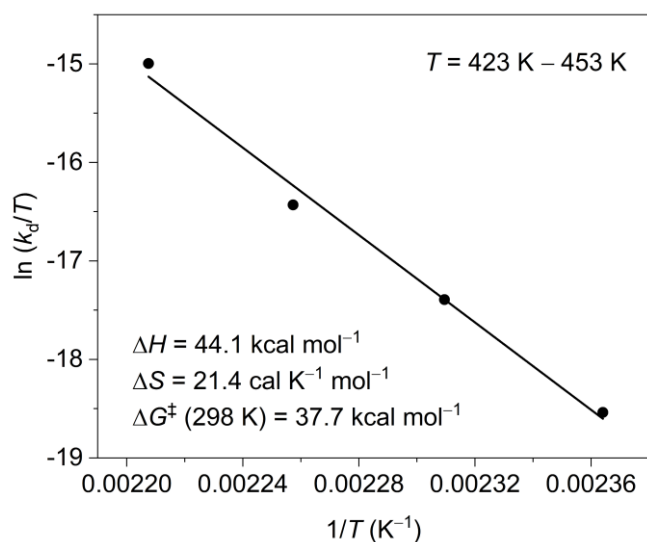


Figure S3b. Plot of $\ln(k_d/T)$ against $1/T$ for **(P, P)-1** fitted linearly to obtain the ΔH and ΔS values.

S5. Photophysical Studies

a. Absorption and Emission Spectroscopy

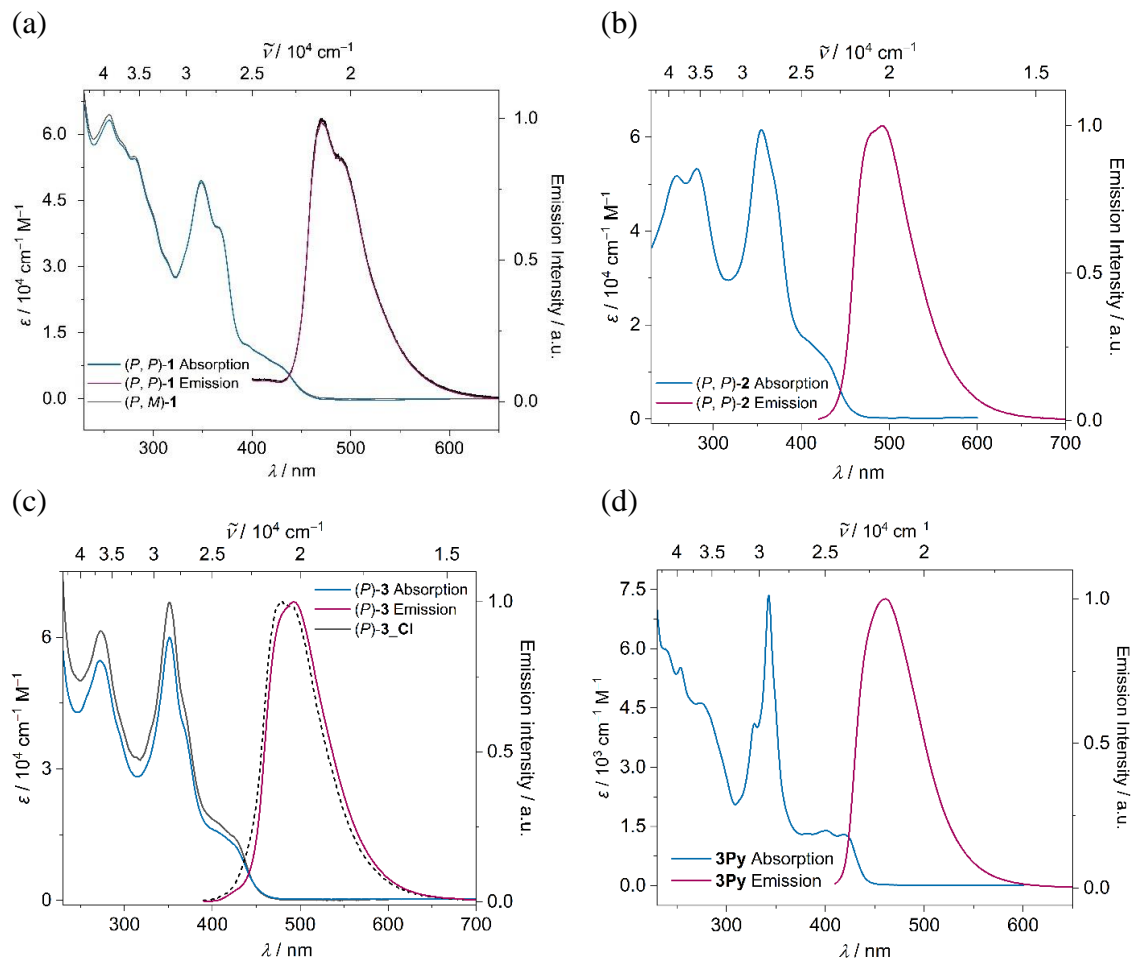


Figure S4. UV–Vis absorption (blue) and emission (red) spectra of (a) (*P, P*)-1 and (*P, M*)-1, (b) (*P, P*)-2, (c) (*P*)-3 and (*P*)-3_Cl, (d) 3Py in dichloromethane ($c \sim 10^{-5}$ M).

Table S2. Summary of (chir)optical parameters.

Compound	λ_{maxabs} (nm)/ ϵ ($\text{cm}^{-1} \text{M}^{-1}$)	λ_{maxem} (nm)	E_g / eV ^a	Φ_{FL}	τ_{FL} / ns	k_{FL} / 10^8 s^{-1}	k_{NR} / 10^8 s^{-1}	g_{abs}^d / 10^{-3}	g_{lum} / 10^{-3}
(<i>P, P</i>)-1	431 (7325)	473	2.83	0.05	5.55 ^b	0.09 ^c	1.72 ^c	2.64 – 1.17	0.63
(<i>P, M</i>)-1	430 (7167)	472	2.83	0.04	5.62 ^b	0.07 ^c	1.71 ^c	–	–
(<i>P, P</i>)-2	425 (13393)	492	2.79	0.15	5.07	0.29	1.68	4.05 – 1.92	1.54
(<i>P</i>)-3	426 (12533)	493	2.80	0.19	5.13	0.37	1.58	2.43 – 1.16	0.54
(<i>P</i>)-3_Cl	428 (13691)	480	2.84	0.22	5.09 ^b	0.43	1.53 ^c	3.46 – 0.87	0.83
3Py	420(1293)	461	2.92	0.21	3.92 ^b	0.54	2.01 ^c	–	–

^aEstimated from a crossing of absorption and fluorescence spectra ^b $\tau_{\text{avg}}^{[14]} = (\alpha_1 \tau_1^2 + \alpha_2 \tau_2^2) / (\alpha_1 \tau_1 + \alpha_2 \tau_2)$ ^cCalculated for τ_{avg} ^dWavelength range 230 – 450 nm

b. Time resolved fluorescence decay.

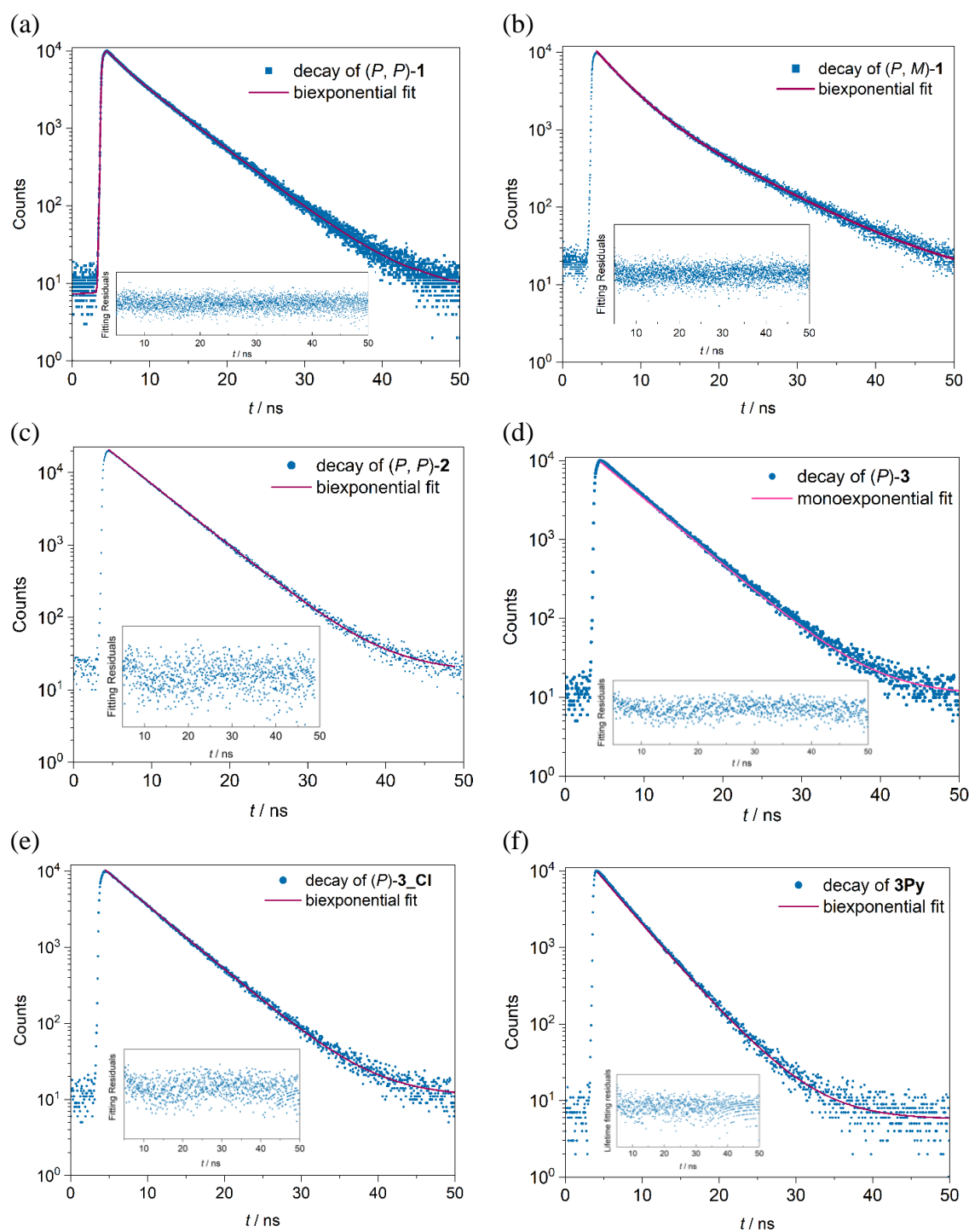


Figure S5. Time resolved fluorescence decay (excited at 24154 cm^{-1}) of (a) (P, P) -1, (b) (P, M) -1, (c) (P, P) -2, (d) (P) -3, (e) (P) -3_CI (f) 3Py in dichloromethane ($c \sim 10^{-5}\text{ M}$). Inset-fitting residuals.

c. ECD and CPL spectroscopy

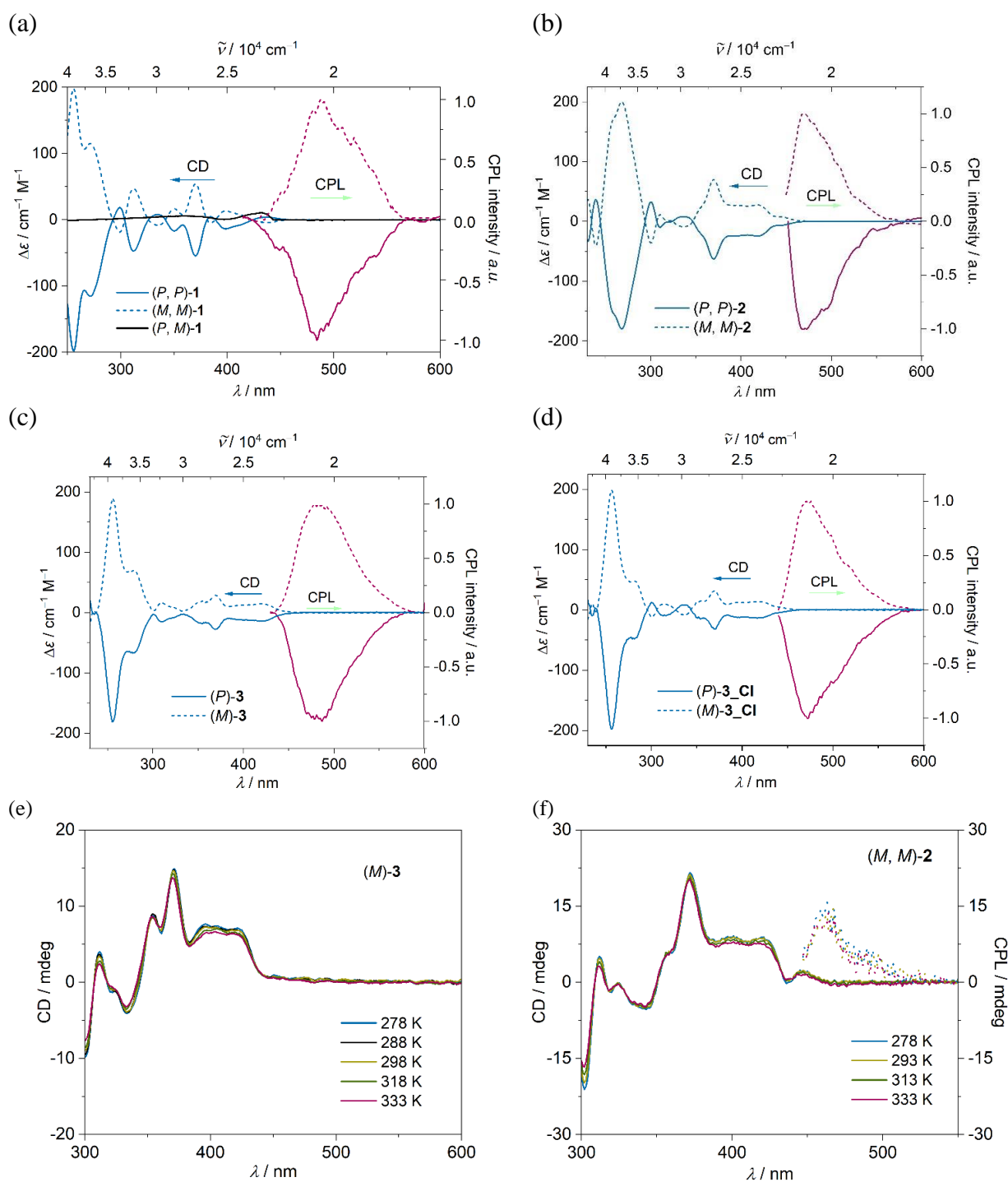


Figure S6. ECD (blue) and CPL (red) spectra of (a) **1**, (b) **2**, (c) **3** and (d) **3-Cl** in dichloromethane and variable temperature ECD (solid) and CPL (dotted) spectra of (e) **(M)-3**, (f) **(M, M)-2** in toluene ($c \sim 10^{-5} \text{ M}$).

d. Absorption and luminescence dissymmetry factors.

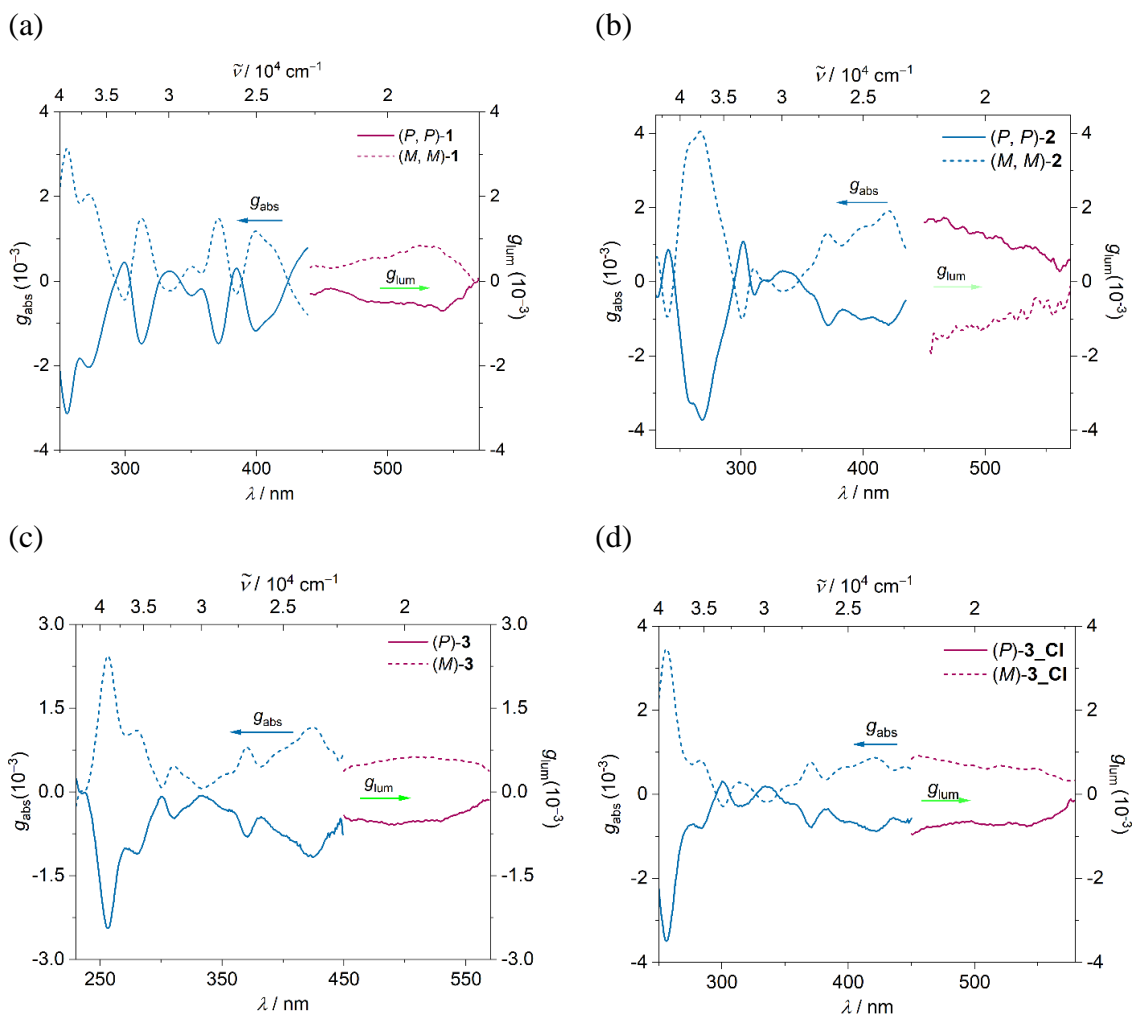


Figure S7. Absorption dissymmetry factor (g_{abs}) (blue) and luminescence dissymmetry factor (g_{lum}) (red) of enantiomers of (a) **1**, (b) **2**, (c) **3** and (d) **3-Cl** in dichloromethane ($c \sim 10^{-5} \text{ M}$).

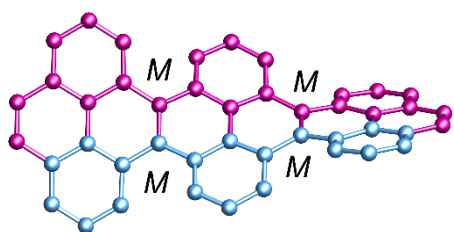
Table S3. Calculated electric and magnetic transition moments, and dissymmetry factor for $S_0 \rightarrow S_1$ and $S_1 \rightarrow S_0$ transitions.

Compound	$S_0 \rightarrow S_1$				$S_1 \rightarrow S_0$			
	$ \mu' / 10^{-20} \text{ esu cm}$	$ m' / 10^{-20} \text{ erg G}^{-1}$	$ \cos\theta' $	$ g_{\text{abs}} / 10^{-3}$	$ \mu / 10^{-20} \text{ esu cm}$	$ m / 10^{-20} \text{ erg G}^{-1}$	$ \cos\theta $	$ g_{\text{lum}} / 10^{-3}$
1	353.23	0.10	0.94	1.0	461.35	0.33	0.31	0.9
2	366.92	0.77	0.96	8.0	395.89	0.80	0.94	7.6
3	356.51	0.13	0.64	0.9	331.29	0.08	0.63	0.6

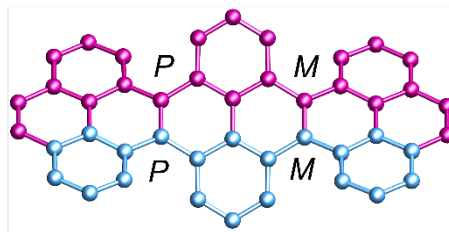
S6. Quantum chemical calculations

Conformational diastereomers: Hydrogen atoms and tert-butyl groups are omitted for clarity.

(a) Relative Gibbs's free energies and optimized geometries of diastereomers of **3Py**.

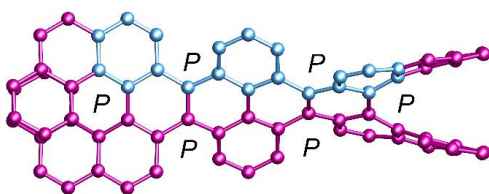


Helical-**3Py**
(0.56 kcal mol⁻¹)

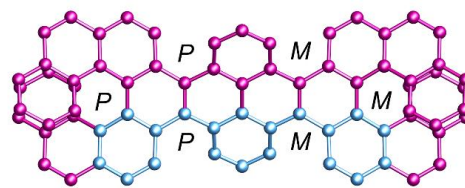


Wagging-**3Py**
(0.0 kcal mol⁻¹)

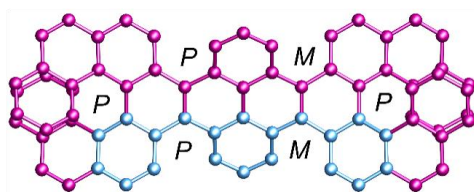
(b) Relative Gibbs's free energies and optimized geometries of diastereomers of **1**.



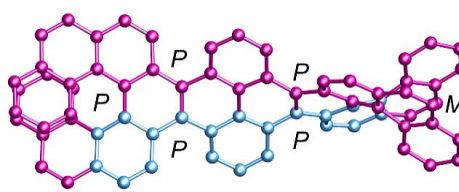
Right handed Helical
(*P,P*)-**1** (8.79 kcal mol⁻¹)



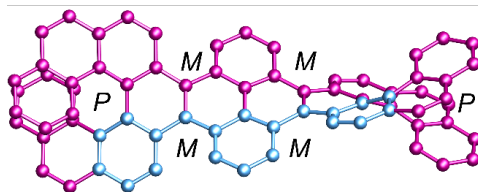
Wagging_2
(*P,M*)-**1** (5.91 kcal mol⁻¹)



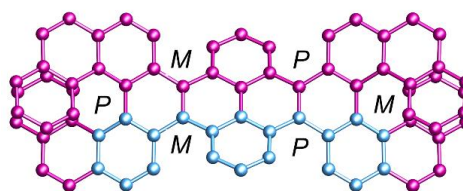
Wagging
(*P,P*)-**1** (4.38 kcal mol⁻¹)



Helical
(*P,M*)-**1** (3.11 kcal mol⁻¹)

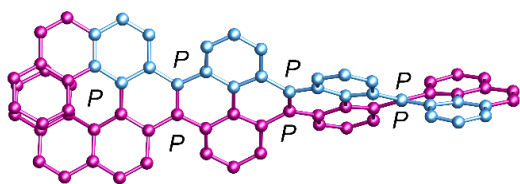


Left handed Helical
(*P,P*)-**1** (0.0 kcal mol⁻¹)

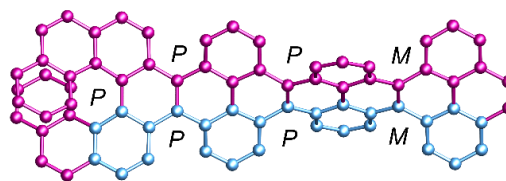


Wagging_1
(*P,M*)-**1** (0.0 kcal mol⁻¹)

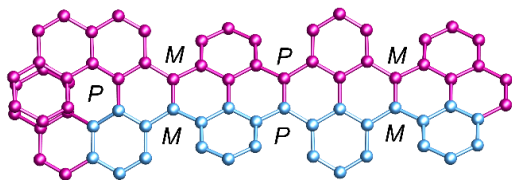
(c) Relative Gibbs's free energies and optimized geometries of diastereomers of (*P*)-**3**.



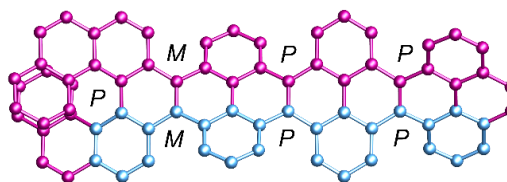
Right handed Helical
(*P*)-**3** (5.17 kcal mol⁻¹)



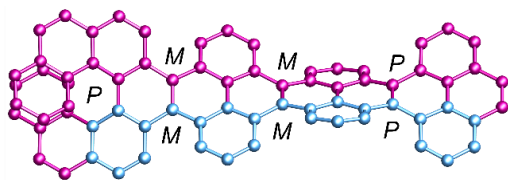
Wagging_4
(*P*)-**3** (5.16 kcal mol⁻¹)



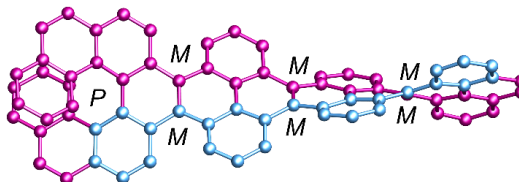
Wagging_3
(*P*)-**3** (2.54 kcal mol⁻¹)



Wagging_2
(*P*)-**3** (2.50 kcal mol⁻¹)

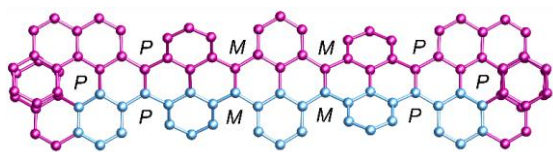


Wagging_1
(*P*)-**3** (1.91 kcal mol⁻¹)

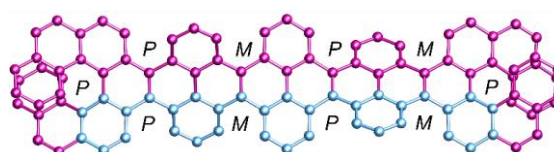


Left handed Helical
(*P*)-**3** (0.0 kcal mol⁻¹)

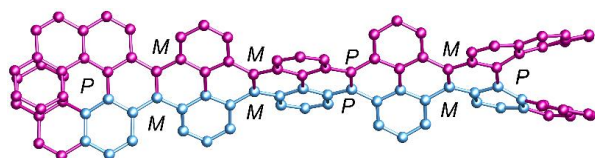
(d) Relative Gibbs's free energies and optimized geometries of diastereomers of (*P,P*)-2.



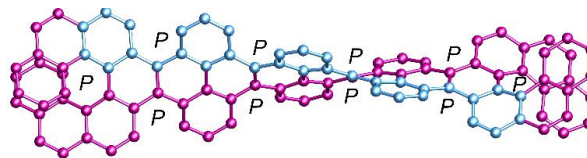
Wagging_6
(*P,P*)-2 (13.29 kcal mol⁻¹)



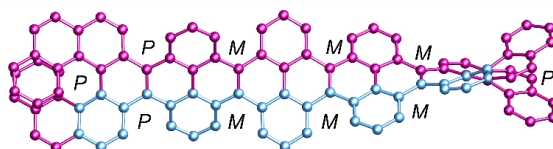
Wagging_5
(*P,P*)-2 (12.23 kcal mol⁻¹)



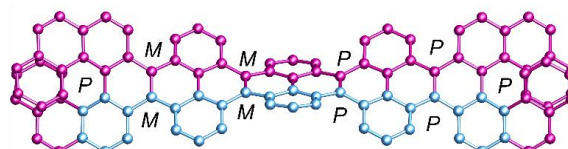
Wagging_4
(*P,P*)-2 (11.15 kcal mol⁻¹)



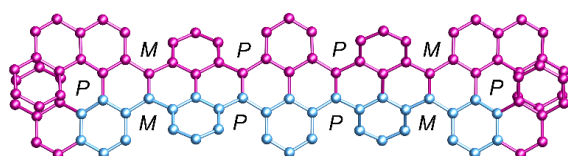
Right handed Helical
(*P,P*)-2 (9.20 kcal mol⁻¹)



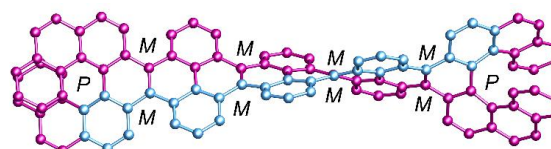
Wagging_3
(*P,P*)-2 (6.98 kcal mol⁻¹)



Wagging_2
(*P,P*)-2 (6.71 kcal mol⁻¹)

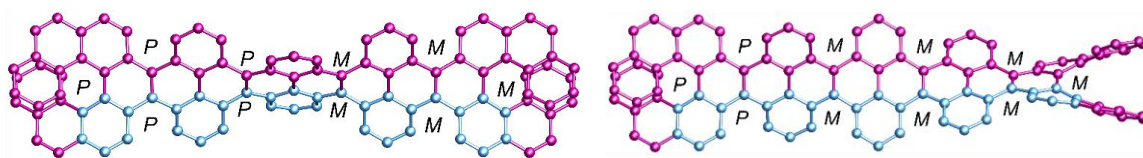


Wagging_1
(*P,P*)-2 (4.37 kcal mol⁻¹)



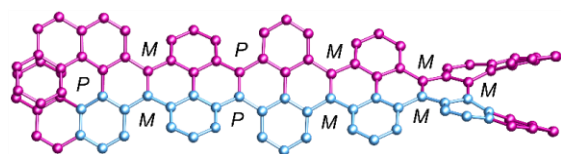
Left handed Helical
(*P,P*)-2 (0.0 kcal mol⁻¹)

(e) Relative Gibbs's free energies and optimized geometries of diastereomers of (P, M) -2.

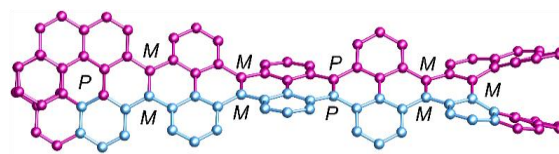


Wagging_6
 (P,M) -2 (7.51 kcal mol⁻¹)

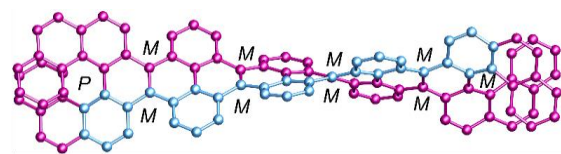
Wagging_5
 (P,M) -2 (6.79 kcal mol⁻¹)



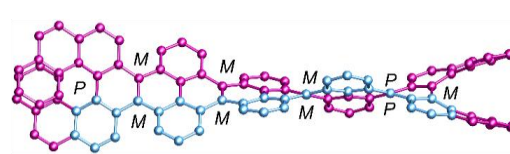
Wagging_4
 (P,M) -2 (4.34 kcal mol⁻¹)



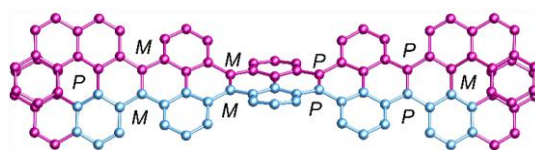
Wagging_3
 (P,M) -2 (4.04 kcal mol⁻¹)



Helical
 (P,M) -2 (2.75 kcal mol⁻¹)

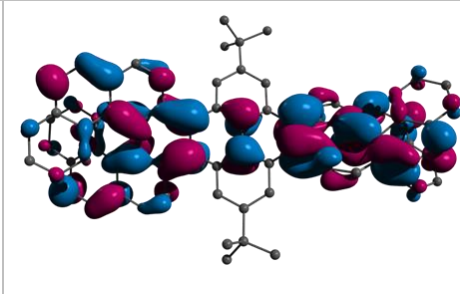
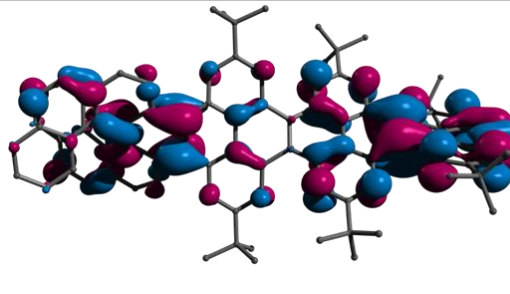
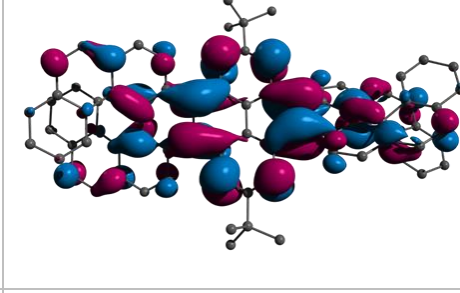
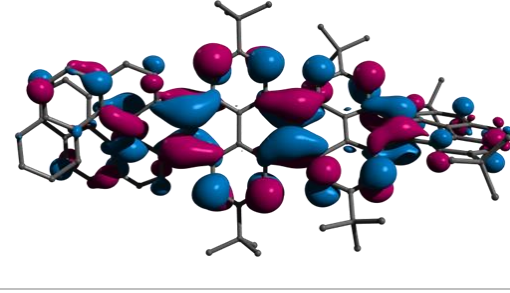
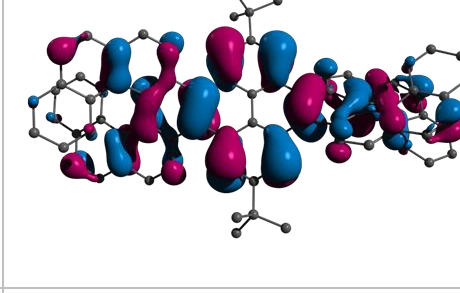
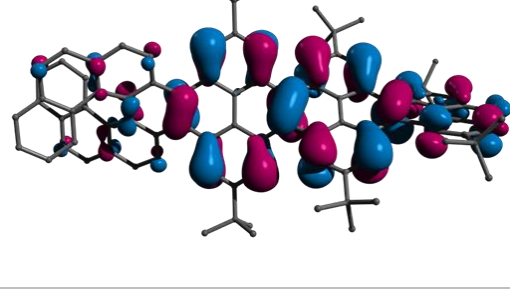
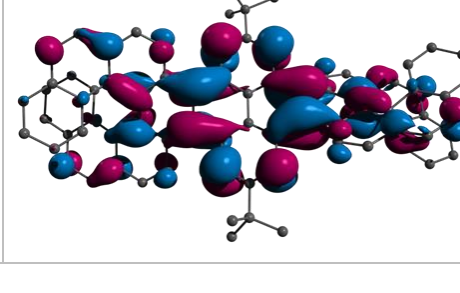
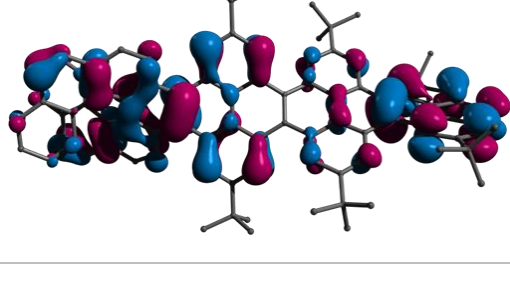


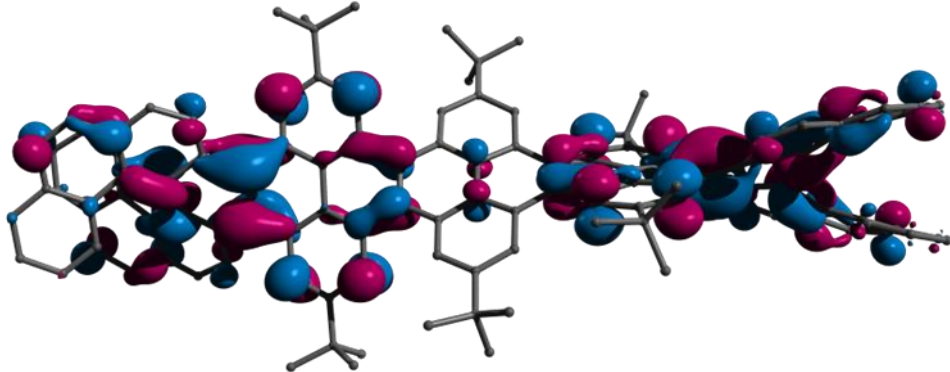
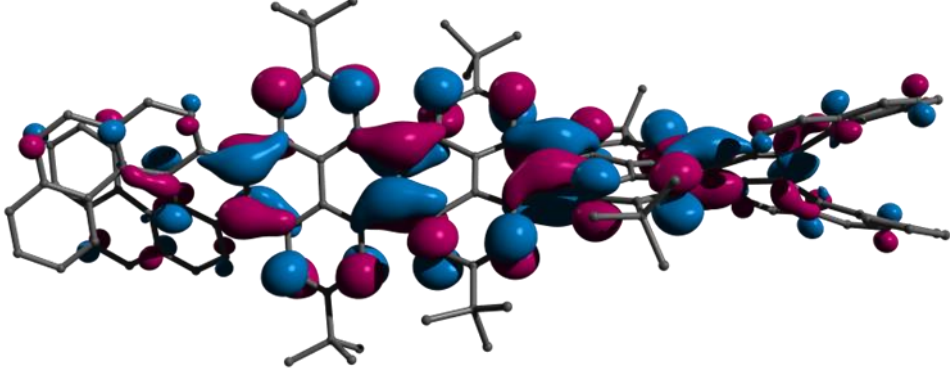
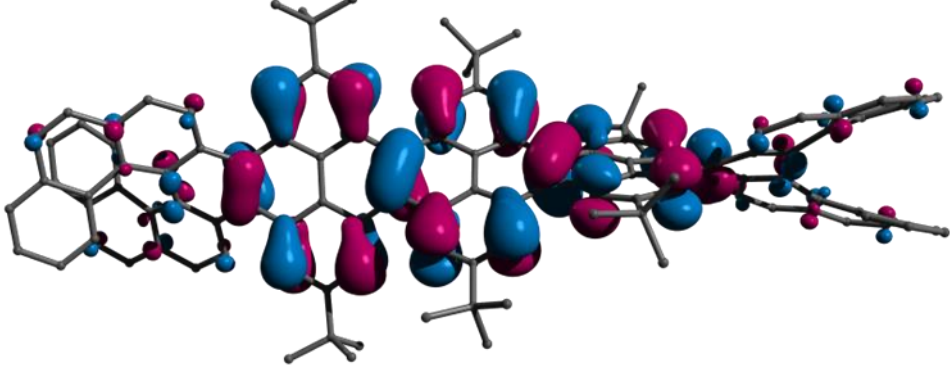
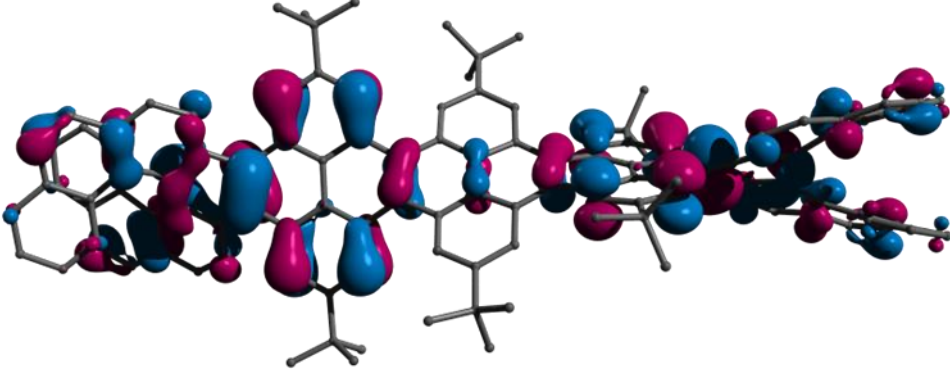
Wagging_2
 (P,M) -2 (0.38 kcal mol⁻¹)



Wagging_1
 (P,M) -2 (0.0 kcal mol⁻¹)

Table S4. Frontier molecular orbitals of **1**, **2** and **3** (isosurface value 0.02). Hydrogen atoms are omitted for clarity.

FMOs	1	3
LUMO+1		
LUMO		
HOMO		
HOMO-1		

FMOs	2
LUMO+1	
LUMO	
HOMO	
HOMO-1	

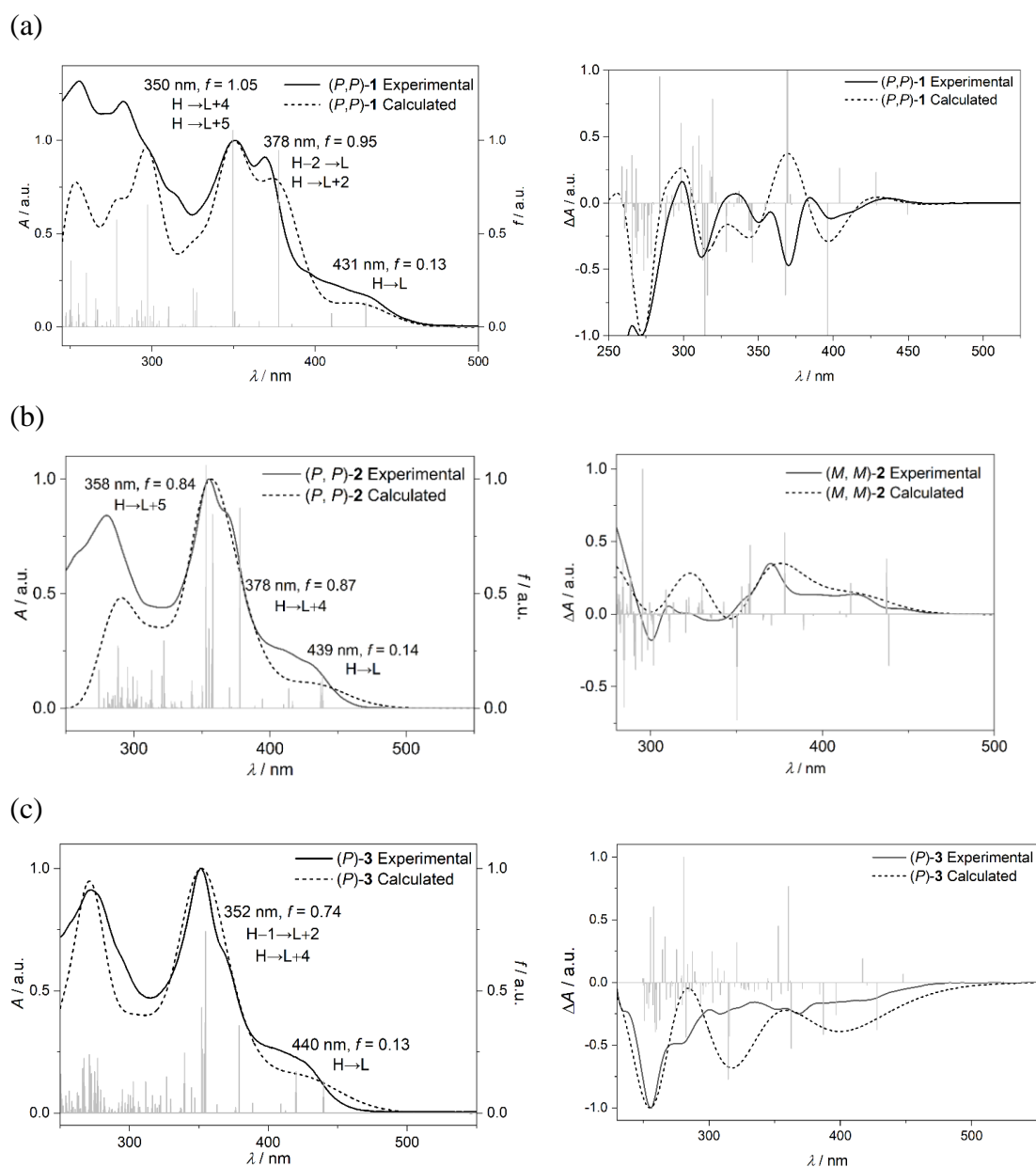


Figure S8. Comparison of experimental (solid) and TD-DFT calculated (dashed) UV-Vis absorption (left) and ECD spectra (right) of (a) (P, P) -1 (shifted by 0.09 eV, 14 nm), (b) (P, P) -2 (shifted by 0.09 eV, 15 nm) and (c) (P) -3 (shifted by 0.08 eV, 13 nm) along with assignments of key transitions. H = HOMO, L = LUMO, f = oscillator strength.

Table S5a. Summary of TD-DFT calculated key low energy transitions of **1**.

Excited singlet state	Wavelength / nm	Energy / eV	Major transitions	Contribution	Oscillator strength (<i>f</i>)
1	431	2.87	HOMO→LUMO	0.69	0.13
2	378	3.28	HOMO-2→LUMO	0.51	0.95
			HOMO→LUMO+2	0.41	
3	350	3.54	HOMO→LUMO+4	0.53	1.05
			HOMO→LUMO+5	0.24	

Table S5b. Summary of TD-DFT calculated key low energy transitions of **2**.

Excited singlet state	Wavelength / nm	Energy / eV	Major transitions	Contribution	Oscillator strength (<i>f</i>)
1	439	2.82	HOMO→LUMO	0.68	0.14
9	378	3.28	HOMO→LUMO+4	0.44	0.87
			HOMO-3→LUMO	0.31	
15	358	3.46	HOMO→LUMO+5	0.34	0.84
			HOMO-1→LUMO+3	0.31	
19	353	3.51	HOMO-1→LUMO	0.36	1.06
			HOMO→LUMO+6	0.28	

Table S5c. Summary of TD-DFT calculated key low energy transitions of **3**.

Excited singlet state	Wavelength / nm	Energy / eV	Major transitions	Contribution	Oscillator strength (<i>f</i>)
1	440	2.82	HOMO→LUMO	0.67	0.13
6	379	3.27	HOMO-2→LUMO	0.47	0.36
10	352	3.52	HOMO→LUMO+4	0.28	0.74
			HOMO-1→LUMO+2	0.41	

NICS calculations: The Nucleus Independent Chemical Shift (NICS) calculations were performed on ω B97XD/6-31G(d,p) optimized geometry at GIAO-B3LYP/6-311+G(2d,p) level. Considering the non-planarity of molecules, the NICS(1)_{zz} values were obtained by placing dummy atom at 1 Å above and below the each ring.

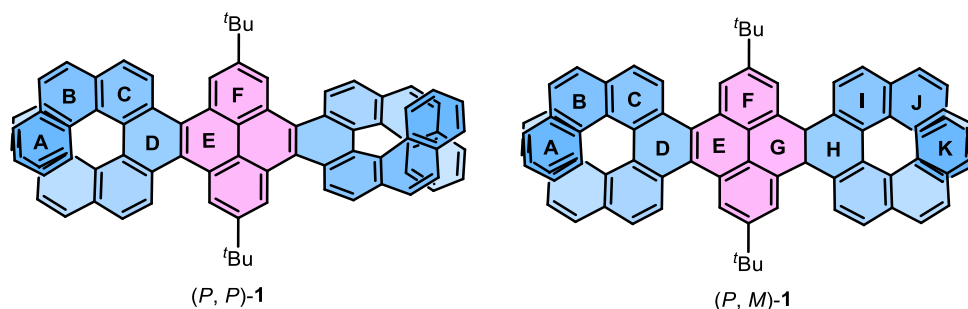


Table S6a. The calculated NICS(0) and NICS(1)_{zz} values for (P, P) -1 and (P, M) -1 .

Ring	(P, P) -1			(P, M) -1		
	NICS(1) _z z (Up)	NICS(1) _z z (Down)	NICS(0) iso	NICS(1) _z z (Up)	NICS(1) _z z (Down)	NICS(0) iso
A	-29.54	-32.46	-9.29	-32.30	-34.16	-9.39
B	-20.89	-20.58	-5.13	-21.88	-21.45	-5.17
C	-15.63	-9.55	-5.05	-18.68	-12.11	-4.98
D	-9.55	-4.52	-1.01	-7.82	-7.82	-1.01
E	-5.83	-5.84	0.57	-3.13	-3.17	1.18
F	-26.33	-26.57	-8.33	-21.53	-28.70	-8.18
G				-3.17	-3.13	1.18
H				-7.81	-7.81	-1.01
I				-18.71	-12.09	-4.98
J				-21.90	-21.47	-5.19
K				-32.11	-34.11	-9.37

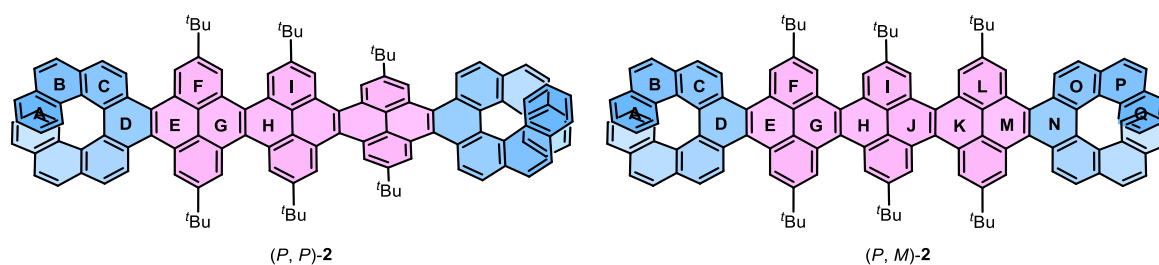


Table S6b. The calculated NICS(0) and NICS(1)_{zz} values for (P, P)-2 and (P, M)-2.

Ring	(P, P)-2			(P, M)-2		
	NICS(1) _z z (Up)	NICS(1) _z z (Down)	NICS(0) iso	NICS(1) zz (Up)	NICS(1) _z z (Down)	NICS(0) iso
A	-11.99	-14.24	-9.37	-27.09	-30.49	-9.31
B	-10.76	-9.28	-5.24	-19.59	-19.17	-5.05
C	-3.15	-1.96	-4.94	-13.37	-7.75	-4.95
D	2.08	1.37	-1.09	-2.88	-3.04	-1.05
E	-2.90	-3.39	1.58	-4.55	-14.55	1.19
F	-20.29	-14.09	-8.23	-26.67	-24.69	-8.23
G	-3.79	-3.83	0.61	-5.29	-5.19	0.98
H	-5.94	-6.18	1.04	-1.32	-1.25	1.23
I	-26.99	-26.88	-8.26	-13.26	-24.02	-8.13
J				-1.20	-1.10	1.30
K				-6.07	-6.11	0.66
L				-26.71	-24.84	-8.21
M				-3.65	-3.72	1.53
N				-3.31	-3.33	-1.13
O				-13.71	-8.01	-4.94
P				-19.69	-19.34	-5.01
Q				-27.51	-30.91	-9.32

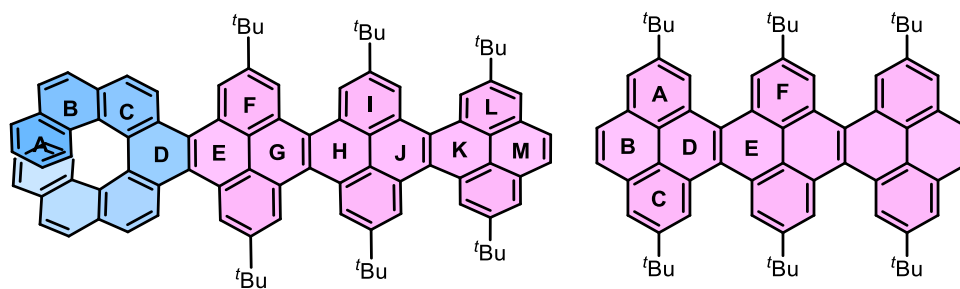


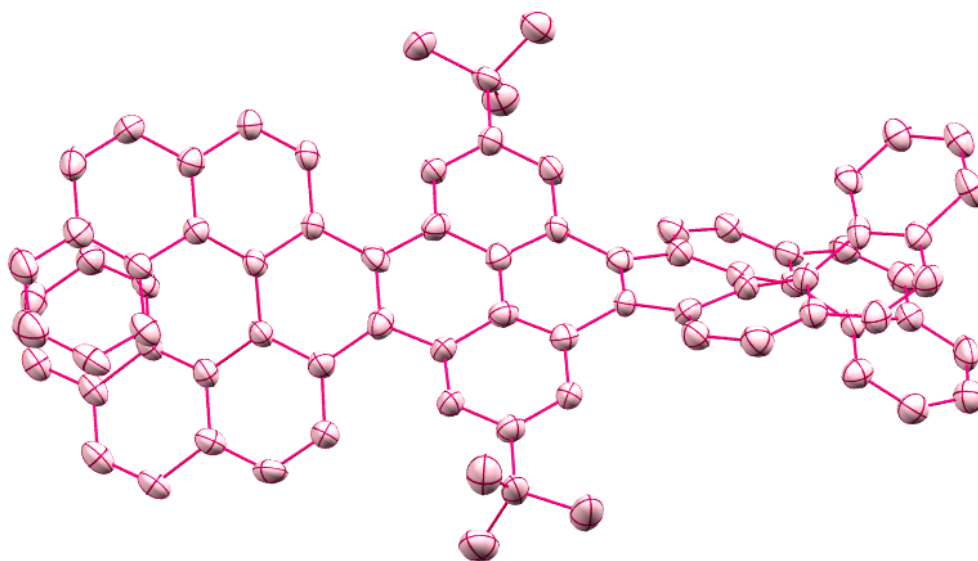
Table S6c. The calculated NICS(0) and NICS(1)_{zz} values for (*P*)-**3** and **3Py**.

Ring	(<i>P</i>)- 3			3Py		
	NICS(1) _z z (Up)	NICS(1) _z z (Down)	NICS(0) iso	NICS(1) zz (Up)	NICS(1) _z z (Down)	NICS(0) iso
A	-11.96	-14.05	-9.35	-26.37	-30.95	-9.40
B	-10.87	-9.22	-5.22	-14.56	-14.56	-2.92
C	-3.26	-1.85	-4.99	-30.95	-26.36	-9.40
D	1.92	1.51	-1.02	-4.04	-4.04	1.36
E	-3.66	-3.88	1.20	-2.74	-2.74	0.99
F	-20.39	-14.34	-8.29	-26.07	-16.19	-8.32
G	-3.28	-3.23	0.88			
H	-6.07	-6.06	1.01			
I	-26.90	-27.24	-8.31			
J	-6.14	-6.51	0.86			
K	-3.45	-3.36	0.58			
L	-15.26	-23.35	-9.54			
M	-7.63	-8.11	-1.99			

S7. X-Ray crystallography

The single crystals were grown by slow diffusion of hexane (HPLC grade) to solution of (*P, P*)-**1** and **3Py** in DCM (HPLC grade) in a NMR tube. Crystallographic data have been deposited with the Cambridge Crystallographic Data Centre as supplementary publication no. CCDC 2315652 and 2315653. These data can be obtained free of charge from the Cambridge Crystallographic Data Centre via www.ccdc.ac.uk/data.request/cif.

(a)



(b)

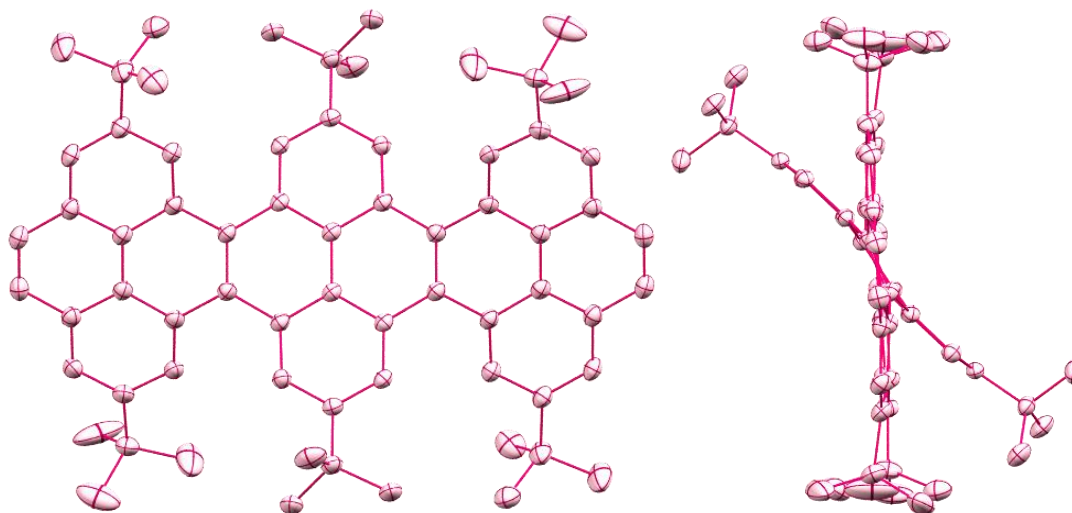


Figure S9. ORTEP diagram of (a) (*P, P*)-**1** and (b) **3Py**. Thermal ellipsoids are shown at the 50% probability level. Hydrogen atoms are omitted for clarity.

Table S7. Crystallographic table for (*P, P*)-**1** and **3Py**.

Data	(<i>P, P</i>)- 1	3Py
CCDC	2315653	2315652
Empirical formula	C ₈₃ H ₆₀ Cl ₆	C ₇₀ H ₇₄ Cl ₄
Formula weight (g·mol ⁻¹)	1270.01	1057.09
Temperature (K)	100.01(10)	100(2)
Radiation, λ (Å)	CuKα, 1.54184	CuKα, 1.54184
Crystal system	triclinic	triclinic
Space group	<i>P</i> 1	<i>P</i> 1
<i>Unit cell dimensions</i>		
<i>a</i> (Å)	14.6922(4)	14.16160(10)
<i>b</i> (Å)	15.4658(4)	14.61250(10)
<i>c</i> (Å)	16.5251(4)	15.92860(10)
α (°)	114.189(3)	66.4050(10)
β (°)	109.595(3)	76.5680(10)
γ (°)	93.418(2)	74.1110(10)
Volume (Å ³)	3140.90(17)	2876.94(4)
<i>Z</i>	2	2
Calculated density (Mg·m ⁻³)	1.343	1.220
Absorption coefficient (mm ⁻¹)	2.862	
<i>F</i> (000)	1320	1124
Theta range for collection	3.191 to 73.493°	3.057 to 75.002°
Reflections collected	31564	123212
Independent reflections	31564	11428
Minimum/maximum transmission	0.64500/1.00000	0.675/1.000
Refinement method	Full-matrix least-squares on <i>F</i> ²	Full-matrix least-squares on <i>F</i> ²
Data / parameters / restraints	31564 / 1648 / 235	11428 / 687 / 413
Goodness-of-fit on <i>F</i> ²	1.052	1.072
Final <i>R</i> indices [<i>I</i> > 2σ(<i>I</i>)]	<i>R</i> ₁ = 0.0936, <i>wR</i> ₂ = 0.2424	<i>R</i> ₁ = 0.0643, <i>wR</i> ₂ = 0.1687
<i>R</i> indices (all data)	<i>R</i> ₁ = 0.1143, <i>wR</i> ₂ = 0.2691	<i>R</i> ₁ = 0.0671, <i>wR</i> ₂ = 0.1710
Maximum/minimum residual electron density (e·Å ⁻³)	0.831 / -0.807	1.170 / -1.228
Flack parameter	0.003(19)	

For (*P, P*)-**1**: Structure was refined as two component twins. Solvent molecules (dichloromethane) were fitted to idealized geometry. Two of these molecules showed positional disorder. Atomic displacement parameters (ADPs) of all disordered atoms were restrained with similarity restraint (SIMU), rigid-body restraint (RIGU) and isotropic restraint (ISOR).

For **3Py**: Two tert-butyl groups were rotationally disordered. The displacement parameters of opposite atoms belonging to these groups were constrained to each other with EADP keyword. Additionally, all ADPs were restrained with RIGU keyword in ShelXL input ('enhanced rigid bond' restraint for all bonds in the connectivity list), similarity restraint SIMU and their *U*_{ii} parameters were restrained with ISOR keyword to approximate isotropic behavior.

S8. NMR spectroscopy

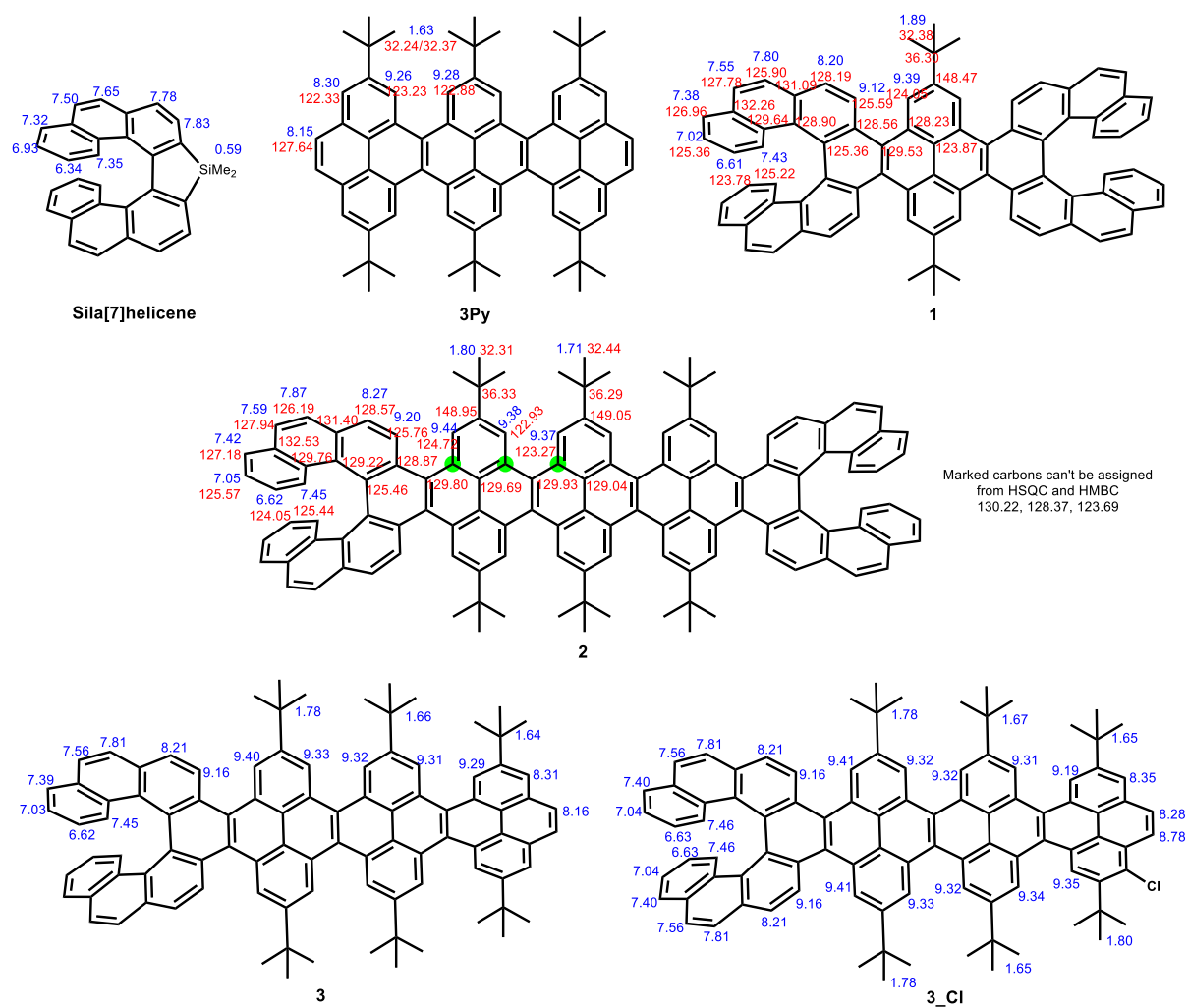


Figure S10. ^1H (blue) and ^{13}C NMR (red) peaks assigned to respective atoms in discussed molecules.

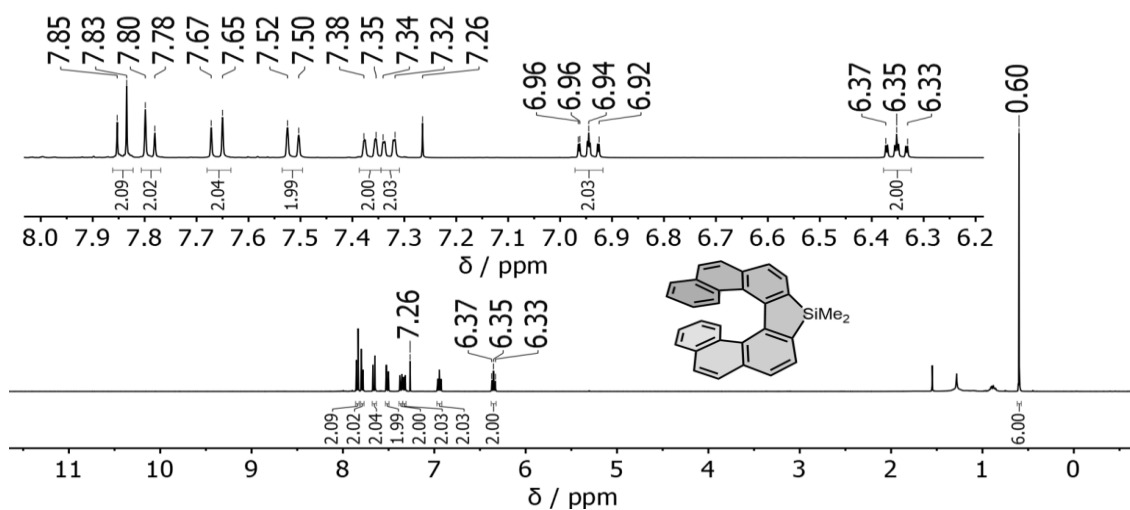


Figure S11. ^1H NMR spectrum of (*P*)-Sila[7]helicene (400 MHz, CDCl_3).

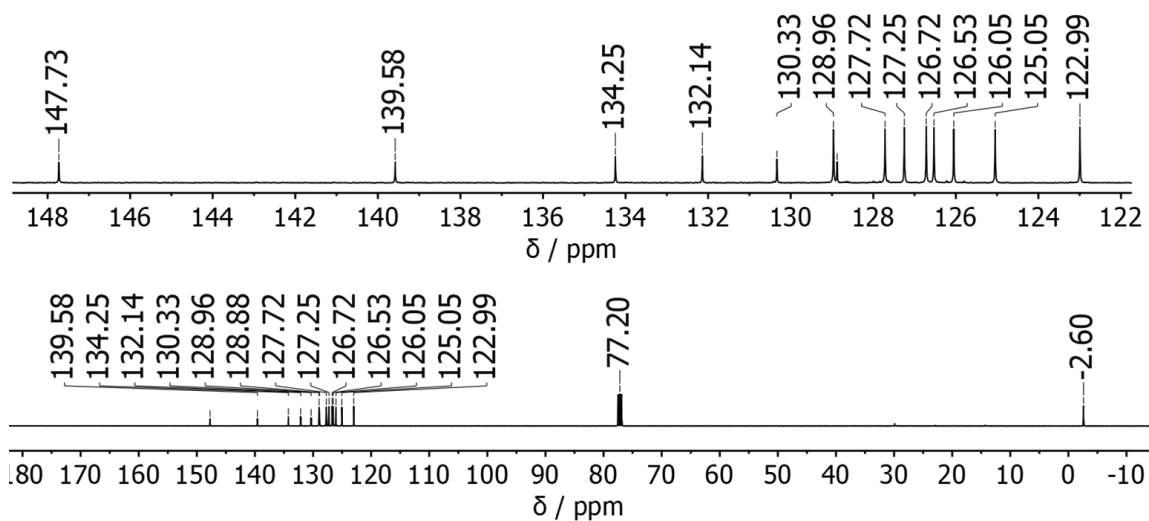


Figure S12. ^{13}C (^1H) NMR spectrum of (*P*)-Sila[7]helicene (101 MHz, CDCl_3).

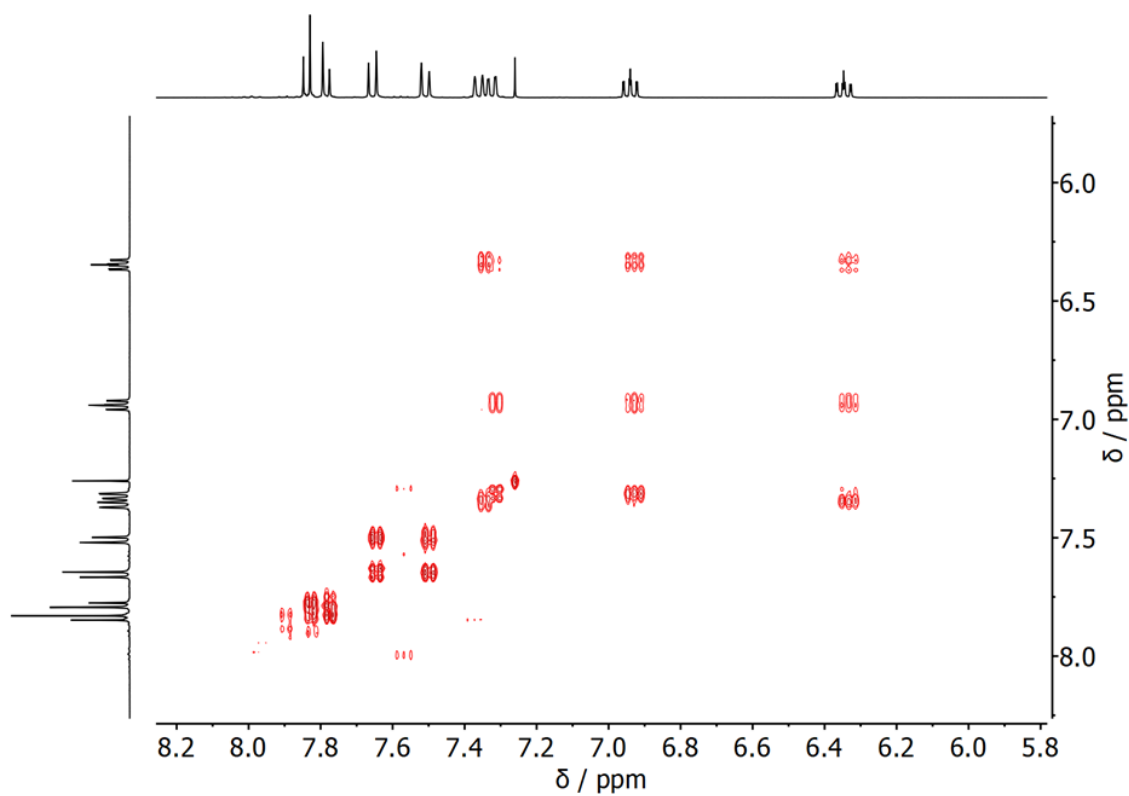


Figure S13. $^1\text{H} - ^1\text{H}$ COSY NMR spectrum of (*P*)-Sila[7]helicene (400 MHz, CDCl_3).

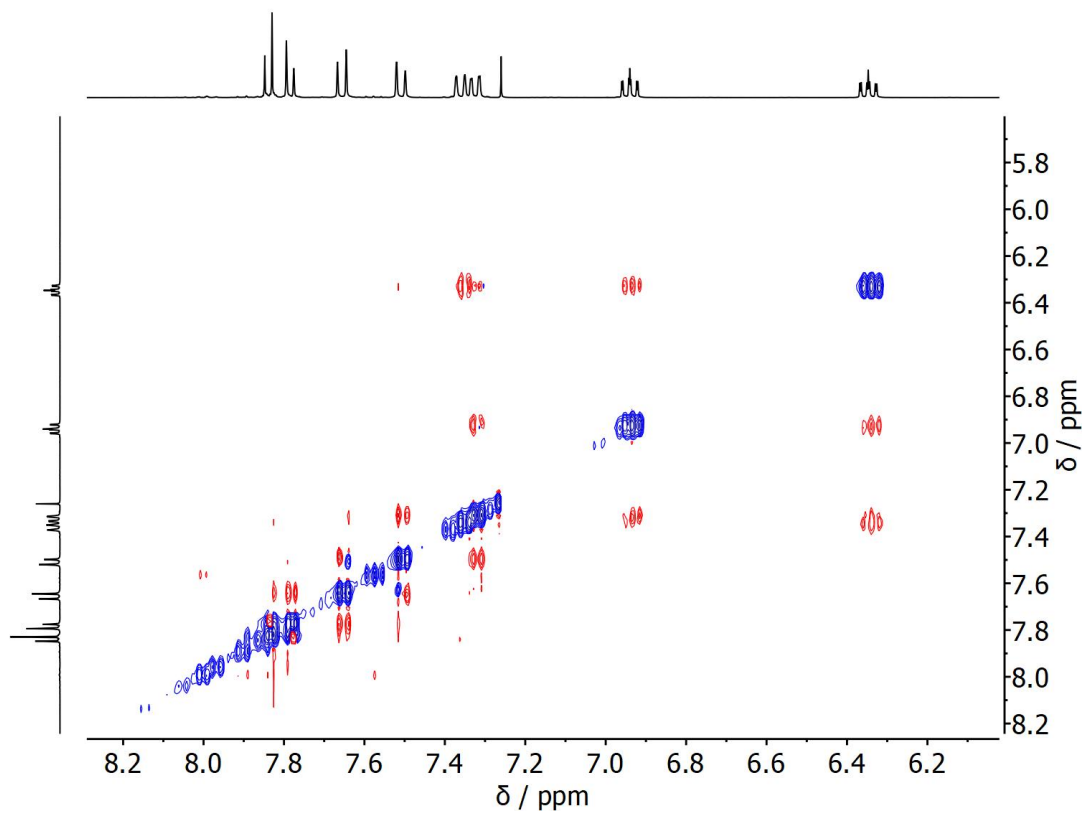


Figure S14. $^1\text{H} - ^1\text{H}$ NOESY NMR spectrum of (*P*)-Sila[7]helicene (400 MHz, CDCl_3).

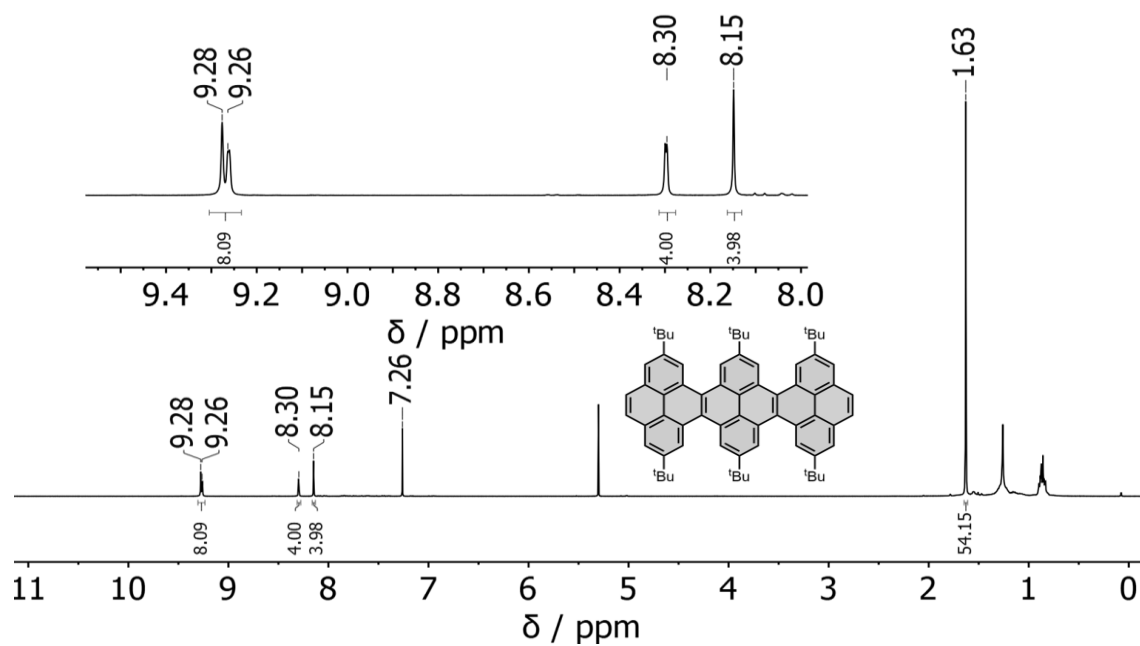


Figure S15. ^1H NMR spectrum of **3Py** (400 MHz, CDCl_3).

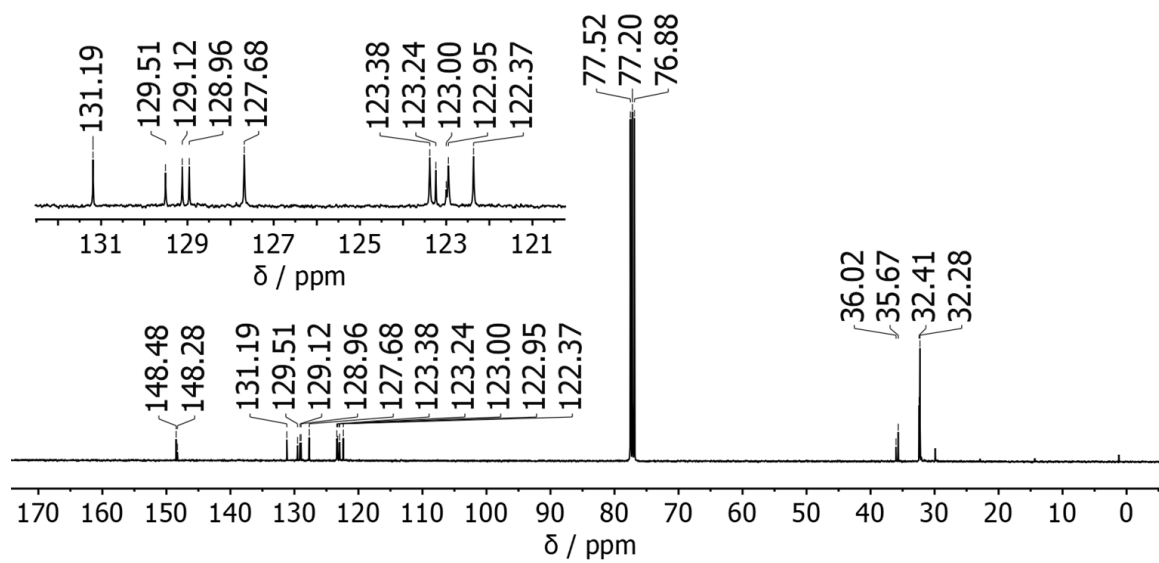


Figure S16. $^{13}\text{C}(^1\text{H})$ NMR spectrum of **3Py** (101 MHz, CDCl_3).

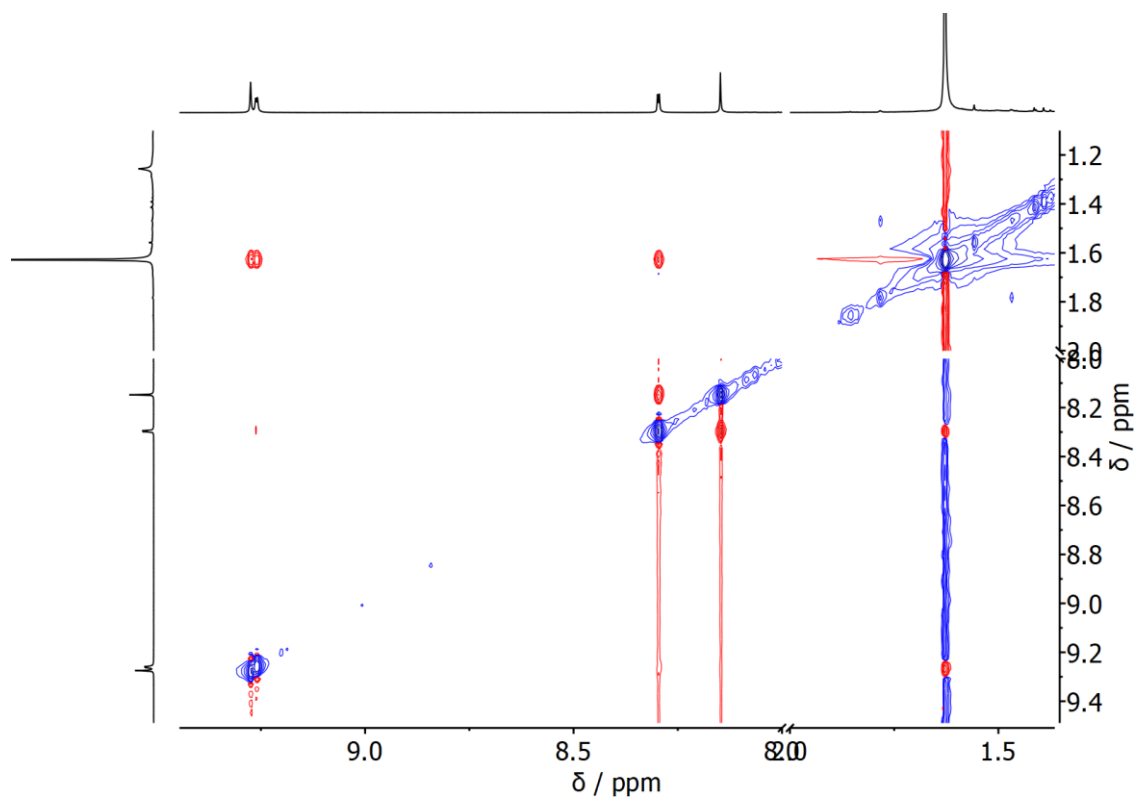


Figure S17. $^1\text{H} - ^1\text{H}$ NOESY NMR spectrum of **3Py** (400 MHz, CDCl_3).

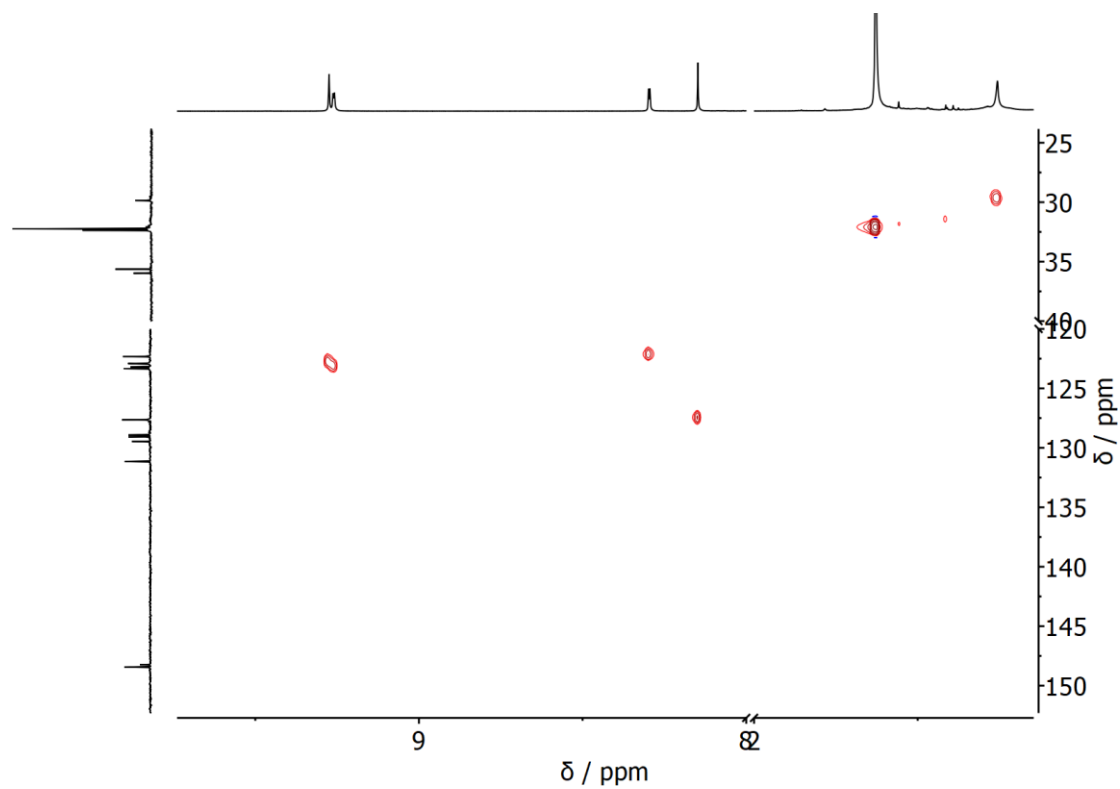


Figure S18. $^1\text{H} - ^{13}\text{C}$ HSQC NMR spectrum of **3Py** (400 MHz, CDCl_3).

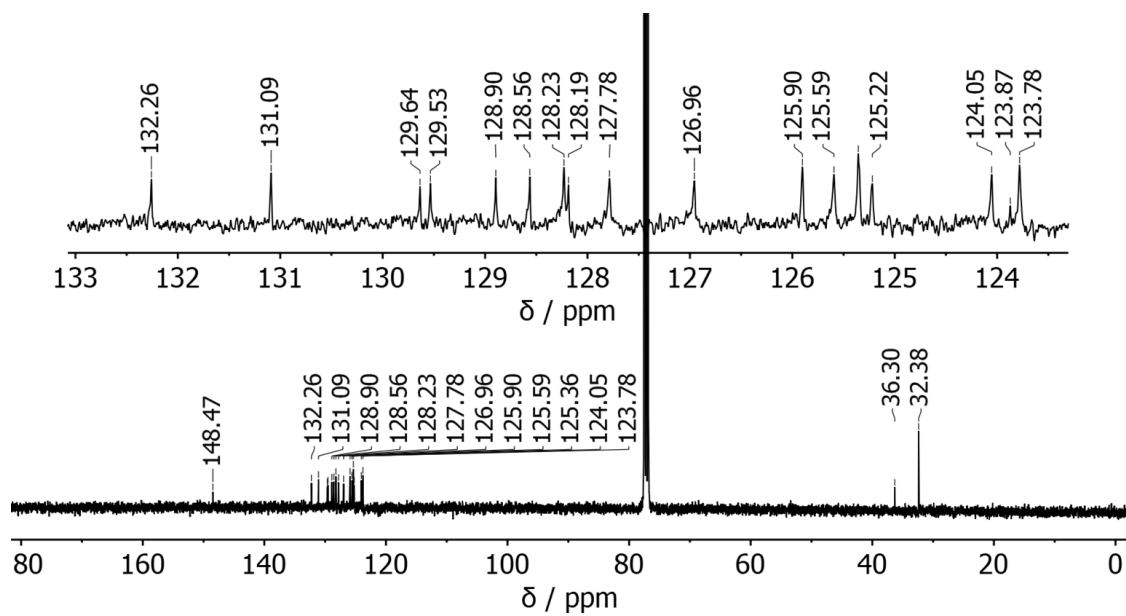


Figure S21. ^{13}C (^1H) NMR spectrum of *(P, P)*-**1** (101 MHz, CDCl_3).

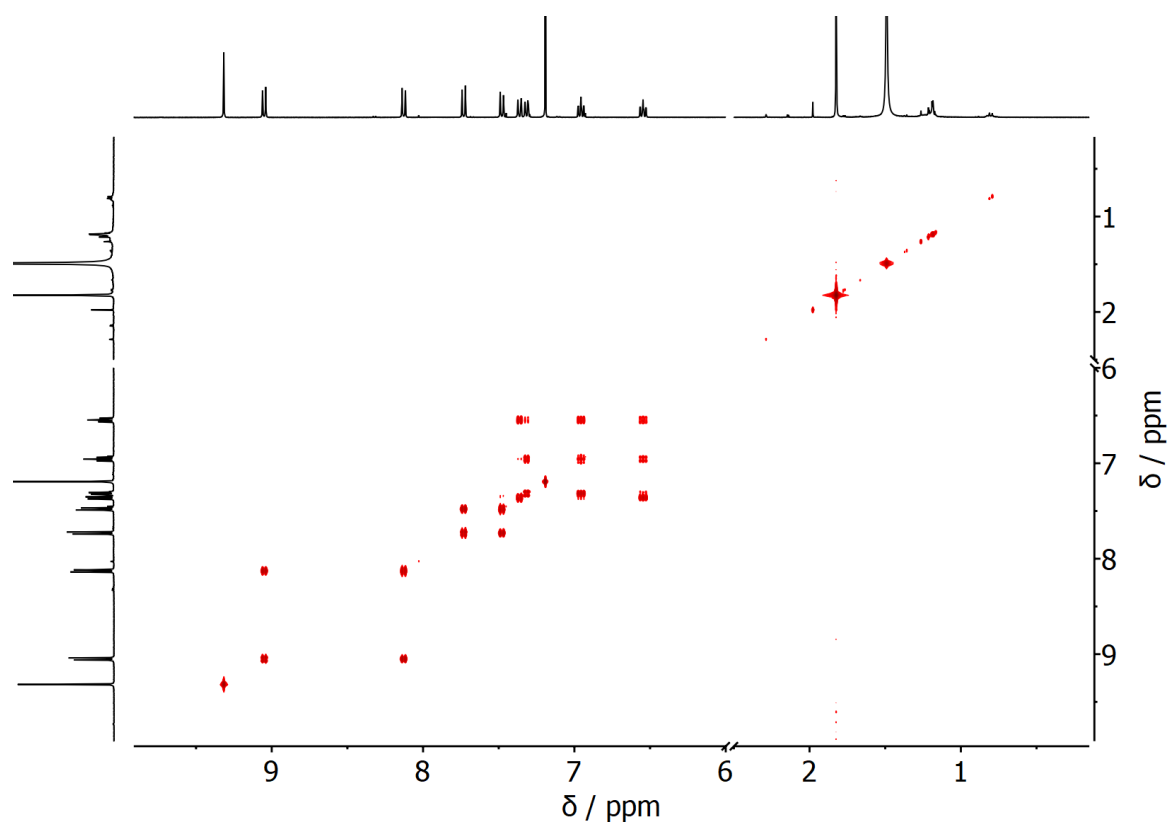


Figure S22. $^1\text{H} - ^1\text{H}$ COSY NMR spectrum of (*P, P*)-**1** (400 MHz, CDCl_3).

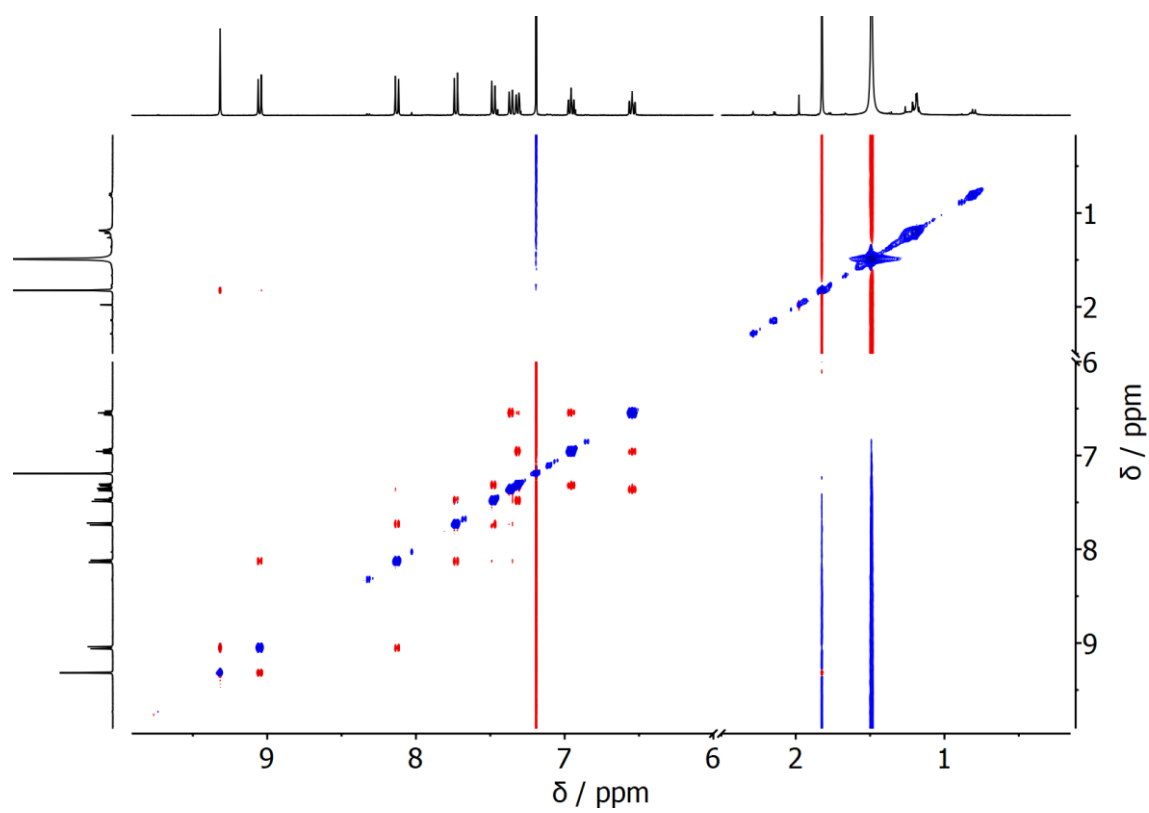


Figure S23. $^1\text{H} - ^1\text{H}$ NOESY NMR spectrum of (*P, P*)-**1** (400 MHz, CDCl_3).

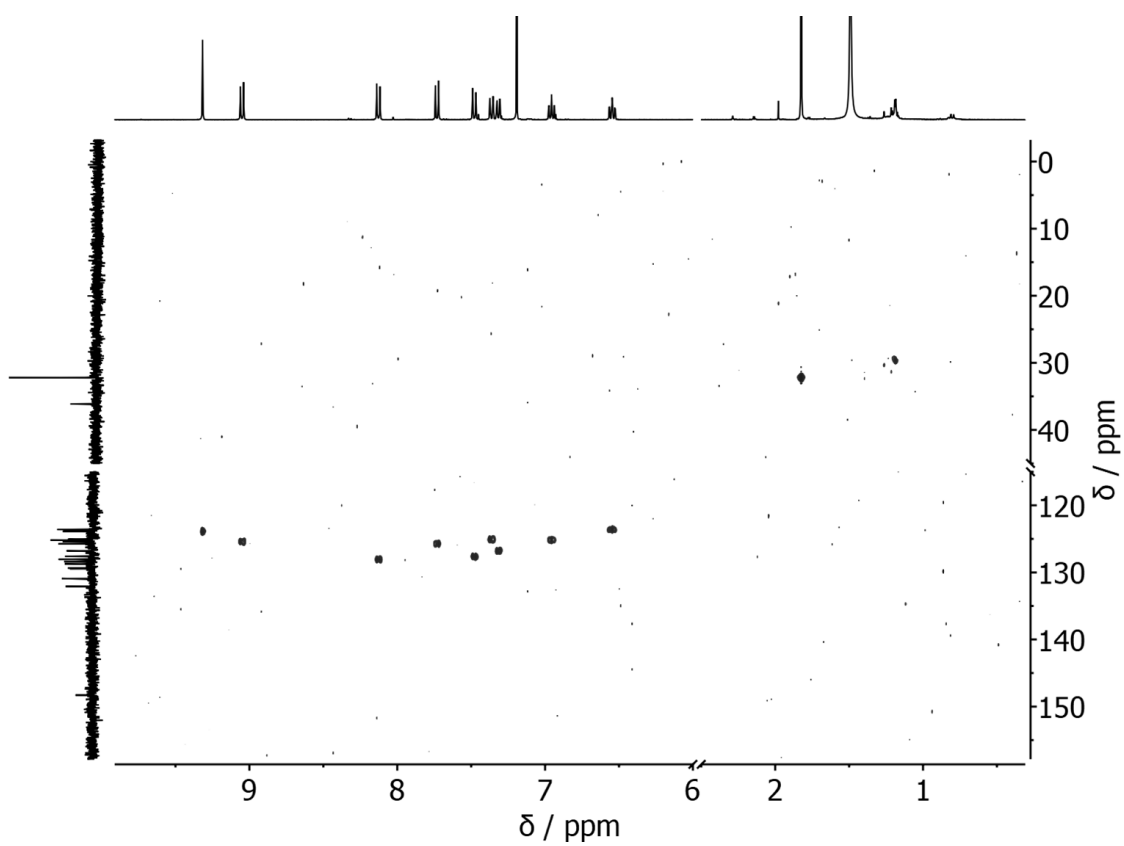


Figure S24. $^1\text{H} - ^{13}\text{C}$ HSQC NMR spectrum of (*P, P*)-**1** (400 MHz, CDCl_3).

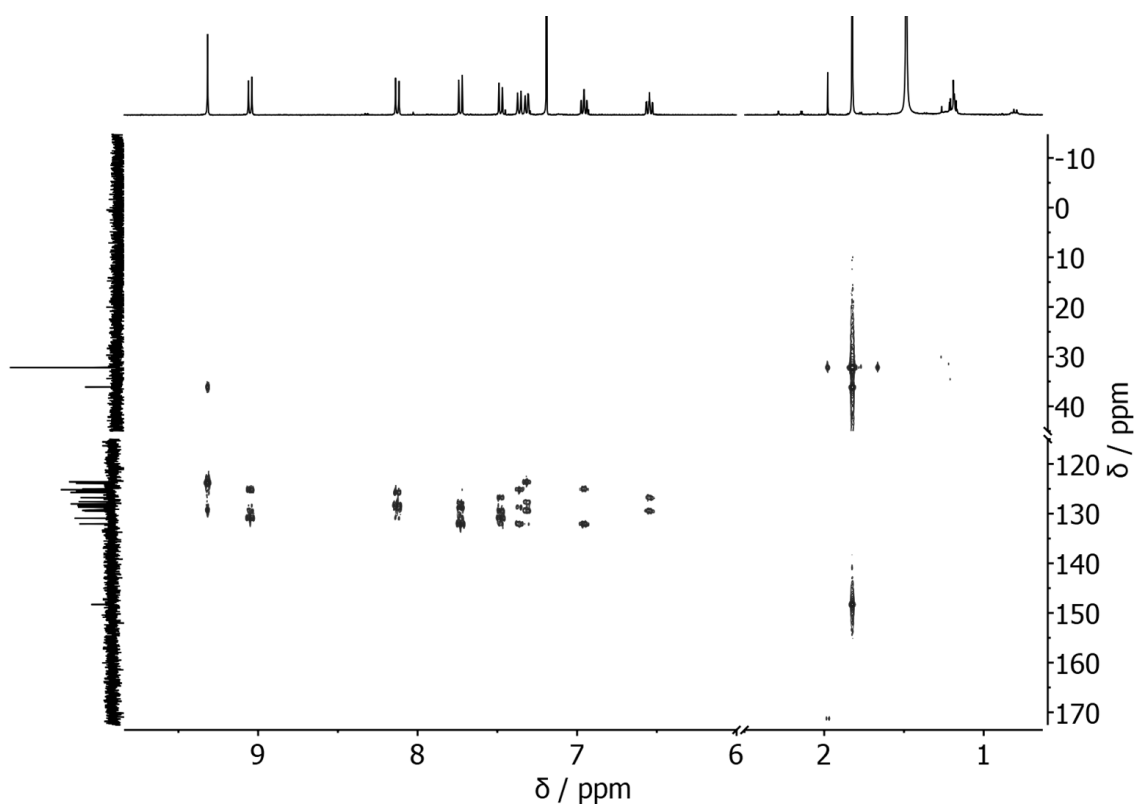


Figure S25. $^1\text{H} - ^{13}\text{C}$ HMBC NMR spectrum of (*P, P*)-**1** (400 MHz, CDCl_3).

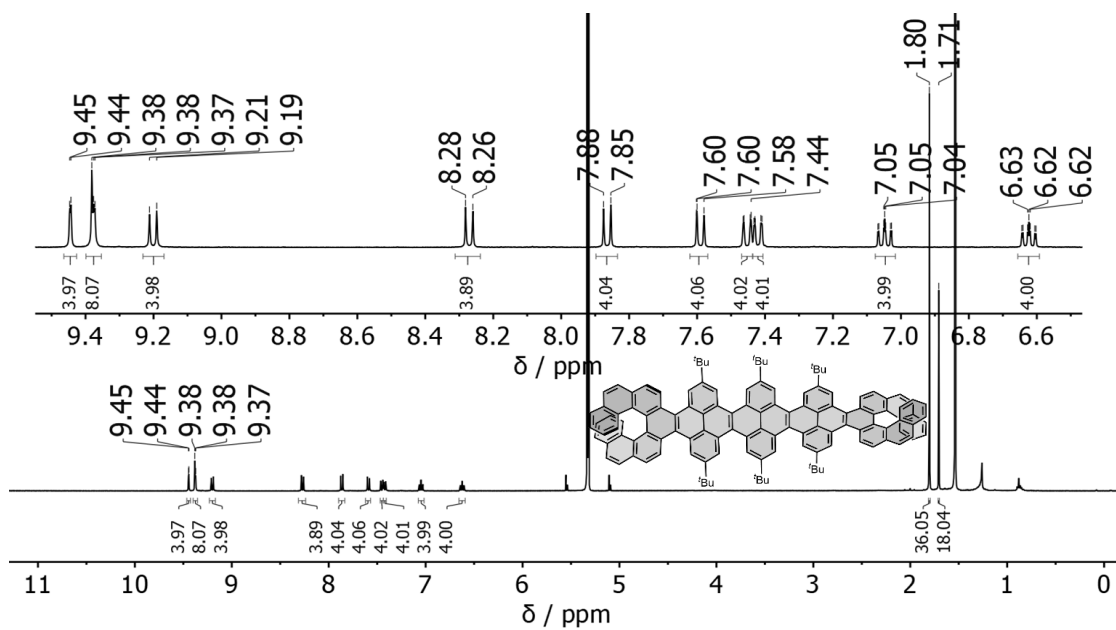


Figure S26. ^1H NMR spectrum of (P, P) -2 (400 MHz, CDCl_3).

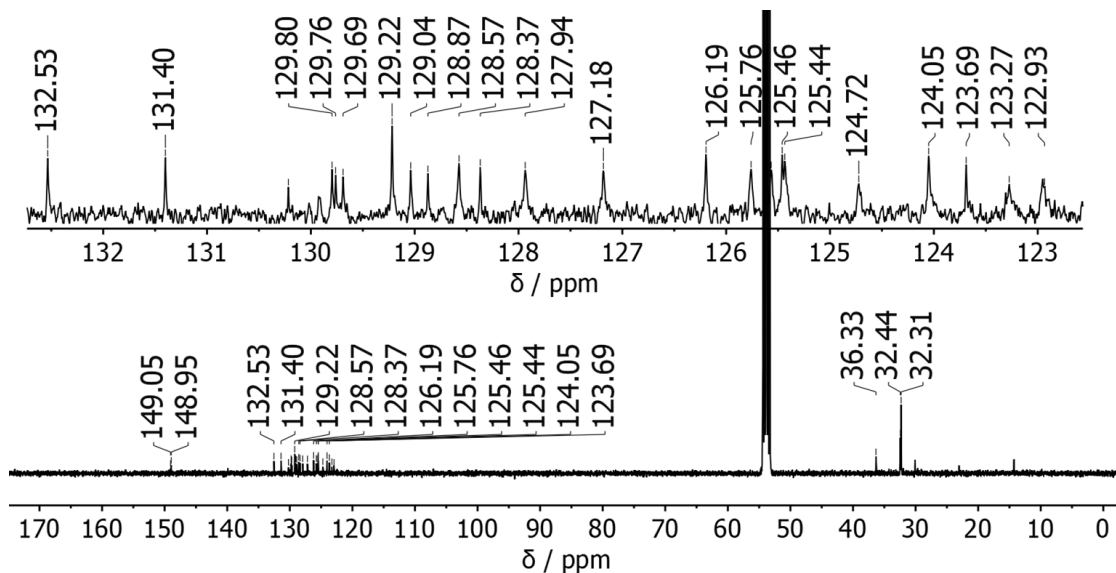


Figure S27. $^{13}\text{C}(^1\text{H})$ NMR spectrum of (P, P) -2 (101 MHz, CDCl_3).

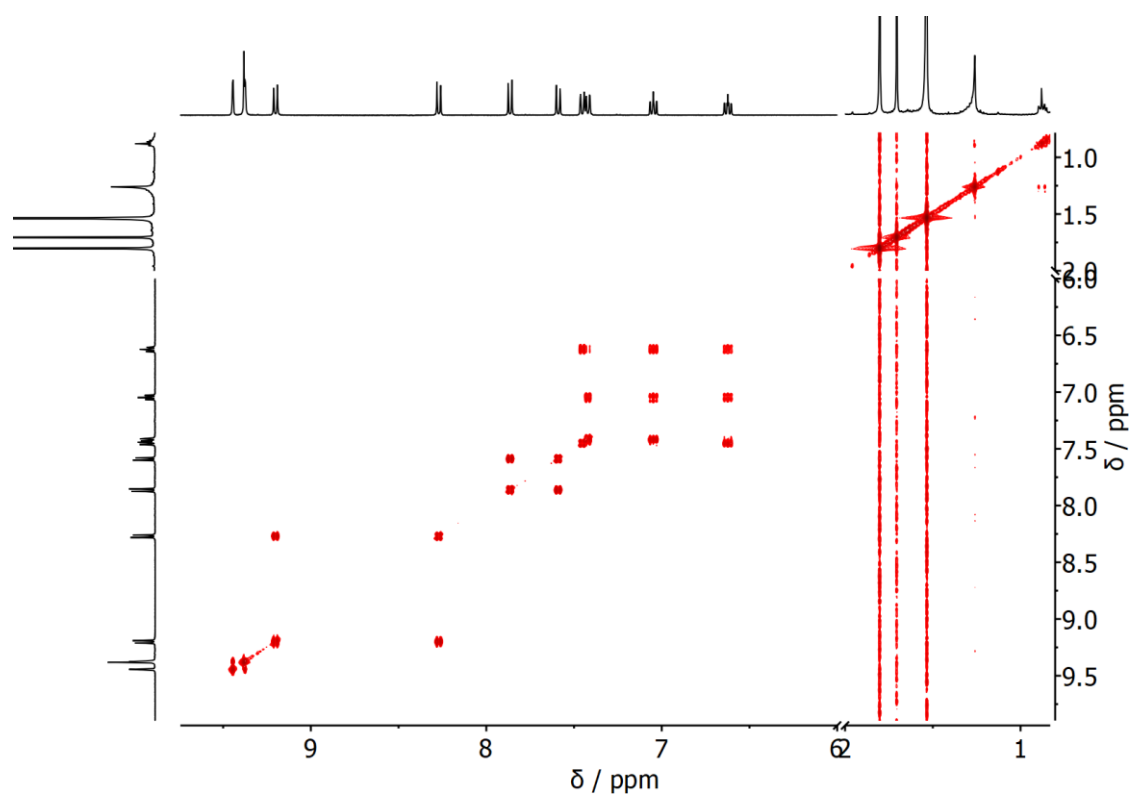


Figure S28. $^1\text{H} - ^1\text{H}$ COSY NMR spectrum of (*P, P*)-**2** (400 MHz, CDCl_3).

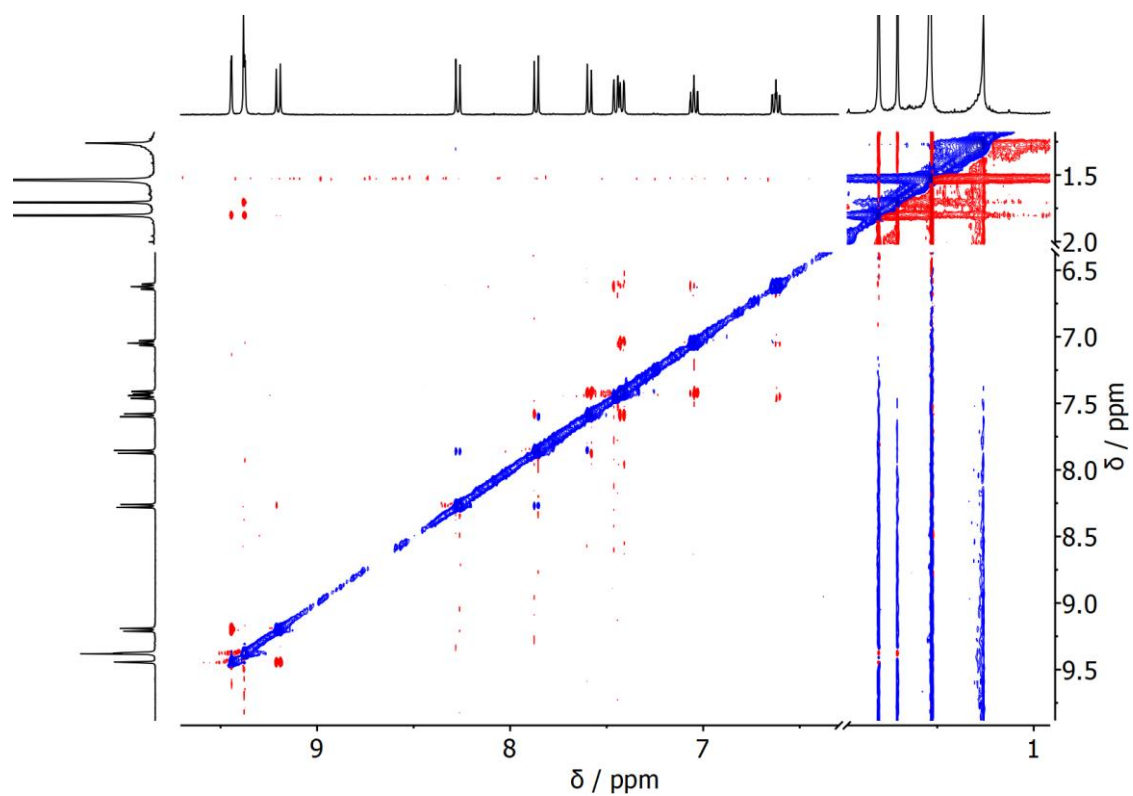


Figure S29. $^1\text{H} - ^1\text{H}$ NOESY NMR spectrum of (*P, P*)-**2** (400 MHz, CDCl_3).

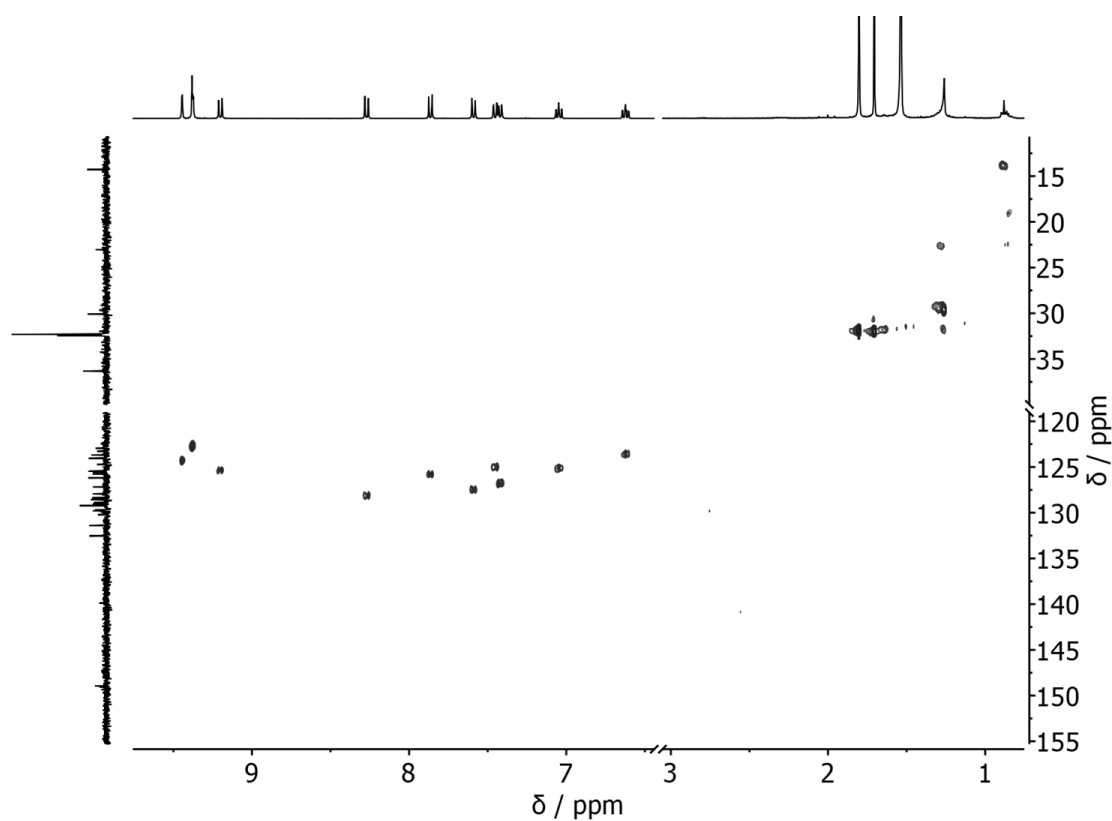


Figure S30. $^1\text{H} - ^{13}\text{C}$ HSQC NMR spectrum of (*P, P*)-**2** (400 MHz, CDCl_3).

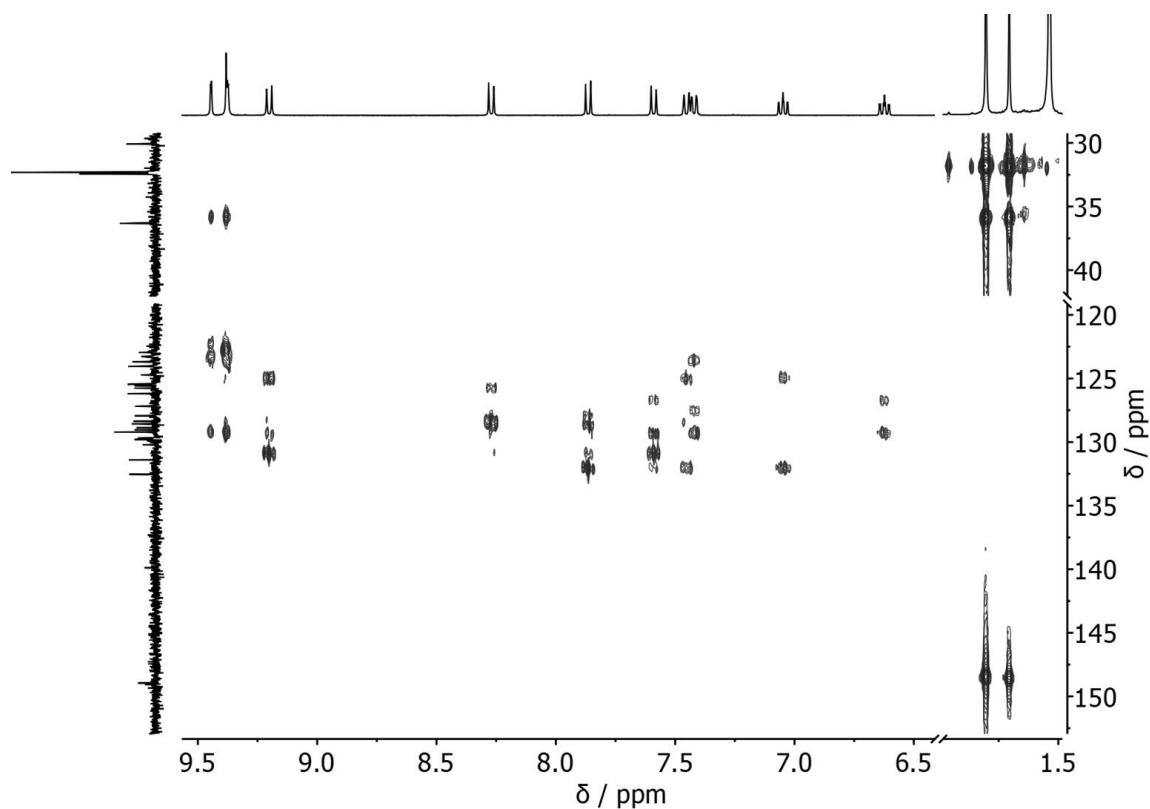


Figure S31. $^1\text{H} - ^{13}\text{C}$ HMBC NMR spectrum of (*P, P*)-**2** (400 MHz, CDCl_3).

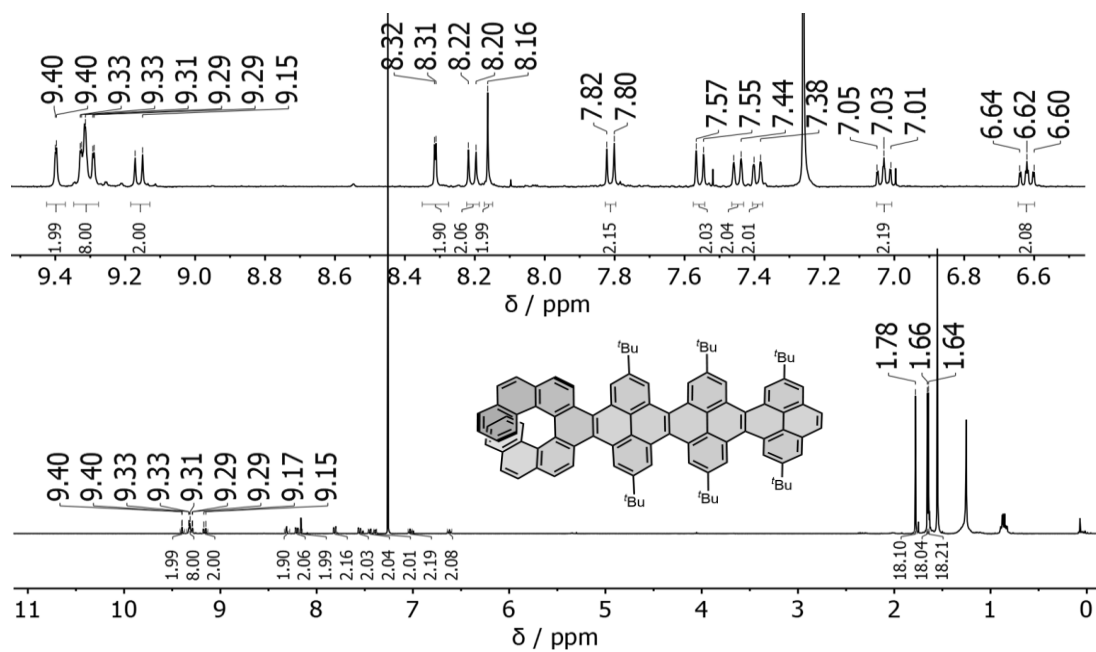


Figure S32. ^1H NMR spectrum of (P) -3 (400 MHz, CDCl_3).

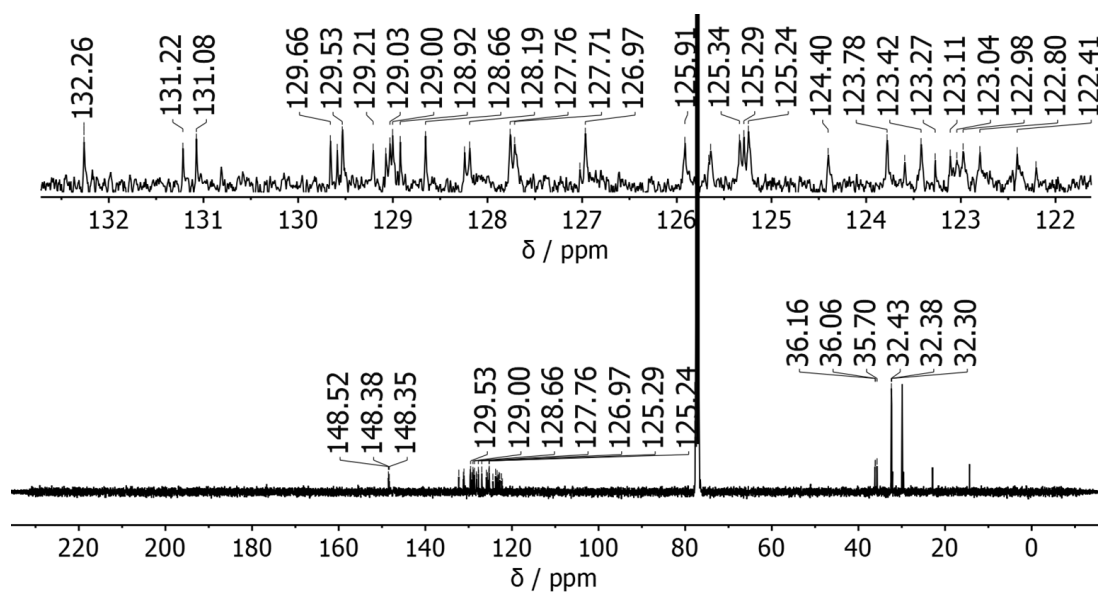


Figure S33. $^{13}\text{C}(^1\text{H})$ NMR spectrum of (P) -3 (101 MHz, CDCl_3).

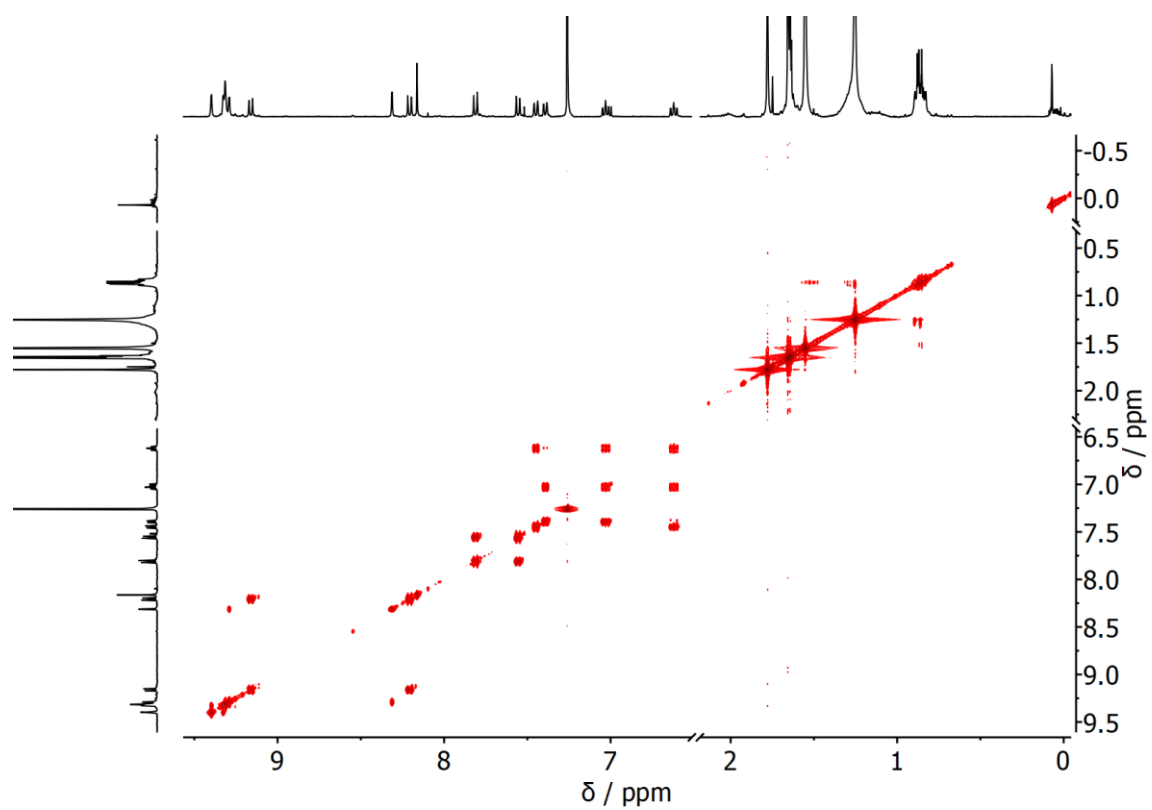


Figure S34. $^1\text{H} - ^1\text{H}$ COSY NMR spectrum of (*P*)-**3** (400 MHz, CDCl_3).

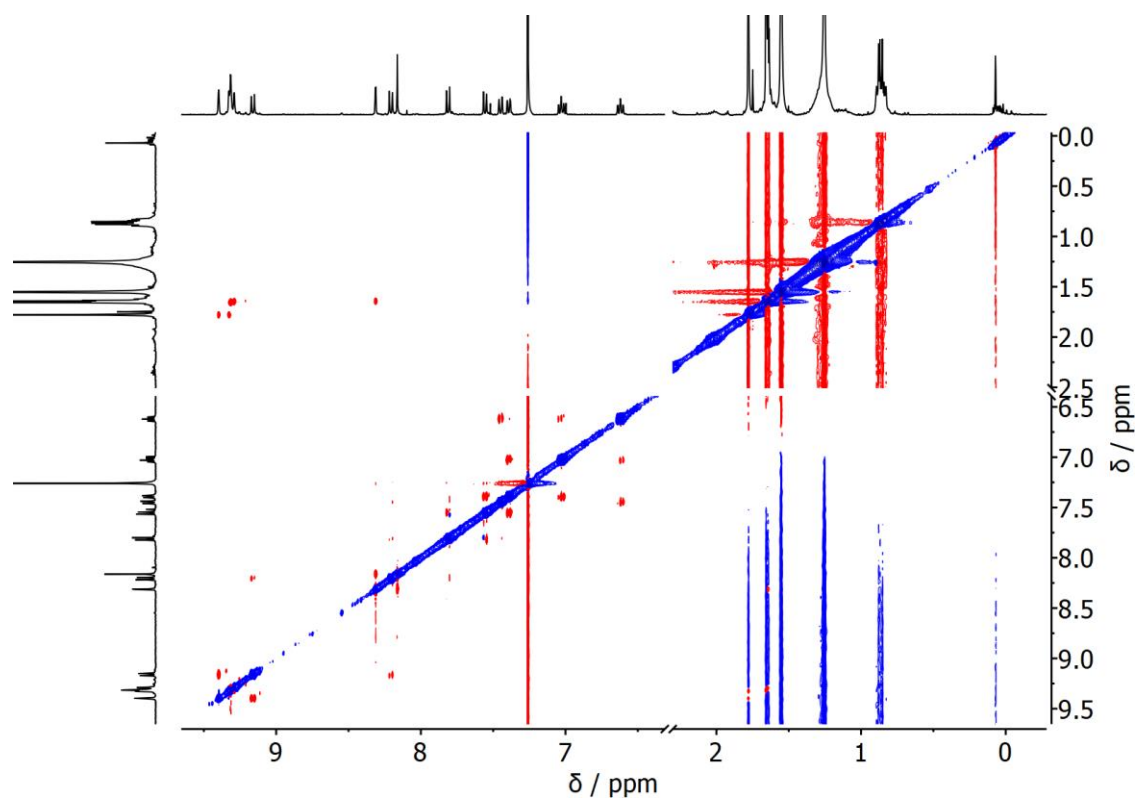


Figure S35. $^1\text{H} - ^1\text{H}$ NOESY NMR spectrum of (*P*)-**3** (400 MHz, CDCl_3).

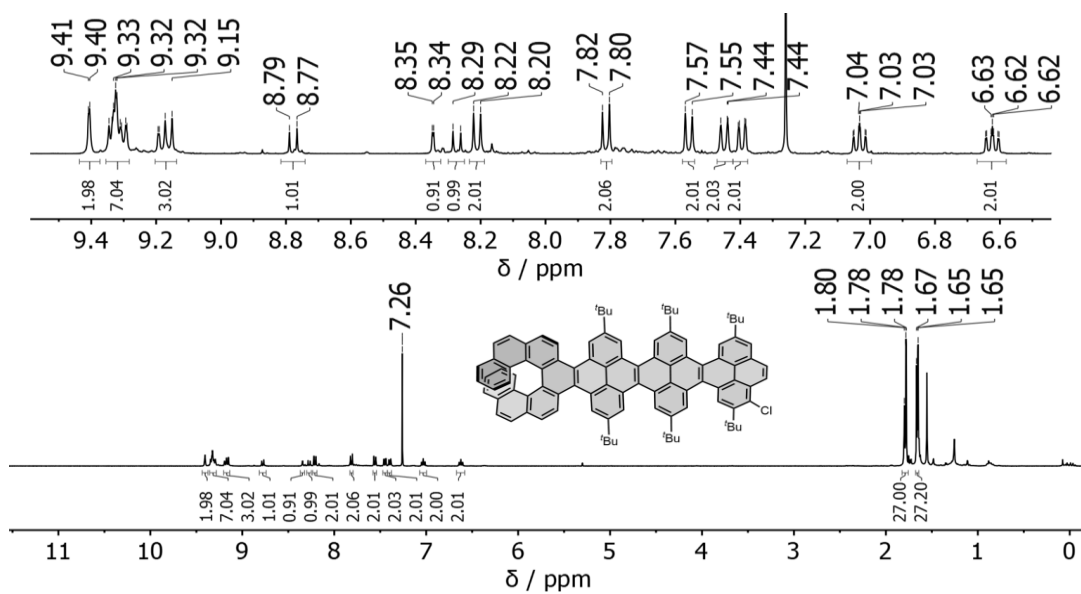


Figure S36. ^1H NMR spectrum of (*P*)-3-Cl (400 MHz, CDCl_3).

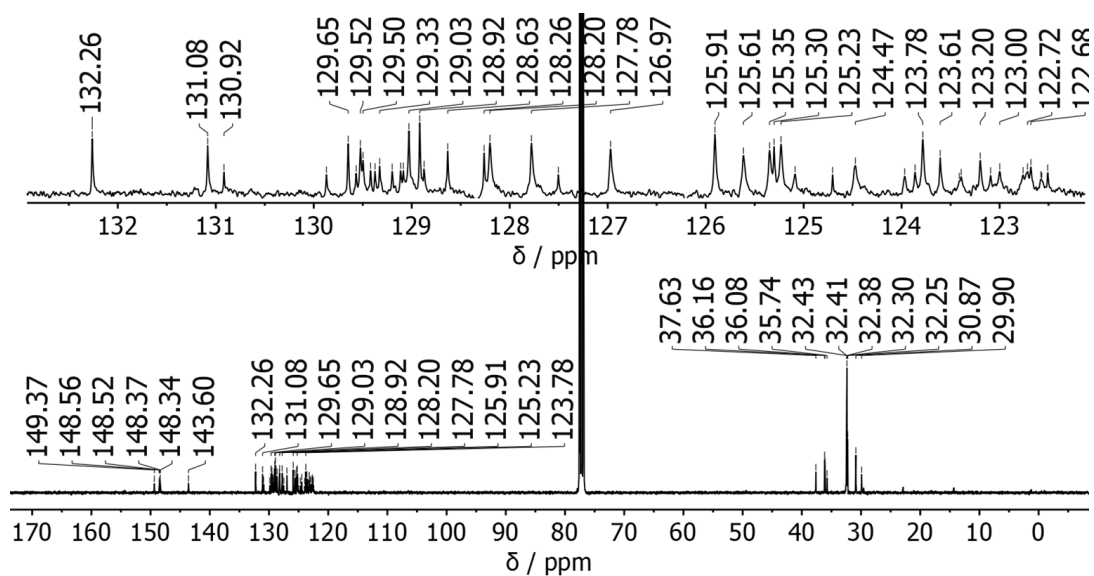


Figure S37. $^{13}\text{C}(^1\text{H})$ NMR spectrum of (*P*)-3-Cl (101 MHz, CDCl_3).

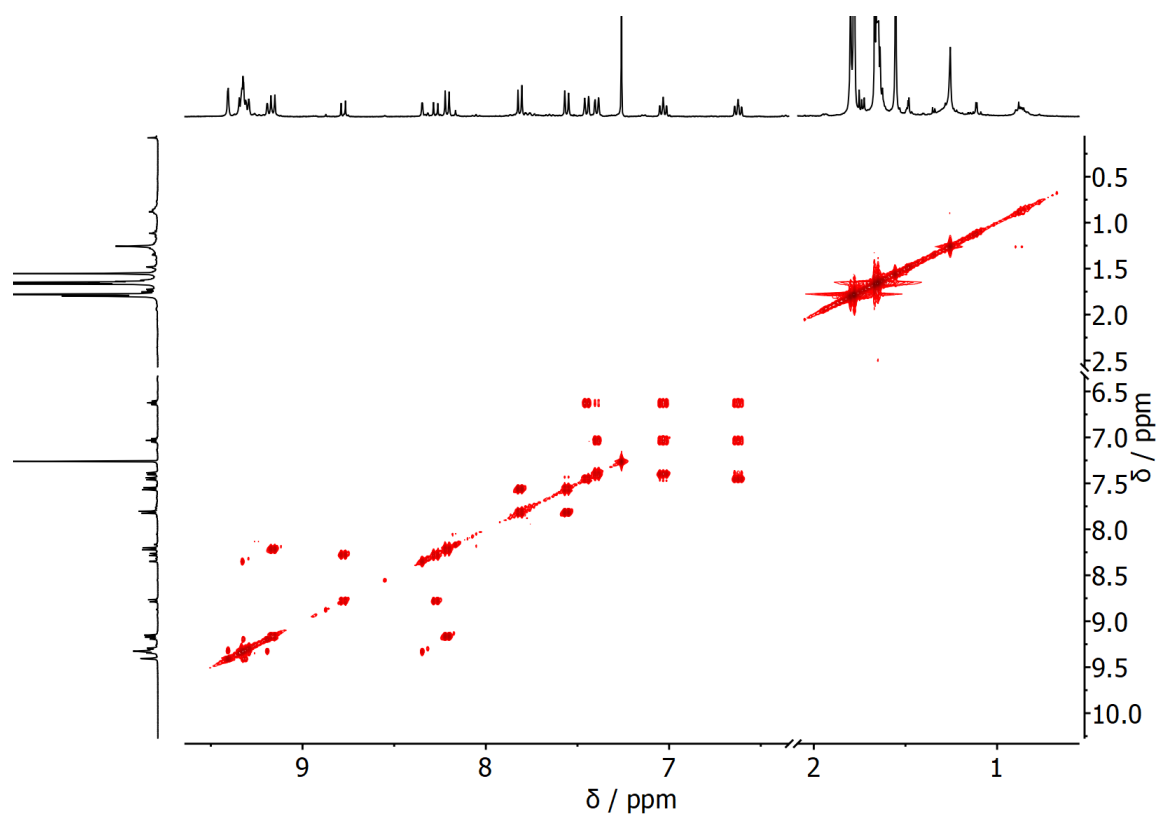


Figure S38. ^1H – ^1H COSY NMR spectrum of (P) -3_Cl (400 MHz, CDCl_3).

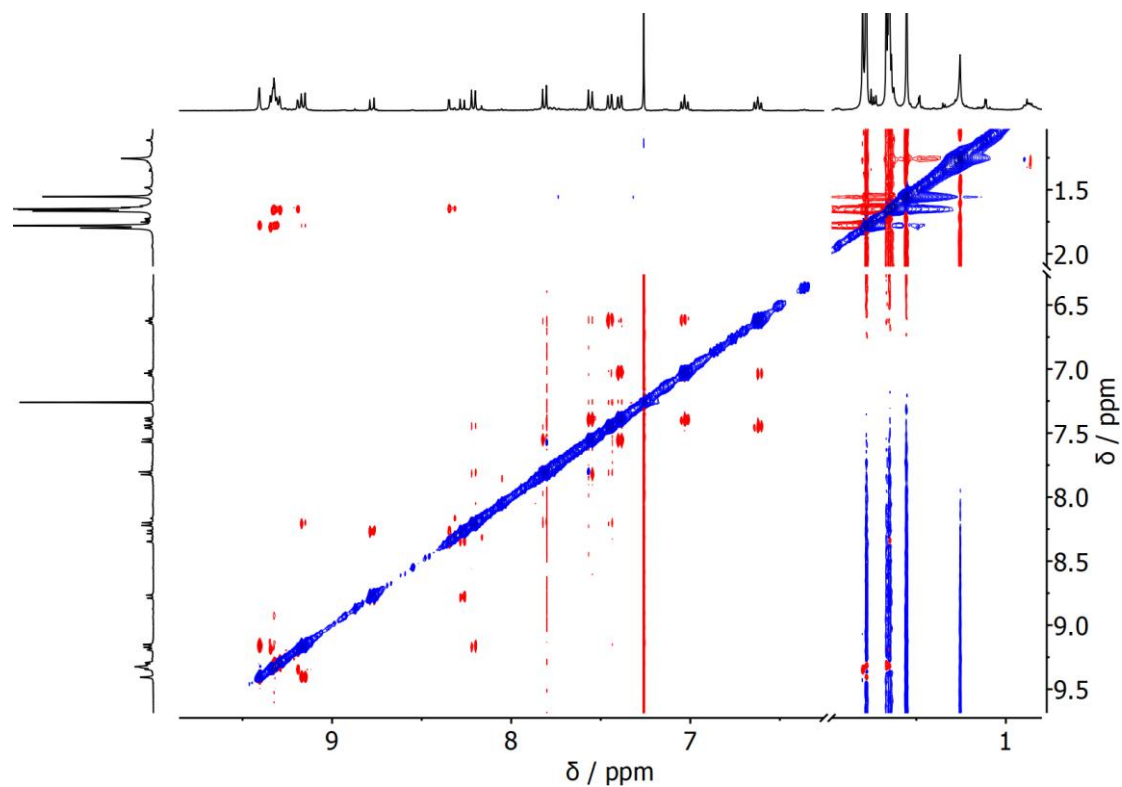


Figure S39. ^1H – ^1H NOESY NMR spectrum of (P) -3_Cl (400 MHz, CDCl_3).

S9. High resolution mass spectrometry (HRMS)

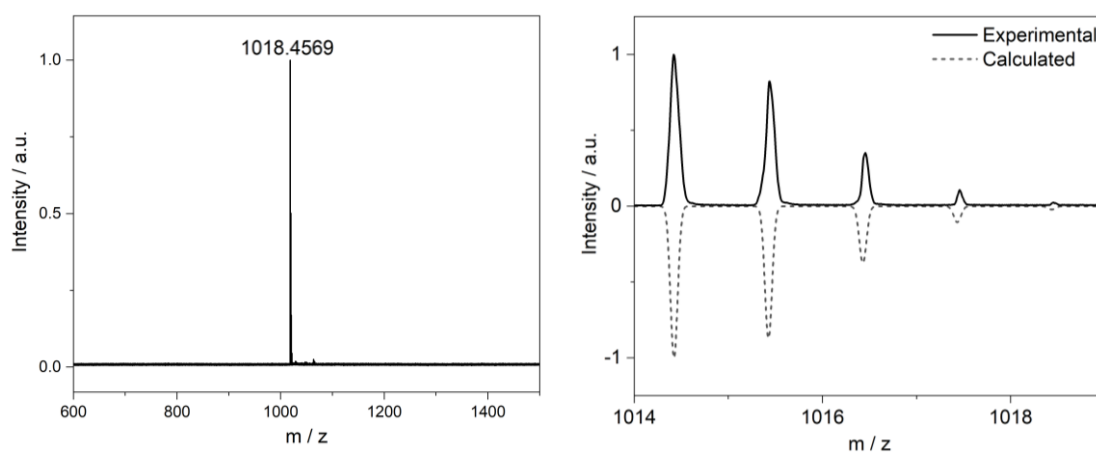


Figure S40. MALDI-TOF HRMS of (P, P)-1.

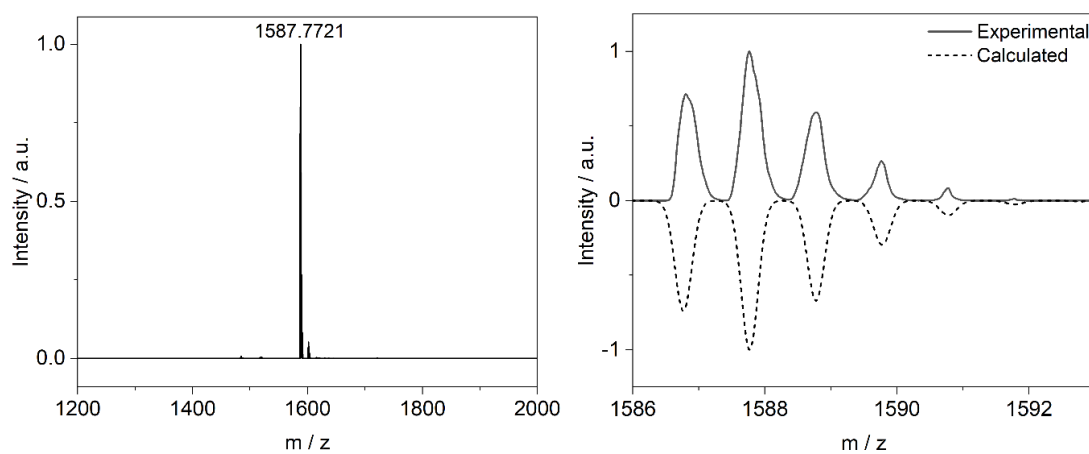


Figure S41. MALDI-TOF HRMS of (P, P)-2.

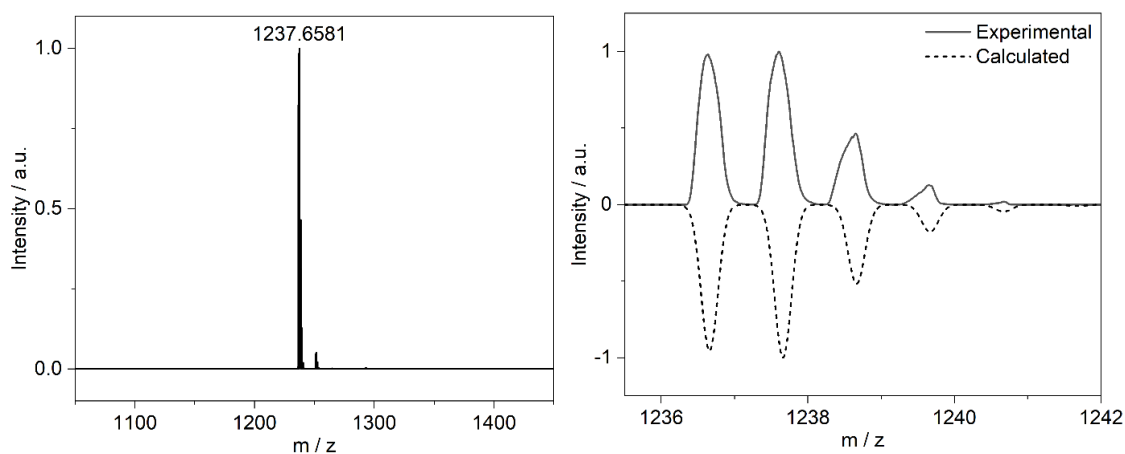


Figure S42. MALDI-TOF HRMS of (P)-3.

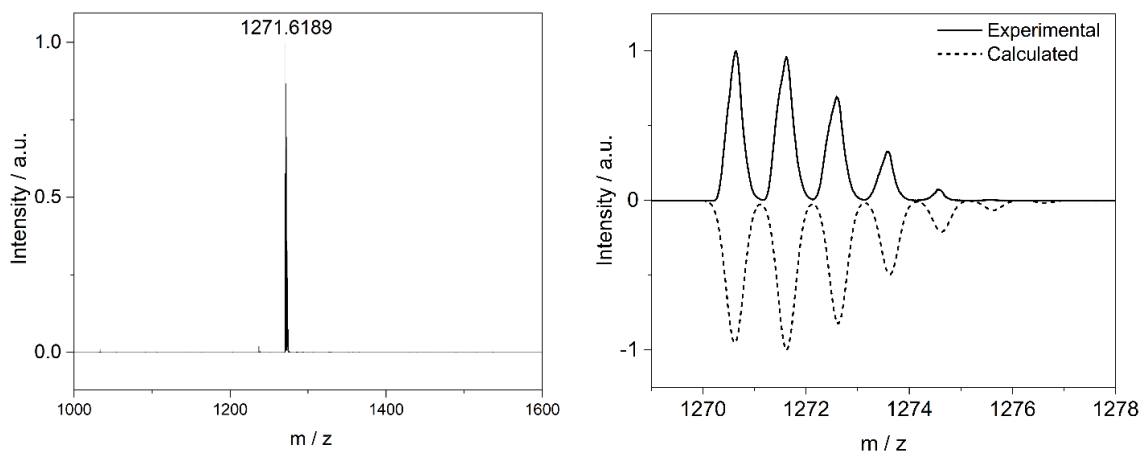


Figure S43. MALDI-TOF HRMS of (P)-3_Cl.

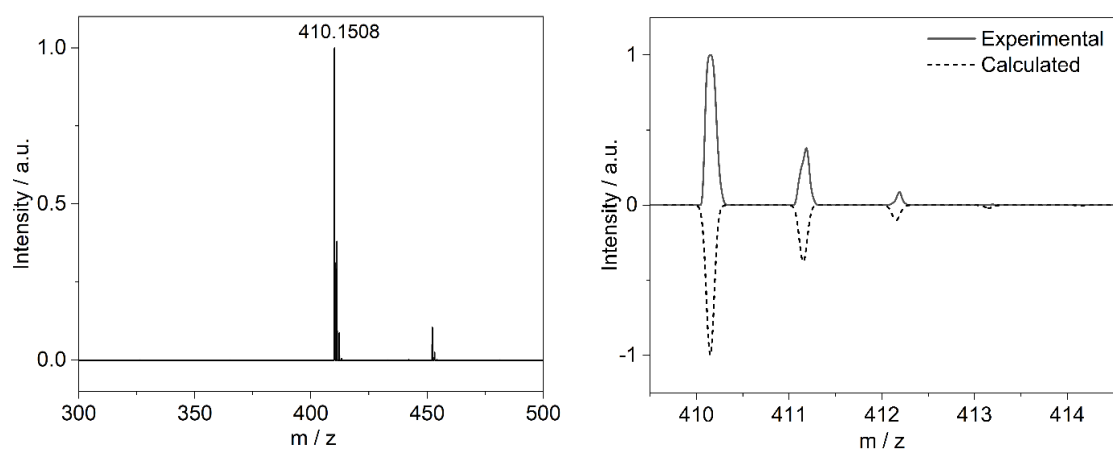


Figure S44. MALDI-TOF HRMS of Sila[7]helicene.

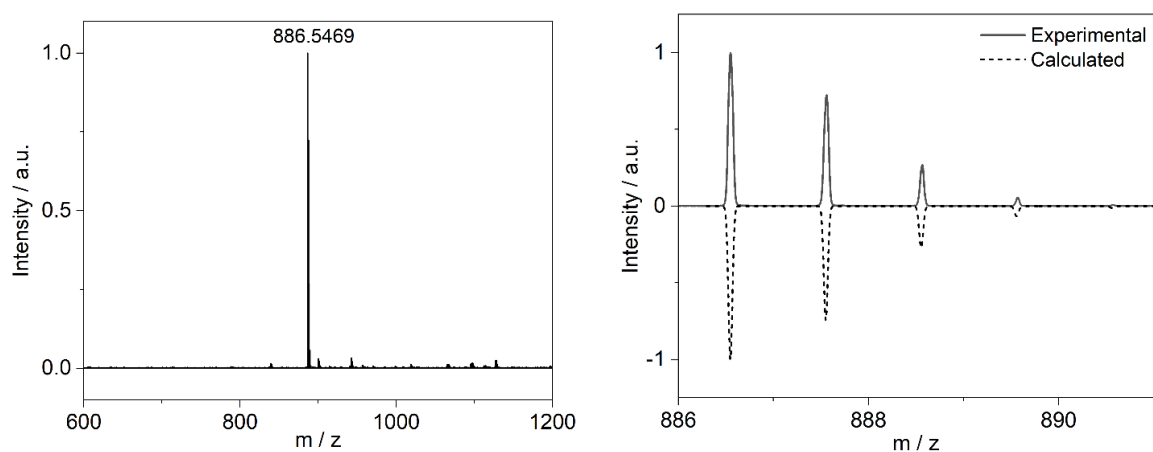


Figure S45. MALDI-TOF HRMS of 3Py.

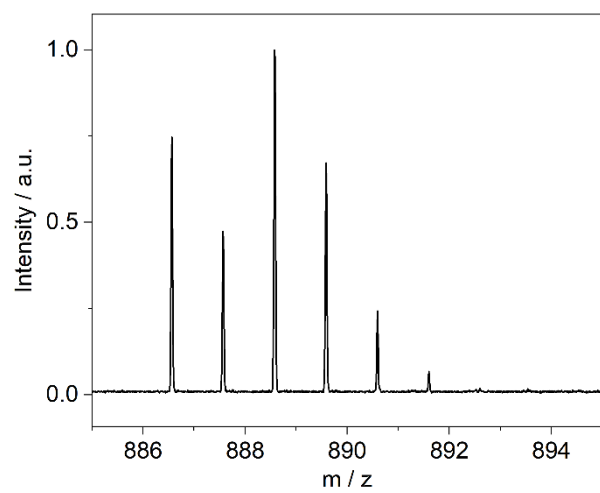


Figure S46. MALDI-TOF MS of crude reaction mixture after Suzuki coupling-C–H activation for preparing **3Py**.

S10. References

- [1] A. K. Swain, K. Radacki, H. Braunschweig, P. Ravat, *J. Org. Chem.* **2022**, *87*, 993-1000.
- [2] Q. Li, J. Li, H. Ren, Z. Gao, D. Liu, *Synth. Commun.* **2011**, *41*, 3325-3333.
- [3] L. Ji, I. Krummenacher, A. Friedrich, A. Lorbach, M. Haehnel, K. Edkins, H. Braunschweig, T. B. Marder, *J. Org. Chem.* **2018**, *83*, 3599-3606.
- [4] Z. Guo, S.-M. Yiu, M. C. W. Chan, *Chem. Eur. J.* **2013**, *19*, 8937-8947.
- [5] K. Ozaki, K. Kawasumi, M. Shibata, H. Ito, K. Itami, *Nat. Commun.* **2015**, *6*, 6251.
- [6] M. Strohm, D. Kavan, P. Novák, M. Volný, V. Havlíček, *Anal. Chem.* **2010**, *82*, 4648-4651.
- [7] G. Sheldrick, *Acta Crystallogr. A* **2015**, *71*, 3-8.
- [8] G. Sheldrick, *Acta Crystallogr. A* **2008**, *64*, 112-122.
- [9] M. J. Frisch, G. W. Trucks, H. B. Schlegel, G. E. Scuseria, M. A. Robb, J. R. Cheeseman, G. Scalmani, V. Barone, G. A. Petersson, H. Nakatsuji, X. Li, M. Caricato, A. V. Marenich, J. Bloino, B. G. Janesko, R. Gomperts, B. Mennucci, H. P. Hratchian, J. V. Ortiz, A. F. Izmaylov, J. L. Sonnenberg, Williams, F. Ding, F. Lipparini, F. Egidi, J. Goings, B. Peng, A. Petrone, T. Henderson, D. Ranasinghe, V. G. Zakrzewski, J. Gao, N. Rega, G. Zheng, W. Liang, M. Hada, M. Ehara, K. Toyota, R. Fukuda, J. Hasegawa, M. Ishida, T. Nakajima, Y. Honda, O. Kitao, H. Nakai, T. Vreven, K. Throssell, J. A. Montgomery Jr., J. E. Peralta, F. Ogliaro, M. J. Bearpark, J. J. Heyd, E. N. Brothers, K. N. Kudin, V. N. Staroverov, T. A. Keith, R. Kobayashi, J. Normand, K. Raghavachari, A. P. Rendell, J. C. Burant, S. S. Iyengar, J. Tomasi, M. Cossi, J. M. Millam, M. Klene, C. Adamo, R. Cammi, J. W. Ochterski, R. L. Martin, K. Morokuma, O. Farkas, J. B. Foresman, D. J. Fox, Wallingford, CT, **2016**.
- [10] T. Bruhn, A. Schaumlöffel, Y. Hemberger, G. Bringmann, *Chirality* **2013**, *25*, 243-249.
- [11] M. D. Hanwell, D. E. Curtis, D. C. Lonie, T. Vandermeersch, E. Zurek, G. R. Hutchison, *J. Cheminformatics* **2012**, *4*, 17.
- [12] H. Oyama, K. Nakano, T. Harada, R. Kuroda, M. Naito, K. Nobusawa, K. Nozaki, *Org. Lett.* **2013**, *15*, 2104-2107.
- [13] F. Liu, X. Shen, Y. Wu, L. Bai, H. Zhao, X. Ba, *Tetrahedron Lett.* **2016**, *57*, 4157-4161.
- [14] A. Sillen, Y. Engelborghs, *Photochem. Photobiol.* **1998**, *67*, 475-486.

9. Individual Contributions

The coauthors of the publications included in this cumulative thesis are informed and agree with the individual contributions as stated below.

***C*₂- and *C*₁-Symmetric Configurationally Stable Pyrene-Fused [5]Helicenes Connected via Hexagonal and Heptagonal Rings**

A. Swain, K. Kolanji, C. Stapper, P. Ravat, *Org. Lett.* **2021**, *23*, 1339–1343.

Author	A.S.	K.K.	C.S.	P.R.	∑ in percent
Research conception	1%	1%		6%	8%
Synthesis and characterization	20%	8%	2%		30%
Photophysical measurements	30%				30%
Calculation of enantiomerization barrier	10%				10%
DFT calculations				2%	2%
Publication writing	3%			5%	8%
Publication correction	2%	1%		4%	7%
Publication coordination	2%			3%	5%
Total	68%	10%	2%	20%	100%

Pyrene-Fused [7]Helicenes Connected Via Hexagonal and Heptagonal Rings: Stereospecific Synthesis and Chiroptical Properties

A. Swain, K. Radacki, H. Braunschweig, P. Ravat, *J. Org. Chem.* **2022**, *87*, 993–1000.

Author	A.S.	K.R.	H.B.	P.R.	∑ in percent
Research conception	3%			6%	9%
Synthesis and characterization	30%				30%
Photophysical measurements	28%				28%
Calculation of enantiomerization barrier	5%				5%
Crystallographic analysis		5%			5%
DFT calculations				2%	2%
Publication writing	6%	1%		3%	10%
Publication correction		1%	2%	3%	6%
Publication coordination	2%			3%	5%
Total	74%	7%	2%	17%	100%

Pyrene Bridged Double[7]helicene Embedded with a Heptagonal ring

A. Swain, P. Ravat, *Org. Chem. Front.*, **2023**, *10*, 3714-3725.

Author	A.S.	P.R.	Σ in percent
Research conception	5%	5%	10%
Synthesis and characterization	30%		30%
Photophysical measurements	30%		30%
Calculation of enantiomerization barrier	10%		10%
DFT calculations		2%	2%
Publication writing	7%	3%	10%
Publication correction		3%	3%
Publication coordination	1%	4%	5%
Total	83%	17%	100%

Helically Twisted Nanoribbons via Stereospecific Annulative π -Extension Reaction Employing [7]Helicene as a Molecular Wrench

A. Swain, K. Radacki, H. Braunschweig, P. Ravat. *Submitted*.

Author	A.S.	K.R.	H.B.	P.R.	Σ in percent
Research conception	3%			6%	9%
Synthesis and characterization	30%				30%
Photophysical measurements	27%				27%
Calculation of enantiomerization barrier	5%				5%
Crystallographic analysis		5%			5%
DFT calculations				3%	3%
Publication writing	6%	1%		3%	10%
Publication correction		1%	2%	3%	6%
Publication coordination	2%			3%	5%
Total	73%	7%	2%	18%	100%

10. Acknowledgement

Above all, I would like to express my deepest appreciation to **Dr. Prince Ravat**, for his unwavering support and guidance throughout my doctoral journey at the Universität Würzburg. His wealth of knowledge, infectious enthusiasm, and constructive criticisms have been instrumental in my growth over the last four years. I am sincerely grateful to **Prof. Dr. Christoph Lambert**, who not only provided invaluable feedback during my Ph.D. program but also graciously allowed me to use the laboratory equipment and spectrometers. I extend my sincere gratitude to **Prof. Dr. Dr. h.c. Todd Marder** and **Prof. Dr. Joanna Wencel-Delord** for reviewing this thesis.

I would like to express my gratitude to **Prof. Dr. Holger Braunschweig** and **Dr. Krzysztof Radacki** for their assistance with single-crystal X-ray diffraction measurements. Additionally, I am sincerely thankful to **Prof. Dr. Frank Würthner**, **Dr. Matthias Stolte**, and **Dr. Bernhard Mahlmeister** for providing access to the CD-CDL spectrometer. Special thanks to **Michael Moos** for diligently handling bureaucratic official documents on my behalf from the beginning until the very end. I would also like to seize this opportunity to extend my heartfelt thanks to **Johannes Hennemann**, my desk neighbor. We had the pleasure of engaging in countless scientific conversations and shared both the joys of success and the frustrations of failed reactions together. I extend a special thanks to **Jonathan Herpich** and **Vincenzo Brancaccio** for their assistance in the measurement of low-temperature NMR and the calculation of Boltzmann populations of conformations.

I thank **Paul Mentzel** and **Leon Euringer** for their invaluable assistance when needed with Fluorescence Spectroscopy. A significant amount of time was spent on column chromatography, mainly using petrol ether and dichloromethane as eluents. I want to express my gratitude to the members of AK Lambert who generously distilled them, starting from **Chantal Roger** all the way to **Tobias Groß**, **Laura Haley**, and **Denise Koppenhöfer**. A special thanks to **Analia D'Orazio** for her assistance in scanning the documents. I would like to express my gratitude to **Frederik Bauer** for his internship with me and for preparing valuable precursors on my behalf. I extend my thanks to **Dr. Joshua Selby**, **Emely Freytag**, **Fangyuan Zhang** and **Fridolin Saal** for their publication collaboration. Lastly, I thank the remaining past and present members of AK Ravat and AK Lambert for helping me in my initial days and for our scientific interactions.

I express my sincere appreciation to **Dr. Matthias Grüne**, **Dr. Juliane Adelman**, **Patricia Altenberger** and **Stefanie Schmitt** for their invaluable assistance with NMR and MS analysis. Additionally, I would like to express my gratitude to **Dr. Christian Stadler** and the other members of the institute's administrative staff for their efforts in ensuring the smooth functioning of management processes.

This PhD journey was impossible without the family and friends who have supported me to this day. Special thanks to **Dr. Praveen Rai** and **Saif Rahman** for their support over the last four years.

.....